SANDIA REPORT

SAND91—0893/2 • UC—721
Unlimited Release
Printed December 1991

Preliminary Comparison with 40 CFR Part 191, Subpart B for the Waste Isolation Pilot Plant, December 1991

Volume 2: Probability and Consequence Modeling

WIPP Performance Assessment Division

Prepared by
Sandia National Laboratories
Albuquerque, New Mexico 87185 and Livermore, California 94550
for the United States Department of Energy
under Contract DE-AC04-76DP00789

Issued by Sandia National Laboratories, operated for the United States Department of Energy by Sandia Corporation.

Available to DOE and DOE contractors from
Office of Scientific and Technical Information
PO Box 62
Oak Ridge, TN 37831

Prices available from (615) 576-8401, FTS 626-8401

Available to the public from
National Technical Information Service
US Department of Commerce
5285 Port Royal Rd
Springfield, VA 22161

NTIS price codes
Printed copy: A16
Microfiche copy: A01

SAND91-0893/2
Unlimited Release
Printed December 1991

Distribution
Category UC-721

PRELIMINARY COMPARISON WITH 40 CFR PART 191, SUBPART B FOR THE WASTE ISOLATION PILOT PLANT, DECEMBER 1991

VOLUME 2: PROBABILITY AND CONSEQUENCE MODELING

WIPP Performance Assessment Division
Sandia National Laboratories
Albuquerque, New Mexico 87185

ABSTRACT

This second volume documents the probability and consequence modeling done by the Performance Assessment Division of Sandia National Laboratories for the 1991 preliminary performance assessment (PA) of the Waste Isolation Pilot Plant (WIPP). The volume provides an overview of the PA calculations; discusses the mechanics of the probability modeling and construction of the complementary cumulative distribution functions (CCDFs); discusses the generic computational models and the applied (or site-specific) models used in consequence analysis and the results that these models predict for both undisturbed conditions (base case) and disturbed conditions (in which one or more hypothetical boreholes intrude the repository during the 10,000-year regulatory period); and tabulates the calculational results used to construct the CCDFs reported in Volume 1.

ACKNOWLEDGMENTS

The WIPP Performance Assessment Division is comprised of both Sandia and contractor employees working as a team to produce these annual preliminary comparisons with EPA regulations, assessments of overall long-term safety of the repository, and interim technical guidance to the program. The on-site team, affiliations, and contributions to the 1991 performance assessment are listed in alphabetical order:

Performance Assessment Division

Name	Affil.	Primary Author of Doc: Sect.	Major Code	Area of Responsibility
R. Anderson	SNL			Division Manager
B. Baker	TEC	V.2:§.6.4		SECO2D, Hydrology, Office Manager
J. Bean	UNM	V.2:§.4.2.1		BRAGFLO & BOASTII, 2-Phase Flow
J. Berglund	UNM	V.2:Ch.7 Editor V.2	CUTTINGS	Task Ldr., Undisturbed Repository, Cuttings/Cavings/ Engr. Mech.
W. Beyeler	SAI	V.2:§.5.3; 6.1;6.3	PANEL GARFIELD	Geostatistics, Analytical Models, CAMCON Systems Codes
K. Brinster	SAI			Geohydrology, Conceptual Models
R. Blaine	ECO			SECO2D & CAMCON Systems Codes
T. Blaine	EPE			Drilling Technology, Exposure Pathways Data
J. Garner	API	V.2:§.5.3	PANEL	Source Term, Sens. Anal.
A. Gilkey	UNM			CAMCON Systems Codes
L. Gomez	SNL			Task Ldr., Safety Assessments
M. Gruebel	TRI	V.1:Ch.1,2, 8,9,10		EPA Regulations
R. Guzowski	SAI	V.1:Ch.4		Geology, Scenario Construction
J. Helton	ASU	V.1:Ch.3,4 V.2:Ch.2,3	CCDFPERM	Task Ldr., Uncert./Sens. Anal., Probability Models
H. Iuzzolino	GC	Editor V.3	CCDFPERM	LHS & CAMCON System Codes
R. Klett	SNL			EPA Regulations
P. Knupp	ECO			STAFF2D & SECOTR, Comp. Fluid Dyn.
C. Leigh	SNL		GENII-S	Exposure Pathways
M. Marietta	SNL	Editor (Set)		Dep. Div. Manager, Tech. Coord.
G. de Marsily	UP	V.2:§.6.2		Task Ldr., Geostatistics
R. McCurley	UNM	V.2:§.4.2.3		SUTRA & CAMCON System Codes
A. Peterson	SNL	Editor V.3		Task Ldr., Inventory
J. Rath	UNM	V.2:§.4.2.3		SUTRA, Engr. Mech.
R. Rechard	SNL	Editor V.2 & V.3		Task Ldr., CAMCON, QA, Ref. Data, Calculations
P. Roache	ECO	V.2:§.6.4	SECO	Task Ldr., Comp. Fluid Dyn.
D. Rudeen	UNM 6.5	V.2:§.4.2.2;		STAFF2D, Transport
J. Sandha	SAI	Editor V.3		INGRES, PA Data Base
J. Schreiber	SAI	V.2:§.4.2.1; 5.2.5 Editor V.3		BRAGFLO & BOASTII, 2-Phase Flow
P. Swift	TRI	V.1:Ch.5,11		Task Ldr., Geology, Climate Var.
M. Tierney	SNL	Editor V.3		Task Ldr., CDF Constr., Probability Models
K. Trauth	SNL			Task Ldr., Expert Panels

P. Vaughn	API	V.2:§.5.1; 5.2; 5.2.5; App.A	BRAGFLO	Task Ldr., 2-Phase Flow & Waste Panel Chemistry
J. Wormeck	ECO			Comp. Fluid Dyn. & Thermodyn.

The foundation of the annual WIPP performance assessment is the underlying data set and understanding of the important processes in the engineered and natural barrier systems. The SNL Nuclear Waste Technology Department is the primary source of these data and understanding. Assistance with the waste inventory comes from WEC and its contractors. We gratefully acknowledge the support of our departmental and project colleagues. Some individuals have worked closely with the performance assessment team, and we wish to acknowledge their contributions individually:

J. Ball	ReS	Computer System Manager
H. Batchelder	WEC	CH & RH Inventories
R. Beauheim	SNL	Natural Barrier System, Hydrologic Parameters
B. Butcher	SNL	Engineered Barrier System, Unmodified Waste-Form Parameters, Disposal Room Systems Parameters
L. Brush	SNL	Engineered Barrier System, Source Term (Solubility) and Gas Generation Parameters
L. Clements	ReS	Computer System Support
T. Corbet	SNL	Natural Barrier System, Geologic & Hydrologic Parameters, Conceptual Models
P. Davies	SNL	Natural Barrier System, Hydrologic & Transport Parameters, & 2-Phase Flow Mechanistic Modeling
P. Drez	IT	CH & RH Inventories
E. Gorham	SNL	Natural Barrier System, Fluid Flow & Transport Parameters
S. Howarth	SNL	Natural Barrier System, Hydrologic Parameters
R. Kehrman	WEC	CH & RH Waste Characterization
R. Lincoln	SNL	Project Integration
F. Mendenhall	SNL	Engineered Barrier System, Unmodified Waste Form Parameters, Waste Panel Closure (Expansion)
D. Munson	SNL	Reference Stratigraphy, Constitutive Models, Physical & Mechanical Parameters
E. Nowak	SNL	Shaft/Panel Seal Design, Seal Material Properties, Reliability
J. Orona	ReS	Computer System Support
J. Tillerson	SNL	Repository Isolation Systems Parameters
S. Webb	SNL	2-Phase Flow Sensitivity Analysis & Benchmarking

API	=	Applied Physics Incorporated
ASU	=	Arizona State University
ECO	=	Ecodynamics Research Associates
EPE	=	Epoch Engineering
GC	=	Geo-Centers Incorporated
IT	=	International Technology
ReS	=	ReSpec
SAI	=	Scientific Applications International Corporation
SNL	=	Sandia National Laboratories
TEC	=	Technadyne Engineering Consultants
TRI	=	Tech Reps, Inc.
UNM	=	Univiversity of New Mexico/New Mexico Engineering Research Institute
UP	=	University of Paris
WEC	=	Westinghouse Electric Corporation

Peer Review

Internal/Sandia

T. Corbet
D. Gallegos
M. LaVenue
S. Hora

Management/Sandia

W. Weart
T. Hunter

PA Peer Review Panel

R. Heath, Chairman	University of Washington
R. Budnitz	Future Resources Associates, Inc.
T. Cotton	JK Research Associates, Inc.
J. Mann	University of Illinois
T. Pigford	University of California, Berkeley
F. Schwartz	Ohio State University

Department of Energy

R. Becker
J. Rhoderick

Expert Panels

Futures

M. Baram	Boston University
W. Bell	Yale University
G. Benford	University of California, Irvine
D. Chapman	The World Bank, Cornell University
B. Cohen	University of Pittsburgh
V. Ferkiss	Georgetown University
T. Glickman	Resources for the Future
T. Gordon	Futures Group
C. Kirkwood	Arizona State University
H. Otway	Joint Research Center (Ispra), Los Alamos National Laboratory
M. Pasqualetti	Arizona State University
D. Reicher	Natural Resources Defense Council
N. Rosenberg	Resources for the Future
M. Singer	The Potomac Organization
T. Taylor	Consultant
M. Vinovski	University of Michigan

Source Term

C. Bruton	Lawrence Livermore National Laboratory
I-Ming Chou	U.S. Geological Survey
D. Hobart	Los Alamos National Laboratory
F. Millero	University of Miami

Retardation

R. Dosch	Sandia National Laboratories
C. Novak	Sandia National Laboratories
M. Siegel	Sandia National Laboratories

Geostatistics Expert Group

G. de Marsily, Chairman	U. of Paris
R. Bras	Massachusetts Inst. of Tech.
J. Carrera	U. Politechnica de Cataluña
G. Dagan	Tel Aviv U.
A. Galli	Ecole des Mines de Paris
A. Gutjahr	New Mexico Tech.
D. McLaughlin	Massachusetts Inst. of Tech.
S. Neuman	U. of Arizona
Y. Rubin	U. of California, Berkeley

Report Preparation (TRI)

Editors:

Volume 1: M. Gruebel (text); S. Laundre-Woerner (illustrations)
Volume 2: D. Scott (text); D. Marchand (illustrations)
Volume 3: J. Chapman (text); D. Pulliam (illustrations)

D. Rivard, D. Miera, T. Allen, and the Word Processing Department
R. Rohac, R. Andree, and the Illustration and Computer Graphics Departments
S. Tullar and the Production Department

J. Stikar (compilation of PA Peer Review Panel comments)

CONTENTS

LIST OF FIGURES

LIST OF TABLES

1. INTRODUCTION—Rob P. Rechard

1.1 Role of Volume 2

The Waste Isolation Pilot Plant (WIPP) is planned as the first mined geologic repository for transuranic (TRU) wastes generated by defense programs of the United States Department of Energy (DOE). Before disposing of waste at the WIPP, the DOE must evaluate compliance with the United States Environmental Protection Agency's Standard, *Environmental Radiation Protection Standards for Management and Disposal of Spent Nuclear Fuel, High-Level and Transuranic Radioactive Wastes* (40 CFR Part 191, U. S. EPA, 1985).

This volume deals primarily with probability and consequence modeling of the WIPP disposal system for evaluating compliance with the quantitative requirements of Subpart B of the EPA Standard. Volume 1 deals primarily with scenario development and the regulations in 40 CFR Part 191 and their application to the WIPP, but also summarizes aspects of this volume. Volume 3 compiles pertinent data from disposal system characterization. Finally, uncertainty/sensitivity analysis is discussed in Volume 4.

1.2 Organization of Volume 2

This introduction to Volume 2 provides an overview of the 1991 PA calculations using the general tasks of the performance assessment methodology as a framework. It also summarizes the CAMCON (Compliance Assessment Methodology CONtroller) computer system used to perform these complex calculations.

The two chapters following the introduction discuss probability modeling and complementary cumulative distribution function (CCDF) construction for the 1991 PA:

- Chapter 2 describes the probability model for computational scenarios in the 1991 calculations.
- Chapter 3 describes the mathematical construction of the CCDF for WIPP performance assessment.

The next four chapters discuss the generic computational models and the applied (or site-specific) models used in consequence analysis and the results that these models predict:

- Chapter 4 discusses predicted undisturbed performance of the repository/shaft system (where no boreholes intrude the repository during the 10,000-year regulatory period). Because no releases beyond the repository shaft are predicted for undisturbed conditions, radionuclide release into the groundwater of the Culebra was not evaluated.
- Chapter 5 discusses disturbed performance of the repository/shaft system (in which one or more hypothetical boreholes intrude the repository during the 10,000-year regulatory period).

- Chapter 6 discusses predicted radionuclide release into the Culebra groundwater for disturbed conditions.
- Chapter 7 discusses predicted radionuclide release by transport of cuttings and eroded material to the surface during borehole intrusion.

Discussion in Chapters 4 through 7 is limited to the seven generic computational models ("codes") and the corresponding applied models used to simulate the major conceptual components of the WIPP disposal system. Details of code development and uses are not presented here; in most cases, that information is available separately in user's manuals for the various codes. Furthermore, details of CAMCON, including information about the codes that link the major models and control data flow, are also not presented here. That information is contained in the CAMCON user's manual (Rechard et al., 1989).

Finally, this volume contains two appendices:

- Appendix A discusses the theory of multiphase flow through porous media. This appendix is included in the report because two of the analysis models, BOAST II (for undisturbed conditions) and BRAGFLO (for disturbed conditions), describe simultaneous flow of brine and gas through porous media.
- Appendix B presents the input and output data for calculations reported in Volumes 1 and 2.

1.3 Background on PA Methodology

The Sandia methodology for assessing the compliance of the WIPP with the Containment Requirements, § 191.13 of 40 CFR Part 191 (U.S. EPA, 1985), hereafter referred to as performance assessment (PA), consists of six general tasks (Figure 1-1):

1. characterization of the WIPP disposal system and regional area
2. scenario development and selection of scenarios to model
3. development and execution of probability models
4. development and execution of consequence models (both generic computational and site-specific models) including uncertainty
5. regulatory compliance assessment
6. uncertainty/sensitivity analysis.

The first task is performed primarily outside the PA organization (except for estimating the radionuclide inventory), and the data are compiled in Volume 3. The other five tasks are performed inside the PA division.

For the WIPP, the PA process is conducted in annual cycles, and the 1991 PA is the second* in a series of annual "Performance Analysis and DOE Documentation" activities shown in the

* The PA process actually started in 1989, but it was primarily a demonstration with a specific example from the WIPP.

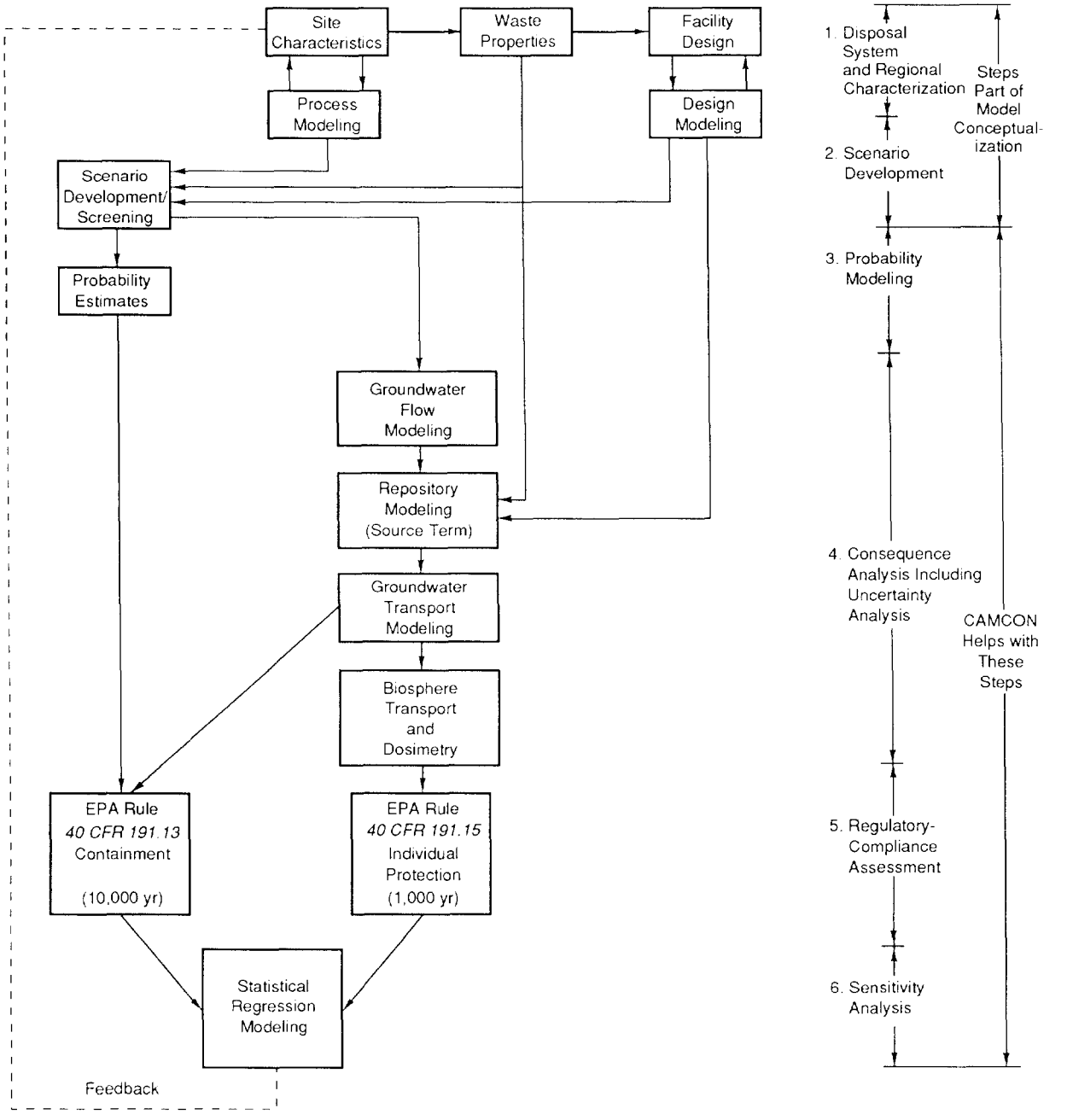

Figure 1-1. Overview of WIPP Performance Assessment Process (after Rechard, 1989, Figure 3.1)

Performance Assessment Time-Phased Activities for the Test Phase (U.S. DOE, 1991). In each cycle, data from the test program are used to update scenarios, update conceptual models (and computational models if necessary), and provide input to applied models to evaluate compliance.

The first two PA tasks listed above are referred to collectively as model conceptualization (Figure 1-1). Characterization of the disposal system and surrounding regional hydrology has been in progress since project inception in 1975 (e.g., Powers et al., 1978) and is nearing completion. Screening of events and processes that may affect performance of the system during the next 10,000 years is also nearly complete, and significant summary scenarios have been identified for consideration in consequence modeling (Guzowski, 1990; and Volume 1).

For Task 3, a probability model has been developed to evaluate probabilities of detailed computational scenarios for analysis, which are a decomposition of the summary scenarios developed above as part of Task 2. The scenarios incorporate stochastic variability (IAEA, 1989) into the performance assessment.

A major portion of the methodology consists of simulating physical processes to estimate the amount of radionuclides released to the accessible environment. This process is referred to as consequence modeling and analysis and actually is a composite function of several models (Task 4) (Figure 1-1). Construction of the modeling system begins with the development of conceptual models that identify the processes that will be simulated. These conceptual models provide a framework in which to interpret observational data and a basis for developing predictive mathematical models. In most cases, the choice of a conceptual model introduces simplifying assumptions about the real world that permit interpretation of entire components of the system using limited available data. In some cases the choice of a conceptual model may also be influenced by the availability of computational models to simulate it. For some processes, available generic computational models required adaptation. For other components of the disposal system, such as the coupled processes of gas generation, brine flow, and creep closure in the repository domain, computational models were developed specifically for the WIPP.

The complexity of the WIPP disposal system and the need to use multiple codes to describe the various components poses operational problems in performing calculations. An executive controller, CAMCON (Compliance Assessment Methodology CONtroller) (Rechard et al., 1989), links codes within the modeling system, manages data flow from one component to the next, and minimizes the opportunities for operator error.

Because of imprecisely known parameters, uncertainty is incorporated into the performance assessment through a Monte Carlo analysis (part of Task 4). As discussed in more detail in Chapter 3 of Volume 1 and compiled in Volume 3, Monte Carlo analysis consists of first identifying the important parameters to vary and assigning ranges and distributions. Second, sample elements are generated from these distributions. In the WIPP performance assessment,

Latin hypercube sampling (LHS) is used to minimize the number of sample elements needed to capture variability in the parameters adequately. And finally, each sample element is propagated through the consequence modeling system. For the 1991 calculations, 60 sample elements were drawn from the distributions assigned to 45 imprecisely known parameters. The repository performance was evaluated for each sample element (a vector of 45 parameter values).

From the consequence results using Monte Carlo analysis, the final two tasks naturally follow. In Task 5, estimated releases are combined into a complementary cumulative distribution function (CCDF) for each sample element. A CCDF (exceedance probability curve) is used for evaluating compliance with § 191.13 of 40 CFR Part 191. The CCDF from each sample element results in a distribution (family) of CCDFs. Summary statistics of the CCDFs (e.g. mean, median, and different quantiles) are also produced. The CCDFs for the WIPP are presented in Volume 1.

In Task 6, sensitivity analyses are used to analyze the results. For example, sensitivity analyses can be used to identify those parameters for which variability in the sampled value had the greatest effect on results, to provide guidance for research that may improve confidence in the estimate of performance. This sixth task is reported in Volume 4. CCDFs using several different modeling assumptions are also presented in Volume 4.

1.4 Overview of Calculations

The following discusses the calculations using the framework of the PA methodology. (Tasks 3 and 4 are particularly pertinent to Volume 2.)

1.4.1 SUMMARY SCENARIOS MODELED

Four summary scenarios from the scenario development task are examined for the 1991 PA: three disturbed (human intrusion) scenarios and the undisturbed (base case) scenario (see Chapter 4, Volume 1). (These same scenarios were examined for the 1990 PA calculations.) Disturbed performance scenarios include the possibility of human disruption of the repository by exploratory drilling or the occurrence of unlikely events. Undisturbed performance forms the base case for scenario development (Guzowski, 1990). As defined in the EPA Standard, "undisturbed performance" means "the predicted behavior of a disposal system, including consideration of the uncertainties in predicted behavior, if the disposal system is not disrupted by human intrusion or the occurrence of unlikely natural events" (U.S. EPA, 1985, § 191.12(p)).

The approach for the calculations for the human intrusion and base case scenarios differs somewhat for the WIPP disposal system. If human intrusion by drilling hypothetically occurs some time in the next 10,000 years, some releases by removal of cuttings are certain (but do not necessarily exceed EPA limits). Furthermore, the long-term consequence from disrupting the

repository must be evaluated. Consequently, a complex modeling effort is required. For undisturbed conditions, a number of deterministic calculations are performed to investigate radionuclide transport in and adjacent to the repository. It is tempting to describe the deterministic calculations as bounding since the conceptual model often appears conservative—but they are not always. For example, in one analysis the disposal region was assumed to be directly in the MB139 anhydrite layer, a potential pathway. However, the selection of conservative values for many of the parameters of these models was problematic since it was often difficult to assess their influence on such a complex system a priori. Thus, median values (not "conservative" values) were typically selected. (The Monte Carlo calculations for undisturbed conditions are described in Volume 4.) Because of the excellent isolating capabilities of the bedded salt in the Salado Formation, the undisturbed scenario has zero releases of radionuclides, and only the region directly around the repository needs to be modeled.

1.4.2 PROBABILITY MODELING AND REGULATORY COMPLIANCE EVALUATION

Following the usual sequential order of the tasks presented above, regulatory assessment (Task 5) would be discussed later. However, because probability modeling is intimately tied to regulatory evaluation, both are discussed here prior to the consequence analysis (Task 4) discussion.

Last year for the 1990 PA, probabilities for the four summary scenarios were determined from (1) professional judgment and (2) assuming a Poisson process. These probabilities were then paired with EPA-summed normalized releases, and the CCDF was constructed.

For the 1991 PA, the probabilities were also evaluated assuming drilling is a Poisson process. However, although the summary scenarios are the same as for the 1990 PA, these summary scenarios were decomposed based on (1) number of drilling intrusions (1 to 15), (2) time of intrusion (5 times—1000, 3000, 5000, 7000, and 9000 years), and (3) the activity level of the waste penetrated by the boreholes (five activity levels—four for contact-handled (CH) and one for remote-handled (RH) waste). This decomposition more fully resolves the CCDF, that is, each individual CCDF has numerous small steps rather than the four large steps (with two being identical) shown in the 1990 PA calculations (Bertram-Howery et al., 1990). The decomposition of the summary scenarios required many more simulations, as described in the following sections of this introduction.

The construction of the CCDF is possible once all the simulations are completed in each of the three modeling systems described below. The code, CCDFCALC, extracts the radionuclide concentration history and the cuttings concentration history calculated in the consequence modeling described below and evaluates cumulative releases and EPA-summed normalized releases. The

actual construction of the CCDF required a new program, CCDFPERM, in addition to CCDFCALC to decompose the summary scenarios. The Poisson probability model for evaluating decomposed scenario probabilities and the theory underlying the CCDF construction are thoroughly described in Chapters 2 and 3, respectively.

1.4.3 CONSEQUENCE MODELING OF DISTURBED CONDITIONS

The consequence modeling of disturbed conditions of the WIPP is discussed first because the modeling for undisturbed conditions is actually a simplification of this complex modeling system.

1.4.3.1 Physical Features Modeled

Of the numerous computer codes required to perform the PA, relatively few generic computational models ("codes") are necessary to simulate the major physical features of the WIPP disposal system (Figure 1-2). Five computational models are used for disturbed conditions. (Four computational models are used for undisturbed conditions, the base case summary scenario [see Section 1.4.5 of this introduction]). Except for PANEL, which implements analytic solutions to the mathematical model to model flow and radionuclide concentration in a WIPP disposal panel, the computer codes are generic and implement a variety of mathematical models using several numerical solution techniques. Hence, some codes were used to model several different physical features of the WIPP disposal system and are repeated in several places. Furthermore, the CAMCON model system was developed so that different codes could be used to model any one physical feature with relative ease; thus some WIPP disposal systems features in Figure 1-2 show more than one code being used. Specifically, three codes (BRAGFLO, STAFF2D, and SUTRA) can be used to simulate flow and transport within the repository environment. PANEL estimates radionuclide concentrations in repository brine and can analytically simulate flow near the repository. CUTTINGS estimates the amount of radioactive material brought to the surface during drilling. SECO_2DH simulates regional groundwater flow within the Culebra Dolomite Member of the Rustler Formation, and STAFF2D simulates local groundwater flow and radionuclide transport within the Culebra.

1.4.3.2 Modeling Systems

Depicting the generic computational models and the physical features they represent is fairly straightforward. However, the actual mechanics of moving through the calculations are more complicated. For modeling, the WIPP disposal system was divided into three modeling systems: repository/shaft/borehole, Culebra groundwater flow and transport, and cuttings. The seven major computational models and the systems they model are listed in Table 1-1. For disturbed conditions, all three modeling systems are used. Each of these modeling systems are analyzed in

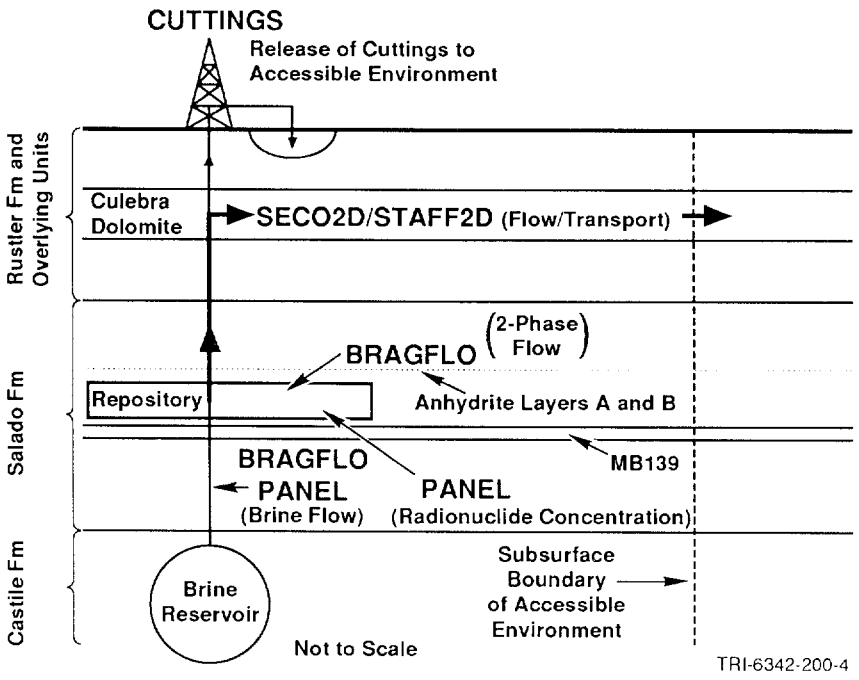

Figure 1-2. Major Computational Models and the Physical Features They Simulate in the WIPP Disposal System (Disturbed Conditions). Five generic computational models used for disturbed conditions.

Table 1-1. The Seven Major Computational Models Grouped According to the Modeling Systems Used in Modeling the WIPP Disposal System in the 1991 PA

Modeling System	Generic Computational Models ("Codes")
Repository/Shaft/Borehole	BOAST II, BRAGFLO SUTRA, STAFF2D, PANEL
Culebra Groundwater Flow and Transport	SECO_2DH, STAFF2D
Cuttings	CUTTINGS

parallel and results are combined during the regulatory compliance assessment (described in the previous section) and sensitivity analysis (described below) tasks.

The modeling systems do not correspond to the geologic and engineered barrier systems associated with physical parts of the WIPP disposal system and defined in the EPA Standard. Rather, these categories are an alternate subdivision of the WIPP disposal system done to facilitate modeling. The modeling subdivision and the identified components may change from year to year as required by the analysis whereas the physical systems described in the EPA Standard are invariant.

Twenty-nine major and support codes are used in these modeling systems (Figure 1-3). Section 1.5 provides a brief description of these codes. A more thorough discussion of the codes is provided in the CAMCON user's manual (Rechard et al., 1989).

The codes and general flow of information used in calculations of disturbed conditions has not substantially changed from the 1990 PA calculations. Specific changes for calculations of disturbed conditions are (1) the full incorporation of BOAST II and BRAGFLO, used to analyze two-phase flow, and CUTTINGS, used to analyze cuttings release, into the procedure rather than their use as subsidiary calculations as in the 1990 PA, (2) the use of the codes GARFIELD (which generates equally likely transmissivity fields), GENOBS (which generates head impulse functions at selected points along the boundary), FITBND (which determines functional relationships between well heads and pressure boundary conditions and optimizes the fit of pressure boundary conditions), and SWIFT II (which models hydrologic flow) during model conceptualization to evaluate uncertainty of the transmissivity field within the Culebra Dolomite Member of the Rustler Formation, and (3) the evaluation of scenario probabilities and the permutation of computational scenarios within CCDFPERM, which calculates decomposed scenario probabilities (Chapter 2). This last change is a result of decomposition of the summary scenarios used in the PA (mentioned earlier). Although the software tools have not substantially changed, the underlying treatment of the calculations, as represented by CCDFPERM, has changed substantially and is described in Chapters 2 and 3.

The overview of the mechanics of the 1991 PA calculations for disturbed conditions is shown in Figure 1-3. Model and parameter selection and the modeling steps in each of the modeling systems are discussed in the following sections.

1.4.3.3 Model and Parameter Selection

The calculations start with model and parameter selection. This can be a time-consuming process, but in short, the process involves evaluating data and then developing conceptual, mathematical, and computational models if necessary. It is then followed by a selection of parameters to vary (45 parameters in the 1991 PA). Following these decisions, data are entered in

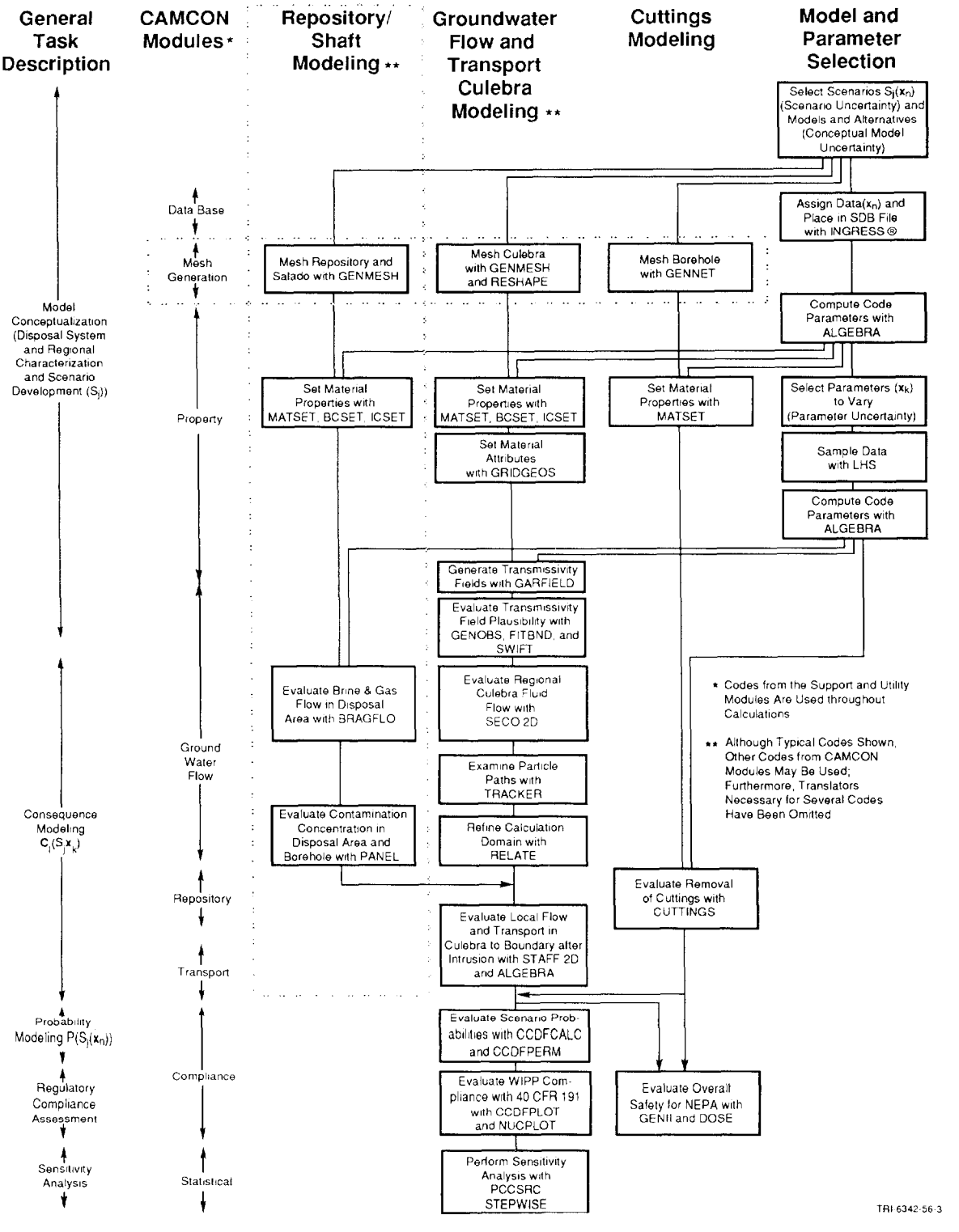

Figure 1-3. Overview of 1991 PA Calculations for Disturbed Conditions (Human Intrusion). Refer to Section 1.5 and CAMCON User's Manual (Rechard et al., 1989) for description of codes listed.

the data base and are sampled. The parameters sampled and the sampled values are presented in Tables B-1 through B-3 in Appendix B. All other data used for the 1991 PA calculations are documented in Volume 3. The fixed data are not repeated in this volume unless the data differed from what is reported in Volume 3. (Differences usually occurred only for the undisturbed calculations because they began in May 1991, prior to final decisions for some parameters.)

Once this critical step is completed, the analysts can begin the task of performing the calculations. (In this volume, the analysts have authored the parts of the calculations for which they are responsible.) As mentioned previously, the next steps are performed in parallel. In general, this consists of preparation of input with several computer codes, followed by the simulation and finally followed by examination of intermediate results and usually very little preparation for use by other codes. The intermediate results, along with the details of the applied models, are the subject of Chapters 4, 5, and 6.

1.4.3.4 Cuttings Modeling

The mechanics of modeling the initial human intrusion by drilling into the repository is fairly simple. It involves input preparation using GENMESH, the mesh generation model of CAMCON, (the mesh is a simple line representing the borehole since the analysis of cuttings is implemented with an analytic solution), extraction of pertinent data from the database using MATSET and sampled parameters from LHS using ALGEBRA. Then the CUTTINGS code is run for each sample element for each time, first assuming an intrusion into contact-handled (CH) waste and then an intrusion into remote-handled (RH) waste. (The time of intrusion was important because of radionuclide decay.) Six hundred simulations are required—two for the RH and CH wastes, five for the time intervals, and 60 for the sample elements. Once the 600* simulations are complete, the output is stored for use by CCDFCALC. The simulation release results for CH and RH waste are presented in Tables B-6 and B-7, respectively (Appendix B).

1.4.3.5 Repository/Borehole Modeling

The repository/borehole modeling system models phenomena around the repository. These phenomena include gas generation from corrosion and microbiological degradation of the waste, brine movement around the waste over time, and the possible saturation of the waste by the brine reservoir following intrusion and creep closure. The two-phase numerical code BRAGFLO and the one-phase analytic code PANEL were developed specifically to model these phenomena. (The creep closure phenomenon is not modeled in the 1991 PA calculations. Rather, constant room state corresponding to high porosity after gas generation was selected.) For most calculations

* The numerous additional simulations required for the sensitivity analysis presented in Volume 4 are not included in these or any of the following simulation counts.

reported in Chapter 5, the brine-phase flow results from the cylindrical approximation of the repository, Castile brine reservoir, and Culebra using BRAGFLO were used by PANEL to evaluate radionuclide concentrations using a equilibrium-mixing cell mathematical model. However, in one case PANEL was also used to evaluate analytically brine inflow from the Salado and brine reservoir to make comparisons with BRAGFLO.

Modeling the repository/borehole area required 600 simulations: 2x5x60; two for the E2 and E1E2 summary scenarios, five for the five time intervals selected to decompose these two scenarios, and 60 for the sample elements used to describe parameter uncertainty. (Based on one-phase and early two-phase simulations, the E1 summary scenario was assumed to be similar to the E2 summary scenario—and bounded by the E1E2 summary scenario. This assumption is more thoroughly examined in Volume 4.)

1.4.3.6 Culebra Groundwater Flow Modeling

Flow and transport are grouped into the same modeling subdivision because they model the same physical features of the same unit, the Culebra Dolomite Member at the Rustler Formation. However, the modeling and number of simulations are different and are separated in this discussion. (Transport modeling is discussed in Section 1.4.3.7 of this introduction.)

The groundwater flow component of the Culebra modeling system was quite complicated. It not only consisted of a normal data-preparation step using GENMESH to set up a planar, two-dimensional mesh at the Culebra and MATSET, BCSET, and ICSET to set fixed material properties and boundary conditions, but as indicated in Figure 1-3 it also consisted of evaluating the uncertainty of the transmissivity fields using GARFIELD, GENOBS, FITBND, and the groundwter flow code SWIFT II.

Specifically, the procedure consisted of using GARFIELD to randomly generate thousands of transmissivity fields of the Culebra, which had the general spatial variance (same variogram) as suggested by the data, after which a set of head impulse functions at selected points along the mesh boundary were generated (40 impulse functions in the 1991 PA), followed by an evaluation of the steady-state, linear response of the thousands of Culebra "systems" (including brine density variation) to these impulse functions using the hydrologic code SWIFT II. Finally, each of the generated transmissivity fields were conditioned to the steady-state equivalent head measurements at wells by using the 40 linear responses to select the optimal pressure conditions on the boundaries of the regional model using FITBND. The first 60 transmissivity fields generated by this procedure that had (1) good agreement with the head measurements and (2) agreement with known general flow directions in the area were retained. (About 1 in 5 meets these selection criteria; thus, about 12,000 simulations (60x40x5) of the steady-state Culebra system were made with SWIFT II.) Uncertainty of the transmissivity fields is the subject of the first part of Chapter 6.

Once the final 60 transmissivity fields were selected, the regional fluid flow assuming constant brine density was determined 60 times with a newly developed hydrologic code, SECO_2DH. The regional analyses included effects from varying head boundary conditions that were related to increases in precipitation. Capabilities of SECO_2DH and the results are the second topic discussed in Chapter 6.

1.4.3.7 Culebra Groundwater Transport

The second part of the Culebra modeling system is the evaluation of radionuclide transport from the intrusion borehole to the 5-km boundary of the accessible environment and through the Culebra. The code RELATE was used to evaluate fluid flow boundary conditions on a greatly decreased local mesh. STAFF2D was then used to evaluate first flow and then transport on this local two-dimensional domain. Note that no borehole model was used; rather, the radionuclide concentrations (mass flux only) from the repository/borehole modeling system were directly injected into the Culebra at a point directly above the center of the disposal area. Following the STAFF2D simulations, the support program ALGEBRA was used to evaluate radionuclide transport across the 5-km boundary of the accessible environment.

While the evaluation of local fluid flow with STAFF2D only required 60 simulations, the evaluation of transport required 600 simulations because 600 different "source terms" come from the repository/borehole modeling system. The transport conceptual model reported here and in Volume 1 is dual porosity. A fracture-porosity-only transport model is reported in Volume 4. The integrated releases from these transport simulations are reported in Tables B-4 and B-5 (Appendix B).

1.4.4 SENSITIVITY ANALYSIS

The final task, sensitivity analysis, can only start after major results have been calculated. Hence, Volume 4, where the sensitivity analysis is described, must of necessity be produced after Volumes 1, 2, and 3. It involves plotting scatter plots and developing regression models between the parameters varied (and their ranks) and various results (e.g., EPA-summed normalized releases for cumulative releases of each radionuclide from the 600 combined simulations or the 600 cuttings simulations) using the Sandia statistics codes PCCSRC (which calculates partial correlation coefficients and standardized regression coefficients) and STEPWISE (which selects the regression model using stepwise techniques). In addition, several other issues such as conceptual model uncertainty is explored in Volume 4, so the number of total simulations increases four or five times.

1.4.5 CONSEQUENCE MODELING SYSTEM FOR UNDISTURBED CONDITIONS

Preliminary results from the 1989 PA demonstration showed no releases to the accessible environment (Marietta et al., 1989) for undisturbed conditions. Consequently, simulations of undisturbed conditions were not performed in 1990; instead, the preliminary results showing no releases were summarized (Bertram-Howery et al., 1990). Simulations of undisturbed conditions were repeated in 1991 with updated data and computational models to verify these results and examine the influence of gas generation in the repository.

Prior to running the two-phase undisturbed calculations with BRAGFLO, much work was expended to gain experience in using several one-phase models (both planar and cross-sectional using STAFF2D and SUTRA) assuming a constant and varying gas drive with modifications to the porosity and permeability to examine various alternative modeling schemes. The modifications to porosity and permeability were based on preliminary calculations using BOAST II because development of BRAGFLO was not complete in May 1991, when these undisturbed calculations were being run. The alternative modeling schemes could find use in providing design criteria for panel and shaft backfill or for examining engineered modifications to the waste where detailed calculations may be necessary and approximations to the two-phase flow formulation may be desirable. The different modeling schemes are presented in Chapter 4. (The physical features modeled and the codes used are shown in Figure 1-4.) The overview of the mechanics of the 1991 PA calculations for undisturbed conditions is shown in Figure 1-5. Thirteen major codes are used in the repository/shaft modeling system.

For the undisturbed calculations incorporating two-phase flow, two cases were run using BRAGFLO. First, the 60 simulations of the cylindrical model for the E2 scenario (without a borehole) were extended to the full 10,000-year performance period. Second, a separate BRAGFLO vertical cross-section model of the repository that included the shaft was also run. This latter two-dimensional model included three-dimensional effects by gradually increasing the thickness of elements as a function of distance from the repository. (Because only fluid-flow comparisons were planned, this latter case used a new LHS sampling with only 22 sampled elements.) These undisturbed calculations with BRAGFLO are reported in Volume 4.

The conclusion has remained the same since the 1989 preliminary calculations: if no one drills into the repository during the 10,000-year performance period, there will be no radionuclide releases from WIPP to the accessible environment, and furthermore, no radionuclide movement outside the Salado Formation.

1.5 Background on the CAMCON System

As shown in Figures 1-3 and 1-5, many different types of software are necessary to investigate various events and physical processes, perform the assessment, and present the final output as a

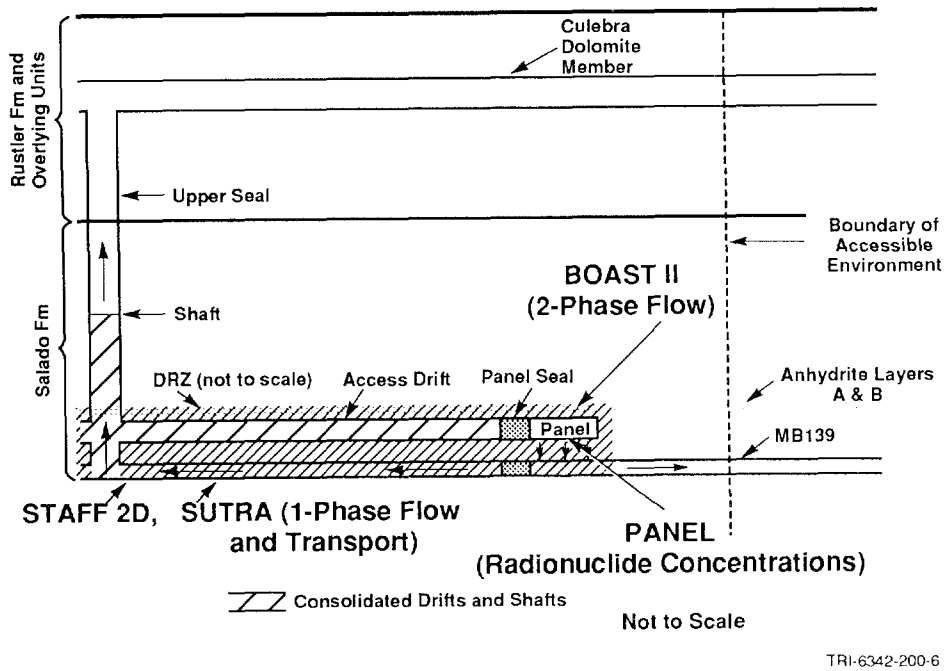

Figure 1-4. Major Computational Models and the Physical Features They Simulate in the WIPP Disposal System (Undisturbed Conditions). Four generic computational models used for undisturbed conditions.

complementary cumulative distribution function (CCDF) for comparison with the probabilistically based release limits in 40 CFR 191. While Figures 1-3 and 1-5 show the modeling mechanics of producing a CCDF, the support structure (framework) for the modeling system is CAMCON (Compliance Assessment Methodology CONtroller). CAMCON manipulates this software as an analysis system (analysis "toolbox") by assisting the flow of information between numerous codes.

1.5.1 ASSISTING THE FLOW OF INFORMATION: THE CAMCON SYSTEM

CAMCON, the analysis toolbox for running the calculations, has two important functions. First, it provides the analyst with the necessary tools and flexibility to build and execute all or portions of an assessment for the WIPP. For example, it allows an analyst to quickly identify available software and the necessary information for using individual codes, enabling the analyst to

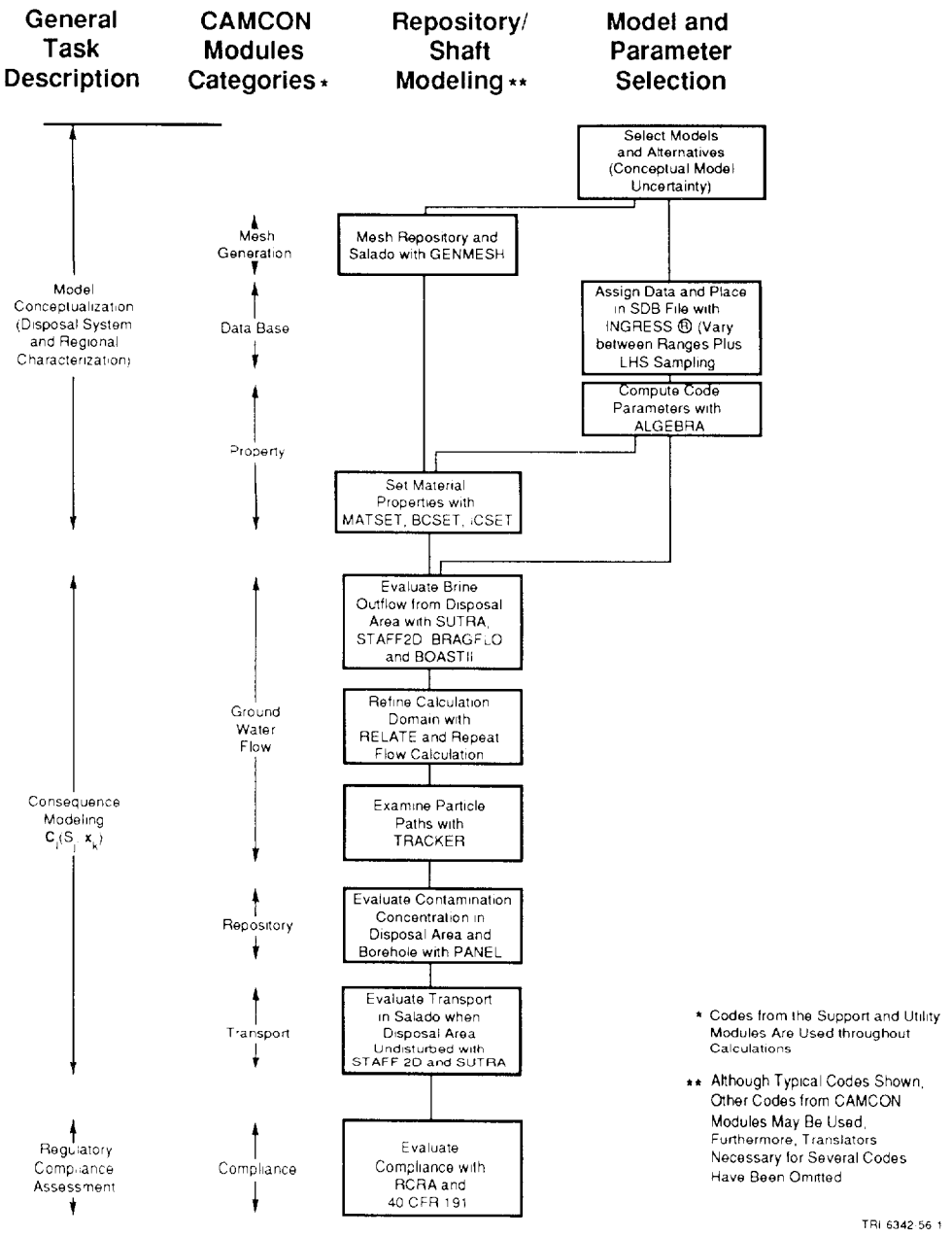

Figure 1-5. Overview of 1991 PA Calculations for Undisturbed Conditions (Base Case)

select the code(s) best suited for a particular study. Second, several of CAMCON's procedures, utility programs, and even directory structure assist in implementing software QA procedures (Rechard et al., 1989). For example, CAMCON serves as a software management system, providing (1) rudimentary configuration control, (2) FORTRAN libraries of commonly used subroutines, and (3) on-line documentation for each code, consisting of a description of the code and its capability, summary of user commands, update history, and examples.

Related to the first function, CAMCON has five main features that help the analyst perform a quality analysis: (1) the ability to read model parameters from one central data base to ensure data consistency; (2) semi-automated linkage of codes, reducing errors in keying in data, (3) a computational data base that stores all data results in one location; (4) codes to algebraically manipulate and plot any intermediate (and final) results for careful scrutiny; and (5) a procedure to help archive analysis input and output.

1.5.2 THE CAMCON SYSTEM PARTS

The primary parts of the CAMCON system consist of (Figure 1-6):

1. Code modules broken down into:
   - seven computational modules (mesh generation, property assignment and Monte Carlo sampling, etc.)
   - one support module (e.g., plotting and algebraic manipulation) (eighth module)
   - one utility module for archiving input files and results, listing programs, reporting code discrepancies, etc. (ninth module)
   - a data base module containing software for storing and/or manipulating the secondary and computational data bases
2. A computational data base, CAMDAT, and several secondary data bases
3. A collection of frequently used subroutines in FORTRAN object libraries (e.g., plot libraries)
4. A suite of procedural files (and symbols to set up the computer environment) for ready access and execution (either batch or interactively) of the computational and support modules. The VAX/VMS procedures are written in DEC (Digital Equipment Corporation) Control Language (DCL).
5. Directory structure and protocols for storing codes for rudimentary configuration control.
6. Help files for on-line documentation.

The CAMCON software (modules, procedures, help files, and libraries) is stored within its own directory on the WIPP 8810 VAX computer.

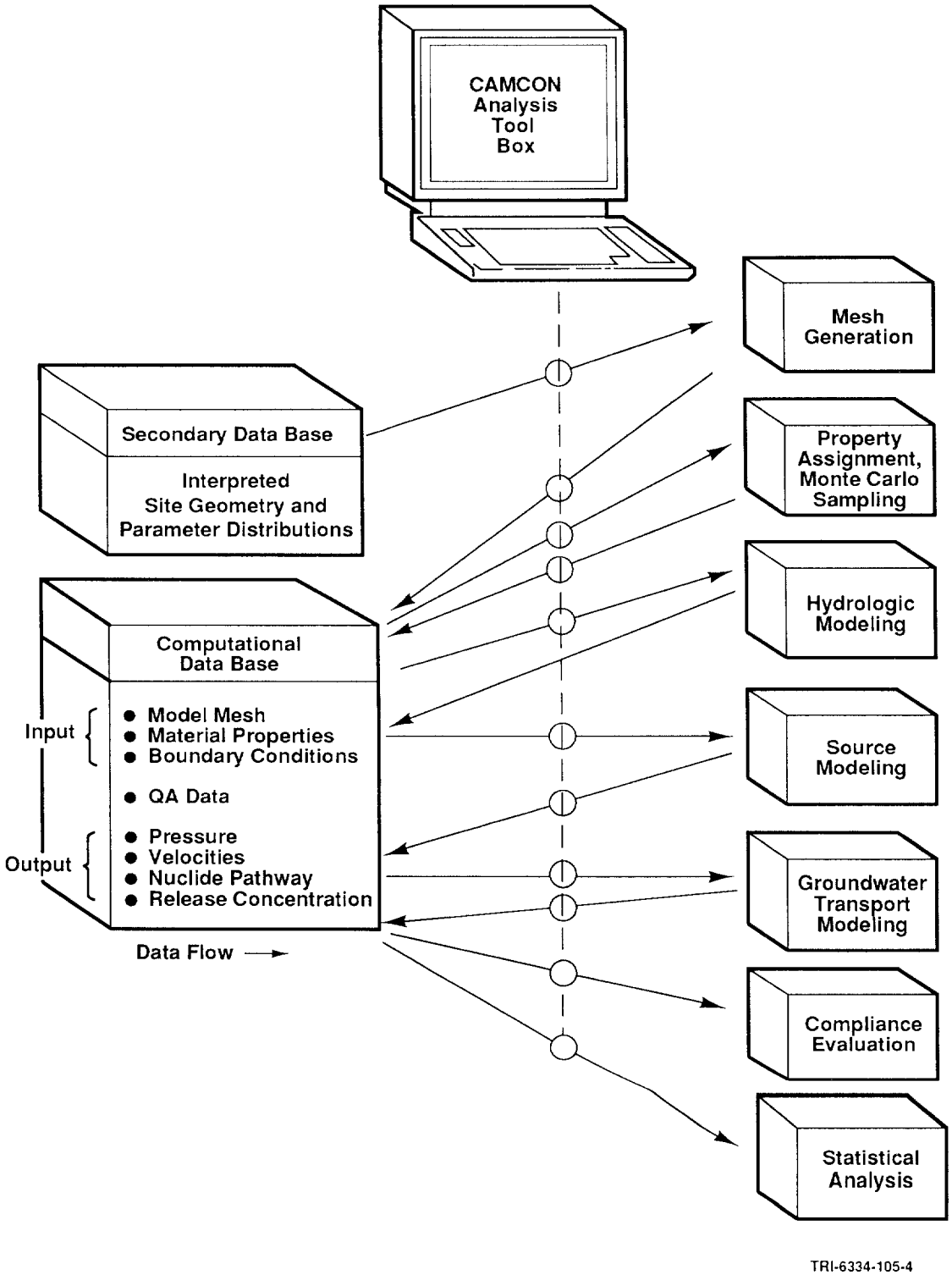

Figure 1-6. The Analysis Tool, CAMCON. CAMCON consists of (1) code modules broken down into seven computational modules, one support module (not shown), one utility module (not shown), and a data base module, a computational data base (CAMDAT), and several secondary data bases, (3) software libraries (not shown), (4) procedural files to access modules (not shown), (5) directory structures and protocols for storing codes (not shown), and (6) help files for on-line documentation (not shown).

1.5.3 CODES AVAILABLE IN THE CAMCON MODULES

The ten code modules (groupings of codes) mentioned above are the (1) mesh generation module, (2) material property module, (3) regional and local hydrologic module, (4) panel module, (5) transport module, (6) compliance calculation module, (7) statistical module, (8) support module, (9) utility module, and (10) data base module.

- The Mesh Generation Module discretizes the models needed for assessing consequences of one scenario.
- The Property (Monte Carlo sampling) Module samples distributions of geologic and hydrologic properties needed for uncertainty and sensitivity calculations.
- The Regional and Local Fluid-Flow Module establishes flow conditions within the controlled area of the repository.
- The Repository Module develops a source term for transport calculations by incorporating the complex processes in the waste container, storage room, drifts, shaft, and seals.
- The Nuclide Transport Module predicts radionuclide migration from the repository source to the accessible environment boundary for EPA standard calculations or the maximally exposed individuals for the NEPA calculations.
- The Compliance Module evaluates the cumulative distribution function (CCDF) from simulations on all scenarios to assess compliance with the EPA Standard.
- The Statistical Module evaluates parameter sensitivity through regression analysis.
- The Support Module provides data base manipulation and plotting codes to support the other modules.
- The Utility Module contains codes that assist in the operation of the CAMCON system (e.g., listing programs, etc.).
- The Property Data Base Module inputs and manipulates the data collected during disposal system characterization.

CAMCON currently consists of about 75 codes and FORTRAN object libraries, which includes those codes and libraries developed external to Sandia, those internal to Sandia but developed in other organizations, and those developed specifically for the WIPP project. The total FORTRAN lines of software written specifically for the WIPP project is about 300,000 (of which about 51% are comment lines). Imported software, much of which was modified for use in the WIPP project, totals about 175,000 (25% comments) but excludes six libraries and codes for which only executables are available. Thus, the total is about 475,000 lines of FORTRAN coding that may be selected by the analyst.

In most cases, a choice of computer codes is available within each module. For example, five codes are available in the groundwater flow module; the selection depends upon the type of problem under consideration. The codes available within each module are listed below:

Mesh Generation Module

- FASTQ: generate finite-element mesh
- GENMESH: generate rectilinear mesh
- GENNET: generate network
- PATEXO: transform PATRAN neutral file to CAMDAT data base format

Property Module

- BCSET: set up boundary condition
- FITBND: determine functional relationships between well heads and pressure boundary conditions and optimize fit of pressure boundary conditions
- GARFIELD: generate equally likely attribute fields, e.g., transmissivity
- GENOBS: generate a set of impulse functions at selected points along the boundary
- GRIDGEOS: interpolate from data to mesh
- ICSET: set up initial conditions
- LHS: sample using Latin hypercube sampling
  - PRELHS: translate from property secondary data base to LHS
  - POSTLHS: translate from LHS output to CAMDAT
- MATSET: set up material properties
- RELATE: interpolate from coarse to fine mesh and fine to coarse mesh (relates property and boundary conditions)
- SORTLHS: reorders LHS vectors

Groundwater Flow Module

- BRAGFLO: model two-phase flow
- BOAST_II: model black oil
  - PREBOAST: translate from CAMDAT to BOAST_II
  - POSTBOAST: translate from BOAST_II to CAMDAT
- HST3D: model hydrologic flow
  - PREHST: translate from CAMDAT to HST3D
  - POSTHST: translate from HST3D to CAMDAT
- SECO_2DH: model 2-D hydrologic flow using head formulation
- SUTRA: model hydrologic flow
  - PRESUTRA: translate from CAMDAT to SUTRA
  - POSTSUTRA: translate from SUTRA to CAMDAT
- SUTRA_GAS: SUTRA modified for fluid as gas instead of liquid

- SWIFT_II: model hydrologic flow
  - PRESWIFT: translate from CAMDAT to SWIFT_II
  - POSTSWIFT: translate from SWIFT_II to CAMDAT

Repository Module

- CUTTINGS: evaluate amount of material removed during drilling
- PANEL: model flow (analytically) and radionuclide concentration (mixing cell) in a WIPP disposal panel

Transport Module

- NEFTRAN: simulate transport with network model
  - PRENEF: translate from CAMDAT to NEFTRAN
  - POSTNEF: translate from NEFTRAN to CAMDAT
- STAFF2D: model transport using finite elements
  - PRESTAFF: translate from CAMDAT to STAFF2D
  - POSTSTAFF: translate from STAFF2D to CAMDAT

Compliance Module

- CCDFCALC: preprocess radionuclide time histories for CCDF
- CCDFPERM: calculate decomposed scenario probabilities
- NUCPLOT: plot box plots of each radionuclide contribution to CCDF
- CCDFPLOT: plot CCDF
- GENII: calculate human doses
- DOSE: calculate doses from transfer factors

Support Module

- ALGEBRA: manipulate data in CAMDAT
- BLOT: plot mesh and results
- GROPE: read CAMDAT file for debugging
- RESHAPE: redefine blocks (i.e., groupings of mesh elements)
- TRACKER: track a neutrally buoyant particle
- UNSWIFT: convert SWIFT_II input files into CAMDAT data base

Statistical Module

- PCCSRC: calculate partial correlation coefficients and standardized regression coefficients
- STEPWISE: select regression model using stepwise techniques

- LHS2STEP: translate from LHS output to STEPWISE or PCCSRC
- CCD2STEP: translate from CCDFCALC to STEPWISE or PCCSRC

Utility Module

- CHAIN: calculate radionuclide chains
- CHANGES: record needed enhancements to CAMCON or codes
- DISTRPLT: plots pdf's given parameters
- FLINT: analyze FORTRAN codes
- HLP2ABS: convert help file to software abstract
- LISTDCL: list DEC command procedural files
- LISTFOR: list programs; summarize comments and active FORTRAN lines
- NEFDIS: plot NEFTRAN discharge history as a function of time

Data Base Module

- GENPROP: enter item into property data base
- INGRES: store and manipulate data (commercial relational data base manager)
- LISTSDB: tabulate data in secondary data base for reports
- PLOTSDB: plot parameter distributions in property secondary data base
- CAM2TXT: convert binary CAMDAT to ASCII format file
- SCANCAMDAT: quickly summarize data in CAMDAT
- TXT2CAM: convert ASCII file to binary CAMDAT data base

2. DRILLING INTRUSION PROBABILITIES—Jon C. Helton

2.1 Introduction

The U.S. Environmental Protection Agency (EPA) has promulgated the following as a requirement for the geologic disposal of radioactive waste (U.S. EPA, 1985):

> *191.13 Containment requirements.*
> *(a) Disposal systems for spent nuclear fuel or high-level or transuranic radioactive wastes shall be designed to provide a reasonable expectation, based upon performance assessments, that the cumulative releases of radionuclides to the accessible environment for 10,000 years after disposal from all significant processes and events that may affect the disposal system shall:*
> *(1) Have a likelihood of less than one chance in 10 of exceeding the quantities calculated according to Table 1 (Appendix A); and*
> *(2) Have a likelihood of less than one chance in 1,000 of exceeding ten times the quantities calculated according to Table 1 (Appendix A).*

The term accessible environment means "(1) the atmosphere; (2) land surfaces; (3) surface waters; (4) oceans; and (5) all of the lithosphere that is beyond the controlled area" [U.S. EPA, 1985, 191.12 (k)]. Further, controlled area means "(1) a surface location, to be identified by passive institutional controls, that encompasses no more than 100 square kilometers and extends horizontally no more than 5 kilometers in any direction from the outer boundary of the original location of the radioactive wastes in a disposal system; and (2) the subsurface underlying such a surface location" [U.S. EPA, 1985, 191.12 (g)]. Table 1 (Appendix A), which is referred to in the preceding containment requirements, is reproduced here as Table 2-1.

For releases to the accessible environment that involve a mix of radionuclides, the limits in Table 2-1 are used to define normalized releases for comparison with the release limits. Specifically, the normalized release for transuranic waste is defined by

$$nR = \sum_i \left(\frac{Q_i}{L_i} \right) \left(1 \times 10^6 \text{ Ci}/C \right), \tag{2-1}$$

where

Q_i = cumulative release (Ci) of radionuclide i to the accessible environment during the 10,000-year period following closure of the repository,

L_i = the release limit (Ci) for radionuclide i given in Table 2-1,

and

C = amount of transuranic waste (Ci) emplaced in the repository.

For the 1991 WIPP performance assessment, $C = 11.87 \times 10^6$ Ci.

Table 2-1. Release Limits for the Containment Requirements
(U.S. EPA, 1985, Appendix A, Table 1)

Radionuclide	Release Limit L_i per 1,000 MTHM* or Other Unit of Waste (Curies)
Americium-231 or -243	100
Carbon 14	100
Cesium-135 or -137	1,000
Iodine-129	100
Neptunium-237	100
Plutonium-238, -239, -240, -or -242	100
Radium-226	100
Strontium-90	1,000
Technetium-99	10,000
Thorium-230, or -232	10
Tin-126	1,000
Uranium-233, -234, -235, -236, or -238	100
Any other alpha-emitting radionuclide with a half-life greater than 20 years	100
Any other radionuclide with a half-life greater than 20 years that does not emit alpha particles	1,000

* Metric tons of heavy metal exposed to a burnup between 25,000 megawatt-days per metric ton of heavy metal (MWd/MTHM) and 40,000 MWd/MTHM.

In addition, the EPA directs that the results of a performance assessment intended to show compliance with the release limits in 191.13 should be assembled into a single complementary cumulative distribution function (CCDF). Specifically, the following statement is made:

> *. . whenever practicable, the implementing agency will assemble all of the results of the performance assessments to determine compliance with [section] 191.13 into a "complementary cumulative distribution function" that indicates the probability of exceeding various levels of cumulative release. When the uncertainties in parameters are considered in a performance assessment, the effects of the uncertainties considered can be incorporated into a single such distribution function for each disposal system considered. The Agency assumes that a disposal system can be considered to be in compliance with [section] 191.13 if this single distribution function meets the requirements of [section] 191.13(a). (U.S. EPA, 1985, Appendix B, p. 38088).*

Construction of the single CCDF requires a clear conceptual representation for a performance assessment. A representation based on a set of ordered triples provides a suitable way to organize a performance assessment and leads naturally to the presentation of the outcome of a performance assessment as a CCDF (Kaplan and Garrick, 1981; Helton et al., 1991). Specifically, the outcome of a performance assessment can be represented by a set of $\mathcal{R}$ ordered triples of the form

$$\mathcal{R} = \left\{ \left(S_i, pS_i, \mathbf{cS}_i \right),\ i = 1, \ldots, nS \right\}, \tag{2-2}$$

where

S_i = a set of similar occurrences,

pS_i = probability that an occurrence in set S_i will take place,

$\mathbf{cS}_i$ = a vector of consequences associated with S_i

and

nS = number of sets selected for consideration.

In terms of performance assessment, the S_i are scenarios, the pS_i are scenario probabilities, and the $\mathbf{cS}_i$ are vectors containing results or consequences associated with scenarios.

The information contained in the pS_i and $\mathbf{cS}_i$ shown in (2-2) can be summarized in CCDFs. With the assumptions that a particular consequence result cS (e.g., normalized release to the accessible environment) is under consideration and that the values for this result have been ordered so that $cS_i \le cS_{i+1}$ for $i = 1, 2, \ldots, nE - 1$, Figure 2-1 shows the resultant CCDF. As illustrated in

Figure 2-2, the EPA containment requirement in 191.13 specifies that the CCDF for normalized release to the accessible environment should fall below a curve defined by the points (1, 0.1) and (10, 0.001). The vertical lines in Figure 2-2 have been added for visual appeal but are not really part of the CCDF. A waste disposal site can be considered to be in compliance with the EPA release limits if the CCDF for normalized release to the accessible environment falls below the bounding curve shown in Figure 2-2.

Since the representation for a performance assessment in (2-2) and the resultant CCDFs in Figures 2-1 and 2-2 involve probabilities, there must be an underlying sample space. For performance assessments conducted to provide comparisons with the EPA release limits, the sample space is the set S defined by

$$S = \{x: x \text{ a single 10,000-year time history beginning at decommissioning of the facility under consideration}\}. \quad (2\text{-}3)$$

Each 10,000-year history is complete in the sense that it provides a full specification, including time of occurrence, for everything of importance to performance assessment that happens in this time interval. The S_i appearing in (2-1) are disjoint subsets of S for which

$$S \triangleq \bigcup_{i=1}^{nS} S_i . \quad (2\text{-}4)$$

In the terminology of probability theory, the S_i are events and the pS_i are the probabilities for these events. It is the discretization of S into the sets S_i that leads to the steps in the estimated CCDFs in Figures 2-1 and 2-2. The use of more sets will reduce the step sizes but will not alter the fact that CCDFs are the basic outcome of a performance assessment (Helton et al., 1991, Chapter VI).

Important parts of any performance assessment are the discretization of S into the sets S_i, commonly referred to as scenario development (Hunter, 1989; Ross, 1989; Cranwell et al., 1990; Guzowski, 1990), and the subsequent determination of probabilities for these sets (Mann and Hunter, 1988; Hunter and Mann, 1989; Guzowski, 1991). For radioactive waste disposal in sedimentary basins, many computational scenarios (i.e., scenarios defined specifically for the construction of CCDFs) result from unintended intrusions due exploratory drilling for natural resources, particularly oil and gas. To construct CCDFs of the form shown in Figures 2-1 and 2-2, the time histories associated with these drilling intrusions must be sorted into disjoint sets such that (1) each S_i is sufficiently homogeneous that it is reasonable to use the same consequence

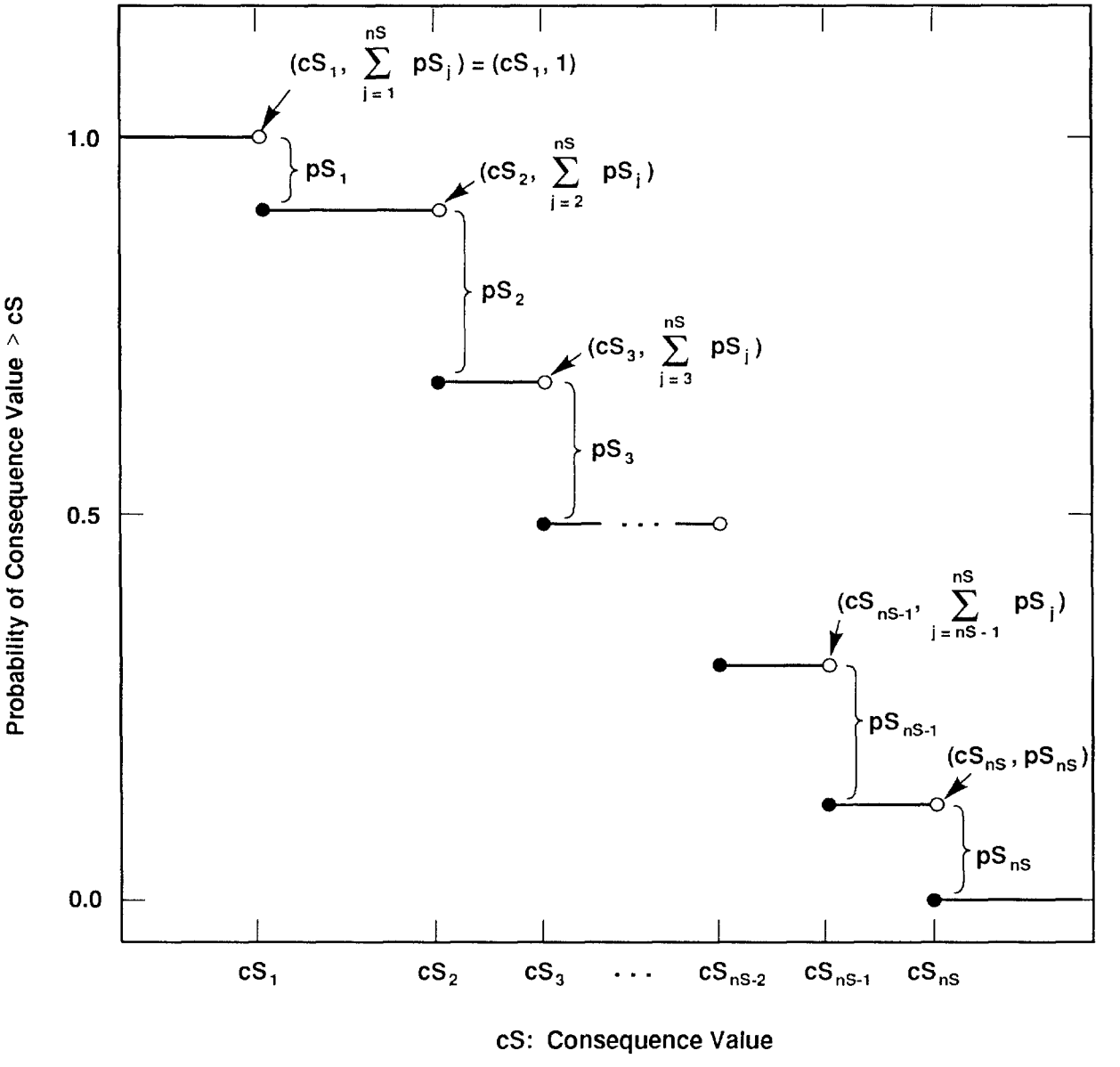

TRI-6342-730-5

Figure 2-1. Estimated Complementary Cumulative Distribution Function (CCDF) for Consequence Result cS. (Helton et al. 1991, Figure VI-1).

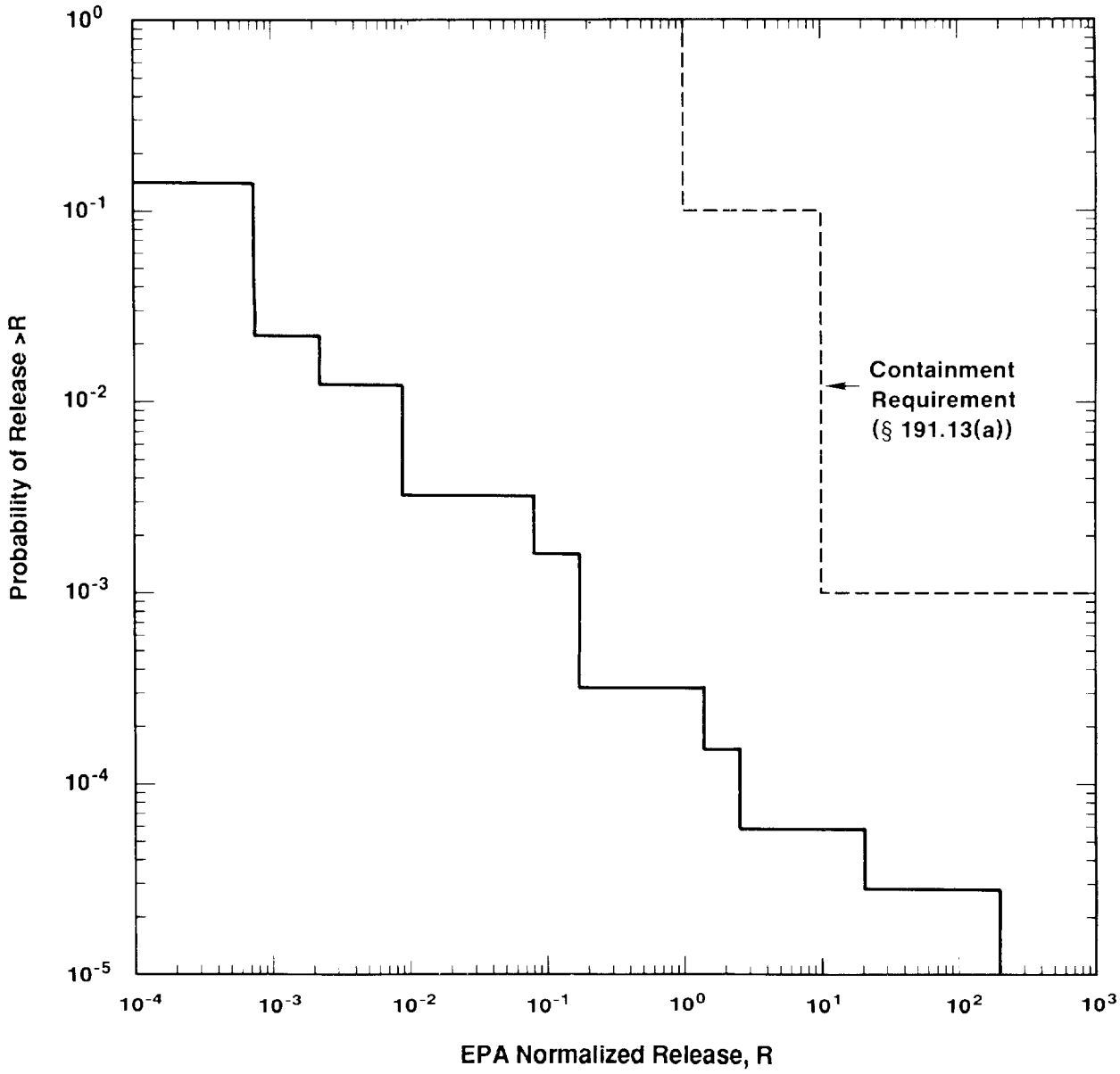

Figure 2-2. Comparison of a CCDF for Normalized Release to the Accessible Environment with the EPA Release Limits.

result $\mathbf{cS}_i$ for all elements of S_i, (2) a probability pS_i can be determined for each S_i, and (3) the computational costs for estimation of pS_i and $\mathbf{cS}_i$ are acceptable.

This chapter describes a decomposition of drilling intrusions into computational scenarios on the basis of number of intrusions and their times of occurrence and derives the necessary formulas to convert from drilling rates to scenario probabilities. For these derivations, the occurrence of individual drilling intrusions is assumed to be random in time and space, although the drilling rate is not assumed to be constant or, for that matter, even continuous through time. A following presentation will describe a computational procedure that can be used to determine CCDFs for intrusions due to drilling (Chapter 3).

2.2 Mathematical Preliminaries

The symbol $\mathcal{S}_k(a,b)$ will be used to denote the subset of $\mathcal{S}$ [see (2-3)] defined by

$$\mathcal{S}_k(a,b)=\{x: x \text{ an element of } \mathcal{S} \text{ that involves exactly } k \text{ drilling intrusions in the time interval } [a,b] \}. \tag{2-5}$$

One of the objectives of this presentation is to derive a probability $p[\mathcal{S}_k(a,b)]$ for $\mathcal{S}_k(a,b)$. Membership in $\mathcal{S}_k(a,b)$ only places a restriction on intrusions in the time interval $[a,b]$ and thus does not preclude intrusions in other time intervals. As a result, an additional objective will be to determine the probability $p\left[\bigcap_{i=1}^{n}\mathcal{S}_{n(i)}(t_{i-1},t_i)\right]$ for the set $\bigcap_{i=1}^{n}\mathcal{S}_{n(i)}(t_{i-1},t_i)$, where $t_0 < t_1 < \cdots < t_n$ and each $n(i)$, $i = 1,2,\ldots,n$, is a nonnegative integer. This corresponds to determining the probability of a computational scenario in which exactly $n(1)$ intrusions occur in time interval $[t_0,t_1]$, exactly $n(2)$ intrusions occur in time interval $[t_1,t_2]$, and so on.

The probability of having exactly one intrusion in the time interval $[u,v]$ will be approximated by a function F such that

$$p[\mathcal{S}_1(u,v)] = F(u,v) + O\left[(v-u)^2\right], \tag{2-6}$$

where the preceding notation is a shorthand for the statement that the ratio

$$\frac{p[\mathcal{S}_1(u,v)] - F(u,v)}{(v-u)^2} \tag{2-7}$$

is bounded as $v-u$ approaches zero. More precisely, the statement in (2-6) is satisfied on a time interval $[a,b]$ if there exists a number B and a sequence of times $a=t_0<t_1<\cdots<t_n=b$ such that, if $1\le i\le n$ and $t_{i-1}\le u<v\le b$, then

$$\left|\frac{p[S_1(u,v)]-F(u,v)}{(v-u)^2}\right|<B\,. \tag{2-8}$$

The expressions in (2-6) and (2-8) are providing a mathematical form for the statement "$F(u,v)$ is a good approximation to $p[S_1(u,v)]$ when $v-u$ is small."

The function F in (2-6) can be defined in a number of ways. The simplest definition is

$$F(u,v)=\lambda(v-u). \tag{2-9}$$

In this case, F corresponds to a Poisson process (Cox and Lewis, 1966; Haight, 1967; Cox and Isham, 1980) with a fixed rate of constant λ (i.e., a homogeneous Poisson process). A step up in complexity is

$$F(u,v)=\lambda(u)(v-u), \tag{2-10}$$

in which case F corresponds to a Poisson process with a time-dependent rate constant (i.e., a nonhomogeneous Poisson process). Results obtained in an expert review process indicate that the WIPP performance assessment may need to use time-dependent values for λ (Hora et al., 1991). Another possibility is

$$F(u,v)=f(u)[g(v)-g(u)], \tag{2-11}$$

where $g(t)$ is the probability that no intrusions will have occurred by time t and $f(t)=-1/g(t)$. As a final example, F might be defined by

$$F(u,v)=\begin{cases}p_i & \text{if } t_{i-1}<u<v=t_i\\ \lambda(v-u) & \text{otherwise,}\end{cases} \tag{2-12}$$

where $t_{i-1}<t_i$ and $0\le p_i\le 1$ for $i=1,2,\cdots$. The preceding example allows nonzero failure, or intrusion, probabilities at fixed points in time; this type of discontinuity is unlikely to arise in radioactive waste disposal problems but does help show the generality of characterizing a Poisson process with an interval function.

The following presentation will require two types of integrals involving interval functions of the type defined in (2-9) through (2-12): sum integrals and product integrals. These integrals, along with some related terminology, are now defined.

Definition 1. The statement that $\mathcal{D} = \{x_i\}_{i=0}^{m}$ is a subdivision of an interval $[a,b]$ means $a = x_0 < x_1 < \cdots < x_m = b$.

Definition 2. The statement that $\mathcal{R}$ is a refinement of a subdivision $\mathcal{D}$ of $[a,b]$ means (1) $\mathcal{R}$ is a subdivision of $[a,b]$ and (2) every point in $\mathcal{D}$ is also a point in $\mathcal{R}$.

Definition 3. The statement that the sum integral $\int_a^b F$ exists means there exists a number L such that, if $\varepsilon > 0$, then there exists a subdivision $\mathcal{D}$ of $[a,b]$ such that, if $\mathcal{R} = \{r_i\}_{i=0}^{n}$ is a refinement of $\mathcal{D}$, then $\left|L - \sum_{i=1}^{n} F(r_{i-1}, r_i)\right| < \varepsilon$.

Definition 4. The statement that the product integral ${}_a\prod^b(1+F)$ exists means there exists a number L such that, if $\varepsilon > 0$, then there exists a subdivision $\mathcal{D}$ of $[a,b]$ such that, if $\mathcal{R} = \{r_i\}_{i=0}^{n}$ is a refinement of $\mathcal{D}$, then $\left|L - \prod_{i=1}^{n}\left[1 + F(r_{i-1}, r_i)\right]\right| < \varepsilon$.

As indicated in the two preceding definitions, the sum and product integrals

$$\int_a^b F \text{ and } {}_a\prod^b(1+F) \tag{2-13}$$

are simply representations for limits involving

$$\sum_{i=1}^{n} F(r_{i-1}, r_i) \text{ and } \prod_{i=1}^{n}\left[1 + F(r_{i-1}, r_i)\right], \tag{2-14}$$

respectively. These definitions lead to the equalities

$$\int_a^b F = \int_a^x F + \int_x^b F \tag{2-15}$$

and

$$ {}_a\prod^b(1+F) = {}_a\prod^x(1+F)\,{}_x\prod^b(1+F) \tag{2-16} $$

for $a \le x \le b$, where

$$ \int_x^x F = 0 \text{ and } {}_x\prod^x(1+F) = 1. \tag{2-17} $$

As shown by the following two theorems, there is a reciprocal relationship between sum and product integrals.

Theorem 1 (Helton, 1973a). If F is an interval function defined on $[a,b]$ and either

(1) $\int_a^b F$ exists and $\int_a^b F^2$ exists,

or

(2) $\int_a^b F$ exists and ${}_a\prod^b(1+F)$ exists and is not zero,

or

(3) each of ${}_a\prod^b(1+F)$ and ${}_a\prod^b(1-F)$ exists and is not zero,

then $\int_x^y F$, $\int_x^y F^2$ and ${}_x\prod^y(1+F)$ exist for $a \le x \le y \le b$.

Theorem 2 (Davis and Chatfield, 1970; Helton, 1973b). If F is an interval function defined on $[a,b]$ and either $\int_a^b F$ exists or ${}_x\prod^y(1+F)$ exists for $a \le x \le y \le b$, then either of the following two statements implies the other:

(1) ${}_x\prod^y(1+F)$ and $\int_x^y F$ both exist and ${}_x\prod^y(1+F) = \exp\left(\int_x^y F\right)$ for $a \le x \le y \le b$,

and

(2) $\int_a^b F^2 = 0$.

The definition of F in (2-9) satisfies both theorems, as does the definition in (2-10) if $\lambda(u)$ is bounded and integrable on $[a,b]$. It is also possible for the definition in (2-11) to satisfy both theorems when g does not have any discontinuities. The definition in (2-12) satisfies Theorem 1 when $\sum_{i=1}^{\infty} p_i$ exists but will not satisfy Theorem 2 unless $p_i = 0$ for $i = 1,2,\cdots$. Theorem 2 is important because it presents the relationship between product integrals and exponentials of sum integrals.

In the discussions that follow, it will be assumed that F is sufficiently well-behaved for the existence of both $\int_a^b F^2$ and ${}_x\prod^y(1+F)$ for $a \le x \le y \le b$. Actually, we will be interested in the existence of ${}_x\prod^y(1-F)$, which follows from Theorem 1 if $\int_a^b F$ and ${}_x\prod^y(1+F)$ both exist, or equivalently, if $\int_a^b F$ and $\int_a^b F^2$ both exist. Further, the exponential relationship in Theorem 2 will be used to simplify relationships under the added assumption that $\int_a^b F^2 = 0$.

Although not widely used, product integrals are a very useful mathematical construction. Additional background and information can be found in several references (Masani, 1947; Helton, 1977; Dollard and Friedman, 1979; Gill and Johansen, 1990).

2.3 Computational Scenario Probabilities for Single Time Intervals

This section presents a derivation for the probability that exactly k intrusions will occur in a fixed time interval. More specifically, the purpose of this section is to determine the probability $p[S_k(a,b)]$ of $S_k(a,b)$. Notation will involve a subdivision $\{t_i\}_{i=0}^n$ of $[a,b]$. Further, limits are assumed to be of the subdivision-refinement type, although the notation does not expressly indicate this. The function F is also assumed to be sufficiently well-behaved for all indicated integrals to exist.

The probability of no intrusions in the interval $[a,b]$ is given by

$$p[S_0(a,b)] = \lim_{n\to\infty} \prod_{i=1}^{n} [1 - F(t_{i-1}, t_i)]$$

$$= {}_a\prod^b (1-F)$$

$$= \exp\left(-\int_a^b F\right) \qquad \left[\text{if } \int_a^b F^2 = 0\right]$$

$$= \exp[-\lambda(b-a)] , \qquad [\text{if } F(r,s) = \lambda(s-r)] \tag{2-18}$$

where the final expression is the usual form for a Poisson process with a fixed rate constant λ. The expressions

$$ {}_a\prod^b (1-F) \text{ and } \exp\left(-\int_a^b F\right) \tag{2-19}$$

give the probability of no intrusions under less restrictive conditions. In particular, the exponential form includes time-dependent values for λ, and the product integral form is sufficiently general to permit nonzero intrusion probabilities at fixed points in time. A discussion of similar derivations in other contexts is given in Gill and Johansen (1990), Section 4.1.

The probability of exactly one intrusion in the interval [a, b] is given by

$$p[S_1(a,b)] = \lim_{n\to\infty} \sum_{i=1}^{n} p[S_0(a,t_{i-1})]F(t_{i-1},t_i)p[S_0(t_i,b)]$$

$$= \int_a^b p[S_0(a,r)]F(r,s)\, p[S_0(s,b)]$$

$$= \int_a^b {}_a\prod^r (1-F)\, F(r,s)\, {}_s\prod^b (1-F)$$

$$= \left[\int_a^b F\right]\left[{}_a\prod^b (1-F)\right] \qquad \left[\text{if} \int_a^b F^2 = 0\right]$$

$$= \left[\int_a^b F\right]\exp\left(-\int_a^b F\right)$$

$$= [\lambda(b-a)]\exp[-\lambda(b-a)], \qquad [\text{if } F(r,s) = \lambda(s-r)] \tag{2-20}$$

where the final expression is again the usual form for a Poisson process with a fixed rate constant λ. The expressions

$$\int_a^b {}_a\prod^r (1-F)\, F(r,s)\, {}_s\prod^b (1-F) \text{ and } \left[\int_a^b F\right]\exp\left(-\int_a^b F\right) \tag{2-21}$$

give the probability of exactly one intrusion under less restrictive conditions.

The probability of exactly two intrusions in the interval $[a,b]$ is given by

$$p[S_2(a,b)] = \lim_{n\to\infty} \sum_{i=1}^{n} p[S_1(a,t_{i-1})]F(t_{i-1},t_i)p[S_0(t_i,b)]$$

$$= \int_a^b p[S_1(a,u)]F(u,v)\, p[S_0(v,b)]$$

$$= \int_a^b \left[\int_a^u {}_a\prod^{r}(1-F)F(r,s)_s\prod^{u}(1-F) \right] F(u,v)_s\prod^{b}(1-F)$$

$$= \int_a^b \left[\int_a^u F \right] \left[{}_a\prod^{u}(1-F) \right] F(u,v)_v\prod^{b}(1-F) \qquad \left[if \int_a^b F^2 = 0 \right]$$

$$= \left\{ \int_a^b \left[\int_a^u F \right] F(u,v) \right\} {}_a\prod^{b}(1-F)$$

$$= \left\{ \int_a^b \left[\int_a^u F \right] F(u,v) \right\} \exp\left(-\int_a^b F \right)$$

$$= \left[\frac{\lambda^2 (b-a)^2}{2} \right] \exp[-\lambda(b-a)], \qquad [\text{if } F(u,v) = \lambda(v-u)] \qquad (2\text{-}22)$$

where the final expression is the usual form for a Poisson process with a fixed rate constant λ. Various representations for a Poisson process under less restrictive assumptions are also given in the preceding sequence of equalities.

The preceding derivations can be continued for $k = 3,4,\cdots$. In general, the probability of exactly k intrusions, $k = 1,2,3,\cdots$, in the interval $[a,b]$ is given by

$$p[S_k(a,b)] = \lim_{n\to\infty} \sum_{i=1}^{n} p[S_{k-1}(a,t_{i-1})]F(t_{i-1},t_i)p[S_0(t_i,b)]$$

$$= \int_a^b p[S_{k-1}(a,u)]F(u,v)\, p[S_o(v,b)]$$

$$= \left[\int_a^b \left\{ \int_a^u \cdots \left[\left(\int_a^r F \right) F(r,s) \right] \cdots \right\} F(u,v) \right] \exp\left(-\int_a^b F \right) \qquad \left[if \int_a^b F^2 = 0 \right]$$

$$= \left[\frac{\lambda^k (b-a)^k}{k!} \right] \exp[-\lambda(b-a)], \qquad [\text{if } F(u,v) = \lambda(v-u)] \qquad (2\text{-}23)$$

where the preceding iterated integral involves k integrals. The final expression is the usual form for a Poisson process with a fixed rate constant λ. As before, the two preceding expressions give

representations for $p[\mathcal{S}_k(a,b)]$ with less restrictive conditions on F. For a formal development, the equalities in (2-23) could be established by mathematical induction.

2.4 Computational Scenario Probabilities for Multiple Time Intervals

This section presents a derivation for the probability of a pattern of intrusions involving multiple time intervals. Suppose $\{t_i\}_{i=0}^{n}$ is a subdivision of the time interval [a, b]. Further, for $i = 1,2,\cdots,n$, let $\mathcal{S}(t_{i-1},t_i)$ denote a subset of $\mathcal{S}$ that is defined on the basis of drilling intrusions occurring in the time interval $[t_{i-1},t_i]$. That is, the conditions that determine whether or not an element x of $\mathcal{S}$ is also an element of $\mathcal{S}(t_{i-1},t_i)$ are specified only for $[t_{i-1},t_i]$, and thus, the possible intrusions associated with x in other time intervals do not affect membership in $\mathcal{S}(t_{i-1},t_i)$.

A set of time histories satisfying the conditions imposed on $\mathcal{S}(t_{i-1},t_i)$ for all i can be obtained by forming the intersection of the sets $\mathcal{S}(t_{i-1},t_i)$. Specifically, the time histories in the set

$$\mathcal{S}(a,b) = \bigcap_{i=1}^{n} \mathcal{S}(t_{i-1},t_i) \tag{2-24}$$

satisfy the conditions imposed on each of the sets $\mathcal{S}(t_{i-1},t_i)$. The intrusion model is based on the assumption that the occurrences of boreholes are independent in time and space. Thus, the sets (i.e., events) $\mathcal{S}(t_{i-1},t_i)$ and $\mathcal{S}(t_{j-1},t_j)$ are independent for $i \neq j$. As a result, the probability of $\mathcal{S}(a,b)$ can be obtained from the relationship

$$p[\mathcal{S}(a,b)] = p\left[\bigcap_{i=1}^{n} \mathcal{S}(t_{i-1},t_i)\right] = \prod_{i=1}^{n} p[\mathcal{S}(t_{i-1},t_i)]. \tag{2-25}$$

In words, the probability of $\mathcal{S}(a,b)$ is the product of the probabilities for the sets $\mathcal{S}(t_{i-1},t_i)$.

The sets $\mathcal{S}(t_{i-1},t_i)$ are often specified by the number of drilling intrusions (i.e., boreholes) occurring within the time interval $[t_{i-1},t_i]$. As indicated in Section 2.2, $\mathcal{S}_{n(i)}(t_{i-1},t_i)$ can be used to denote the subset of $\mathcal{S}$ such that $x \in \mathcal{S}_{n(i)}(t_{i-1},t_i)$ only if x involves exactly $n(i)$ intrusions within the time interval $[t_{i-1},t_i]$. Then,

$$\mathcal{S}(a,b) = \bigcap_{i=1}^{n} \mathcal{S}_{n(i)}(t_{i-1},t_i) \tag{2-26}$$

denotes the set of time histories in which exactly $n(1)$ intrusions occur in the time interval $[t_0,t_1]$, exactly $n(2)$ intrusions occur in the time interval $[t_1,t_2]$, and so on. As shown in (2-25), the probability of $\mathcal{S}(a,b)$ is given by

$$p[\mathcal{S}(a,b)] = \prod_{i=1}^{n} p\left[\mathcal{S}_{n(i)}(t_{i-1},t_i)\right]. \tag{2-27}$$

Section 2.3 provides computational formulas for the probabilities $p\left[\mathcal{S}_{n(i)}(t_{i-1},t_i)\right]$. These formulas in conjunction with the relationship in (2-27) provide a means to determine the probabilities of a wide variety of scenarios involving drilling intrusions.

Several examples are now presented to illustrate the use of the formula in (2-27). The first example is for a single borehole in time interval $\left[t_{j-1},t_j\right]$ and no intrusions in all other intervals, which is equivalent to

$$n(i) = \begin{cases} 1 \text{ if } i = j \\ 0 \text{ if } i \neq j. \end{cases} \tag{2-28}$$

In this case,

$$p[\mathcal{S}(a,b)] = \prod_{i=1}^{n} p\left[\mathcal{S}_{n(i)}(t_{i-1},t_i)\right] \qquad \text{[from (2-27)]}$$

$$= \left\{\prod_{i=1}^{j-1} p\left[\mathcal{S}_0(t_{i-1},t_i)\right]\right\}\left\{p\left[\mathcal{S}_1(t_{j-1},t_j)\right]\right\}\left\{\prod_{i=j+1}^{n} p\left[\mathcal{S}_0(t_{i-1},t_i)\right]\right\}$$

[from (2-28)]

$$= \left\{\prod_{i=1}^{j-1}\left[t_{i-1}\prod^{t_i}(1-F)\right]\right\}\left\{p\left[\mathcal{S}_1(t_{j-1},t_j)\right]\right\}\left\{\prod_{i=j+1}^{n}\left[t_{i-1}\prod^{t_i}(1-F)\right]\right\}$$

[from (2-18)]

$$= \left\{ {}_{a}\prod^{t_{j-1}} (1-F) \right\} \left\{ p\left[S_1\left(t_{j-1}, t_j\right) \right] \right\} \left\{ {}_{t_{i-1}}\prod^{t_i} (1-F) \right\} . \tag{2-29}$$

The value for $p\left[S_1\left(t_{j-1}, t_j\right)\right]$ is given in (2-20) and results in the equality

$$p[S(a,b)] = \left\{ {}_{a}\prod^{t_{j-1}} (1-F) \right\} \left\{ \int_{t_{j-1}}^{t} {}_{t_{j-1}}\prod^{u} (1-F) F(u,v) {}_{v}\prod^{t_j} (1-F) \right\}$$

$$\bullet \left\{ {}_{t_j}\prod^{b} (1-F) \right\}. \tag{2-30}$$

The preceding representation for $p[S(a,b)]$ was developed with no restrictions on F other than the existence of the integrals involved. Simpler representations result when additional restrictions are placed on F.

When the requirement that $\int_a^b F^2 = 0$ is added, the representation in (2-30) becomes

$$p[S(a,b)] = \left\{ \exp\left(-\int_a^{t_{j-1}} F \right) \right\} \left\{ \left[\int_{t_{j-1}}^{t_j} F \right] \exp\left(-\int_{t_{j-1}}^{t_j} F \right) \right\} \left\{ \exp\left(-\int_{t_j}^{b} F \right) \right\}$$

$$= \left[\int_{t_{j-1}}^{t_j} F \right] \exp\left(-\int_a^b F \right). \tag{2-31}$$

Further, the representation in (2-30) becomes

$$p[S(a,b)] = \left[\lambda\left(t_j - t_{j-1}\right) \right] \exp[-\lambda(b-a)] \tag{2-32}$$

when the additional requirement that $F(u,v) = \lambda(v-u)$ is added.

The intrusion pattern indicated in (2-28) is equivalent to no intrusions in the time intervals $\left[a, t_{j-1}\right]$ and $\left[t_j, b\right]$ together with exactly 1 intrusion in the time interval $\left[t_{j-1}, t_j\right]$. When this decomposition is used, the representation for $p[S(a,b)]$ is

$$p[S(a,b)] = \left\{ p\left[S_0\left(a, t_{j-1}\right) \right] \right\} \left\{ p\left[S_1\left(t_{j-1}, t_j\right) \right] \right\} \left\{ p\left[S_0\left(t_j, b\right) \right] \right\}$$

$$= \left\{ {}_a\prod^{t_j} (1-F) \right\} \left\{ p\left[S_1\left(t_{j-1}, t_j\right) \right] \right\} \left\{ {}_{t_j}\prod^{b} (1-F) \right\}, \qquad (2\text{-}33)$$

[from (2-27)]

which is the same as the representation in (2-29).

The second example is for exactly k boreholes in time interval $\left[t_{j-1}, t_j\right]$ and no intrusion in all other intervals, which is equivalent to

$$n(i) = \begin{cases} k \text{ if } i = j \\ 0 \text{ if } i \neq j \end{cases}. \qquad (2\text{-}34)$$

As indicated in both (2-29) and (2-33), this case leads to

$$p[S(a,b)] = \left\{ {}_a\prod^{t_{j-1}} (1-F) \right\} \left\{ p\left[S_k\left(t_{j-1}, t_j\right) \right] \right\} \left\{ {}_{t_j}\prod^{b} (1-F) \right\}. \qquad (2\text{-}35)$$

The form taken by $p\left[S_k\left(t_{j-1}, t_j\right) \right]$ is shown in (2-29), which leads to

$$p[S(a,b)] = \left\{ {}_a\prod^{t_{j-1}} (1-F) \right\} \left\{ \int_{t_{j-1}}^{t_j} p\left[S_{k-1}\left(t_{j-1}, u\right) \right] F(u,v)\, p\left[S_0\left(v, t_j\right) \right] \right\} \left\{ {}_{t_j}\prod^{b} (1-F) \right\} \qquad (2\text{-}36)$$

for the general case,

$$p[S(a,b)] = \left[\int_{t_{j-1}}^{t_j} \left\{ \int_{t_{j-1}}^{u} \cdots \left[\left(\int_{t_{j-1}}^{r} F \right) F(r,s) \right] \cdots \right\} F(u,v) \right] \exp\left(-\int_a^b F \right) \qquad (2\text{-}37)$$

for the case $\int_a^b F^2 = 0$, and

$$p[S(a,b)] = \left[\frac{\lambda^k \left(t_j - t_{j-1}\right)^k}{k!} \right] \exp[-\lambda(b-a)] \qquad (2\text{-}38)$$

for the case $F(u,v) = \lambda(v-u)$.

The third example is for exactly k boreholes in time interval $[t_{j-1}, t_j]$, exactly m boreholes in time interval $[t_{l-1}, t_l]$, and no intrusions in all other intervals, which is equivalent to

$$n(i) = \begin{cases} k & \text{if } i = j \\ m & \text{if } i = l \\ 0 & \text{otherwise.} \end{cases} \tag{2-39}$$

Derivations similar to those shown in (2-29) and (2-33) lead to

$$p[S(a,b)] = \left\{ {}_a\prod^{t_{j-1}} (1-F) \right\} \left\{ p\left[S_k\left(t_{j-1}, t_j\right) \right] \right\} \left\{ {}_{t_j}\prod^{t_{l-1}} (1-F) \right\}$$

$$\bullet \left\{ p\left[S_m\left(t_{l-1}, t_l\right) \right] \right\} \left\{ {}_{t_l}\prod^{a} (1-F) \right\}, \tag{2-40}$$

with the assumption that $t_j < t_l$. The forms taken by $p\left[S_k\left(t_{j-1}, t_j\right)\right]$ and $p\left[S_m\left(t_{l-1}, t_l\right)\right]$ are shown in (2-29) and can be substituted into (2-40) to produce expressions corresponding to those shown in (2-36), (2-37) and (2-38). The general case and the case for $\int_a^b F^2 = 0$ will involve two pairs of iterated integrals. The relatively simple expression

$$p[S(a,b)] = \left[\frac{\lambda^{k+m} \left(t_j - t_{j-1}\right)^k \left(t_l - t_{l-1}\right)^m}{k!\,m!} \right] \exp[-\lambda(b-a)] \tag{2-41}$$

is produced for the case $F(u,v) = \lambda(v-u)$.

This section concludes by returning to the general case shown in (2-27) in which exactly $n(i)$ intrusions occur for each time interval. Equation (2-29) provides computational formulas for the probabilities $p\left[S_{n(i)}\left(t_{i-1}, t_i\right)\right]$ appearing in (2-27). Thus, a general formula for $p[S(a,b)]$ could be generated by substituting the relations in (2-29) into (2-27). The resultant relationships for the general case and the case $\int_a^b F^2 = 0$ are notationally messy due to the many iterated integrals involved. However, the relatively compact relationship

$$p[S(a,b)] = \left\{ \prod_{i=1}^{n} \left[\frac{\lambda^{n(i)} \left(t_i - t_{i-1}\right)^{n(i)}}{n(i)!} \right] \right\} \exp[-\lambda(b-a)] \tag{2-42}$$

results for the case $F(u,v) = \lambda(v-u)$.

2.5 Computational Scenario Probabilities for Pressurized Brine Pockets

Field data indicate that part of the waste panels at the WIPP may be underlain by one or more pressurized brine pockets in the Castile formation (Earth Technology Corp., 1987). The possible location of these pockets is shown in Figure 2-3. As a result, a potentially important summary scenario involves two or more boreholes through a waste panel in which at least one borehole penetrates a pressurized brine pocket and at least one borehole does not. The significance of this summary scenario results because fluid may flow up one borehole from the pressurized brine pocket, through the panel, and then out through another borehole. This was referred to as the E1E2 scenario in the 1990 WIPP performance assessment for the case involving two boreholes through a panel in which one borehole penetrates a pressurized brine pocket, one borehole does not penetrate a pressurized brine pocket, and the borehole seals fail in a pattern that induces flow through the panel as shown in Figure 2-4 (Bertram-Howery et al., 1990).

Determination of probabilities for E1E2-type computational scenarios is based on the subsets $\mathcal{BP}_k^+(l;a,b)$ and $\mathcal{BP}_k^-(l;a,b)$ of $\mathcal{S}$, where

$$\mathcal{BP}_k^+(l;a,b) = \{x : x \text{ an element of } \mathcal{S} \text{ that involves exactly } k \text{ drilling intrusions through waste panel } l \text{ in the time interval } [a,b] \text{ that penetrate a pressurized brine pocket}\} \quad (2\text{-}43)$$

and

$$\mathcal{BP}_k^-(l;a,b) = \{x : x \text{ an element of } \mathcal{S} \text{ that involves exactly } k \text{ drilling intrusions through waste panel } l \text{ in the time interval } [a,b] \text{ that do not penetrate a pressurized brine pocket}\}. \quad (2\text{-}44)$$

Computational scenarios of the E1E2-type are defined by the intersection of sets of the form shown in (2-43) and (2-44).

As shown in (2-18) and (2-23), the probabilities for $\mathcal{BP}_k^+(l;a,b)$ and $\mathcal{BP}_k^-(l;a,b)$ are given by

$$p\left[\mathcal{BP}_0^+(l;a,b)\right] = {}_a\prod^b \left[1 - F^+(l;u,v)\right], \quad (2\text{-}45)$$

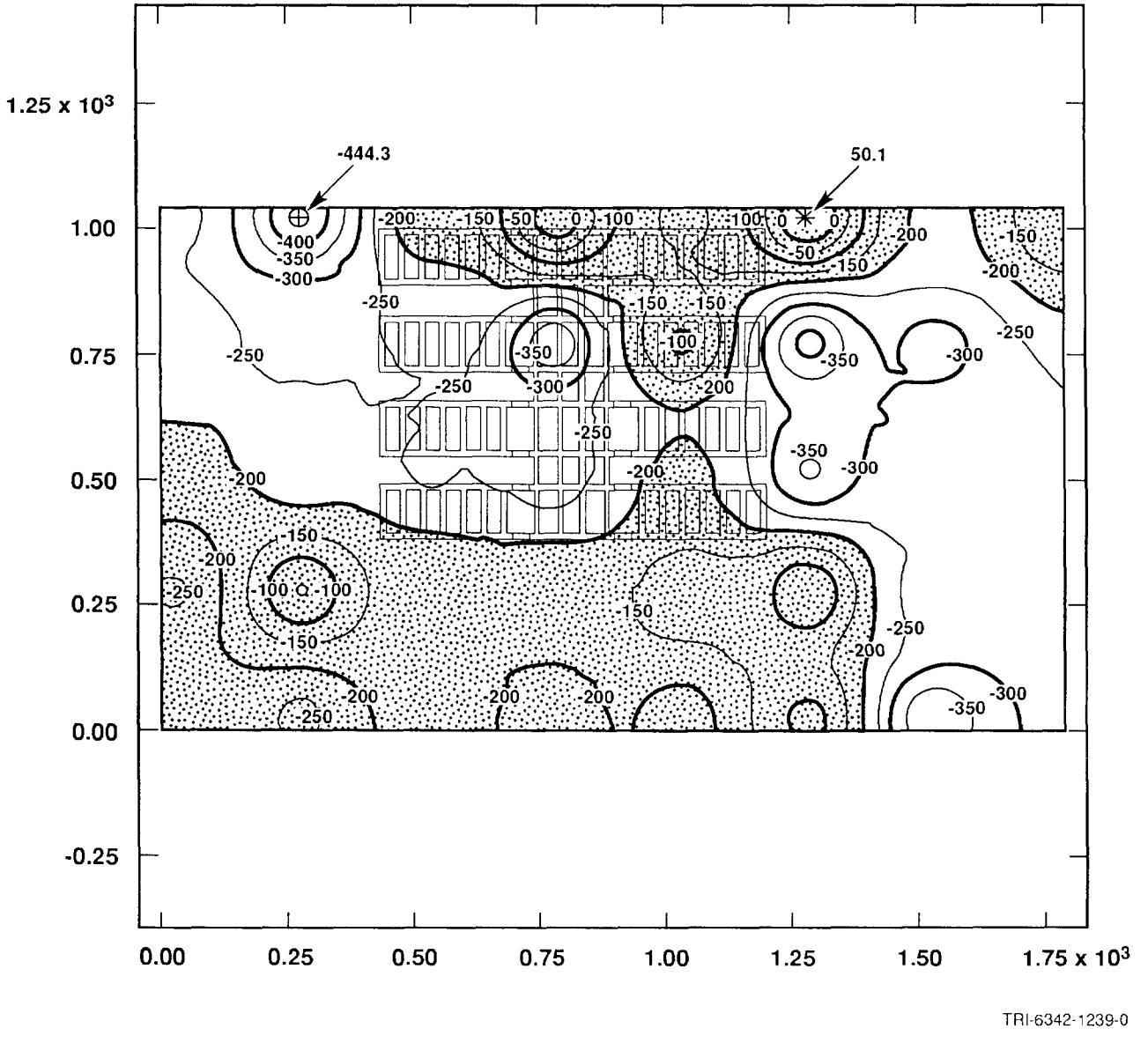

Figure 2-3. Contour Map of Elevation to First Major Conductor below WIPP Disposal Area (after Earth Technology Corp., 1987) (see Section 5.1.1 of Volume 3 of this report).

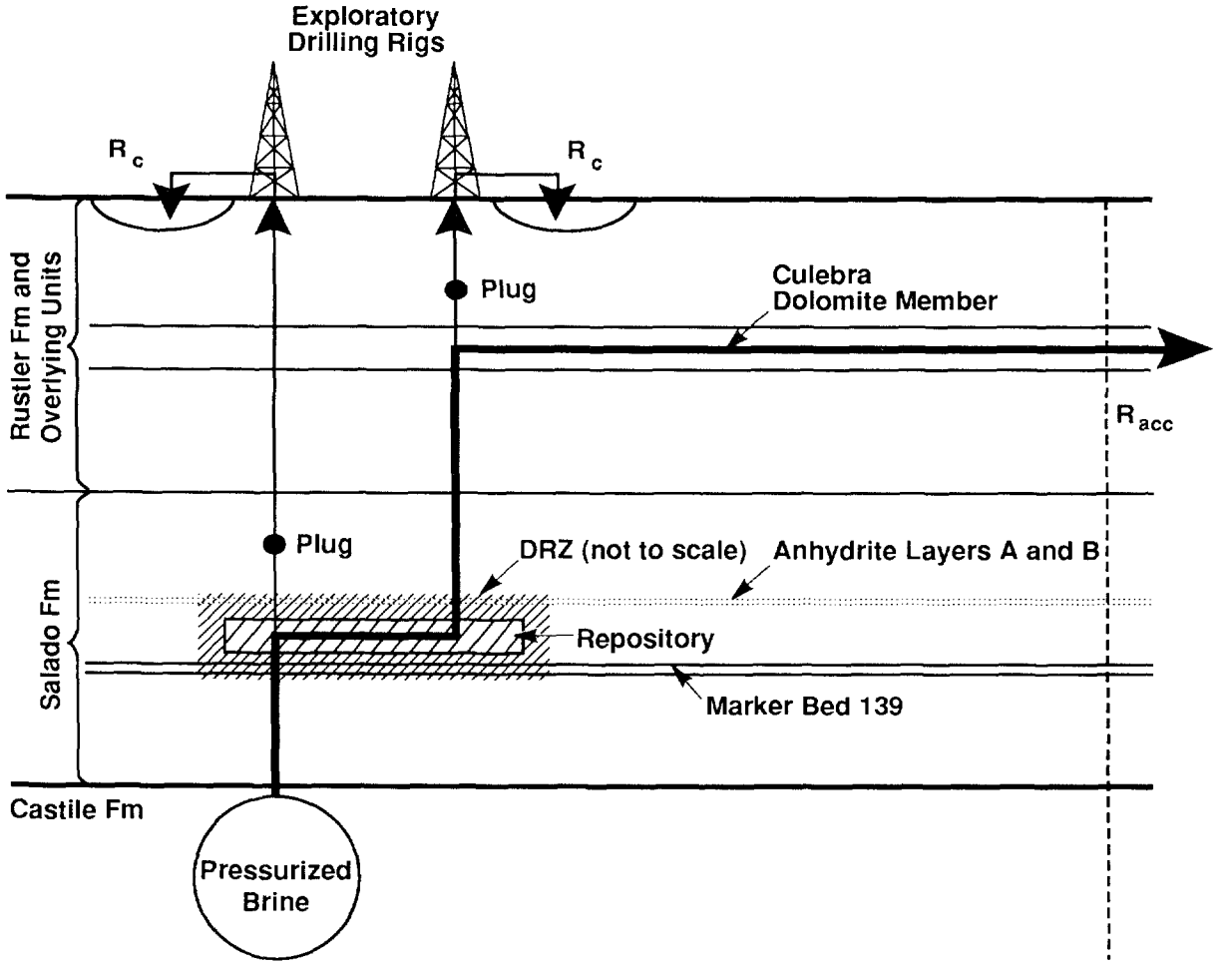

R_c = Release of Cuttings and Eroded Material

R_{acc} = Release at the Subsurface Boundary of the Accessible Environment

DRZ = Disturbed Rock Zone

TRI-6342-217-3

Figure 2-4. Conceptual Model for Scenario E1E2 (Bertram-Howery et al., 1990, Fig. IV-6). Arrows indicate direction of flow. The indicated plugs are assumed to be intact; other possible plugs are assumed to be degraded.)

$$p\left[\mathcal{BP}_k^+(l;a,b)\right] = \int_a^b p\left[\mathcal{BP}_{k-1}^+(l;a,u)\right] F^+(l;u,v)\, p\left[\mathcal{BP}_0^+(l;v,b)\right], \tag{2-46}$$

$$p\left[\mathcal{BP}_0^-(l;a,b)\right] = \prod_a^b \left[1 - F^-(l;u,v)\right], \tag{2-47}$$

and

$$p\left[\mathcal{BP}_k^-(l;a,b)\right] = \int_a^b p\left[\mathcal{BP}_{k-1}^-(l;a,u)\right] F^-(l;u,v)\, p\left[\mathcal{BP}_0^-(l;v,b)\right], \tag{2-48}$$

where $k = 1,2,\cdots$ in (2-46) and (2-48) and the functions $F^+(l;u,v)$ and $F^-(l;u,v)$ approximate the probability of drilling through panel l in time interval $[u,v]$ and penetrating a pressurized brine pocket $\left(F^+\right)$ and not penetrating a pressurized brine pocket $\left(F^-\right)$, respectively.

Since drilling is assumed to be random in time and space, $F^+(l;u,v)$ and $F^-(l;u,v)$ are related to the function F used in Sections 2.3 and 2.4 by

$$\begin{aligned} F^+(l;u,v) &= \left(\frac{aBP(l)}{aTOT(l)}\right)\left(\frac{aTOT(l)}{aTOT}\right)F(u,v) \\ &= \left(\frac{aBP(l)}{aTOT}\right)F(u,v) \end{aligned} \tag{2-49}$$

and

$$\begin{aligned} F^-(l;u,v) &= \left(\frac{aTOT(l) - aBP(l)}{aTOT(l)}\right)\left(\frac{aTOT(l)}{aTOT}\right)F(u,v) \\ &= \left(\frac{aTOT(l) - aBP(l)}{aTOT}\right)F(u,v), \end{aligned} \tag{2-50}$$

respectively, where

$aBP(l)$ = area (m^2) of pressurized brine pocket under waste panel l,
$aTOT(l)$ = total area (m^2) of waste panel l,

and

$aTOT$ = total area (m^2) of all waste panels.

For the special case in which $F(u,v) = \lambda(v-u)$, the functions $F^+(l;u,v)$ and $F^-(l;u,v)$ are defined by

$$F^+(l;u,v) = \alpha(l)(v-u) \text{ and } F^-(l;u,v) = \beta(l)(v-u), \tag{2-51}$$

where

$$\alpha(l) = \left(\frac{aBP(l)}{aTOT}\right)\lambda \text{ and } \beta(l) = \left(\frac{aTOT(l) - aBP(l)}{aTOT}\right)\lambda. \tag{2-52}$$

The probability of having an E1E2-type computational scenario involving waste panel l during the time interval $[a,b]$ is given by

$$p\left[\mathcal{BP}_1^+(l;a,b) \cap \mathcal{BP}_1^-(l;a,b)\right] = p\left[\mathcal{BP}_1^+(l;a,b)\right] p\left[\mathcal{BP}_1^-(l;a,b)\right], \tag{2-53}$$

where $p\left[\mathcal{BP}_1^+(l;a,b)\right]$ and $p\left[\mathcal{BP}_1^-(l;a,b)\right]$ are defined in (2-46) and (2-48). For the special case in which $F(u,v) = \lambda(v-u)$, the preceding expression becomes

$$\begin{aligned} & p\left[\mathcal{BP}_1^+(l;a,b) \cap \mathcal{BP}_1^-(l;a,b)\right] \\ &= \left\{\alpha(l)(b-a)\exp[-\alpha(l)(b-a)]\right\}\left\{\beta(l)(b-a)\exp[-\beta(l)(b-a)]\right\} \\ &= \alpha(l)\beta(l)(b-a)^2 \exp\left\{-[\alpha(l)+\beta(l)][b-a]\right\} \\ &= \left\{\frac{aBP(l)[aTOT(l) - aBP(l)]}{aTOT^2}\right\}\lambda^2(b-a)^2 \exp\left\{-[aTOT(l)/aTOT]\lambda(b-a)\right\}, \end{aligned} \tag{2-54}$$

where $\alpha(l)$ and $\beta(l)$ are defined in (2-52) and the values for $p\left[\mathcal{BP}_1^+(l;a,b)\right]$ and $p\left[\mathcal{BP}_1^-(l;a,b)\right]$ follow from a derivation analogous to the one shown in (2-20).

In a similar manner the probability of having an E1E2-type computational scenario for the time interval [a, b] in which r boreholes pass through waste panel l and subsequently penetrate a pressurized brine pocket and s boreholes pass through waste panel l but do not penetrate a pressurized brine pocket is given by

$$p\left[\mathcal{BP}_r^+(l;a,b)\cap\mathcal{BP}_s^-(l;a,b)\right]=p\left[\mathcal{BP}_r^+(l;a,b)\right]\;\;p\left[\mathcal{BP}_s^-(l;a,b)\right]. \tag{2-55}$$

For the special case in which $F(u, v) = \lambda(v-u)$, the preceding expression becomes

$$\begin{aligned}
&p\left[\mathcal{BP}_r^+(l;a,b)\cap\mathcal{BP}_s^-(l;a,b)\right]\\
&\quad=\left\{\left[\alpha(l)\right]^r[b-a]^r\exp\left[\alpha(l)(b-a)\right]\right\}\left\{\left[\beta(l)\right]^s[b-a]^s\exp\left[\beta(l)(b-a)\right]\right\}\\
&\quad=\left\{\left[aBP(l)\right]^r\left[aTOT(l)-aBP(l)\right]^s/aTOT^{r+s}\right\}\lambda^{r+s}(b-a)^{r+s}\\
&\qquad\bullet\exp\left\{\left[aTOT(l)/aTOT\right]\lambda(b-a)\right\},
\end{aligned} \tag{2-56}$$

which reduces to the expression in (2-54) when $r = s = 1$.

Rather than basing the probability of an E1E2-type computational scenario for waste panel l on the sets $\mathcal{BP}_1^+(l;a,b)$ and $\mathcal{BP}_1^-(l;a,b)$, a more conservative (i.e., larger) probability can be obtained by using the sets

$$\mathcal{BP}^+(l;a,b)=\{x:x \text{ an element of } \mathcal{S} \text{ that involves one or more drilling intrusions through waste panel } l \text{ in the time interval } [a,b] \text{ that penetrate a pressurized brine pocket}\} \tag{2-57}$$

and

$$\mathcal{BP}^-(l;a,b)=\{x:x \text{ an element of } \mathcal{S} \text{ that involves one or more drilling intrusions through waste panel } l \text{ in the time interval } [a,b] \text{ that do not penetrate a pressurized brine pocket}\}. \tag{2-58}$$

In this case, the probability for an E1E2-type computational scenario is given by

$$\begin{aligned}
&p\left[\mathcal{BP}^+(l;a,b)\cap\mathcal{BP}^-(l;a,b)\right]=p\left[\mathcal{BP}^+(l;a,b)\right]\;\;p\left[\mathcal{BP}^-(l;a,b)\right]\\
&\quad=\left\{1-{}_a\prod^b\left[1-F^+(l;u,v)\right]\right\}\left\{1-{}_a\prod^b\left[1-F^-(l;u,v)\right]\right\},
\end{aligned} \tag{2-59}$$

where the second equality follows from (2-18). For the special case in which $F(u,v) = \lambda(v-u)$, the preceding expression becomes

$$p\left[\mathcal{BP}^{+}(l;a,b) \cap \mathcal{BP}^{-}(l;a,b)\right] = \left\{1-\exp\left[-\alpha(l)(b-a)\right]\right\}\left\{1-\exp\left[-\beta(l)(b-a)\right]\right\}, \tag{2-60}$$

where $\alpha(l)$ and $\beta(l)$ are defined in (2-52).

Thus far, this section has dealt with E1E2-type computational scenarios that involve a single waste panel. A complete performance assessment requires consideration of all waste panels. This leads to computational scenarios defined by sets of the form

$$\mathcal{BP}_{11}^{+-}(a,b) = \{x : x \text{ an element of } S \text{ in which at least one waste panel is penetrated by exactly two boreholes during the time interval } [a,b], \text{ of which one penetrates a pressurized brine pocket and one does not}\}.$$

$$= \bigcup_{l=1}^{nP} \left\{\mathcal{BP}_1^{+}(l;a,b) \cap \mathcal{BP}_1^{-}(l;a,b)\right\}, \tag{2-61}$$

where nP is the number of waste panels in the repository. The probability of $\mathcal{BP}_{11}^{+-}(a,b)$ is then given by

$$\begin{aligned} p\left[\mathcal{BP}_{11}^{+-}(a,b)\right] &= p\left[\bigcup_{l=1}^{nP}\left\{\mathcal{BP}_1^{+}(l;a,b) \cap \mathcal{BP}_1^{-}(l;a,b)\right\}\right] \\ &\doteq \sum_{l=1}^{nP} p\left[\left\{\mathcal{BP}_1^{+}(l;a,b) \cap \mathcal{BP}_1^{-}(l;a,b)\right\}\right] \\ &= \sum_{l=1}^{nP} p\left[\mathcal{BP}_1^{+}(l;a,b)\right] p\left[\mathcal{BP}_1^{-}(l;a,b)\right]. \end{aligned} \tag{2-62}$$

As indicated in (2-54), the preceding relation becomes

$$p\left[\mathcal{BP}_{11}^{+-}(a,b)\right] \doteq \sum_{l=1}^{nP}\left[\alpha(l)\beta(l)(b-a)^2 \exp\left\{-\left[\alpha(l)+\beta(l)\right][b-a]\right\}\right] \tag{2-63}$$

when $F(u,v)=\lambda(v-u)$, where $\alpha(l)$ and $\beta(l)$ are defined in (2-52).

As shown in conjunction with (2-60), it is also possible to determine a more conservative probability for E1E2-type computational scenarios by considering one or more boreholes rather than the single boreholes associated with the sets $\mathcal{BP}_1^+(l;a,b)$ and $\mathcal{BP}_1^-(l;a,b)$. This leads to computational scenarios defined by sets of the form

$\mathcal{BP}^{+-}(a,b)=\{x: x$ an element of $\mathcal{S}$ in which at least one waste panel is penetrated by two or more boreholes during the time interval $[a,b]$, of which at least one penetrates a pressurized brine pocket and at least one does not$\}$

$$= \bigcup_{l=1}^{nP} \left\{ \mathcal{BP}^+(l;a,b) \bigcap \mathcal{BP}^-(l;a,b) \right\}. \tag{2-64}$$

As shown in (2-62), the probability of $\mathcal{BP}^{+-}(a,b)$ can be approximated by

$$p\left[\mathcal{BP}^{+-}(a,b)\right] \doteq \sum_{l=1}^{nP} p\left[\mathcal{BP}^+(l;a,b)\right] p\left[\mathcal{BP}^-(l;a,b)\right]. \tag{2-65}$$

Further, when the condition that $F(u,v)=\lambda(v-u)$ is added, it follows from (2-60) that

$$p\left[\mathcal{BP}^{+-}(a,b)\right] \doteq \sum_{l=1}^{nP} \left\{1-\exp\left[-\alpha(l)(b-a)\right]\right\}\left\{1-\exp\left[-\beta(l)(b-a)\right]\right\}, \tag{2-66}$$

where $\alpha(l)$ and $\beta(l)$ are defined in (2-52).

The approximations appearing in (2-62), (2-63), (2-65) and (2-66) result from use of the identity

$$p\left(\bigcup_{i=1}^{N} S_i\right) = \sum_{i=1}^{N} p(S_i) - \sum_{i_1<i_2} p\left(S_{i_1} \bigcap S_{i_2}\right) + \cdots + (-1)^{n+1} \sum_{i_1<i_2<\cdots<i_n} p\left(S_{i_1} \bigcap S_{i_2} \bigcap \cdots \bigcap S_{i_n}\right)$$

$$+ \cdots + (-1)^{N+1} p\left(S_1 \bigcap S_2 \bigcap \cdots \bigcap S_N\right), \tag{2-67}$$

which leads to the inequality

$$p\left(\bigcup_{i=1}^{N} S_i\right) \le \sum_{i=1}^{N} p(S_i). \tag{2-68}$$

Thus, the relations in (2-62), (2-63), (2-65) and (2-66) actually provide bounds on the probabilities involved. Strict equalities could be derived. However, as indicated by (2-67), the resultant relationships would be very cumbersome.

As indicated in (2-52), $\alpha(l)$ and $\beta(l)$ depend on the ratios

$$aBP(l)/aTOT \text{ and } \left[aTOT(l) - aBP(l)\right]/aTOT. \tag{2-69}$$

Thus, as shown in (2-63) and (2-66) for $F(u,v) = \lambda(v-u)$, $p\left[\mathcal{BP}_{11}^{+-}(a,b)\right]$ and $p\left[\mathcal{BP}^{+-}(a,b)\right]$ also depend on these ratios. When only an estimate for

$$aBP = \sum_{l=1}^{nP} aBP(l) \tag{2-70}$$

is available, where aBP is the total brine pocket area under the waste panels, $aBP(l)$ can be estimated by

$$aBP(l) = aBP/nP, \tag{2-71}$$

which leads to

$$\alpha(l) = \left(\frac{aBP}{nP\ aTOT}\right)\lambda \text{ and } \beta(l) = \left(\frac{aTOT(l) - aBP/nP}{aTOT}\right)\lambda. \tag{2-72}$$

The preceding values for $\alpha(l)$ and $\beta(l)$ can be used in conjunction with (2-63) and (2-66) to estimate the probabilities for $\mathcal{BP}_{11}^{+-}(a,b)$ and $\mathcal{BP}^{+-}(a,b)$, which correspond to E1E2-type computational scenarios involving exactly one intrusion of each type and one or more intrusions of each type, respectively.

2.6 Example Results

The 1990 WIPP performance assessment (Bertram-Howery et al., 1990) used a value of

$$\lambda = 3.28 \times 10^{-4}\ \mathrm{yr}^{-1} \tag{2-73}$$

for drilling intrusions, which was derived from an assumption of 30 boreholes per square kilometer per 10,000-years (U.S. EPA, 1985) and an excavated disposal area of 1.09 x 10^5 m^2 (Volume 3 of this report). For illustration, Table 2-2 shows the probability of various computational scenarios involving drilling during different 2,000-year time intervals over a 10,000-year time period.

For a specified number of intrusions, the first column in Table 2-2 indicates the time interval in which the first intrusion takes place, the second column indicates the time interval in which the second intrusion takes place, and so on. The last column lists the probability for each combination of intrusions. For example, the row

I_1	I_2	I_3	I_4	Prob
⋮	⋮	⋮	⋮	⋮
1	3	4		1.062×10^{-2}
⋮	⋮	⋮	⋮	⋮

under 3 Intrusions indicates that the first, second and third intrusions occur during the time intervals [0, 2000], [4000, 6000] and [6000, 8000], respectively, and that the probability of this pattern of intrusions (i.e., scenario) is 1.062×10^{-2}. When expressed with previously used notation, this row indicates that

$$p\Big[S_1(0,2000) \bigcap S_0(2000,4000) \bigcap S_1(4000,6000) \bigcap S_1(6000,8000) \bigcap S_0(8000,10000)\Big] = 1.062 \times 10^{-2}. \tag{2-74}$$

The probabilities appearing in Table 2-2 were calculated with the relationship shown in (2-42).

For each specified number of intrusions, say k, in Table 2-2, the resultant number of cases, or scenarios, is the total number of combinations of the 2,000-year intervals taken k at a time with repetition. In general, the number of combinations of n elements taken k at a time with repetition is given by (Gellert et al., 1977, p. 578)

$$^{n}C_{k} = \binom{n+k-1}{k}. \tag{2-75}$$

For Table 2-2, $n = 5$ and $k = 1, 2, ..., 15$.

The EPA standard allows a 100-year period of administrative control to be assumed after the decommissioning of a waste disposal facility in which no disruptions due to human intrusion can

occur. Table 2-3 shows the result of recalculating the scenario probabilities in Table 2-2 with an assumed 100-year period of administration control (i.e., no drilling intrusions can occur in the first 100-years after decommissioning, which is equivalent to assuming that $\lambda = 0$ in the time interval [0, 100]). As comparison of Tables 2-2 and 2-3 shows, the assumption of a 100-year period of administrative control has little effect on scenario probabilities defined by a Poisson process over a 10,000-year period.

Probabilities for E1E2-type computational scenarios are shown in Table 2-4. The probabilities in this table are actually approximations due to the use of the relations in (2-62), (2-65) and (2-66). Exact results can be obtained but the formulas are very involved. The values used for $aBP(\ell)$, $aTOT(\ell)$ and $aTOT$ in the generation of Table 2-4 are shown in Table 2-5. For comparison, Table 2-6 shows the probabilities that result when an initial 100-year period of administrative control is assumed. As previously seen in Tables 2-2 and 2-3, the exclusion of drilling for a 100-year period does not have a large impact when a 10,000-year period is under consideration.

Probabilities for various types of drilling scenarios are shown in Tables 2-2, 2-3, 2-4 and 2-6. Another factor that can enter into computational scenario definition is the distribution of activity levels (i.e., Ci/m^2) within the waste emplaced in the repository. A projected distribution for the activity levels in waste that will be shipped to the WIPP is shown in Table 2-7. Chapter 3 of this volume discusses how activity loading can be incorporated into both the definition and probability of individual computational scenarios and the CCDF that can be determined for comparison with the EPA release limits.

Table 2-2. Probabilities for Computational Scenarios Involving Multiple Intrusions over 10,000-years for $\lambda = 3.28 \times 10^{-4} yr^{-1}$ and 2,000-Year Time Intervals. For a specified number of intrusions, the first column indicates the time interval in which the first intrusion occurs, the second column indicates the time interval in which the second intrusion occurs, and so on, where 1 ~ [0,2000], 2 ~ [2000,4000], 3 ~ [4000,6000], 4 ~ [6000,8000] and 5 ~ [8000,10000]; the last column lists the probability for each pattern of intrusions calculated with the relationship in (2-42).

0 Intrusions
(prob = 3.763E-02)
(cum prob = 3.763E-02)
(comb of intrusions = 1)

1 Intrusion
(prob = 1.234E-01)
(cum prob = 1.610E-01)
(comb of intrusions = 5)

I_1	I_2	I_3	I_4	Prob
1				2.468E-02
2				2.468E-02
3				2.468E-02
4				2.468E-02
5				2.468E-02
				1.234E-01

2 Intrusions
(prob = 2.024E-01)
(cum prob = 3.635E-01)
(comb of intrusions = 15)

I_1	I_2	I_3	I_4	Prob
1	1			8.096E-03
1	2			1.619E-02
1	3			1.619E-02
1	4			1.619E-02
1	5			1.619E-02
2	2			8.096E-03
2	3			1.619E-02
2	4			1.619E-02
2	5			1.619E-02
3	3			8.096E-03
3	4			1.619E-02
3	5			1.619E-02
4	4			8.096E-03
4	5			1.619E-02
5	5			8.096E-03
				2.024E-01

3 Intrusions
(prob = 2.213E-01)
(cum prob = 5.848E-01)
(comb of intrusions = 35)

I_1	I_2	I_3	I_4	Prob
1	1	1		1.770E-03
1	1	2		5.311E-03
1	1	3		5.311E-03
1	1	4		5.311E-03
1	1	5		5.311E-03
1	2	2		5.311E-03
1	2	3		1.062E-02
1	2	4		1.062E-02
1	2	5		1.062E-02
1	3	3		5.311E-03
1	3	4		1.062E-02
1	3	5		1.062E-02
1	4	4		5.311E-03
1	4	5		1.062E-02
1	5	5		5.311E-03
2	2	2		1.770E-03
2	2	3		5.311E-03
2	2	4		5.311E-03
2	2	5		5.311E-03
2	3	3		5.311E-03
2	3	4		1.062E-02
2	3	5		1.062E-02
2	4	4		5.311E-03
2	4	5		1.062E-02
2	5	5		5.311E-03
3	3	3		1.770E-03
3	3	4		5.311E-03
3	3	5		5.311E-03
3	4	4		5.311E-03
3	4	5		1.062E-02
3	5	5		5.311E-03
4	4	4		1.770E-03
4	4	5		5.311E-03
4	5	5		5.311E-03
5	5	5		1.770E-03
				2.213E-01

4 Intrusions
(prob = 1.815E-01)
(cum prob = 7.662E-01)
(comb of intrusions = 70)

I_1	I_2	I_3	I_4	Prob
1	1	1	1	2.903E-04
1	1	1	2	1.161E-03
.	.	.	.	.
.	.	.	.	.
.	.	.	.	.
1	2	3	4	6.968E-03
.	.	.	.	.
.	.	.	.	.
.	.	.	.	.
4	5	5	5	1.161E-03
5	5	5	5	2.903E-04
				1.815E-01

5 Intrusions
(prob = 1.190E-01)
(cum prob = 8.853E-01)
(comb of intrusions = 126)

6 Intrusions
(prob = 6.508E-02)
(cum prob = 9.503E-01)
(comb of intrusions = 210)

7 Intrusions
(prob = 3.049E-02)
(cum prob = 9.808E-01)
(comb of intrusions = 330)

Table 2-2. Probabilities for Computational Scenarios Involving Multiple Intrusions over 10,000-years for $\lambda = 3.28 \times 10^{-4} yr^{-1}$ and 2,000-Year Time Intervals. (Concluded)

8 Intrusions (prob = 1.250E-02) (cum prob = 9.933E-01) (comb of intrusions = 495)	11 Intrusions (prob = 4.456E-04) (cum prob = 9.998E-01) (comb of intrusions =1365)	14 Intrusions (prob = 7.200E-06) (cum prob = 1.000E+00) (comb of intrusions =3060)
9 Intrusions (prob = 4.556E-03) (cum prob = 9.979E-01) (comb of intrusions = 715)	12 Intrusions (prob = 1.218E-04) (cum prob = 1.000E+00) (comb of intrusions =1820)	15 Intrusions (prob = 1.574E-06) (cum prob = 1.000E+00) (comb of intrusions =3876)
10 Intrusions (prob = 1.494E-03) (cum prob = 9.994E-01) (comb of intrusions =1001)	13 Intrusions (prob = 3.073E-05) (cum prob = 1.000E+00) (comb of intrusions =2380)	

Table 2-3. Probabilities for Computational Scenarios Involving Multiple Intrusions over 10,000-years for $\lambda = 3.28 \times 10^{-4} yr^{-1}$, a 100-year Period Of Administrative Control During Which No Drilling Intrusions Can Occur, and 2,000-Year Time Intervals. For a specified number of intrusions, the first column indicates the time interval in which the first intrusion occurs, the second column indicates the time interval in which the second intrusion occurs, and so on, where 1 ~ [0,2000], 2 ~ [2000,4000], 3 ~ [4000,6000], 4 ~ [6000,8000] and 5 ~ [8000,10000]; the last column lists the probability for each pattern of intrusions calculated with the relationship in (2-42).

0 Intrusions
(prob = 3.888E-02)
(cum prob = 3.888E-02)
(comb of intrusions = 1)

1 Intrusion
(prob = 1.263E-01)
(cum prob = 1.651E-01)
(comb of intrusions = 5)

I_1	I_2	I_3	I_4	Prob
1				2.423E-02
2				2.551E-02
3				2.551E-02
4				2.551E-02
5				2.551E-02
				1.263E-01

2 Intrusions
(prob = 2.050E-01)
(cum prob = 3.701E-01)
(comb of intrusions = 15)

I_1	I_2	I_3	I_4	Prob
1	1			7.551E-03
1	2			1.590E-02
1	3			1.590E-02
1	4			1.590E-02
1	5			1.590E-02
2	2			8.366E-03
2	3			1.673E-02
2	4			1.673E-02
2	5			1.673E-02
3	3			8.366E-03
3	4			1.673E-02
3	5			1.673E-02
4	4			8.366E-03
4	5			1.673E-02
5	5			8.366E-03
				2.050E-01

3 Intrusions
(prob = 2.219E-01)
(cum prob = 5.920E-01)
(comb of intrusions = 35)

I_1	I_2	I_3	I_4	Prob
1	1	1		1.569E-03
1	1	2		4.953E-03
1	1	3		4.953E-03
1	1	4		4.953E-03
1	1	5		4.953E-03
1	2	2		5.214E-03
1	2	3		1.043E-02
1	2	4		1.043E-02
1	2	5		1.043E-02
1	3	3		5.214E-03
1	3	4		1.043E-02
1	3	5		1.043E-02
1	4	4		5.214E-03
1	4	5		1.043E-02
1	5	5		5.214E-03
2	2	2		1.829E-03
2	2	3		5.488E-03
2	2	4		5.488E-03
2	2	5		5.488E-03
2	3	3		5.488E-03
2	3	4		1.098E-02
2	3	5		1.098E-02
2	4	4		5.488E-03
2	4	5		1.098E-02
2	5	5		5.488E-03
3	3	3		1.829E-03
3	3	4		5.488E-03
3	3	5		5.488E-03
3	4	4		5.488E-03
3	4	5		1.098E-02
3	5	5		5.488E-03
4	4	4		1.829E-03
4	4	5		5.488E-03
4	5	5		5.488E-03
5	5	5		1.829E-03
				2.219E-01

4 Intrusions
(prob = 1.801E-01)
(cum prob = 7.722E-01)
(comb of intrusions = 70)

I_1	I_2	I_3	I_4	Prob
1	1	1	1	2.444E-04
1	1	1	2	1.029E-03
.	.	.	.	.
.	.	.	.	.
.	.	.	.	.
1	2	3	4	6.841E-03
.	.	.	.	.
.	.	.	.	.
.	.	.	.	.
4	5	5	5	1.200E-03
5	5	5	5	3.000E-04
				1.801E-01

5 Intrusions
(prob = 1.170E-01)
(cum prob = 8.891E-01)
(comb of intrusions = 126)

6 Intrusions
(prob = 6.331E-02)
(cum prob = 9.525E-01)
(comb of intrusions = 210)

7 Intrusions
(prob = 2.937E-02)
(cum prob = 9.818E-01)
(comb of intrusions = 330)

Table 2-3. Probabilities for Computational Scenarios Involving Multiple Intrusions over 10,000-years for $\lambda = 3.28 \times 10^{-4} yr^{-1}$, a 100-year Period Of Administrative Control During Which No Drilling Intrusions Can Occur, and 2,000-Year Time Intervals. (Concluded)

8 Intrusions (prob = 1.192E-02) (cum prob = 9.937E-01) (comb of intrusions = 495)	11 Intrusions (prob = 4.123E-04) (cum prob = 9.999E-01) (comb of intrusions =1365)	14 Intrusions (prob = 6.464E-06) (cum prob = 1.000E+00) (comb of intrusions =3060)
9 Intrusions (prob = 4.301E-03) (cum prob = 9.980E-01) (comb of intrusions = 715)	12 Intrusions (prob = 1.116E-04) (cum prob = 1.000E+00) (comb of intrusions =1820)	15 Intrusions (prob = 1.399E-06) (cum prob = 1.000E+00) (comb of intrusions =3876)
10 Intrusions (prob = 1.397E-03) (cum prob = 9.994E-01) (comb of intrusions =1001)	13 Intrusions (prob = 2.787E-05) (cum prob = 1.000E+00) (comb of intrusions =2380)	

Table 2-4. Probabilities for E1E2-Type Computational Scenarios (i.e., boreholes through a single panel in which at least one borehole penetrates a pressurized brine pocket and at least one borehole does not penetrate a pressurized brine pocket) over 10,000-years for $\lambda = 3.28 \times 10^{-4} yr^{-1}$ and 2,000-Year Time Intervals.

Time Intervals	2 Boreholes[a] (Eqs 2-63, 2-52)	≥2 Boreholes[b] (Eqs 2-66, 2-52)	2 Boreholes[c] (Eqs 2-63, 2-72)	≥ 2 Boreholes[d] (Eqs.2-66, 2-72)
[0, 2000]	0.005635	0.005825	0.009964	0.010304
[2000, 4000]	0.005635	0.005825	0.009964	0.010304
[4000, 6000]	0.005635	0.005825	0.009964	0.010304
[6000, 8000]	0.005635	0.005825	0.009964	0.010304
[8000, 10000]	0.005635	0.005825	0.009964	0.010304

a. At least one waste panel penetrated by exactly two boreholes during the indicated time interval, of which one penetrates a pressurized brine pocket and one does not. Calculation uses approximation in (2-63) with $\alpha(l)$ and $\beta(l)$ defined in (2-52). Values for aBP(l), aTOT(l) and aTOT consistent with Figure 2-3.

b. At least one waste panel penetrated by two or more boreholes during the indicated time interval, of which at least one penetrates a pressurized brine pocket and at least one does not. Calculation uses approximation in (2-66) with $\alpha(l)$ and $\beta(l)$ defined in (2-52). Values for aBP(l), aTOT(l) and aTOT consistent with Figure 2-3.

c. Same as a. but $\alpha(l)$ and $\beta(l)$ defined in (2-72) and aBP(l), aTOT(l) and aTOT defined to be consistent with Figure 2-3.

d. Same as b. but $\alpha(l)$ and $\beta(l)$ defined in (2-71) and aBP(l), aTOT(l) and aTOT defined to be consistent with Figure 2-3.

Table 2-5. Parameter Values Used in Example Calculation of Probabilities for E1E2-type Computational Scenarios (Source: Table 5.1-1 of Vol. III of this report with depth to pressurized brine assumed to be less than 1250 m).

	$aTOT(l)^a$	$aBP(l)^b$	$aBP(l) / aTOT(l)$
Panel 1	11,530	11,530	1.0000
Panel 2	11,530	8,249	0.7154
Panel 3	11,530	3,548	0.3077
Panel 4	11,530	8,869	0.7692
Panel 5	11,530	4,833	0.4192
Panel 6	11,530	0	0.0000
Panel 7	11,530	0	0.0000
Panel 8	11,530	7,432	0.6446
Southern Panel	8,413	3,786	0.4500
Northern Panel	8,701	1,044	0.1200

Additional Values:

$$aTOT = \sum_{l=1}^{10} aTOT(l) = 109,354$$

$$aBP = \sum_{l=1}^{10} aBP(l) = 49,291$$

$$aBP / aTOT = 0.45075$$

[a] $aTOT(l)$ = area (m^2) of waste panel l

[b] $aBP(l)$ = area (m^2) of pressurized brine under waste panel l

Table 2-6. Probabilities for E1E2-Type Computational Scenarios (i.e., boreholes through a single panel in which at least one borehole penetrates a pressurized brine pocket and at least one borehole does not penetrate a pressurized brine pocket) over 10,000-years for $\lambda = 3.28 \times 10^{-4} yr^{-1}$, a 100-year Period of Administrative Control During Which No Drilling Intrusions Can Occur, and 2,000-Year Time Intervals.

Time Intervals	2 Boreholes[a] (Eqs 2-63, 2-52)	≥2 Boreholes[b] (Eqs 2-66, 2-52)	2 Boreholes[c] (Eqs 2-63, 2-72)	≥ 2 Boreholes[d] (Eqs 2-66, 2-72)
[0, 2000]	0.005102	0.005266	0.009022	0.009315
[2000, 4000]	0.005635	0.005825	0.009964	0.010304
[4000, 6000]	0.005635	0.005825	0.009964	0.010304
[6000, 8000]	0.005635	0.005825	0.009964	0.010304
[8000, 10000]	0.005635	0.005825	0.009964	0.010304

a. At least one waste panel penetrated by exactly two boreholes during the indicated time interval, of which one penetrates a pressurized brine pocket and one does not. Calculation uses approximation in (2-63) with $\alpha(l)$ and $\beta(l)$ defined in (2-52). Values for aBP(l), aTOT(l) and aTOT consistent with Figure 2-3.

b. At least one waste panel penetrated by two or more boreholes during the indicated time interval, of which at least one penetrates a pressurized brine pocket and at least one does not. Calculation uses approximation in (2-66) with $\alpha(l)$ and $\beta(l)$ defined in (2-52). Values for aBP(l), aTOT(l) and aTOT consistent with Figure 2-3.

c. Same as a. but $\alpha(l)$ and $\beta(l)$ defined in (2-72) and aBP(l), aTOT(l) and aTOT defined to be consistent with Figure 2-3.

d. Same as b. but $\alpha(l)$ and $\beta(l)$ defined in (2-71) and aBP(l), aTOT(l) and aTOT defined to be consistent with Figure 2-3.

Table 2-7. Projected Activity Levels (Ci/m^2) in Waste That is Currently Stored and May be Shipped to the WIPP (based on Table 3.4-11 in Volume 3 of this report).

Activity Level	Type[a]	Probability[b]	Time (years) 0	1000	3000	5000	7000	9000
1	CH	0.4023	3.4833	0.2718	0.1840	0.1688	0.1575	0.1473
2	CH	0.2998	34.8326	2.7177	1.8401	1.6875	1.5748	1.4729
3	CH	0.2242	348.326	27.177	18.401	16.875	15.748	14.729
4	CH	0.0149	3483.26	271.77	184.01	168.75	157.48	147.29
5	RH	0.0588	117.6717	0.1546	0.1212	0.1139	0.1082	0.1030
Average for CH Waste:			150.7905	11.7648	7.9658	7.3053	6.8174	6.3764

[a] CH designates contact handled waste; RH designates remote handled waste

[b] Probability that a randomly placed borehole through the waste panels will intersect waste of activity level (l), $l = 1,2,3,4,5$.

3. CONSTRUCTION OF COMPLEMENTARY CUMULATIVE DISTRIBUTION FUNCTIONS—Jon C. Helton

3.1 Introduction

Sandia National Laboratories is conducting an ongoing performance assessment for the Waste Isolation Pilot Plant (WIPP) in southeastern New Mexico (Bertram-Howery and Hunter, 1989; Lappin et al., 1989). At present, a performance assessment is performed each year to summarize what is known about the WIPP and to provide guidance for future work (Marietta et al., 1989; Bertram-Howery et al., 1990). It is anticipated that these iterative performance assessments will continue until the WIPP is either licensed for the disposal of transuranic wastes or found to be unsuitable for such disposal.

The result of greatest interest obtained in these performance assessments is a complementary cumulative distribution function (CCDF) that is used for comparison with the U. S. Environmental Protection Agency (EPA) release limits for radioactive waste disposal (U.S. EPA, 1985). As discussed in the preceding chapter (Chapter 2 of this volume), the EPA standard requires that the normalized releases to the accessible environment be expressed as a single CCDF and that this CCDF fall under certain specified bounds. At present, drilling intrusions are believed to be the most severe potential disruptions that need be considered at the WIPP (Guzowski, 1990 and 1991). Thus, the construction of this CCDF for the WIPP is based on summary scenarios that result from drilling intrusions.

This presentation will describe how a CCDF can be constructed for comparison against the EPA release limits when the disruptions to the waste disposal site under consideration result from drilling intrusions. For the results presented here, the drilling intrusions are assumed to follow a Poisson process (i.e., occur randomly in time and space) (Cox and Lewis, 1966; Haight, 1967; Cox and Isham, 1980) with a fixed rate constant. However, the described approach would work with any probability model for drilling intrusions.

With regard to the risk representation

$$\mathcal{R} = \left\{ \left(\mathcal{S}_i, pS_i, \mathbf{cS}_i \right), i = 1, \ldots, nS \right\} \tag{3-1}$$

described in the preceding chapter and elsewhere (Kaplan and Garrick, 1981; Helton et al., 1991), $\mathcal{S}_i$ is a set of similar time histories defined on the basis of drilling intrusions, pS_i is the probability for $\mathcal{S}_i$, and $\mathbf{cS}_i$ contains the EPA normalized release for $\mathcal{S}_i$. The $\mathcal{S}_i$ appearing in (3-1) are obtained by discretizing a suitable sample space. For comparisons with the EPA release limits, this sample space is

$$\mathcal{S}=\{x: x \text{ a single 10,000-year time history beginning at decommissioning of the facility under consideration}\}. \quad (3\text{-}2)$$

In what follows, an approach will be described for defining the $\mathcal{S}_i$, assigning probabilities pS_i and consequences $\mathbf{cS}_i$ to these $\mathcal{S}_i$, and then constructing the resultant CCDF.

3.2 Construction of a CCDF

The following factors will be used to define the computational scenarios $\mathcal{S}_i$ appearing in (3-1): number and time of the intrusions (see Tables 2-2 and 2-3), flow through a panel due to penetration of a pressurized brine pocket in the Castile formation (see Tables 2-4 and 2-6), and activity level of the waste penetrated by a borehole (see Table 2-7). The preceding factors all relate to stochastic or type A uncertainty (Kaplan and Garrick, 1981; Helton et al., 1991; International Atomic Energy Agency, 1989) since they lead to values for the probabilities appearing in (3-1) and ultimately to a CCDF. Scenarios defined at this level of detail are referred to as computational scenarios in the WIPP performance assessment due to their role in defining the actual calculations that must be performed in the construction of a CCDF for comparison with the EPA release limits.

As shown in Tables 2-2 and 2-3 of this volume, even a fairly coarse gridding on time leads to far too many computational scenarios to perform a detailed calculation for each of them. Construction of a CCDF for comparison against the EPA release limits requires the estimation of cumulative probability through the 0.999 level. Thus, depending on the value for the rate constant λ in the Poisson model for drilling, this may require the inclusion of computational scenarios involving as many as 10 to 12 drilling intrusions, which results in a total of several thousand computational scenarios. Further, this number does not include the effects of different activity levels in the waste. To obtain results for such a large number of computational scenarios, it is necessary to plan and implement the overall calculations very carefully. The manner in which this can be done is not unique. In the following, one computational procedure for calculating a CCDF for comparison with the EPA release limits is described.

The 10,000-year time interval that must be considered for comparison with the EPA release limits can be divided into disjoint subintervals

$$[t_{i-1}, t_i], \quad i = 1, 2, \ldots, nT, \quad (3\text{-}3)$$

where nT is the number of time intervals selected for use. The following results can be calculated for each time interval (e.g., with the assumption the intrusion takes place at the middle of the time interval):

rC_i = EPA normalized release to the surface environment for cuttings removal due to a single borehole in time interval i with the assumption that the waste is homogeneous (i.e., waste of different activity levels is not present), (3-4)

rC_{ij} = EPA normalized release to the surface environment for cuttings removal due to a single borehole in time interval i that penetrates waste of activity level j, (3-5)

$rGW1_i$ = EPA normalized release to the surface environment for groundwater transport initiated by a single borehole in time interval i, (3-6)

and

$rGW2_i$ = EPA normalized release to the surface environment for groundwater transport initiated by two boreholes in the same waste panel in time interval i, of which one penetrates a pressurized brine pocket and one does not [i.e., an E1E2-type summary scenario (Bertram-Howery et al., 1990)]. (3-7)

In general, rC_i, rC_{ij}, $rGW1_i$ and $rGW2_i$ will be vectors containing a large variety of information; however, for notational simplicity, a vector representation will not be used.

For the WIPP performance assessment, the cuttings release to the accessible environment (i.e., rC_i and rC_{ij}) is determined by the CUTTINGS (Rechard et al., 1989) program, and the groundwater release to the accessible environment (i.e., $rGW1_i$ and $rGW2_i$) is determined through a sequence of linked calculations involving the SECO_2DH (draft of SAND90-7096, Roache et al., in preparation; also see Chapter 6 of this volume), BRAGFLO (Chapter 5 of this volume), PANEL (Rechard et al., 1989) and STAFF2D (Huyakorn et al., 1989) programs. The overall operation of these programs is controlled by a driver called CAMCON (Rechard et al., 1989). Additional information on the actual calculations that must be performed to obtain rC_i, rC_{ij}, $rGW1_i$ and $rGW2_i$ is available elsewhere (Chapters 5 through 7 of this volume).

The releases rC_i, rC_{ij}, $rGW1_i$ and $rGW2_i$ can be used to construct the releases associated with the many individual scenarios that must be used in the construction of a CCDF for comparison with the EPA release limits. The following assumptions are made:

1. With the exception of E1E2-type computational scenarios, no synergistic effects result from multiple boreholes, and thus, the total release for a scenario involving multiple intrusions can be obtained by adding the releases associated with the individual intrusions.

2. An E1E2-type computational scenario can only take place when the necessary boreholes occur within the same time interval $[t_{i-1}, t_i]$.

3. An E1E2-type computational scenario involving more than two boreholes will have the same release as an E1E2-type computational scenario involving exactly two boreholes.

The preceding assumptions can now be used systematically to construct the releases for individual computational scenarios.

Computational scenarios that involve *nBH* intrusions, but not an E1E2-type intrusion, are considered first. For a time history involving exactly *nBH* intrusions over 10,000 yrs, let

$$\mathbf{l} = [l(1), l(2), \ldots, l(nBH)] \tag{3-8}$$

$$\mathbf{m} = [m(1), m(2), \ldots, m(nBH)] \tag{3-9}$$

and

$$\mathbf{n} = [n(1), n(2), \ldots, n(nT)] \tag{3-10}$$

represent vectors such that $l(j)$ designates the activity level penetrated by the j^{th} borehole, $m(j)$ designates the time interval in which the j^{th} borehole occurs, and $n(i)$ equals the number of intrusions that occur in the i^{th} time interval. Each element $l(j)$ of $\mathbf{l}$ will take on an integer value between 1 and nL, where nL is the number of activity levels into which the waste has been classified, and each element $m(j)$ of $\mathbf{m}$ will take on an integer value between 1 and nT, where nT is the number of time intervals in use. Similarly, each element $n(i)$ of $\mathbf{n}$ will take on an integer value between 0 and nBH. The elements of $\mathbf{m}$ satisfy the ordering $m(j) \le m(j+1)$, and the elements of $\mathbf{n}$ satisfy the equality $\Sigma_i n(i) = nBH$. Further, a reciprocal relationship exists between $\mathbf{m}$ and $\mathbf{n}$ in the sense that, if either is known, then the other can be determined.

The vectors $\mathbf{l}$, $\mathbf{m}$ and $\mathbf{n}$ can be used to define computational scenarios in a manner that will lead naturally to the calculation of their probabilities and consequences. Specifically, let

$$\mathcal{S}(\mathbf{n}) = \{x: x \text{ an element of } \mathcal{S} \text{ for which exactly } n(i) \text{ intrusions occur in time interval } [t_{i-1}, t_i] \text{ for } i = 1,2,\ldots,nT\} \quad (3\text{-}11)$$

and

$$\mathcal{S}(\mathbf{l},\mathbf{n}) = \{x: x \text{ an element of } \mathcal{S} \text{ for which the } j^{th} \text{ borehole encounters waste of activity } l(j) \text{ and exactly } n(i) \text{ intrusions occur in time interval } [t_{i-1}, t_i] \text{ for } i = 1,2,\ldots,nT\}. \quad (3\text{-}12)$$

The computational scenarios $\mathcal{S}(\mathbf{n})$ and $\mathcal{S}(\mathbf{l},\mathbf{n})$ are related by

$$\mathcal{S}(\mathbf{n}) = \bigcup_{\mathbf{l}} \mathcal{S}(\mathbf{l},\mathbf{n}), \quad (3\text{-}13)$$

where, for a fixed value of $\mathbf{n}$, the union is taken over all possible values for $\mathbf{l}$ (i.e., over all possible combinations of activity loading that the boreholes specified by $\mathbf{n}$ might encounter).

It follows from Eq. (2-42) that the probability $pS(\mathbf{n})$ for $\mathcal{S}(\mathbf{n})$ is given by

$$pS(\mathbf{n}) = \left\{ \prod_{i=1}^{nT} \left[\frac{\lambda^{n(i)} (t_i - t_{i-1})^{n(i)}}{n(i)!} \right] \right\} \exp\left[-\lambda (t_{nT} - t_0)\right] \quad (3\text{-}14)$$

when drilling follows a Poisson process with a rate constant λ. Further, the probability $pS(\mathbf{l},\mathbf{n})$ for $\mathcal{S}(\mathbf{l},\mathbf{n})$ is given by

$$pS(\mathbf{l},\mathbf{n}) = \left(\prod_{j=1}^{nBH} pL_{l(j)} \right) pS(\mathbf{n}), \quad (3\text{-}15)$$

where $pS(\mathbf{n})$ is defined in (3-14) and $pL_{l(j)}$ is the probability that a randomly placed borehole in the repository will encounter waste of activity level $l(j)$.

The normalized releases rC_i, rC_{ij} and $rGW1_i$ can be used to construct the EPA normalized releases for computational scenarios $\mathcal{S}(\mathbf{n})$ and $\mathcal{S}(\mathbf{l},\mathbf{n})$. For $\mathcal{S}(\mathbf{n})$, the normalized release to the accessible environment can be approximated by

$$cS(\mathbf{n}) = \sum_{j=1}^{nBH} \left(rC_{m(j)} + rGW1_{m(j)} \right), \tag{3-16}$$

where $\mathbf{m}$ is the vector defined in (3-9). As indicated earlier, $\mathbf{m}$ is uniquely determined once $\mathbf{n}$ is specified. The computational scenario $S(\mathbf{n})$ contains no information on the activity levels encountered by the individual boreholes, and so $cS(\mathbf{n})$ was constructed with the assumption that all waste is of the same average activity. However, $S(\mathbf{l},\mathbf{n})$ does contain information on activity levels, and the associated normalized release to the accessible environment can be approximated by

$$cS(\mathbf{l},\mathbf{n}) = \sum_{j=1}^{nBH} \left(rC_{m(j),l(j)} + rGW1_{m(j)} \right), \tag{3-17}$$

which does incorporate the activity levels encountered by the individual boreholes.

Computational scenarios of the E1E2-type are now considered. This is a relatively unlikely type of computational scenario (see Tables 2-4 and 2-6) but has the potential to cause large releases due to flow between two boreholes within a single panel. Specifically, E1E2-type computational scenarios are defined by

$$S^{+-}(t_{k-1},t_k) = \{x : x \text{ an element of } S \text{ involving two or more boreholes that penetrate the same waste panel during the time interval } [t_{k-1},t_k], \text{ at least one of these boreholes penetrates a pressurized brine pocket and at least one does not penetrate a pressurized brine pocket}\}. \tag{3-18}$$

Further, the computational scenario $S^{+-}(t_{k-1},t_k)$ can be subdivided on the basis of the activity levels encountered by the boreholes, which produces computational scenarios of the form

$$S^{+-}(\mathbf{l};t_{k-1},t_k) = \{x : x \text{ an element of } S^{+-}(t_{k-1},t_k), \text{ for which the } jth \text{ borehole encounters waste of activity level } l(j)\}. \tag{3-19}$$

It follows from Eqs. (2-63) and (2-66) that the probability for $S^{+-}(t_{k-1},t_k)$ can be approximated by

$$pS^{+-}(t_{k-1},t_k) \triangleq \sum_{l=1}^{nP}\left[\alpha(l)\beta(l)(t_k - t_{k-1})^2\right]\exp\left\{-\left[\alpha(l)+\beta(l)\right]\left[t_k - t_{k-1}\right]\right\} \tag{3-20}$$

or

$$pS^{+-}(t_{k-1},t_k) \triangleq \sum_{l=1}^{nP}\left\{1-\exp\left[-\alpha(l)(t_k - t_{k-1})\right]\right\}\left\{1-\exp\left[-\beta(l)(t_{k-1},t_k)\right]\right\}, \tag{3-21}$$

where

$\alpha(l)$ = $[aBP(l)]\lambda / aTOT$,

$\beta(l)$ = $[aTOT(l) - aBP(l)]\lambda / aTOT$,

$aBP(l)$ = area (m^2) of pressurized brine pocket under waste panel l,

$aTOT(l)$ = total area (m^2) of waste panel l,

$aTOT$ = total area (m^2) of waste panels,

nP = number of waste panels,

and drilling is assumed to follow a Poisson process with a rate constant λ. The expression for $pS^{+-}(t_{k-1},t_k)$ in (3-21) was derived for two or more drilling intrusions and thus provides a somewhat larger value for $pS^{+-}(t_{k-1},t_k)$ than the expression in (3-20), which was derived for exactly two intrusions. However, as illustrated in Tables 2-4 and 2-6, there is not a large difference in the values for $pS^{+-}(t_{k-1},t_k)$ obtained for these two expressions. If desired, an exact probability can be obtained with the relationship in Eq. (2-67) in Chapter 2 of this volume. Further,

$$pS^{+-}(\mathrm{I};t_{k-1},t_k) = \left(\prod_{j=1}^{nB} pL_{l(j)}\right) pS^{+-}(t_{k-1},t_k). \tag{3-22}$$

Before continuing, it is pointed out that the expression in (3-21) is actually greater than $pS^{+-}(t_{k-1},t_k)$ (see Eqs. (2-67) and (2-68)) and also incorporates the probability for the occurrence of an E1E2-type computational scenario in two different waste panels during the time interval $[t_{k-1},t_k]$.

The normalized release to the accessible environment for $S^{+-}(t_{k-1},t_k)$ can be approximated by

$$cS^{+-}(t_{k-1},t_k) = 2\ rC_k + rGW2_k, \tag{3-23}$$

where it is assumed that all waste is of the same average activity for cuttings removal. Similarly, the normalized release $cS^{+-}(\mathbf{l};t_{k-1},t_k)$ for $S^{+-}(\mathbf{l};t_{k-1},t_k)$ can be approximated by

$$cS^{+-}(\mathbf{l};t_{k-1},t_k) = \sum_{j=1}^{2} rC_{k,l(j)} + rGW2_k, \tag{3-24}$$

which incorporates the activity level of the waste. The approximations for $cS^{+-}(t_{k-1},t_k)$ and $cS^{+-}(\mathbf{l};t_{k-1},t_k)$ in (3-23) and (3-24) are based on exactly two intrusions in the time interval $[t_{k-1},t_k]$. More complicated expressions could be developed to define releases for multiple E1E2-type intrusions. However, due to the low probability of such patterns of intrusion (e.g., compare the probabilities for 2 and ≥2 boreholes in Tables 2-4 and 2-6), the use of such expressions would have little impact on the CCDFs used for comparison with the EPA release limits.

The results contained in this section can be used in conjunction with the risk representation in (3-1) to calculate CCDFs for comparison with the EPA release limits. The choices for S_i, pS_i and $\mathbf{cS}_i$ with and without the consideration of activity level for cuttings removal are summarized in Table 3-1.

Table 3-1. Calculation of a CCDF for Comparison with the EPA Release Limits with and without the Effects of Activity Loading

	S_i	pS_i	$\mathbf{cS}_i$
Without Activity Loading	$S(\mathbf{n})$, $S^{+-}(t_{k-1},t_k)$ (Eqs. 3-11, 3-18)	$pS(\mathbf{n})$, $pS^{+-}(t_{k-1},t_k)$ (Eqs. 3-14, 3-20, 3-21)	$cS(\mathbf{n})$, $cS^{+-}(t_{k-1},t_k)$ (Eqs. 3-16, 3-23)
With Activity Loading	$S(\mathbf{l},\mathbf{n})$, $S^{+-}(\mathbf{l};t_{k-1},t_k)$ (Eqs. 3-12, 3-19)	$pS(\mathbf{l},\mathbf{n})$, $pS^{+-}(\mathbf{l};t_{k-1},t_k)$ (Eqs. 3-15, 3-22)	$cS(\mathbf{l},\mathbf{n})$, $cS^{+-}(\mathbf{l};t_{k-1},t_k)$ (Eqs. 3-17, 3-24)

Example CCDFs calculated with the techniques discussed in this section are given in Section 3.4. However, there is a numerical problem that must be addressed first. The computational scenarios $\mathcal{S}(\mathbf{l},\mathbf{n})$ are based on taking all possible combinations of activity levels that might be encountered by the boreholes associated with $\mathcal{S}(\mathbf{n})$. As the number of boreholes increases, the number of activity level combinations increases rapidly and becomes too large to permit a systematic consideration of every possible combination. A numerical procedure for determining the distribution of cuttings releases that results from the consideration of activity loading is presented in Section 3.3. This procedure is then used in the generation of the CCDFs presented in Section 3.4.

3.3 Computation of Activity Loading Effects

The computational scenario $\mathcal{S}(\mathbf{n})$ defined in (3-11) involves nBH drilling intrusions (i.e., $\Sigma_i n(i) = nBH$) and nT time intervals; in addition, the computational scenario $\mathcal{S}(\mathbf{l},\mathbf{n})$ defined in (3-12) involves nL levels for activity loading. This results in

$$\binom{nT+nBH-1}{nBH} \text{ and } nL^{nBH}\binom{nT+nBH-1}{nBH} \tag{3-25}$$

possible values for $\mathcal{S}(\mathbf{n})$ and $\mathcal{S}(\mathbf{l},\mathbf{n})$, respectively [Eq. (2-75)]. As illustrated in Table 3-2, the number of possible computational scenarios increases rapidly with increases in nBH.

Construction of the CCDF for comparison with the EPA release limits may require the consideration of as many as 10 to 12 drilling intrusions when the suggested default drilling rate of 30 boreholes/km^2/10,000 yrs is used (Tables 2-2 and 2-3). As examination of Table 3-2 shows, use of the computational scenarios $\mathcal{S}(\mathbf{n})$ and their associated consequences in the construction of a CCDF should be possible. However, a systematic incorporation of each computational scenario $\mathcal{S}(\mathbf{l},\mathbf{n})$ into a CCDF is likely to require an unreasonable amount of computation. This is especially true when sampling-based uncertainty/sensitivity studies are used to investigate the possible variation in the CCDF used for comparison with the EPA release limits (Helton et al., 1991, Chapter VI).

Table 3-2. Number of Possible Computational Scenarios for Varying Numbers of Intrusions (nBH), Time Intervals (nT) and Levels for Activity Loading (nL)

nBH	$nT = 3$, $nL = 3$		$nT = 5$, $nL = 5$		$nT = 10$, $nL = 5$	
	$\mathcal{S}(\mathbf{n})$	$\mathcal{S}(\mathbf{l},\mathbf{n})$	$\mathcal{S}(\mathbf{n})$	$\mathcal{S}(\mathbf{l},\mathbf{n})$	$\mathcal{S}(\mathbf{n})$	$\mathcal{S}(\mathbf{l},\mathbf{n})$
0	1	1	1	1	1	1
1	3	9	5	25	10	50
2	6	54	15	375	55	1375
3	10	270	35	4375	220	27500
4	15	1215	70	43750	715	446875
5	21	5103	126	393750	2002	6.26×10^{6}
6	28	20412	210	3.28×10^{6}	5005	7.82×10^{7}
7	36	78732	330	2.58×10^{7}	11440	8.94×10^{8}
8	45	295245	495	1.93×10^{8}	24310	9.50×10^{9}
9	55	1.08×10^{6}	715	1.40×10^{9}	48620	9.50×10^{10}
10	66	3.90×10^{6}	1001	9.78×10^{9}	92378	9.02×10^{11}
11	78	1.38×10^{7}	1365	6.67×10^{10}	167960	8.20×10^{12}
12	91	4.84×10^{7}	1820	4.44×10^{11}	293930	7.18×10^{13}
13	105	1.67×10^{8}	2380	2.91×10^{12}	497420	6.07×10^{14}
14	120	5.74×10^{8}	3060	1.87×10^{13}	817190	4.99×10^{15}
15	136	1.95×10^{9}	3876	1.18×10^{14}	1307504	3.99×10^{16}

Computational costs associated with the construction of a CCDF involving the computational scenarios $\mathcal{S}(\mathbf{l},\mathbf{n})$ can be controlled by considering all computational scenarios for relatively small values of nBH and then switching to a Monte Carlo procedure for larger values of nBH. Further, storage requirements can be significantly reduced by sorting the individual consequence results into groups based on size and accumulating the associated probability as the calculation progresses. In essence, this constructs the desired CCDF as the calculation progresses and removes the need to save results for the large number of individual computational scenarios until the end of the calculation. These ideas are now elaborated on.

First, a "binning" system must be established to accumulate the probabilities for the individual computational scenarios as the calculation progresses. To this end, the range of possible

consequence results (i.e., normalized releases to the accessible environment) is partitioned by a sequence of values of the form

$$cS_0 < cS_1 < \cdots < cS_{m-1} < cS_m, \tag{3-26}$$

where cS_0 is less than or equal to the smallest anticipated consequence value and cS_m is greater than or equal to the largest anticipated consequence value. The increments

$$\Delta(cS_i) = cS_i - cS_{i-1} \tag{3-27}$$

will determine the horizontal step sizes in the final CCDF. After each consequence value cS in the integrated calculation has been determined, the integer i such that

$$cS_{i-1} < cS \le cS_i \tag{3-28}$$

is determined and the probability for the associated computational scenario is accumulated in a variable pS_i. At the end of the calculation, the pS_i will determine the vertical step sizes in the final CCDF.

Second, a systematic coverage of the computational scenarios $\mathcal{S}(\mathbf{l},\mathbf{n})$ is performed for small values of nBH (e.g., ≤5). For each of these computational scenarios, $cS(\mathbf{l},\mathbf{n})$ will be calculated, an integer i will be determined such that

$$cS_{i-1} < cS(\mathbf{l},\mathbf{n}) \le cS_i, \tag{3-29}$$

and $pS(\mathbf{l},\mathbf{n})$ will be accumulated in pS_i. Since there are relatively few of them, the scenarios $\mathcal{S}^{+-}(\mathbf{l};t_{k-1},t_k)$ can be handled similarly at this point.

Third, a Monte Carlo procedure can be used to incorporate computational scenarios for larger values of nBH (e.g., >5). For a fixed nBH and each associated computational scenario $\mathcal{S}(\mathbf{n})$, a distribution must be estimated for the releases $cS(\mathbf{l},\mathbf{n})$ defined in (3-17). The variable in this estimation is the vector $\mathbf{l}$, which characterizes the activity levels encountered by the individual boreholes. Each element $l(j)$ of $\mathbf{l}$ is an integer-valued variable defined by the discrete distribution

$$(1,pL_1),(2,pL_2),\ldots,(nL,pL_{nL}). \tag{3-30}$$

Specifically, $I(j) = l$ occurs with probability pL_l and indicates that the j^{th} borehole encountered waste of activity level l. Since drilling is assumed to be random in time and space, the individual elements of $\mathbf{I}$ have the same distribution but are independent of each other. Random or Latin hypercube sampling (McKay et al., 1979) in conjunction with the distribution indicated in (3-8) can be used to generate a sample

$$\mathbf{I}_s = [I_s(1), I_s(2), \ldots, I_s(nBH)], \quad s = 1,2,\ldots,nR, \tag{3-31}$$

from the set of all possible values for $\mathbf{I}$, where nBH is the total number of boreholes associated with $\mathcal{S}(\mathbf{n})$ and nR is the sample size. The following assignments are made for each sample element $\mathbf{I}_s$:

$$pS_s = \frac{p\mathcal{S}(\mathbf{n})}{nR} \text{ and } cS_s = cS(\mathbf{I}_s, \mathbf{n}). \tag{3-32}$$

For each sample element $\mathbf{I}_s$, the integer i such that

$$cS_{i-1} < cS_s \leq cS_i \tag{3-33}$$

is determined and pS_s is accumulated in pS_i. The preceding procedure must be repeated for all nBH selected for consideration and all $\mathcal{S}(\mathbf{n})$ associated with each nBH. The number of $\mathcal{S}(\mathbf{n})$ associated with various values of nBH is shown in Table 3-2.

Fourth, once the calculations are completed for all nBH, the probabilities pS_i and the associated consequence values cS_i can be used to construct the desired CCDF. Specifically, this CCDF is given by the function

$F(x)$ = probability that cS exceeds a specific consequence value x

$$= \sum_{j=i}^{m} pS_j, \tag{3-34}$$

where i is the smallest integer such that $cS_i > x$.

An observation on computational logistics with respect to the sampling procedure in the third step is now made. The most computationally efficient approach would be to generate the sample shown in (3-31) for a large value of nBH (e.g., nBH = 15) and then use this sample for all values of nBH and associated computational scenarios in the analysis. For any specific value of nBH, only the first nBH values in each vector would be used. The advantage of this approach is that the

generation of only one sample is required. Another approach would be to generate a new sample for each computational scenario, which has the advantages that (1) the systematic biases that might result from the repeated use of the same sample would not be present and (2) a fuller coverage of the possible combinations of activity loadings would be obtained. However, as shown in Table 3-2, many thousands of samples would be required for large values of nBH. For example, 1001 samples would be required to provide a different sample for each $\mathcal{S}(\mathbf{n})$ when $nT = 5$ and $nBH = 10$. An intermediate approach would be to generate a new sample for each value of nBH and then to use this sample for all computational scenarios $\mathcal{S}(\mathbf{n})$ associated with nBH. Examples of CCDFs constructed with the techniques described in this section are given in Section 3.4.

3.4 Examples of CCDF Construction

As indicated in (3-1), the outcome of a performance assessment for the WIPP can be represented by a set $\mathcal{R}$ of ordered triples. In practice, many imprecisely known variables are required in the determination of $\mathcal{R}$. When these variables are included, the representation for $\mathcal{R}$ becomes

$$\mathcal{R}(\mathbf{x}) = \left\{\left[\mathcal{S}_i(\mathbf{x}), pS_i(\mathbf{x}), \mathbf{cS}_i(\mathbf{x})\right], \quad i = 1, \cdots, nS(\mathbf{x})\right\} \tag{3-35}$$

where the vector $\mathbf{x}$ denotes these imprecisely known variables. The 1991 WIPP performance assessment considered the 45 imprecisely known variables listed in Tables 6.01-1, 6.0-2 and 6.0-3 of Volume 3 of this report. The impact of these variables on $\mathcal{R}$ was assessed by generating a Latin hypercube sample (McKay et al., 1979) of size 60 from these variables and then evaluating $\mathcal{R}$ for each sample element $\mathbf{x}_j$. This produced the sequence of sets

$$\mathcal{R}(\mathbf{x}_j) = \left\{\left[\mathcal{S}_i(\mathbf{x}_j), pS_i(\mathbf{x}_j), \mathbf{cS}_i(\mathbf{x}_j)\right], \quad i = 1, \cdots, nS(\mathbf{x}_j)\right\} \tag{3-36}$$

for $j = 1, \cdots, 60$.

One or more CCDFs can be constructed for each set $\mathcal{R}(\mathbf{x}_j)$. In particular, Figure 3-1 shows the distribution of CCDFs for releases to the accessible environment due to groundwater transport, and Figure 3-2 shows the distribution of CCDFs for releases to the accessible environment due to cuttings removal. Further, Figure 3-3 shows the distribution of CCDFs for total release to the accessible environment (i.e., groundwater transport and cuttings removal combined). Each set $\mathcal{R}(\mathbf{x}_j)$ shown in (3-36) leads to a single CCDF in Figures 3-1, 3-2 and 3-3, although Figure 3-1

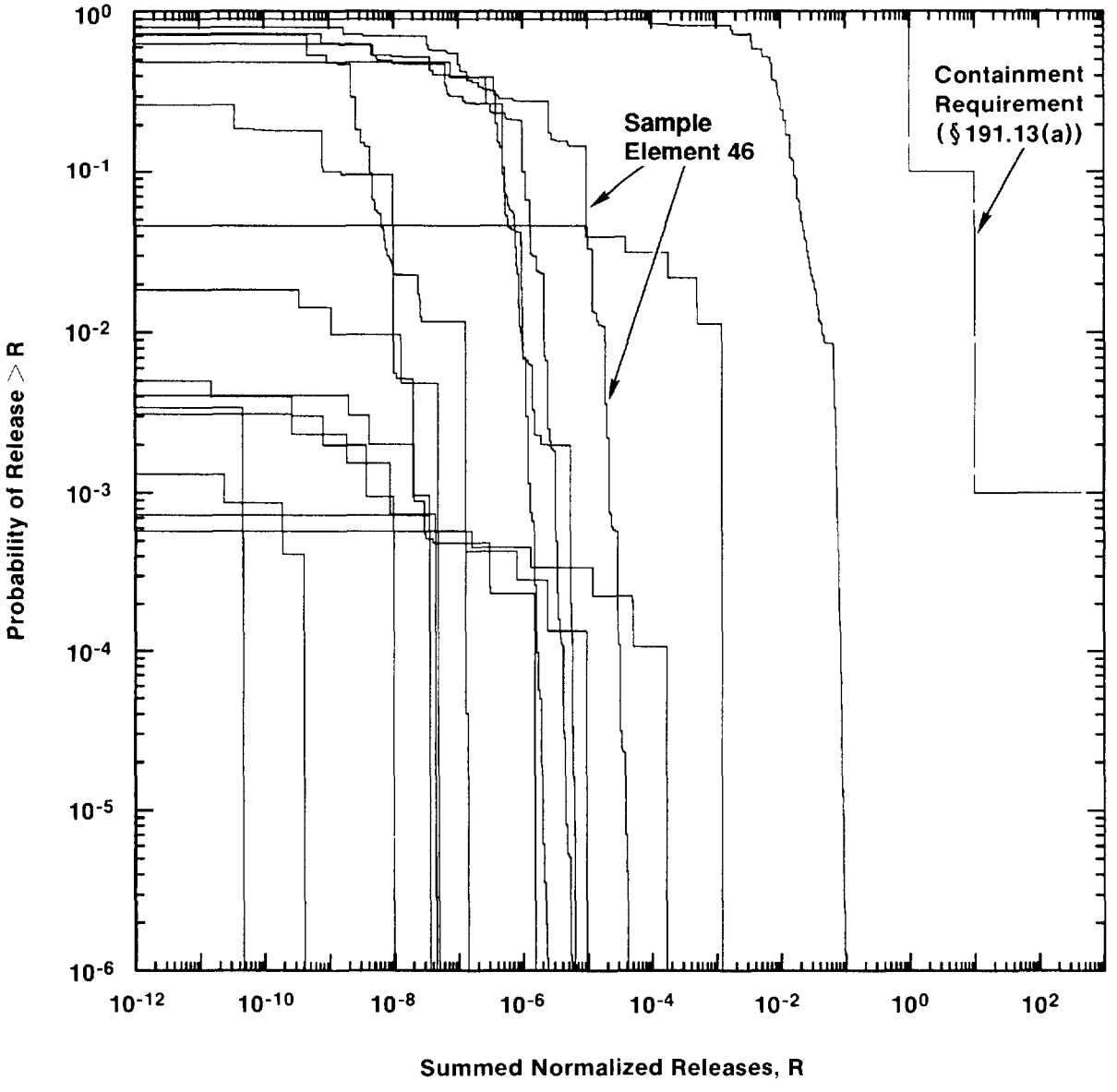

TRI-6342-1295-1

Figure 3-1. Distribution of CCDFs For Normalized Releases to the Accessible Environment Due to Groundwater Transport with a Dual Porosity Model for the Culebra Formation. Each CCDF shown in this figure results from one of the sets $\mathcal{R}(\mathbf{x}_j)$ shown in (3-36).

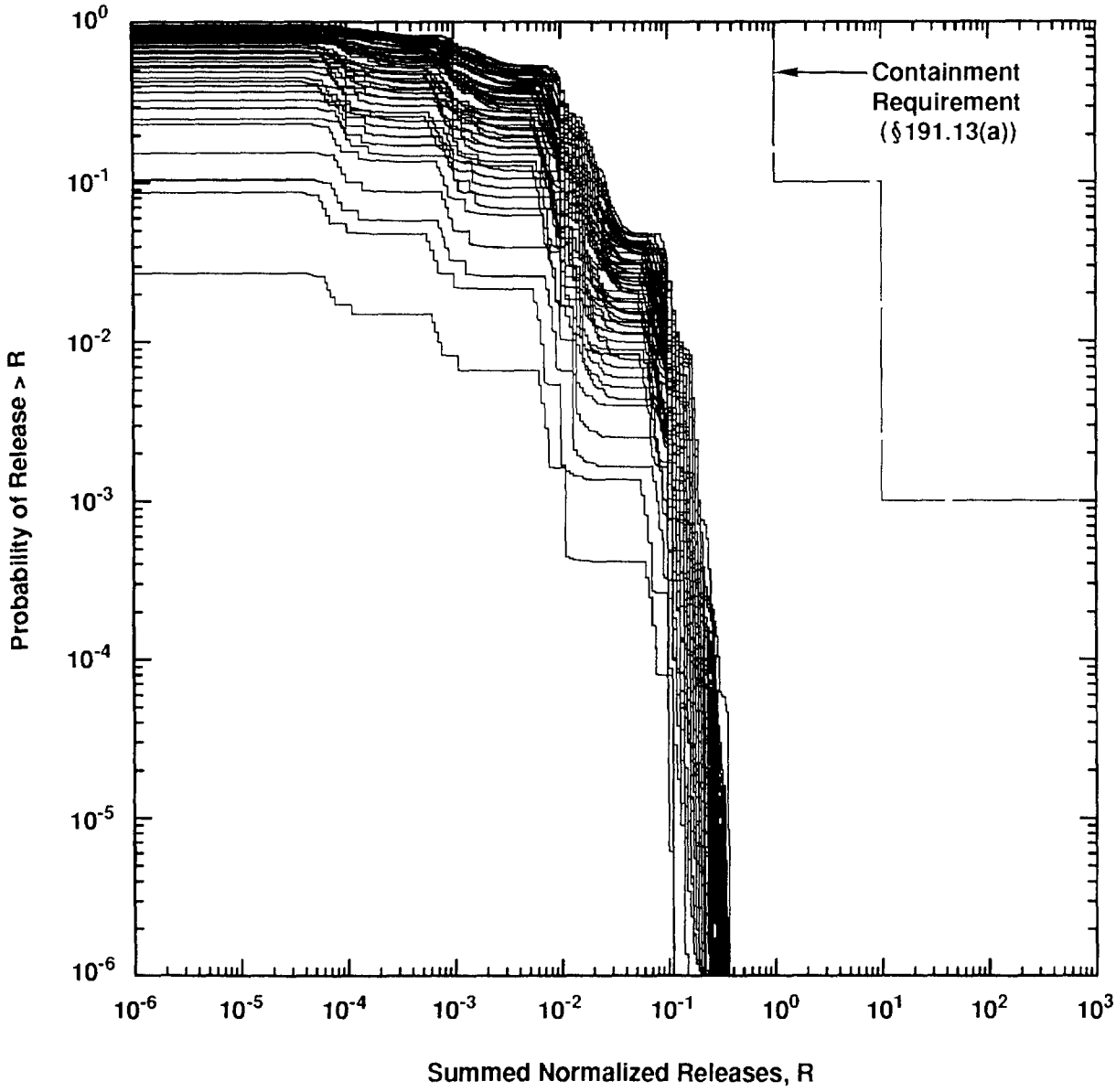

TRI-6342-1383-0

Figure 3-2. Distribution of CCDFs For Normalized Releases to the Accessible Environment Due to Cuttings Removal. Each CCDF shown in this figure results from one of the sets $\mathcal{R}(\mathbf{x}_j)$ shown in (3-36).

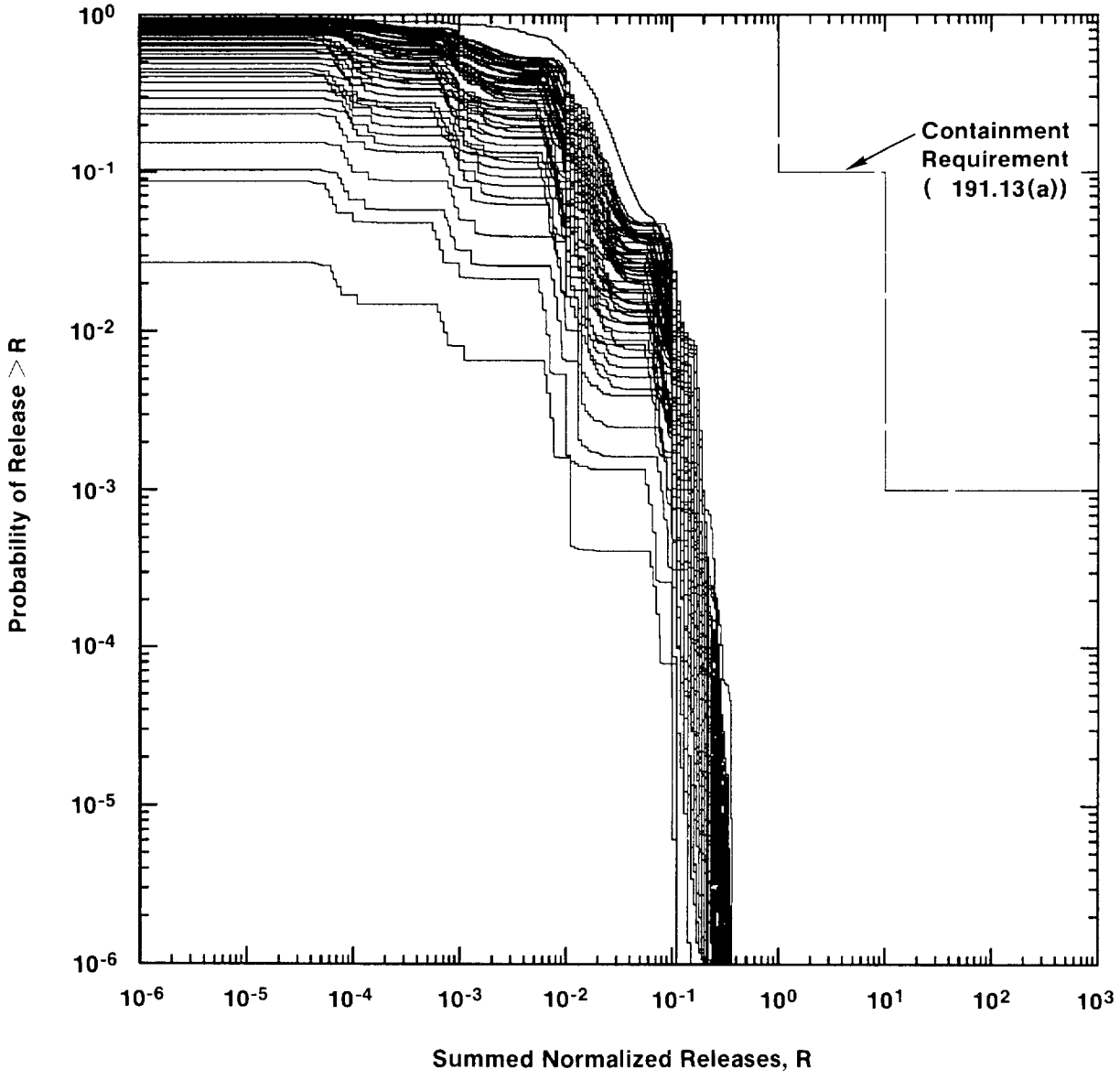

TRI-6342-1293-0

Figure 3-3. Distribution of CCDFs For Normalized Releases to the Accessible Environment Due to Both Cuttings Removal and Groundwater Transport with a Dual Porosity Model for the Culebra. Each CCDF shown in this figure results from one of the sets $\mathcal{R}(\mathbf{x}_j)$ shown in (3-36).

contains less than 60 CCDFs because some sample elements result in no groundwater releases to the accessible environment.

This section will use results associated with one of the sample elements on which Figures 3-1, 3-2 and 3-3 are based to illustrate CCDF construction. In particular, results associated with sample element $j = 46$ will be used. The variable values associated with sample element 46 are listed in Appendix B of this volume. For perspective, the CCDF for groundwater releases associated with this sample element is identified in Figure 3-1; further, sample element 46 results in one of the higher-probability CCDFs in Figure 3-2 for cuttings releases and also in Figure 3-3 for the total release due to both groundwater transport and cuttings removal.

As discussed in Section 3.2, the cuttings releases rC_i and rC_{ij} indicated in (3-4) and (3-5) and the groundwater releases $rGW1_i$ and $rGW2_i$ indicated in (3-6) and (3-7) are used to construct CCDFs for comparison with the EPA release limits. The values that resulted for these variables for sample element 46 are listed in Table 3-3.

The computational scenarios $\mathcal{S}(\mathbf{n})$ and $\mathcal{S}^{+-}(t_{k-1},t_k)$ are defined in (3-11) and (3-18), respectively. Further, probabilities for these scenarios are defined in (3-14) and (3-21), respectively, and the associated releases to the accessible environment under the assumption that all waste is of the same average activity level are defined in (3-16) and (3-23), respectively. The ratio of brine pocket area to total repository area (i.e., $aBP/aTOT$, where aBP is the area (m^2) of pressurized brine under the panels and $aTOT$ (m^2) is the total area of the panels) was a sampled variable in the 1991 WIPP performance assessment. As examination of the terms $\alpha(l)$ and $\beta(l)$ appearing in the approximations for $pS^{+-}(t_{k-1},t_k)$ in (3-20) and (3-21) shows, calculation of $pS^{+-}(t_{k-1},t_k)$ requires the ratio of brine pocket area under waste panel l to total area under waste panel l (i.e., $aBP(l)/aTOT(l)$). As only the ratio $aBP/aTOT$ is known for each sample element, the approximations

$$aBP(l)/aTOT(l) = aBP/aTOT \text{ and } aTOT(l) = aTOT/nP \tag{3-37}$$

are used in the determination of $\alpha(l)$ and $\beta(l)$, where $nP = 10$ is the number of waste panels. With the preceding approximations,

$$\alpha(l) = \lambda(aBP/aTOT)/nP,\ \beta(l) = \lambda(1 - aBP/aTOT)/nP, \tag{3-38}$$

and the representations for $pS^{+-}(t_{k-1},t_k)$ in (3-20) and (3-21) become

$$pS^{+-}(t_{k-1},t_k) \doteq \left[\left(\frac{aBP}{aTOT}\right)\left(1-\frac{aBP}{aTOT}\right)(t_k-t_{k-1})^2\lambda^2/nP\right]\exp\left[-\lambda(t_k-t_{k-1})/nP\right] \quad (3\text{-}39)$$

and

$$pS^{+-}(t_{k-1},t_k) \doteq nP\left\{1-\exp\left[-\lambda\frac{aBP}{aTOT}(t_k-t_{k-1})/nP\right]\right\} \cdot\left\{1-\exp\left[-\lambda\left(1-\frac{aBP}{aTOT}\right)(t_k-t_{k-1})/nP\right]\right\}, \quad (3\text{-}40)$$

respectively. It is the form of (3-21) given in (3-40) that was actually used in the construction of CCDFs in the 1991 WIPP performance assessment.

The results of the indicated probability and release calculations are illustrated in Table 3-4 for sample element 46. Examples of the computational scenarios $\mathcal{S}(\mathbf{n})$ appear in the first column of Table 3-4 as $\mathcal{S}(0,0,0,0,0),\mathcal{S}(1,0,0,0,0),\cdots,\mathcal{S}(1,0,0,0,15)$. As a reminder, five time intervals are being used, and so the vector $\mathbf{n}$ has five elements (i.e., $\mathbf{n}=(0,0,0,0,0),(1,0,0,0,0),\cdots,(0,0,0,0,15)$ in Table 3-4). The scenarios $\mathcal{S}^{+-}(t_{k-1},t_k)$ appear as the last five entries in the first column (i.e., $\mathcal{S}^{+-}(0,2000),\cdots,\mathcal{S}^{+-}(8000,10000)$). The remaining columns present the probabilities and normalized releases for the individual scenarios. Probabilities are presented with and without a 100 year period of administrative control in which drilling intrusions cannot take place. As comparison of the two probability columns shows, assumption of a 100 year period of administrative control has little effect on the scenario probabilities.

The computational scenarios $\mathcal{S}(\mathbf{l},\mathbf{n})$ and $\mathcal{S}^{+-}(\mathbf{l};t_{k-1},t_k)$ incorporating activity loading effects for the cuttings releases are defined in (3-12) and (3-19), respectively. Further, probabilities for these scenarios are defined in (3-15) and (3-22), respectively, and the associated releases to the accessible environment are defined in (3-17) and (3-24), respectively. The results of the indicated probability and release calculations are illustrated for $\mathcal{S}(\mathbf{l},\mathbf{n})$ in Table 3-5 for sample element 46. The calculations for $\mathcal{S}^{+-}(\mathbf{l};t_{k-1},t_k)$ are similar and are not shown.

The CCDFs appearing in the 1991 WIPP performance assessment are constructed from computational scenarios with probabilities and normalized releases of the form shown in Tables 3-4 and 3-5. When only groundwater releases are under consideration, it is possible to systematically incorporate all the computational scenarios indicated in Table 3-4 into a CCDF.

Table 3-3. Normalized Radionuclide Releases Used to Illustrate Scenario Construction Procedures. The releases presented in this table were calculated for sample element 46 in the 1991 WIPP performance assessment (see Appendix B, Vol. 2).

Time[a]	$rGW1_i$[b]	$rGW2_i$[c]	rC_i[d]	rC_{i1}[e]	rC_{i2}[e]	rC_{i3}[e]	rC_{i4}[e]	rC_{i5}[e]
1	9.92E-06	1.48E-05	7.39E-03	1.71E-04	1.71E-03	1.71E-02	1.71E-01	6.96E-03
2	2.51E-06	5.08E-06	5.01E-03	1.16E-04	1.16E-03	1.16E-02	1.16E-01	4.72E-03
3	3.61E-07	1.34E-06	4.60E-03	1.06E-04	1.06E-03	1.06E-02	1.06E-01	4.33E-03
4	7.72E-08	3.16E-07	4.29E-03	9.92E-05	9.92E-04	9.92E-03	9.92E-02	4.04E-03
5	0.00E+00	5.08E-08	4.02E-03	9.28E-05	9.28E-04	9.28E-03	9.28E-02	3.78E-03

a Time at which intrusion occurs, where 1~1000 yr, 2~3000 yr, 3~5000 yr, 4~7000 yr, 5~9000 yr.

b EPA normalized release (dimensionless) to the accessible environment for groundwater transport (with a dual porosity model in the Culebra Formation) initiated by a single borehole in time interval i.

c EPA normalized release (dimensionless) to the accessible environment for groundwater transport (with a dual porosity model in the Culebra Formation) initiated by two boreholes in the same waste panel in time interval i, of which one penetrates a pressurized brine pocket and one does not (i.e., an E1E2-type scenario).

d EPA normalized release (dimensionless) to the surface environment for cuttings removal due to a single borehole in time interval i with the assumption that the waste is homogeneous (i.e., waste of different activity levels is not present). Calculation of the rC_i used the average activity level shown in Table 2-7.

e EPA normalized release (dimensionless) to the surface environment for cuttings removal due to a single borehole in time interval i that penetrates waste of activity level j. Calculation of the rC_{ij} used the activity levels corresponding to j=1,2,3,4,5 shown in Table 2-7.

Table 3-4. Probabilities and Normalized Releases for Computational Scenarios Used to Illustrate Scenario Construction Procedures without the Inclusion of Activity Loading Effects on the Cuttings Releases. The probabilities presented in this table were calculated for sample element 46 in the 1991 WIPP performance assessment (see Appendix B, Vol. 2), which resulted in the rate constant in the Poisson model for drilling (i.e., λ) equaling 8.4424E-05 yr^{-1} and the area ratio for the pressurized brine pocket (i.e., aBP/aTOT) equaling 0.44981; the normalized releases were constructed from the values shown for $rGW1_j$, $rGW2_j$, and rC_j in Table 3-3.

a Computational Scenario	b Probability w/o Control	c Probability w Control	d Cuttings Release	e Groundwater Release	f Total Release
$\mathcal{S}(0,0,0,0,0)$	0.429886	0.433530	0.000E+00	0.000E+00	0.000E+00
$\mathcal{S}(1,0,0,0,0)$	0.072585	0.069540	6.961E-03	9.922E-06	6.971E-03
$\mathcal{S}(0,1,0,0,0)$	0.072585	0.073200	4.716E-03	2.507E-06	4.719E-03
$\mathcal{S}(0,0,1,0,0)$	0.072585	0.073200	4.329E-03	3.610E-07	4.329E-03
$\mathcal{S}(0,0,0,1,0)$	0.072585	0.073200	4.042E-03	7.724E-08	4.042E-03
$\mathcal{S}(0,0,0,0,1)$	0.072585	0.073200	3.784E-03	0.000E+00	3.784E-03
$\mathcal{S}(2,0,0,0,0)$	0.006128	0.005577	1.392E-02	1.984E-05	1.394E-02
$\mathcal{S}(1,1,0,0,0)$	0.012256	0.011742	1.168E-02	1.243E-05	1.169E-02
$\mathcal{S}(1,0,1,0,0)$	0.012256	0.011742	1.129E-02	1.028E-05	1.130E-02
$\mathcal{S}(1,0,0,1,0)$	0.012256	0.011742	1.100E-02	1.000E-05	1.101E-02
$\mathcal{S}(1,0,0,0,1)$	0.012256	0.011742	1.074E-02	9.922E-06	1.075E-02
$\mathcal{S}(0,2,0,0,0)$	0.006128	0.006180	9.433E-03	5.013E-06	9.438E-03
$\mathcal{S}((0,1,1,0,0)$	0.012256	0.012360	9.045E-03	2.868E-06	9.048E-03
$\mathcal{S}(0,1,0,1,0)$	0.012256	0.012360	8.759E-03	2.584E-06	8.761E-03
$\mathcal{S}(0,1,0,0,1)$	0.012256	0.012360	8.500E-03	2.507E-06	8.503E-03
$\mathcal{S}(0,0,2,0,0)$	0.006128	0.006180	8.657E-03	7.220E-07	8.658E-03
$\mathcal{S}(0,0,1,1,0)$	0.012256	0.012360	8.371E-03	4.382E-07	8.371E-03
$\mathcal{S}(0,0,1,0,1)$	0.012256	0.012360	8.112E-03	3.610E-07	8.113E-03
$\mathcal{S}(0,0,0,2,0)$	0.006128	0.006180	8.085E-03	1.545E-07	8.085E-03
$\mathcal{S}(0,0,0,1,1)$	0.012256	0.012360	7.826E-03	7.724E-08	7.826E-03
$\mathcal{S}(0,0,0,0,2)$	0.006128	0.006180	7.568E-03	0.000E+00	7.568E-03
$\mathcal{S}(3,0,0,0,0)$	0.000345	0.000298	2.088E-02	2.977E-05	2.091E-02
$\mathcal{S}(2,1,0,0,0)$	0.001035	0.000942	1.864E-02	2.235E-05	1.866E-02
$\mathcal{S}(2,0,1,0,0)$	0.001035	0.000942	1.825E-02	2.021E-05	1.827E-02
$\mathcal{S}(2,0,0,1,0)$	0.001035	0.000942	1.796E-02	1.992E-05	1.798E-02
$\mathcal{S}(2,0,0,0,1)$	0.001035	0.000942	1.771E-02	1.984E-05	1.773E-02
$\mathcal{S}(1,2,0,0,0)$	0.001035	0.000991	1.639E-02	1.494E-05	1.641E-02
$\mathcal{S}(1,1,1,0,0)$	0.002069	0.001983	1.601E-02	1.279E-05	1.602E-02
$\mathcal{S}(1,1,0,1,0)$	0.002069	0.001983	1.572E-02	1.251E-05	1.573E-02

Table 3-4 (Continued).

a Computational Scenario	b Probability w/o Control	c Probability w Control	d Cuttings Release	e Groundwater Release	f Total Release
$\mathcal{S}(1,1,0,0,1)$	0.002069	0.001983	1.546E-02	1.243E-05	1.547E-02
$\mathcal{S}(1,0,2,0,0)$	0.001035	0.000991	1.562E-02	1.064E-05	1.563E-02
$\mathcal{S}(1,0,1,1,0)$	0.002069	0.001983	1.533E-02	1.036E-05	1.534E-02
$\mathcal{S}(1,0,1,0,1)$	0.002069	0.001983	1.507E-02	1.028E-05	1.508E-02
$\mathcal{S}(1,0,0,2,0)$	0.001035	0.000991	1.505E-02	1.008E-05	1.506E-02
$\mathcal{S}(1,0,0,1,1)$	0.002069	0.001983	1.479E-02	1.000E-05	1.480E-02
$\mathcal{S}(1,0,0,0,2)$	0.001035	0.000991	1.453E-02	9.922E-06	1.454E-02
$\mathcal{S}(0,3,0,0,0)$	0.000345	0.000348	1.415E-02	7.520E-06	1.416E-02
$\mathcal{S}(0,2,1,0,0)$	0.001035	0.001043	1.376E-02	5.374E-06	1.377E-02
$\mathcal{S}(0,2,0,1,0)$	0.001035	0.001043	1.347E-02	5.091E-06	1.348E-02
$\mathcal{S}(0,2,0,0,1)$	0.001035	0.001043	1.322E-02	5.013E-06	1.322E-02
$\mathcal{S}(0,1,2,0,0)$	0.001035	0.001043	1.337E-02	3.229E-06	1.338E-02
$\mathcal{S}(0,1,1,1,0)$	0.002069	0.002087	1.309E-02	2.945E-06	1.309E-02
$\mathcal{S}(0,1,1,0,1)$	0.002069	0.002087	1.283E-02	2.868E-06	1.283E-02
$\mathcal{S}(0,1,0,2,0)$	0.001035	0.001043	1.280E-02	2.661E-06	1.280E-02
$\mathcal{S}(0,1,0,1,1)$	0.002069	0.002087	1.254E-02	2.584E-06	1.255E-02
$\mathcal{S}(0,1,0,0,2)$	0.001035	0.001043	1.228E-02	2.507E-06	1.229E-02
$\mathcal{S}(0,0,3,0,0)$	0.000345	0.000348	1.299E-02	1.083E-06	1.299E-02
$\mathcal{S}(0,0,2,1,0)$	0.001035	0.001043	1.270E-02	7.992E-07	1.270E-02
$\mathcal{S}(0,0,2,0,1)$	0.001035	0.001043	1.244E-02	7.220E-07	1.244E-02
$\mathcal{S}(0,0,1,2,0)$	0.001035	0.001043	1.241E-02	5.155E-07	1.241E-02
$\mathcal{S}(0,0,1,1,1)$	0.002069	0.002087	1.215E-02	4.382E-07	1.216E-02
$\mathcal{S}(0,0,1,0,2)$	0.001035	0.001043	1.190E-02	3.610E-07	1.190E-02
$\mathcal{S}(0,0,0,3,0)$	0.000345	0.000348	1.213E-02	2.317E-07	1.213E-02
$\mathcal{S}(0,0,0,2,1)$	0.001035	0.001043	1.187E-02	1.545E-07	1.187E-02
$\mathcal{S}(0,0,0,1,2)$	0.001035	0.001043	1.161E-02	7.724E-08	1.161E-02
$\mathcal{S}(0,0,0,0,3)$	0.000345	0.000348	1.135E-02	0.000E+00	1.135E-02
$\mathcal{S}(4,0,0,0,0)$	0.000015	0.000012	2.784E-02	3.969E-05	2.788E-02
$\mathcal{S}(3,1,0,0,0)$	0.000058	0.000050	2.560E-02	3.227E-05	2.563E-02
.					
.					
.					
$\mathcal{S}(1,1,1,1,0)$	0.000349	0.000335	2.005E-02	1.287E-05	2.006E-02
.					
.					
.					
$\mathcal{S}(0,0,0,0,4)$	0.000015	0.000015	1.514E-02	0.000E+00	1.514E-02
.					
.					
.					
$\mathcal{S}(0,0,0,0,15)$	8.497E-25	8.569E-25	5.676E-02	0.000E+00	5.676E-02

Table 3-4 (Concluded).

Computational Scenario [a]	Probability w/o Control [b]	Probability w Control [c]	Cuttings Release [d]	Groundwater Release [e]	Total Release [f]
$\mathcal{S}^{+-}$(0, 2000)	0.000700	0.000632	1.392E-02	1.480E-05	1.394E-02
$\mathcal{S}^{+-}$(2000, 4000)	0.000700	0.000700	9.433E-03	5.082E-06	9.438E-03
$\mathcal{S}^{+-}$(4000, 6000)	0.000700	0.000700	8.657E-03	1.342E-06	8.659E-03
$\mathcal{S}^{+-}$(6000, 8000)	0.000700	0.000700	8.085E-03	3.162E-07	8.085E-03
$\mathcal{S}^{+-}$(8000,10000)	0.000700	0.000700	7.568E-03	5.080E-08	7.568E-03

a $\mathcal{S}(\mathbf{n})$and $\mathcal{S}^{+-}(t_{k-1},t_k)$ are defined in (3-11) and (3-18), respectively.

b Probabilities for $\mathcal{S}(\mathbf{n})$ (defined in 3-14)) and $\mathcal{S}^{+-}(t_{k-1},t_k)$ (defined in (3-21) and (3-40)), without a 100 yr period of administrative control in which drilling intrusions cannot take place.

c Same as b but with a 100 yr period of administrative control in which drilling intrusions cannot take place.

d Cuttings releases for $\mathcal{S}(\mathbf{n})$ and $\mathcal{S}^{+-}(t_{k-1},t_k)$ are defined in (3-16) and (3-23), respectively, with the groundwater component of the release set to zero.

e Groundwater releases for $\mathcal{S}(\mathbf{n})$ and $\mathcal{S}^{+-}(t_{k-1},t_k)$ are defined in (3-16) and (3-23), respectively, with the cuttings component of the release set to zero.

f Total releases for $\mathcal{S}(\mathbf{n})$ and $\mathcal{S}^{+-}(t_{k-1},t_k)$ are defined in (3-16) and (3-23), respectively.

Table 3-5. Probabilities and Normalized Releases for Computational Scenarios Used to Illustrate Scenario Construction Procedures with the Inclusion of Activity Loading Effects on the Cuttings Releases. The probabilities presented in this table were calculated for observation number 46 in the 1991 WIPP performance assessment (see Appendix B, Vol. 2), which resulted in the rate constant in the Poisson model for drilling (i.e., λ) equaling 8.4424E-05 yr^{-1}, and the activity loading distribution given in Table 2-7; the normalized releases were constructed from the values shown for $rGW1_i$ and rC_{ij} in Table 3-3.

a	b	c	d	e	f
Computational Scenario	Probability w/o Control	Probability w Control	Cuttings Release	Groundwater Release	Total Release
$\mathcal{S}$(0,0,0,0,0)	0.429886	0.433530	0.000E+00	0.000E+00	0.000E+00
$\mathcal{S}$(I;1,0,0,0,0)					
I=(1)	0.029201	0.027976	1.708E-04	9.922E-06	1.807E-04
I=(2)	0.021761	0.020848	1.708E-03	9.922E-06	1.718E-03
I=(3)	0.016274	0.015591	1.708E-02	9.922E-06	1.709E-02
I=(4)	0.001082	0.001036	1.708E-01	9.922E-06	1.708E-01
I=(5)	0.004268	0.004089	9.712E-05	9.922E-06	1.070E-04
	---	---			
	0.072585	0.069540			
$\mathcal{S}$(I;0,1,0,0,0)					
I=(1)	0.029201	0.029449	1.157E-04	2.507E-06	1.182E-04
I=(2)	0.021761	0.021945	1.157E-03	2.507E-06	1.160E-03
I=(3)	0.016274	0.016412	1.157E-02	2.507E-06	1.157E-02
I=(4)	0.001082	0.001091	1.157E-01	2.507E-06	1.157E-01
I=(5)	0.004268	0.004304	7.615E-05	2.507E-06	7.865E-05
	---	---			
	0.072585	0.073200			
$\mathcal{S}$(I;0,0,1,0,0)					
.					
.					
.					
$\mathcal{S}$(I;0,0,0,1,0)					
.					
.					
.					
$\mathcal{S}$(I;0,0,0,0,1)					
.					
.					
.					
$\mathcal{S}$(I;2,0,0,0,0)					
I=(1,1)	0.000992	0.000903	3.416E-04	1.984E-05	3.615E-04
I=(1,2)	0.000739	0.000673	1.879E-03	1.984E-05	1.899E-03
I=(1,3)	0.000553	0.000503	1.725E-02	1.984E-05	1.727E-02
I=(1,4)	0.000037	0.000033	1.710E-01	1.984E-05	1.710E-01
I=(1,5)	0.000145	0.000132	2.679E-04	1.984E-05	2.878E-04
I=(2,1)	0.000739	0.000673	1.879E-03	1.984E-05	1.899E-03
I=(2,2)	0.000551	0.000501	3.416E-03	1.984E-05	3.436E-03

Table 3-5 (Continued)

a Computational Scenario	b Probability w/o Control	c Probability w Control	d Cuttings Release	e Groundwater Release	f Total Release
.					
.					
.					
I=(5,5)	0.000021	0.000019	1.942E-04	1.984E-05	2.141E-04
	---	---			
	0.006128	0.005577			
$\mathcal{S}$(I;1,1,0,0,0)					
I=(1,1)	0.001984	0.001900	2.865E-04	1.243E-05	2.989E-04
I=(1,2)	0.001478	0.001416	1.328E-03	1.243E-05	1.340E-03
I=(1,3)	0.001105	0.001059	1.174E-02	1.243E-05	1.175E-02
I=(1,4)	0.000073	0.000070	1.159E-01	1.243E-05	1.159E-01
I=(1,5)	0.000290	0.000278	2.470E-04	1.243E-05	2.594E-04
I=(2,1)	0.001478	0.001416	1.824E-03	1.243E-05	1.836E-03
I=(2,2)	0.001102	0.001055	2.865E-03	1.243E-05	2.878E-03
.					
.					
.					
I=(5,5)	0.000042	0.000041	1.733E-04	1.243E-05	1.857E-04
	---	---			
	0.012256	0.011742			
$\mathcal{S}$(I;1,0,1,0,0)					
.					
.					
.					
$\mathcal{S}$(I;0,0,0,0,2)					
.					
.					
.					
$\mathcal{S}$(I;3,0,0,0,0)					
I=(1,1,1)	0.000022	0.000019	5.124E-04	2.977E-05	5.422E-04
I=(1,1,2)	0.000017	0.000014	2.050E-03	2.977E-05	2.079E-03
I=(1,1,3)	0.000013	0.000011	1.742E-02	2.977E-05	1.745E-02
.					
.					
.					
I=(2,3,5)	0.000001	0.000001	1.889E-02	2.977E-05	1.892E-02
.					
.					
.					
I=(5,5,5)	0.000000	0.000000	2.914E-04	2.977E-05	3.211E-04
	---	---			
	0.000345	0.000298			
$\mathcal{S}$(I;2,1,0,0,0)					
.					
.					
.					
$\mathcal{S}$(I;0,0,0,0,3)					

Table 3-5 (Concluded)

Computational Scenario [a]	Probability w/o Control [b]	Probability w Control [c]	Cuttings Release [d]	Groundwater Release [e]	Total Release [f]
.					
.					
.					
$\mathcal{S}(\mathbf{l};4,0,0,0,0)$					
.					
.					
.					

a $\mathcal{S}(\mathbf{l},\mathbf{n})$ is defined in (3-12).

b Probability for $\mathcal{S}(\mathbf{l},\mathbf{n})$ as defined in (3-15) without a 100 yr period of administrative control in which drilling intrusions cannot take place.

c Same as b but with a 100 yr period of administrative control in which drilling intrusions cannot take place.

d Cuttings release for $\mathcal{S}(\mathbf{l},\mathbf{n})$ from (3-17) with the groundwater component of the release set to zero.

e Groundwater release for $\mathcal{S}(\mathbf{l},\mathbf{n})$ from (3-17) with the cuttings component of the release set to zero.

f Total release for $\mathcal{S}(\mathbf{l},\mathbf{n})$ from (3-17).

The result of this calculation is shown in Figure 3-4. Specifically, the CCDF labeled "Groundwater" in Figure 3-4 was constructed from the probabilities and releases in the columns "Probability w Control" and "Groundwater Release" in Table 3-4. This is also the CCDF identified in Figure 3-1 as resulting from sample element 46. Similarly, when activity loading effects on the cuttings releases are not considered (i.e., all waste is assumed to be of the same average activity level), it is possible to systematically incorporate all the computational scenarios indicated in Table 3-4 into a CCDF for cuttings release and also into a CCDF for total release (i.e., cuttings release and groundwater release combined). The CCDF labeled "Cuttings without Activity Loading" in Figure 3-4 was constructed from the probabilities and releases in the columns "Probability w Control" and "Cuttings Release" in Table 3-4. Due to the small releases for groundwater transport, the CCDF constructed with the releases in the column "Total Release" is identical in appearance to the "Cuttings without Activity Loading" CCDF in Figure 3-4.

When activity loading effects for the cuttings releases are considered, it is necessary to use results of the form shown in Table 3-5. Due to the large number of computational scenarios that result from the many possible combinations of cuttings releases, it is not possible to systematically cover all scenarios of the form listed in Table 3-5. Rather, as described in Section 3.3, these computational scenarios are covered systematically up to a certain number of intrusions and then a switch is made to a Monte Carlo procedure. For the 1991 WIPP performance assessment, computational scenarios of the form shown in Table 3-5 were systematically covered up to $nB = 4$ boreholes; then, a switch was made to a Monte Carlo procedure that used a Latin hypercube sample of size $nR = 100$ for each computational scenario involving more than $nB = 4$ boreholes. The results of this calculation for cuttings release is shown in Figure 3-4. Specifically, the CCDF labeled "Cuttings with Activity Loading" in Figure 3-4 was constructed from the probabilities and releases in the columns "Probability w Control" and "Cuttings Release" in Table 3-5. This is also the CCDF for sample element 46 in Figure 3-2, although its exact identification is difficult due to the large number of closely placed CCDFs in this figure.

Activity loading effects can also be incorporated into the CCDF for total release. This involves use of the results in the column "Total Release" in Table 3-5 together with similar results for computational scenarios of the form $\mathcal{S}^{+-}(\mathbf{I}; t_{k-1}, t_k)$. Due to the small groundwater releases associated with sample element 46, this results in a CCDF for total release that is identical in appearance to the CCDF labeled "Cuttings with Activity Loading" in Figure 3-4. The CCDF that results from this construction procedure for sample 46 also appears in Figure 3-3, but is difficult to identify.

The CCDFs appearing in Figures 3-1 through 3-4 were constructed with the program CCDFPERM, which is part of the CAMCON system. Probabilities and normalized releases for computational scenarios are determined by CCDFPERM with the procedures illustrated in this section. To reduce storage requirements, CCDFPERM uses a binning algorithm of the type indicated in conjunction with (3-28) to accumulate the probabilities associated with individual computational scenarios. For the 1991 WIPP performance assessment, the binning algorithm used 100 increments per order of magnitude on the release axis. To reduce unnecessary calculations, CCDFPERM provides a mechanism to stop the CCDF construction procedure. Specifically, CCDFPERM determines the smallest integer n such that the probability of having exactly n boreholes over 10,000 years is less than B, where B is a user-specified quantity. Then, CCDFPERM only uses computational scenarios that involve less than or equal to n boreholes. For the 1991 WIPP performance assessment, B was specified to be 1×10^{-6}, which resulted in the omitted scenario probability being far below the 0.001 point used in defining the EPA release limits. Since the λ in the Poisson model was a sampled variable in the 1991 WIPP performance

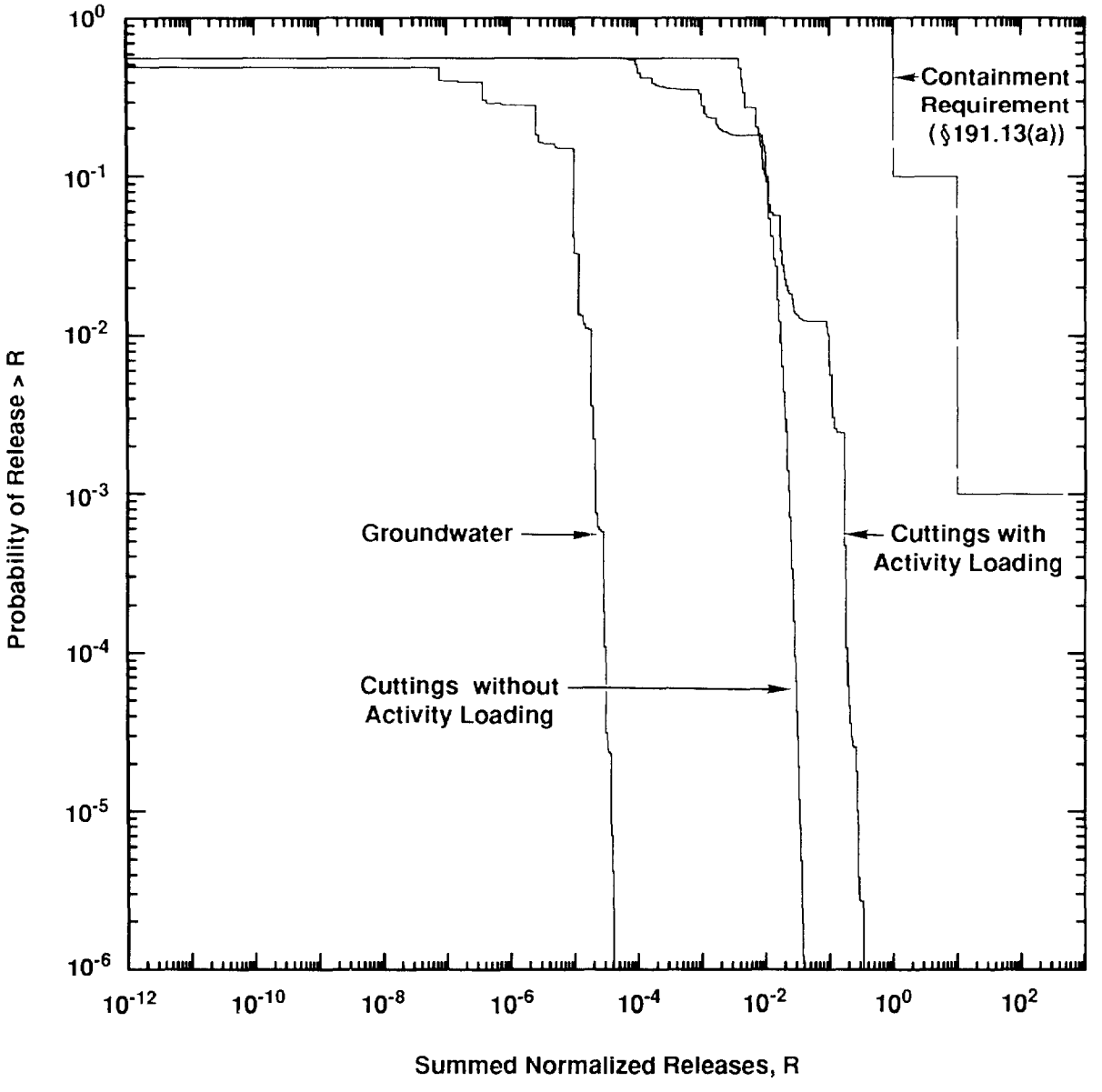

TRI-6342-1382-0

Figure 3-4. Estimated CCDFs for Sample Element 46.

assessment, the maximum number of boreholes used in CCDF construction varied from sample element to sample element.

There is actually some overlap (i.e., intersection) between the computational scenarios $S(\mathbf{n})$ and $S^{+-}(t_{k-1},t_k)$. That is, no correction has been made for the fact that some time histories in computational scenarios of the form $S(\mathbf{n})$ also belong to computational scenarios of the form $S^{+-}(t_{k-1},t_k)$. Further, as indicated in conjunction with (2-68), probabilities for the $S^{+-}(t_{k-1},t_k)$ are approximated with conservative relationships that actually bound the probabilities. As the probabilities for the scenarios $S(\mathbf{n})$ sum to 1, the total estimated probabilities for the computational scenarios $S(\mathbf{n})$ and $S^{+-}(t_{k-1},t_k)$ will be somewhat greater than 1. For example, the total probability for the computational scenarios indicated in Table 3-4 is 1.003432 when 100 years of administrative control is assumed. If desired, the probabilities for the individual computational scenarios could be defined with greater resolution, but the resultant relationship would be very complicated (e.g., see (2-67)). At present, the added complexity that these refined probabilities would require is not justified. Specifically, they would produce few visually identifiable shifts in the CCDFs shown in Figures 3-1 through 3-4, and the effects that they did produce would tend to shift the CCDFs downward. However, as a low-level correction, CCDFPERM does normalize the probabilities for computational scenarios involving two or more boreholes so that total computational scenario probability sums to 1.

The probability normalization performed by CCDFPERM is based on the ratio

$$R = \frac{\sum_{k=1}^{nT} pS^{+-}(t_{k-1},t_k)}{\sum_{\mathbf{n}\in\mathcal{A}} pS(\mathbf{n})}, \tag{3-41}$$

where $\mathbf{n}\in\mathcal{A}$ only if $\mathbf{n}$ has an element greater than or equal to 2 (i.e., if $S(\mathbf{n})$ designates a set of time histories in which two or more drilling intrusions can occur in the same time interval). Thus, R is the ratio between the estimated probability for all E1E2-type computational scenarios and the probability for all computational scenarios $S(\mathbf{n})$ that could contain an E1E2-type intrusion.

Once R is determined, CCDFPERM systematically goes through all computational scenarios $S(\mathbf{l},\mathbf{n})$ selected for consideration. For each $S(\mathbf{l},\mathbf{n})$, the probability $pS(\mathbf{l},\mathbf{n})$ and release $cS(\mathbf{l},\mathbf{n})$ are determined as shown in (3-15) and (3-17), respectively. If $\mathbf{n}\notin\mathcal{A}$, no modification to $pS(\mathbf{l},\mathbf{n})$ is made. If $\mathbf{n}\in\mathcal{A}$, then the probability $pS(\mathbf{l},\mathbf{n})$ is redefined to be $(1\text{-}R)\ pS(\mathbf{l},\mathbf{n})$. Further, $S^{+-}(\mathbf{l},\mathbf{n})$ is assigned the probability

$$pS^{+-}(\mathbf{l},\mathbf{n}) = R\, pS(\mathbf{l},\mathbf{n}), \tag{3-42}$$

where $pS(\mathbf{l},\mathbf{n})$ is the initial probability for $S(\mathbf{l},\mathbf{n})$ defined in (3-15) and

$$S^{+-}(\mathbf{l},\mathbf{n}) = \{x: x \text{ an element of } S(\mathbf{l},\mathbf{n}) \text{ in which at least one waste panel is penetrated by two or more boreholes during a time interval } [t_{i-1},t_i], \text{ of which at least one penetrates a pressurized brine pocket and at least one does not}\}. \tag{3-43}$$

The set $S^{+-}(\mathbf{l},\mathbf{n})$ is assigned the normalized release $S^{+-}(\mathbf{l};t_{k-1},t_k)$ in (3-24), where k is the smallest integer such that $S^{+-}(\mathbf{l},\mathbf{n}) \subset S^{+-}(\mathbf{l};t_{k-1},t_k)$. As $pS(\mathbf{l},\mathbf{n})$, $cS(\mathbf{l},\mathbf{n})$, $pS^{+-}(\mathbf{l},\mathbf{n})$ and $cS^{+-}(\mathbf{l},\mathbf{n})$ are determined, the probabilities $pS(\mathbf{l},\mathbf{n})$ and $pS^{+-}(\mathbf{l},\mathbf{n})$ are accumulated within the binning algorithm used in CCDFPERM.

The outcome of the preceding normalization procedure is that (1) probabilities for computational scenarios $S(\mathbf{l},\mathbf{n})$ that do not contain time histories also contained in a set $S^{+-}(\mathbf{l};t_{k-1},t_k)$ are unchanged, (2) probabilities for computational scenarios $S(\mathbf{l},\mathbf{n})$ that do contain time histories also contained in a set $S^{+-}(\mathbf{l};t_{k-1},t_k)$ are scaled down by a factor of $1-R$, (3) total probability for the computational scenarios $S^{+-}(\mathbf{l};t_{k-1},t_k)$ is unchanged, and (4) total probability for all computational scenarios sums to 1. Other normalizations are also possible. For example, a normalization could be used that also produces a downward scaling in the probabilities for $S^{+-}(\mathbf{l};t_{k-1},t_k)$, which are known to be overestimates. However, no "reasonable" normalization would have had a significant impact on the CCDFs produced for the 1991 WIPP performance assessment.

4. UNDISTURBED PERFORMANCE OF REPOSITORY/SHAFT

4.1 Conceptual Model

The overall hypothesized sequence of events in the disposal area for undisturbed conditions is summarized in the scenario discussion in Chapter 4 of Volume 1 and is repeated in more detail in Chapter 5 of Volume 1. The reader is encouraged to refer to the figures and the discussion in Volume 1 when reading about the models discussed in the remainder of Volume 2.

Generally, the repository/shaft system models for the undisturbed case consist of at most six components (or features): (1) a room or disposal region, (2) a panel and drift seal, (3) drift backfill, (4) shaft backfill and seal, (5) Salado Formation salt, and (6) anhydrite interbeds (MB139 and layers a and b, which are combined). These features comprise both the natural and engineered barriers to migration from waste panels during undisturbed conditions.

Groundwater flow and radionuclide migration are driven by gas generation in the waste disposal panels. Creep closure of the repository can also affect brine flow; however, the dynamics of this effect are not currently modeled. Two pathways for groundwater flow and radionuclide transport will likely dominate the disposal system (Figure 4-6 in Volume 1). In both, radionuclides enter MB139, either through fractures in salt or directly as a result of rooms and drifts intersecting the marker bed during construction or room closure. The head gradient tends to force radionuclide-bearing brine into MB139 beneath the panel, along the fractures in MB139 to the base of the shaft. Radionuclides may then move up the shaft to the Culebra dolomite member, and downgradient in the Culebra to the accessible environment. The second conceivable pathway is along MB139 to the subsurface extension of the accessible environment (5 km boundary) from the waste-disposal area (Figure 4-6 in Volume 1).

For the undisturbed scenario type, four primary generic computational models were used to assess the response of the repository/shaft system to this base case: BOAST II, a three-dimensional, multiphase code for isothermal Darcy flow; PANEL, an analytical model that estimates the discharge of radionuclides from a repository panel breached by a borehole; SUTRA, a two-dimensional, saturated or unsaturated, coupled flow and transport code; and STAFF2D, a two-dimensional, single-phase, flow or transport code.

The simulations described examine the importance of the principal migration pathways for radionuclides to reach the accessible environment during the undisturbed scenario. The hypothesized migration paths assume that under undisturbed conditions brine with dissolved radionuclides is expelled from the storage rooms by gas generated from anoxic corrosion of the containers and microbiological degradation of the waste. Because the computer codes SUTRA and STAFF2D model single-phase-flow instead of two-phase flow, liquid (brine) replaces gas in these simulations and the pores of the waste are assumed to be completely filled with liquid. An effect

of substituting a liquid source for the gas drive is that the liquid tends to leave the storage area in all directions, while gas-driven brine would be expected to leave the repository mainly through the floor (because the waste-generated gas rises to the top of the waste panels). To account for the presence of undissolved gas in an approximate sense using the single-phase codes SUTRA and STAFF2D, the material properties (permeability and porosity) can be modified to reflect the changes that occur as the result of varying gas saturation. These changes, in terms of brine (or gas) saturation, relative permeability, and porosity can be determined from a separate calculation with the two-phase code BOAST II, which does account for both gas generation and combined brine and gas flow.

SUTRA, STAFF2D, and PANEL were used to evaluate the flow of brine and the transport of dissolved radionuclides from the repository in the undisturbed case. Vertical cross-sections through the repository, anhydrite layers a and b, MB139, the drift, and the shaft were modeled to determine the path and extent of transport from the repository. Calculations assuming single-phase flow with and without properties modified by the effects of gas were performed.

Recognizing that radionuclide migration from the repository is three dimensional, additional calculations were performed with SUTRA modeling a horizontal plane through the repository. MB139 has been hypothesized to be the principal brine pathway out of the repository. In these calculations it was assumed that the entire waste repository was located within MB139. This conservative assumption eliminated any resistance to flow afforded by the DRZ between the repository and MB139, maximizing the advective flow in MB139.

STAFF2D and PANEL were the two codes used to quantify the transport of radionuclides up the shaft and away from the repository within MB139. Using these codes it was determined that the quantity of radionuclides passing a point 20 m up the shaft from the repository horizon and through a boundary 100 m away from the repository within MB139 were several orders of magnitude less than the EPA normalized limit of one. The SUTRA code was used primarily to verify the extent of transport calculated by STAFF2D and to assess the importance of transient gas pressures. SUTRA was also used to investigate some of the three-dimensional aspects of flow away from the repository. The BOAST II code was used to calculate the transient pressure from waste-generated gas and to provide relative permeabilities and porosities for use in the single-phase codes SUTRA and STAFF2D.

Subpart B of 40 CFR Part 191 (The Standard) limits the probabilities of cumulative releases of radionuclides to the accessible environment for 10,000 years and limits the dose to individuals for 1000 years after disposal (Volume 1, Chapter 1). Bounding calculations that show that no releases reach the accessible environment can be used to satisfy the requirement of the Standard for undisturbed conditions. It is not always intuitively obvious, however, that the selection of

extreme values for input parameters for computation have the effect of providing an upper bound on radionuclide transport.

In the following calculations for undisturbed performance, many of the assumptions were indeed conservative, tending to maximize transport away from the waste panel. However, this was not wholly true for all parameters; often average or median properties were used. Therefore, it cannot be claimed that these calculations are truly bounding. Indeed, it may not be possible to prove that any fixed set of assumed input parameters will produce a bounding result.

These calculations had several objectives:

- To determine the path and extent of migration of radionuclides from the waste panels, and to quantify the magnitude of radionuclide transport up the shaft.
- To evaluate (in an approximate sense) the effect of waste-generated undissolved gas on migration of radionuclides for undisturbed conditions.
- To assess the importance of three-dimensional effects on radionuclide migration in MB139.
- To cross-verify the results from the two single-phase codes SUTRA and STAFF2D.

4.2 Consequence Models

4.2.1 BOAST II AXISYMMETRIC APPROXIMATION OF TWO-PHASE FLOW—James E. Bean and James D. Schreiber

4.2.1.1 Model Overview

For undisturbed conditions, the generation of gas by corrosion and microbial degradation of waste is the principal driving force that moves brine and dissolved radionuclides out of the repository. The presence of an undissolved gas phase also affects the brine saturation and other material properties governing flow in and around the repository.

To account for these effects, the three-phase code BOAST II was used to calculate the pressure history, brine saturations and relative permeabilities within and adjacent to the repository waste panel. These parameters could then be used to modify material parameters (e.g., porosity and permeability) and calculate brine flow using the single-phase codes SUTRA and STAFF2D.

Since BOAST II was originally written as a petroleum reservoir model, the three phases normally considered are gas, oil, and water. In using BOAST II to simulate flow of brine and gas in and adjacent to the repository, only two of the three phases in the model are used. What is referred to as "oil" in BOAST II is given properties of brine. "Gas" is given properties of hydrogen gas. "Water" is not used. "Oil," rather than "water," is used to simulate brine simply as a matter of convenience. As long as the correct properties are used, the same results will be obtained regardless of which phase is used to simulate brine.

The following description of BOAST II hinges largely on a conceptualization of multiphase flow through porous media described in detail in Appendix A. The reader is encouraged to refer to Appendix A for a broader view of the underlying assumptions.

4.2.1.2 Model Description

Nomenclature

Symbols may appear with subscripts g (gas), o (oil), or w (water) substituted for phase subscript symbol p.

B_p = Formation volume factor for phase p [m^3 @ reservoir conditions/m^3 @ reference conditions]
CG_p = Collections of terms for phase p, defined by equations (4-15), (4-16), and 4-17 [s^{-1}]
c_p = Compressibility of phase p [Pa^{-1}]
c_r = Compressibility of rock [Pa^{-1}]
c_t = Total compressibility [Pa^{-1}]
g = Gravitational acceleration [m/s^2]
K = Absolute permeability [m^2]
k_{rp} = Relative permeability of phase p [dimensionless]
p_p = Pressure of phase p [Pa]
q_p = Well injection rate for phase p [m^3/s]
R_{sp} = Solubility of gas in phase p [m^3 gas/m^3 phase p]
S_p = Saturation of phase p [m^3 phase p/m^3 void]
v_p = Darcy velocity (or flux) of phase p [m^3 phase p/(s•m^2 cross-section flow area)]
λ_p = Mobility of phase p [$(Pa•s)^{-1}$]
μ_p = Viscosity of phase p [Pa•s]
ρ_p = Density of phase p [kg/m^3]
ϕ = Porosity [m^3 void/m^3 rock]
∇ = Gradient operator [m^{-1}]
$\nabla \bullet$ = Divergence operator [m^{-1}]

Description

BOAST II (Black Oil Applied Simulation Tool, enhanced version) is a petroleum reservoir model that simulates isothermal Darcy flow in three dimensions. BOAST II assumes that reservoir fluids can be described by three fluid phases, two that are immiscible fluids and a third that is conceptually a gas soluble in each of the other two. Each phase has a constant composition with physical properties that depend only on pressure. All three phases, as well as the porous medium, are assumed to be compressible. A complete description of BOAST II and its capabilities

is found in Fanchi et al. (1987). The model description that follows is based closely on the presentation in Fanchi et al. (1982).

BOAST II uses a finite-difference, implicit-pressure, explicit-saturation (IMPES) numerical technique to solve the three differential mass balance equations that describe the simultaneous flow of the three phases. In the IMPES procedure, the mass balance for gas is recast in terms of fluid pressures, and the equations for the other two phases are written in terms of the saturations of each phase. This procedure simplifies the solution, but the explicit solution of the pressure equation results in certain limitations. For example, neither the pressure or the saturations can change rapidly (as in "coning" situations where liquid flow converges rapidly toward a well) because the IMPES solution technique then requires an impracticably small time step. This problem will also occur if the capillary pressure is not constant. The system of algebraic equations resulting from discretizing the differential equations can be solved using either direct or iterative techniques. Boundary conditions other than no-flow conditions must be specified by wells. Well models in BOAST II allow rate or pressure constraints on well performance to be specified so that gas generation and brine sinks can be simulated in a variety of realistic ways. Time steps are adjusted automatically to ensure accurate solutions. Permeabilities can be varied in each of the three orthogonal directions, and porosities can vary from cell to cell.

BOAST II solves the flow equations for three fluid phases in three dimensions in a porous medium. In the discussion that follows, the three fluid phases are referred to as oil, water, and gas, in keeping with the original development of BOAST II as an oil reservoir simulator (Fanchi et al., 1982). The flow, or mass conservation, equations for each phase, in their simplest form, are:

$$-\nabla \bullet \frac{\vec{v}_o}{B_o} - \frac{q_o}{\rho_{osc}} = \frac{\partial}{\partial t}\left(\phi S_o / B_o\right) , \tag{4-1}$$

$$-\nabla \bullet \frac{\vec{v}_w}{B_w} - \frac{q_w}{\rho_{wsc}} = \frac{\partial}{\partial t}\left(\phi S_w / B_w\right) , \tag{4-2}$$

and

$$-\nabla \bullet \left(\frac{\vec{v}_g}{B_g} + \frac{R_{so}}{B_o}\vec{v}_o + \frac{R_{sw}}{B_w}\vec{v}_w \right) - \frac{q_g}{\rho_{gsc}} = \frac{\partial}{\partial t}\left[\phi \left(\frac{S_g}{B_g} + \frac{R_{so}\, S_o}{B_o} + \frac{R_{sw}\, S_w}{B_w} \right) \right] . \tag{4-3}$$

where the symbol $\nabla \bullet \vec{v}_p$ is shorthand for the divergence of the velocity of phase p:

$$\nabla \bullet \vec{v}_p = \frac{\partial}{\partial x} v_{xp} + \frac{\partial}{\partial y} v_{yp} + \frac{\partial}{\partial z} v_{zp} \ . \tag{4-4}$$

The parameters B_O, B_w, and B_g are formation volume factors in units of volume at reservoir conditions/volume at reference or standard conditions. (The subscript *sc* refers to standard conditions.) R_{so} and R_{sw} are solubilities of gas in oil and water, respectively.

The phase densities are related to formation volume factors and gas solubilities by

$$\rho_O = \frac{1}{B_O}\left[\rho_{osc} + R_{so}\rho_{gsc}\right], \tag{4-5}$$

$$\rho_w = \frac{1}{B_w}\left[\rho_{wsc} + R_{sw}\rho_{gsc}\right], \tag{4-6}$$

and

$$\rho_g = \frac{\rho_{gsc}}{B_g}. \tag{4-7}$$

The velocities $\vec{v}_p$ are assumed to be Darcy velocities and their x-components are

$$v_{xp} = -K_x\lambda_p\frac{\partial}{\partial x}\left[p_p - \rho_p g z\right]. \tag{4-8}$$

Similar expressions can be written for the y and z components. This equation is generally valid for incompressible fluids (oil and water). It is also valid for compressible fluids (gas), as long as the flow is irrotational and the fluid density is a function of pressure only (Bear, 1972), which is true for the simulations done using BOAST II.

The phase mobility λ_p is defined as the ratio of the relative permeability to flow of the phase divided by its viscosity; thus,

$$\lambda_p = k_{rp}/\mu_p. \tag{4-9}$$

The presence of oil, water, and gas phase pressures in (4-8) complicates the problem. For many situations, the difference between phase pressures is much smaller than the individual phase potentials and can be either ignored or treated less rigorously mathematically. The handling of the phase pressures and potentials in the flow equations can be simplified by using the capillary pressure concept. BOAST II defines the difference in phase pressures as

$$p_{cow} = p_O - p_w \tag{4-10}$$

and

$$p_{cgo} = p_g - p_o \cdot \tag{4-11}$$

The differences p_{cow} and p_{cgo} are the capillary pressures of oil-to-water and gas-to-oil phases, respectively. Experimentally p_{cow} and p_{cgo} have been observed to be principally functions of water and gas saturations, respectively.

Combining (4-1) through (4-3) with (4-8), (4-9), (4-10), and (4-11) and rearranging yields

Oil

$$\nabla \bullet \left[\vec{K} \bullet \left(\frac{\lambda_o}{B_o} \right) \nabla p_o \right] + CG_o - \frac{q_o}{\rho_{osc}} = \frac{\partial}{\partial t} \left(\phi \frac{S_o}{B_o} \right) \tag{4-12}$$

Water

$$\nabla \bullet \left[\vec{K} \bullet \left(\frac{\lambda_w}{B_w} \right) \nabla p_o \right] + CG_w - \frac{q_w}{\rho_{wsc}} = \frac{\partial}{\partial t} \left(\phi \frac{S_w}{B_w} \right) \tag{4-13}$$

and Gas

$$\nabla \bullet \left[\vec{K} \bullet \left(\frac{\lambda_g}{B_g} + \frac{R_{so}\lambda_o}{B_o} + \frac{R_{sw}\lambda_w}{B_w} \right) \nabla p_o \right] + CG_g - \frac{q_g}{\rho_{gsw}}$$

$$= \frac{\partial}{\partial t} \left[\phi \left(\frac{S_g}{B_g} + \frac{R_{so}S_o}{B_o} + \frac{R_{sw}S_w}{B_w} \right) \right] \tag{4-14}$$

The notation $\vec{K}$ signifies that permeability is a second-order tensor. The common assumption is made that the coordinate axes of the reference system are aligned along the principal axes of $\vec{K}$. The gravity and capillary contributions to the phase pressures have been collected in the terms CG_o, CG_w, and CG_g:

$$CG_o = -\nabla \bullet \left[\vec{K} \bullet \left(\frac{\lambda_o}{B_o} \right) \nabla (\rho_o g z) \right] \tag{4-15}$$

$$CG_w = -\nabla \bullet \left[\vec{K} \bullet \left(\frac{\lambda_w}{B_w} \right) \nabla(\rho_w g z + p_{cow}) \right] \tag{4-16}$$

and

$$CG_g = \nabla \bullet \left\{ \vec{K} \bullet \left(\frac{\lambda_g}{B_g} \nabla\left(p_{cgo} - \rho_g g z\right) - \frac{R_{so}\lambda_o}{B_o} \nabla(\rho_o g z) - \frac{R_{sw}\lambda_w}{B_w} \nabla\left(p_{cow} + \rho_w g z\right) \right) \right\} \tag{4-17}$$

Essentially BOAST II's task is to solve (4-12) through (4-14) and (4-18) (discussed below) for the four unknowns p_o, S_o, S_w, and S_g. All other physical properties in the equations are known, in principle, as functions of the four unknowns, or from field and laboratory data.

The procedure BOAST II uses to solve the flow equations requires combining (4-12) through (4-14) with the equality

$$S_o + S_w + S_g = 1 \tag{4-18}$$

such that only one equation for the unknown pressure p_o remains:

$$\left(B_o - R_{so}B_g\right)\left[\nabla \bullet \left(\vec{K} \bullet \frac{\lambda_o}{B_o} \nabla p_o \right) + CG_o - \frac{q_o}{\rho_{osc}} \right]$$

$$+\left(B_w - R_{sw}B_g\right)\left[\nabla \bullet \left(\vec{K} \bullet \frac{\lambda_w}{B_w} \nabla p_o \right) + CG_w - \frac{q_w}{\rho_{wsc}} \right]$$

$$+B_g\left\{ \nabla \bullet \left[\vec{K} \bullet \left(\frac{\lambda_g}{B_g} + \frac{R_{so}\lambda_o}{B_o} + \frac{R_{sw}\lambda_w}{B_w} \right) \nabla p_o \right] + CG_g - \frac{q_g}{\rho_{gsc}} \right\} = \frac{\phi c_t \partial p_o}{\partial t} \tag{4-19}$$

The equation in (4-19) is called the pressure equation because no explicit time derivatives of saturations are present. BOAST II solves the three-dimensional, three-phase flow equations by first numerically solving the pressure equation for p_o, then using the results in (4-20), (4-21), and (4-18) to find the phase saturations.

Oil

$$\frac{\partial}{\partial t}\left(\phi\frac{S_o}{B_o}\right)=\nabla\bullet\left(\vec{\vec{K}}\bullet\frac{\lambda_o}{B_o}\nabla p_o\right)+CG_o-\frac{q_o}{\rho_{osc}} \tag{4-20}$$

Water

$$\frac{\partial}{\partial t}\left(\phi\frac{S_w}{B_w}\right)=\nabla\bullet\left(\vec{\vec{K}}\bullet\frac{\lambda_w}{B_w}\nabla p_o\right)+CG_w-\frac{q_w}{\rho_{wsc}} \tag{4-21}$$

The oil, water, gas, rock, and total compressibilities are identified as

$$c_o=-\frac{1}{B_o}\frac{\partial B_o}{\partial p_o}+\frac{B_g}{B_o}\frac{\partial R_{so}}{\partial p_o}\ , \tag{4-22}$$

$$c_w=-\frac{1}{B_w}\frac{\partial B_w}{\partial p_o}+\frac{B_g}{B_w}\frac{\partial R_{sw}}{\partial p_o}\ , \tag{4-23}$$

$$c_g=-\frac{1}{B_g}\frac{\partial B_g}{\partial p_o}\ , \tag{4-24}$$

$$c_r=\frac{1}{\phi}\frac{\partial\phi}{\partial p_o}\ , \tag{4-25}$$

and

$$c_t=c_r+c_oS_o+c_wS_w+c_gS_g \tag{4-26}$$

respectively.

Code Modifications for CAMCON Version

A number of improvements have been incorporated into the version used in CAMCON.

- BOAST II has been tied into CAMCON via the preprocessor, PREBOAST, and the postprocessor, POSTBOAST.
- Darcy velocities of each phase in each direction can be calculated and included in the output along with time-dependent phase pressures and saturations.
- Interpolation between values of physical properties in lookup tables has been improved for greater speed.
- Rock compressibility calculations have been modified from the original version. Non-zero capillary pressures can now be used although the IMPES formulation may require the capillary pressure to be constant to maintain reasonable time steps.

- An algebraic multigrid (AMG) solver (Ruge and Stuben, 1987) has been added; it is much faster and requires far less memory than the direct solver and is more accurate and robust than the other iterative solvers in BOAST II. The multigrid solution is checked by following it with at least one iteration of a point-successive overrelaxation solver. The advantage of AMG over simple iterative or even direct methods commonly used in groundwater flow and transport programs is more pronounced with finer meshes.

4.2.1.3 Spatial Grid

Although BOAST II has three-dimensional capabilities, the complexity of the WIPP repository or even of a waste panel precludes using BOAST II in three dimensions. Consequently, the geometry used in the two-phase model for undisturbed performance represents a cylindrical, equivalent panel surrounded by the Salado Formation with anhydrite layers above and below (Figure 4-1). The region modeled extends upward to the Culebra, downward to the Castile Formation, and outward approximately 21 kilometers. The Castile and Culebra were included because they represent the major sources and sinks for brine flow to and from the repository. The far-field boundary is intended to be far enough away to justify the use of a no-flow boundary without the boundary affecting the behavior of the repository. Anhydrite layers a and b immediately above the repository have been consolidated into a single layer with a thickness equal to the combined thicknesses of a and b and located at the elevation of layer b. The panel thickness was chosen to be 2 m. The floor area of the cylindrical panel is the same as the enclosed area of an actual equivalent panel, including the area occupied by pillars. To account for the inclusion of the pillars, the porosity of the panel is adjusted (decreased) from the original waste porosity. The initial brine saturation is also adjusted for the presence of pillars fully saturated with brine. The disturbed rock zone (DRZ) extends vertically upward through the anhydrite layer and downward through MB139. Beyond the outer radius of the panel, both the anhydrite layers and the Salado are intact.

4.2.1.4 Material Properties, Boundary Conditions, and Initial Conditions

The generation of hydrogen as a result of corrosion and microbial action was simulated by means of gas injection wells in the repository grid blocks. Gas generation resulting from anoxic corrosion was assumed to occur for the first 450 years at a fixed rate of 2 moles per equivalent drum per year (Brush and Lappin, 1990), with the repository capacity being 556,000 equivalent drums. During the first 600 years, microbial action was assumed to generate gas at a fixed rate of 1 mole per equivalent drum per year (Brush and Lappin, 1990). Thus, the total gas generation rate from 0 to 450 years was 3 moles per drum per year, and from 450 to 600 years, the rate was 1 mole per drum per year. All corrodible metal was assumed to be reacted in 450 years, so corrosion

ceased then. Biodegradable material in the waste was completely consumed in 600 years, so gas generation by microbial processes ended then. The injection rates actually used in the model were on the basis of a unit volume of repository, or panel, grid block: 2.5×10^{-9} m^3 H_2/ ($s \cdot m^3$ panel) for years 0 to 450, 8.3×10^{-10} m^3 H_2/ ($s \cdot m^3$ panel) for years 450 to 600, and 0 m^3 H_2/ ($s \cdot m^3$ panel) for years 600 to 10,000. The gas generation rates used for anoxic corrosion and biodegradation were based on values available at the time the calculations were performed and do not necessarily correspond to values given in Volume 3 of this report. Currently, anoxic corrosion at 2 moles per drum equivalent corresponds to twice the maximum rate for humid conditions and a biodegradation rate of 1 mole per drum equivalent corresponds to the maximum rate for humid conditions (see Brush, July 8, 1991, memo, Volume 3).

For initial conditions, the brine saturation in the waste was assumed to be 13%; when averaged in with the pillars in the enclosed panel, which were assumed to be fully saturated with brine, the panel average saturation was 19.2% (80.8% gas saturation). The value chosen for initial brine saturation (13%) was selected from literature values reported for analogous materials. The uncertainty in this value was addressed in the calculations for Disturbed Conditions by varying it from zero to the residual saturation of the waste, 27.6%, but for the Undisturbed Conditions, the fixed value of 13% was used. In all other regions, an initial brine saturation of 100% was used.

The initial pressure in the equivalent panel was 0.1 MPa (1 atm). Initial far-field pressures were not known with any certainty, so a value midway between hydrostatic (~7 MPa at the repository elevation) and lithostatic pressure (~15 MPa at the elevation of the repository) was chosen, 11 MPa. An average gradient midway between hydrostatic and lithostatic was used to vary the far-field pressure with depth. No-flow boundary conditions were used on all six sides of the region modeled.

Because of the Implicit Pressure-Explicit Saturation formulation used in BOAST II, stability requirements initially resulted in time steps that were too small for 10,000-year simulations. To overcome this limitation, the capillary pressure, which is a nonlinear function of saturation, was assumed to be constant and equal to the threshold displacement pressure. The threshold displacement pressure is the pressure that is just large enough for gas to enter and move through a fully brine-saturated porous medium and displace some brine from it. This assumption allows simulations to proceed at a reasonable time step size. A fully implicit code, such as BRAGFLO (see Chapter 5), is less sensitive to the nonlinearities of the capillary pressure function; however, this code was not ready for use when these calculations were done, and was used only for the calculations for disturbed conditions with borehole intrusion.

4.2.1.5 Results and Discussion

Figure 4-2 illustrates the pressure in the repository as a function of time. As a result of gas generation, the pressure increases from 0.1 MPa initially to approximately 15.5 MPa after about 500 years. The pressure at that time exceeds lithostatic (~15 MPa). The effect of internal pressure near lithostatic would cause an actual waste panel to inflate slightly, forcing salt to creep outward to relieve the rising pressure in the repository. BOAST II ignores these creep effects.

Figures 4-3 and 4-4 provide vertical slices through the grid near the repository panel boundary of the brine relative permeability and the brine saturation. It can be seen in Figure 4-4 that gas has moved up into the DRZ and anhydrite layers within the first 1000 years (31.5×10^9 s). At 1000 years and later, the brine saturation was greater than residual saturation (0.276). Because the initial brine saturation in the waste was below residual saturation, there had to be a period of time during the first 1000 years in which brine flowed into the waste, some of it draining from the DRZ and some flowing in from the anhydrite layers and MB 139. This brought the brine saturation in the waste above residual saturation, thus allowing brine to brine flow. After 1000 years, the relative permeability to brine flow in the waste decreases continuously to 10,000 years, which indicates that brine saturation is decreasing. Therefore, brine is flowing out of the waste, transporting radionuclides away from the repository.

To determine the amount of radionuclides that leave the repository, a transport model such as SUTRA or STAFF2D, rather than just a flow model such as BOAST II, was needed. However, since SUTRA and STAFF2D are single-phase models, it was necessary to modify the material properties to simulate the effect of gas generation on brine flow. The relative permeability results from these BOAST II calculations, as shown in Figure 4-3, were used to modify the waste, DRZ, and anhydrite permeabilities used by STAFF2D and SUTRA in order to model the effects of gas on radionuclide transport. These calculations are discussed in Sections 4.2.2 and 4.2.3.

4.2.2 STAFF2D VERTICAL CROSS SECTION SIMULATIONS—David K. Rudeen

4.2.2.1 Model Overview

Gas generation within the repository is expected to be the primary driving force causing radionuclides to be driven out of the waste repository into the adjacent halite and anhydrite layers. To determine the primary pathways and estimate the magnitude of the release, finite-element flow and transport calculations were performed in a vertical cross section that passed through the repository, drift, shaft, and surrounding geology. The intent of these calculations is *not* to predict the actual behavior of the repository, but to show with conservative calculations that release to the accessible environment will not exceed current EPA standards. Models and most parameters were chosen to maximize release yet still be within expected ranges.

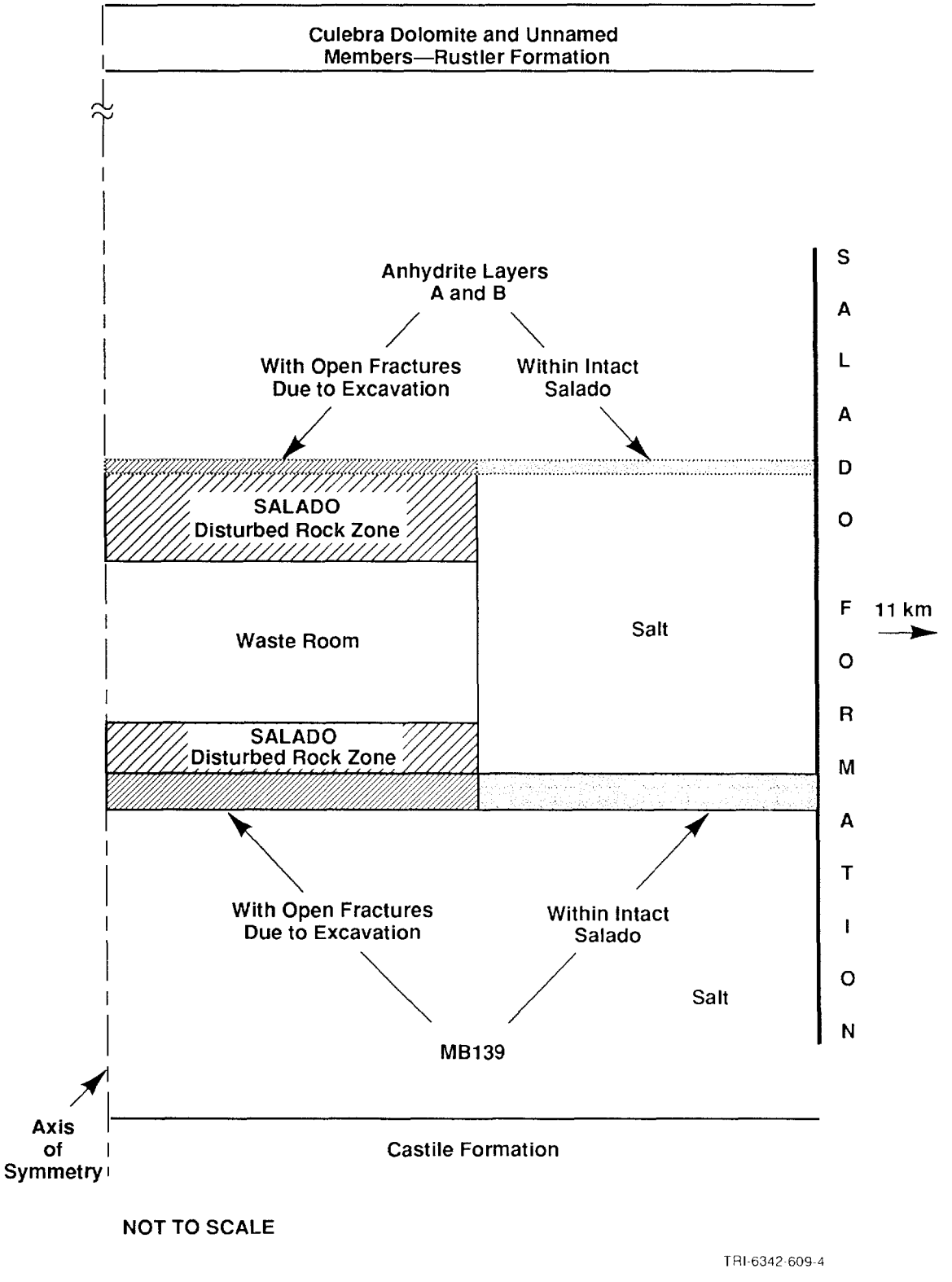

Figure 4-1. BOAST II Geologic/Waste Panel.

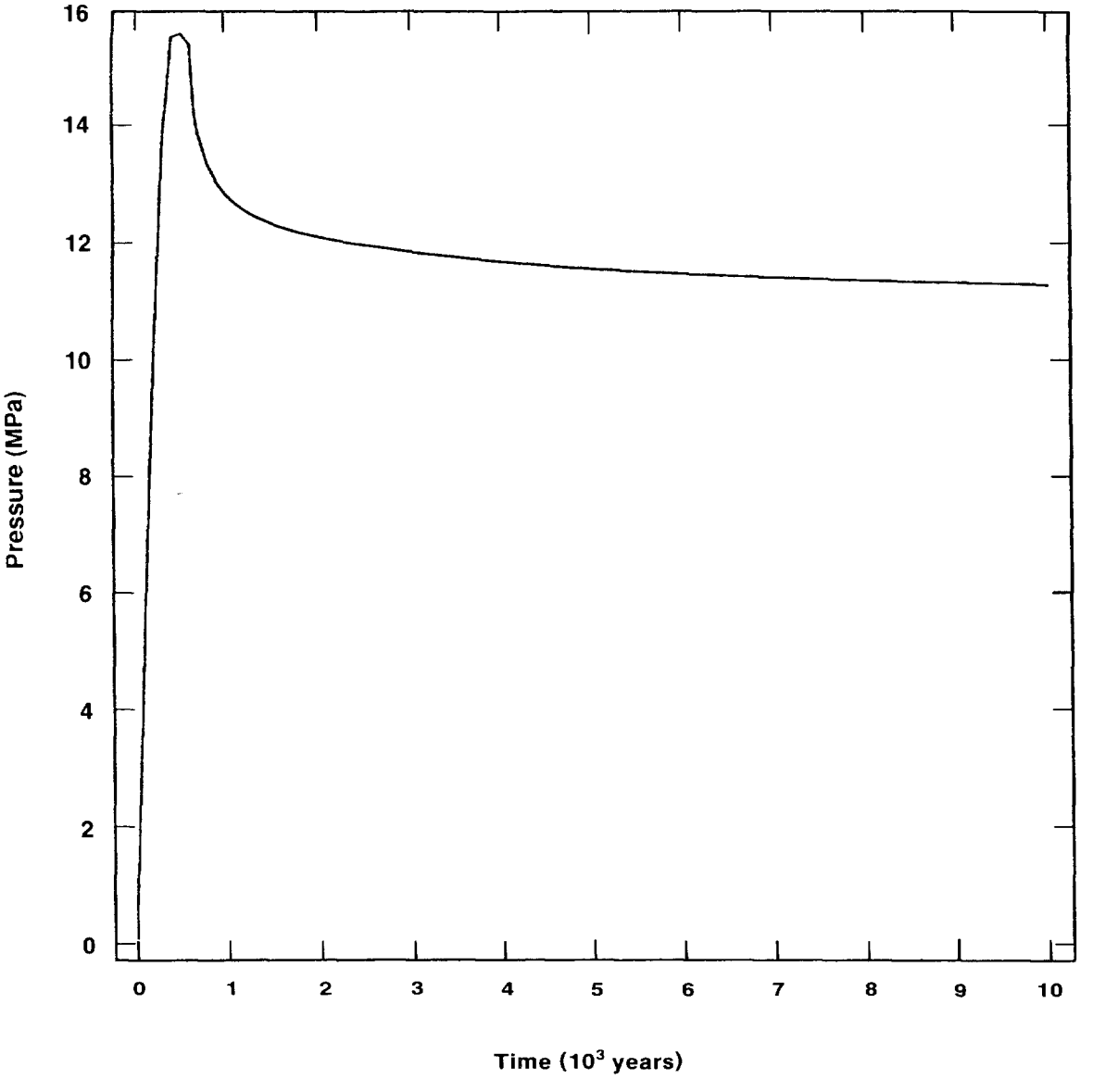

Figure 4-2. Equivalent Panel Pressure as a Function of Time

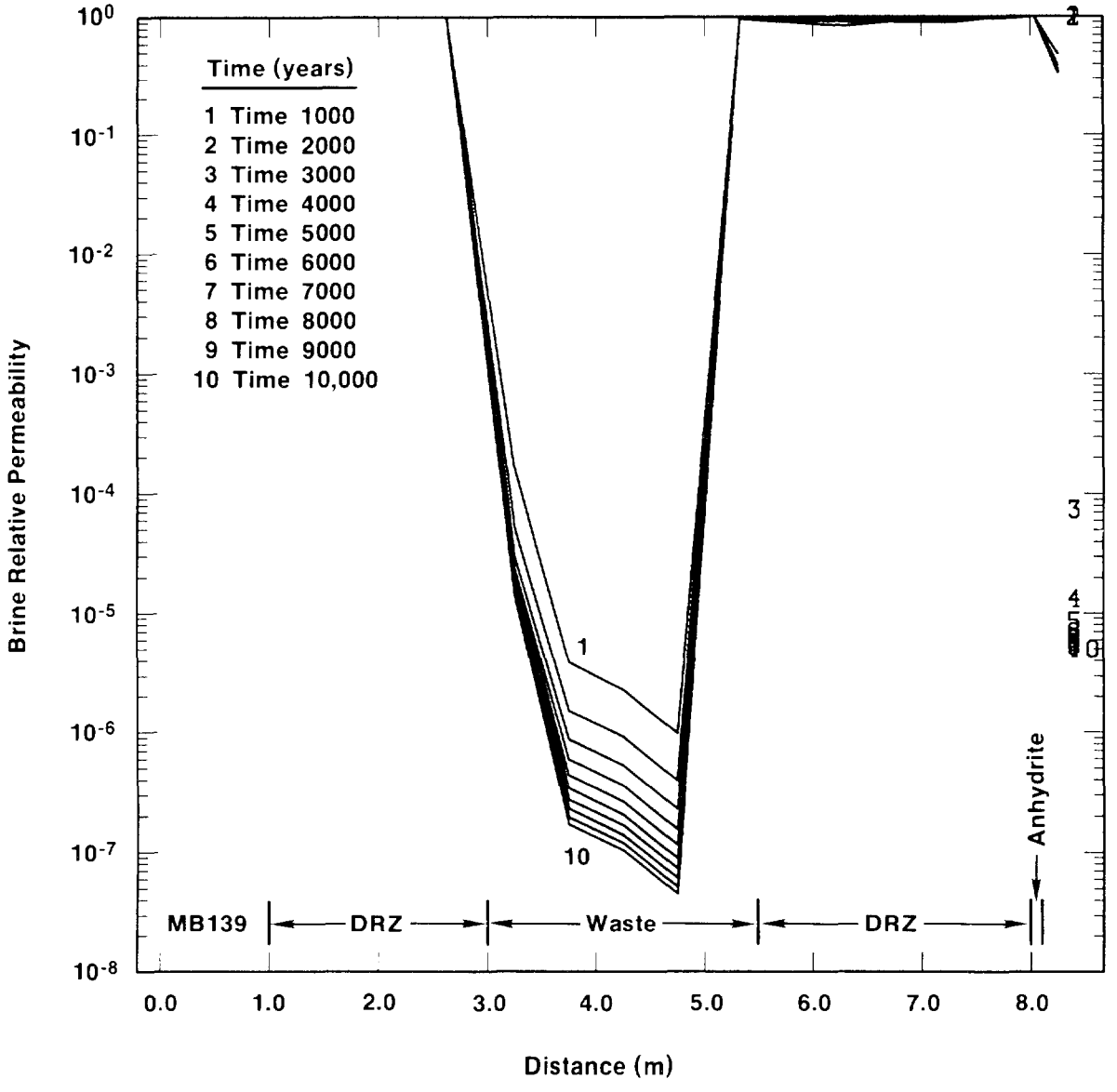

Figure 4-3. Brine Relative Permeability Profile From Bottom of MB139 to Top of Anhydrite

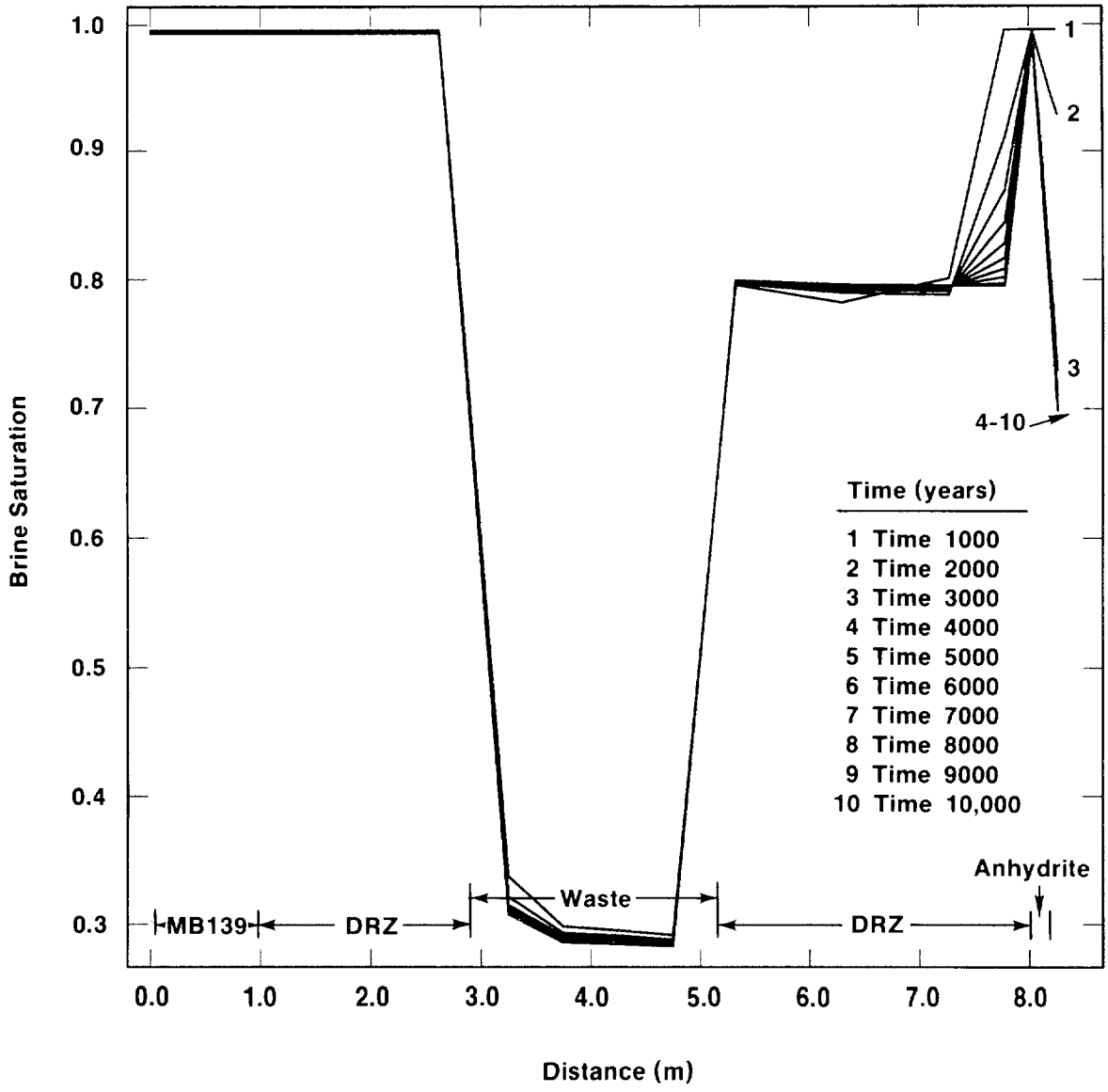

Figure 4-4. Brine Saturation Vertical Profile from Bottom of MB139 to Top of Anhydrite

The simulations in the model described here are designed to study the effect of the repressurization of the repository as the result of gas generation. The hypothesized episodes described in Section 4.1 assume that under undisturbed conditions, the repository remains in a gas-filled state after brine is expelled. Brine is expelled from the repository by the gas, which is generated from anoxic corrosion of the containers and microbiological degradation of the waste. The generation of gas causes a decrease in the brine volume in the pores. There is less brine available for transport and it is more disconnected; therefore the effective porosity, effective permeability, and effective diffusion are reduced. Because STAFF2D models saturated groundwater flow instead of gas, liquid (brine) replaces the gas in these simulations, and the repository is assumed to be completely saturated. Pressurized pore liquid becomes the force driving brine out of the repository. The brine generation is not realistic but an artifact of the pressure boundary condition applied to the nodes in the interior of the repository. An influx of brine is required to maintain the pressure above ambient. The effect of substituting a brine source for the gas drive is that brine leaves the storage area in all directions; gas-driven brine would be expected to leave primarily through the floor (because gas rises to the top of the repository) and then circle outward and up within the DRZ and host rock. The effect of gas generation on effective properties will be examined in later sections of this report (see Section 4.2.3 and Pseudo-Unsaturated Flow discussion in Section 4.2.2.6).

These calculations are an extension of those reported in the parameter sensitivity studies of Rechard et al. (1990b). In the current calculations, (1) the undisturbed MB139 is included beyond the repository, (2) the anhydrite layers above the repository are also included, (3) the drift seals have been removed, (4) the entire repository is modeled rather than only one room, (5) material properties have been updated to the current best estimates (Volume 3), particularly the effective diffusion coefficient, which includes tortuosity. STAFF2D requires the input of an effective diffusion coefficient ($D^o\tau$) where D^o (length^2/time) is the free water diffusion coefficient and τ (length/length) is the tortuosity. Including tortuosity has the effect of dropping the effective diffusion by about one order of magnitude. This results in less radionuclide diffusion into the surrounding host rock making more radionuclides available for advective transport along (or "within") MB139. Solute diffusing into the surrounding rock does not diffuse back because, with the constant pressure and concentration source, there is no solute pulse propagating away from the repository. Diffusion is constantly away from the repository, which is another conservative aspect of the model.

Analysis was performed primarily with two computer codes: STAFF2D and PANEL. The STAFF2D finite-element code calculated the steady-state flow and transient transport of a passive solute from the waste repository assuming a constant panel pressure. The choice of a constant

pressure tends to maximize flow away from the repository over 10,000 years.* Calculations with STAFF2D used either median properties or effective properties adjusted to account for desaturation. The source concentration of the passive solute was 1 kg/m^3. Simple scaling was then be used to estimate field concentrations for radionuclides with specific source concentration determined by their solubility limits. Steady-state flow was driven by a constant pressure of 17 MPa within the repository. The value chosen was the peak pressure seen from preliminary two-phase calculations similar to Section 4.2.1.5 that had been completed at the time this analysis was initiated. The PANEL code was used to calculate the quantity of radionuclides dissolved in the brine passing through the repository. The PANEL results, which take into account repository and radionuclide properties, were assumed to be source values that were scaled by the STAFF2D normalized concentrations to obtain conservative estimates of concentrations for specific radionuclides.

4.2.2.2 Model Description

STAFF2D (Solute Transport and Fracture Flow in 2 Dimensions) is a two-dimensional, finite-element code designed to simulate groundwater flow and solute transport in fractured or porous aquifers (Huyakorn et al., 1991). The original version was developed through a joint effort by HydroGeoLogic, Inc., and the International Ground Water Modeling Center of the Holcomb Research Institute. Improved versions of the code have since been commercially available through HydroGeoLogic, the latest being Version 3.2. CAMCON originally adapted Version 2.0 of the code and has since included upgrades from Version 3.2. Additional changes to the code have been made to accommodate CAMCON input/output requirements and tailor code inputs to the WIPP database (Rechard et al., 1989). The model description that follows is based closely on the presentation in Huyakorn et al. (1991).

Governing Physical Equations

Fluid Flow. The model description for fluid flow that follows is based closely on the presentation in Huyakorn et al. (1991). The governing equation for fluid flow in STAFF2D is

$$\frac{\partial}{\partial x_i}\left(T_{ij}\frac{\partial h}{\partial x_j}\right) = S\frac{\partial h}{\partial t} - \Lambda - q, \; i = 1,2 \tag{4-27}$$

where,

* Steady-state calculations neglect the effects of flow transients. To address this, transient STAFF2D flow and transport calculations using a constant repository pressure were performed after the bulk of this report went to press and consequently could not be reported here in detail. Briefly, the transient integrated flow and transport results were within 10% of the results determined using a steady flow assumption. The reader is also directed to the SUTRA calculations of Section 4.3.3.2, where fully transient calculations were performed.

h = hydraulic head (length)

T_{ij} = transmissivity tensor (length^2/time)

S = storage coefficient (dimensionless)

Λ = volumetric rate of fluid transfer per unit area from porous matrix blocks to the fracture when using dual-porosity flow (length^3/(time•length^2))

q = volumetric rate of fluid flow per unit area for sources or sinks (length^3/(time•length^2))

In accordance with standard definitions for transmissivity and storage coefficient, T_{ij} and S can be expressed as

$$T_{ij} = \phi_f H K_{ij} \tag{4-28}$$

and

$$S = \phi_f H S_s \text{ for confined aquifers} \tag{4-29}$$

where,

H = formation thickness (length)

K_{ij} = hydraulic conductivity tensor (length/time)

ϕ_f = porosity (fracture or secondary porosity for dual porosity) (dimensionless)

S_s = specific storage coefficient (1/length).

The term Λ represents the interaction between the porous rock matrix and fractures and is analogous to the Γ_ℓ in the transport equation. For the flow calculated here, Λ is assumed to be zero. The fluid exchange between the matrix and fractures in the Culebra dolomite is assumed to negligible. The q term is also zero. The fluid injected into the Culebra at the intrusion borehole that carries dissolved nuclides is assumed to have negligible effect on the existing flow field.

Transport. STAFF2D can perform both fluid flow and transport problems. The governing equations for transport in STAFF2D are

$$\frac{\partial}{\partial x_i}\left(D_{ij}\frac{\partial c_\ell}{\partial x_j}\right) - V_i\frac{\partial c_\ell}{\partial x_i} = \phi R_\ell \frac{\partial c_\ell}{\partial t} + \phi R_\ell \lambda_\ell c_\ell - \sum_{m=1}^{M} \xi_{\ell m}\phi R_m \lambda_m c_m - q\left(c_\ell^* - c_\ell\right) - \Gamma_\ell$$

$$\ell = 1, 2, \ldots, M \quad species, \tag{4-30}$$

where,

c_ℓ = concentration (mass/volume) of species ℓ,

D_{ij} = hydrodynamic dispersion tensor (length^2/time),

V_i = Darcy velocity (length/time) of the flow field,

ϕ = porosity (dimensionless),

λ_ℓ = first order decay constant (time^{-1}) of species ℓ,

R_ℓ = retardation coefficient (dimensionless) of species ℓ,

$\xi_{\ell m}$ = fraction of parent species m (dimensionless) that transforms into daughter species ℓ,

q = rate of fluid injection per unit volume of formation (time^{-1}),

c_ℓ^* = concentration of species ℓ in the injected fluid, and

Γ_ℓ = rate of material transfer of component ℓ from the rock matrix to the fracture (mass/(volume•time)) (see dual-porosity model, Section 6.5)

In the transport mode, the Darcy velocity is considered as input to the code and is obtained from STAFF2D or other flow codes. The dispersion tensor is defined as (Scheidegger, 1960),

$$D_{11} = \frac{\alpha_L V_1^2 + \alpha_T V_2^2}{|V|} + \phi D_1^*$$

$$D_{12} = (\alpha_L - \alpha_T)\frac{V_1 V_2}{|V|}$$

$$D_{22} = \frac{\alpha_L V_2^2 + \alpha_T V_1^2}{|V|} + \phi D_2^* \qquad (4\text{-}31)$$

where α_L and α_T are the longitudinal and transverse dispersivities, and D_1^* and D_2^* are the effective coefficients of molecular diffusion.

The decay constant is

$$\lambda = \frac{\ln(2)}{T_{1/2}} \qquad (4\text{-}32)$$

where $T_{1/2}$ is the half-life of species ℓ.

Retardation is given by

$$R_\ell = 1 + \frac{\rho_s(1-\phi)}{\phi} K_{d,\ell} \qquad (4\text{-}33)$$

where $K_{d,\ell}$ is the distribution coefficient, and ρ_s is the solid density.

In (4-30), Γ_ℓ represents a source term modeling the matrix-fracture interaction when using the dual-porosity model. The undisturbed calculations did not use the dual porosity capability, so $\Gamma_\ell = 0$. Also, for a passive solute with an infinite half-life and no retardation, $\lambda_\ell = 0$ and $R_\ell = 1.0$.

The finite-element approximation technique applied to the convective-dispersive equation is an upstream-weighted residual technique (Huyakorn and Pinder, 1983) designed to overcome oscillations of the numerical solutions when the convective terms are dominant.

Physical Assumptions and Limitations

Assumptions are as follows:

- The code is limited to two dimensions.
- Transport is governed by Fick's Law.
- The dispersivity is assumed to correspond to an isotropic porous medium so that only two constants, the longitudinal and transverse dispersivity, are important.
- Adsorption and decay of radionuclides obey a linear equilibrium isotherm.
- Solute concentration effects on fluid density are ignored.

CAMCON Enhancement: Spatially Varying Material Properties

The HydroGeoLogic version of STAFF2D is limited to having distinct material regions over which physical properties do not vary. In the transport case, these include porosity and tortuosity. In addition, the free-water molecular diffusion parameter is independent of species in Version 3.2. The CAMCON data base contains spatially varying data for tortuosity and porosity and species-dependent molecular diffusion parameters. The CAMCON version of STAFF2D was modified to permit input and use of these data.

Benchmark Tests

Several benchmark calculations have been performed to compare STAFF2D with analytical solutions. Generally, good agreement with the analytic solutions is claimed. Unfortunately, for the case of multiple species transport, analytic solutions are confined to one-dimensional model problems. The following list of documented benchmark problems is discussed in Huyakorn et al. (1991):

- longitudinal transport in fractures and transverse matrix diffusion
- longitudinal transport in fractures and spherical matrix diffusion
- one-dimensional transport of a three-member radioactive decay chain
- radial transport in fractures and transverse matrix diffusion
- two-well transport in a porous medium system

4.2.2.3 Summary of Results

A brief summary of results and conclusion is presented here. Details of the calculations including spatial and temporal grids, material properties, and boundary conditions follow. Results from STAFF2D indicate that the primary migration pathway is from the repository down into

MB139, and within MB139 to the shaft. Solute is transported up the shaft at concentrations much less than 1% of the source. The effect of desaturation via effective properties on flow and transport was minimal. An estimate of the normalized EPA sum of radionuclides passing a point 20 m up the shaft was several orders of magnitude less than the normalized EPA limit of 1, during the 10,000-year regulatory period. A similar result was obtained for radionuclides moving in MB139 away from the repository and shaft.

Flow rates up the shaft are less than 0.03 m^3 /yr with no shaft seal system, and concentrations in the shaft are much less than 1% of the source. A six order-of-magnitude decrease in shaft permeability, from 10^{-12} m^2 (permeability of sand) to 10^{-18} m^2 (permeability of initially placed salt), drops the flux up the shaft by only a factor of three. The shaft seals were not included in the original model, again to maximize flow up the shaft. Varying the shaft permeability in a parameter study showed that the properties of an engineered shaft seal would have to approach the properties of the intact Salado before it would have an effect on the undisturbed performance.

4.2.2.4 Spatial and Temporal Grids

Two grids were initially used for these simulations. A very large, coarse grid was used for a regional simulation to establish boundary conditions on a much smaller, finely zoned local simulation. Comparisons of both pressure and concentration contours from both calculations show that the extra step was not necessary. The large regional grid adequately resolved the flow and transport within MB139 and up the shaft. Therefore, all remaining results are for the large, coarse grid.

The region covered by the grid extended from 1,000 m below the MB139 to the top of the Culebra dolomite and for 1,000 m downgradient from the shaft to 1,500 m up gradient from the repository (Figure 4-5). Details of the grid are shown in Figure 4-6 at the shaft/drift intersection. The MB139 and anhydrite layers were modeled using one element through the thickness. Two and three elements were used through the thickness of the Salado DRZ below and above the repository respectively. Three zones were used through the thickness of the repository. One element was used through the thickness of the shaft. Along the drift, the zones increased in length from 5 to about 40 m; in the repository they were approximately 30 m long. Zones expanded in all directions away from the repository/shaft system. The zoning resulted in some rather large aspect ratios (e.g., greater than 30). However, they did not cause numerical problems for flow, as evidenced by a comparison with the fine-zoned mesh discussed above.

The two-dimensional calculations are for a 1-meter-thick cross section through the center of the repository, drift, and shaft. The code calculates specific flux ($m^3/(s \cdot m^2)$) or Darcy velocity (m/s) per unit thickness. The reported fluxes are scaled to the actual shaft dimension by assuming

a 25-m^2 shaft cross-sectional area. The assumption is conservative in that the repository, drift, and shaft are assumed to be infinite in the direction orthogonal to the plane of the calculation.

4.2.2.5 Material Properties, Boundary Conditions, and Initial Conditions

Material properties used in the simulations are given in Volume 3 of this report. The entire shaft has been modeled with upper shaft properties (no lower shaft seal system) to maximize flow up the shaft. The shaft permeability was varied between 10^{-12} and 10^{-18} m^2 in a parameter study to obtain a possible bound on properties of the engineered barrier-shaft seal system. The region below the repository is assumed to be entirely Salado. The Castile formation has been excluded. The effect is assumed to be minimal.

Boundary conditions are shown schematically in Figure 4-7. It has been hypothesized that the initial fluid pore pressure at the repository is between Salado brine hydrostatic (7.0 MPa) and lithostatic (14.9 MPa); a value of 11 MPa has been selected. Generating the quasi-hydrostatic conditions using a fluid density of 1200 kg/m^3 and a pressure of 11 MPa at the repository horizon results in a hydrostatic pressure of about 6 MPa at the Culebra dolomite. The other choices required either an artificially high fluid density to get realistic fluid pressure at the Culebra or result in boundary-condition-induced vertical flow. To enhance the flow up the shaft, a no-flow boundary was used along the top of the Culebra, except at the shaft, which had a 2.8 MPa pressure corresponding to the actual hydrostatic pressure due to a column of brine extending to the ground surface. Flow is induced by an 17-MPa pressure boundary condition in the waste part of the repository. For the STAFF2D simulations, these pressure, boundary, and initial conditions were converted to hydraulic head. A steady-state governing equation was used. The solute source in the repository was modeled with a constant normalized concentration boundary condition of 1.0 kg/m^3.

4.2.2.6 Results and Discussion

The results are summarized in Figure 4-8 as pressure and total hydraulic head contours and in Figure 4-9 as normalized solute contours at 10,000 years. The pressure and head contours show the gradients away from the repository, between the repository and the shaft, and up the shaft. Compared to other regions near the repository in the computational plane, there is very little gradient between the base of the shaft and the Culebra and therefore very little flow. The solute contours show that vertical transport into surrounding host rock adjacent to the waste panel is small compared to transport along MB139 (note the magnified vertical scale in Figure 4-9). The primary migration pathway is from the repository to MB139, and within MB139 to the shaft. Concentrations in the shaft are less than 1% of the source. Solute under the influence of increased

pressure primarily moves into the disturbed region (Salado and MB139) below the repository and drift.

The fluid flux up the shaft is about 0.026 m^3/yr. For U234 with a current median solubility limit of $1.0x10^{-4}$ molar, this corresponds to $4.68x10^{-6}$ kg/yr or $4.68x10^{-2}$ kg/10,000 yr. For PU239 with a current median solubility of $6x10^{-10}$ molar, it corresponds to $2.86x10^{-5}$ kg/10,000 yr. U234 and Pu239 are the primary radionuclides contributing to the normalized EPA sum.

The permeability and porosity values of the shaft (10^{-12} m^2 and 0.10, respectively) are for unconsolidated salt. To estimate the properties of an engineered shaft seal system that would be effective in reducing transport up the shaft, a series of simulations was performed with varying shaft permeabilities. Two and four order-of-magnitude decreases in permeability (10^{-14} m^2 and 10^{-16} m^2) resulted in essentially no change in the flow up the shaft. A permeability of 10^{-18} m^2 resulted in a factor-of-three decrease in flow. This implies for undisturbed conditions an engineered shaft seal has little effect unless the permeability approaches that of the intact Salado.

In conclusion, for fully saturated conditions, no significant quantity of radionuclides move up a shaft, even when it is filled with a material with a permeability of 10^{-12} m^2. The permeability of the shaft backfill must be within a few (2 to 3) orders of magnitude of the surrounding host rock to reduce this already insignificant migration even further. These results are consistent with results reported earlier by Rechard et al., 1990.

Release Estimates

Nuclide release up the shaft was estimated conservatively by combining the normalized concentration from STAFF2D with actual source concentration for radionuclides as calculated using the PANEL code (Section 5.3). PANEL uses the repository inventory, radionuclide properties, repository properties and intrusion borehole flow history to calculate radionuclide mass flux up an intrusion borehole. For this problem the steady-state flow up the shaft of 0.026 m^3/yr as calculated in the undisturbed simulations discussed above was used as an intrusion borehole flow history. The flow rate was calculated from the Darcy velocity times the shaft cross-sectional area. Transport up the shaft as calculated by PANEL assumes that the shaft intersects a waste panel. The effect is that there is no time delay or diffusion due to travel down the MB139 from the repository to the shaft and consequently no concentration gradient; what comes out of the repository goes directly up the shaft. The resulting radionuclide discharge is very conservative. PANEL-calculated discharges up a shaft are much larger than they would be up a shaft 366 m away. Releases calculated by PANEL were then scaled by the normalized concentrations at locations of interest up the shaft as calculated in the STAFF2D undisturbed simulations to account for the transport and time delay due to transport down the MB139.

Three PANEL calculations were run using two sets of radionuclide solubilities (median and maximum, see Volume 3) and two values of repository pore water volume (1 m^3 and 4000 m^3). The pore water volume of 4000 m^3 corresponds to an inundated waste panel and was used in the December 1990 PA. The value of 1 m^3 was used to generate concentration of the radionuclides near their solubility limits. It provides a bound to release but not a least upper bound or a maximum. PANEL mixes the in-flowing fluid with the fluid in the repository and then releases it with dissolved radionuclides. Larger volumes of pore water result in lower release concentrations.

The normalized EPA sum (Section 2.1) for the three calculations are shown in Table 4-1 for the release as calculated by PANEL (column 4). These releases are then reduced to account for the actual 366 m separation of the repository and shaft by combining the PANEL and STAFF2D results. For Case 1 (column 4), 99% of the EPA sum comes from the activity of AM241, which is released from the repository in the first 200 yr. AM241 can be excluded from the EPA sum since the average travel time down the MB139 is over 10,000 years and the half-life of AM241 is 432 years. This results in the values shown in column 5. There are similar results for Case 2 where AM241 contributes 70% of the EPA sum. The values shown in columns 6 and 7 have been scaled by the normalized concentrations 366 m from the repository and 20 and 50 m up the shaft (above the repository horizon)—0.001 and 0.0001, respectively.

Other factors that would significantly reduce radionuclide release up the shaft would be retardation, reduced solubilities, larger pore water volume, travel time delays for all radionuclides, and time varying concentrations. For the analysis presented the concentration scale factors are constant at their value at 10,000 yr. They are actually much smaller early in time when releases from PANEL are large.

Another pathway for release from the undisturbed scenario is within MB139 directly to the accessible environment. Darcy velocities 100 m from the far side of the repository (away from the shaft) are 0.03 times the velocities in the shaft; however the flux area is significantly larger—on the order of 3600 m^2 assuming discharge at 100 m from all four sides of the repository. Normalized concentrations are $5x10^{-5}$ 100 m from the repository within MB139. The associated EPA sum would be $2.2x10^{-4}$ ($5x10^{-5}$*0.03*3600/25) times the release calculated by PANEL or one-fifth as large as the release 20 m up the shaft, column 8. Concentrations drop off considerably with distance away from the repository. At 200 m the scale factor is $8.4x10^{-7}$ or 250 times smaller than at 100 m, column 9. In summary, the results in Table 4-1 show that normalized EPA sums for release up the shaft and out the MB139 when conservatively estimated by PANEL and appropriately scaled to account for diffusion and travel time down the MB139 are several orders of magnitude below the EPA limit.

Verification

The STAFF2D calculations were verified by performing the same simulations with the SUTRA code and comparing results. The CAMCON system made this process quite simple as only the CAMDAT data base had to be modified to include a few properties required by SUTRA. Figure 4-10 shows a comparison of the 1% contour for both the SUTRA and STAFF2D simulations at 10,000 years. The comparison shows SUTRA transporting solute slightly farther from the repository due to the subtle modeling differences and/or different numerics. The main difference between the two models is that the porosity fields are slightly different. STAFF2D uses element-centered porosity as it is stored in the CAMDAT Data Base. SUTRA interpolates the porosities to the nodes resulting in average porosities at material boundaries.

Table 4-1. Normalized EPA Sums for Release up the Shaft in the Undisturbed Scenario From All Waste Panels

			EPA SUM					
Case	Solu-	Pore - Water		No	shaft		MB139	
	bility	Vol.	PANEL	AM241	20m	50m	100m	200m
(1)	(2)	(3)	(4)	(5)	(6)	(7)	(8)	(9)
1	max.	1	1407	4.6	4.6×10^{-3}	4.6×10^{-4}	1.0×10^{-3}	4.0×10^{-6}
2	max.	4000	6.25	1.8	1.8×10^{-3}	1.8×10^{-4}	3.9×10^{-4}	1.6×10^{-6}
3	median	4000	0.11	0.11	1.1×10^{-4}	1.1×10^{-5}	2.4×10^{-5}	9.6×10^{-8}

Notes on columns 4 through 9:

(4) PANEL results including AM241 for shaft intersecting repository.
(5) Same as (4) but without AM241 in EPA sum.
(6) (5) scaled by relative concentration 20 m up shaft from STAFF2D.
(7) (5) scaled by relative concentration 50 m up shaft from STAFF2D.
(8) (5) scaled by relative concentration 100 m from repository within MB 139.
(9) (5) scaled by relative concentration 200 m from repository within MB 139.

Nuclides used in EPA sum: AM241, NP237, PB210, PU238, PU239, PU240, PU242, RA226, RA228, TH229, TH230, TH232, U233, U234, U236, U238.

Pseudo-Unsaturated Flow

In the previous calculations, STAFF2D was run assuming that the permeability and porosity were unaffected by the presence of waste-generated gas. The effect of gas was included only in so far as it provided a pressure of 17 MPa to nodes within the repository. In the following calculations with STAFF2D, gas generation effects on effective properties were included in a second STAFF2D simulation by modifying the properties of the waste, Salado DRZ, and MB139DRZ based on results of two-phase flow simulations performed with BOAST II (Section 4.2.1). Gas-generation effects are accounted for by effective properties that arise due to desaturation of the pores and by a constant 17 MPa repository source pressure. Note that saturation refers to the ratio of volume of brine to volume of pores. Saturation of 1 is fully brine saturated; a value of 0 implies the pores are void (empty). Effective porosity and effective diffusion were calculated based on brine saturation in the pores. Effective permeability was calculated using relative permeability, which is a function of brine saturation in the pores. Profiles of relative permeability on a vertical slice through the repository were shown in Figure 4-3. The waste material was broken into three layers. Permeability in the three layers was decreased by seven, six, and five orders of magnitude from top to bottom based on relative permeability. This reflects the higher gas saturations (lower brine saturation) near the ceiling. To maximize desaturation effects, permeabilities in the Salado-DRZ and MB139-DRZ were decreased by a factor of 10. Porosity in the waste, Salado DRZ and MB139DRZ were decreased by a factor of three based on the saturation profiles shown in Figure 4-4. Effective diffusion, which is a strong function of fluid saturation, was decreased by a factor of 100. Dispersivity coefficients were unchanged since saturation effects on dispersion are accounted for via the flow velocity.

The results, summarized as a concentration contour of 1% of the source value, are compared to the original saturated flow simulations in Figure 4-11. The effective property changes due to gas generation and desaturation as modeled here had little effect on solute transport; a little more solute is transported downward and a little less solute is transported laterally along MB139. The results above the repository appear to be noisy. Very little change in results will occur until effective waste and DRZ properties approach those of the intact Salado properties. This conclusion is consistent with effects of shaft seal properties on flow up the shaft. The solute transport is advection- and dispersion- (fluid velocity) dominated. The velocities are a function of hydraulic conductivity and head gradient. One would expect the fluid velocity and transport to decrease with decreased hydraulic conductivity; however, head gradients increased resulting in velocities similar to the those using unmodified properties. Gas generation in the *undisturbed* repository is *not* expected to cause releases to the accessible environment or beyond the 5-km boundary in excess of the EPA limit. In fact, the releases calculated here are several orders of magnitude lower than the limit only a few hundred meters away from the repository. Gas generation effects on radionuclide

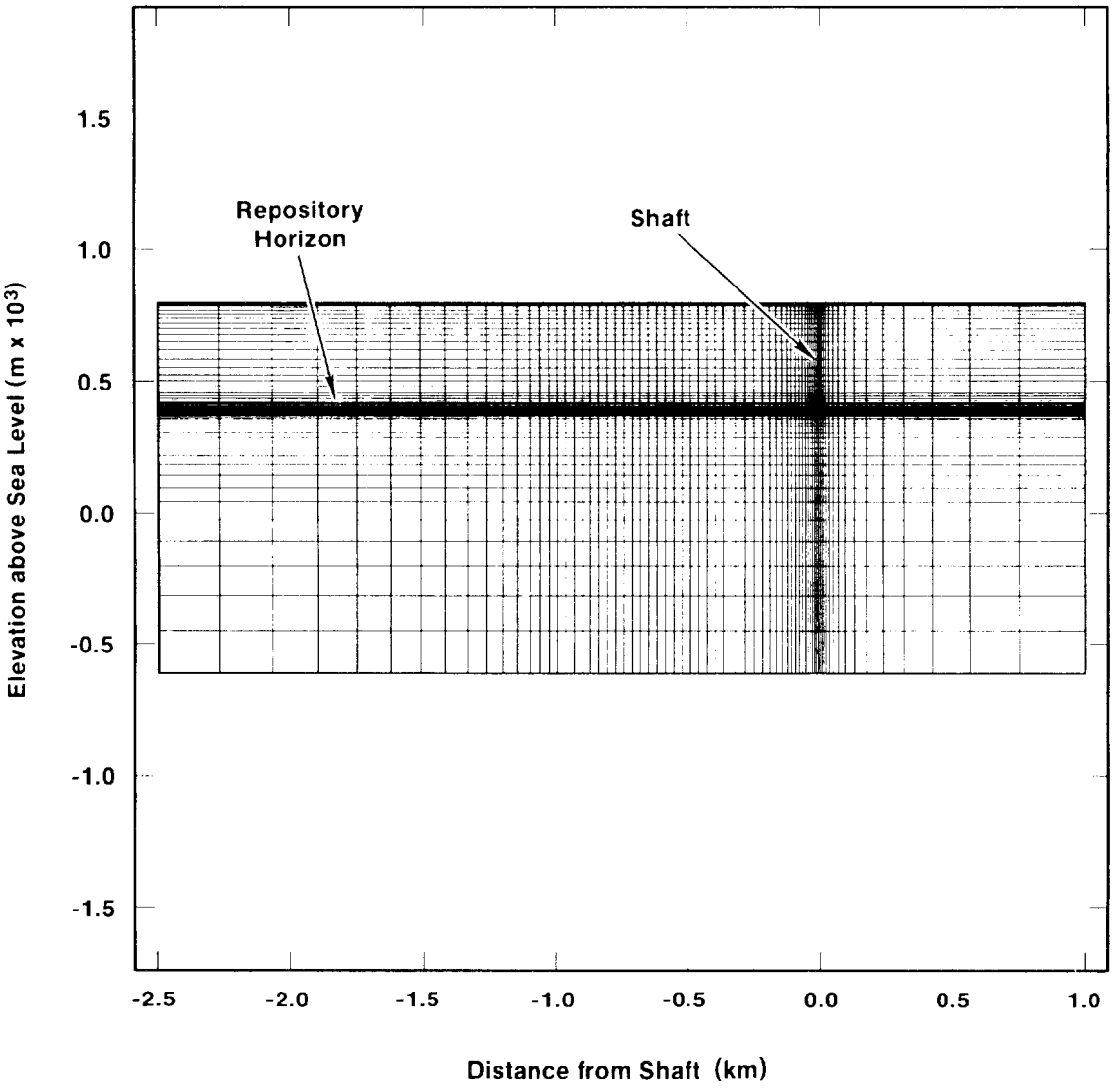

Figure 4-5. Spatial Grid for Undisturbed Simulation with Saturated Flow

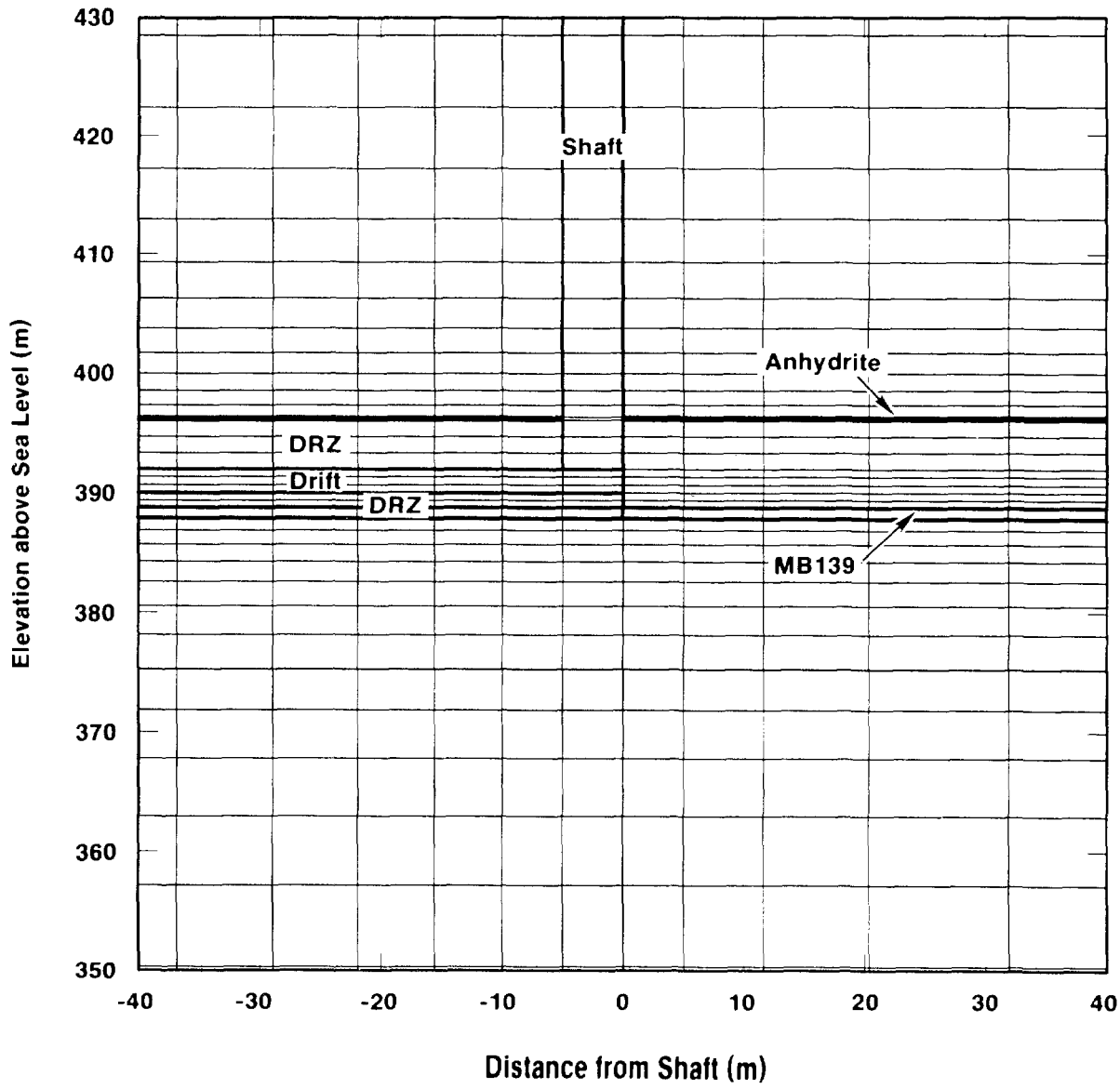

TRI-6342-1306-0

Figure 4-6. Spatial Grid Details Near Shaft/Drift Intersection

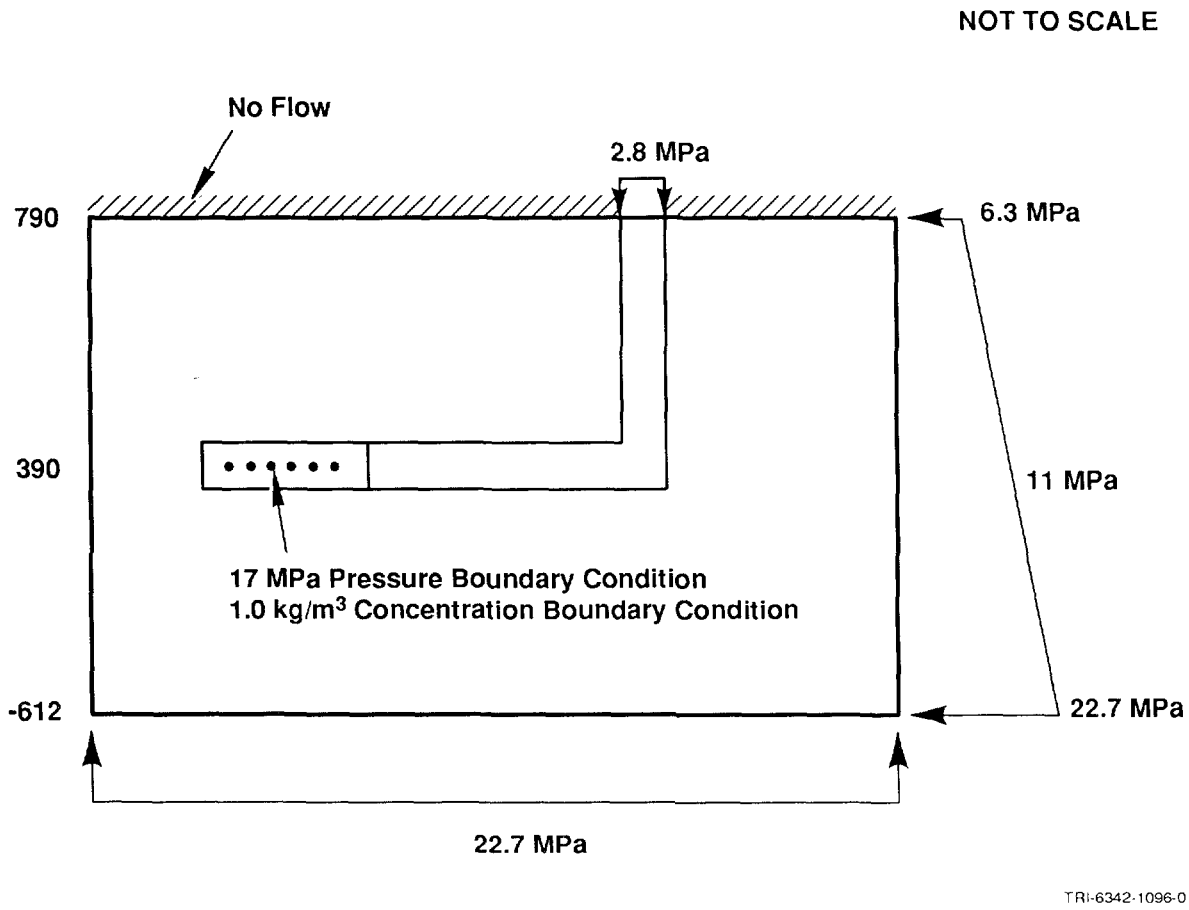

Figure 4-7. Boundary Conditions for Undisturbed Repository Performance

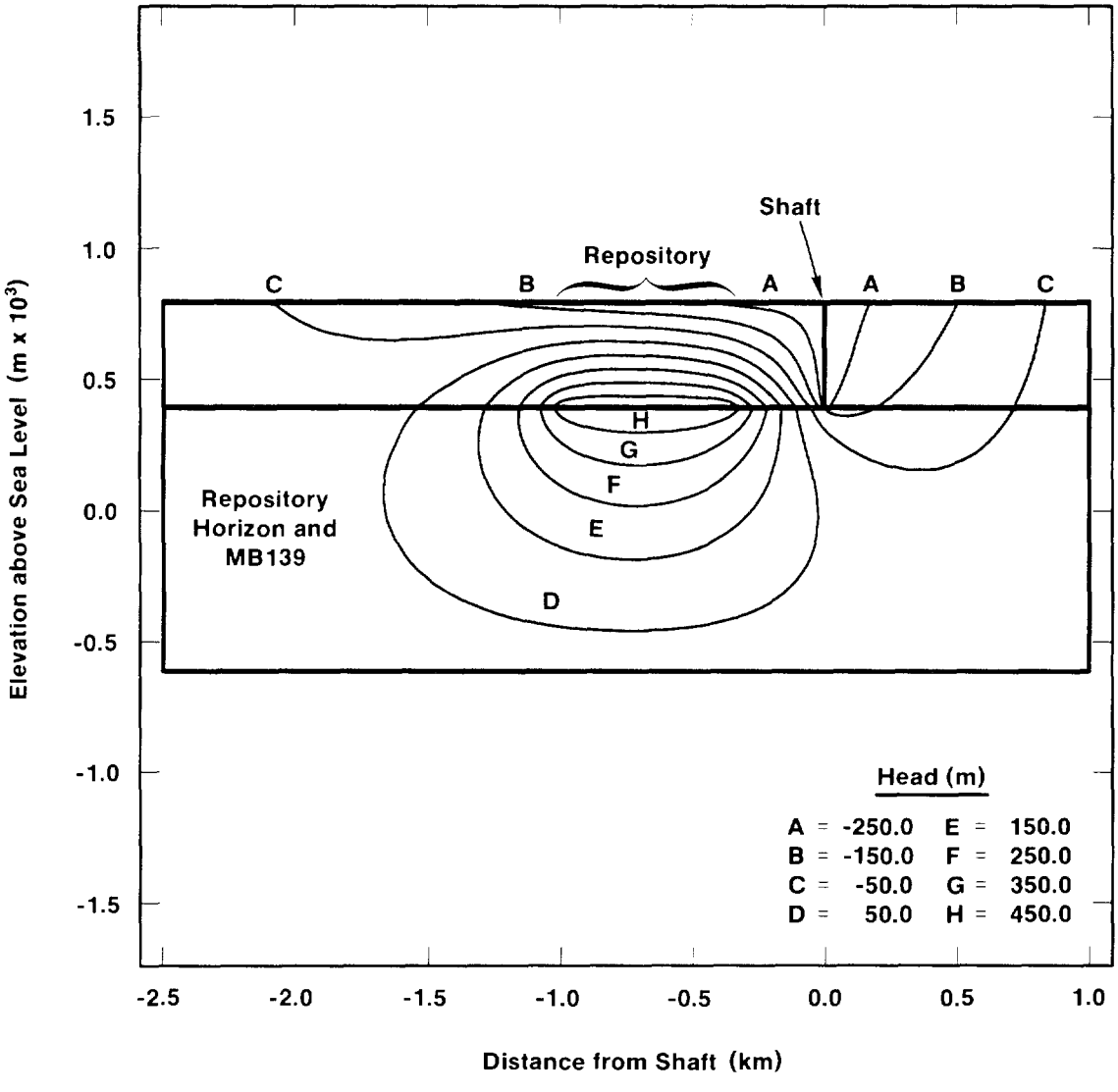

Figure 4-8a. Hydraulic Head Contours for Undisturbed Simulation with Steady-State Saturated Flow

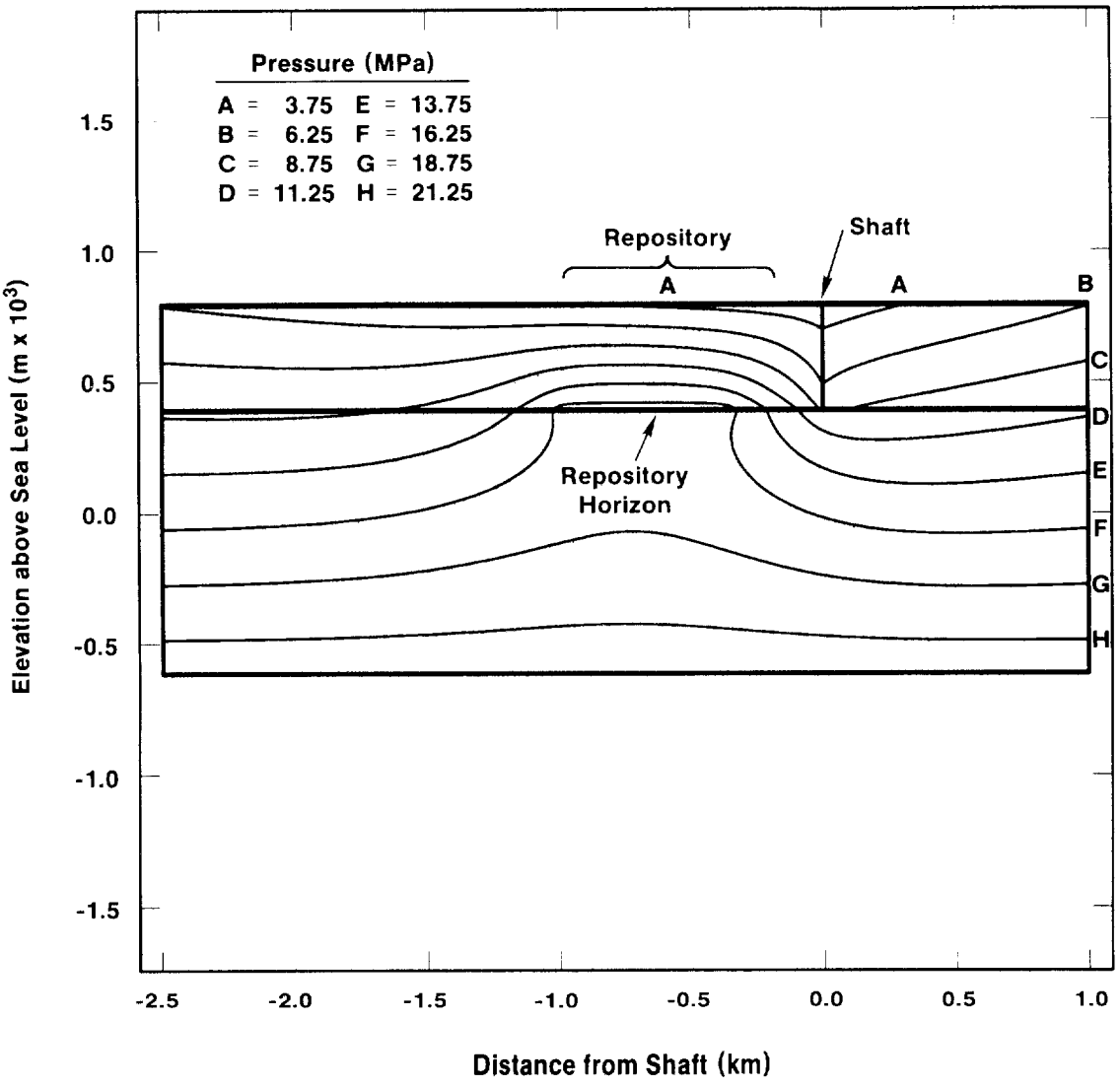

Figure 4-8b. Pressure Contours for Steady-State Saturated Flow for Undisturbed Repository Performance

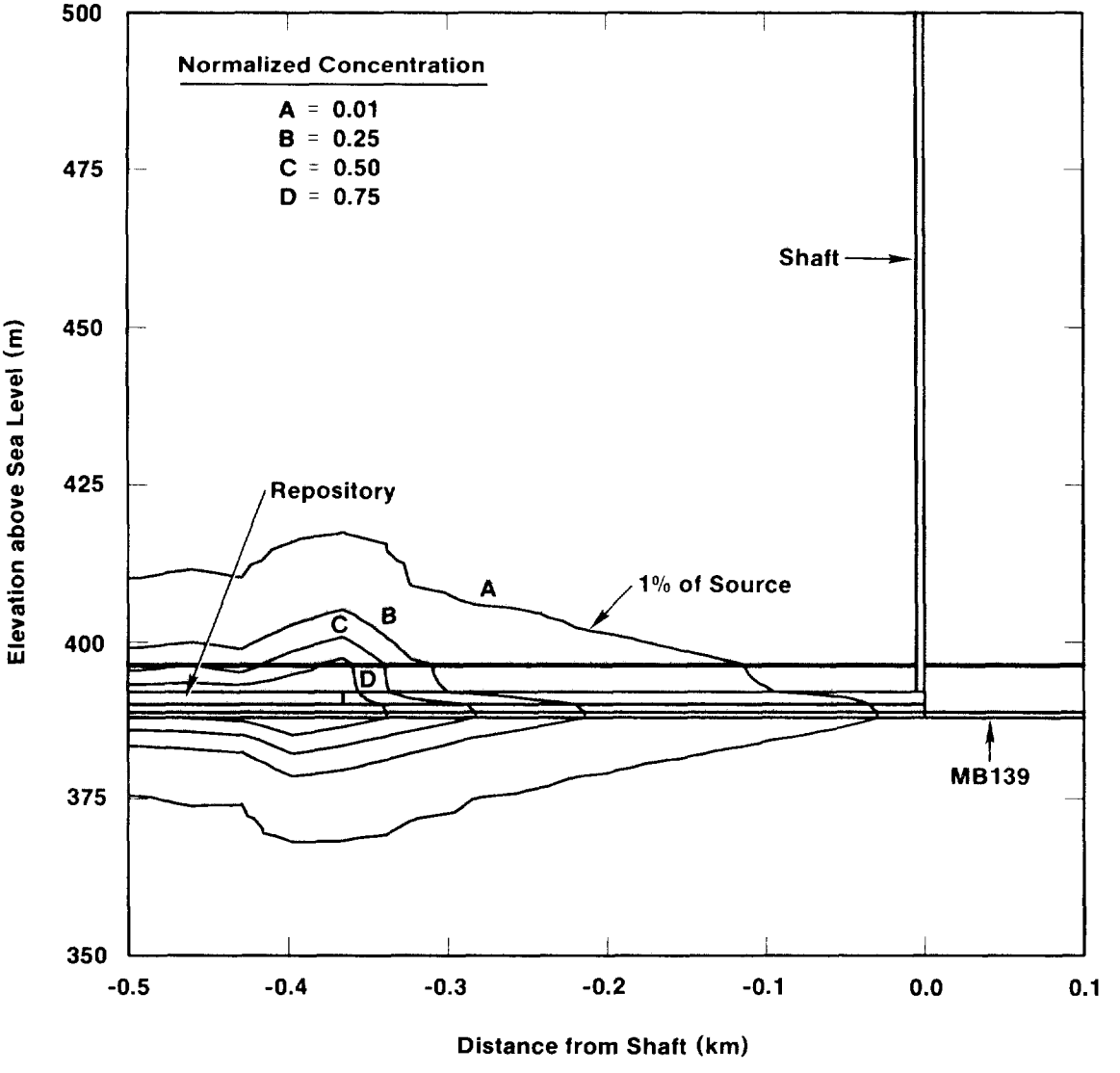

Figure 4-9. Normalized Solute Concentration Contours at 10,000 Years

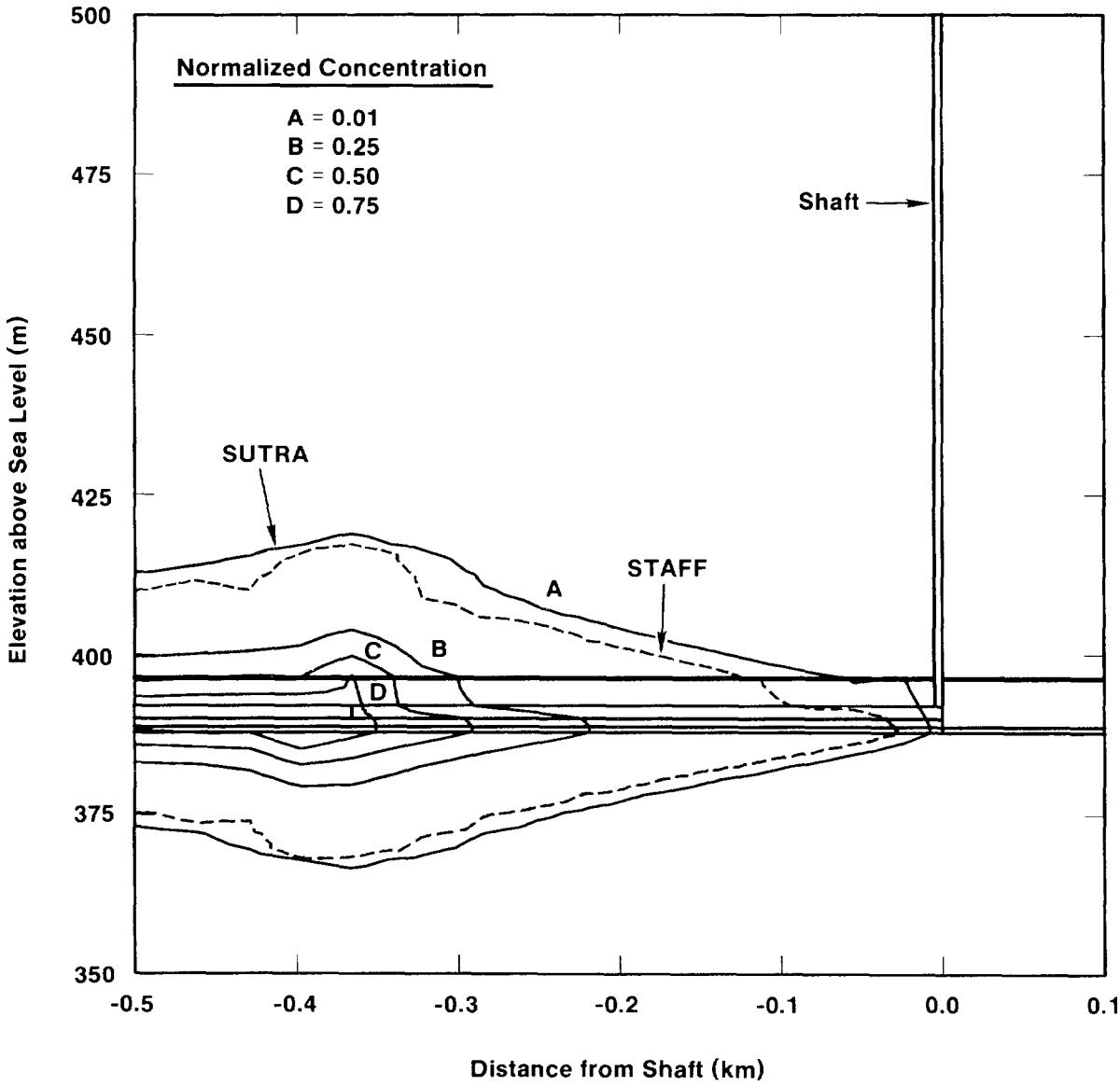

Figure 4-10. Solute Concentration Contours at 10,000 Years for SUTRA Undisturbed Simulation and Comparison with STAFF

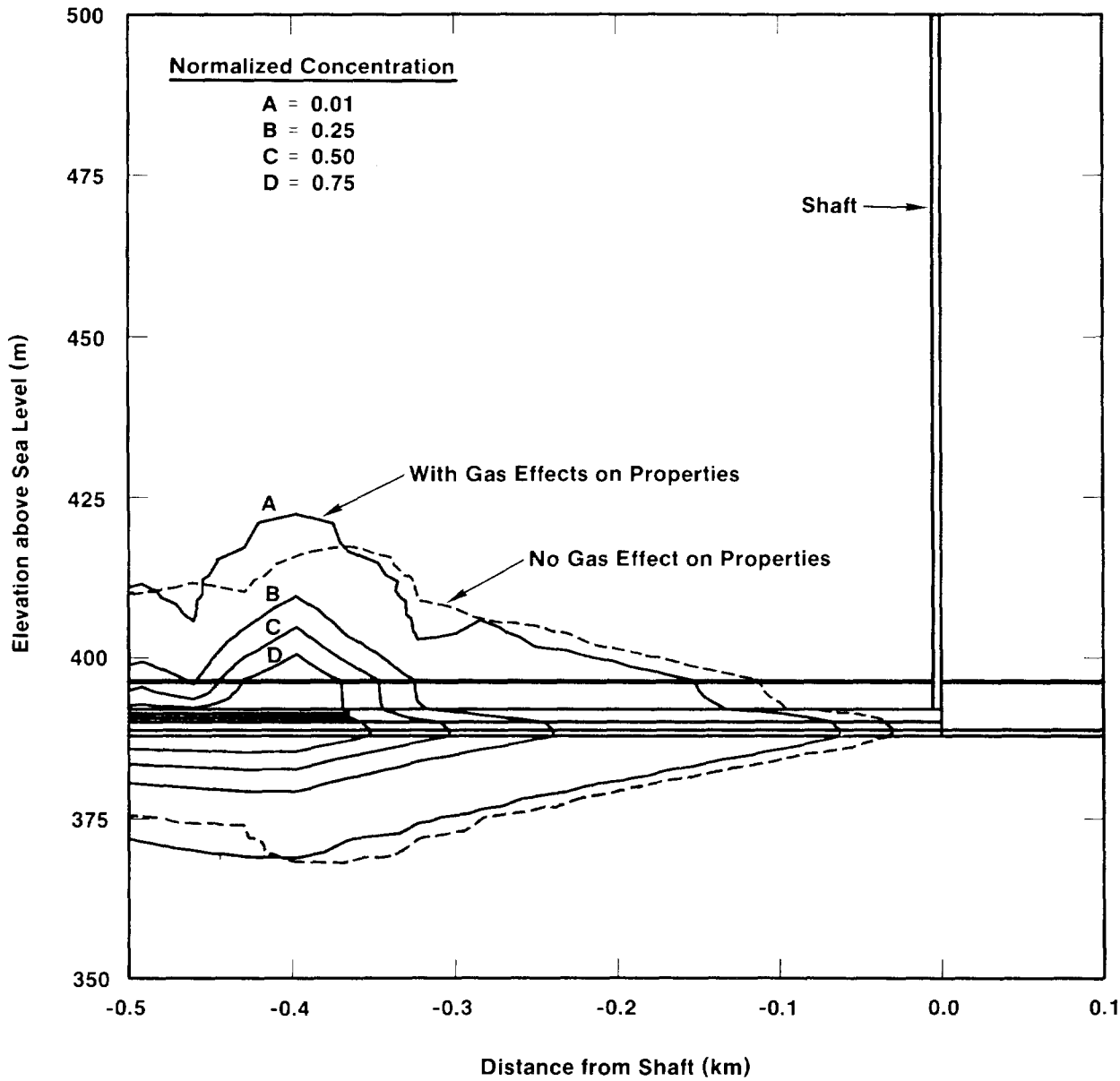

Figure 4-11. Solute Concentration Contours with Properties Modified Based on Two-Phase Simulation with BOAST (at 10,000 Years)

transport (due to property changes) are confined to a region between the repository and access shafts. The results presented here for time-constant "effective" properties are preliminary, for demonstration purposes only. They are the initial effort in an ongoing investigation into possible methods of calculating transport in the presence of two-phase flow. Other areas include fully coupling transport into a two-phase flow code (such as BRAGFLO), uncoupling two-phase flow and transport, or coupling the two-phase flow to a single-phase transport code and using time-dependent transport properties that are derived from the two-phase flow field.

4.2.3 SUTRA SIMULATIONS—Jonathan S. Rath and Ron D. McCurley

In addition to the STAFF2D calculations, the SUTRA code was also used in a vertical cross-section through the repository to verify further the results of STAFF2D (see the steady-state verification discussion in Section 4.2.2.6) and to study in greater detail the effects of transient gas pressures and time-varying material properties as generated by BOAST II. The SUTRA calculations for the vertical cross-section (Section 4.2.3.2), as opposed to STAFF2D, were run in a fully transient mode utilizing the time-varying gas pressure and material permeabilities. Additional calculations were carried out with SUTRA modeling a horizontal plane through the repository (Section 4.2.3.3). The purpose of these calculations was to investigate some of the three-dimensional aspects of flow out of the waste repository.

4.2.3.1 Model Description

The model description that follows is based closely on the presentation in Voss (1984). SUTRA (Saturated-Unsaturated TRAnsport) (Voss, 1984) evaluates density-dependent, saturated or unsaturated groundwater flow in rigid, porous media with either (1) transport of a single-species solute subject to non-linear equilibrium adsorption and zero- and first-order production or decay or (2) transport of thermal energy in the groundwater and solid matrix of an aquifer. SUTRA employs a two-dimensional hybrid finite-element and integrated finite-difference method to approximate the governing equations. The primary results are fluid pressures, velocities, and either solute mass fractions or temperatures as they vary with time. SUTRA solves partial differential equations for coupled flow and transport using backwards finite differencing time discretization for time derivatives appearing in the conservation equations. Groundwater flow is simulated through the numerical solution of a fluid mass balance. Similarly, transport of either solute mass or energy is solved numerically by satisfying a solute mass or energy balance equation. SUTRA's finite element approximation equations are derived by using the Galerkin-type method of weighted residuals. Isoparametric, bilinear, 4-node quadrilateral elements are used exclusively by SUTRA.

In addition, SUTRA allows (1) steady or transient flow, (2) radial or Cartesian coordinate systems, (3) areal (in plane) or cross-sectional solution domains, (4) equilibrium non-linear

adsorption, (5) zero and first-order production or decay for a single species, (6) saturated or unsaturated flow, (7) material-dependent storativity and grain density, (8) time-dependent boundary conditions and/or sources and sinks, and (9) time-dependent material properties. Items 7, 8, and 9 are enhancements developed for the CAMCON version.

Groundwater Flow Equation

The governing partial differential equation describing conservation of fluid mass in an unsaturated porous medium is given by (Voss, 1984),

$$\left\{S_l \rho_f G + \left(\varepsilon \rho_f\right)\frac{\partial S_l}{\partial p}\right\}\frac{\partial p}{\partial t} + \left\{\left(\varepsilon S_l\right)\frac{\partial \rho_f}{\partial \hat{C}}\right\}\frac{\partial \hat{C}}{\partial t} = \nabla \bullet \left\{\left[\frac{\underline{\underline{k}} k_{rl} \rho_f}{\mu_l}\right] \bullet \left[\nabla p - \rho_f \underline{g}\right]\right\} + Q_l \qquad (4\text{-}34)$$

where,

S_l = ratio of fluid saturation to total void volume (dimensionless),

ρ_f = fluid density (M/L^3),

G = specific storativity (t^2/M),

ε = porosity (dimensionless),

p = pore pressure ($M/(Lt^2)$),

t = time (t),

$\hat{C}$ = solute mass fraction (M/M),

$\underline{\underline{k}}$ = permeability tensor (L^2),

k_r = relative permeability (dimensionless),

μ_l = fluid kinematic viscosity (ML/t),

∇p = pressure gradient ($M/(L^2t^2)$),

$\underline{g}$ = gravitational acceleration vector (L/t^2), and

Q_l = fluid mass source or sink (including pure fluid plus solute mass dissolved in fluid) ($M/(L^3t)$).

k_{rl} = relative permeability (dimensionless)

Relative permeability, k_{rl}, expresses what fraction of the total permeability remains when the void space is partially fluid-filled. Thus, for a saturated fluid, $S_l = 1$, and $k_{rl} = 1$. If the fluid density is not allowed to vary as a function of solute mass fraction ($\partial \rho_f / \partial \hat{C} = 0$), the second term of (4-34) drops out. Thus, the resulting fluid mass balance equation is no longer coupled to solute transport.

Solute Transport Equation

SUTRA allows a single solute species to be transported conservatively, or the single solute species may be subjected to equilibrium sorption (through linear, Freundlich, or Langmuir

isotherms). Single species solute may also be produced or decay through first- or zero-order reaction processes. SUTRA's solute transport simulation allows for a single species mass stored in fluid solution as solute and species mass stored as adsorbate on the surfaces of solid matrix grains. Solute concentration, $\hat{C}$, and adsorbate concentration, C_s, are related through equilibrium adsorption isotherms. Assuming that species mass stored as adsorbate on the surfaces of solid matrix grains does not occur, $C_s = 0$ (i.e., no adsorbate mass transfer occurs, and thus solute is transported conservatively). The governing partial differential equation describing conservation of solute mass fraction in a saturated, $S_l = 1$, porous medium is given by Voss (1984),

$$\varepsilon\rho_f \frac{\partial \hat{C}}{\partial t} = \nabla \bullet \left\{ \left[\varepsilon\rho_f \left(D_p \underline{\underline{I}} + \underline{\underline{D}} \right) \right] \bullet \nabla \hat{C} \right\} - \varepsilon\rho_f \underline{v} \bullet \nabla \hat{C} + Q_l \left(C^* - \hat{C} \right) \tag{4-35}$$

where,

D_p = molecular diffusion coefficient in porous media (L^2/t),

$\underline{\underline{I}}$ = identity tensor (dimensionless),

$\underline{\underline{D}}$ = dispersion tensor (L^2/t)

$\nabla \hat{C}$ = gradient of solute mass fraction (L^{-1}),

$\underline{v}$ = interstitial velocity vector (L/t), and

C^* = solute mass fraction of fluid mass source (M/M).

The term involving the interstitial fluid velocity vector, $\underline{v}$, of (4-35) represents the average advection into or out of the local volume. For saturated flow, $S_l = k_{rl} = 1$, this velocity term is calculated in SUTRA from a generalized form of Darcy's law as,

$$\underline{v} = -\left[\frac{\underline{\underline{k}}}{\varepsilon\mu_l} \right] \bullet \left(\nabla p - \rho_f \underline{g} \right) \tag{4-36}$$

SUTRA employs an algorithm for determination of fluid velocities that alleviates typical spurious numerical errors common with standard finite element methods for systems with variable fluid density. Such errors are a result of fundamental numerical inconsistencies in spatial and temporal approximations for the pressure gradient, ∇p, and the density-gravity term, $\rho_f \underline{g}$, of (4-36), which are used in computing the velocity field (Voss, 1984). Consistent evaluation of the velocity is also necessary for the assembly of the dispersion tensor, $\underline{\underline{D}}$. SUTRA's method of velocity calculation applies a consistent spatial and temporal discretization to the term $(\nabla p - \rho_f \underline{g})$. Thus, SUTRA produces consistently evaluated velocities and allows stable and accurate transport modeling.

The term involving molecular diffusivity of the solute, D_p, and the dispersion tensor, $\underline{\underline{D}}$, of (4-35) represents the contribution of solute diffusion and dispersivity to the temporal solute mass

gradient. The diffusion contribution is based on a true physical process frequently neglected at the field scale. The dispersion term approximates the irregularity of the velocity field and the flow field's mixing, which are not accounted for by average solute advection. Subsequent mixing is due to the presence of non-uniform, convective velocities in three dimensions about the average interstitial velocity, $\underline{v}$, and is conceptualized in two dimensions as a diffusion-like process with anisotropic dispersivities.

For a system with isotropic permeabilities, SUTRA's dispersion tensor, $\underline{\underline{D}}$, components can be written in matrix form as,

$$[D] = \begin{bmatrix} D_{LL} & D_{TL} \\ D_{LT} & D_{TT} \end{bmatrix}, \tag{4-37}$$

where the tensor components are symmetric, defined as,

$$D_{LL} = \frac{1}{v^2}\left(\alpha_L v_L^2 + \alpha_T v_T^2\right),$$

$$D_{TT} = \frac{1}{v^2}\left(\alpha_T v_L^2 + \alpha_L v_T^2\right), \text{ and}$$

$$D_{TL} = D_{LT} = \frac{1}{v^2}\left(\alpha_L v_L v_T - \alpha_T v_L v_T\right),$$

where

α_L = longitudinal dispersivity of solid matrix (L),

α_T = transverse dispersivity of solid matrix (L), and

v = magnitude of the velocity vector, $\|\underline{v}\|$.

When such an isotropic media model is applied to a particular field situation where aquifer inhomogeneities are much smaller than the field transport scale, dispersivities α_L and α_T may be considered to be fundamental transport properties of a system in the same sense that permeability is a fundamental property of flow through porous media (Voss, 1984).

For an anisotropic permeability field, SUTRA uses an ad-hoc model of flow-direction-dependent longitudinal dispersion. SUTRA's anisotropic-media dispersion algorithm splits longitudinal dispersivity into two principal space directions aligned with the principal directions of permeability. Since anisotropic permeability's transverse dispersivity is typically only a fraction of the longitudinal dispersivity, the transverse dispersivity is ignored. Dropping the transverse dispersivity term can also be justified by the limitations of mesh refinement for accurate simulation of low transverse dispersion. Thus, the effect of any direction-dependence of tranverse dispersivity would be obscured by the numerical discretization errors in a typical mesh. SUTRA's value of longitudinal dispersivity as dependent on the flow direction for an anisotropic permeability media is given as

$$\alpha_L = \frac{\alpha_{L\min}\alpha_{L\max}}{\alpha_{L\min}(\cos\theta_{kv})^2 + \alpha_{L\max}(\sin\theta_{kv})^2}, \quad (4\text{-}38)$$

where

$\alpha_{L\min}$ = longitudinal dispersivity in the minimum permeability direction (L),

$\alpha_{L\max}$ = longitudinal dispersivity in the maximum permeability direction (L), and

θ_{kv} = angle from maximum permeability direction to the local flow direction ($\underline{v}/\|\underline{v}\|$).

4.2.3.2 Vertical Cross Section Simulations

Model Overview

Introduction. The following describes SUTRA calculations using vertical cross-sectional geometry to examine the phenomenology of solute transport in and near the repository. This phenomenology includes transport due to advection and dispersion related to the movement of fluid (brine) through the repository and surrounding rock matrix, and to molecular diffusion.

The SUTRA simulations described in this section differ from the STAFF2D calculations (described in Section 4.2.2) in the following ways: (1) The SUTRA calculations solved for transient flow and transient transport simultaneously; STAFF2D used a two-step process—steady-state flow followed by transient transport. (2) SUTRA used smaller time steps (100 years). (3) The modeled pressure in the waste (due to gas-generation) is time-dependent in SUTRA calculations, (4) In one SUTRA calculation, the permeabilities in several materials are allowed to vary with time. Otherwise, mesh geometry, material properties, and boundary and initial conditions are the same as those of the STAFF2D calculations.

The results of the SUTRA calculations confirm and augment the findings of other studies of transport in the undisturbed scenario. One significant and unique result of this study shows qualitatively different and quantitatively less transport than STAFF2D, due to time-varying permeabilities (from gas invasion into porous spaces generated by waste decomposition, etc.) and due to time-varying gas pressure.

Summary of Results. The results from SUTRA are consistent with those generated by STAFF2D (Sections 4.2.2.3 and 4.2.2.6). Again, as with STAFF2D, the primary migration pathway is down into MB139 and laterally within MB139 towards the shaft. When SUTRA used the transient gas pressures generated by BOAST II and no gas modified material properties, the 1% source concentration contour at 10,000 years did not extend as far down MB139 as the STAFF2D 1% source concentration contour run steady state with a constant, higher repository driving pressure (17 MPa). When SUTRA and STAFF2D were both run with steady-state pressures (Section 4.2.2.6), the 1% SUTRA contours preceded the STAFF2D contour. It should be noted

that the normalized concentrations calculated in STAFF2D (given as a percent of the initial concentration) are equivalent to normalized mass fractions (given as a percent of the initial mass fraction) as calculated by SUTRA. When the repository and surrounding geologic permeabilities are modified as a function of time as the result of gas generation, the SUTRA generated concentration contours show further retardation; the 1% source concentration contour in this case is approximately 50 m farther from the shaft than for the unmodified material case. Transport along MB139 without the effects of a shaft present reveals that the 1% source concentration contour extends out from the repository by approximately 120 m (see in-plane SUTRA calculation, Section 4.2.3.3).

Geometry, Spatial Grid, and Temporal Grid

For undisturbed conditions, SUTRA was exercised with a constant source term of solute mass fractions, no adsorption, and no decay. The modeled geologic matrix defined a slice perpendicular to the plane (referred to, hereafter, as the out-of-plane geometry) of and through the axis of the repository. This vertical slice included, in addition to the waste, the drift and the lower shaft, the surrounding intact host rock, the nearby disturbed rock zones, an anhydrite layer (combining layers a and b), and MB139. Disturbed rock zone regions (in the Salado) and disturbed regions in the anhydrite and MB139 layers underlying and overlying the repository are distinct materials with distinct flow properties.

The physical domain included the geological strata below the waste up to the top of the Culebra dolomite member. To simplify modeling the geometry of the geology, no account was taken for bending or changing thickness of layers. The thickness of the consolidated waste was assumed to be 2.0 meters in the vertical direction. Adjustments were required to preserve the elevation (or depth) of the repository (the original thickness is 4.0 meters). The layer thickness of the disturbed rock zone in the Salado above the repository was increased by 2.0 meters to preserve elevations of other layers. The far-field boundaries and computational mesh was the same as those used for the STAFF2D calculations (Section 4.2.2).

Two computational domains, a coarse and a fine grid, were created. The coarse grid was intended to establish and examine transient flow and concentration fields over a large domain. Due to constraints such as the large extent of the modeled domain and relative thicknesses of modeled geologic layers, there was a large variation of element size and aspect ratio (refer to Figures 4-12, and 4-13.). A finely meshed grid was created to examine flow and transport more accurately and to study the effect of mesh geometry (e.g., element aspect ratios) on transport. The results from the coarse grid were used to establish boundary conditions for a fine grid. These analyses involved several individual SUTRA calculations utilizing several pre-and post-processors. The entire series of calculations may be summarized in the following sequence (refer to Figure 1-4 in Chapter 1:

1. A coarse mesh with boundary conditions and material properties was developed using CAMCON tools GENMESH, MATSET, BCSET, and ICSET. The size of the computational domain was chosen to be the same as that used in the STAFF2D calculations (see Section 4.2.2.4).

2. Transient flow transport calculations using the computational domain developed in Step 1 were used to investigate transport phenomena and sensitivity to variations of time-step and diffusivity. (The term diffusivity used here and by SUTRA is the product of the pure fluid molecular diffusivity and the tortuosity of the porous media [sometimes referred to as the coefficient of molecular diffusion].) These transient calculations used no-flow ($\partial Q/\partial n = 0$, $\partial \hat{C}/\partial n = 0$, where n = outward or normal direction) far-field boundary conditions. Results from BOAST II (Section 4.2.1) for gas-generated time-dependent pore pressures were used as internal boundary conditions inside the waste. The rationale for the particular gas-generation rate used to determine BOAST II results used here is discussed in Section 4.2.1.5. In some cases time-dependent effective permeabilities and porosities were implemented. Care was taken to use time steps sufficiently small to reflect adequately the time-dependent functionality of results from BOAST II. The time step used in most of the calculations done here was 100 years. A smaller time step of 10 years was used only to study the effect of smaller time steps on the transport results.

3. Finally ALGEBRA, BLOT, and TRACKER were used to display results.

Material Properties, Boundary and Initial Conditions

As noted above, in some calculations the effective permeabilities of selected materials were allowed to vary with time. The time variation was determined by relative brine permeabilities predicted by BOAST II due to gas-generation in the waste. Plots of results predicted by BOAST II showing changes in relative brine permeability as a function of time for different regions in and near the repository are shown in Figures 4-14a, b, c, d. These time-dependent relative permeabilities were used to modify geologic permeabilities in SUTRA in order to make them time-dependent. The expression used to do this was $k(t) = k_0 k_r(t)$, where $k(t)$ is the derived time-dependent permeability, k_0 is the permeability and $k_r(t)$ is the time-dependent relative permeability from BOAST II. In all calculations SUTRA was used in the fully saturated mode ($S_l = 1$). The time variation in permeabilities was introduced to account for some of the effects of gas generation in the waste and two-phase flow in the surrounding geology.

A plot showing changes in drift permeability, due to time-dependent consolidation, is also included as Figure 4-14e. This figure is taken from Rechard et al. (1990b). The waste material

was subdivided into lower and upper regions in the model using time-varying permeabilities (see Figure 4-15). This was both reasonable and desirable because results from BOAST II showed significantly different permeability variations in the two regions. The upper region had dramatic decreases (many orders of magnitude) in brine permeability due to gas saturation; the lower region (the bottom row of elements) showed only small changes (less than an order of magnitude). Refer to Figures 4-14a and 14b.

The material and fluid properties used in these calculations were identical to those listed in the data report (Volume 3), with the exception of those shown in Tables 4-2 and 4-3. Included in these tables are material properties of the lower shaft that are to be determined by engineering design (Table 4-2). Also, as already indicated, the diffusivity used is a representative value of inventory radionuclides (Table 4-3).

Table 4-2. SUTRA Material Properties that Differ from those Found in Volume 3

	Property Value			
Zone	Dns Grain	Perm x	Perm y	Porosity
	(kg/m^3)	(m^2)	(m^2)	(dimensionless)
Anhydrite (DRZ)	___	___	___	0.1
Anhydrite (FF)	___	$1.00x10^{-19}$	$1.00x10^{-19}$	___
Culebra	___	___	___	$1.50x10^{-3}$
Drift	$2.19x10^{3}$	___	___	___
MB139 (DRZ)	___	___	___	___
MB139 (FF)	___	$1.00x10^{-19}$	$1.00x10^{-19}$	___
Salado (DRZ)	___	___	___	___
Salado (FF)	___	$3.50x10^{-21}$	$3.50x10^{-21}$	___
Shaft	___	$1.00x10^{-12}$*	$1.00x10^{-12}$*	$1.00x10^{-1}$*
Waste	$2.70x10^{3}$	___	___	___

* Undetermined engineered value.

Table 4-3. SUTRA Brine Properties that Differ from those Found in Volume 3

Brine Property	Value
Compressibility (Pa^{-1})	2.70×10^{-10}
Density (kg/m^3)	1.20×10^{3}
Viscosity (Pa•sec)	1.60×10^{-3}
Diffusivity (m^2/sec)	1.40×10^{-11}*

* Generic radionuclide.

The initial flow field for the coarse-zoned transport calculations was established in the following way. The pore pressure at the repository elevation was assigned a value of 11.0 MPa. This value represents a median value between hydrostatic pore pressure at that depth (7.0 MPa) and lithostatic pressure (15.0 MPa). The pressure in the repository itself is initially 0.1 MPa (atmospheric). The pore pressures at other elevations in the grid are determined by using a brine density of 1200 kg/m^3, gravitational acceleration of 9.8 m/s^2 and the relation

$$p(z) = p|_{z=391m} + \rho g(z - 391\,\mathrm{m}) \tag{4-39}$$

where z is the elevation of a node in the grid, g is the gravitational constant, ρ is the brine density and p is pore pressure (see Figure 4-16). (The repository is located at an elevation of 391 m above sea level.)

Far-field boundary conditions are no-flow ($\partial Q/\partial n = 0$), except at the top boundary of the shaft where the pressure is brine hydrostatic (due to a column of brine up to the surface). The boundary pressures inside the repository were determined by BOAST II calculations and were applied uniformly to all internal nodes of the waste in these calculations. Nodes on the edges of the waste are excluded because this would introduce artificially large flow velocities in the elements in surrounding regions having these nodes as corners. Gas-generation predictions from BOAST II show pressures building quite rapidly initially (a peak pressure of about 15.5 MPa is attained by 500 years) and then decaying gradually to ambient pressure (11 MPa) in 10,000 years (see Section 4.2.1 and Figure 4-2). Pressure contours at 600 years are shown in Figure 4-17.

A constant solute source term of 2.0×10^{-7} kg solute/kg solution (mass fraction) was input at those nodes in the waste where a gas pressure boundary has been applied. The value, 2.0×10^{-7} comes from using an arbitrary source of atomic weight 240 (specifically Pu-240). The solubility

limit for $^{240}Pu^{+4}$ is about 10^{-6} molar. A simple calculation gives the value of 2×10^{-7} for mass fractions.

Results and Discussion

Figures 4-18 and 4-19 show the combined effects of advection, dispersion, and diffusion on mass fraction (the ratio of solute mass to total fluid mass) contours at 10,000 years for calculations with both time-dependent pressure and time-dependent properties and with time-dependent gas-generated pressures only (no time-dependent properties), respectively. (To obtain concentrations as used in STAFF2D, mass-fraction must be multiplied by fluid density.) In Figures 4-18 through 4-23 the scale on the *Y* axis has been magnified by four to show the contours more clearly. Results show that (1) contours of 1% of original waste concentrations do not intersect the shaft at 10,000 years, and (2) when changes in brine permeability due to gas generation are taken into account, that transport of the solute is reduced relative to calculations with constant (in time) brine permeability.

Interestingly, if one examines mass fraction contours where permeability in the anhydrite above the repository has changed due to gas invading the pore spaces, a notable effect can be seen. Transport along the anhydrite layers above the repository is enhanced for the case of no-gas-modified properties (Figure 4-19). This enhancement disappears when gas-modified properties are introduced (Figure 4-18).

Calculations using diffusivities of zero, 1.4×10^{-11}, and 1.4×10^{-9}, and with advection essentially turned off (by eliminating head gradients in the near field of the waste) were done to study both the effect of changing the value of diffusivity on solute transport and the relative effect of diffusion compared to advection (advection includes dispersion). The middle value (of diffusivity) was chosen as representative of a generic radionuclide (Rechard et al., 1990a). The upper value was chosen merely to show clearly the effect of increasing the diffusivity.

Plots (Figures 4-20 and 4-21) of mass fraction contours at 1000 years show a dramatic spreading of plume widths using diffusivity of 1.4×10^{-9} rather than 1.4×10^{-11}. No other effects are evident. Comparisons of Figures 4-20 and 4-22 (diffusivity=0.0 in Figure 4-22) indicate that the value of 1.4×10^{-11} used for diffusivity gave a negligible diffusion effect (note negligible differences in mass-fraction contours).

It is unclear how important diffusion is in specific local regions. The value of diffusivity used in SUTRA is a global value and does not attempt to reflect local geologic differences due to variations of tortuosity. Along the marker bed, diffusion may be relatively more significant with respect to vertical movement of particles, especially for larger values of diffusivity (refer to the statements above regarding plume width).

Comparisons of transport results in SUTRA calculations using the in-plane (of the repository) geometry (see discussion of calculations in Section 4.2.3.3) and the out-of-plane (vertical cross-section) geometry used in these calculations, show that both configurations predict similar transport away from the repository, but that the in-plane geometry predicts somewhat different transport plume dimensions. The in-plane geometry models predict more uniform movement in all in-plane directions away from the repository. The out-of-plane calculations described here and calculations done using STAFF2D all show eccentricities in the direction of the shaft. However, the in-plane geometry does not include simulation of the shaft. To see the effect of the presence of the shaft in the out-of-plane geometry, a calculation was done with the shaft absent (Figure 4-23). This calculation shows that without the shaft, the vertical model produced transport results comparable to the in-plane results (see Section 4.2.3.3). A closer examination of contour plots of mass-fractions indicates that the (small) differences may be due, in part, to the relatively large dimensions of elements along the direction parallel to the repository. Because of the limitations of computational resources and the increase of computational time with grid size, large aspect ratios in a large number of mesh elements are unavoidable.

Effects due to reduction of time step in coarse mesh were studied. A limited study of time step change show a small effect on the spread of the concentration plume (of particulates). Smaller time steps result in slight (less than 1%) magnification of plume intensity (i.e., the contours spread further from the source with 10 year time steps as compared to 100 year time steps). In all calculations a constant time step was used.

4.2.3.3 In-Plane Calculations

Model Overview

Introduction. Calculations with SUTRA (vertical cross section) and STAFF2D (Sections 4.2.3.2 and 4.2.2.3) showed that the principal pathway for radionuclides driven out of the waste panels by waste-generated gas was downward from a waste panel, into MB139 and then laterally through MB139. These results are based on a vertical two-dimensional model of an essentially three-dimensional phenomenon. Of course, once brine from the repository reaches MB139 the flow spreads in all directions in the plane defined by the thin (approximately 1.0 m thick) MB139.

To assess transport in this horizontal plane the SUTRA code was used to model several waste panels assuming that its entire contents were located in MB139. This assumption essentially neglects any flow resistance afforded by the DRZ in the small thickness of halite between the repository and MB139. SUTRA was run with the transient gas pressure history generated within the repository by the BOAST II code. See Section 4.2.1.5 and Figure 4-2. No gas-modified material properties were used and the shaft was not included. These calculations provide an estimate of the spatial extent of transport in the MB139 medium and can be compared to results

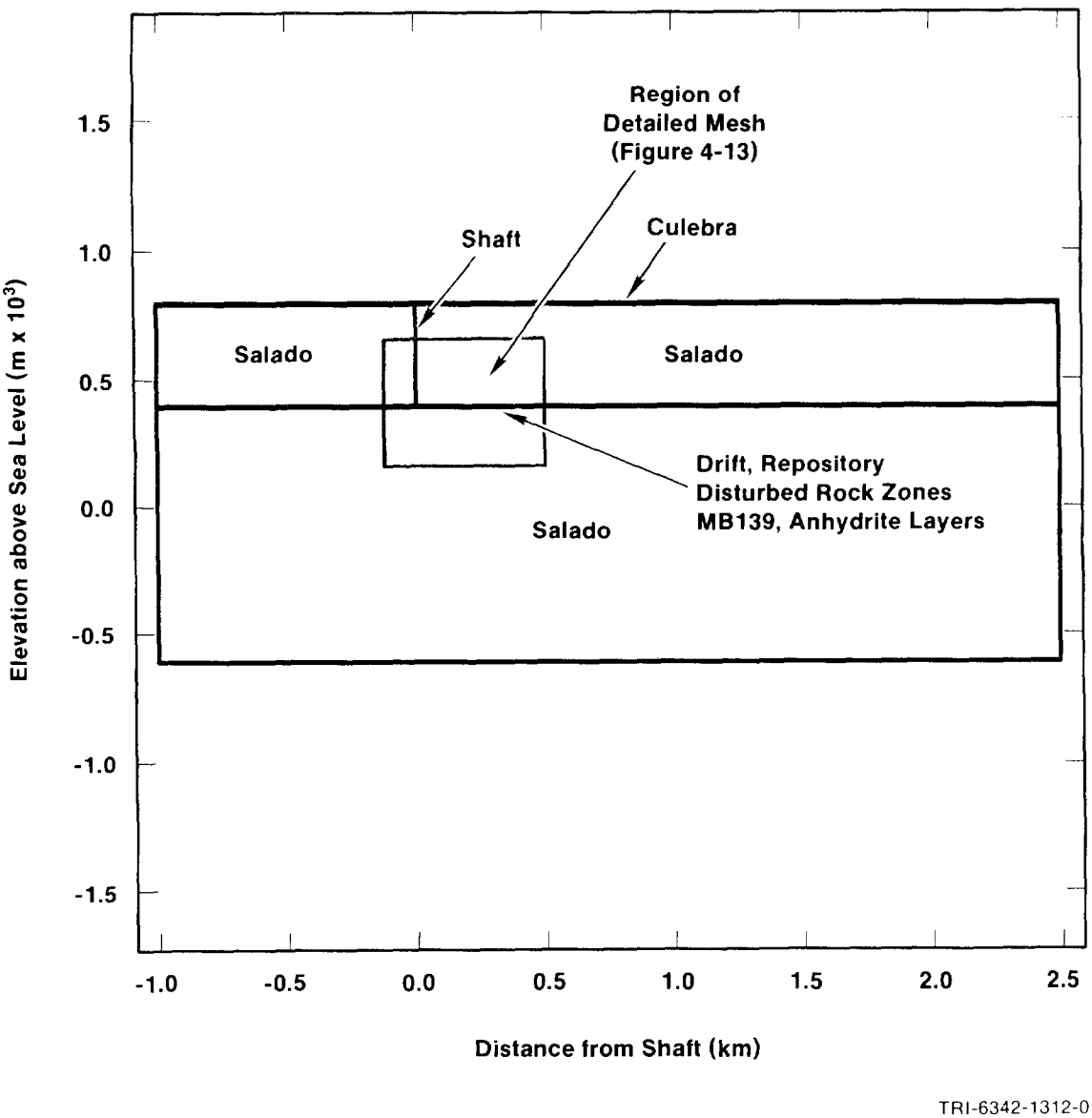

Figure 4-12. Large-Scale View of Coarse Mesh for SUTRA Boundary Conditions

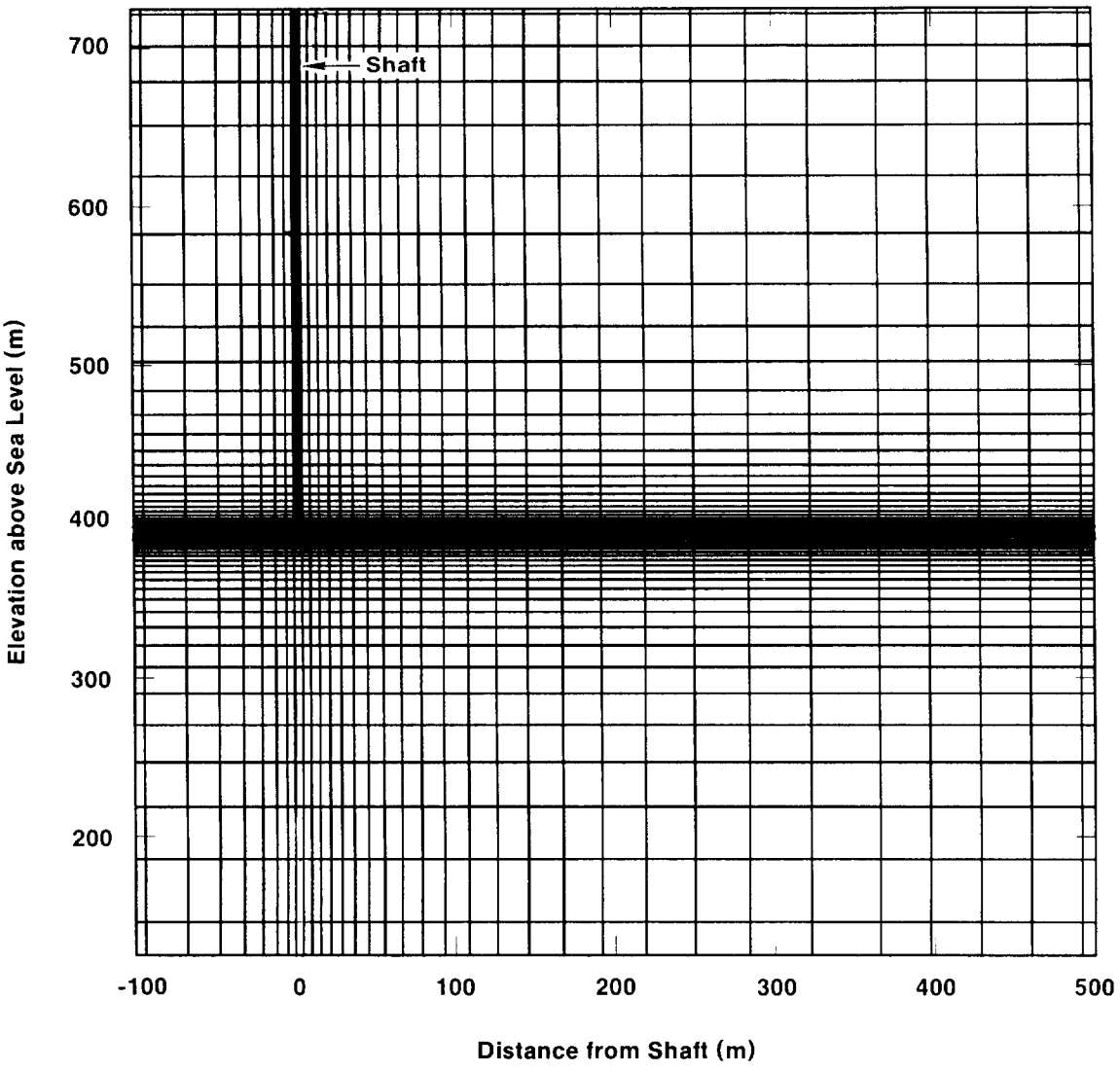

TRI-6342-1313-0

Figure 4-13. Detailed View of Coarse Mesh for SUTRA Boundary Conditions

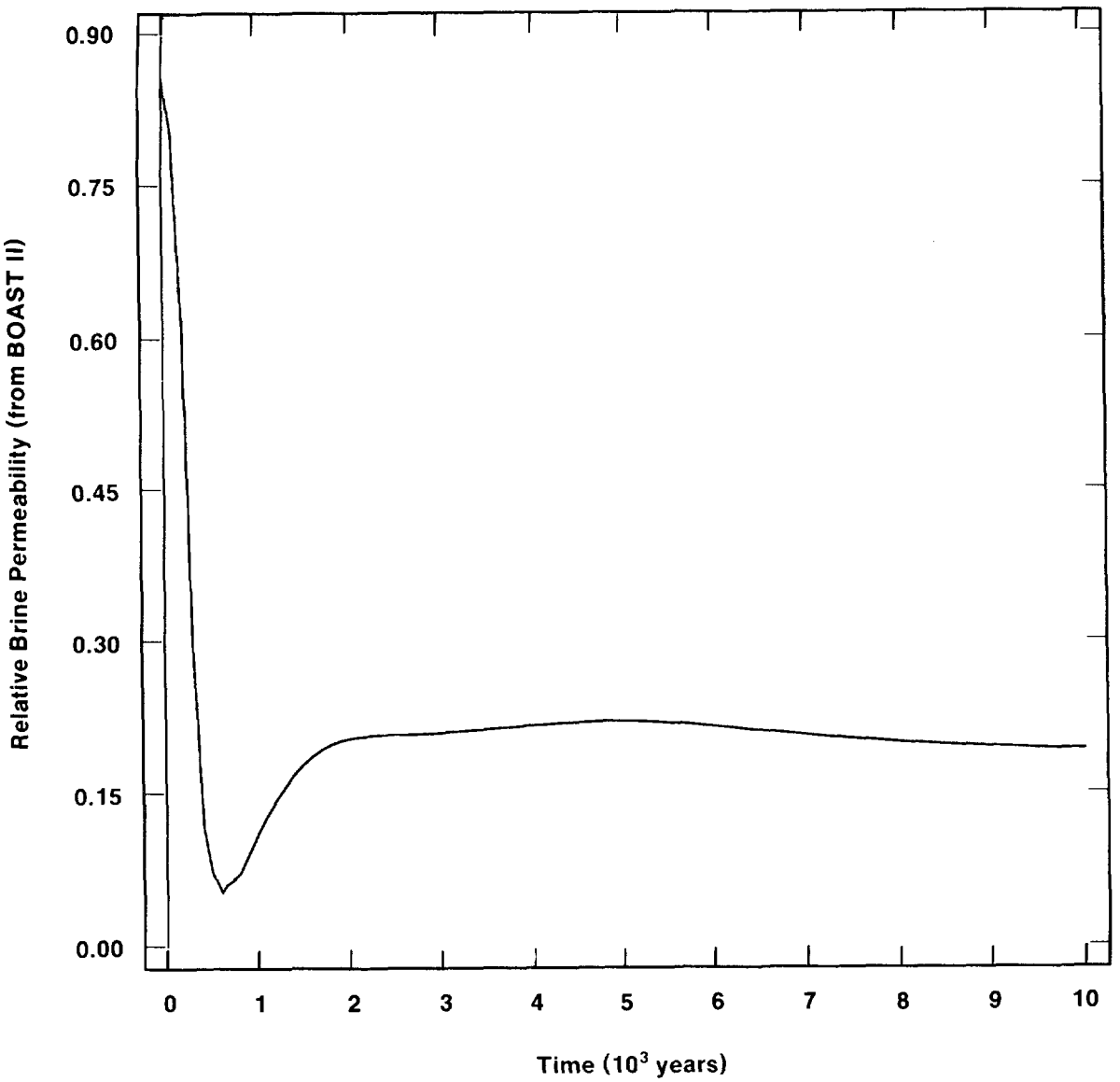

Figure 4-14a. Relative Permeability in Lower Region of Waste Due to Gas Generation

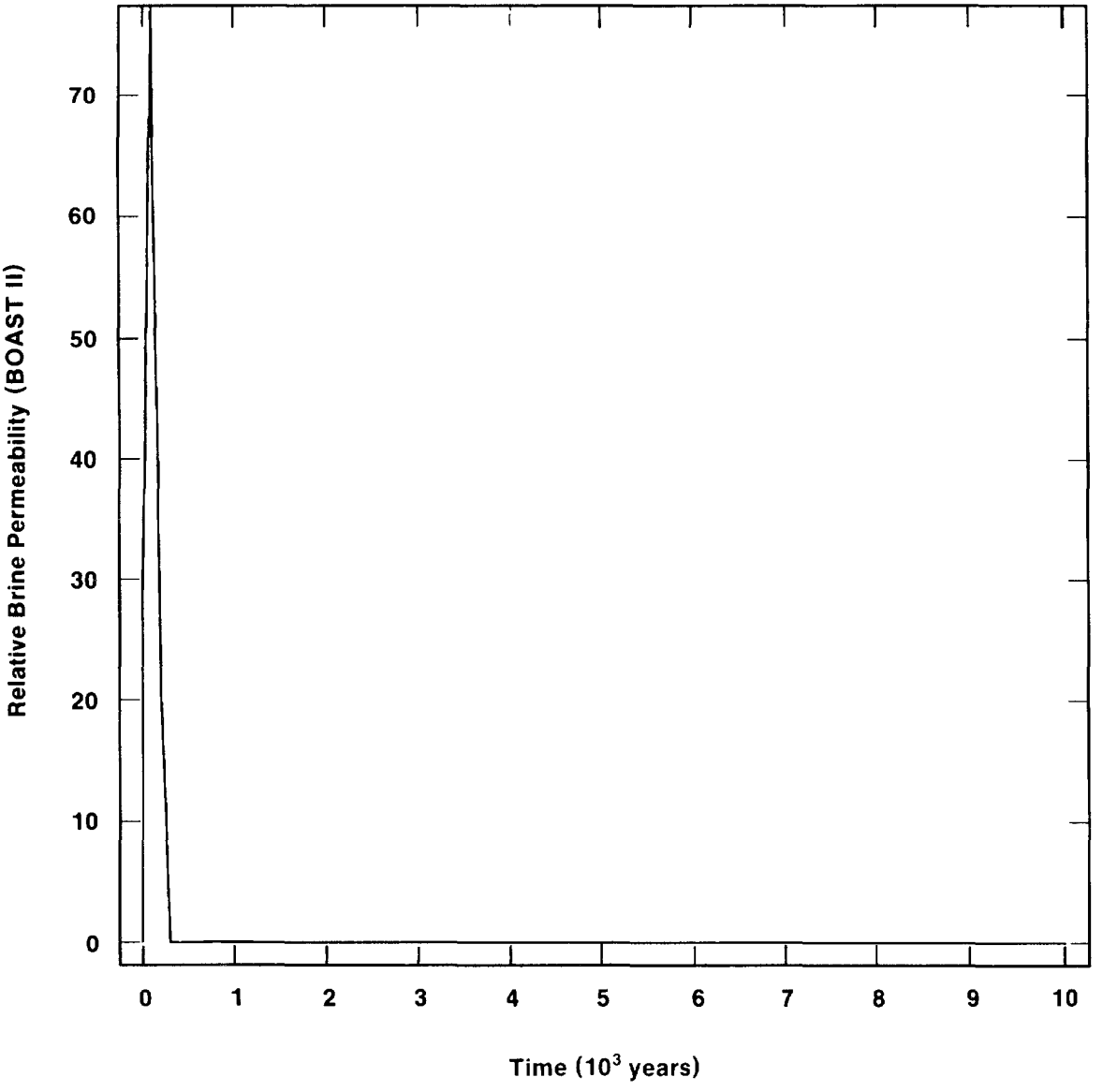

Figure 4-14b. Relative Permeability in Upper Region of Waste Due to Gas Generation

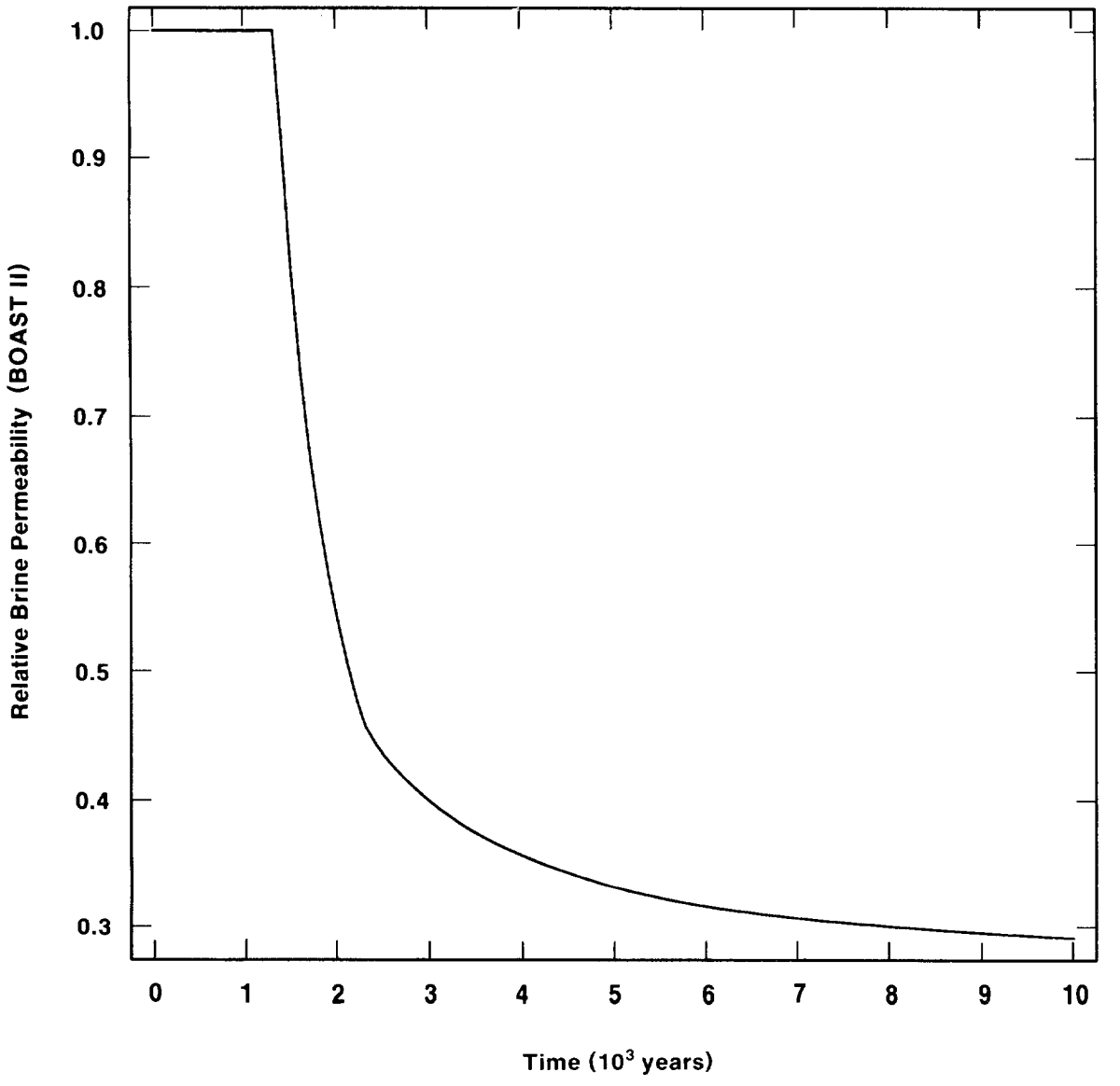

Figure 4-14c. Relative Permeability in Anhydrite

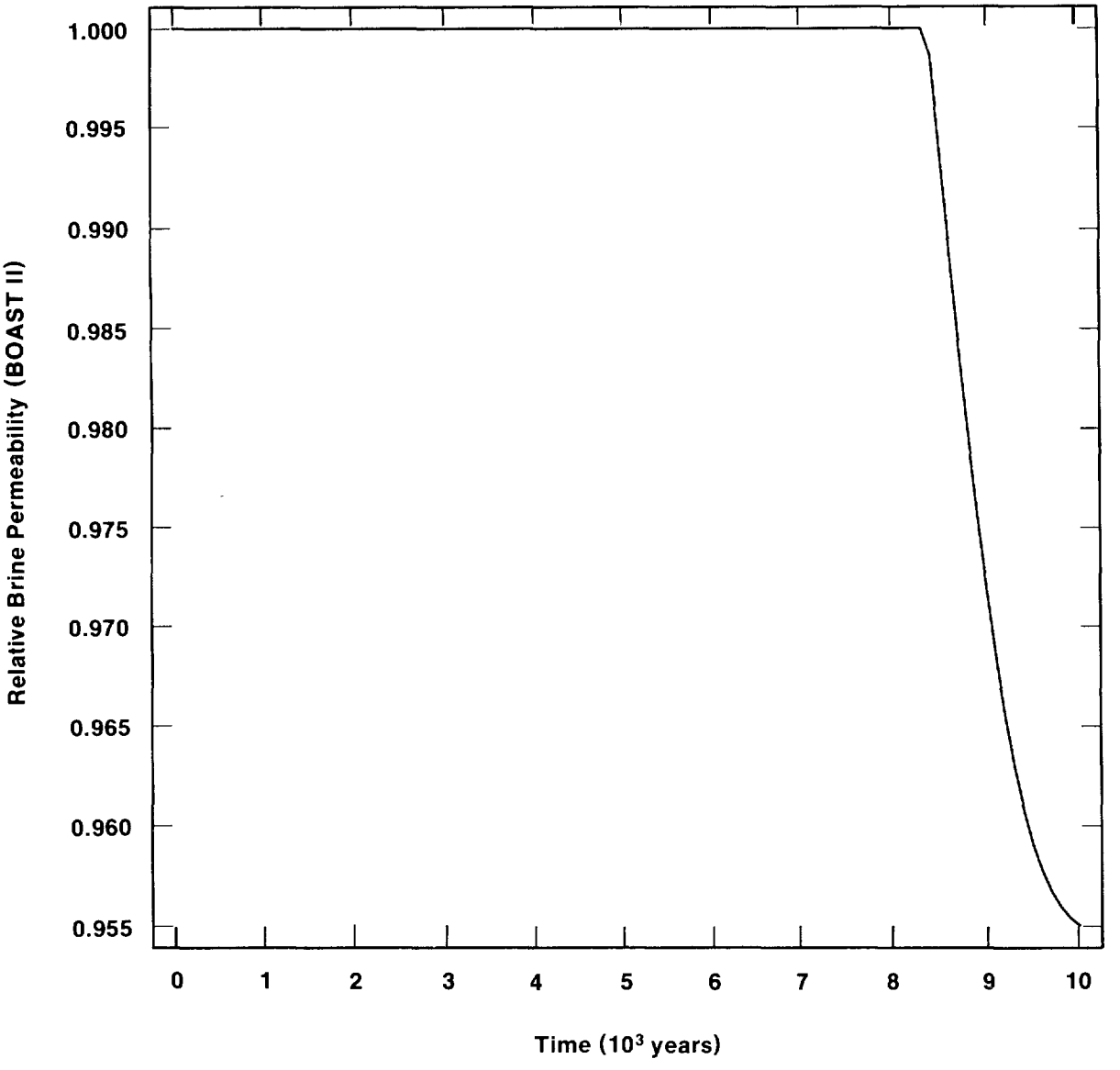

Figure 4-14d. Relative Permeability in Upper Salado DRZ (Above Repository)

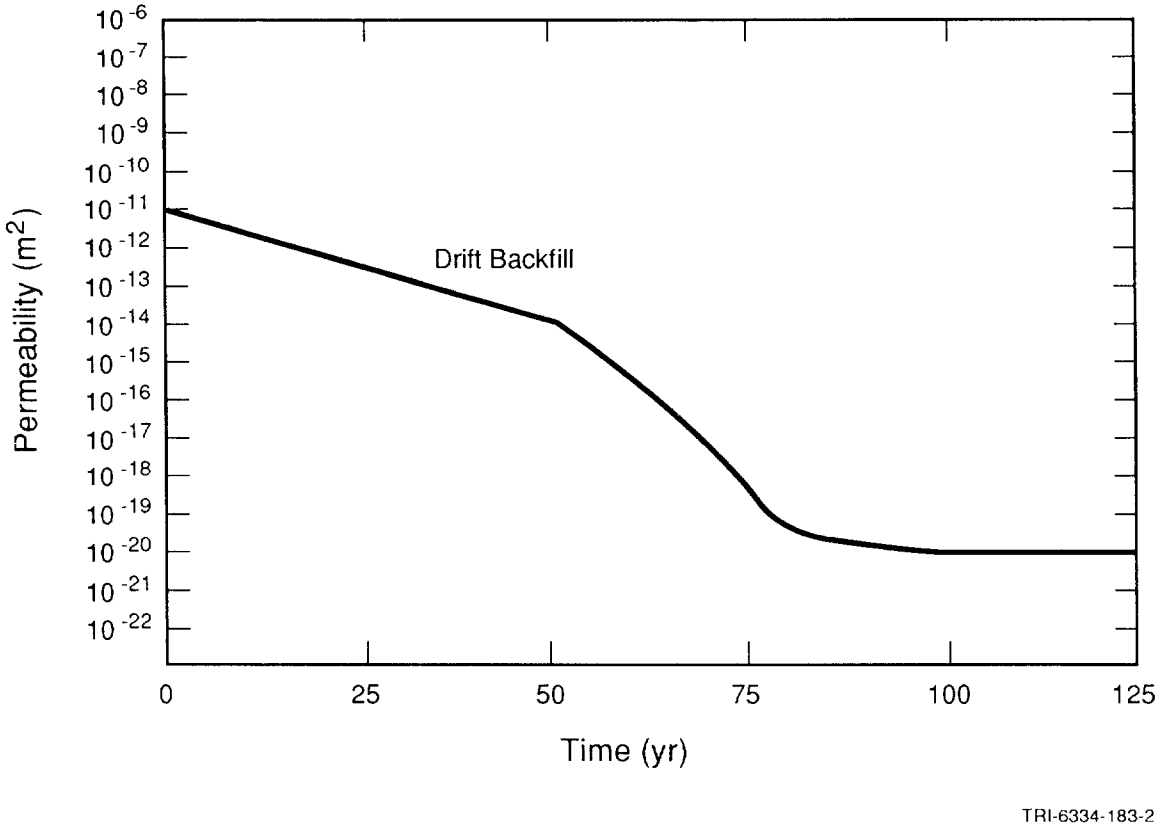

Figure 4-14e. Time Variation of Drift Permeability Due to Consolidation of Drift (from Rechard et al., 1990b, p. 74))

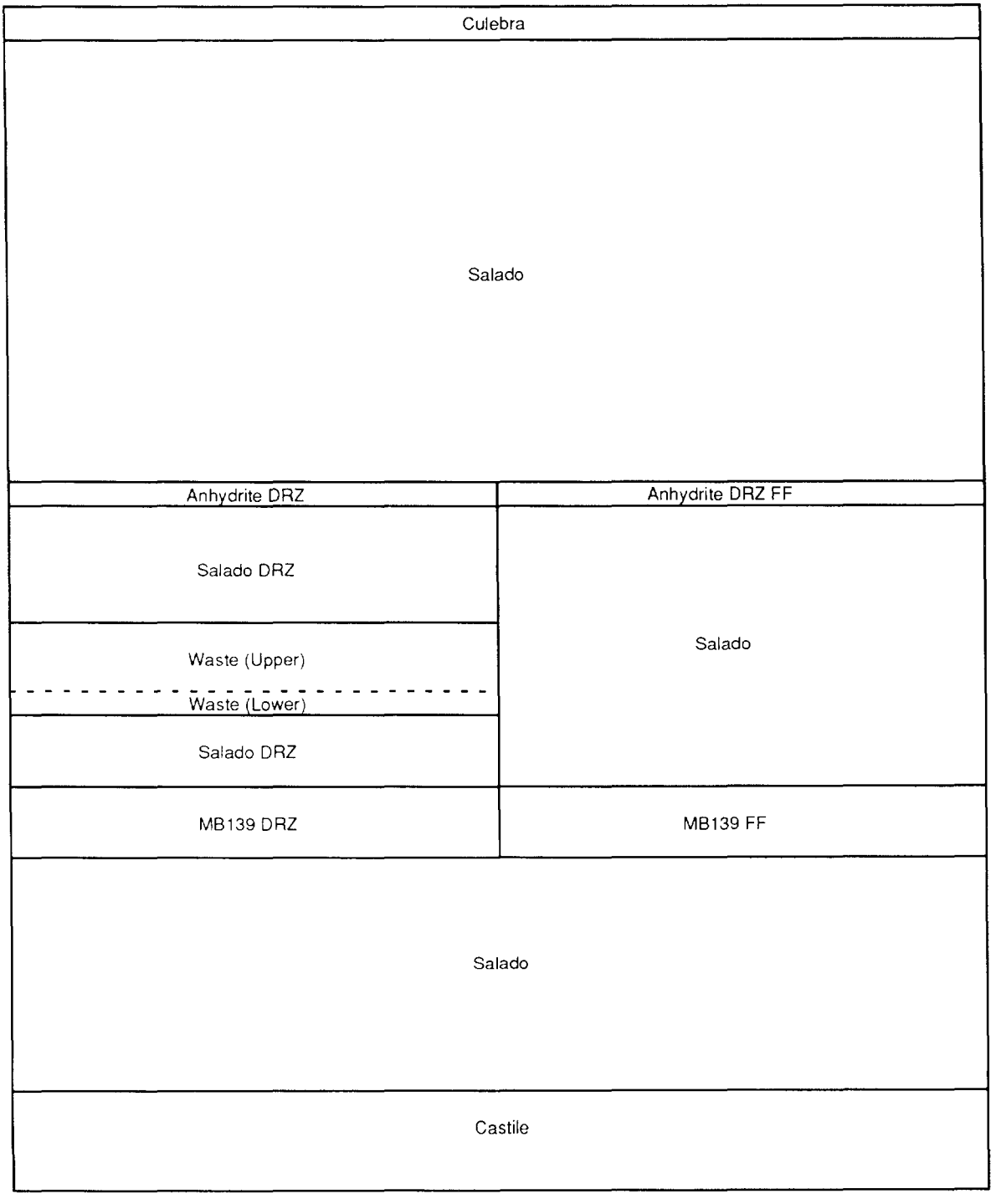

TRI-6342-1376-0

Figure 4-15. BOAST Regions

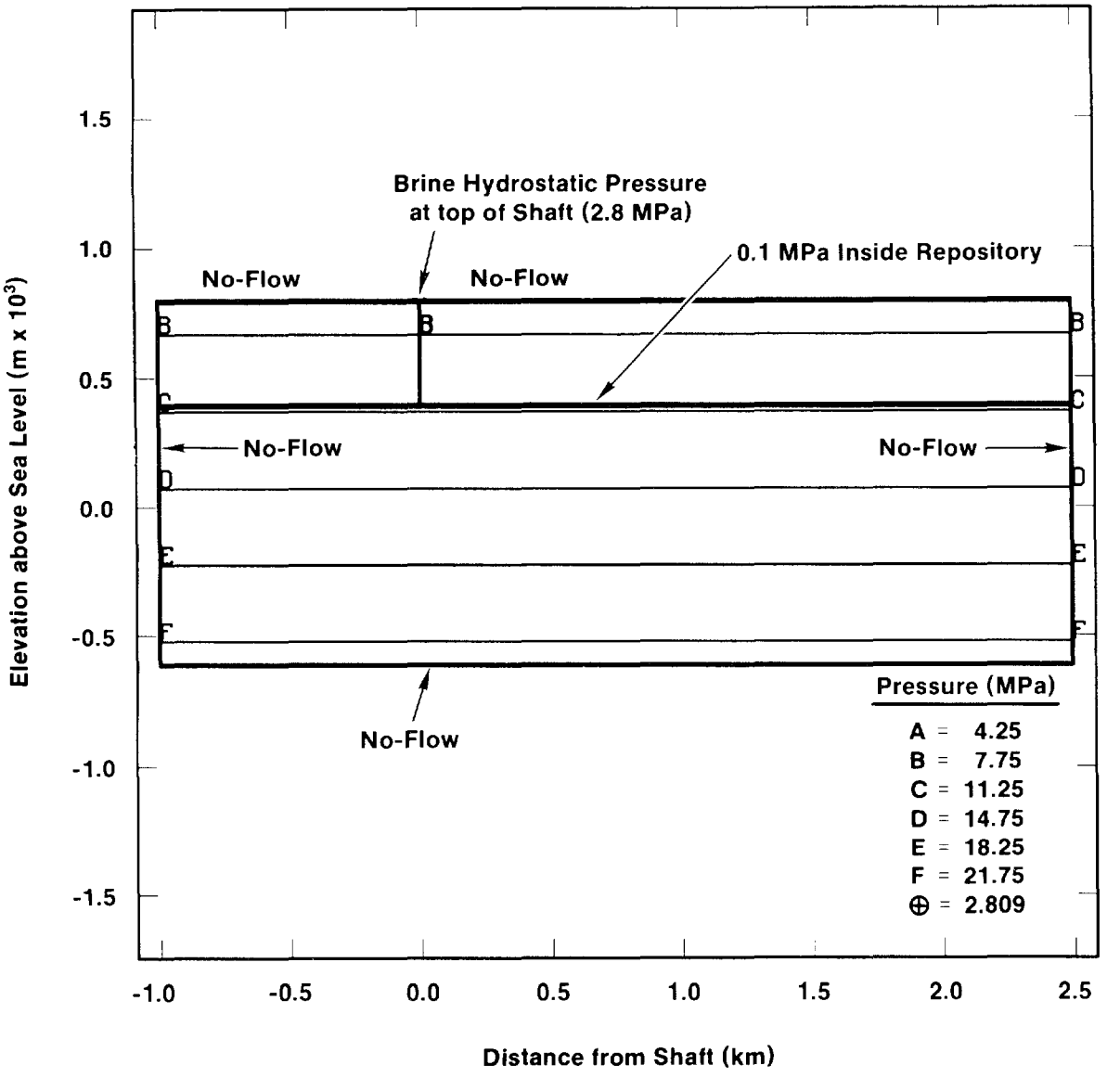

TRI-6342-1319-0

Figure 4-16. Initial Pressure Conditions

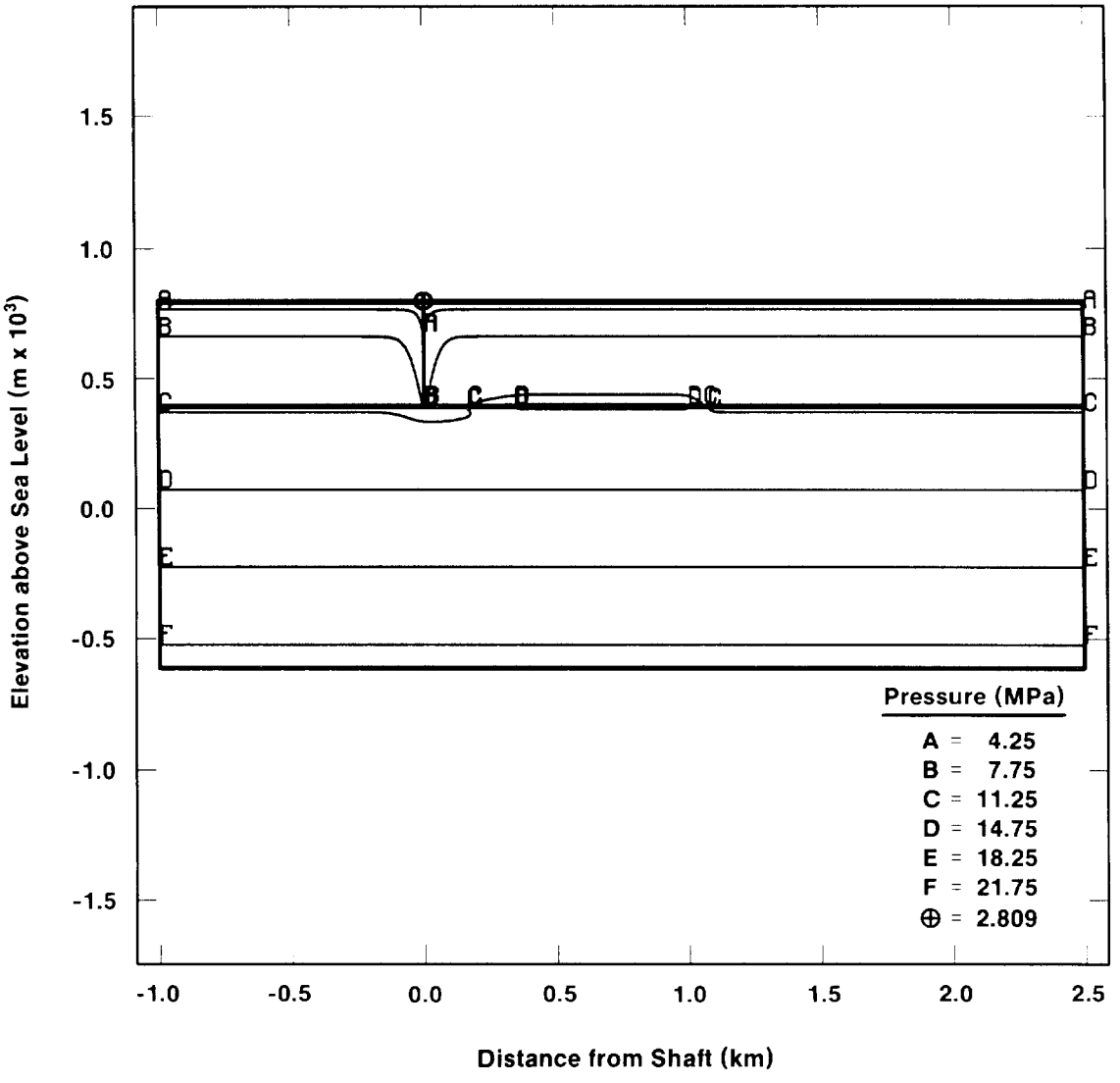

TRI-6342-1320-0

Figure 4-17. Pressures at 600 Years

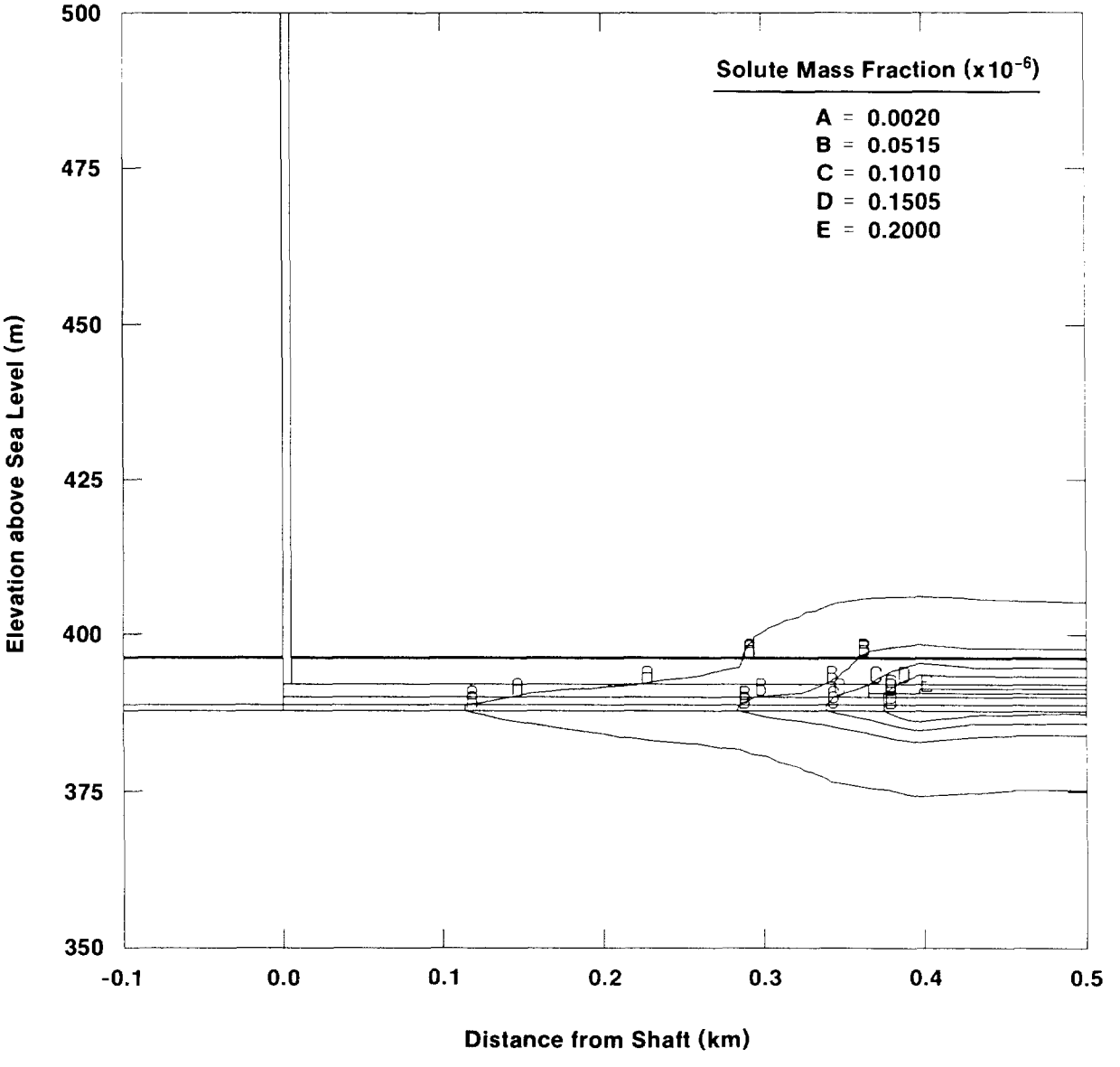

TRI-6342-1322-0

Figure 4-18. Mass Fraction Contours for Undisturbed Vertical Cross Section, Time-Dependent Gas Pressures and Permeabilities (from BOAST II), Step=100 Years, Diffusivity=1.4e-11, Total Time=10,000 years

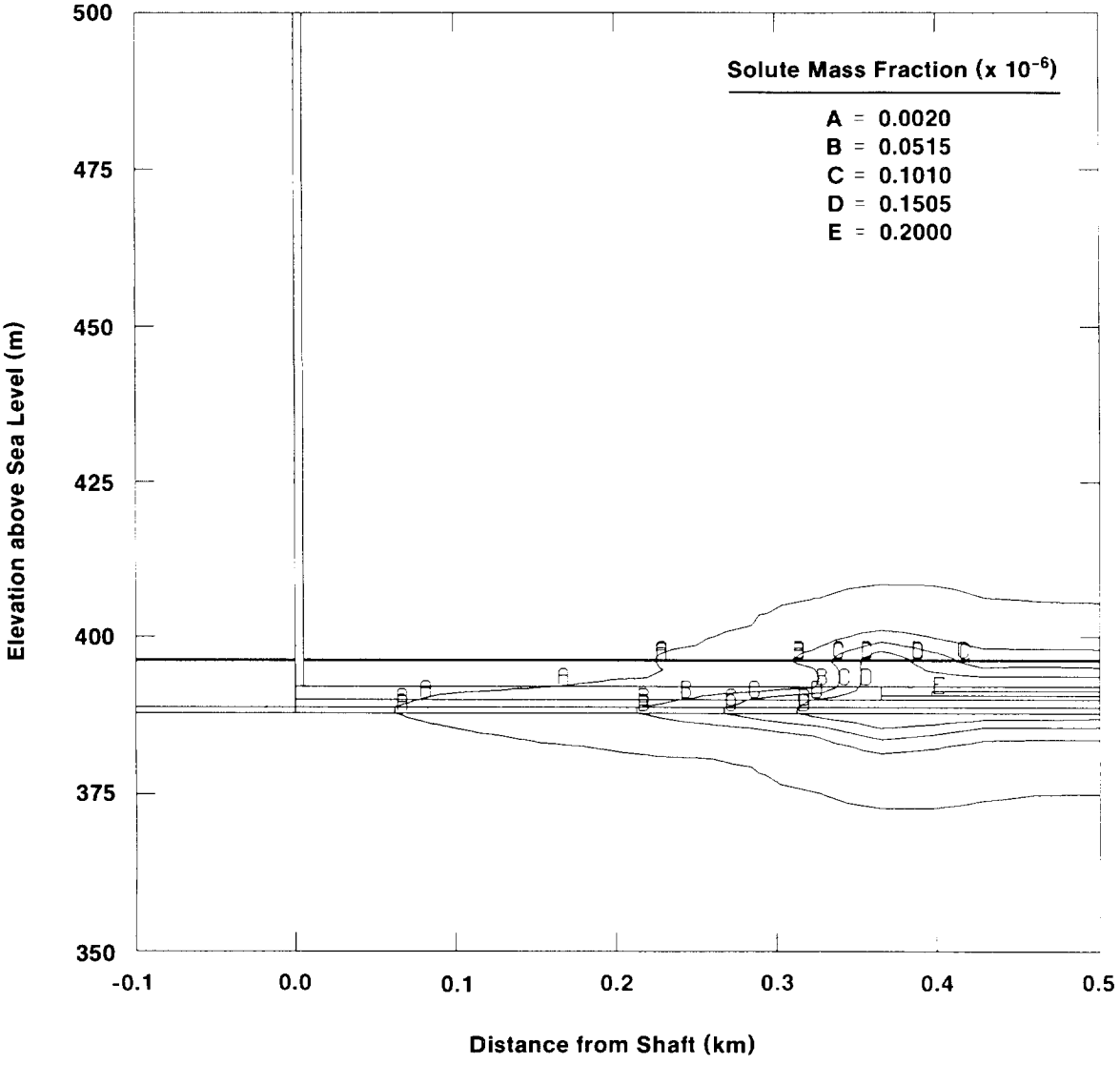

Figure 4-19. Mass Fraction Contours for Undisturbed Vertical Cross Section, Time-Dependent Gas Pressure Only (BOAST II), Time Step=100 Years, Diffusivity = 1.4e-11, Total Time=10,000 years

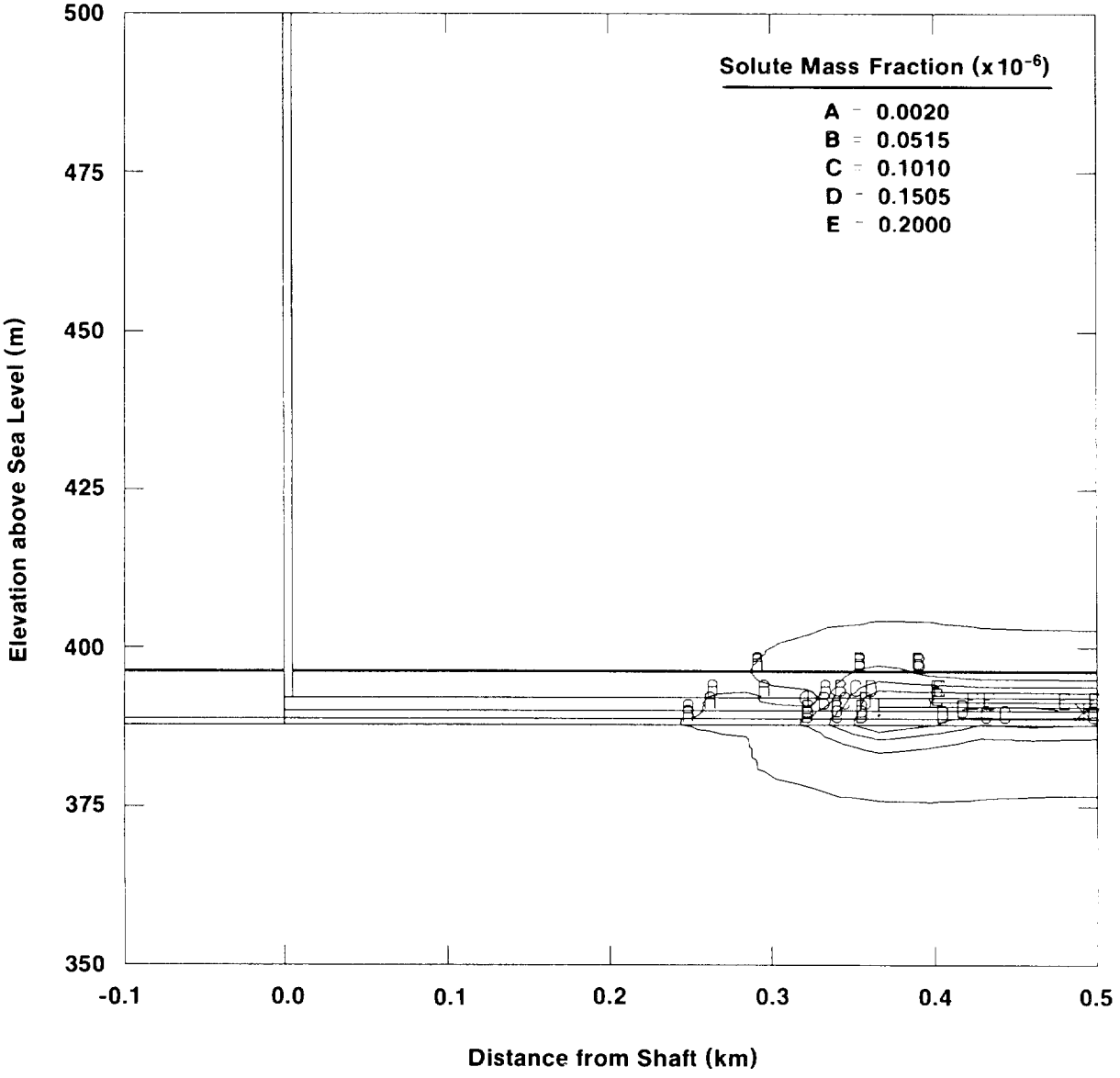

TRI-6342-1321-0

Figure 4-20. Mass Fraction Contours for Undisturbed Vertical Cross Section, Time-Dependent Gas Pressure Only (BOAST II), Diffusivity=1.4e-11, Total Time=1000 years

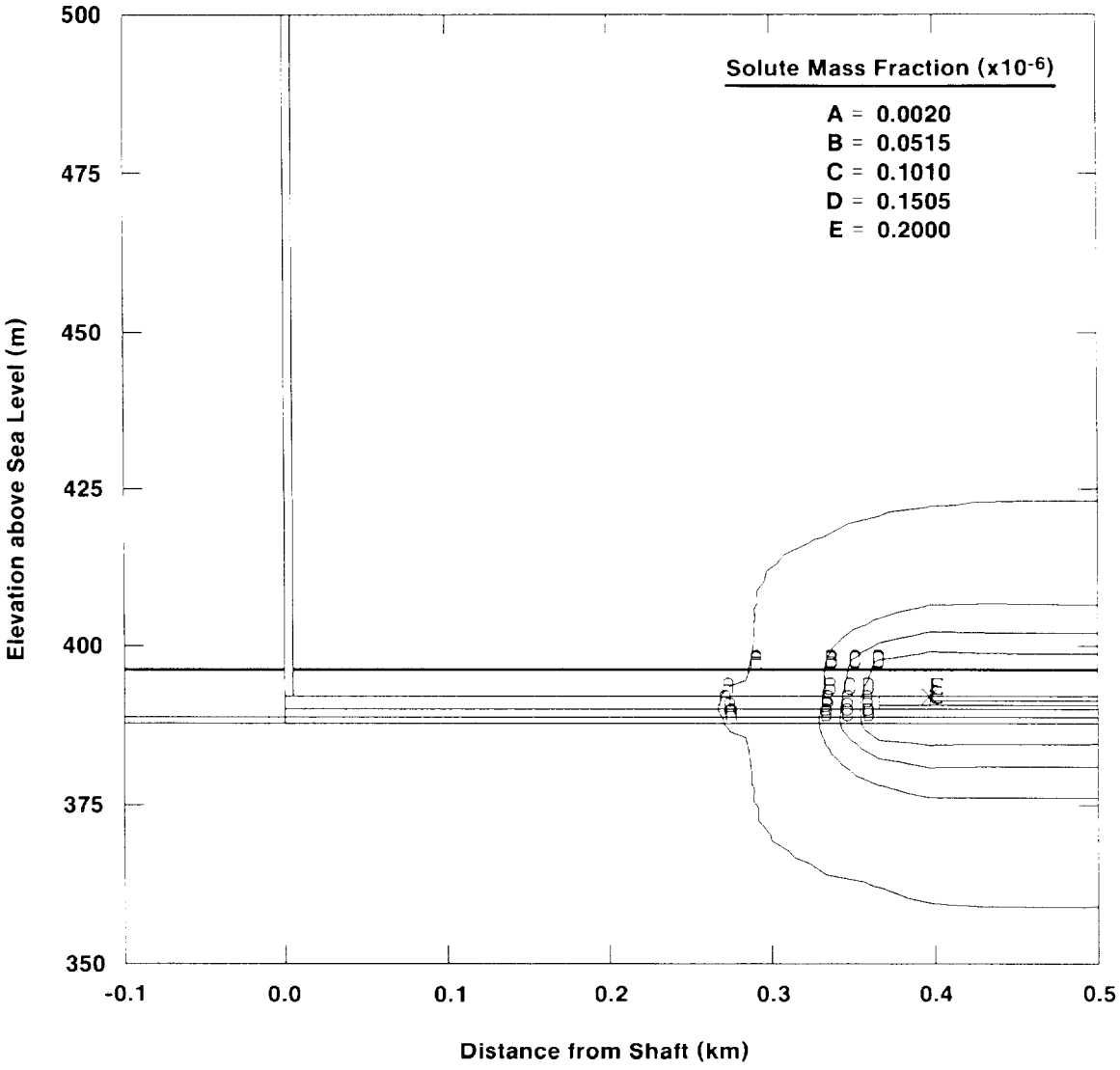

Figure 4-21. Mass Fraction Contours for Undisturbed Vertical Cross Section, Time-Dependent Gas Pressure Only (BOAST II), Diffusivity=1.4e-9, Total Time=1000 years

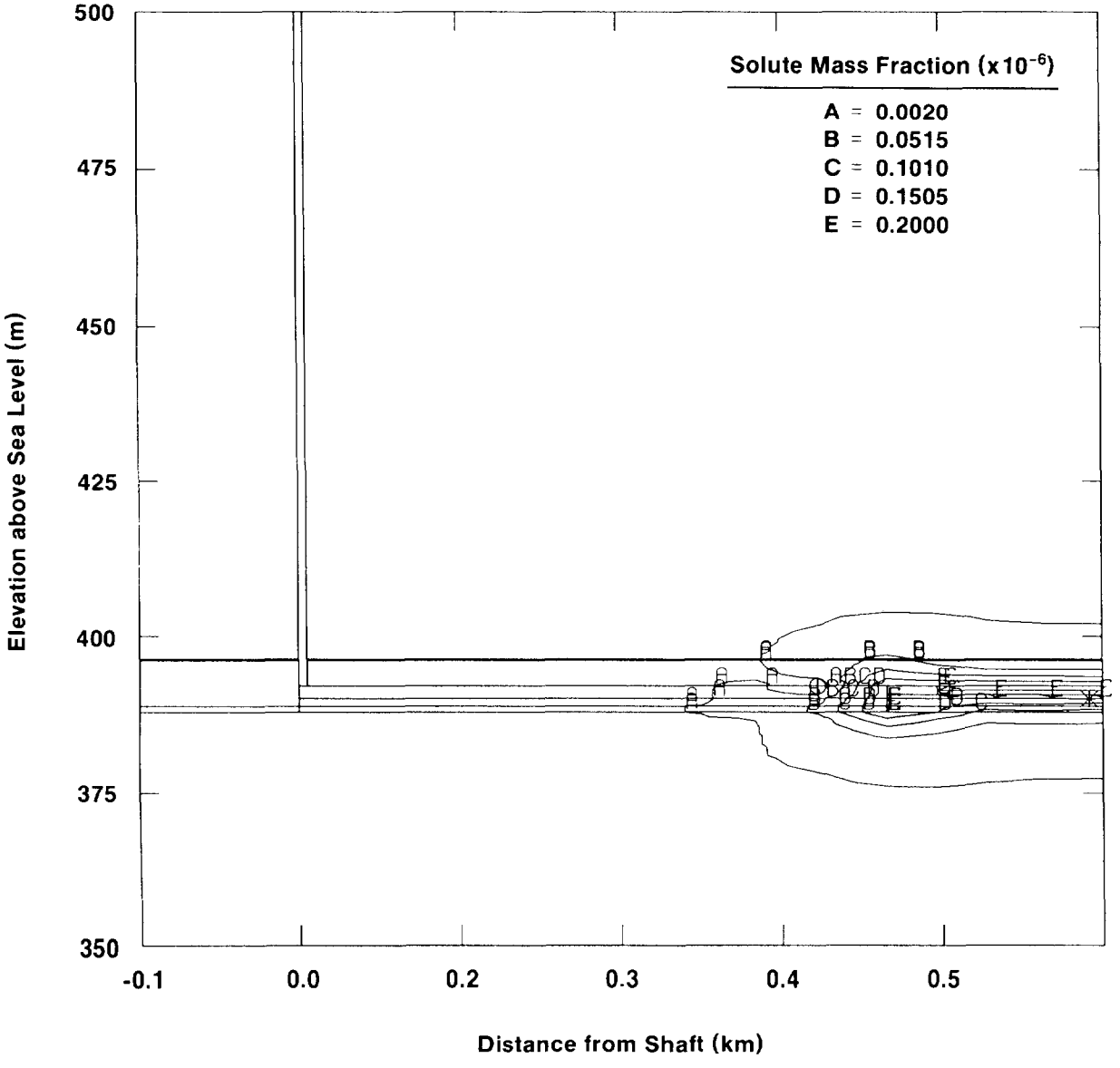

Figure 4-22. Mass Fraction Contours for Undisturbed Vertical Cross Section, Time-Dependent Gas Pressure Only (BOAST II), No Diffusion, Total Time=1000 years

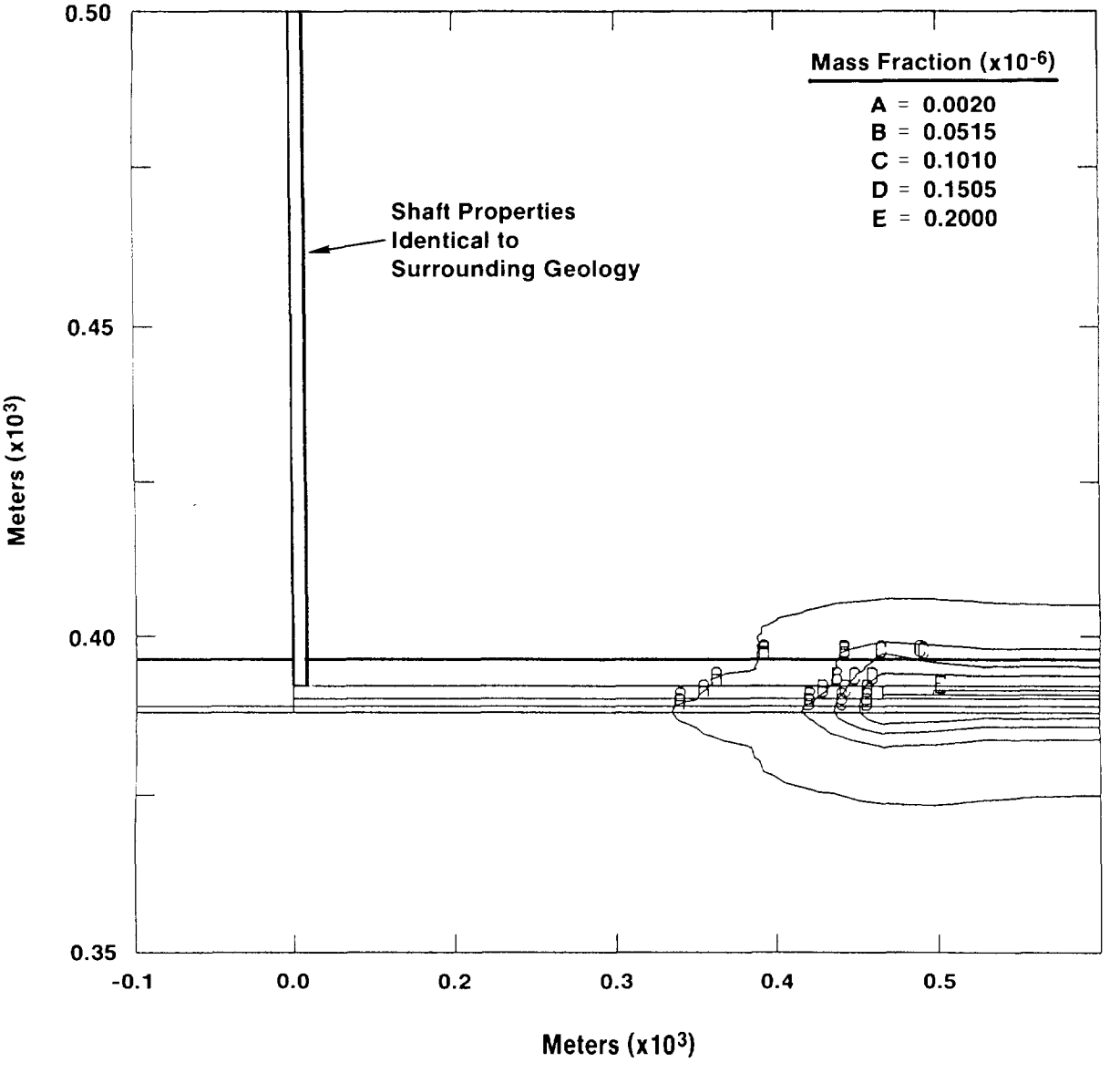

TRI-6342-1327-0

Figure 4-23. Mass Fraction Contours for Undisturbed Vertical Cross Section, Time-Dependent Gas Pressure Only (BOAST II), No Shaft, Total Time 10,000 Years

obtained from calculations performed in a vertical cross section (Section 4.2.3.2). Since the calculations have been performed utilizing single-phase groundwater flow theory, no adsorbate mass transfer, and since the panels are assumed to lie within MB139, the following results represent a conservative estimate of transport phenomena away from the panels in the MB139 medium. References to variables and equations used in SUTRA correspond to definitions provided in Section 4.2.3.1.

Summary of Results. Contours of solute concentrations were plotted at different times and at the end of the 10,000 year regulatory period. At 10,000 years the 1% source-concentration contour extended 75 to 110 m from the repository boundary. These results are consistent with the SUTRA results obtained in a vertical cross-section (approximately 120 m, Section 4.2.3.2) and tend to confirm the validity of the two-dimensional methods used.

Spatial and Temporal Grids

SUTRA was used to investigate transport phenomena as if the WIPP repository fed directly into the fractured anhydrite of MB139. This assumption eliminates the resistance to brine flow that exists in the DRZ just below the repository and maximizes the flow in MB139. Using symmetry and areal geometry (in plane), only one-fourth of the waste panel's shadow projected onto the MB139 layer needs to be modeled. To simulate accurately the gas-generation effects, a pressure history (obtained from BOAST II; see Figure 4-2) was applied to interior repository nodes that lie in the disturbed zone. All calculations were run to 10,000 years. The effect of the shaft is not included.

Simulations using SUTRA were performed assuming single-phase, saturated flow ($S_l = 1$), no adsorbate mass production (i.e., $C_s = 0$), single-species solute without decay, and no density change with concentration. Since density was not allowed to vary as a function of concentration change, ($\partial \rho_f / \partial \hat{C} = 0$), SUTRA's coupling process between flow and transport was eliminated. This is a valid assumption since the initial mass fraction is quite small compared to the initial brine solution density. The assumption that adsorption does not occur is conservative. The model used SUTRA's time-dependent boundary-condition capability to handle the transient pressure condition from BOAST II calculated due to gas generation (Figure 4-2).

Two different spatial and temporal grids were used to model the repository/MB139 medium. A coarse finite-element (FE) mesh used 2,160 elements (45 x 48 elements and 46 x 49 nodes) with a maximum element length (El) of 78.50 m (Figure 4-24). The fine FE mesh of 2,116 elements (46 x 46 elements and 47 x 47 nodes) modeled a smaller domain within the coarse mesh. With a maximum element length of 39.25 m, the exterior boundaries of the fine mesh are also shown in Figure 4-24. The coarse mesh calculation was run to provide boundary conditions for the fine mesh calculations. The first temporal grid used 100 100-year time steps. The second temporal

grid used 200 50-year time steps. The coarse spatial mesh was initially constructed to maintain a mesh Peclet number (Pe_m) less than 10 (the mesh Peclet number estimates the ratio of advection to transport, and can be approximated as $Pe_m=MAX(E_l)/\alpha_L$). The fine mesh was used to study the sensitivity of the model to smaller mesh Peclet numbers. The first temporal scale of 100-year time steps was chosen to handle accurately the pressure history simulating gas generation. Although SUTRA uses an implicit time integration scheme (backwards time-differencing method), a finer temporal scale of 50-year time steps was applied to both coarse and fine spatial grids. The smaller time-step runs were used to investigate sensitivity of time-step size when using time-dependent boundary conditions. The SUTRA codes states that spatial stability is usually guaranteed when $Pe_m \leq 4$. Since the E_ℓ of the fine mesh was 39.25 m and the longitudinal dispersivity of both MB139 materials modeled was 15.00 m, the resulting $Pe_m \approx 2.619$.

Material Properties, Boundary Conditions, and Initial Conditions

Excavation damage and creep damage is expected to modify the properties of MB139 directly under the repository (Lappin et al., 1989). Consequently, two material regions were modeled with both the fine and coarse FE grids: MB139FF and MB139DRZ. (The suffix FF represents "Far Field"; DRZ denotes "Disturbed Rock Zone.") The required SUTRA flow properties are (1) grain density (of solid matrix), (2) fluid density, (3) permeability (assumed isotropic for this calculation), (4) bulk compressibility (of solid matrix), and (5) fluid compressibility. The required SUTRA transport properties are (1) dispersivity, (2) diffusion, (3) fluid density, and (4) fluid viscosity. The material property values of both MB139FF and MB139DRZ are for the most part given in Volume 3 of this report. Certain parameters differed, however, from those found in Volume 3 of this report. For MB139FF a permeability of $1.0\text{x}10^{-19}$ m^2 was used (as opposed to the report value of $2.87\text{x}10^{-20}$ m^2) and for MB139DRZ a porosity of 0.06 was used as opposed to a value of 0.055 reported in Volume 3 of this report. The SUTRA input variable for solid (bulk) compressibility, corresponding to the MB139 bulk compressibility was calculated as the inverse of the solid mechanics bulk modulus (K_{bulk}). Therefore the bulk compressibility equals $3(1-2\nu)/E$, where ν and E are Poisson's ratio and Young's modulus, respectively. It is assumed that the anhydrite material and MB139 material have equivalent bulk compressibilities. Both ν and E values are referenced from Table A-8 of Rechard et al. (1990a). The MB139 fluid's molecular diffusion, density, compressibility, and viscosity were assumed equivalent to Salado brine properties found in Table A-9 of Rechard et al. (1990b).

The SUTRA code uses a coefficient of apparent molecular diffusivity of solute in solution in a porous medium, including tortuosity effects (D_p, Section 4.2.3.1), for the diffusion term of the transport partial differential equation (PDE). Thus, for diffusive/dispersion-dominated transport, solute concentration is highly sensitive to the input diffusion and dispersivity values. The

apparent molecular diffusivity term used in SUTRA calculations was computed as the product of the free-water molecular diffusion in a pure fluid, D^*, and tortuosity, τ (1.000×10^{-10} m^2/s and 0.140, respectively).

Dirichlet boundary conditions (of p=11.00 MPa and $\hat{C}$ = 0.000 kg/kg) for the coarse grid were applied to the far-field boundaries. The far-field pressure of 11.00 MPa was taken as the median value of brine pressure at the repository level found in Rechard et al. (1990b). Neumann boundary conditions ($\partial p/\partial u = 0$ and $\partial \hat{C}/\partial u = 0$, where u = outward normal direction) were applied to the one-fourth repository/MB139 symmetric boundaries as shown in Figure 4-25. In addition, time-dependent pressure conditions were applied at interior nodes of the MB139DRZ to simulate gas generation effects. The time-dependent conditions (a pressure history function) from BOAST II (see Figure 4-2) were applied exclusively to interior nodes of the MB139DRZ because SUTRA computes an associated fluid-flux term at each pressure boundary condition node. According to Voss (1984), SUTRA computes specified pressures at nodes through cellwise addition of fluid flux, Q_{bc}^i (where i denotes a node number) [L^3/t], as

$$Q_{bc}^i = v\left(p_{bc} - p^i\right) \tag{4-40}$$

where v is the conductance [$L^4 t/M$], p^i is the specified pressure node [M/Lt^2], and p_{bc} is the specified pressure value [M/Lt^2].

SUTRA defines a "cell" as a node centered among four separate quadrants of four neighboring elements. Thus for a cell in which a large number is assigned to v, the flux term Q_{bc}^i dominates the fluid mass balance equation. This results in $p^i \cong p_{bc}$ and achieves the specified pressure at the node representing cell i. It is because of this "cellwise" fluid-flux terminology involving fluid sources and flows across boundaries that the time-dependent pressures were applied only to the interior nodes of material MB139DRZ. Thus, applying a pressure condition on the material boundary of MB139FF/MB139DRZ would invoke unrealistic fluid-flux terms. Figures 4-26a and 4-26b display the MB139DRZ material and the interior nodes at which the BOAST II pressure function was applied for both spatial grids. In conjunction with the pressure function, a constant concentration (SUTRA's concentration is actually a mass fraction: mass solute per mass total solution) of 2.000×10^{-7} kg/kg was also set at the interior MB139DRZ nodes. This value of concentration is about the maximum solubility limit of brine solution transporting radionuclide $^{240}Pu^{+4}$.

At first, the fine FE mesh calculations used two sets of time-dependent conditions, transient boundary conditions and a transient source function (pressure history and constant concentration applied on the MB139DRZ interior nodes). To remain consistent with the coarse FE mesh

calculations, the fine grid's boundary pressures and concentrations were interpolated at each time step from the coarse mesh solution. (Note that the fine mesh is nested completely within the coarse mesh as shown in Figure 4-24). However, the interpolated fine mesh boundary values at each time step were found to be identical to the coarse mesh constant boundary values. Thus, the same constant coarse mesh boundary conditions were applied to the fine mesh boundaries and the coarse grid calculations were, in fact, not necessary.

Initial conditions of the two primary variables (pressure and concentration) for both the coarse and fine grids were p = 11.00 MPa and $\hat{C}$ = 0.000 kg/kg, applied at the nodes of the MB139FF material and at nodes of the MB139FF/MB139DRZ boundary.

Results and Discussion

Because the interior nodes of MB139DRZ are initially at a lower pressure than the nodes of MB139FF (MB139DRZ at atmospheric pressure and MB139FF at a far-field pore pressure of p=11.00 MPa), the SUTRA solution resulted in flow into the MB139DRZ material until the gas generation source function (pressure history) reached 11.00 MPa. After that time, the MB139DRZ pressure exceeded the MB139FF far-field pore pressure, and flow was driven outward from the MB139DRZ material.

Viewing the concentration contour plots, it can be seen that both grid size and time-step size have a noticeable effect on transport. Studying the coarse mesh analyses, it was found that decreasing the time-step size from 100 to 50 years had no affect on the transport distance of the 1% source concentration contour line (2.0×10^{-9} kg/kg) after 10,000 years (Figures 4-27a and 4-27b). In contrast, the fine mesh SUTRA calculations were more sensitive to smaller size time steps. The fine mesh analyses resulted in a greater transport distance of the 1% source-concentration line for 50-year time steps than for 100-year time steps. Yet, decreasing the time-step size even further (10-year time steps) showed no difference from using the 50-year time steps. The effects of concentration transport due to decreased time-step size on the fine mesh after 1,000 years are shown in Figures 4-28a, 28b, and 28c. Comparing the coarse and fine mesh calculations for 50-year time steps, it can be seen in Figures 4-27b and 4-29 that the fine mesh shows the 1% source-concentration contour line traveling much further and around both "fingers" of the one-fourth repository's shadow in the MB139 layer. Since the fine mesh SUTRA calculations revealed that decreasing the time step to 10 years had no effect compared to the calculations using 50-year time steps, it follows that 50-year time steps are adequate for temporal discretization. This SUTRA transport calculation (fine mesh and 50-year time steps) predicts that after 10,000 years the 1% source-concentration contour line (2.000×10^{-9} kg/kg) has traveled approximately 75 m from the MB139DRZ-MB139FF material intersection (Figure 4-29).

To verify that this model is not diffusion/dispersion dominant, additional calculations setting the velocity field equal to zero would be necessary. If the velocity contribution of the transport PDE were omitted from equation (4-35), the resultant PDE becomes more parabolic,

$$\varepsilon\rho_f \frac{\partial \hat{C}}{\partial t} = \nabla \bullet \left\{ \left[\varepsilon\rho_f \left(D_p \underline{\underline{I}} + \underline{\underline{D}} \right) \right] \bullet \nabla \hat{C} \right\} \tag{4-41}$$

where,

ε = porosity (dimensionless),

ρ_f = fluid density (M/L^3),

∇ = del operator,

$\bullet$ = dot product,

D_p = diffusion coefficient (L^2/t),

$\underline{\underline{I}}$ = identity tensor (dimensionless),

$\underline{\underline{D}}$ = dispersivity tensor (L^2/t), and

$\nabla \hat{C}$ = concentration gradient (L^{-1}).

Equation (4-41) reveals that if the dispersivity tensor, $\underline{\underline{D}}$, components were small (functions of the velocity components), the transport PDE would be diffusion, D_p, dominated. A brief study was made to investigate the influence of diffusion on contaminated groundwater transport. Rather than use a zero-velocity field ($\underline{v}$=0) to study the uncoupled effects of diffusion, a calculation was performed using an order-of-magnitude increase in the apparent molecular diffusion coefficient, D_p (1.400×10^{-10} m^2/s), with the fine FE mesh and a temporal grid of 100-year time steps. As seen in Figure 4-30a, the resulting calculation's increased diffusion in the transport is noticeable when compared to the fine mesh calculation with the original diffusion coefficient(1.4×10^{-11} m^2/s of Figure 4-30b (especially between the "fingers" where the 1% source-concentration contour line has traveled farther). However, the increased diffusion does not dominate the solution (concentration-contour lines), and since Pe_m = 2.619, the model is not completely diffusion-dominated and advection should not be ignored.

An additional calculation was performed to study the effect of placing source concentration nodes on the boundary of the MB139FF and MB139DRZ materials. This slight modification to the boundary conditions retained the flow equation's time-varying Dirichlet conditions applied to the interior MB139DRZ nodes, while extending the transport equation's constant Dirichlet conditions to all interior MB139DRZ nodes and MB139DRZ/MB139FF boundary nodes. Previous calculations assumed that the source terms for transport were applied only to the interior MB139DRZ nodes. Thus employing the fine mesh, a temporal discretization of 50-year time steps, identical initial conditions, and these slightly modified boundary conditions, the calculation was run to 10,000 years. As displayed in Figure 4-31, the 1% source concentration contour line

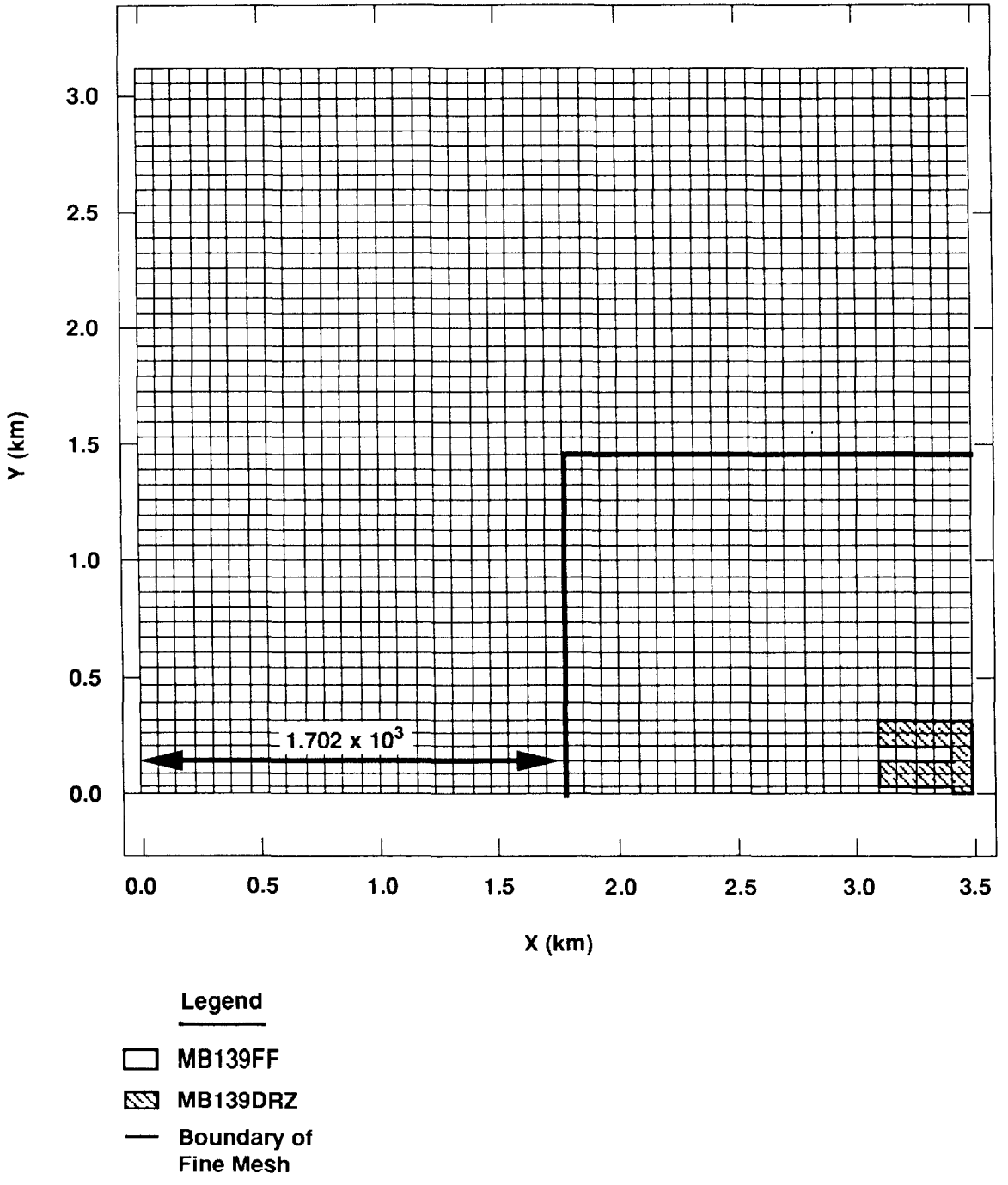

TRI-6342-1386-0

Figure 4-24. Coarse FE Mesh for In-Plane Calculations

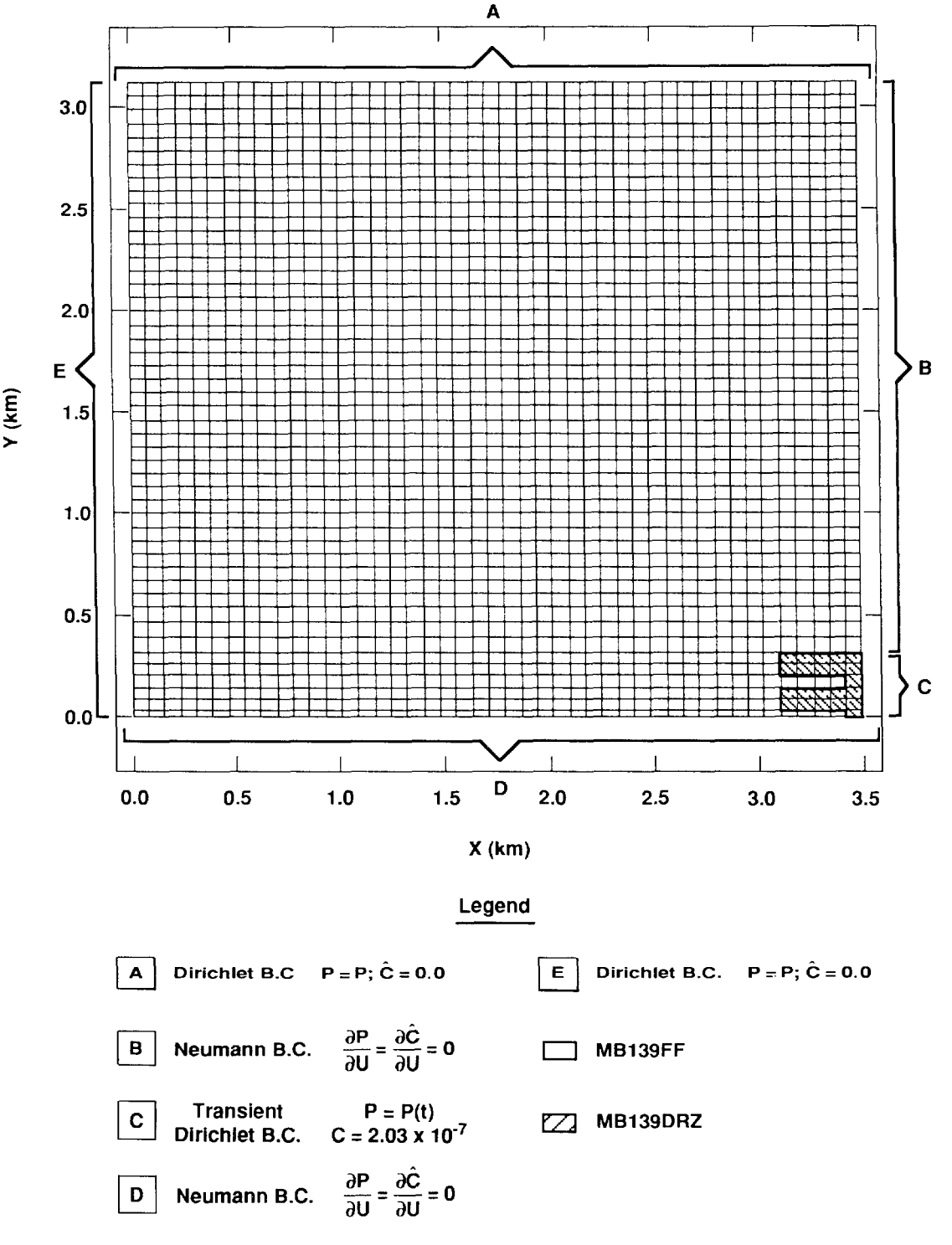

Figure 4-25. Boundary Conditions for In-Plane Calculations

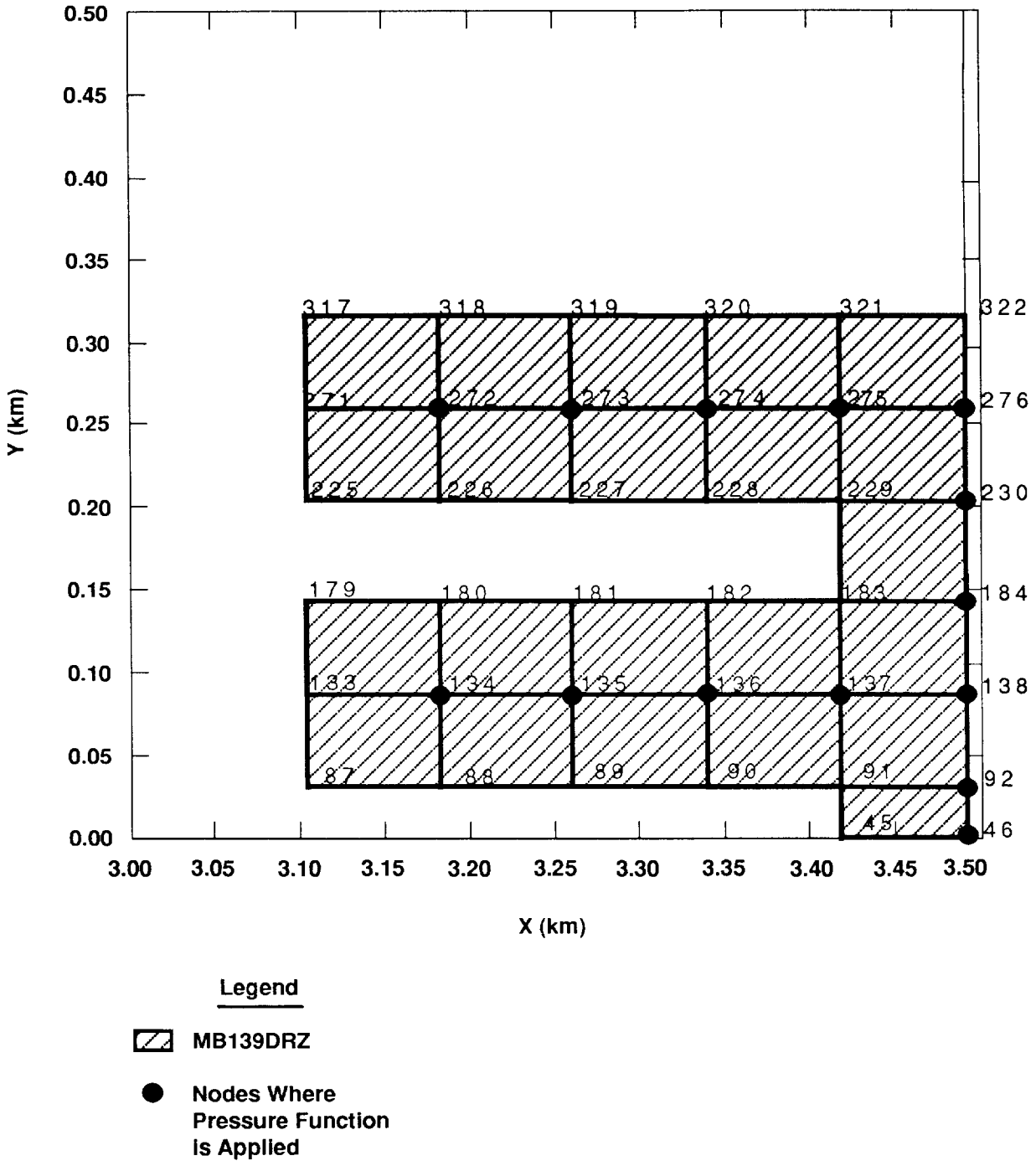

TRI-6342-1384-0

Figure 4-26a. Location of Nodes of Coarse FE Mesh for Applied Pressure Function

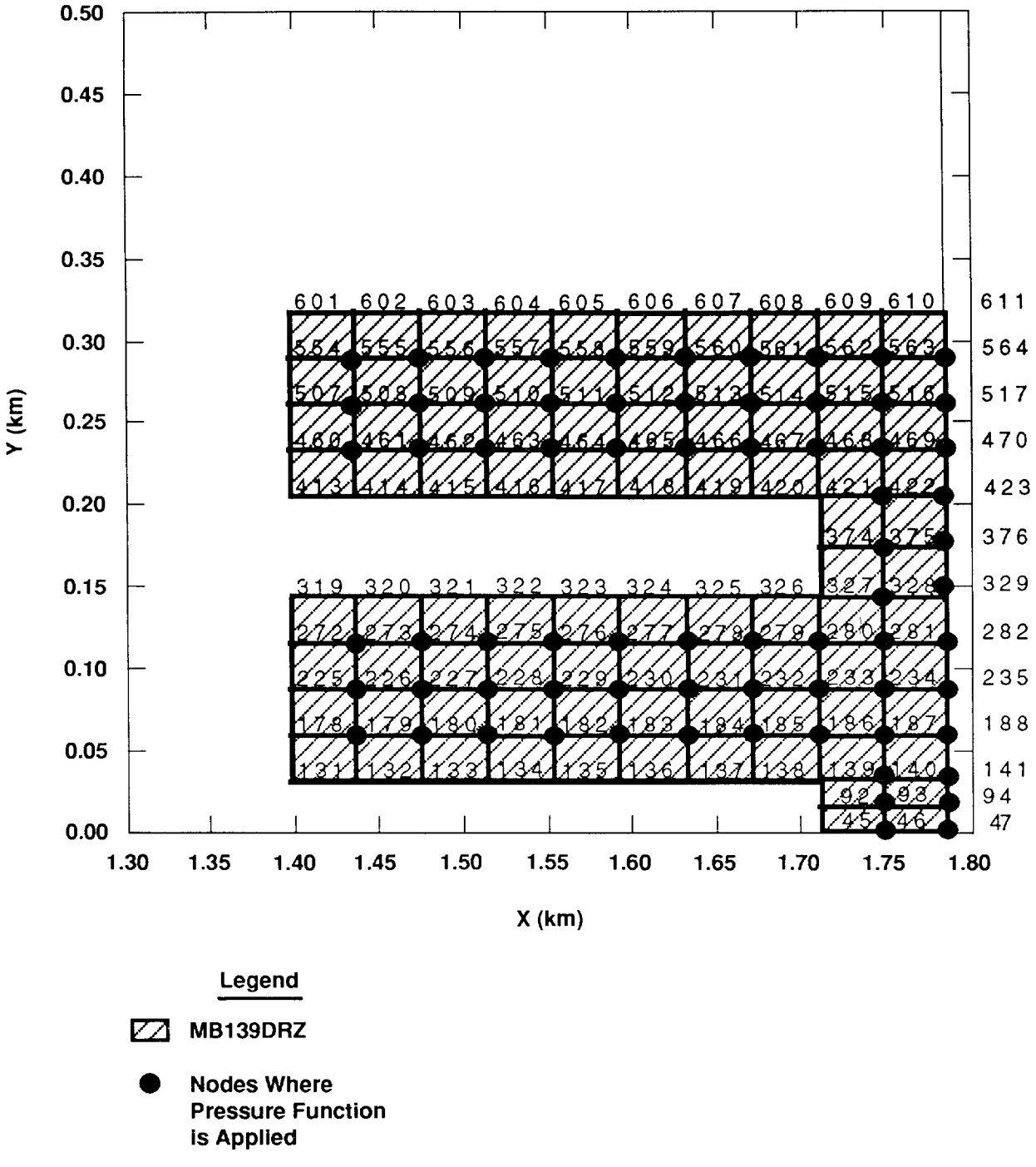

TRI-6342-1385

Figure 4-26b. Location of Nodes of Fine FE Mesh for Applied Pressure Function

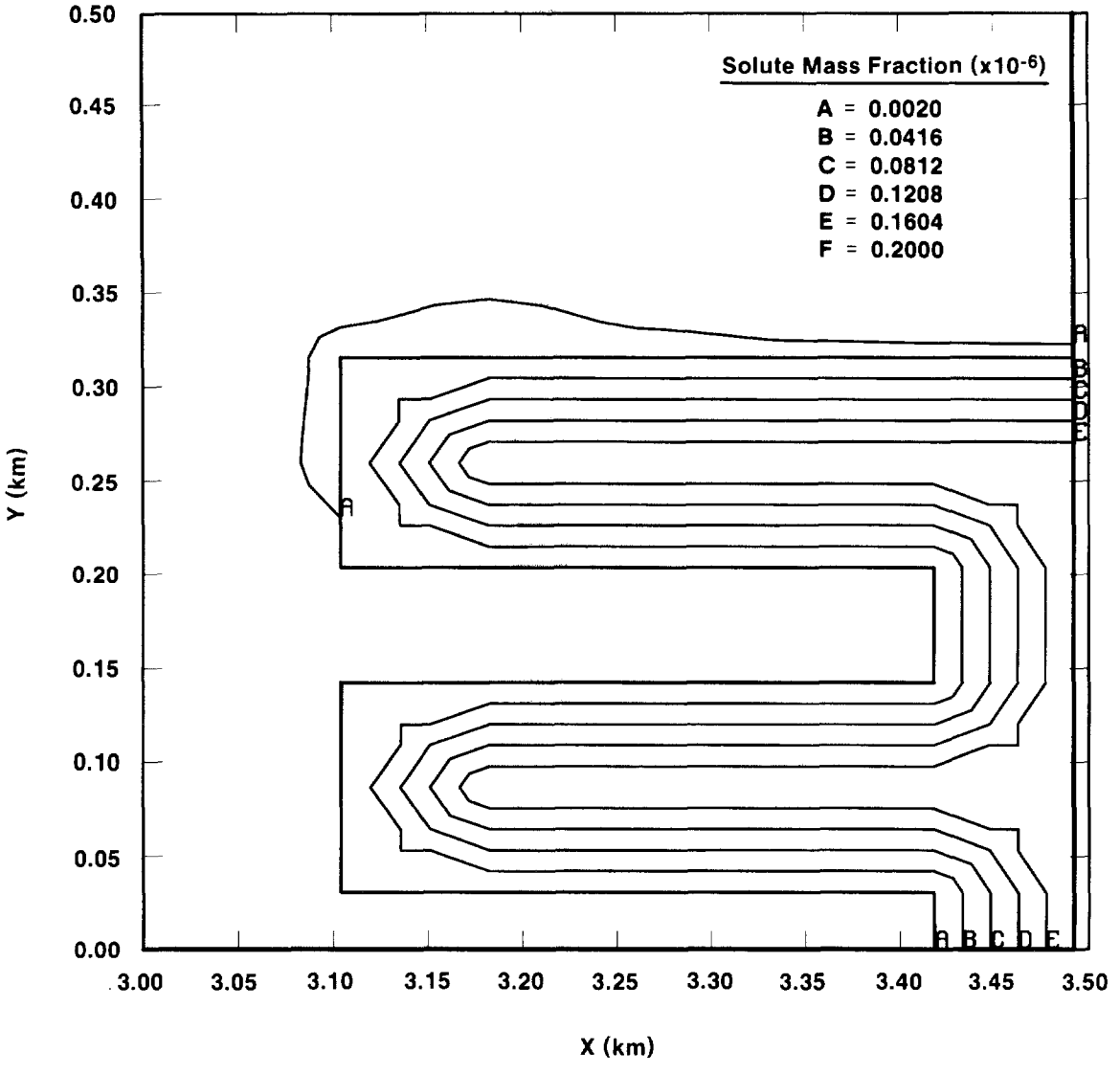

TRI-6342-1332-0

Figure 4-27a. Solute Concentration Contours at 10,000 Years (Coarse Mesh, Δt = 100 Years)

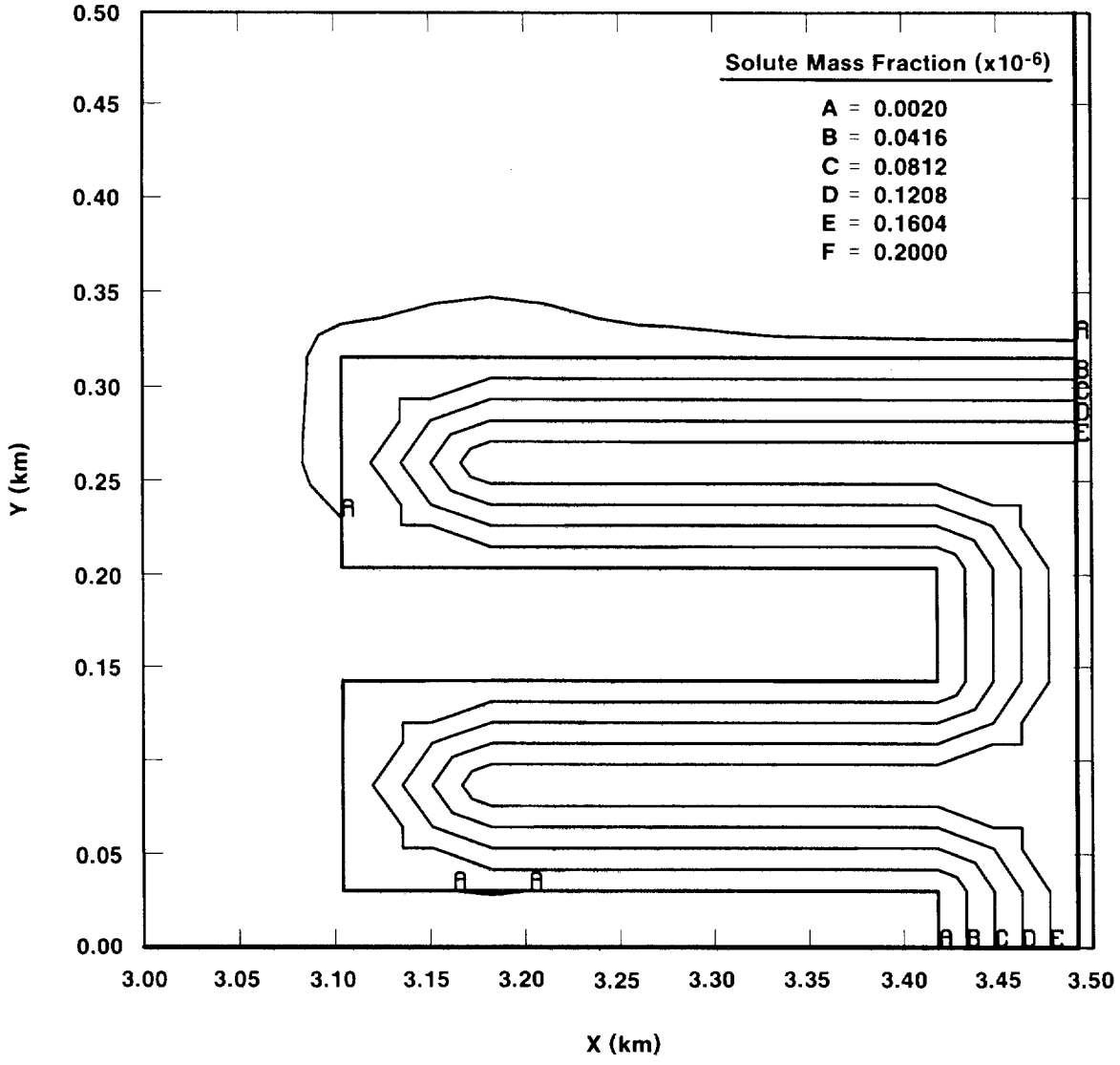

Figure 4-27b. Solute Concentration Contours at 10,000 Years (Coarse Mesh, Δt = 50 Years)

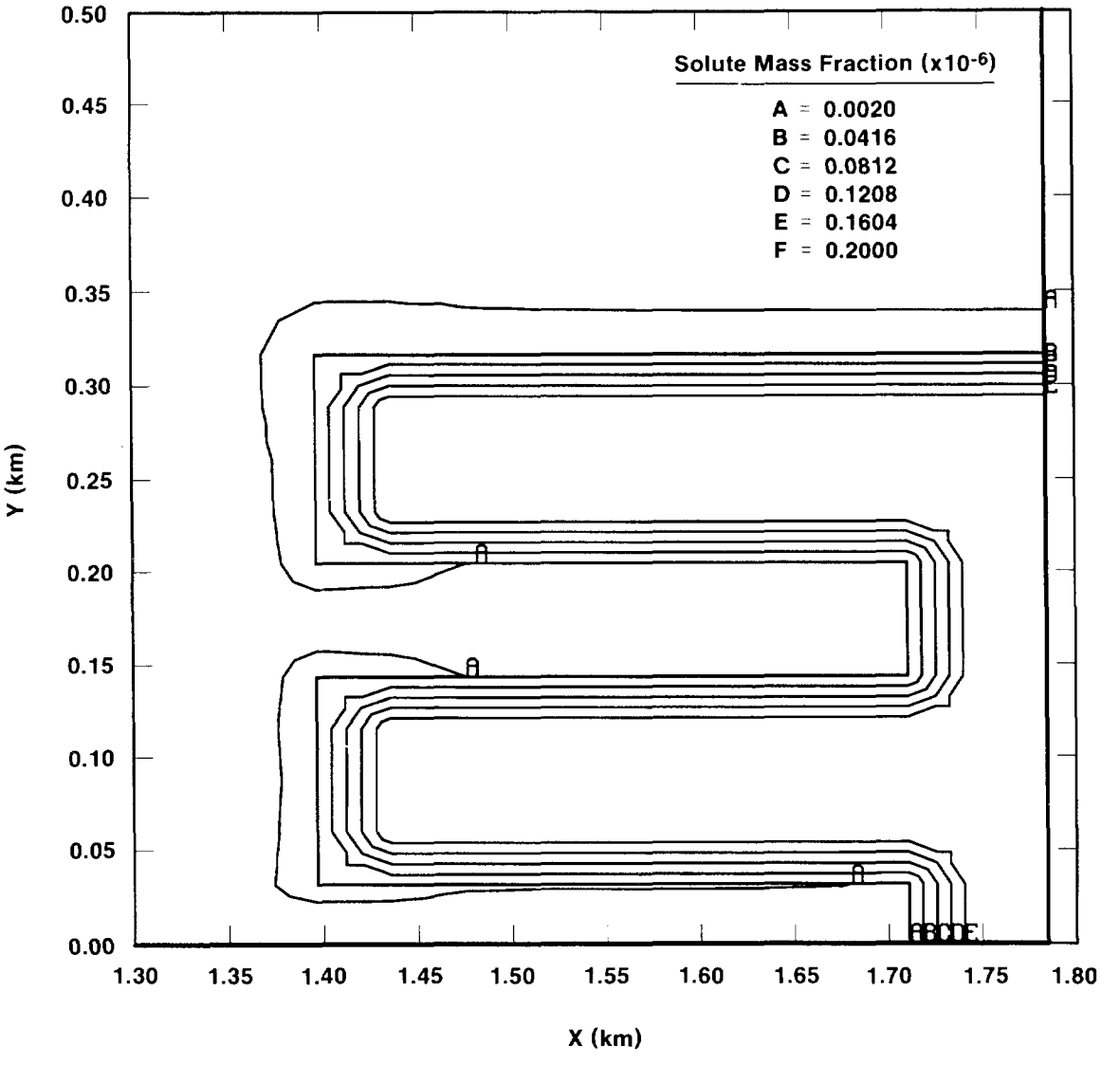

Figure 4-28a. Solute Concentration Contours at 1000 Years (Fine Mesh, Δt = 100 Years)

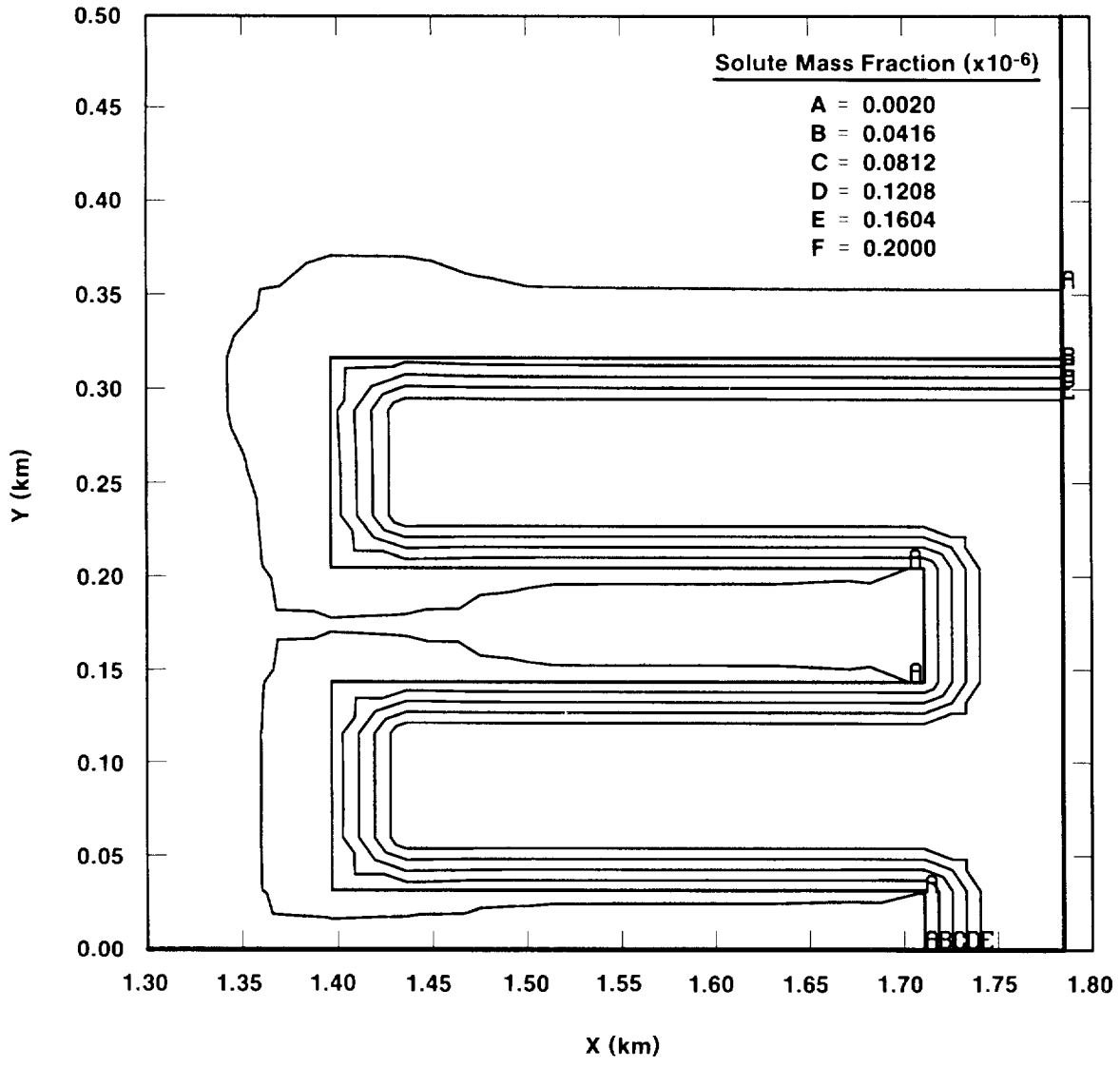

TRI-6342-1335-0

Figure 4-28b. Solute Concentration Contours at 1000 Years (Fine Mesh, Δt = 50 Years)

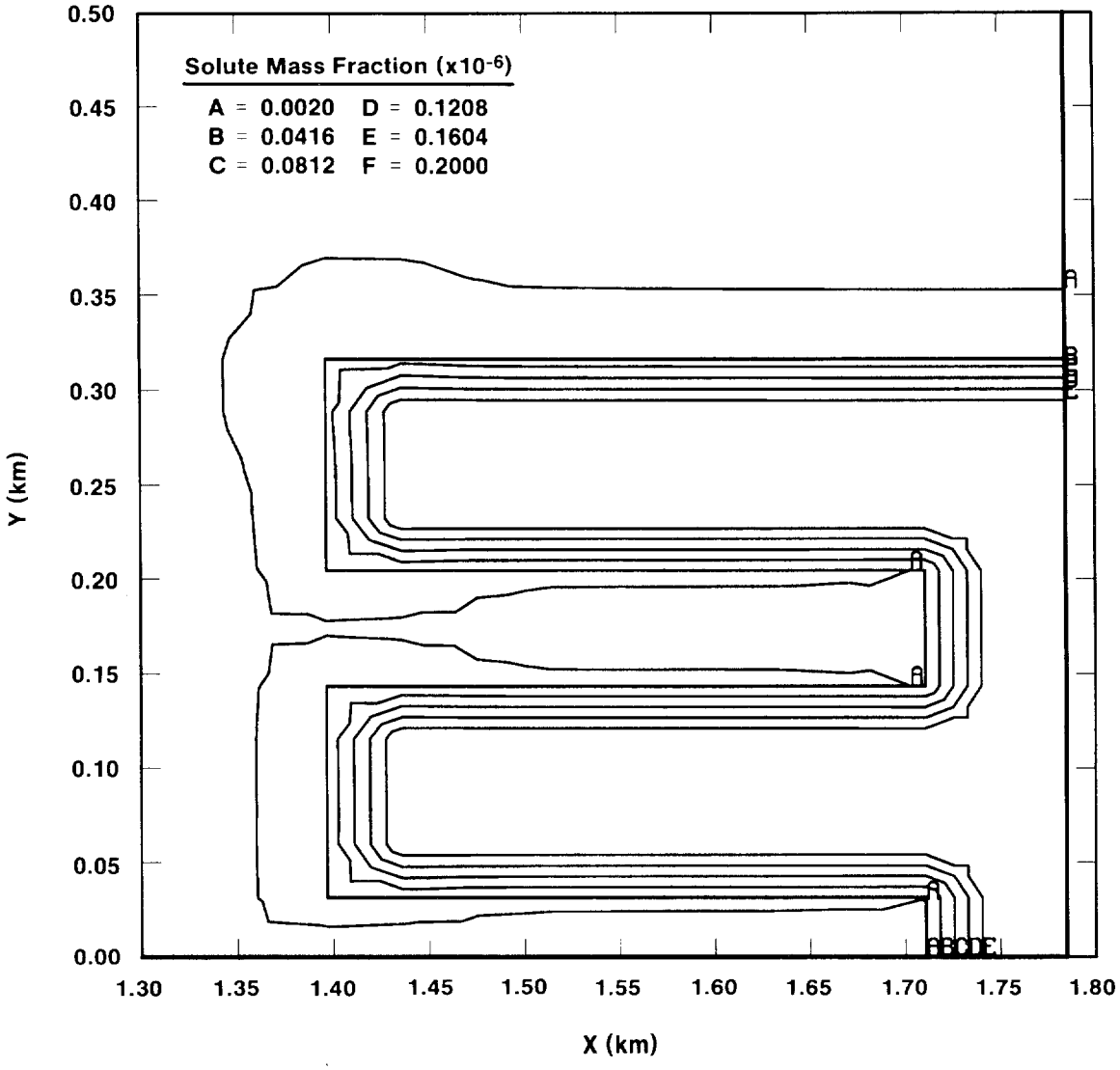

TRI-6342-1336-0

Figure 4-28c. Solute Concentration Contours at 1000 Years (Fine Mesh, Δt = 10 Years)

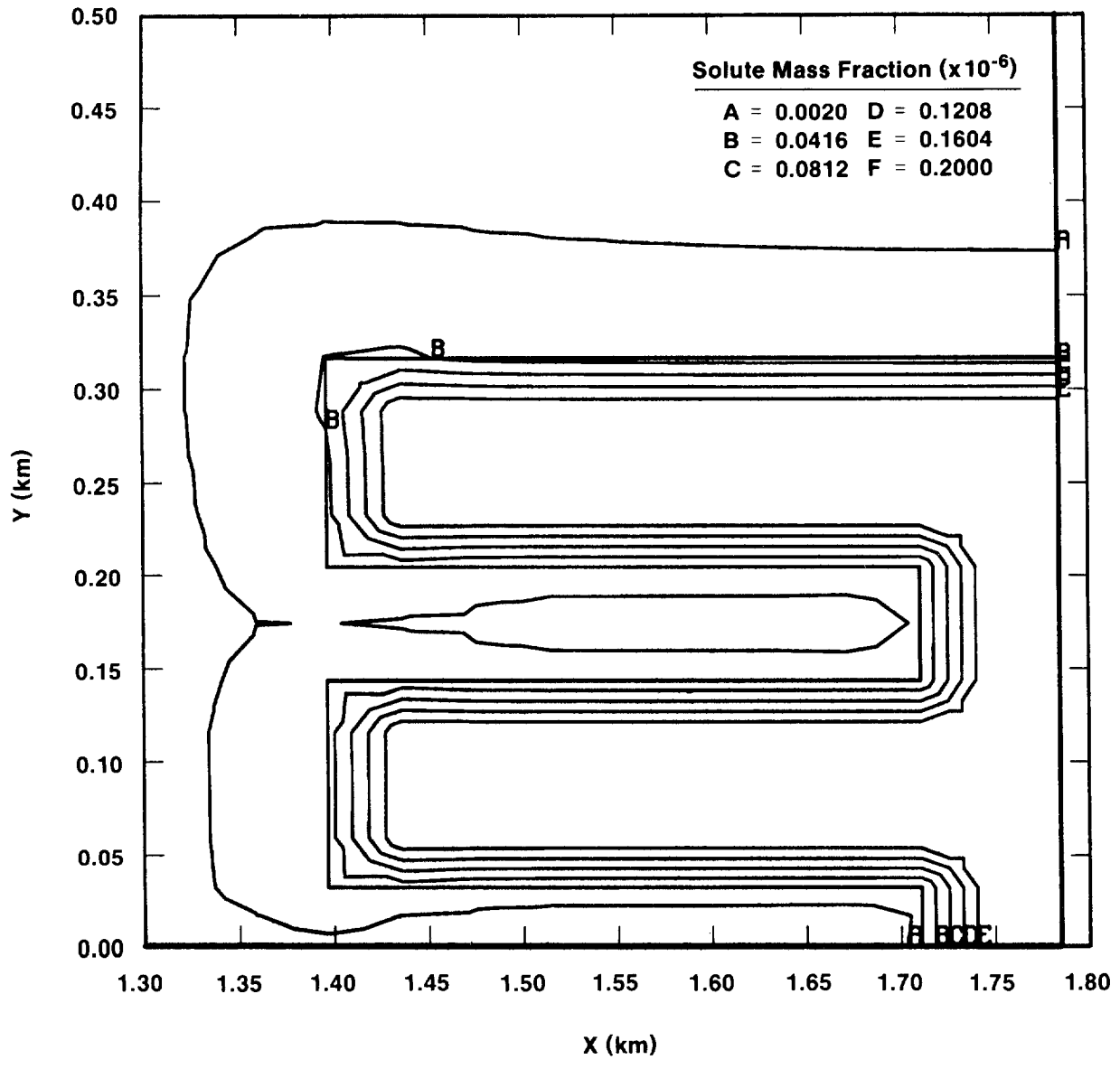

Figure 4-29. Solute Concentration Contours at 10,000 Years (Fine Mesh, Δt = 50 Years)

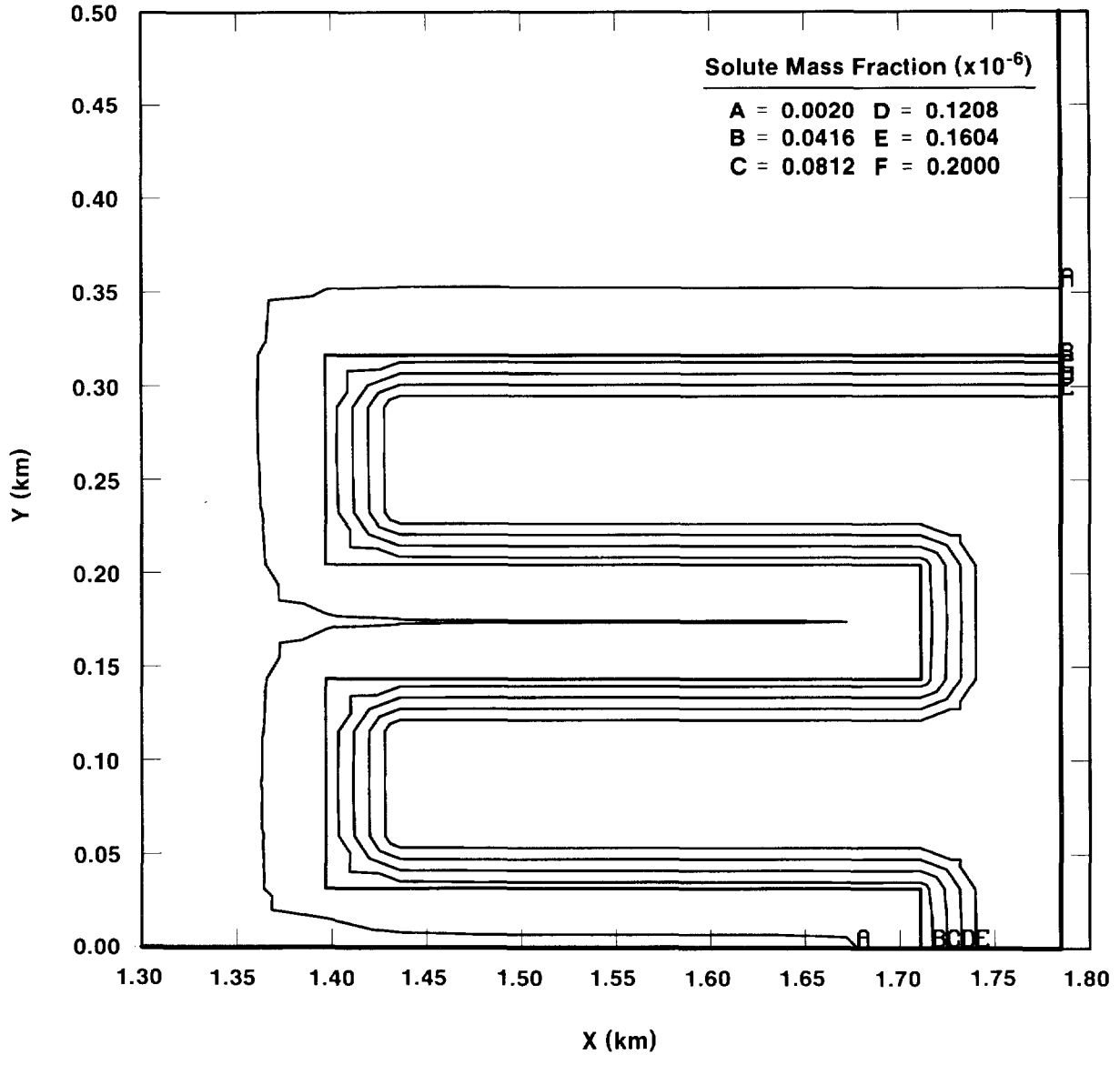

Figure 4-30a. Solute Concentration Contours at 10,000 Years With Increased Diffusion Coefficient (Fine Mesh, Δt = 100 Years)

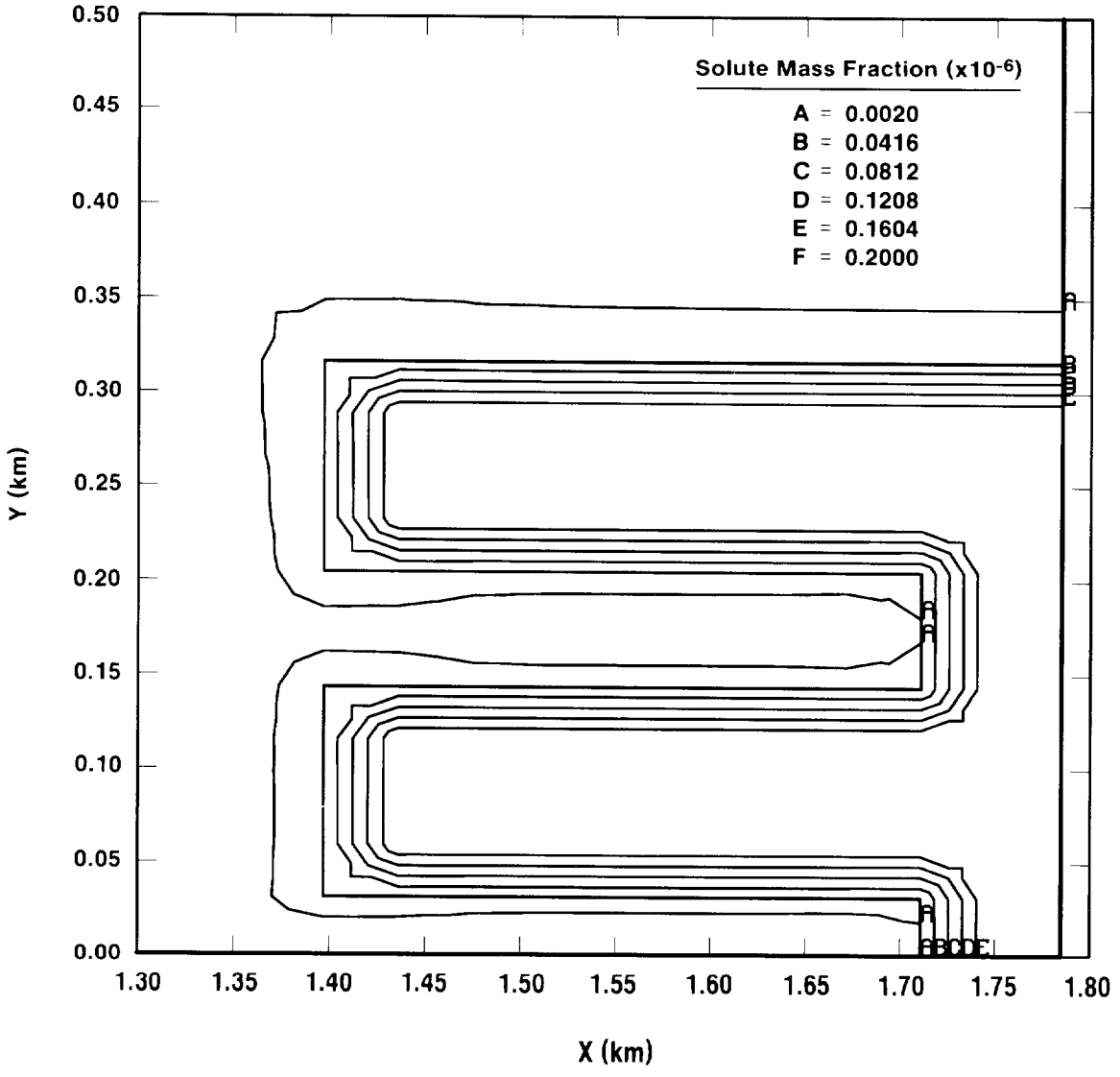

TRI-6342-1339-0

Figure 4-30b. Solute Concentration Contours at 10,000 Years With Original Diffusion Coefficient (Fine Mesh, Δt = 100 Years)

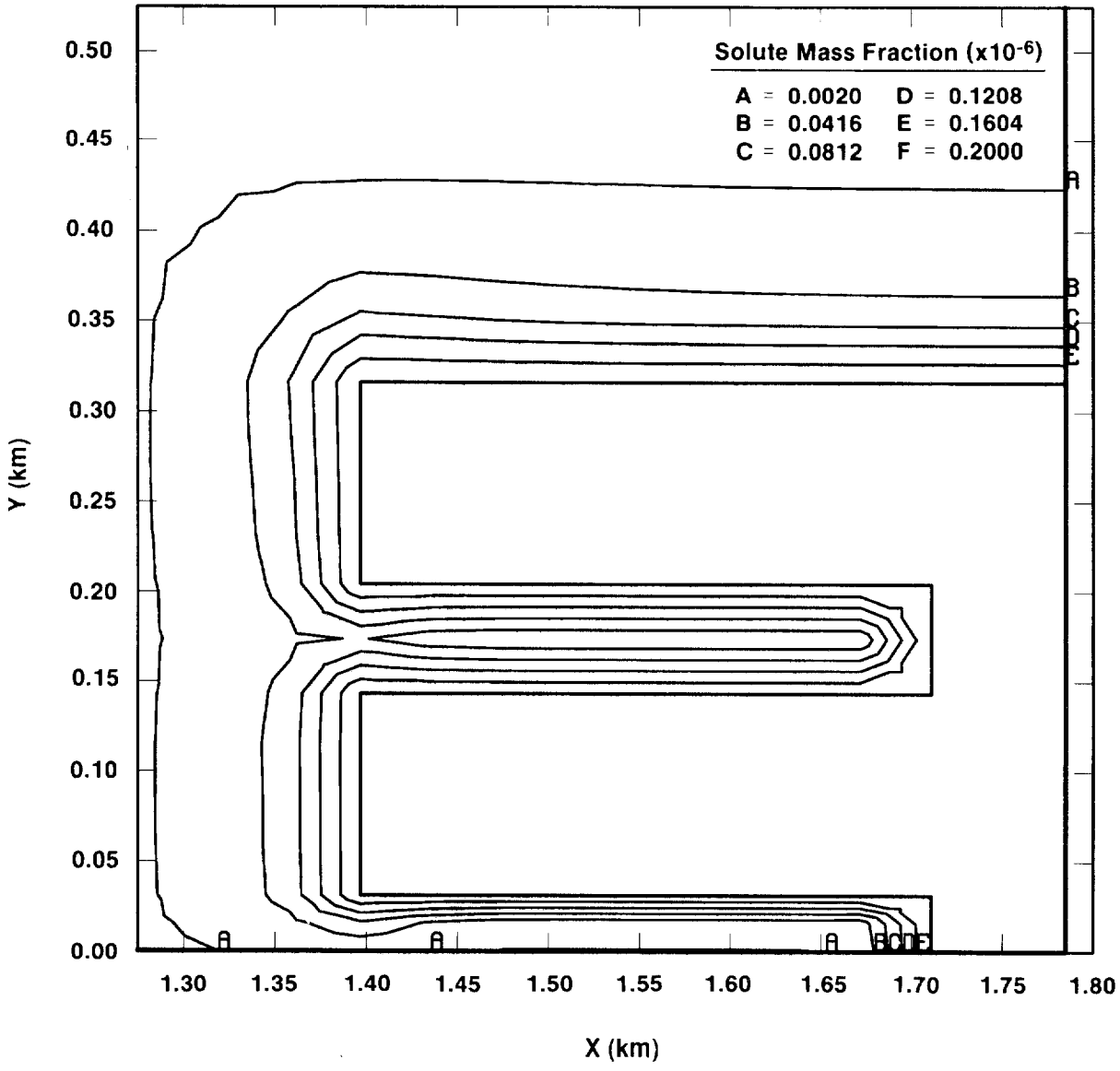

TRI-6342-1340-0

Figure 4-31. Solute Concentration Contours at 10,000 Years With Modified Concentration Source Placement (Fine Mesh, Δt = 50 Years)

has traveled 110 m into the MB139FF material, whereas previous calculations indicated a distance of 75 m (Figure 4-29). In addition, the concentration contours of Figure 4-31 depict no internal concentration gradients within the MB139DRZ material. This calculation is more conservative and provides an upper bound for transport phenomena in the MB139FF medium for this set of calculations.

4.3 Summary of Results for Undisturbed Performance of the Repository/Shaft

The calculations performed to assess the undisturbed performance of the Repository/Shaft System had four objectives

- To determine the path and extent of migration of radionuclides from the waste panel, and to quantify the magnitude of radionuclide transport up the shaft.
- To evaluate (in an approximate sense) the effect of waste-generated, undissolved gas on migration of radionuclides for undisturbed conditions.
- To assess the importance of three-dimensional effects on radionuclide migration in MB139.
- To cross-verify the results from the two single-phase codes SUTRA and STAFF2D.

To address these objectives, the four codes BOAST II, STAFF2D, SUTRA and PANEL were used in one or more configurations with varying material properties and operational assumptions. In utilizing these codes an attempt was made to use conservative assumptions that tend to maximize migration of dissolved radionuclides away from the waste panels. However, this was not done for all parameters where often average or median values were used. Thus the results from the calculations cannot be claimed to be a worst-case or a bounding result. In fact, it may not be possible to prove that any set of assumed input parameters will produce a bounding result. The results from the calculations are summarized below.

1. In determining the pathway and extent of movement of radionuclides from the repository an effort was made to use assumptions that were believed to be conservative and that would tend to maximize the extent of migration. Using STAFF2D as the principal computational tool and aided with results from BOAST II and PANEL, it was determined that the primary pathway of dissolved radionuclides out of the repository, as the result of pressurized gas generated by the corrosion and biodegradation of the waste, is downward through the small thickness of fractured Salado halite below the repository into MB139. The greater permeability of MB139 compared to the surrounding Salado channels the movement of dissolved radionuclides along the MB139 primarily toward the shaft. Movement of radionuclides along MB139 in the direction away from the shaft is slower than toward the shaft by approximately a factor of 2. Radionuclide concentrations

decrease steadily toward the shaft and also after the primary flow path turns upward into the shaft. The quantity of radionuclides passing a level of 20 m up the shaft from the repository in 10,000 years was calculated and shown to be several orders of magnitude less than the EPA limit of 1 for releases to the accessible environment at five kilometers from the waste emplacement panels. Similar results were shown for radionuclide migration away from the repository and shaft in MB139 at distances of 100 m from the repository.

Decreases in shaft permeabilities of 2 and 4 orders of magnitude (10^{-12} m^2 to 10^{-14} m^2 and 10^{-12} m^2 to 10^{-16} m^2) resulted in essentially no change in flow up the shaft. This implies that for undisturbed conditions the presence of an engineered shaft seal has little effect in restricting flow up the shaft unless the permeability of the seal approaches that of the intact surrounding Salado.

2. As configured in the undisturbed calculations, both SUTRA and STAFF2D considered only a single phase (brine) in assessing flow in and around the repository. The two-phase BOAST II code was used in the undisturbed calculations to provide input source pressures for the SUTRA calculations, and gas-modified material properties for both SUTRA and STAFF2D. The use of gas-modified material properties in SUTRA and STAFF2D allowed these single-phase codes to account for (in an approximate sense) the presence of undissolved gas in the waste and surrounding geology. Calculations with gas-modified material properties in SUTRA and STAFF2D revealed that the presence of undissolved gas has little effect on solute transport compared to the unmodified (fully saturated) case. The principal effect of the presence of gas is to delay the transport of dissolved radionuclides along the primary pathway to the shaft (MB139).

3. The majority of calculations for the undisturbed case were performed using a two-dimensional vertical cross-section through the repository, drift, and shaft. This two-dimensional representation neglects potential three-dimensional effects that may be important. In an effort to investigate this, two-dimensional SUTRA calculations were performed using a computational grid based on a horizontal plane through the repository and surrounding geology. Moreover, an additional conservative assumption was made that divided the permeabilities in the computational plane into two regions—one that corresponds to the excavation-disturbed MB139 and the other to the undisturbed MB139. These assumptions had the effect of placing the contents of the waste repository within MB139, the primary transport medium. In this configuration, the magnitude of the radial solute transport away from the repository (in MB139) was found to be entirely consistent with SUTRA vertical cross-section calculations, which were run with the same source pressure and where the shaft was assumed to be absent. These results suggest that the

two-dimensional vertical cross-section calculations with SUTRA and STAFF2D performed to ascertain the pathway and spatial extent of migration of solute are valid.

4. The calculations performed for a vertical cross-section through the waste panel, drift, and shaft were accomplished with the two codes, SUTRA and STAFF2D. These codes, based on the same governing equations, nevertheless use different centering schemes for some element variables such as porosity. A comparison of results from the two codes, modeling the same problem, reveal similar results based on solute-concentration contours. The SUTRA solution is somewhat more numerically dispersive than the STAFF2D solutions. In spite of these slight differences, for the calculations performed, the two codes tend to cross-verify one another.

5. DISTURBED CONDITIONS OF REPOSITORY/SHAFT

In addition to the undisturbed performance, the Standard (40 CFR 191, Subpart B) requires a study of combinations of hypothetical events and processes (scenarios) in which a waste repository is intruded by humans (see Chapter 4 of Volume 1). In these scenarios, the primary component of the geologic barrier (the Salado Formation) has been breached leaving only the waste form, possibly intervening panel and borehole seals, and the Culebra Dolomite as barriers. Thus, characterizing the behavior of the disposal system is much more important under these conditions than for the undisturbed scenario and requires the use of several additional simulation models (e.g., CUTTINGS, SECO_2DH, GENOBS, BRAGFLO and others) (see Figure 1-3 in Chapter 1).

5.1 Conceptual Model—Palmer Vaughn

In Sections 5.1 and 5.2 the term "flow" is used repeatedly. Unless otherwise stated, "flow" is meant to represent the cumulative volume of contaminated brine that has flowed up the intrusion borehole in 10,000 years and enters the Culebra. The term "flow rate" is the rate of this flow.

Currently, two summary scenarios are directly used in performance-assessment analysis during disturbed conditions: (1) one or more intrusion boreholes terminating in a disposal panel (E2) and (2) one intrusion borehole terminating in a disposal panel followed by a second borehole penetrating the same panel and terminating in a lower Castile brine pocket (E1E2). The computational scenarios used in modeling consequences of these summary scenarios are further distinguished by the number of intrusions and the time of intrusion. Consequences of the E1 summary scenario, in which an intrusion borehole intersects both a disposal panel and a lower Castile brine pocket, are not calculated for the 1991 analysis and are assumed to be the same as E2 consequences (see Section 5.1.2). The E1, E2, and E1E2 summary scenarios are defined in detail in Chapter 4, Volume 1 of the report.

The E2 summary scenario consists of one or more boreholes that penetrate a waste-filled room or drift in a panel. Shortly after completion, plugs are placed to isolate any aquifers (i.e., above and below the Culebra) and the well is abandoned and packed with concrete. The concrete remaining in the borehole degrades with time into a sand-like material. The borehole below the Culebra creeps partially closed due to movement of halite in the surrounding Salado. All plugs except the one above the Culebra degrade thus forcing any flow out through the Culebra. This maximizes the possible release through the Culebra. During multiple E2 well intrusions no interaction between wells occurs (Volume 1, Chapter 5).

The E1E2 summary scenario consists of one or more boreholes that penetrate a waste-filled room or drift in a panel and another borehole that penetrates a panel and a pressurized brine pocket in the Castile formation. The boreholes are abandoned, plugged, and creep partially closed as in the E2 summary scenario. The plugs also degrade as before except that a plug located between the

panel and Culebra in all but one of the wells that terminate in the panel remains intact. This forces all brine leaving the pressurized brine pocket through the waste panel before it flows out a well connected to the Culebra (Volume 1, Chapter 5).

When an intrusion of a waste panel first occurs, the room quickly depressurizes (the entire panel does not) and gas escapes through the borehole. As suggested in Appendix B of the Standard, the intruders "soon" (interpreted as less than one month) detect that the area is incompatible with their intended use and they seal and abandon the well. The room repressurizes either from continued gas generation or from a redistribution of pressure and saturation from the surrounding formation. Over time (less than 75 years) the borehole degrades and partially creeps closed. The net effect is a permeable and porous borehole that provides communication between the repository and the Culebra formation. After this period of degradation, the remaining gas moves out of the panel and brine will flow toward the panel and well bore. During the E2 scenario the primary path of this brine in-flow is along MB139 from the far field and up through the DRZ into the panel near the panel/Salado boundary. During an E1E2 scenario the primary source of brine in-flow is from the Castile brine pocket, although some Salado brine flows along MB139 toward the panel. Little brine flows into the panel from the intact Salado during the E2 or E1E2 scenarios because of its low permeability. Brine flowing through the upper anhydrite layers takes longer to reach the panel because the gas drive during room pressurization forces brine out the anhydrite farther than it is forced out MB139 and gravity drainage tends to saturate the lower MB139 to a greater extent than the upper anhydrite. Once brine saturations in the room exceed residual, interconnected brine pathways are formed in the void space and brine eventually reaches the well. Brine may then be forced out the well, up toward the Culebra against hydrostatic pressures in the well. Exactly how far up the well or how much brine reaches the Culebra during the regulatory 10,000 years depends, in part, upon how much gas flow can dissipate room pressure.

5.1.1 APPROXIMATION TO E1E2 SUMMARY SCENARIO

The E1E2 summary scenario is modeled by BRAGFLO (see Section 5.2) as an E1 scenario with the important conservative assumption that all of the Castile brine mixes with all of the waste. This conservative approximation is a necessary result of the limitations in modeling the waste panel in two dimensions as a cylinder with an axis of symmetry coincident with the intrusion well (Section 5.2.3). While a second borehole in the E1E2 summary scenario could be modeled in three-dimensional Cartesian or radial geometry, there is no convenient way of locating a second well in the two-dimensional radial representation while accurately describing well interactions and individual well flow. The assumption of total mixing of Castile brine with the waste overestimates the contamination of the brine compared to a true two-well E1E2 scenario

since the flow paths between two separated wells located anywhere in the panel results in less than 100% of the waste volume being in contact with brine.

The cumulative "flow" of brine in a true two-well E1E2 summary scenario also cannot exceed this conservative single-well approximation. In a true E1E2 summary scenario, the two intrusion wells are spatially separated. The flow path in this case is longer and is through the less permeable waste material (compared to the borehole) than in the single well E1 approximation to the E1E2 scenario. This lengthens the time required for brine to reach the Culebra through the borehole and increases pressure drop requirements to maintain flow up the borehole in the true E1E2 compared to the conservative E1E2 approximation. The existence of a second borehole in the true E1E2 scenario also increases the total void space available for brine. More time is required to saturate the panel with brine. Except for occasional gas pockets, the panel must be brine saturated before brine can flow up the borehole that connects the panel to the Culebra. Therefore, in a true E1E2 summary scenario, less brine reaches the Culebra after 10,000 years than would for the conservative E1 scenario approximation of an E1E2 scenario.

5.1.2 APPROXIMATION TO E1 SUMMARY SCENARIO

The consequences of E1 summary scenarios have been assumed to fall in the same consequence "bin" as those of the E2 summary scenarios. Results from the two-phase flow calculations using BRAGFLO indicate that for many scenario vectors the "flow" resulting from the E2 summary scenario bounds that from the E1 scenarios. The "flow" associated with the E1 summary scenarios is obtained from the E1E2 BRAGFLO simulation results assuming that the Castile brine does not mix with the waste after the waste panel becomes saturated with brine. In Figure 5-1 the "flow" from the E1 scenario vectors is compared to the "flow" from the E2 scenario vectors for each of the five intrusion times (1000, 3000, 5000, 7000, 9000 years). Points above the indicated 45 degree line correspond to E2 scenario "flows" in excess of E1 scenario flows. The cases where the "flows" from the E1 scenario exceed those from the E2 scenario either occur at low or zero E2 "flow" or are close to each other (near the 45 degree line).

In Figure 5-1 a clustering of data points according to intrusion time is also observed. For instance, the large releases tend to be dominated by the 1000-year intrusion scenarios followed by 3000-, 5000- and 7000-year intrusions. All 9000-year intrusion vectors produce no release. In addition, the relative degree to which the E2 "flows" exceed the E1 "flows" for the high E2 "flow" vectors is qualitatively preserved among the various intrusion times. This suggests some scaling or correlation factor may exist to relate "flow" at one intrusion time to "flow" at another intrusion time.

In the case assuming single-phase flow of brine and a fully brine-saturated panel, the "flows" from E2 summary scenarios bound those from the E1 summary scenarios if Castile brine bypasses

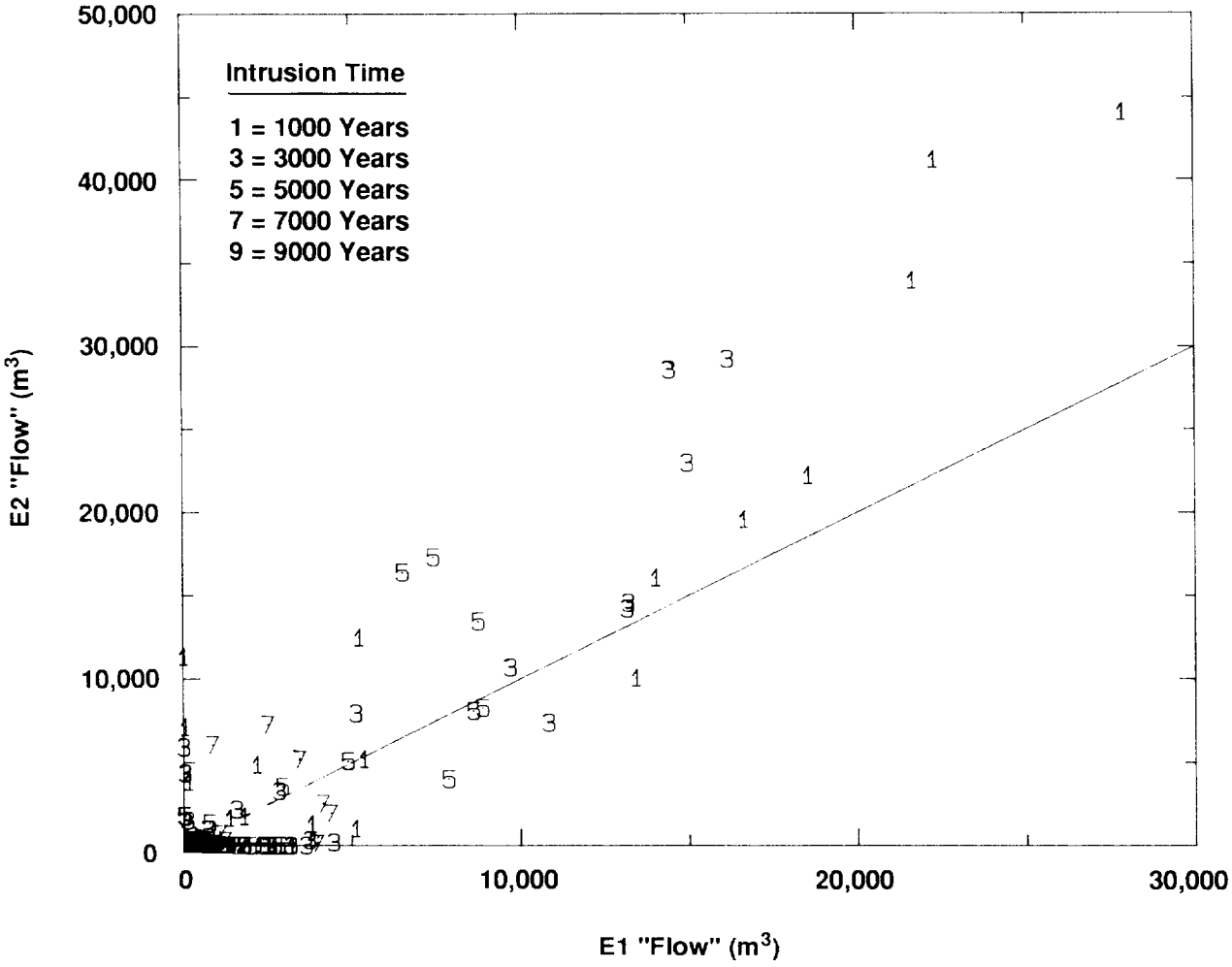

"Flow" = Volume of contaminated brine entering Culebra and accumulated over 10,000 years

TRI-6342-1356-0

Figure 5-1. Comparisons of E1 Flows with E2 Flows Assuming Two-Phase Flow at 1000-, 3000-, 5000-, 7000-, and 9000-Year Intrusion Times

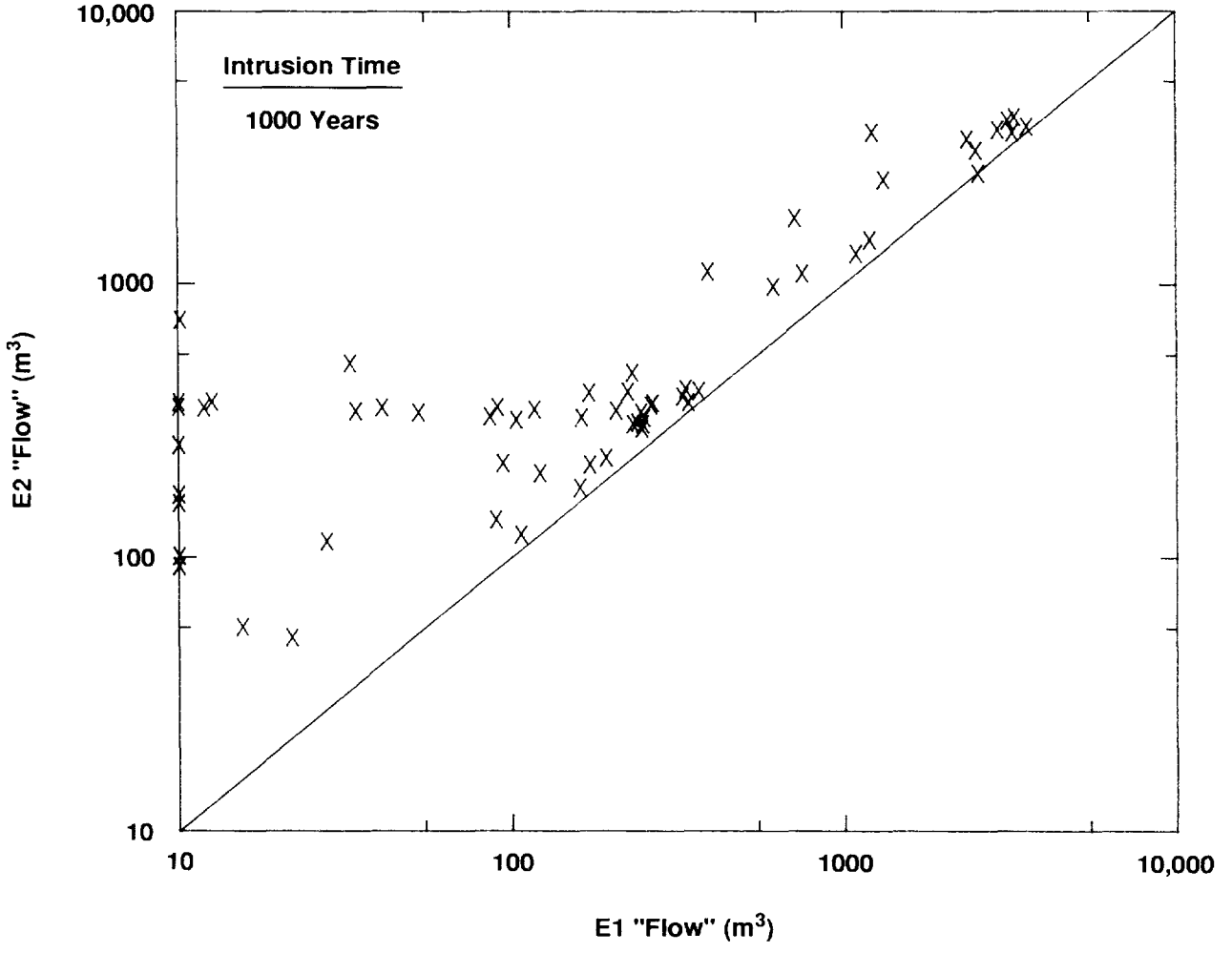

"Flow" = Volume of contaminated brine entering Culebra and accumulated over 10,000 years

TRI-6342-1357-0

Figure 5-2. Comparisons of E1 and E2 Flows (Full Brine Saturation and No Castile Brine Mixing Assumed) at 1000-Year Intrusion Time

the contaminated waste in the panel. Figure 5-2 compares the "flow," resulting from E1 summary scenarios with that resulting from E2 summary scenarios. The "flows" are accumulated over 10,000 years for a well intrusion at 1000 years. On the figure the E2 "flows" are plotted on the vertical axis against the E1 "flows" on the horizontal axis; logarithmic scales are used for both axes. All data pairs fall above the indicated 45 degree-sloped line, indicating that the E2 "flows" bound the E1 "flows" under the conditions and assumptions used. These results are obtained from the analytic model, PANEL, a single-phase flow model (Section 5.3) in which it is assumed that the waste panel is fully saturated with brine and that a negligible amount of Castile brine mixes with waste panel brine.

When two-phase flow is considered, E2 scenarios do not necessarily bound E1 scenarios, particularly at lower levels of "flow." When considering two-phase flow, brine does not flow up the intrusion shaft from the panel to the Culebra until the portion of the panel surrounding the shaft becomes highly saturated with brine. Those E2 scenario vectors that result in no "flow" are vectors in which the panel is not brine filled in 10,000 years. When the panel is connected to a pressured brine pocket by an intrusion well, less time is required to fill the panel with brine and flow toward the Culebra may begin earlier.

At the higher release levels, the E2 "flows" bound the E1 "flows." This primarily reflects the higher brine pocket pressure retarding the flow of brine into the waste panel from the far field along the anhydrite layers. Once the intrusion occurs, the Culebra, panel, and Castile become connected. When the gas is displaced from the panel and the panel is brine-filled a nearly linear pressure gradient will be established between Culebra pressure and brine pocket pressure. This can result in the establishment of a higher panel pressure in the E1 summary scenarios compared to the panel pressure established in the E2 summary scenarios. The higher panel pressures reduce the pressure gradient between the panel and far field, and consequently less Salado brine flows into the panel from the far field along the anhydrite layers. For the high "flow" vectors compared to the low "flow" vectors, the panel becomes brine saturated earlier and the Culebra to Castile pressure gradient is established and remains for a longer period of time.

In summary, E2 "flows" bound E1 "flows" for large release vectors because the established panel pressure retards or reverses Salado brine in-flow toward the panel. E1 "flows" bound E2 "flows" for small release vectors because the flow of Castile brine decreases the time required to fill the panel with brine so that brine may begin to flow toward the Culebra.

5.2 Two-Phase Flow: BRAGFLO—Palmer Vaughn

5.2.1 MODEL OVERVIEW

BRAGFLO is used to evaluate the effect of gas on the flow of brine through the repository and up an intrusion borehole. (BRAGFLO is based on conceptualizations of porous media and multiphase flow presented in Appendix A.) The presence of gas and its rate of production may be extremely important in evaluating the flow characteristics of the repository. With respect to contaminants transported primarily in the brine phase (radionuclides and dissolved chemicals) gas may have negative and positive impacts. A potential negative impact is the increased brine phase mobility because of increased dissolved gas, possibly causing lower brine viscosity and higher relative permeability. Gas may additionally increase the driving force for moving brine away from the repository and may increase permeability through fracture development. Positive impacts associated with gas include the partial occupation of pore space by gas and the associated reduction in brine relative permeability and its mobility. Gas pressurization may drive brine from the room along the anhydrite layers to the far field creating unsaturated conditions around the waste. In addition, if the mechanism for gas generation consumes brine, then brine saturation may be reduced well below residual levels in the waste resulting in immobile brine at the time of intrusion.

In addition to quantifying the brine and gas flow fields in and around the repository for consequence analysis calculations, BRAGFLO is used to evaluate the effect of gas generation on the flow of brine. The comparisons are made to evaluate our hypothesis that the assumptions of no gas generation and predominantly single-phase brine flow is conservative with respect to predicting brine flow through the repository and borehole.

5.2.2 MODEL DESCRIPTION

5.2.2.1 Nomenclature

The following nomenclature is used throughout the model description of the two-phase flow model BRAGFLO:

English

$C_{M\ell}$	mass fraction of component M dissolved or miscible in phase ℓ
D	depth in reservoir measured from surface [L], [m]
g	gravitational acceleration constant [$L\,t^{-2}$], [m s^{-2}]

G	vector obtained in evaluating the finite differences analogs of the conservation equations at each grid block location [$ML^{-3}t^{-1}$], [kg m^{-3} s^{-1}]
H	length in the direction normal to the flow phase [L], [m]
J	shorthand notation for the Jacobian Matrix
k	absolute permeability of the reservoir [L^2], [m^2]
k_x	absolute permeability in the x direction [L^2], [m^2]
k_y	absolute permeability in the y direction [L^2], [m^2]
$k_{r\ell}$	relative permeability to phase ℓ [dimensionless]
P_C	capillary pressure [$ML^{-1}t^{-2}$], [Pa]
P_ℓ	pressure of phase ℓ [$ML^{-1}t^{-2}$], [Pa]
P_ℓ^*	potential of phase ℓ defined as $P_\ell - \rho_\ell\ g\ D$ [$ML^{-1}t^{-2}$], [Pa]
q_ℓ	mass rate of well injection (or production, if negative) per unit volume of reservoir [$ML^{-3}\ t^{-1}$], [kg m^{-3} s^{-1}]
$q_{r\ell}$	mass rate of products produced (or reactant consumed, if negative) per unit volume of reservoir due to chemical reaction [$ML^{-3}\ t^{-1}$], [kg m^{-3} s^{-1}]
q_v	volumetric flow rate of water per unit cross sectional area normal to the flow direction [$L^3\ L^{-2}\ t^{-1}$]
S_ℓ	saturation of phase ℓ [dimensionless]
$T_{\ell x}$	shorthand for the group $\rho_\ell\ k_x\ k_{r\ell}\ /\ u_\ell$ for phase ℓ
$T_{\ell y}$	shorthand for the group, $\rho_\ell\ k_y\ k_{re}\ /\ u_\ell$ for phase ℓ
x,y	spatial dimensions (x-horizontal, y-vertical)

Greek

α	geometric factor (in three dimensions, $\alpha = 1$; in two dimensions, α = length; in one dimension, α = area
∇	gradient, shorthand for vector $\partial / \partial x$, $\partial / \partial y$ in two dimensions
$\nabla \bullet$	divergence, shorthand for $\partial / \partial x + \partial / \partial y$ in two dimensions
Δt	time step [t], [s]
Δz_m^k	maximum change in dependent variable values during time step, k (see equation (5-9))

Δz^*		the change in dependent variable values during a time step such that the new estimate for time step size remains the same as the current time step size (see equation (5-9))
$\bar{\delta}^k$		solution vector of dependent variable changes for time step k
ϕ		reservoir porosity [dimensionless]
ρ_ℓ		density of phase ℓ [$M^1\ L^{-3}$], [kg^1 m^{-3}]
u_ℓ		viscosity of phase ℓ [$ML^{-1}\ t^{-1}$], [cp]

Subscripts

B	brine component
b	brine phase
G	gas component
g	gas phase
N	nonwetting component
n	nonwetting phase
W	wetting component
w	wetting phase

5.2.2.2 Background

BRAGFLO is a computational model that describes the multiphase flow of gas and brine through a porous, heterogeneous reservoir. BRAGFLO was developed in-house for the Sandia National Laboratories WIPP Performance Assessment (PA) Division and is used by PA to simulate two-phase flow in and around the WIPP repository waste rooms. The roots of the BRAGFLO formulation are in TSRS, a multiphase compositional thermal reservoir simulator used to model the in-situ processing of tar sand (Vaughn, 1986). TSRS was developed for the DOE through an agreement with Western Research Institute, Laramie, WY. The version of BRAGFLO currently used by PA represents a significant improvement beyond its predecessor. A technical user's manual for BRAGFLO is being prepared and should become available in the latter part of 1992.

BRAGFLO is a necessary tool for PA primarily because no other public domain model was available for simulating the convergent flow of brine and gas to an intrusion well in a heterogeneous reservoir under conditions of gas generation and brine consumption. Repeated attempts using BOAST II during disturbed conditions resulted in excessively small time steps and unstable oscillations in saturations. The causes of these problems are characteristic of the IMPES

(implicit-pressure, explicit-saturation) solution technique, which BOAST II uses. BRAGFLO, because of its fully implicit numerical formulation, does not suffer from the stability and time-step restrictions that hamper BOAST II.

BRAGFLO was developed as a research tool capable of expanding and evolving to accommodate our changing conceptual models. Its highly structured architecture facilitates making future enhancements. The description that follows is a summary of the version of BRAGFLO used for this year's calculation, BRAGFLO 1.0; additional enhancements to the model are anticipated. Because the theory of BRAGFLO has not been previously documented, the summary for BRAGFLO is more extensive than the summaries presented in this volume on the other WIPP PA consequence analysis models.

5.2.2.3 Benchmark Results

Prior to its use in PA calculations, BRAGFLO was put through a series of benchmark tests. This verification process consisted of running three multiphase reservoir codes (BRAGFLO, BOAST II, and TOUGH) and comparing the results. The results of four one-dimensional, radial benchmarks (with/without dissolved gas and with/without gas generation) showed excellent agreement between the three codes, supporting our confidence in using BRAGFLO. For example, in Figures 5-3 and 5-4 the results of repository pressure and brine saturation are compared among BRAGFLO, BOAST, and TOUGH for the one-dimensional, constant gas generation benchmark. In this problem the repository is initially fully gas saturated and gas is generated at a rate of 2×10^{-7} kg/s/m^3. No well intrusion occurs and the simulation continues for 700 years. Pressure in the repository rises due to gas generation from the initial pressure of 0.1 MPa to 13 MPa at 700 years. The gas saturation (initially 100%) in the room falls to 15% in the first 100 years as brine flows into the repository from the Salado, after which increased pressure in the repository reverses the direction of brine flow. Gas saturation increases for the remainder of the simulation.

The results of a more realistic two-dimensional simulation with an intrusion well and the inclusion of the repository stratification and material zoning also showed excellent agreement between BOAST II and BRAGFLO up until the time of intrusion. (BOAST was unable to proceed beyond intrusion.) In the two-dimensional benchmark the repository is bounded top and bottom by a disturbed rock zone, anhydrite layers, and Salado and is surrounded by Salado in the horizontal direction. Gas is generated at two rates to simulate differing corrosion and biodegradation reaction rates: 1.7×10^{-10} kg/s/m^3 for 525 years followed by 5.7×10^{-11} kg/s/m^3 for 185 years. The repository panel volume is 5.6×10^4 m^3. The panel is initially 80% gas saturated with a porosity of 8.4%. In Figure 5-5 the repository pressures predicted by BRAGFLO are compared to those of BOAST for the first 1200 years (the time of well intrusion). The high pressures predicted by both models are primarily a result of the gas generation rates and the low repository porosity used. The

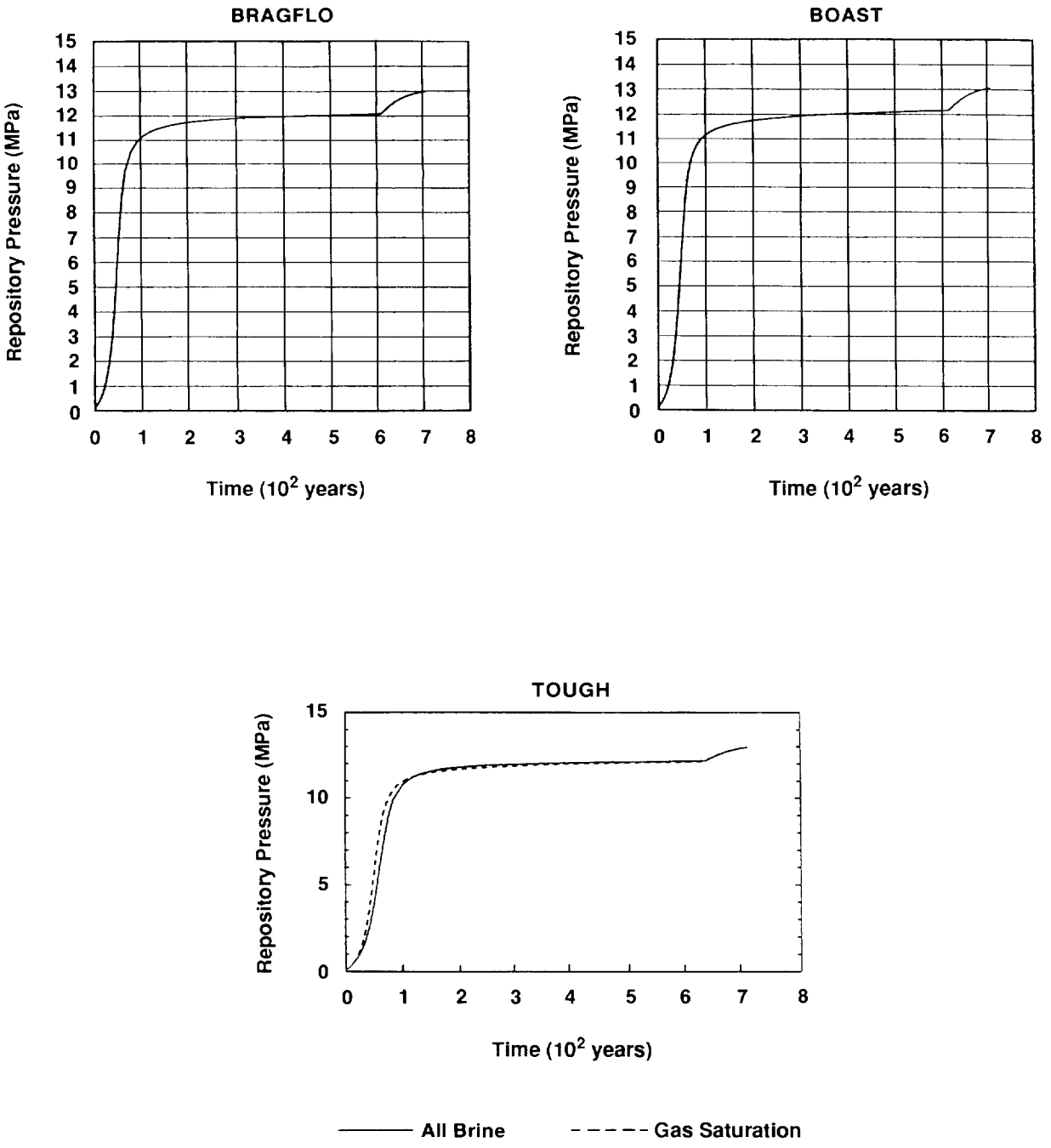

Figure 5-3. Repository Pressure Comparisons for Benchmark 2

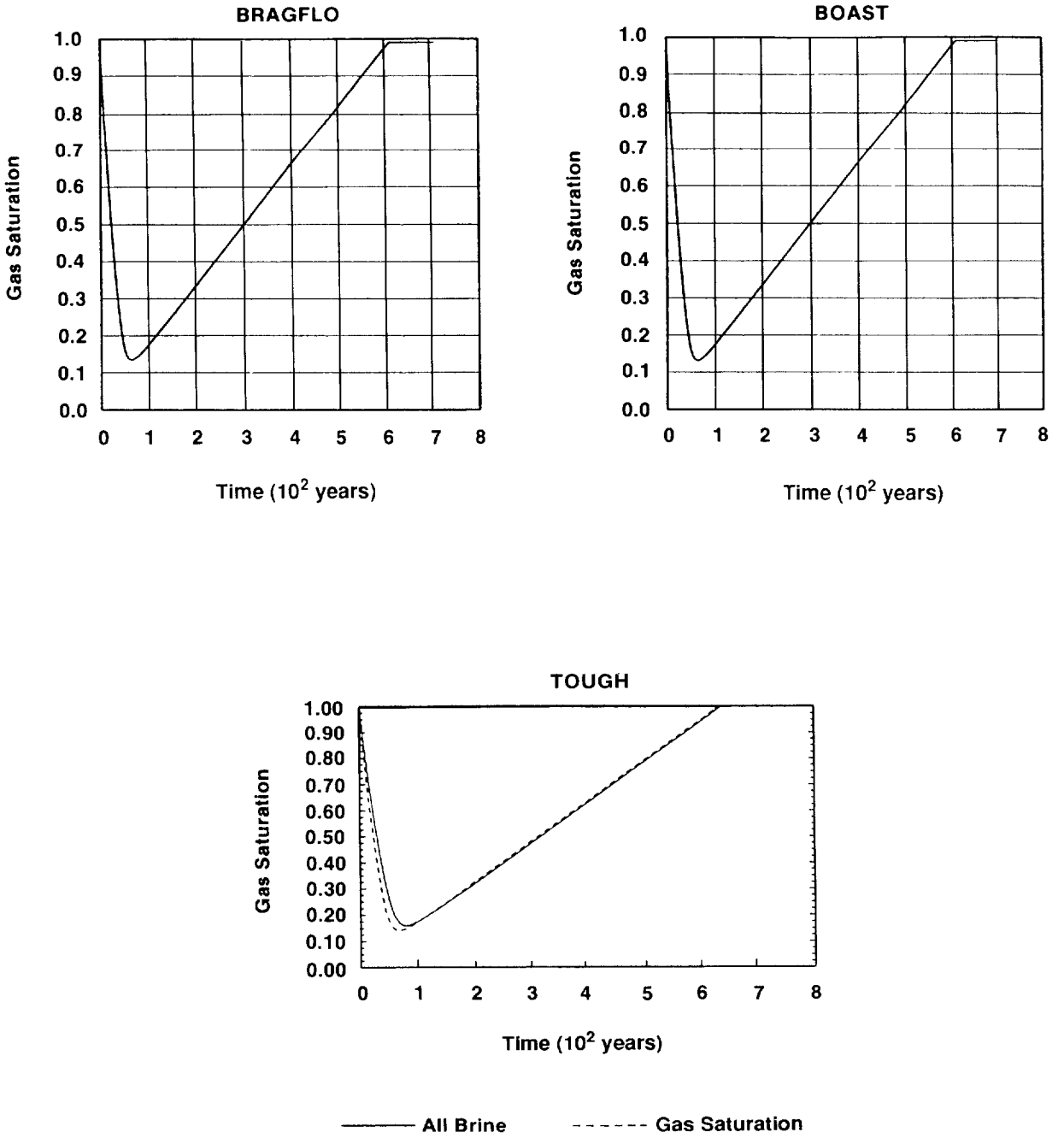

Figure 5-4. Repository Gas Saturation Comparisons for Benchmark 2

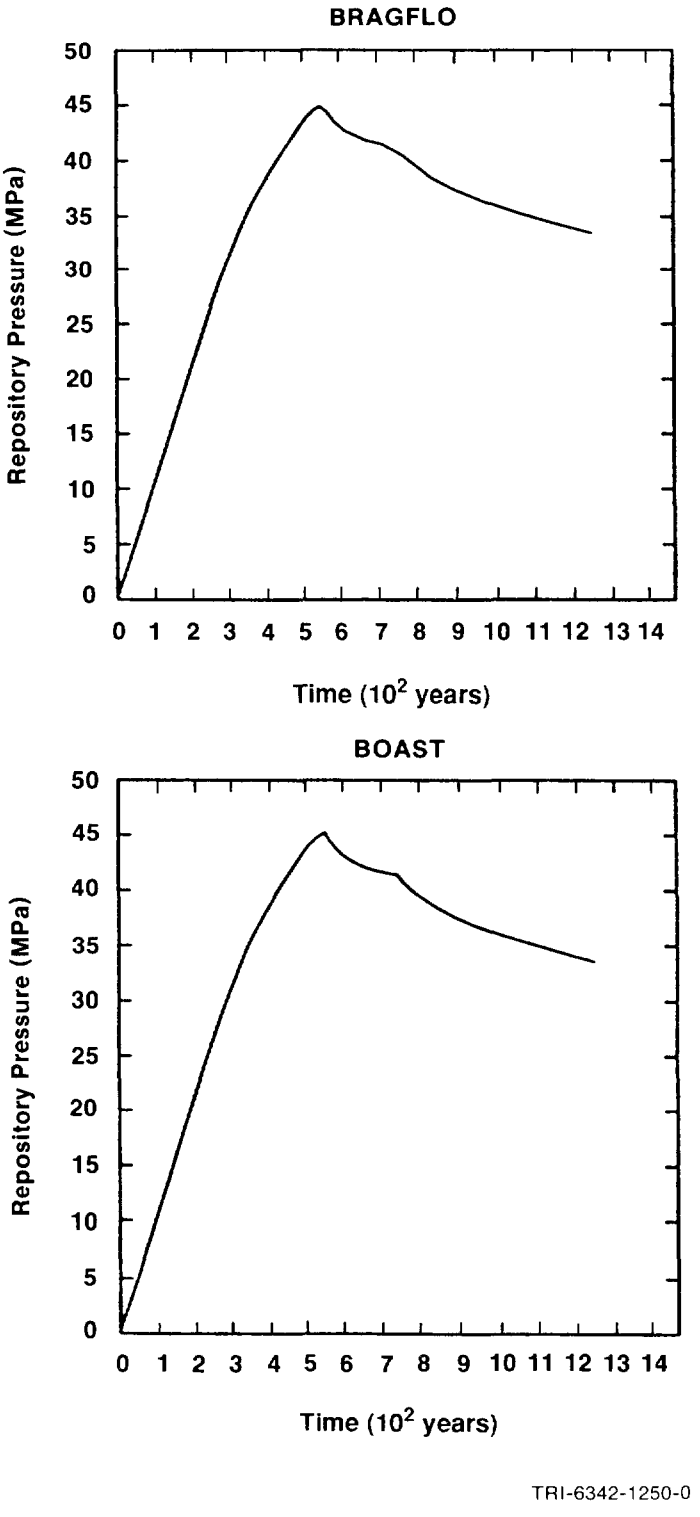

Figure 5-5. Repository Pressure Comparisons for Two-Dimensional Benchmark

comparisons of other resulting parameters such as saturations similarly showed excellent agreement. Results from TOUGH on this two-dimensional benchmark are unavailable at this time.

5.2.2.4 Fundamental Equations

BRAGFLO solves simultaneously the partial differential equations (PDEs) that describe the mass conservation of each mobile component (gas and brine) along with appropriate constraint equations, initial conditions, and boundary conditions. The fundamental equations can be found in Peaceman (1977) and Crichlow (1977). A total of five independent equations (two component mass conservation PDEs and three constraints) can be written to define the two-phase flow phenomena:

Gas Component Conservation:

$$\nabla \bullet \left[\frac{\alpha \rho_n K k_{rn}}{\mu_n} \left(\nabla P_n - \rho_n g \nabla D \right) + \frac{\alpha C_{Nw} \rho_w K k_{rw}}{\mu_w} \left(\nabla P_w - \rho_w g \nabla D \right) \right] + \alpha q_n + \alpha q_{rn}$$

$$= \alpha \frac{\partial \left(\phi \rho_n S_n + \phi C_{Nw} \rho_w S_w \right)}{\partial t} \tag{5-1}$$

Brine Component Conservation:

$$\nabla \bullet \left[\frac{\alpha C_{Ww} \rho_w K k_{rw}}{\mu_w} \left(\nabla P_w - \rho_w g \nabla D \right) \right] + \alpha q_w + \alpha q_{rw} = \alpha \frac{\partial \left(\phi C_{Ww} \rho_w S_w \right)}{\partial t} \tag{5-2}$$

Saturation Constraint:

$$S_n + S_w = 1 \tag{5-3}$$

Mass Fraction Constraint:

$$C_{Nw} + C_{Ww} = 1.0 \tag{5-4}$$

Capillary Pressure Constraint:

$$P_n - P_w = P_c \tag{5-5}$$

In the above equations uppercase subscripts refer to components while lowercase subscripts refer to phases. The subscript n or N refers to the nonwetting phase or component (assumed to be gas), while the subscript w or W refers to the wetting phase or component (assumed to be brine). In the case of the mass fraction terms (C_{Nw}, C_{Ww}), the first subscript refers to the component while the second refers to phase. In other words, C_{Nw} is the mass fraction of the nonwetting component (gas) in the wetting phase (brine), and C_{Ww} is the mass fraction of the wetting component (brine) in the wetting phase (brine). The term α in (5-1) and (5-2) is a geometric factor that generalizes the equations regardless of spatial dimension. In two dimensions, α is the "thickness" in the direction perpendicular to flow. The rest of the nomenclature is defined in Section 5.2.2.1.

In casting the PDEs in this form, a number of assumptions have been made. For instance, the conservation equations are balances on components and not phases. Because of the possibility of transfer of components between phases, it would not be appropriate to conserve the mass of each phase. Instead, the total mass of each component must be conserved. Equations (5-1) and (5-2) describe the simplest two-component, two-phase compositional mode. We have assumed that gas may exist in the gas phase as well as in the brine phase (as dissolved gas). We have further assumed that brine only exists in the brine phase (zero vapor pressure) so that $C_{Nn} = 1$ and $C_{Wn} = 0$. The amount of gas which is dissolved in the brine is described by a gas solubility parameter which may vary with pressure. The gas solubility parameter is defined as the ratio of the volume of dissolved gas (measured at standard conditions) to a unit volume of brine and can be related to C_{Gb}, the mass fraction of gas dissolved in brine. Imbedded in the PDEs is the assumption that Darcy's law, which linearly relates flow rate and pressure drop, remains valid.

The equation in (5-1) states that the net change in gas flow rate into and out of a control volume in pure or dissolved form, plus any gas added to or taken out of the control volume due to well or chemical reaction, equals the rate of gas accumulation in the control volume. The equation in (5-2) states the same for the brine component except there is no gas phase contribution to brine flow. The equation in (5-3) states that the volumes of the two mobile phases must occupy all of the void space. The equation in (5-4) states that the oil phase consists of brine and dissolved gas. Finally, (5-5) defines the concept of capillary pressure.

Because the amount of dissolved gas can be expressed as a function of pressure and the capillary pressure can be expressed as a function of saturation, the six unknowns can be reduced to four (brine and gas pressure and brine and gas saturations); two of these unknowns can be aligned with two PDEs and the other two found by application of the constraints expressed in (5-3) and (5-5). Other combinations of alignment may be more efficient. In the current version of BRAGFLO, (5-1) is aligned with gas saturation while (5-2) is aligned with brine pressure. We

have found no difference when (5-1) and (5-2) are aligned with gas pressure and brine saturation respectively during test cases.

In two dimensions (5-1) and (5-2) become respectively:

$$\frac{\partial}{\partial x}\left(HT_{gx}\frac{\partial P_g^*}{\partial x}\right)+\frac{\partial}{\partial y}\left(HT_{gy}\frac{\partial P_g^*}{\partial y}\right)+\frac{\partial}{\partial x}\left(HT_{bx}C_{Gb}\frac{\partial P_b^*}{\partial x}\right)+\frac{\partial}{\partial y}\left(HT_{by}C_{Gb}\frac{\partial P_b^*}{\partial y}\right)+Hq_g+Hq_{rg}$$

$$=H\frac{\partial}{\partial x}\left(\phi\rho_g S_g+\phi\rho_b S_b C_{Gb}\right) \tag{5-6}$$

and

$$\frac{\partial}{\partial x}\left(HT_{bx}C_{Bb}\frac{\partial P_b^*}{\partial x}\right)+\frac{\partial}{\partial y}\left(HT_{by}C_{Bb}\frac{\partial P_b^*}{\partial y}\right)+Hq_b+Hq_{rb}=H\frac{\partial}{\partial t}\left(\phi\rho_b S_b C_{Bb}\right). \tag{5-7}$$

In (5-6) and (5-7) the n, N, w and W subscripts have been replaced with g, G (gas) and b, B (brine) respectively. In addition, H (thickness in meters) has replaced α, T is shorthand for the group $\rho K k_r/\mu$ and P^* is $P-\rho gD$. In writing (5-6) and (5-7) we distinguish anisotropic permeability by expressing it in terms of k_x and k_y, which are contained in the groupings for T_x and T_y.

The equations in (5-6), (5-7), (5-3), (5-4), and (5-5), along with appropriate boundary and initial conditions and material physical property relationships, form the basis of the model's fundamental equations. All of the physical properties may be functions of any of the dependent variables (saturations and pressures) or independent variables (spatial position and time).

5.2.2.5 Wells

In reservoir models, wells are used to inject or withdraw fluids at specific locations in the reservoir. In BRAGFLO wells may be accommodated by using simple well models or by directly including well geometry and properties into the numerical mesh. In addition to describing the human intrusion borehole, wells can be used to approximate the gas generation process in the waste during corrosion and biodegradation and to modify the boundary condition from no-flow to fixed pressure or non-zero flow.

The well models treat a well as a point source or sink. Because of the finite size of the grids making up the numerical mesh of the reservoir, a true point source or sink can only be approximated. A true point source has infinite flow rate per unit volume of reservoir at the well and zero elsewhere (Peaceman, 1977). Instead, for finite-sized grids, the well is assumed to be

located in the center of a grid block of volume V_B. The mass flow rate per unit volume of reservoir into the grid block then is the well flow rate divided by the block volume. Outside the block the well does not directly contribute to flow rate. Wells are described according to type (injection or production) and operation (pressure or rate controlled). Injection wells may be of either operation while production wells are always pressure controlled. Injection wells only inject, and production wells only produce. If a production well is specified, but the well pressure exceeds reservoir pressure, fluid will not be drawn into the reservoir from the well; flow will be zero. If a well is to function as both an injector or producer, two wells are specified at the same location. This may be desirable when specifying a pressure along a boundary. Flow may then occur in either direction dependent on the direction of the pressure gradient.

In BRAGFLO wells may be accommodated by using simple well models or by directly including the well geometry and properties into the numerical mesh. The well model approach is more computationally efficient; however, the parameters that describe the flow properties of the well are unknown in advance. These parameters are typically determined from historical production or reservoir pressure and flow data. Because collection of such data at the WIPP is not feasible, current calculations do not use the well models to simulate the human intrusion boreholes. Instead the borehole dimensions, permeability, and porosity are directly incorporated into the numerical grid.

The well model, however, is used in certain areas along the far-field boundary where a constant pressure condition rather than a no-flow condition is desirable. Such an area is in the Culebra zone. The no-flow boundary condition is valid only to the extent its location is far enough removed such that events in the repository do not produce responses at the boundary over the simulated time frame. This may be questionable in the Culebra zone for some of the vectors associated with human intrusion scenarios. The relatively high permeability in the borehole and throughout the Culebra may cause pressure and saturation to fluctuate at the Culebra's far-field boundary. By specifying both an injection well and a production well characterized by a large injectivity and productivity index, constant pressure and saturation can be maintained at the Culebra boundary. This allows for the possibility of flow across the Culebra far-field boundary, thus avoiding unrealistic pressure buildup in the Culebra.

While wells can also be used to approximate gas generation in the waste, more sophisticated descriptions of the gas-generating reactions and their dependence on brine saturation have been included in BRAGFLO. Inclusion of separate corrosion and biodegradation reaction descriptions allow sensitivities associated with inventory variability and brine saturation variability to be evaluated. These sensitivities cannot be evaluated directly using a well model representation for reaction sources.

5.2.2.6 Numerical Solution Techniques

The numerical techniques in BRAGFLO are based on a fully implicit finite difference representation of the nonlinear conservation equations. In implicit methods the dependent variable at a particular location is evaluated as a function of the current values of its neighbors and the current value of any coefficients. In explicit methods current values of the dependent variables are evaluated as a function of previously determined (or past-dated) values of dependent variables and coefficients. Implicit methods are inherently more numerically stable compared to their explicit or hybrid (IMPES) counterparts (Fanchi et al., 1982; Carnahan et al., 1969; and Smith, 1965). The penalty for this increased stability is the increased computational effort associated with the simultaneous solution of the resulting finite difference analogs of the conservation equations at each grid block center.

In BRAGFLO the Newton-Raphson (Hildebrand, 1974; Carnahan et al., 1969; and Peaceman, 1977) iteration technique is used to generate solutions to the nonlinear partial differential equations. In the Newton-Raphson method a sequence of dependent variable values are produced which come increasingly close to the solution of the nonlinear analogs. The Newton-Raphson technique is chosen because of its quadratic convergence behavior (provided a good initial guess is available), its robustness (Carnahan, 1969; and Hildebrand, 1974), and its proven track record in solving multi-phase flow problems arising in petroleum reservoir modeling (Peaceman, 1977; Rubin, Vinsom, 1980; Coats, 1980; Crookston, Culham, Chen, 1979; Vaughn, 1986; and Price and Coats, 1974).

Five steps comprise our implementation of the Newton-Raphson solution method. The first is the linearization of the finite difference analogs of the conservation equations by truncation of a Taylor series expansion around the solution at each grid block center.

The second step is forming the recurrence formulas which relate values at successive intra-time step iteration levels. In matrix notation the recurrence equations become

$$J\left(\overline{Z}^{k}\right)\overline{\delta}^{k} = -G\left(\overline{Z}^{k}\right) \tag{5-8}$$

where k is the iteration level, $\overline{\delta}^{k}$ is the solution vector of corrections to the dependent variables $\overline{Z}$, $G\left(\overline{Z}^{k}\right)$ is a vector of the finite difference analogs evaluated at each grid block position, and $J\left(\overline{Z}^{k}\right)$ is the Jacobian matrix (Smith, 1965; and Hildebrand, 1974). The Jacobian matrix consists of the values of the partial derivative of finite difference analogs with respect to each dependent variable evaluated at each grid block center. In our implementation, the recurrence formula relates the changes in dependent variable values at successive iterations rather than the values themselves. This simplifies the computational process somewhat. The solutions to this system of equations

are then the changes in (or updated corrections to) the dependent variable values from the values converged to in the previous time step.

The third step is the evaluation of the elements in the Jacobian matrix. If the nonlinear analog functions are known analytically, then in principle analytical forms of their partial derivatives with respect to the dependent variables may be obtained. If the functions are not analytic or are complicated through coefficients which depend nonlinearly on the dependent variables, it becomes more practical or necessary to evaluate the Jacobian elements numerically. We choose the numerical approach in BRAGFLO for the reasons above as well as the increased flexibility which results from the ability to replace or modify property (coefficient) functionalities without requiring re-derivation of the analytical partial derivatives. The numerical evaluation of the Jacobian elements does not significantly affect the convergence characteristics provided the change in dependent variables for calculating the derivatives numerically is small enough that it captures the true nature of the slope at the point required. The change should not be so small; however, that machine precision errors dominate. We have found that changes on the order of 0.1 to 0.01 percent of the dependent variable values are satisfactory.

The fourth step is the solution of the system of equations resulting from the recurrence equations in step 2. The finite difference analog functions which appear in the recurrence equations and are used in forming the Jacobian relate the value of a dependent variable (or its change), a grid block (i, j) to values of the dependent variable evaluated at the four closest grid blocks: $(i-1, j)$, $(i+1, j)$, $(i, j-1)$, and $(i, j+1)$. This may be represented by a 5-point stencil (Figure 5-6) (Smith, 1965). The structure of the Jacobian made from the 5-point stencil is sparse (contains many 0 elements), consisting of five diagonal bands with a minimum bandwidth that may be calculated from grid block dimensions (Price and Coats, 1974; and Smith, 1965). The solution techniques available in BRAGFLO take advantage of the sparseness. For large problems this becomes a necessity from both storage and computational considerations.

Four solution options are available in BRAGFLO for solving the matrix equations. Two techniques are iterative solvers (Smith, 1965), PSOR (Point Successive Over Relaxation) and a Multi-Grid Algorithm. The third and fourth options are direct solvers using a banded LU decomposition (Conte and de Boor, 1972) and an LU decomposition routine from LINPACK (Dongarra et al., 1979). The Multi-Grid solver has the potential for being the most efficient technique for meshes in excess of 16 by 16 blocks while the LU solver is less efficient for large systems. Unfortunately for the current WIPP application, modeling matrix conditioning numbers (an indication of the determinant of the Jacobian matrix) are such that both iterative solvers suffer from extremely slow convergence to a solution. These conditioning numbers are calculated during

the LINPACK implementation of the LU decomposition method. This results in the LU solver being the most efficient and robust solver of the three options for this particular application.

In general the Jacobian matrix must be evaluated and solved for each intra-time step iteration. Fortunately, experience has shown for this particular application that the Jacobian can be evaluated only once at the start of each time step and left unchanged throughout the time step without significant impact on convergence or on the results. This results in a great computational savings since only one matrix evaluation and decomposition is required for each time step. All other intra-time step iterations only require the right-hand side of the matrix equation (5-8) to be updated and a back substitution to obtain the iterate solution vector, $\overline{\delta}^k$.

The fifth step in Newton-Raphson procedure is to update the dependent variables and check for convergence. The updating is done as $\overline{Z}^{k+1} = \overline{Z}^k + \overline{\delta}^k$, where k is the iteration level. Convergence is assumed when the right-hand side function vector of (5-8) is within a small tolerance of zero and all the δ^k's are within a specified tolerance of zero.

There are a few caveats associated with the application of Newton-Raphson technique to the multiphase flow of brine and gas at the WIPP. One is that the if the time step is too large an overshoot of gas saturation ($S_g > 1$) or an undershoot ($S_g < 0$) can occur during the iterations. It is not appropriate to accept these values even if they occur when convergence is satisfied. Internal checks in BRAGFLO flag these situations and cause the time step calculations to be repeated at a reduced time step. The selection of time step is another important issue.

Secondly, during the simulation when saturation and/or pressure are changing rapidly smaller time steps are required than when variables change slowly. In BRAGFLO the time step is updated continuously and is proportional to the change in dependent variables by

$$\Delta t^{k+1} = \Delta t^k \left[\frac{2\Delta z^*}{\Delta z^* + \Delta z_m^k} \right] \tag{5-9}$$

In (5-9), Δz^* is input and is the change in dependent variable (pressure and saturation) such that $\Delta t^{k+1} = \Delta t^k$. Δz_m^k is the maximum change in a dependent variable across all grid blocks defined as $z^{k+1} - z^k$. The time step is further restricted such that $\Delta t_{\min} < \Delta t^k < \Delta t_{\max}$ and $\Delta t^{k+1} / \Delta t^k < \Delta t_r$. $\Delta t_{\min}$, $\Delta t_{\max}$ and Δt_r are all user specified. The time step calculated above is reduced if required so that the resulting elapsed simulation time is coincident with the times required for specifying a change in well data, material property data, or for printing output.

A third issue concerns the spatial location where the various coefficients in the finite difference analogs of the conservation equations, (5-6) and (5-7), are evaluated. These coefficients involve the

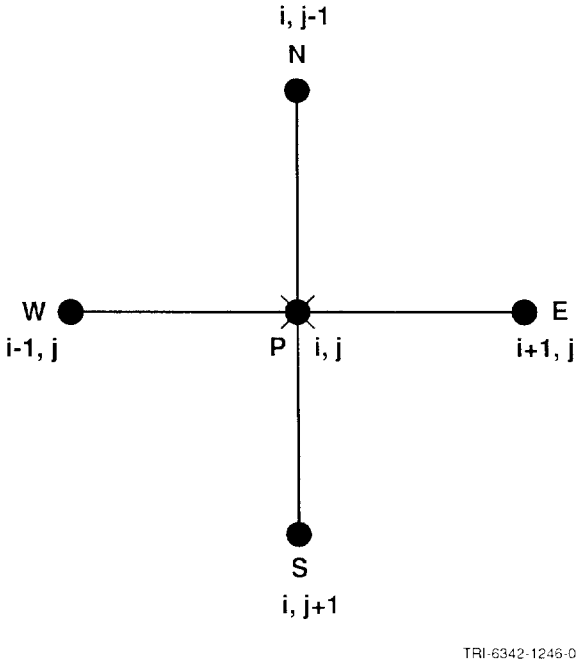

Figure 5-6. Five-Point Finite Difference Stencil.

grouping of parameters, $(\rho_b k_\ell C_{Bb}/\mu_b)\bullet(k_{rb})$ in the brine phase and $(\rho_g k_\ell C_{Gb}/\mu_b)\bullet(k_{rg})$ in the gas phase in the direction ℓ. The discretization of (5-6) and (5-7) about a grid block center located at i, j as used in BRAGFLO necessitates the evaluation of these coefficients at the interfaces between i, j and its four neighboring grid block centers (i.e., at $(i+1, j)$, $(i-1, j)$, $(i, j+1)$, and $(i, j-1)$). This raises the following question: How should the values of the coefficients evaluated at adjacent grid block centers be correctly averaged to obtain the interface value?

Mass balances about the interface between two grid blocks indicate that a harmonic average of its coefficients evaluated at adjacent grid block centers conserves mass, (Fanchi et al., 1982; Peaceman, 1977). Furthermore, experience (Crichlow, 1977; Rubin and Vinsome, 1980; Peaceman, 1977; Crookston et al., 1979; Coats, 1980) has shown that use of a relative permeability in the block that has the larger phase potential of the two neighboring blocks yields more reliable results. This is called "upstream weighting" in the reservoir modeling literature. The formulation in BRAGFLO combines the upstream weighted relative permeability with the harmonic average of remaining grouping of parameters in the coefficients to yield interface coefficient values.

Upstream weighting of relative permeability produces more realistic results compared to complete harmonic averaging. This can be best understood by considering the flow of a phase

between two adjacent grid blocks for the case when the grid block having the lower potential also has none of the flowing phase present (i.e., relative permeability = 0). In this case, using a straight harmonic average would never allow any of the phase to flow into the lower potential block. In other words, assuming only potential flow, once a phase saturation in part of the reservoir is reduced to below its residual saturation it will remain below residual saturation regardless of the potential gradient. Upstream weighting eliminates this unrealistic behavior. Upstream weighting also produces more stable results allowing larger time steps to be taken. Unfortunately, upstream weighting also tends to increase numerical dispersion producing a smoothing of sharp fronts (in saturation and pressure fields) particularly around interfaces between differing materials. The shape and magnitude of the fronts may become distorted (broadened); however, the area under (or spatial integral of) the saturation or pressure distribution is conserved.

5.2.3 SPATIAL AND TEMPORAL GRIDS—James D. Schreiber

The geometry used in the two-phase disturbed conditions modeling is similar to that used in the undisturbed calculations. It represents an axisymmetric approximation to an equivalent panel. Cylindrical geometry was necessary for two reasons. First, the actual geometry of the WIPP repository is too complex for PA modeling; a mesh having all the detail of the repository, or even of a single panel, would be prohibitively large and would require more computation time than is available for a single year's PA calculation. Second, BRAGFLO is currently a two-dimensional model; cylindrical geometry allows the most important aspects of flow over a large areal extent to be simulated in only two dimensions. Specifically, the convergence of flow radially toward a point sink can be modeled more accurately in cylindrical geometry than in rectangular geometry. This is important because on a large scale the flow is radial toward the intrusion borehole, which is located along the axis of symmetry. Even within a panel, because of the relatively high permeability of the waste, flow will be essentially radial, though constrained by the pillars to be more rectilinear. For flow into a panel from the far field, the most important features of a panel are its perimeter, both the length and the distance of the perimeter from the center where an intrusion well is assumed located, and the enclosed volume. How these parameters are averaged into a cylinder is somewhat arbitrary, and compromises are necessary.

In modeling a panel for PA purposes, the panel is treated as a cylinder having the same enclosed floor area as an actual panel, including the area occupied by the pillars. This results in a cylinder having a radius of 96.78 m. To account for the inclusion of the pillars, which have a very low porosity, the porosity of the panel is adjusted from the final porosity of the waste alone. The initial brine saturation is also adjusted for the presence of pillars that are fully saturated with brine. These calculations are discussed in Section 3.4.8 of Volume 3.

The region modeled includes the cylindrical equivalent panel and the surrounding Salado formation with anhydrite layers above and below (see Figure 4-1). The borehole is coincident with the axis of symmetry. The region extends upward to the top of the Culebra, downward to the bottom of the Castile brine reservoir, and outward approximately 22.3 km. By including the Castile and Culebra, the major sources and sinks for brine flow to and from the repository are represented in a single model. The far-field boundary is intended to be far enough away to justify the use of a no-flow boundary, which is required in BRAGFLO, without the boundary affecting the behavior of the repository. While a further removed boundary might be desirable for greater accuracy with this model, the formations being modeled actually extend only about 10 km north of the repository (see Figure 1.5-2, Volume 3). Anhydrite layers a and b immediately above the repository have been consolidated into a single layer with a thickness equal to the combined thicknesses of a and b and located at the elevation of layer b, the one closer to the repository. The panel thickness was varied, depending on the final porosity of the waste, which in turn depends on the composition of the waste and the total gas generation potential. The procedure for calculating the panel height and porosity, and the assumptions used, are described in Section 3.4.8 of Volume 3. The DRZ extends vertically upward through the anhydrite layer and downward through MB139. Beyond the outer radius of the panel, both the anhydrite layers and the Salado are intact. The center of the intrusion borehole is located at the axis of symmetry.

5.2.4 MATERIAL PROPERTIES AND BOUNDARY AND INITIAL CONDITIONS

Specification of boundary and initial conditions are required to complete the formulation. Upon examination of equations (5-6) and (5-7) it is evident that they are second-order with respect to gas pressure (P_g) and brine pressure (P_b). Thus two boundary conditions are required for each phase pressure in each dimension (two on P_g and P_b in x and two on P_g and P_b in y). BRAGFLO handles boundary conditions in a way that typifies reservoir models; that is the reservoir of interest is enclosed by a boundary across which there is no flow in the direction normal to it. Mathematically these types of conditions are Neumann boundary conditions in which the normal derivative of pressure to the boundary is zero. In BRAGFLO this is accomplished by assigning a zero value to the normal transmissibilities along each of the boundaries for both the gas and brine phase.

Through the use of wells, BRAGFLO has the capability to override the no-flow conditions. By locating pressure-constrained or flow-constrained fictitious wells along the boundaries, fixed pressures along the boundary or non-zero flow into or out of the reservoir across the boundary can be approximated.

The calculations of this report are based on the assumption of no-flow boundaries with the exception of a constant pressure condition located at the far field in the Culebra. The no-flow conditions occur on two types of boundary lines: (1) along the far-field boundary and above and below the repository and (2) along a vertical line of symmetry that passes through the center of a panel (the smallest unit of the repository that is assumed to be hydrologically isolated). For application to WIPP, an implicit assumption is that the boundaries of the no-flow type are located far enough away from the repository that they have a negligible influence on the flow behavior in and around the repository over the 10,000-year time span. A constant-pressure well is located at the far-field Culebra boundary because the Culebra zone is the most permeable material in our reservoir model. The constant pressure well allows for the possibility of flow across the boundary in the event that the flow fields affect the pressures and saturation near this boundary.

A number of variables and properties must be specified at time t=0. These initial conditions consist of: (1) the two dependent variables aligned with (5-6) and (5-7) (S_g and P_b), (2) the reservoir properties of porosity and the directional permeabilities, and (3) the concentrations of metal and cellulose. These variables must be specified throughout the simulation volume and along the boundaries. All other material (fluid and reservoir properties) must also be specified; however, properties such as relative permeabilities, capillary pressures, densities, viscosities, dissolved gas, etc., are functions of the previously specified dependent variables and are calculated in BRAGFLO. (Details on material, fluid, and reservoir properties used in BRAGFLO calculations are provided in Volume 3 of this report.)

5.2.5 RESULTS AND DISCUSSION—Palmer Vaughn and James D. Schreiber

5.2.5.1 Overall Results

PA calculations using BRAGFLO have been completed for the 1991 "snap-shot." The results from the 600 two-phase-flow simulations quantify the flow fields in and around the repository over 10,000 years for all the vectors comprising the E2 and E1E2 summary scenarios. A vector is a set of model input parameter values obtained from one particular sampling of parameter value probability distributions. The flow fields from the E1 scenarios are inferred from the E1E2 results as justified earlier, in Section 5.1.2. In addition to the 600 simulations used in the consequence analysis, an additional 120 simulations were completed for comparing the effects of gas generation with no gas generation.

A detailed analysis of all the BRAGFLO results is an ambitious task and is not available at this time. Such an analysis is focused on analyzing the output of all 600 simulations with respect to pressures, saturations, gas generation, iron concentrations, and cellulosic concentrations in order

that phenomenological differences resulting from the wide disparity in parameter values associated with each vector may be evaluated.

A number of general conclusions that have important impact and implications on the final CCDFs can be made at this time. The discussion of results in this section is focused on the intermediate flow-field results from BRAGFLO and not on final CCDFs. A discussion of the final CCDFs and the effect of gas on radionuclide release is summarized in Chapter 6, Volume 1 of this report. Unless otherwise defined, the term "flow" in this section is used to represent the cumulative amount of contaminated brine (in m^3) that flows up an intrusion well and enters the Culebra over the 10,000 years following emplacement.

The first conclusion is that for each vector of the E2 and E1E2 scenarios the "flow" decreases for later-occurring intrusions. In Figures 5-7 and 5-8 the "flows" are plotted for each vector at the selected intrusion times of 1000, 3000, 5000, 7000, and 9000 years after the repository is sealed. Figure 5-7 corresponds to the E2 scenario while Figure 5-8 corresponds to the E1E2 summary scenario. In all cases the flow not only decreases with increasing intrusion time but it decreases at an increasing rate as the time of intrusion increases.

This is an important conclusion. The trend in "flow" versus intrusion time had been observed in the case of single-phase, fully brine-saturated flow, but was unverified, until now, for the case of simultaneous flow of brine and gas with gas generation. This suggests that the release of brine from early intrusion times may bound that of latter times. As long as CCDFs based on early time release comply with the regulation there may be no need to consider late intrusion time scenarios. This conclusion does not apply when considering Resource Conservation and Recovery Act (RCRA) compliance and may not hold for other conceptual models or other combinations of parameters.

A second conclusion is that the "flows" from the E1E2 summary scenario exceed the "flows" from the E2 scenarios in all vectors for each intrusion time investigated. Figures 5-7 and 5-8 described earlier support this conclusion. The larger E1E2 "flows" compared to E2 are dominated by the flow of Castile brine rather than the flow of Salado brine. The flow of Castile brine into the waste panel and up the intrusion borehole is larger than that from the Salado for a number of reasons. First, the borehole connecting the Castile brine pocket to the waste panel is much more permeable (4 to 6 orders of magnitude in m^2 units) than are the anhydrite layers (the primary flow paths for Salado brine to reach the panel). Second, the Castile rock compressibility, which is calculated from the bulk storage coefficient, is larger than that of the anhydrite. The larger rock compressibility results in a smaller pressure decline per unit volume of brine removal from the brine pocket than that which occurs in the anhydrite. Thus the potential difference (the potential for flow) between the brine pocket and the waste panel does not decline as rapidly as that difference between the anhydrite and the panel. Third, the brine volume available in the anhydrite is small

compared to that of the brine pocket and the brine which flows out of the anhydrite is replaced slowly by the surrounding Salado due to low Salado permeability. Finally, good connectivity between the panel and the brine pocket and the high brine pocket pressure generally causes the panel to pressurize more rapidly and to a higher level in the E1E2 compared to the E2, thus reducing further the component of flow from the far field along the anhydrite in the E1E2 compared to the E2. However, this is more than offset by the large contribution to borehole flow from the brine pocket.

A third conclusion is that gas generation produces lower "flow" than in the absence of gas generation for all of the vectors in the E2 and E1E2 1000-year intrusion time summary scenarios. Comparisons for the E1 scenario are believed to result in the same conclusion. In Figures 5-9 and 5-10, the flows from the 120 input vectors are compared to the flow from the same input vectors with zero gas generation rates. The zero reaction rates are the only differences between the two input vector sets. Figure 5-9 corresponds to the E2 scenario class, while Figure 5-10 corresponds to the E1E2 scenario class. The intrusion time is 1000 years (the intrusion time which produces the highest releases). The "flows" from the gas generation simulation are lower and the amount or percentage of reduction in "flow" differs from vector to vector.

The effect of gas generation on "flow" is more pronounced in the E2 scenarios than in the E1E2 with respect to the percent reduction in "flow" because of the smaller "flows" associated with the E2 cases. The amount of the reductions are, however, consistently larger for the E1E2 scenarios. An analysis of the results presented in Figures 5-9 and 5-10 indicate that for the E2 scenario the average "flow" of the 60 vectors is reduced from $9.0 \times 10^3 m^3$ to $4.0 \times 10^3 m^3$, a reduction of $5.0 \times 10^3 m^3$ or 55% when gas generation occurs. The number of E2 vectors resulting in zero "flow" increases from 0 to 22 when gas is considered. The average "flow" of the 60 E1E2 vectors is reduced from 8.2×10^4 to 7.0×10^4, a reduction of 1.2×10^4 or 15%. The large flow rates of Castile brine into the panel compared to the flow rates of brine from Salado into the panel once the repository and brine pocket is breached is partially responsible for the lower percentage reduction in flow observed in the E1E2 scenario compared to E2. The large flow from the brine pocket occurs in spite of rising gas pressure in the waste panel because at the 1000 year time of intrusion the pressure in the panel is still significantly lower than that of the brine pocket and the connection between the brine pocket and panel is quite permeable.

The percent reduction in "flow" is expected to be larger in E1E2 scenarios at later intrusion times provided gas generation still occurs for at least two reasons. First, the higher pressures from continued gas generation at the latter intrusion times will slow the flow of Castile brine. Second, the longer reaction times before intrusion result in increased brine consumption and gas generation. The larger presence of gas in the panel at the time of intrusion results in lower brine

mobilities so not only must a larger amount of gas be displaced from the panel before brine flows up the intrusion well but it is displaced at a slower rate.

Conclusion 4 is that the "flows" produced during E2 summary scenarios do not bound the flows produced during the E1 summary scenario in some vectors. For reasons discussed earlier in Section 4.2.3, the E2 "flows" exceed those from E1 at the higher E2 "flow" vectors except for many of the vectors that produced little or no E2 flow. In those vectors where E1 "flow" exceeds E2 flow, the "flows" are close in magnitude to each other. In generating the final CCDFs, the releases from E1 are approximated by those from the E2 scenario. This is justified since the E2 releases either bound those of E1 or the magnitudes of the E1 releases are sufficiently close to those of E2 that they fall in the same discretized release "bins" used in calculating the CCDFs.

Conclusion 5 is that the "flow" produced during E1 summary scenarios at early intrusion times does not bound that which is produced at later intrusion times for some vectors. This is different behavior than is seen for flows produced from E2 and E1E2 summary scenarios. In Figure 5-11 "flow" produced during E1 summary scenarios is presented for each vector at the five intrusion times (1000, 3000, 5000, 7000, and 9000 years). At the higher "flow" magnitudes (in excess of 5000 m^3) the early intrusion "flows" exceed the "flows" at later intrusion times for all vectors. At low "flow" magnitudes (less than 5000 m^3) the early intrusion "flows" do not necessarily exceed the "flows" at later intrusion times when comparing "flows" resulting from the 1000-, 3000-, and 5000-year intrusion times (vector 18 and 38 for example). Because the releases for these particular vectors are low this behavior does not appreciably affect the CCDFs. The causes of these trends at low "flow" magnitude are being investigated and while interesting from a phenomenological or mechanistic point of view, they are not at this time believed to be important with respect to compliance assessment.

Preliminary examination of some of the details in pressure, saturation, and reaction rate profiles from vector 58 (a vector where "flow," although small, is greater for the 3000-, 5000-, and 7000-year intrusion time than for the 1000-year intrusion time) suggest that the increase in E1 "flow" at later intrusion times may be a result of increased gas generation. In this vector a large gas pocket forms in the panel shortly after flow from the panel through the intrusion well begins. The gas pocket is located in the upper part of the panel some 20 to 50 m from the well, isolating a portion of the panel from the brine. The gas pocket continues to expand throughout the 10,000 years and drives brine predominantly toward the well but also out along the MB 139 as well. During the 1000-year intrusion time scenario this gas pocket does not form and the subsequent "gas drive" does not occur. The additional contribution to "flow" from the gas drive is believed to result in some of the later intrusion times having larger releases. Gas pockets typically do not persist throughout the 10,000 years. They tend to dissipate shortly after intrusion. Exactly how they form and under what conditions they form is being investigated.

5.2.5.2 Results for a Typical Vector

A "typical" vector is analyzed to illustrate the significant features and behavior of two-phase flow under disturbed conditions when an intrusion borehole opens at 1000 years. Vector 18 was chosen as typical in that brine releases were very low, but nonzero, in the E2 scenario (the majority of the 60 vectors showed zero release) when gas generation was included. Without gas generation, the release was higher by a factor of about 6, well within the range of differences seen among the 60 E2 scenario vectors. In the E1E2 scenario, the release for vector 18 was near the mean for the 60 vectors when gas generation was modeled. With no gas generation, the release was just slightly higher, as was generally the case.

The behavior seen in vector 18 appears typical, particularly the pressure history in the waste, which, in the case of gas generation, shows a rapid buildup followed by an even more rapid pressure release when the intrusion borehole opens at 1000 years. The pressure builds up again, rapidly in the E1E2 scenario, and very slowly in the E2 scenario. Without gas generation, the pressure in the waste simply rises monotonically approximately to hydrostatic pressure at the time of borehole opening, then the pressure levels off and remains nearly constant for the remainder of the 10,000-year period.

Comparison of E2 With E1E2, With Gas Generation

During the first 1000 years, the behavior of the two scenarios is identical, since the Castile brine reservoir is modeled as being completely isolated from the Salado by an impermeable layer of Castile anhydrite. Pressure in the waste rises rapidly to 9.2 MPa primarily as a result of gas generation. Small amounts of brine also flow in from the anhydrite layer above the repository and from MB139, which tends to equalize the pressure in the waste with the pressure in the far field, which is at 12.8 MPa. In this vector, gas generation by anoxic corrosion occurs rapidly compared to other vectors; approximately 55% of the corrodible metal in the waste is consumed by 1000 years. The biodegradation rate is slower, but the amount of biodegradable material is one of the lowest among the 60 vectors, and it is fully consumed in about 350 years.

The intrusion borehole opens at 1000 years, resulting in rapid depressurization in both scenarios. In the E1E2 scenario, the pressure (Figure 5-12) bottoms out at 2.5 MPa 280 years later. (It should be noted that in the WIPP repository and the surrounding geologic media, "rapid" changes occur over centuries, not days, weeks, or a few years.) During this period, a gas column (i.e., a gas-filled degraded borehole plug) connects the waste panel with the Culebra. Since the pressure in the Culebra remains fairly constant at about 1.05 MPa, the pressure in the waste could continue to drop to this level. Countering the drop in pressure is continued gas generation by anoxic corrosion, which finally consumes all corrodible metal by 1630 years. At the same time,

brine flow from the Castile is rapidly filling the panel. By 1540 years, the waste panel is connected to the Culebra by a column of brine, and the pressure in the waste rises above hydrostatic. Because the pressure in the Castile (11.57 MPa) is above hydrostatic, a gradient higher than hydrostatic is maintained in the borehole, resulting in the pressure being higher than hydrostatic in the waste. The panel pressure peaks at 7.9 MPa immediately after connection is made with the Culebra, and drops very slowly over the rest of the 10,000-year period to 7.7 MPa. Hydrostatic pressure at the repository level, with the Culebra pressure fixed at 1.053 MPa and brine density of 1230 kg/m^3, is 6.04 MPa. The pressure in the waste is actually slightly greater than even the gradient from the Castile would impose. This is probably caused by brine flow from the far field, which will tend to elevate the pressure closer to the far field pressure of 12.8 MPa, as long as there is some resistance to flow up the borehole. The pressure in the waste drops slowly over time because the Castile brine reservoir pressure is slowly decreasing as brine is withdrawn. Because of the high storage capacity of the brine reservoir, the pressure there drops only from 11.57 MPa initially to 11.51 MPa after 10,000 years. During the 8500 years that brine flows upward from the waste panel, about 31,500 m^3 of brine is released (Figure 5-13).

In the E2 scenario, the pressure in the panel (Figure 5-14) continues to decrease long after the borehole opens. Gas continues to be generated by anoxic corrosion until all corrodible metal is reacted after 4100 years, but the production rate is low because the brine saturation is low owing to the slow recharge from the far field and consumption of brine by the corrosion reaction. The borehole is filled with gas and offers little resistance to gas flow, so as gas is generated, it simply flows up to the Culebra, where the relatively high permeability results in nearly constant pressures of 1.05 MPa. Thus, waste pressure bottoms out at 1.09 MPa after 5400 years. Brine is flowing in from MB139 and from the anhydrite layer during this time, and once corrosion ceases, the panel slowly fills up. After 7700 years, the panel is finally filled and a brine column fills the borehole to the Culebra after 7700 years, at which time the pressure in the waste climbs to just above hydrostatic. It continues to rise very slowly for the remainder of the 10,000 years, presumably as a result of inflow from the far field and some resistance to flow in the borehole. Until the panel and borehole are filled with brine, there is actually a downward flow of brine from the borehole into the panel (see Figure 5-15). This brine is seeping into the borehole from the Salado along the 400 m of Salado between the repository and the Culebra. Once the panel is filled, at 7700 years, the direction of brine flow in the borehole reverses, and 1300 m^3 of brine flows from the panel over the next 2300 years.

There are clearly some major differences in behavior between the E2 and the E1E2 scenarios, owing to the high pressure in the Castile brine reservoir. Without that large source of brine, releases from the waste panel are delayed 6700 years, and the rate of release is far lower. Over the

10,000-year regulatory period, the amount of brine released in the E2 scenario is only 1300 m^3, compared with 31,500 m^3 when a pressurized brine reservoir is intercepted.

Comparison of E1E2, With Gas Generation, With E1E2, Without Gas Generation

Without gas generation, the pressure in the waste rises slowly at first (Figure 5-16), the only mechanism for increasing pressure being inflow of brine from MB139 and the anhydrite layer. Only when the panel is nearly full of brine does the pressure rise rapidly. This occurs just prior to the borehole opening. When the borehole does open at 1000 years, the pressure in the panel has not yet reached hydrostatic. Brine then drains into the panel by way of the borehole from the Salado DRZ, the anhydrite layer and the lower Salado above the repository, and pressure in the neighborhood of hydrostatic is achieved. Only a small amount of the gas that was present initially flows into the borehole (less than 0.2 m^3 at reference conditions); the rest has been compressed to less than residual saturation and remains trapped in the waste. The borehole then fills with brine up to the Culebra. The pressure holds nearly constant for the remainder of the 10,000 years, as was the case with gas generation, except that the pressure is very slightly lower without gas generation than with gas generation. The greatest effect of gas generation is on the brine flow out of the waste (Figure 5-17). Although the time when the brine first flows out is about the same in both cases, the flow rate is higher (4.32 m^3/yr at 10,000 years, vs. 4.08 m^3/yr) and the total flow out over the 10,000 years is greater when no gas is generated. Cumulative releases of brine are 31,500 m^3 with gas generation and 37,300 m^3 without. The process of filling the panel, driving out enough gas for brine to make the connection to the Culebra, and starting flow out of the panel seems to take nearly as long whether or not gas is generated.

There are several reasons for the higher releases when no gas is generated. With gas generation, the panel initially fills with gas over the first 1000 years; and at the same time, brine is consumed by anoxic corrosion, further reducing the brine content of the panel. Gas production via corrosion consumes about 2660 m^3 of brine. The rapid pressure buildup with gas generation restricts the flow of brine from the anhydrite layer and MB139 during the first 1000 years preventing another 150 m^3 of brine from coming in through MB139, compared with when gas is generated. (Flow through the anhydrite layer is largely unaffected during this time period.) Without gas generation, essentially all the gas that is present is compressed down to residual saturation or less before the borehole opens. Thus, there is no resistance to brine flow imposed by the presence of gas. With gas generation, there is gas present in some part of the panel at saturations greater than residual for the full 10,000 years. This restricts flow from the far field and flow through the panel from the Castile, even after the panel is sufficiently filled with brine that it flows upward to the Culebra, which is delayed 540 years while the panel fills. The result is

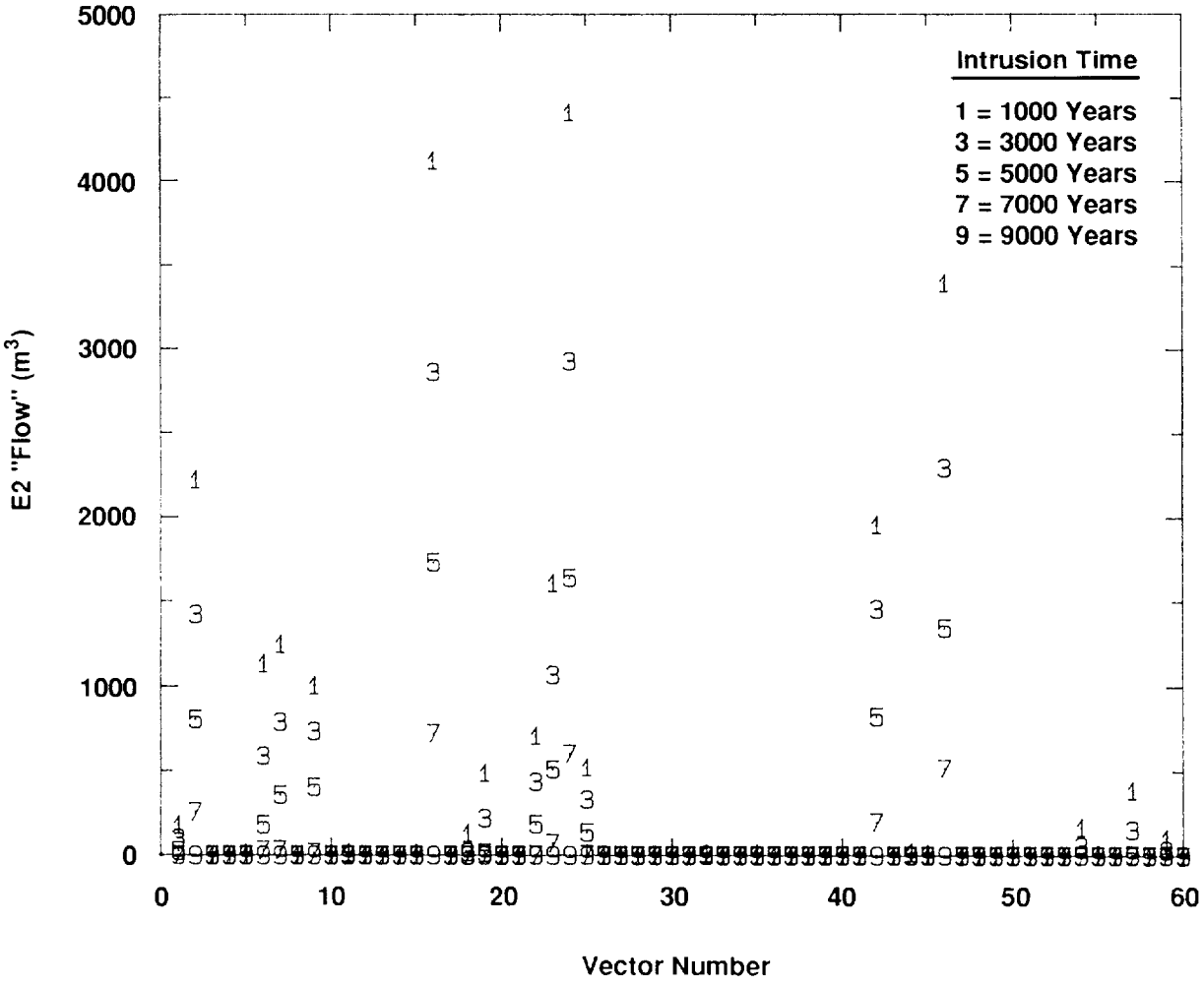

"Flow" = Volume of contaminated brine entering
Culebra and accumulated over 10,000 years

TRI-6342-1397-0

Figure 5-7. Borehole "Flow" From BRAGFLO During E2 Summary Scenarios

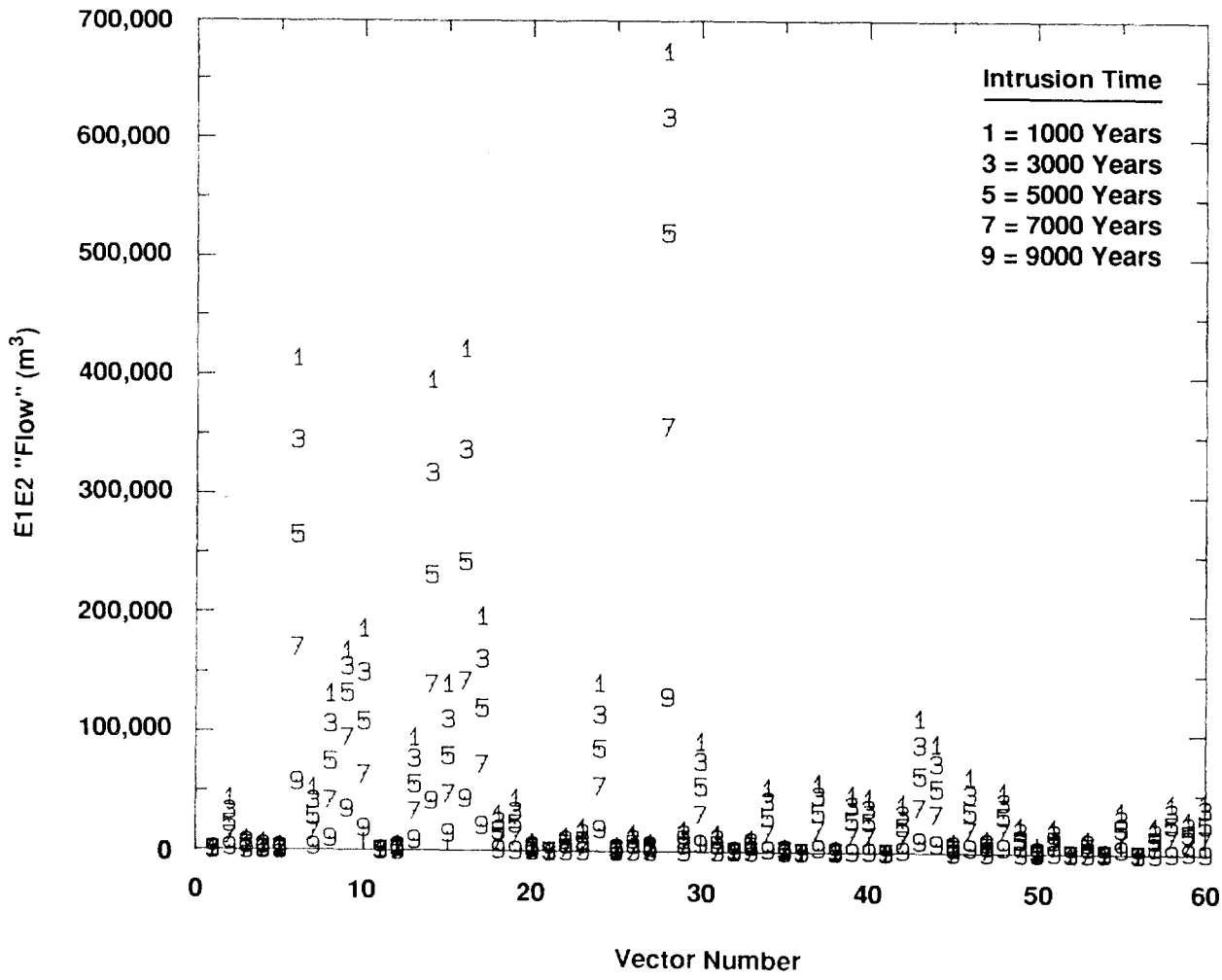

"Flow" = Volume of contaminated brine entering Culebra and accumulated over 10,000 years

TRI-6342-1398-0

Figure 5-8. Borehole "Flow" From BRAGFLO During E1E2 Summary Scenarios

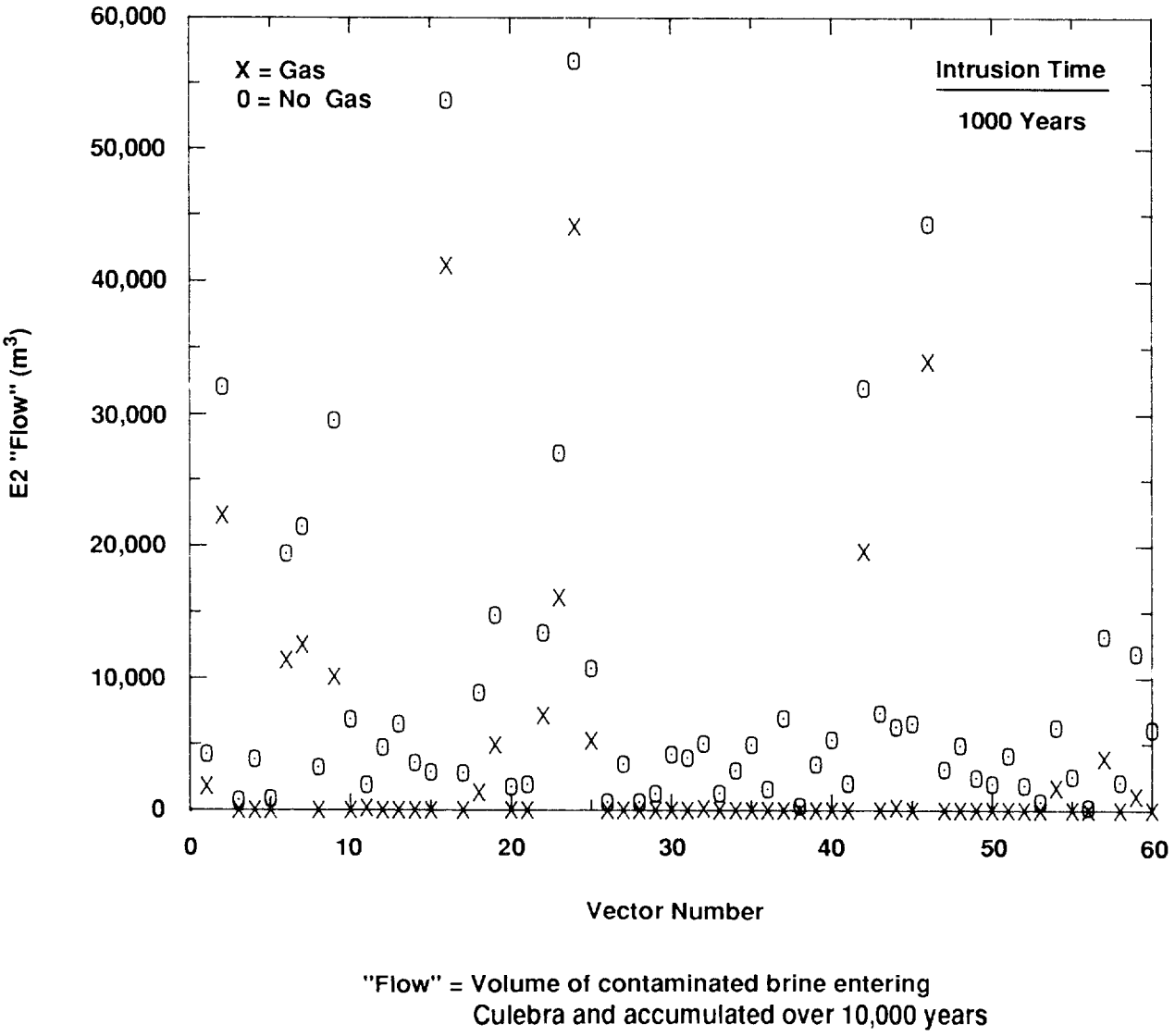

Figure 5-9. Borehole "Flow" Results From BRAGFLO: Effect of Gas Generation In E2 1000-Year Intrusion Summary Scenario

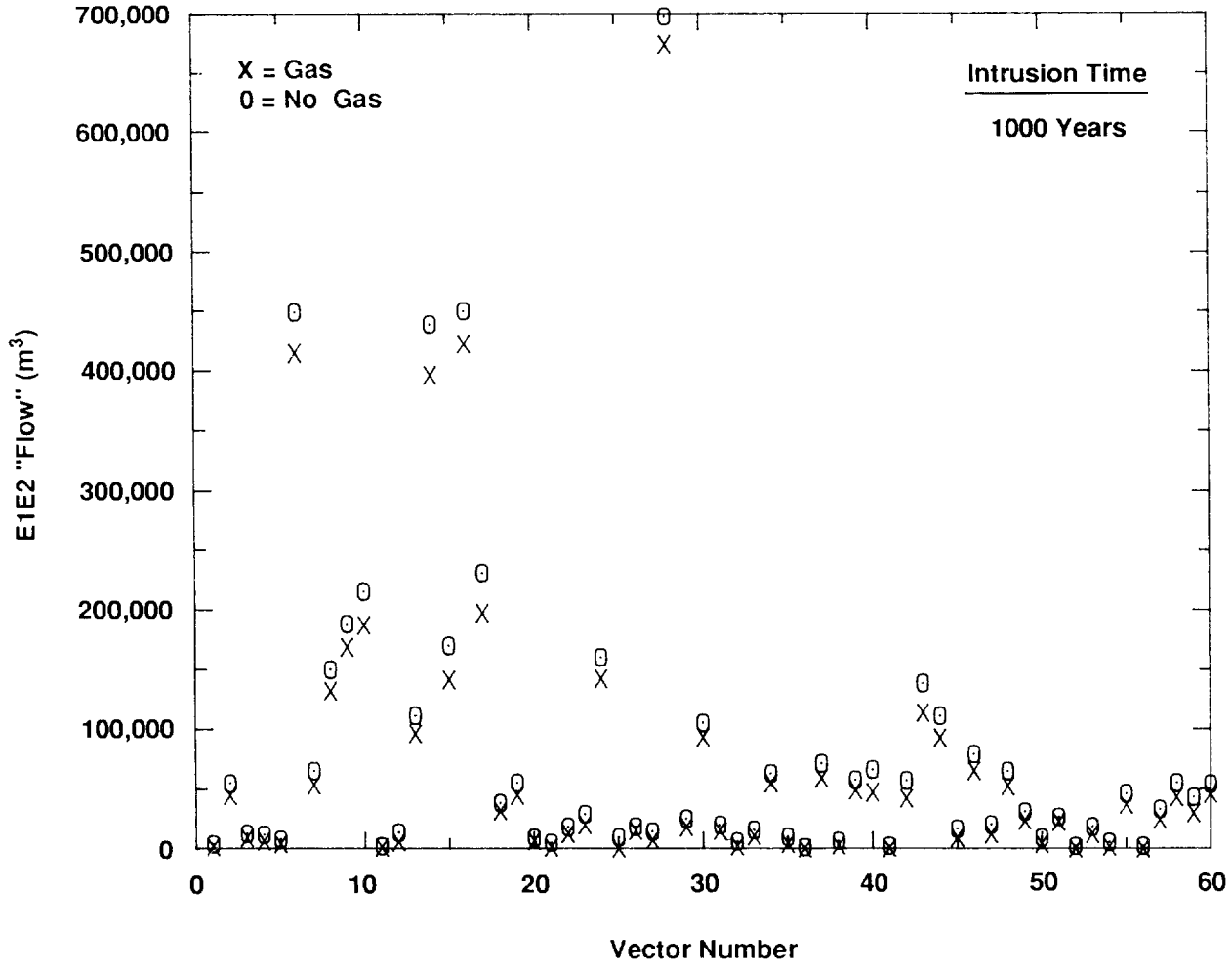

"Flow" = Volume of contaminated brine entering Culebra and accumulated over 10,000 years

TRI-6342-1359-0

Figure 5-10. Borehole "Flow" Results From BRAGFLO: Effect of Gas Generation In E1E2 1000-Year Intrusion Summary Scenario

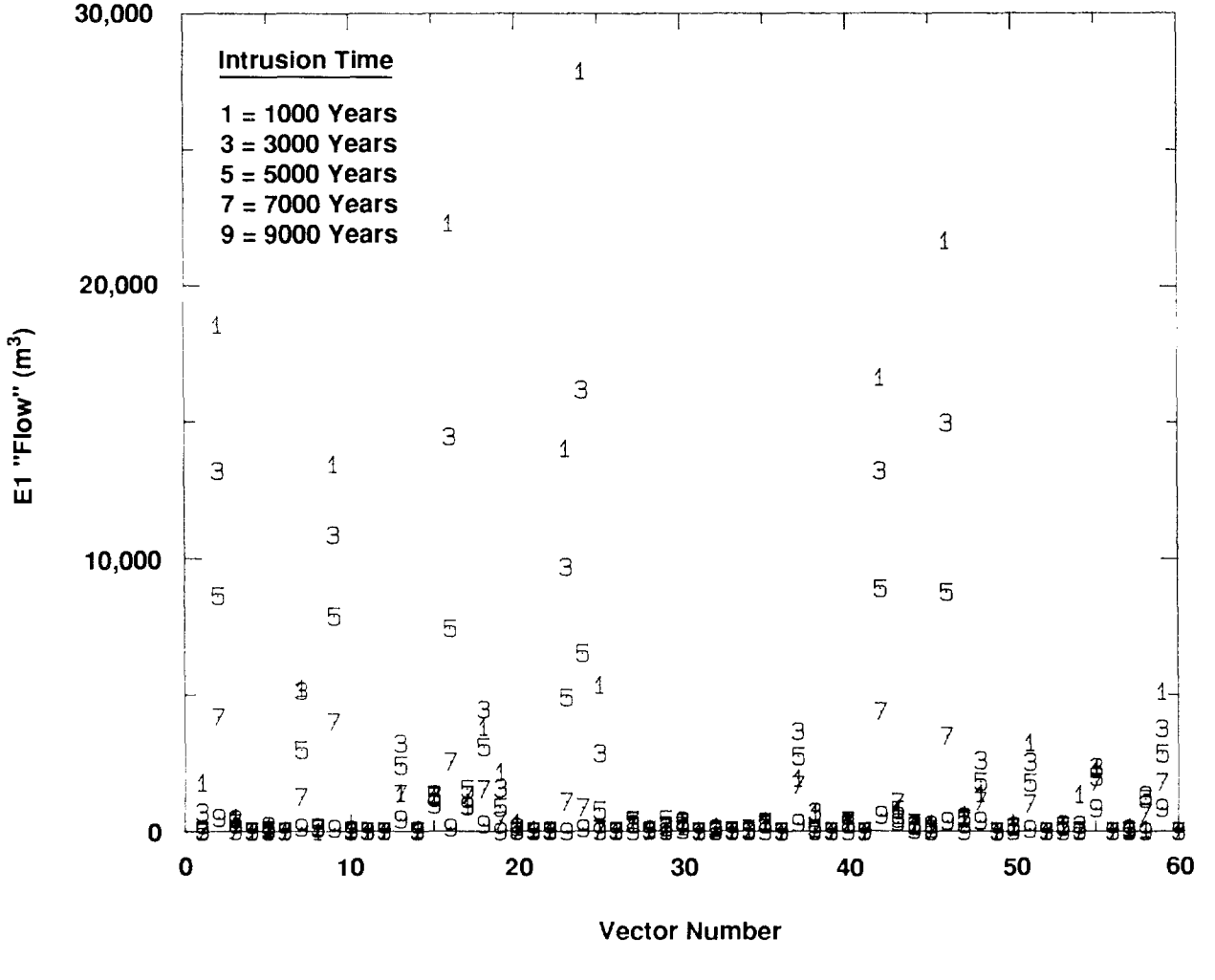

Figure 5-11. Borehole "Flow" Results From BRAGFLO During E1 Summary Scenarios

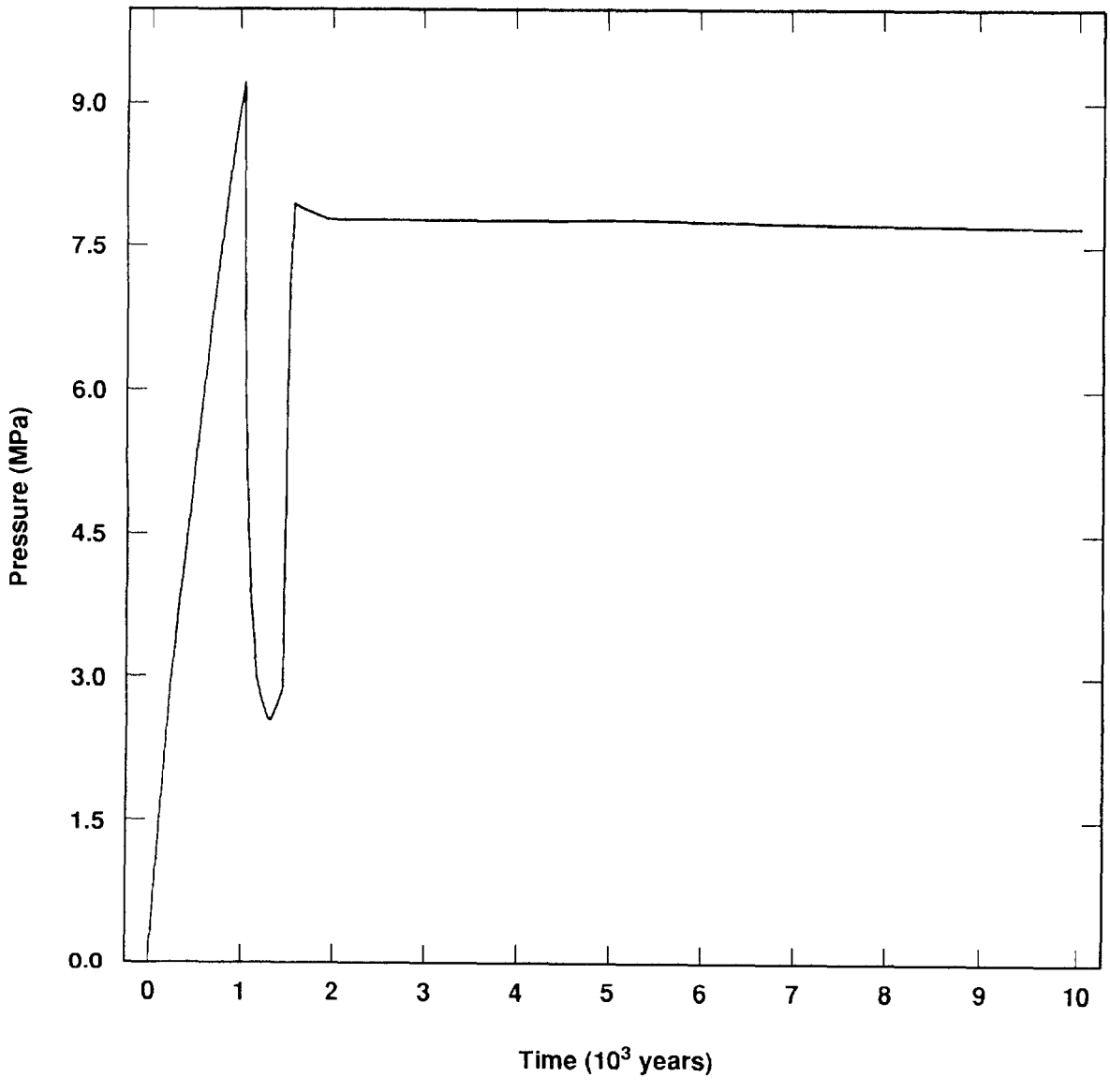

Figure 5-12. Pressure in Waste (E1E2 Scenario, With Gas Generation)

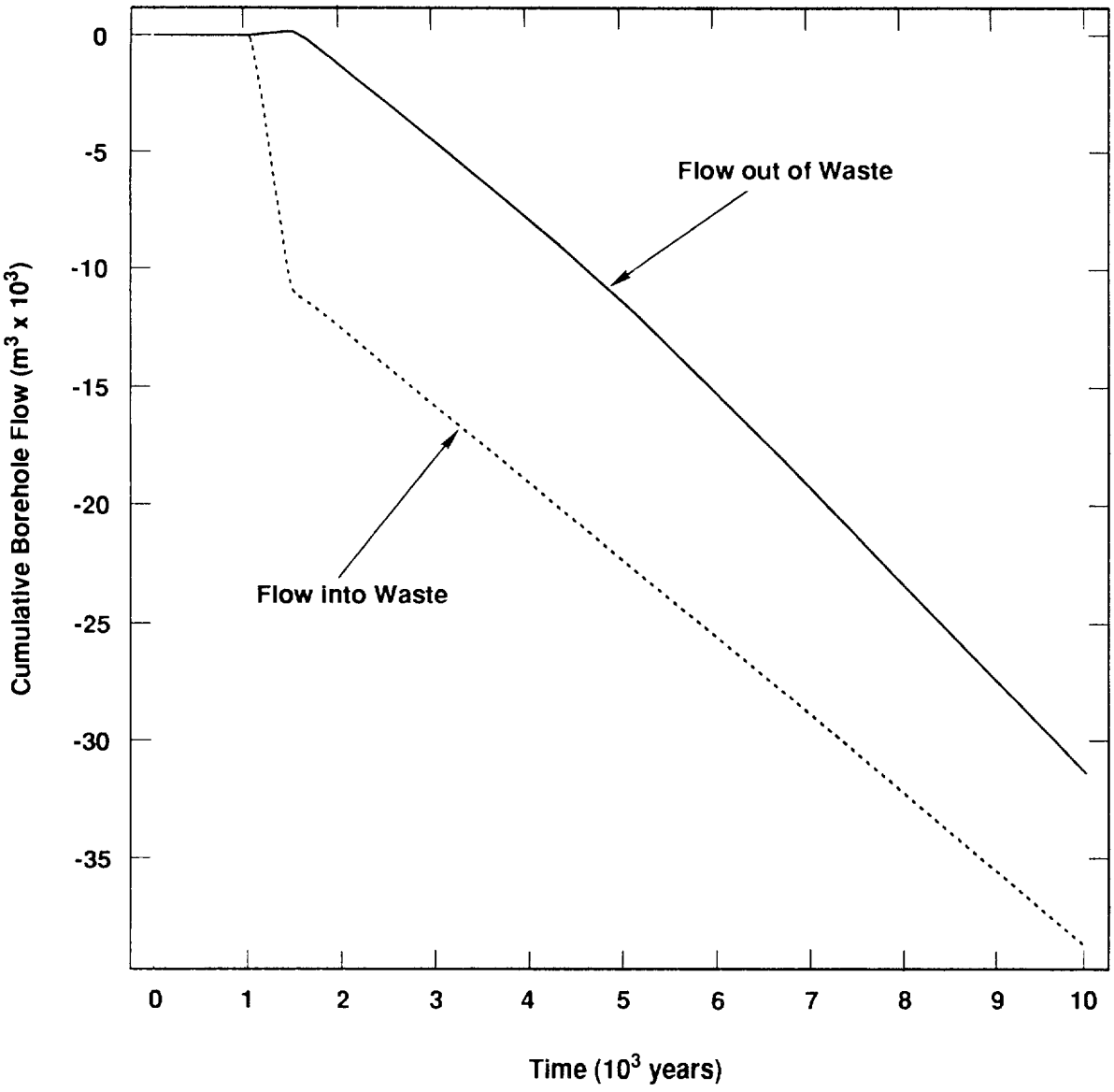

TRI-6342-1349-0

Figure 5-13. Cumulative Borehole Flows Into and Out of Waste (E1E2 Scenario, With Gas Generation)

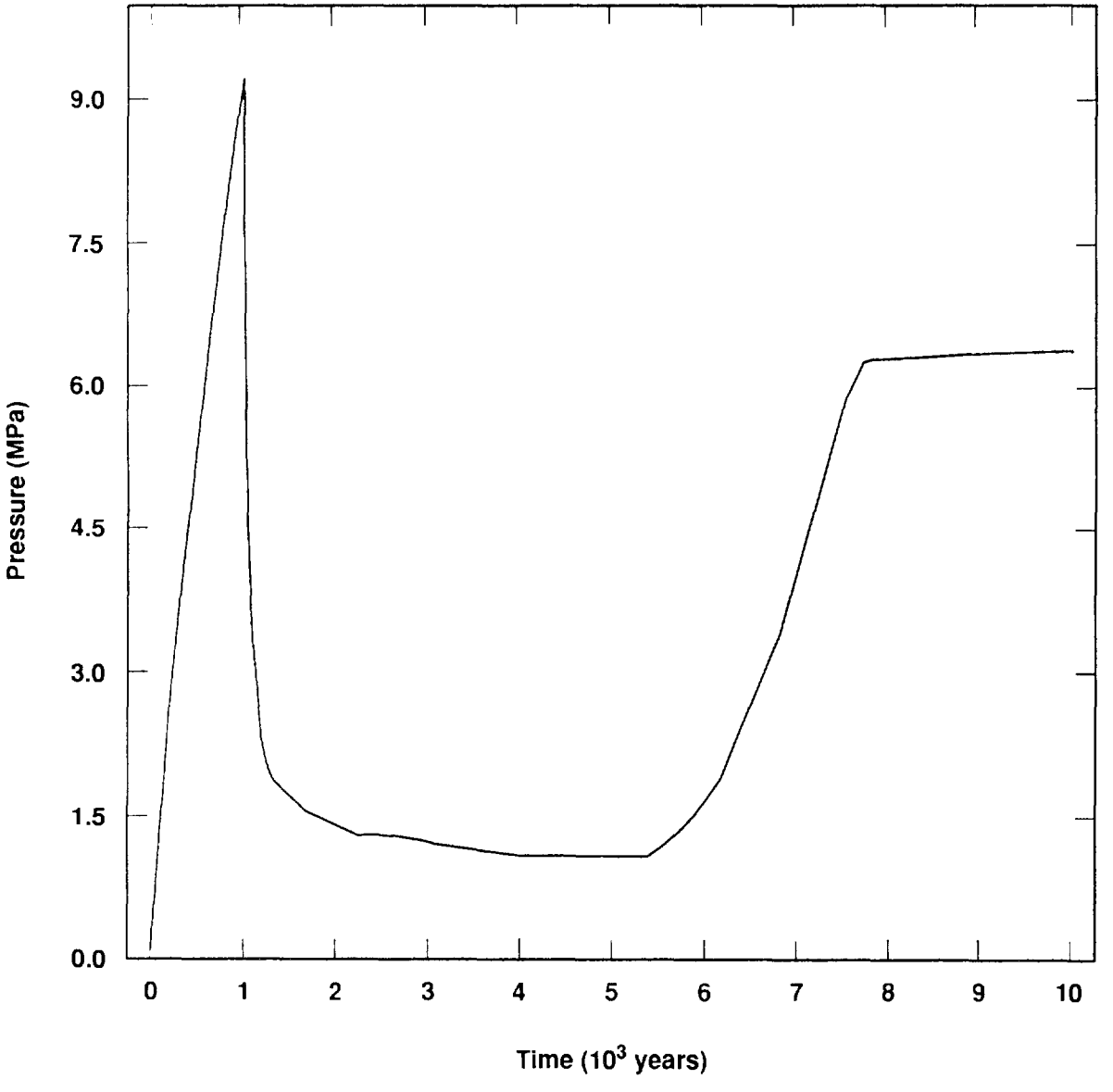

Figure 5-14. Pressure in Waste (E2 Scenario, With Gas Generation)

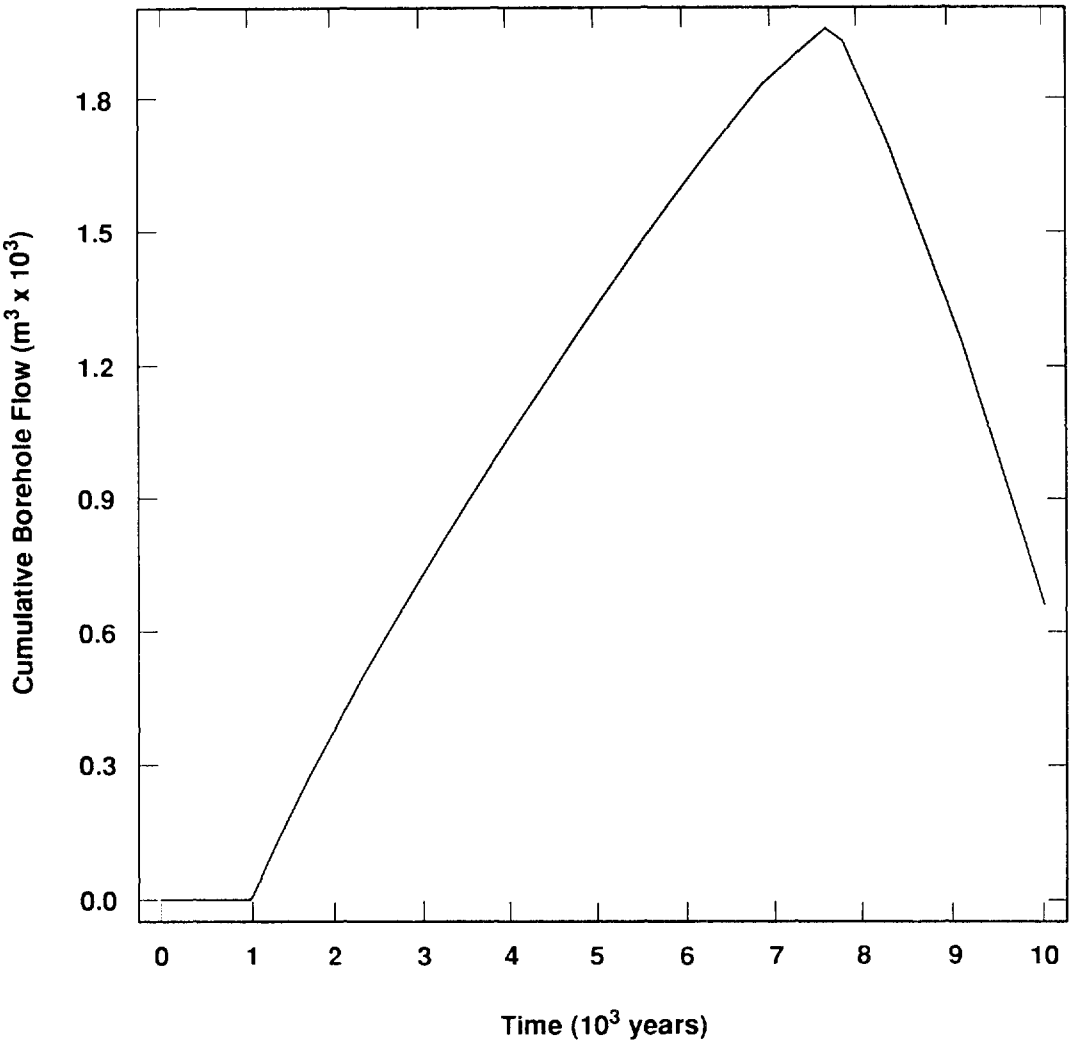

TRI-6342-1351-0

Figure 5-15. Cumulative Borehole Flow Out of Waste (E2 Scenario, With Gas Generation)

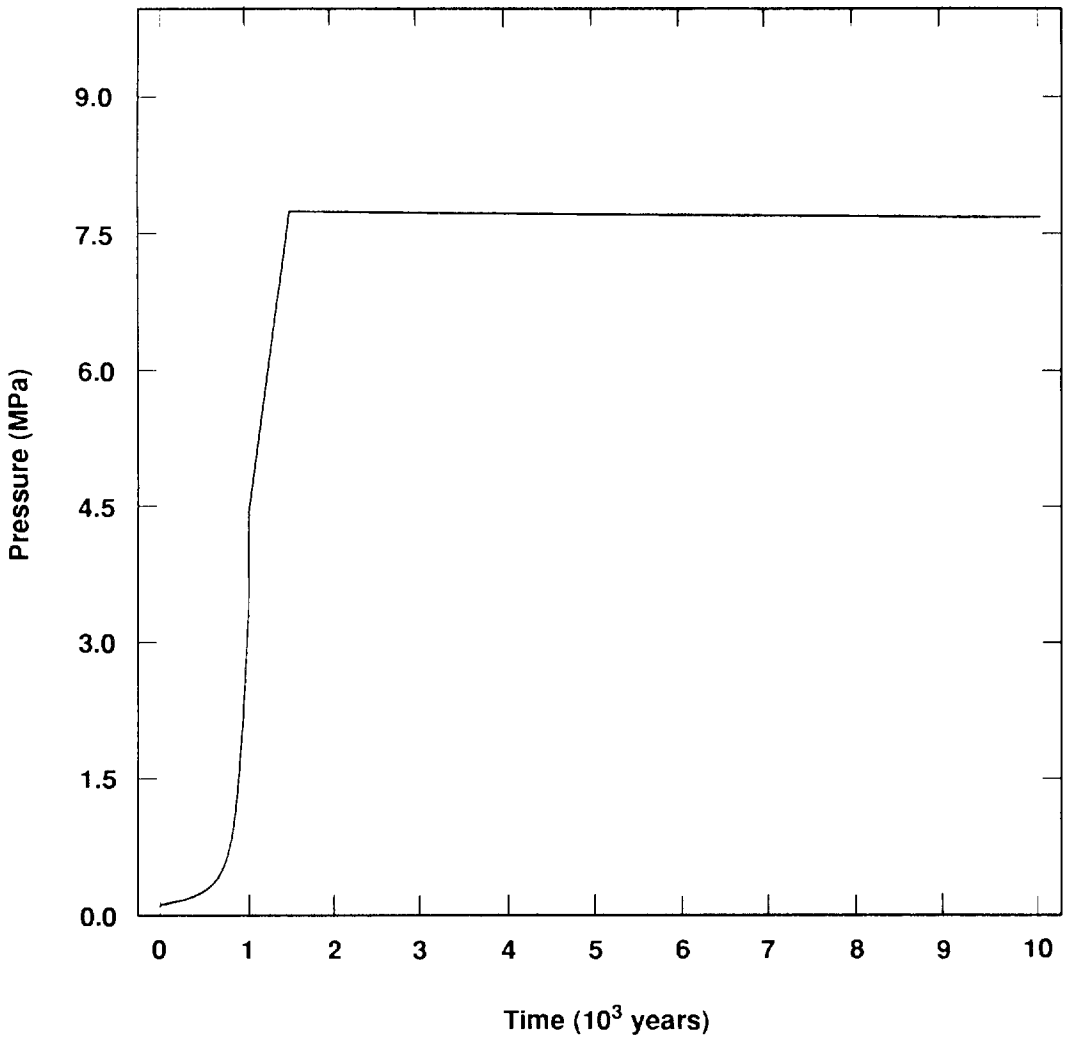

Figure 5-16. Pressure In Waste (E1E2 Scenario, Without Gas Generation)

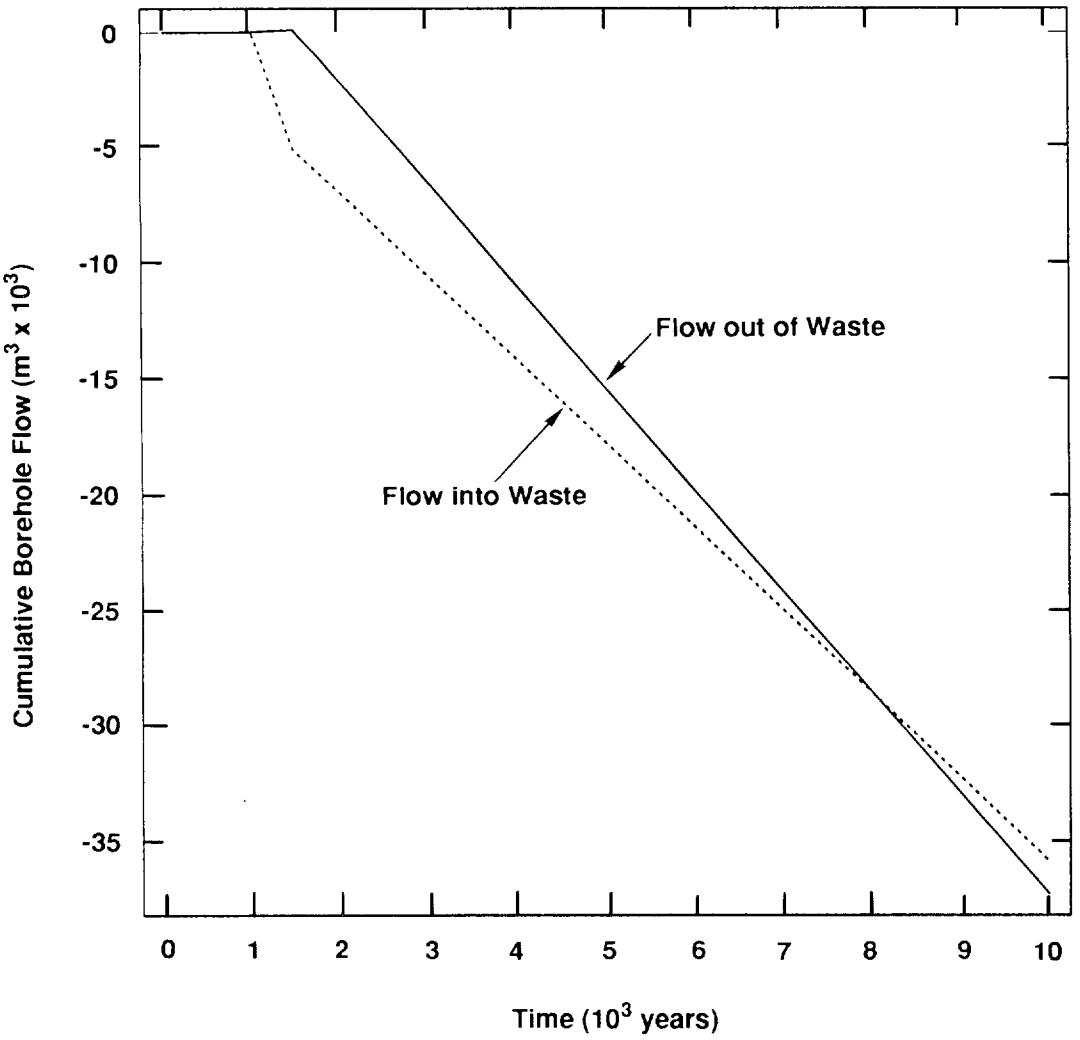

TRI-6342-1353-0

Figure 5-17. Cumulative Borehole Flows Into and Out of Waste (E1E2 Scenario, Without Gas Generation)

slightly higher pressure in the panel. At the same time, the gas bubble driven up into the Culebra is restricting flow there, resulting in higher pressures in the Culebra at the top of the borehole. The pressure there is high enough that the pressure drop from the panel to the Culebra is lower than when no gas is generated, which also reduces the flow rate of brine from the panel.

Comparison of E2, With Gas Generation, With E2, Without Gas Generation

As with the E1E2 scenario, the E2 scenario shows no pressure spike when no gas is generated (Figure 5-18). The pressure in the panel reaches hydrostatic in about 1850 years. When the borehole opens at 1000 years, the pressure is still below hydrostatic, and brine drains down from above to fill and pressurize the panel. The source of this brine is the Salado DRZ, the overlying anhydrite layer, and the lower Salado Formation above the repository. Flow upward to the Culebra (Figure 5-19) begins after 1760 years. The effect of gas generation is clear in this case: With gas generation, the time lag between borehole intrusion and brine flow out of the panel is 6730 years; without gas generation, the time lag is only 760 years. This shorter lag time results in far greater releases of brine: 8430 m^3 vs. 1300 m^3 with gas generation. When no gas has been generated, only residual saturation remains a short time after the borehole opens, so gas imposes no resistance to flow of brine through the waste from the anhydrite layer or MB139, as it does when gas is generated. Thus, the flow rate out of the panel is higher even after 10,000 years when no gas is generated: 0.92 m^3/yr vs. 0.68 m^3/yr with gas.

5.3 Repository Discharge (PANEL)—Walt Beyeler and James W. Garner

Boreholes penetrating a waste panel and possibly a Castile brine pocket can initiate the flow of brine and dissolved radionuclides between the repository and the Culebra Dolomite. Based on coupled models of fluid flow and the geochemical processes occurring within the repository, the discharge rate can be calculated with the code PANEL.

This model estimates rates of discharge of radionuclides and brine to the Culebra resulting from interconnection by one or more boreholes of the Culebra, repository, and possibly a Castile brine pocket underlying the repository. Radionuclide discharge depends on flow through the waste. Flow rates may be calculated internally in PANEL, or may be specified from a separate model (e.g., BRAGFLO). The 1991 calculations of the consequence analysis for disturbed conditions used flow rates calculated by BRAGFLO and not those of PANEL. Only the waste mobilization and transport model of PANEL is used.

Figure 5-20 is a schematic diagram of the Castile, repository panels, and Culebra following penetration.

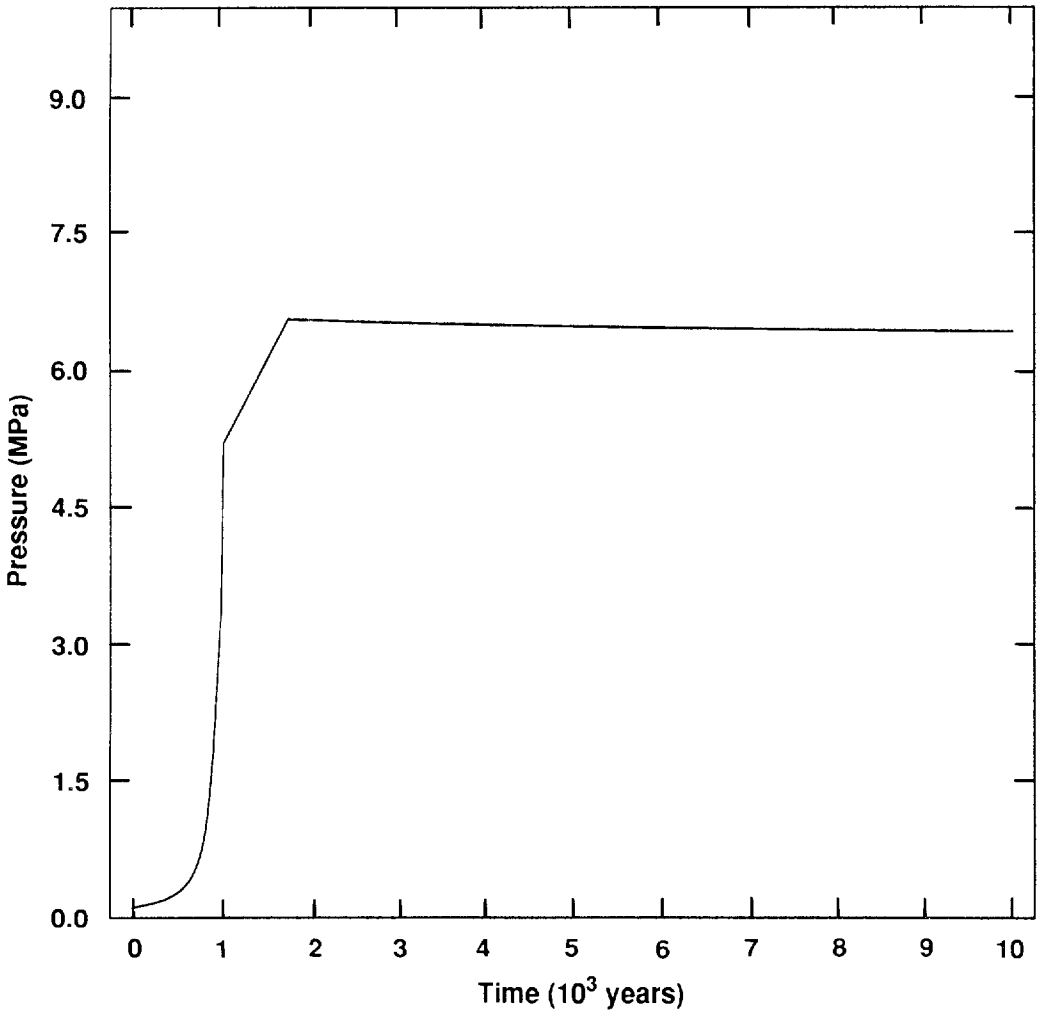

TRI-6342-1354-0

Figure 5-18. Pressure in Waste (E2 Scenario, Without Gas Generation)

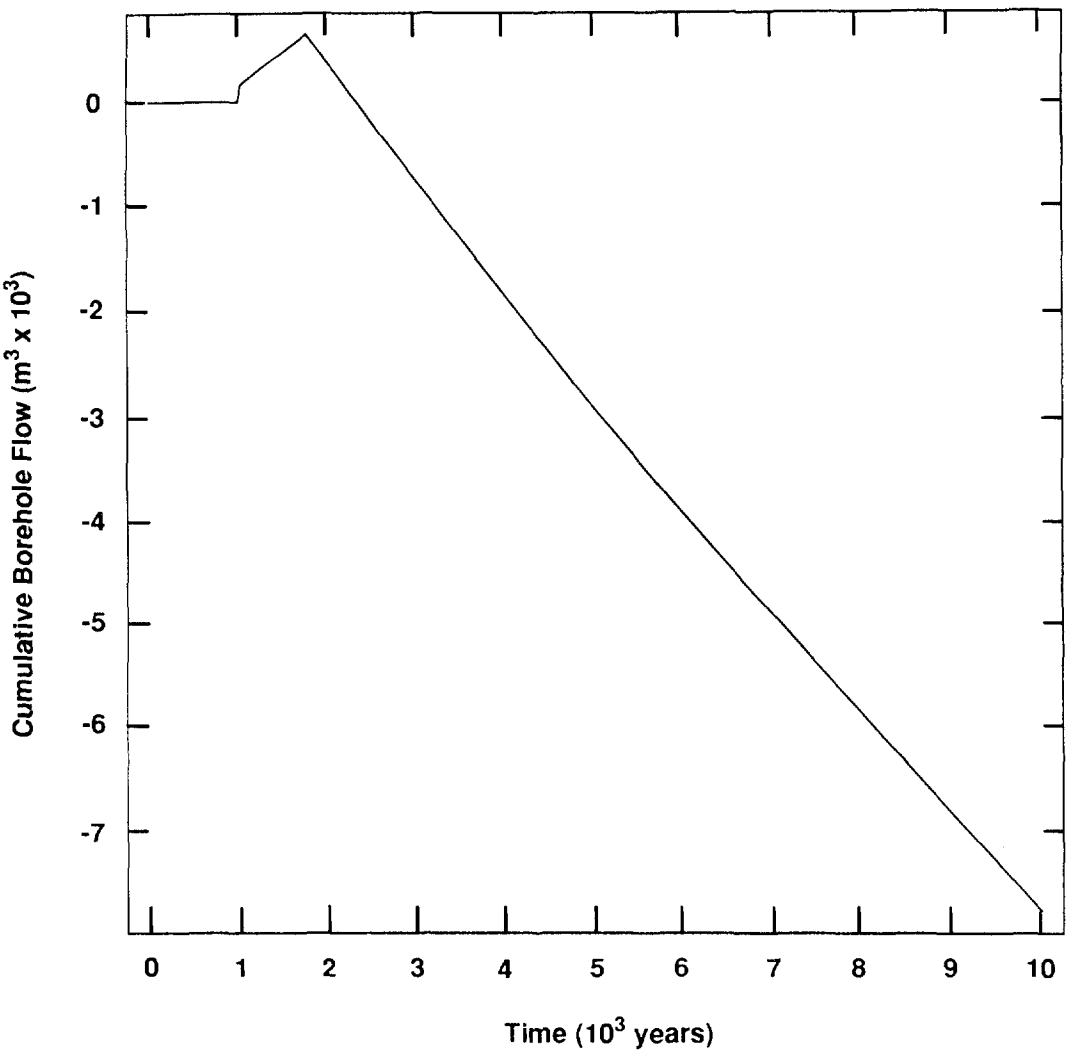

Figure 5-19. Cumulative Borehole Flow Out of Waste (E2 Scenario, Without Gas Generation)

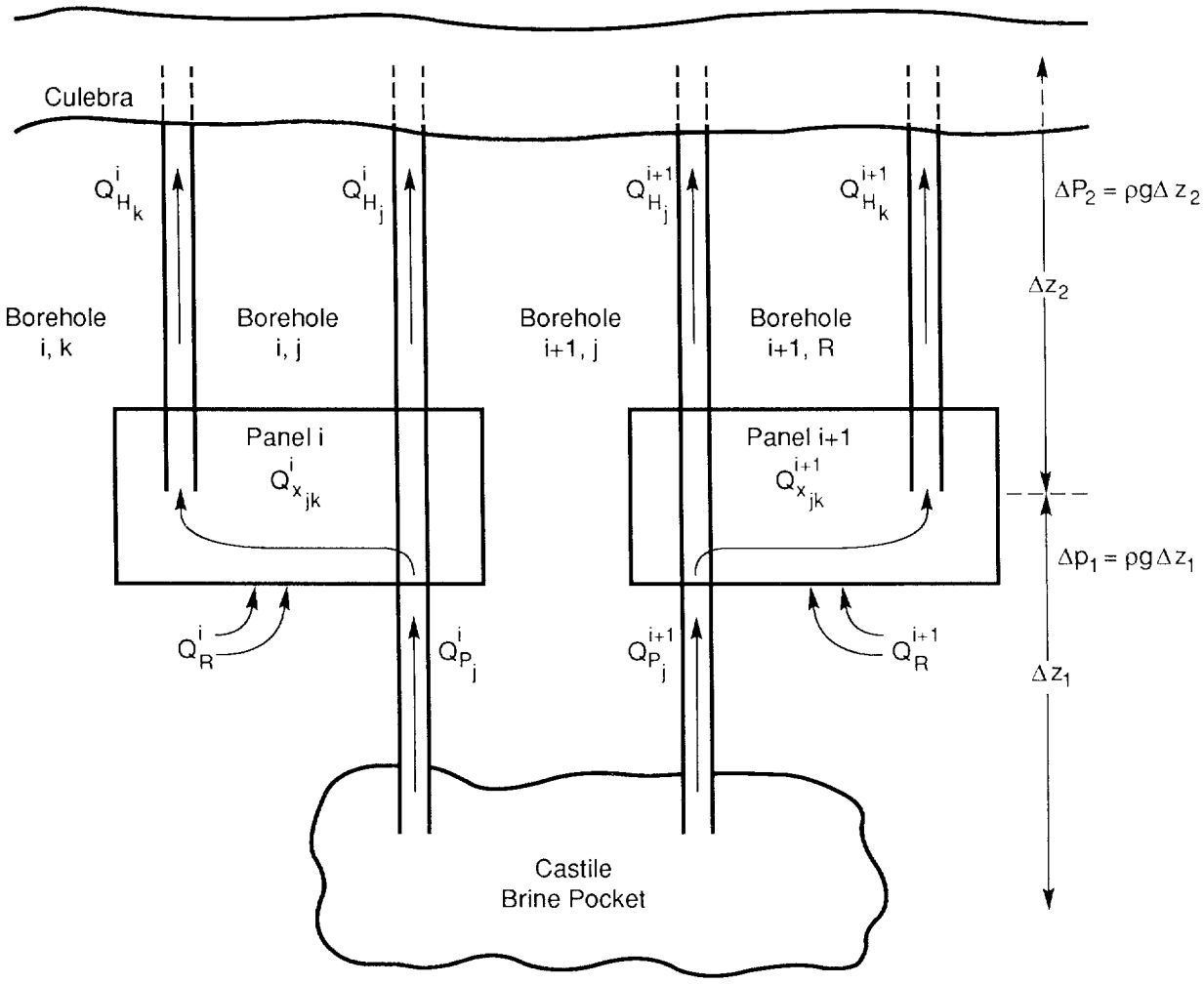

Figure 5-20. Borehole Penetration of Repository Panels and Brine Pockets

Chemical/physical processes governing radionuclide flux are:

a. Dissolution of solid waste in the repository,

b. Radioactive decay, and

c. Advection of dissolved radionuclides from the repository to the Culebra.

Processes considered in the internal flow model are:

a. Upward flow through each borehole (Q_p^i $[L^3T^{-1}]$) from the Castile reservoir due to the difference between the reservoir pressure and the pressure in the panel at the borehole location;

b. Flow into each repository panel from the Salado (Q_R^i $[L^3T^{-1}]$);

c. Flow between boreholes k and j within a panel ($Q_{X_{kj}}^i$ $[L^3T^{-1}]$),

d. Upward flow through each borehole from the repository to the Culebra ($Q_{H_j}^i$ $[L^3T^{-1}]$).

The following describes the mathematical models used to represent the above process.

5.3.1 FLUID FLOW MODEL

5.3.1.1 Assumptions

While the fluid-flow model of PANEL was not used during the consequence analysis calculations, it was used for preliminary screening and comparison calculations. For this reason a discussion of PANEL's fluid-flow model follows.

All flow is assumed to occur as a single fluid phase. Possibly relevant processes which are neglected in this simplified approach include gas generation within the waste, exsolution of gases from Castile brine, and precipitation in the wellbore resulting from chemical or thermal disequilibrium between Castile brine and borehole fluid. All components of the flow system which are explicitly included in the model (see below) are assumed to be governed by Darcy's law. Hydrologic properties of each component are therefore completely characterized by hydraulic conductivity, specific storativity, and component geometry.

Volume 3 discusses ranges of values of these properties for the Castile, borehole fill, waste, and Culebra.

Using these properties, an analysis of the hydrologic response of these components following interconnection by a borehole of the Castile, repository, and Culebra suggests the following (Rechard et al., 1990b):

a. During discharge, pressure in the Culebra is not significantly elevated above its initial value;

b. Time constants for internal pressure transients in the Castile (both large and small fracture sets), borehole, and waste range from less than a year to tens of years;

c. The discharge time of the Castile reservoir ranges from thousands to hundreds of thousands of years.

On this basis, the following assumptions about the Castile, boreholes, waste, and Culebra have been made in the fluid flow model:

a. The Culebra acts as a fixed pressure discharge for all boreholes.

b. The transient behavior of the system over the period of interest is governed by the depletion of the brine reservoir, rather than by internal pressure transients within any component. Accordingly, all components are assumed to be at steady state with respect to boundary pressures at any given time.

c. The evolution of boundary pressures is controlled by depletion of the brine reservoir. Pressure change is assumed to be a linear function of the change in reservoir brine volume (e.g., due to linear elastic expansion of reservoir fluid and anhydrite):

$$\Delta V_p = S_b \Delta P_p \tag{5-10}$$

In terms of parameters of the Darcy flow model, the storativity of all components other than the brine reservoir is assumed to be zero. The conductivities of the brine reservoir and Culebra are assumed to be infinite.

Brine inflow rates from the Salado are assumed to be described by a differential equation which is linear in boundary pressure (such as the Darcian flow equation). In addition, pressure gradients within the panel due to flow from the Salado are assumed to be small, so that the pressure at the waste/Salado interface is effectively equal to an equivalent panel pressure P_{0_i}. Salado brine inflow for an arbitrary pressure history in the panel can be estimated by convolution.

5.3.1.2 Mathematical Formulation

Volume balance expressions are written for each borehole at the point of penetration of the waste panel (Figure 5-21) as follows:

$$Q^i_{H_j} = Q^i_{R_j} + Q^i_{X_j} + Q^i_{P_j} \tag{5-11}$$

where Q^i_R is that portion of Q^i_R discharged through the control volume.

Darcy's law allows all flow components at each junction to be expressed in terms of the discharge (Culebra) pressure (p_D), pressure in the panel at each wellbore (P^i_j), the pressure in the panel at other wellbores (P^i_k) and the instantaneous pressure in the brine reservoir (P_p):

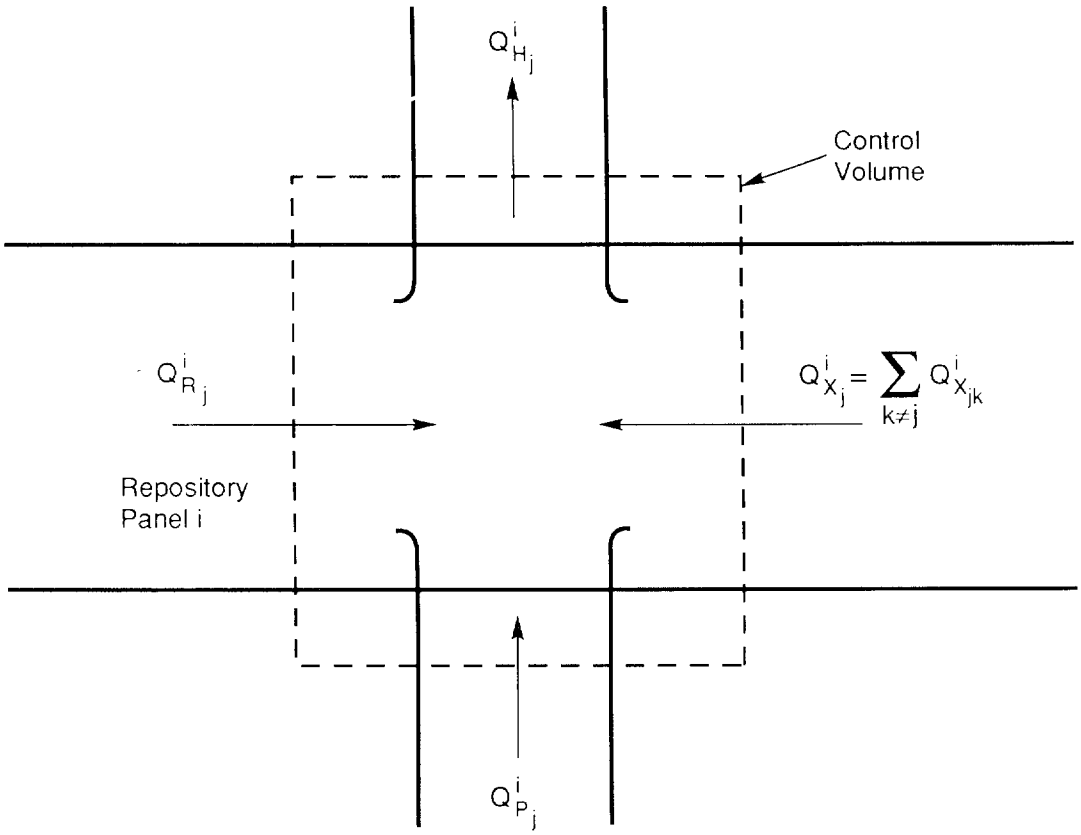

Figure 5-21. Waste Panel Penetration

$$Q_{H_j}^i = \zeta_{\omega_j}^i \left(P_j^i - P_D - \Delta P_2 \right) \tag{5-12}$$

$$Q_{R_j}^i = \zeta_{W_j}^i \left(P_0^i - P_j^i \right) \tag{5-13}$$

$$Q_{X_j}^i = \sum_{k \neq j} Q_{X_{kj}}^i = \sum_{k \neq j} \zeta_{X_{jk}}^i \left(P_k^i - P_j^i \right) \tag{5-14}$$

$$Q_{P_j}^i = \zeta_{L_j}^i \left(P_p - P_j^i - \Delta P_1 \right) \tag{5-15}$$

The connection terms $\zeta \bullet$ are the effective hydraulic conductances (in units of $m^3/s/Pa$) of the pathways associated with each flow component. $\zeta_{U_j}^i$ and $\zeta_{L_j}^i$ are the conductances of the upper and lower portions of wellbore is as follows:

$$\zeta_{U_j}^i = \frac{KA_j^i}{\Delta Z_2 \rho g} \tag{5-16}$$

$$\zeta_{L_j}^i = \frac{KA_j^i}{\Delta Z_1 \rho g} \tag{5-17}$$

where,

- K = hydraulic conductivity of the borehole fills,
- A = borehole cross-sectional area,
- ΔZ_1 = lengths of the lower segment of the borehole,
- ΔZ_2 = lengths of the upper segment of the borehole,
- ρ = fluid density, and
- g = gravitational acceleration.

The effects of alteration of borehole hydraulic properties through plug degradation and closure may be included by varying the product KA for each borehole with time.

Q_R^i is allocated among wellbores in panel i based on the wellbore radius (via the wellbore/waste conductance term $\zeta_{W_j}^i$) and the pressure at the wellbore (via the far-field waste pressure p_0). Accordingly, the individual discharges $Q_{R_j}^i$ must collectively satisfy

$$Q_R^i = \sum_j Q_{R_j}^i \tag{5-18a}$$

The instantaneous inflow rate to the panel, Q_R^i, is given by the pressure history in panel i and the unit pressure response function h(t):

$$Q_R^i = \left(P_I - P_0^i\right) * h \tag{5-18b}$$

where P_I is the equilibrium (far field) pressure at the repository elevation.

The wellbore/waste conductance is estimated as the steady-state conductance between the wellbore radius $r_{W_j}^i$ and a radius r_∞ equal to one-half the width of a panel excavation:

$$\zeta_{W_j}^i = \frac{2\pi K_R b}{\ln\left(\frac{r_\infty}{r_{W_j}^i}\right)\rho g} \tag{5-19}$$

where K_R is the hydraulic conductivity of the waste, and b is the panel height.

ζ is the conductance between boreholes within the same waste panel, and is given by:

$$\left(\zeta_{X_{jk}}^i\right)^{-1} = \left(\zeta_{W_j}^i\right)^{-1} + \left(\zeta_{W_k}^i\right)^{-1} + \left(\zeta_{R_{jk}}^i\right)^{-1} \tag{5-20}$$

where $\zeta_{R_{jk}}^i$ is that portion of the inter-borehole conductance due to borehole separation, i.e., the conductance of the paths between the far fields of each borehole (Figure 5-22).

Substituting for flow terms in (5-11) gives:

$$\zeta_{U_j}^i\left(P_j^i - P_D - \Delta P_2\right) = \zeta_{W_j}^i\left(P_0^i - P_j^i\right) + \sum_{k \neq j} \zeta_{X_{jk}}^i\left(P_k^i - P_j^i\right)$$

$$+\zeta_{L_j}^i\left(P_p - P_j^i - \Delta P_1\right) \tag{5-21}$$

The linear relationship between Castile brine reservoir pressure decline and total reservoir discharge volume can be written:

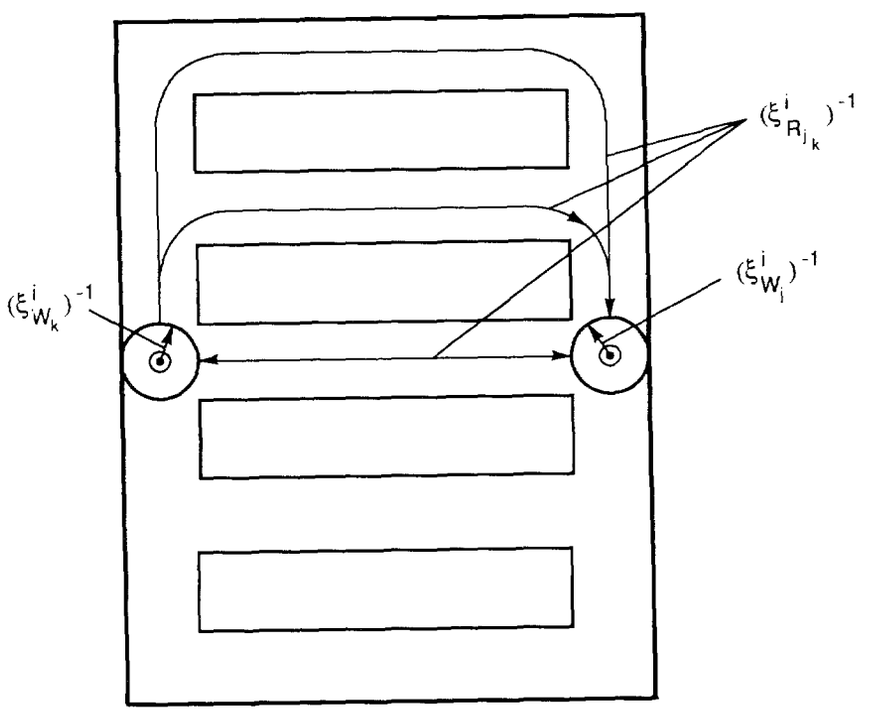

Figure 5-22. Conductance Between Boreholes Within the Same Waste Panel

$$P_p(t_2) = P_p(t_1) - \frac{1}{S_b}\int_{t_1}^{t_2} \sum_i \sum_j Q^i_{p_j}\, dt \tag{5-22}$$

Because of the possibility of time-varying borehole properties (see above), coefficients of (5-21) are not constant. The system is therefore solved numerically using a semi-implicit expression for $Q^i_{p_j}$ in (5-22) to approximate P_p:

$$P_p(t_2) = P_p(t_1) - \frac{t_2 - t_1}{S_b} \sum_i \sum_j Q^i_{p_j} \tag{5-23}$$

$$\overline{Q}^i_{P_j} = \overline{\zeta}^i_{L_j}\left\{\frac{1}{2}\left[P_p(t_1) + P_p(t_2)\right] - \frac{1}{2}\left[P^i_j(t_1) + P^i_j(t_2)\right] - \Delta P_1\right\} \tag{5-24}$$

where $\overline{\zeta}^i_{L_j}$ is an effective conductance for the lower portion of the borehole over the interval $(t_1 \rightarrow t_2)$, estimated from the harmonic mean of the end point values:

$$\overline{\zeta}^i_{L_j} = \frac{\zeta^i_{L_j}(t_1) * \zeta^i_{L_j}(t_2)}{\frac{1}{2}\left[\zeta^i_{L_j}(t_1) + \zeta^i_{L_j}(t_2)\right]} \tag{5-25}$$

Substituting (5-24) into (5-23) and defining

$$\overline{W}_L(x) = \frac{\Delta t}{2S_b} \sum_{\ell} \sum_m \overline{\zeta}_{L\ell m} \cdot x \tag{5-26a}$$

$$\Delta t = t_2 - t_1 \tag{5-26b}$$

yields

$$P_p(t_2) = \frac{1}{1 + \overline{W}_l(1)}\left\{\left[1 - \overline{W}_L(1)\right]P_p(t_1) + \overline{W}_L\left[P_{\ell m}(t_1)\right] + \overline{W}_L\left[P_{\ell m}(t_2)\right] + 2\Delta P_1 \overline{W}_L(1)\right\} \tag{5-27}$$

Collecting junction pressure terms p^i_j in (5-21) gives:

$$\left(\zeta^i_{U_j}+\zeta^i_{W_j}+\sum_{k\neq j}\zeta^i_{X_{kj}}+\zeta^i_{L_j}\right)P^i_j-\sum_{k\neq j}\zeta^i_{X_{kj}}P^i_k-\zeta^i_{L_j}P_p$$

$$=\zeta^i_{U_j}(P_D+\Delta P_2)+\zeta^i_{W_j}P^i_0-\zeta^i_{L_j}\Delta P_1 \qquad (5\text{-}28)$$

Substituting for P_p in (5-28) and collecting pressure terms at time t_2 on the left hand side yields:

$$\left(\zeta^i_{U_j}+\zeta^i_{W_j}+\sum_{k\neq j}\zeta^i_{X_{kj}}+\zeta^i_{L_j}\right)P^i_j(t_2)-\frac{\zeta^i_{L_j}}{1+\overline{W}_L(1)}\overline{W}_L\left[P_m(t_2)\right]$$

$$-\sum_{k\neq j}\zeta^i_{X_{kj}}P^i_k(t_2)$$

$$=\zeta^i_{U_j}(P_D+\Delta P_2)+\zeta^i_{W_j}P^i_0-\zeta^i_{L_j}\Delta P_1$$

$$+\frac{\zeta^i_{L_j}}{1+\overline{W}_L(1)}\left\{P_p(t_1)\left[1-\overline{W}_L(1)\right]+\overline{W}_L\left[P_m(t_1)\right]+2\Delta P_1\overline{W}_L(1)\right\} \qquad (5\text{-}29a)$$

Substituting for $Q^i_{R_j}$ from (5-13) into (5-18),

$$\sum_j\zeta^i_{W_j}\left(P^i_0-P^i_j\right)=Q^i_R=\left(P_I-P^i_0\right)*h \qquad (5\text{-}29b)$$

Convolution in (5-29b) is approximated from tabulated values of $h(t)$ and accumulated values of P^i_0, expanded around $P^i_0(t)$:

$$\left(P_I-P^i_0\right)*h=Q^i_0+\alpha^i\left[P_I-P^i_0(t)\right] \qquad (5\text{-}30)$$

giving

$$\sum_j\zeta^i_{W_j}\left(P^i_0-P^i_j\right)=Q^i_0+\alpha^i\left[P_I-P^i_0\right] \qquad (5\text{-}31)$$

or

$$\sum_j \zeta^i_{W_j}\left(P^i_0 - P^i_j\right) + \alpha^i P^i_0 = Q^i_0 + \alpha P_I \tag{5-32}$$

Equations (5-29a) and (5-29b) can then be solved for the pressures at each junction in each panel P^i_j and for the equivalent far-field pressure in each panel P^i_0.

In practice, the waste conductance terms $\zeta^i_{X_{jk}}$, $\zeta^i_{W_j}$ are usually much larger than the borehole conductance terms. Small inaccuracies in calculated junction pressures can produce large mass balance errors within the waste panel. To overcome this problem, flow rates in each borehole are first calculated assuming infinite waste conductivity (pressure equilibrium in the waste). These flow rates are then used with the waste conductivity and borehole locations to calculate an upper bound on pressure variation induced at each borehole as a result of resistance to flow through the waste. If this variation is within some specified tolerance, the infinite-conductivity approximation is retained. If not, the full system, including waste permeability [i.e., equation (5-29)], is solved.

5.3.1.3 Required Parameters

The following parameters are required by the model:

a. Culebra discharge pressure;
b. Length, area, location, fill hydraulic conductivity, and time of construction for each borehole;
c. Waste hydraulic conductivity;
d. Rate of brine inflow from the Salado as a function of time for some fixed pressure change at the waste/Salado boundary;
e. Castile reservoir initial pressure and bulk storage coefficient (change in volume per unit change in pressure).

In addition, the product of the hydraulic conductivity and area of the borehole may be made to vary in an arbitrary way with time, in order to represent (e.g.) the effects of plug degradation and closure.

5.3.2 WASTE MOBILIZATION AND TRANSPORT MODEL

Assumptions. The following are the waste mobilization and transport assumptions:

a. Concentrations of all species are assumed to be uniform throughout the waste panel.
b. Concentrations of all species are assumed to be in equilibrium at any time.

c. Solubility limits for a given element are allocated among its isotopes on the basis of relative abundance.

5.3.2.1 Mathematical Formulation

Radionuclide concentration and discharge are calculated at discrete time steps as follows:

a. The total volume of fluid entering the panel over the interval displaces an identical volume of fluid with the appropriate concentrations of all isotopes. This volume is limited to no more than 10% of the pore volume of a panel by selection of the time step.

b. Concentrations within the panel are updated by:

   1. Mixing the remaining panel pore fluid with the introduced fluid volume;

   2. Updating the existing inventory of all species from radioactive decay during the interval; the amount of each radionuclide at time $T + \Delta T$ is $A_I(T + \Delta T)$ with decay constant λ_I is defined as $A_I(T + \Delta T) = A_I(T)\ell^{\lambda_I \Delta T}$ + Parental, Grandparental and Great-Grandparental contributions as defined by Bateman Equations (see discussion in CUTTINGS, Chapter 7).

   3. Calculating the new equilibrium concentrations of all species with respect to dissolution. The amount in solution for each element is the solubility limit (molar) * 1,000 liters/m^3 * volume of panel (m^3). If this amount is more than the amount of the element in the panel, the amount in solution is the entire amount of the element.

   The concentration of each radionuclide is the mass of its corresponding element in solution times the moles of this radionuclide in the panel/the total moles for its corresponding element in the panel. Since this is a mixing-cell model, there are no local variations.

5.3.2.2 Parameters

The following are the waste mobilization and transport required parameters:

a. Initial inventory of all isotopes in each panel;

b. Half-lives and daughters for each isotope;

c. Solubility limits for each element;

d. Pore volume of each panel;

e. Rate of fluid flow through the waste (derived from the fluid model discussed above or specified from results of another model, e.g. BRAGFLO).

5.3.3 FLUID-FLOW/WASTE MODEL COUPLING

Two components of the flow system may potentially mobilize waste; flow from the Salado to a borehole, and flow from one borehole to another. The sum of these components at any time provides an estimate of the rate of flow through the waste. In the event of a single intrusion, only

provides an estimate of the rate of flow through the waste. In the event of a single intrusion, only flow from the Salado is assumed to pass through the waste. In the E1E2 scenario, flow from the Castile is also assumed to pass through the waste. Integration of fluid flow rate through the waste over some time interval provides an estimate of the volume of contaminated fluid (with concentrations calculated as described under waste mobilization) discharged to the Culebra through the intrusion boreholes. Final flow rates and concentrations discharged to the Culebra from a given borehole are estimated from the mixing of fluid entering the borehole from the waste with fluid flowing through the borehole from the Castile. This procedure ignores any decay or sorption in transport through the upper half of the borehole. Short travel times and expected borehole fill material suggest that the effect of these would be negligible.

5.3.4 RESULTS

The total flow input to PANEL from the BRAGFLO (Section 5.2.5.1) calculations varied from 0 m^3 to 44,000 m^3 for intrusions that did not intersect a brine pocket and from 0 m^3 to 675,000 m^3 for intrusions that intersected a brine pocket. These flows, coupled with solubilities that varied over many orders of magnitude produced releases of the various radionuclides from PANEL that varied from zero to the inventory of one panel. These releases were then used as input to the program STAFF2D. The EPA normalized releases from PANEL are shown in Figures 5-23 and 5-24. A comparison of Figure 5-23 with 5-7 (the "flows" from BRAGFLO) reveals that large flows are a necessary condition for large releases, but not a sufficient condition (compare vectors 16 and 24). Also, comparing E2 releases and E1E2 releases for vectors 15 and 16 indicates that vector 16 has large releases for both E2 and E1E2, but vector 15 has a near zero release for E2 and a maximum release for E1E2.

PANEL can also be run in a mode that does not require fluid flows produced by BRAGFLO. In this mode, it calculates internally the flows through the waste. The runs made in this mode were used as a diagnostic tool for BRAGFLO. This type of calculation was not used in any of the results reported.

5.4 Summary of Results for Disturbed Performance of the Repository/Shaft

The calculations performed to assess the disturbed performance of the Repository/Shaft System had two primary objectives:

- To determine the path and extent of flow of contaminated brine and to determine migration and transport of radionuclides from the waste panel up an intrusion borehole.
- To evaluate the effect of waste-generated gas on the flow of contaminated brine and on the migration of radionuclides.

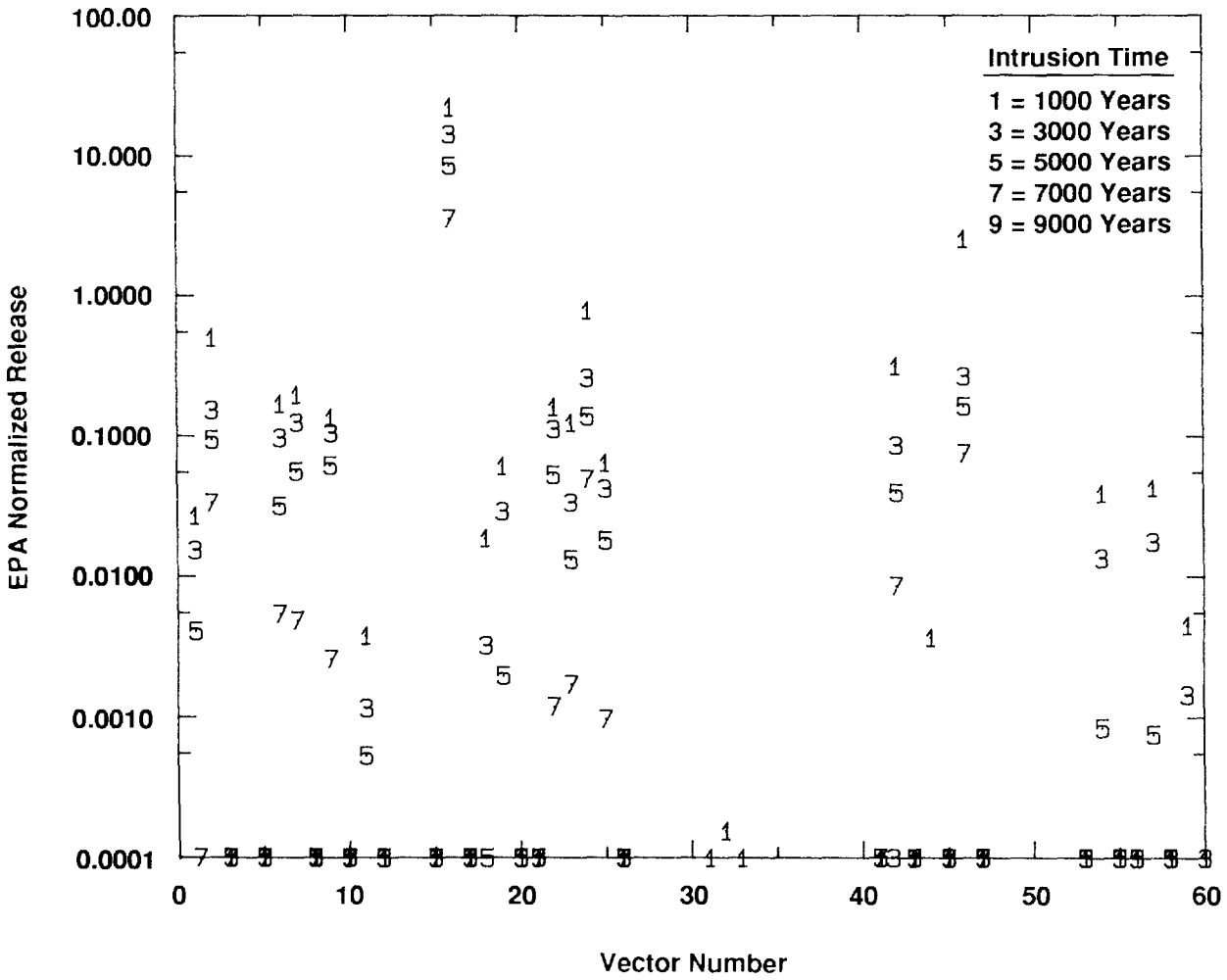

Figure 5-23. E2 Releases from PANEL at Various Times of Intrusion

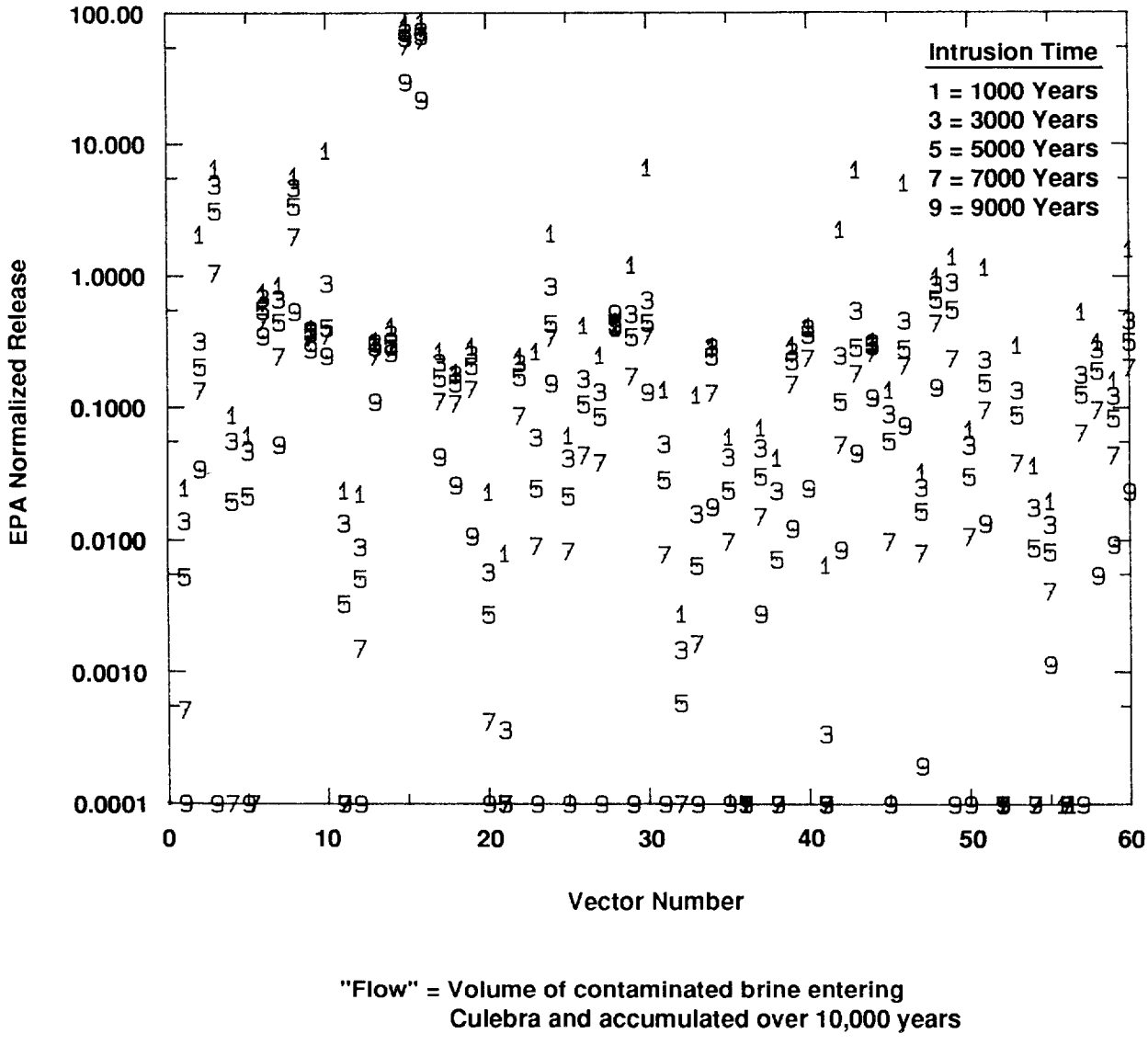

Figure 5-24. E2 Releases from PANEL at Various Times of Intrusion

To address these objectives, two computer codes (BRAGFLO and PANEL) were used with varying material, reservoir, and waste properties. A Latin hypercube sampling procedure was used for selection of the parameter values from parameter probability distributions documented in Volume 3 of this report. The sampling procedure resulted in 60 vectors (differing sets of sampled input parameter values) for each of two summary scenarios E2 and E1E2. The E2 summary scenario is single intrusion of the waste panel, the E1E2 summary scenario is a multiple intrusion of the repository with one well terminating in the waste panel and a second well passing through the panel and terminating in a pressurized brine pocket. The consequences of a third scenario summary the E1 (in which a single borehole penetrates the waste and a brine pocket) was assumed identical to the E2 summary scenario. All three summary scenarios were further sub-divided according to the time of intrusion (1000, 3000, 4000, 7000, and 9000 years). A total of 600 BRAGFLO and PANEL simulations were performed for assessing the disturbed performance of the repository 300 E2 and 300 E1E2 simulation sets.

In PA the calculations, BRAGFLO was used to quantify the two-phase flow fields in and around the repository. PANEL was used for calculating the radionuclide concentration and discharge of radionuclide from the waste through the intrusion borehole. The time-dependent flow fields, phase saturations, and waste porosity from BRAGFLO served as input to PANEL. The well bore flow rates and radionuclide concentrations in the brine resulting from BRAGFLO and PANEL are source terms for models such as SECO2D and STAFF2D (Chapter 6), which quantify the flow fields and radionuclide transport in the Culebra dolomite member of the Rustler formation, considered to be the most likely subsurface pathway to the accessible environment during human intrusion.

Results for a typical vector were described to illustrate the significant features and behavior of two-phase flow under disturbed conditions when an intrusion borehole opens at 1000 years. The E2 and E1E2 scenarios, with gas generation occurring, were compared. Then the effects of gas generation were examined by comparing the results of each scenario with and without gas being generated.

The following general conclusions are based on analysis of the BRAGFLO and PANEL intermediate results. (The term "flow" is defined as the accumulated volume of contaminated brine which enters the Culebra from an intrusion borehole during a 10,000-year interval following panel sealing.)

- "Flow" and radionuclide release decreased for later- occurring intrusions.
- "Flow" and radionuclide release was larger during E1E2 summary scenarios than during E2 summary scenarios.

- Waste generated gas reduced "flow" and radionuclide release during the 1000-year intrusion E2 and E1E2 summary scenarios for the range in waste properties and gas generation rates sampled.
- The "flows" produced during E2 summary scenarios were of similar magnitude to those of E1 summary scenarios but did not necessarily bound the E1 produced "flows" for all vectors.
- Large "flow" was a necessary but not a sufficient condition for producing a large radionuclide release from the waste panel.

6. DISTURBED GROUNDWATER FLOW AND TRANSPORT

6.1 Conceptual Model—Walt Beyeler

The Culebra Dolomite member of the Rustler Formation is considered to be the most likely subsurface pathway for radionuclide transport to the accessible environment in the event of human intrusion into the repository (Volume 1 of this report). Because of its perceived importance to site performance, conceptual and numerical models of the Culebra continue to receive much attention. The conceptual model of the Culebra Dolomite underlying the current performance assessment calculations describes the hydrologic state and behavior of the Culebra Dolomite within the model domain shown on Figure 6-1. The conceptual model consists of the following assumptions:

- **Single-porosity Darcian flow.** Results of hydrologic tests on wells completed in the Culebra are consistent with the response of a heterogeneous medium obeying Darcy's law. Results of some well tests indicate double-porosity response during the early part of the tests (see, for example, Beauheim, 1987). This is interpreted to be caused by disequilibrium between pressure in coextensive fracture and matrix porosity sets. Because the time of pressure equilibration between the porosity sets is much smaller than the time scale of processes considered in the human-intrusion scenario, the Culebra Dolomite is modeled as a heterogeneous single-porosity medium for the purpose of fluid flow calculations. (Dual porosity effects on transport are considered, however).

- **Two-dimensional flow.** Most hydrologic test wells in the Culebra Dolomite are completed across the entire vertical extent of the Culebra. Parameters derived from tests on these wells are therefore composite or average values over the vertical extent of the member. Although flow is known to be localized to particular elevations within the Culebra at several wells (Mercer and Orr, 1979), there is insufficient information to characterize vertical variability of hydrologic properties within the Culebra Dolomite. A vertically integrated two-dimensional model has therefore been adopted.

- **No flow through upper and lower boundaries.** Potentiometric differences between the Culebra and other members of the Rustler suggest that vertical flow between the members is extremely slow over the WIPP and in much of the surrounding study area. The present conceptual model includes impermeable upper and lower boundaries on the Culebra.

- **Parallel-to-axis-flow along the axis of Nash Draw.** Nash Draw is believed to be a major sub-surface drain for the Rustler in the vicinity of the WIPP (Davies, 1989;

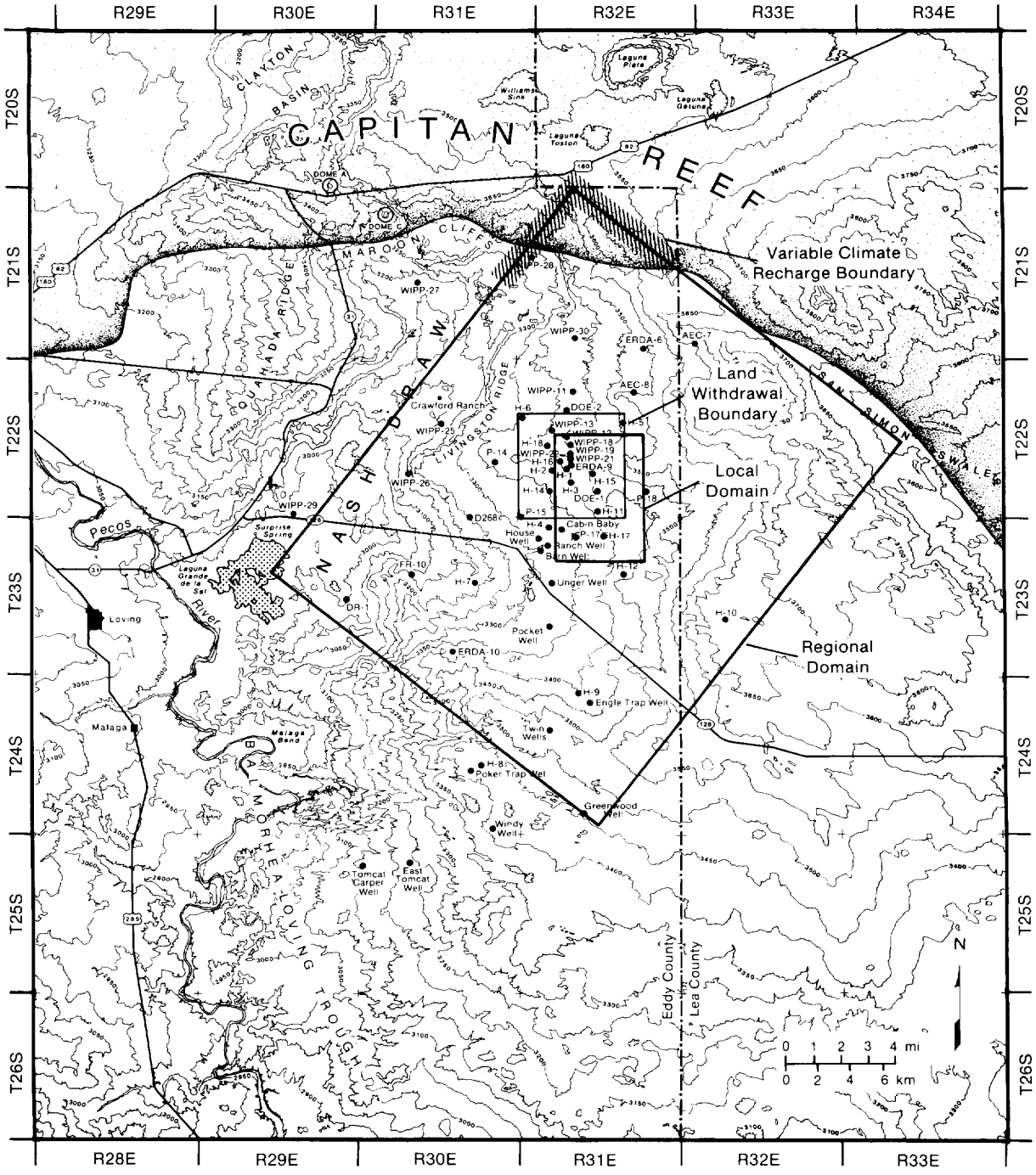

TRI-6342-612-5

Figure 6-1. Model Domain of the Culebra Dolomite Member

Brinster, 1991). Flow in the Rustler would therefore follow the axis of Nash Draw; the axis of the draw is treated as a streamline (no-flow) boundary.

- **Pressure equilibrium and flow prior to WIPP construction.** Time constants of pressure changes due to compression of the fluid and matrix are small compared to time constants of fluid density change, transmissivity evolution, or other transient processes affecting pressure. For any subdomain of the Culebra, and in the absence of fluid sources or sinks within the subdomain, the Culebra pressure is assumed to be currently in equilibrium with pressures around the boundary of the subdomain.

- **Future flow-field transients induced by external changes.** The future state of the Culebra flow field is assumed to differ from the present state through regional climate change. Climate change is assumed to affect recharge and discharge rates external to the model domain, and therefore to influence flow within the model domain through a change in boundary pressures.

- **Transport decoupled from flow.** In the human intrusion scenario, one or more boreholes create a long-term connection between the repository and the Culebra. Hydrologic properties of the borehole fill limit potential fluid discharge to the Culebra to approximately 80 m^3/yr. This rate of fluid injection is assumed to have no impact on the prevailing Culebra flow field (Reeves et al., 1991). In addition, fluid injected from the repository is assumed to have negligible effect on the Culebra fluid density. Estimation of the Culebra flow field, and estimation of radionuclide transport through this flow field resulting from intrusion, are therefore considered as separate problems.

- **Dual-porosity transport.** Matrix and fracture porosities that are coextensive and communicating can result in local disequilibrium in radionuclide concentrations between the fracture and matrix. The time constant associated with this disequilibrium is determined by the rate of exchange of radionuclides between the two porosity sets, and the radionuclide storage capacity of the fracture and matrix. Because this equilibration time may be significant in comparison to the time scale of source-term concentration change, a dual-porosity transport model has been adopted.

- **Linear equilibrium sorption of radionuclides.** In addition to hydrodynamic processes, radionuclide concentrations in Culebra groundwater are assumed to be affected by geochemical interactions with the host rock. Reversible sorption is assumed to be the only

mechanism of interaction of the radionuclides with the Culebra Dolomite. Sorption is further assumed to follow a linear Freundlich isotherm, with different coefficients describing sorption on the Culebra matrix and on clays in Culebra fractures.

Several assumptions made in the present conceptual model are tentative and may be revised after evaluation of more comprehensive models of the regional flow system. Specific areas being investigated by Sandia's Fluid Flow and Transport research group include:

- The extent to which leakage between the Culebra and adjacent units can be neglected. While this assumption may be acceptable in many areas, it is not universally valid. For example, extensive dissolution of Rustler halite and anhydrite in lower Nash Draw has resulted in the Rustler becoming highly fractured, forming a single unconfined aquifer. A more accurate description of vertical flow may be made on the basis of existing data, regional fluid balance requirements, and geologic considerations.
- Geochemical interaction of radionuclides with the Culebra may not be adequately described by a linear sorption model A more detailed representation of the specific interactions between radionuclides, pore fluid, and matrix may be required to predict potential migration rates.

6.1.1 PARAMETERS OF THE CULEBRA MODEL

The Darcian flow model requires values for transmissivity, storage coefficient, fluid density, and initial pressure defined throughout the model domain, in addition to boundary conditions and internal fluid sources and sinks. The dual-porosity transport model requires a fluid seepage velocity field (derived from the Darcian flow model), fracture and matrix porosities, effective matrix diffusivity, fracture dispersivity and diffusivity, and isotope-specific geochemical parameters (retardation factors in both porosity sets) defined over the model domain, as well as specification of internal sources. Parameter values used in the performance assessment are discussed in Volume 3.

6.1.2 MODEL IMPLEMENTATION

Separability of the flow and transport problems allows the release associated with intrusion to be estimated as follows:

- estimation of the prevailing Culebra flow field
- estimation of integrated release due to radionuclide sources introduced into the Culebra flow field.

Because of the complexity of the spatial distribution of transmissivity, and the resulting spatial variability of the flow field, numerical approximations are used to simulate flow and transport processes. Uncertainty in release due to uncertainty in model parameters is addressed by

creating equally likely realizations of the set of parameters controlling transport. Most parameters are assumed to have a single value over the entire model domain for each realization. Because of the large variability of transmissivity, the dependence of transmissivity on location, and the large number of estimates of transmissivity over the site, spatial variability of transmissivity is explicitly included in the model. Realizations of transmissivity are required to honor the point estimates at well locations as well as indirect constraints imposed by the Culebra head distribution, as described below.

6.2 Generation of Transmissivity Fields by Geostatistics—Walt Beyeler

Previous WIPP Performance Assessments used a simple zonal approach for including uncertainty in the transmissivity (T) field within the Culebra Dolomite Member of the Rustler Formation. The zonal method divides the regional and local computational domains into geographic regions; 8, 13, and 15 regions have been used for different analyses reported in Marietta et al. (1989) and Bertram-Howery et al. (1990). In each region, a distribution was constructed using transmissivity measurements from available wells. This empirical distribution was sampled and one constant value used for the transmissivity in each zone. Each zone was sampled independently, so a single simulation used 8 (or 13 or 15) transmissivity values to represent the regional T field. Some simulations used distributions constructed from pilot point values (LaVenue et al., 1990) at locations assigned during calibration in addition to actual measurements at well locations.

This approach can be improved in two ways:

- The reason for varying transmissivity over geographic zones is to include spatial variability in the T field. Correlations exist in the T field over distances greater than five kilometers; however, assuming that the 8 (or 13 or 15) zones are independent during sampling is only a first approximation. Spatial dependence should be included over the whole model domain.
- The T fields generated by the simple zonal approach directly used transmissivity measurements whereas other information was included indirectly through pilot point values. Many other data are available, and it would be better to incorporate these data directly, e.g. hydraulic head measurements and geologic information.

Several methods have been proposed in the scientific literature to resolve these two issues. Most suggestions have relied on geostatistical techniques combined with inverse methods (de Marsily, 1986; Yeh, 1986). To obtain fast guidance on development of a package for WIPP PA to use in the final compliance assessment, a Geostatistics eXpert Group (GXG) was convened. The GXG was asked to provide advice given the modeling work completed, calibrated transmissivity

field, data collected, and the above two objectives listed for improvement of the earlier zonal approach. The group's recommendations were organized into three categories:

- Proposing methods for generating conditional random fields to be used in the present assessment.
- Proposing methods for including conceptual model uncertainty.
- Proposing methods for including geological information.

These recommendations are summarized in the following discussion.

6.2.1 GENERATION OF CONDITIONAL RANDOM FIELDS

Transmissivities display a variability in space that can be characterized using measured data, e.g. pump tests, by geostatistical analyses. This spatial variability was found to be stationary in the mean (LaVenue et al., 1990), but intrinsic in the second moment (IRF = 0) with a linear variogram without nugget effect (i.e., locally described by a constant with random perturbations that increase in variance with distance. Several techniques are available to generate random fields having this spatial structure: turning bands, inversion of the full covariance matrix, and spectral methods. Many such realizations could be generated and each realization could be used as one input for a system simulation. Each realization would then have the correct spatial structure of the true field, and would satisfy the first objective above.

However, these realizations would not be fully coherent with the actual measurements, and would overestimate the uncertainty in the T field. Making realizations of random fields coherent with measured information is called conditioning, which was the major focus of the GXG. For WIPP PA, conditioning can be performed on at least four types of information:

- Measured T values at the wells.
- Measured or estimated head values at the wells in pre-excavation steady-state conditions.
- Measured head values during various transient hydraulic tests (e.g., long-term pump tests, shaft excavation).
- Indirect geologic data that can be correlated with transmissivity (such as overburden thickness, or presence of evaporites in the Culebra or Rustler).

Conditioning on the measured T values is one available technique (Delhomme, 1979). A second technique, conditioning on steady-state and transient head data is discussed below. Conditioning on geologic information will be discussed later.

Six methods of conditioning on head data were discussed by the GXG. These methods range from the simple to the complex. Each method has potential advantages and disadvantages. The GXG will compare these methods on the WIPP data base, and make a recommendation for the final compliance assessment. Given the time constraints for the present PA, only the first method could be implemented. A brief description of the six methods follows.

1. The first method considered by the GXG was used in the 1991 Preliminary Comparison reported in Volume 1 of this document set. Random fields conditioned on T measurements at well locations and on values assigned during manual calibration were assigned to pilot point locations where no measurements were available (LaVenue et al., 1990). Forty-one measured-T and 41 pilot-point values are available. The pilot point values were assigned to insure coherence of the calibrated T field with the measured head data (both steady-state and transient conditions) so conditioning on head data is indirectly included.

   This approach still needs to be validated on the transient data. An advantage of this method is that it does not require any assumption on the acceptable range of variability of T ($\mathrm{Var}(T)$). Many methods require that the $\mathrm{Var}(\ln T) > 1$, and in the Culebra the $\mathrm{Var}(\ln T)$ is about 3.5. This first method also allows using a variable-density fluid-flow model which may be important in the Culebra (Davies, 1989). Other methods are linear, but can only accommodate constant-density fluid-flow models. A second advantage is computational efficiency because the Cholesky decomposition only needs to be performed once regardless of the number of simulations.

2. The second method considered by the GXG was to apply method one only on measured T values. Conditioning on head values (steady-state and transient) would be accomplished simply by screening out T fields not satisfying an assigned acceptance criterion on observed head. Upon testing, the rejection rate proved to be high, so this method was not pursued further.

3. The third method considered by the GXG was to use an available code, INVS (Bras and Kitanidis, 1991; Kitanidis and Vomvoris, 1983; Hoeksema and Kitanidis, 1984, 1985 a and b), that conditions on both measured T values and also steady-state head values, with or without using pilot point values. However, this method is restricted to $\mathrm{Var}(\ln T) < 1$ because of linearization of the flow equations (only constant-density fluid flow). The present code assumes full stationarity of $\ln T$ with an exponential covariance function, and automatically fits the corresponding covariance of the head and cross-covariance functions. The relationship between these covariances is derived analytically assuming that average flow direction and gradient are constant. Uniform rectilinear grids with less than about 10^3 blocks are also required. After automatic fitting of the covariances, an optimal T field can be estimated by co-kriging, and conditional simulations can be generated.

   A similar method relying on spectral techniques (Gutjahr, 1989) is also part of the ongoing comparison exercise between methods 1 and 3.

4. The fourth method considered by the GXG is an extension of the pilot point approach used for the calibration of the Culebra T field. This method should generate random fields conditioned on T measurements, steady-state, and transient head data without restriction on $\mathrm{Var}(\ln T)$ and with variable-density fluid-flow models. This method, if successful, will be used for the 1992 PA.

   First, random T fields conditioned only on the measured T values are generated. These fields are further conditioned on the head data by calibrating them with the pilot point approach both on steady-state and transient data. To generate a large number of calibrated random fields, the procedure will be automated. Order of pilot point selection and the uniqueness of the resulting T field are issues to be examined during operational tests and sensitivity analyses.

5. The fifth method considered by the GXG was a semi-analytical approach (Rubin and Dagan, 1987a and b, 1988; Rubin, 1990; Rubin 1991, in press). This method is similar to method 3, but uses semi-analytical expressions. It will be added to the comparison exercise with methods 1, 3, and 4.

6. The sixth method considered by the GXG is complex relying on a maximum likelihood approach (Carrera and Neuman, 1986 a,b, and c). This method conditions on both steady-state and transient head data, assumes linearity iteratively (in the vicinity of the optimal solution), and constant-density fluid-flow. It may also be added to the comparison exercise.

The comparison exercise will expose potential discrepancies among these six methods. Depending upon the resolution of these discrepancies, the GXG will recommend a method(s) for use in the final PA.

6.2.2 INCLUDING GEOLOGICAL INFORMATION

Geological information should be included in the estimation of the T field because of

- An apparent non-stationarity of the T field; an increasing trend from east to west exists in the data.
- An observed difference between kriged T field and the conditionally simulated fields above.
- A large amount of available geologic information that has not been directly used in either the calibration or the conditional simulations.

The GXG discussed two proposals. First, relevant geologic information such as thickness of the overburden, total estimated thickness of evaporites in the Rustler, slope or curvature of Culebra, density of lineaments, chemical data, etc. should be tested by co-kriging with transmissivity. If a candidate geologic data set(s) is found to improve the T estimation, it can be

retained, and a new T estimation procedure developed. Second, after a new co-kriging procedure using geologic data sets is developed, co-kriged estimates should be compared with measured values at well locations to look for any systematic bias. If a bias is found, the quality of those measurements would be questioned. This would allow well measurements which have been questioned (e.g., well P-18) to be evaluated objectively.

6.2.3 INCLUDING CONCEPTUAL MODEL UNCERTAINTY

After considering the detailed problem of residual uncertainty in the *T* field of the Culebra, the GXG discussed the general problem of how to include conceptual model uncertainty in WIPP PA. The approach discussed was the same as used in previous analyses (Marietta et al, 1989; Bertram-Howery et al., 1990). For each conceptual model, the underlying parameter uncertainty is characterized, and different sets of CCDFs are produced as described in Volume 1, Chapter III. These sets of CCDFs are compared with respect to potential impact on a compliance decision that would be based on a mean CCDF constructed from one or more of these conceptual model sets of CCDFs with an assigned weighting. If a conceptual model produces a set of CCDFs that would have negligible impact on the eventual compliance decision, it can be discarded. The goal is then to identify possible alternative conceptual models that are qualitatively different, and can be calibrated on the available data.

Preliminary approaches for identifying such alternative conceptual models were discussed:

- A fractal model of the Culebra transmissivity was proposed (Grindrod and Capon, 1991). Using a fractal approach allows an extension of the spatial variability in the transmissivity fields to scales less than the measured scale. In this way the effect of possible smaller scale features than have been observed can be evaluated.
- Basin-scale hydrologic modeling over past geologic time scales could evaluate the steady-state assumption of the present PA modeling. Sensitivity studies with such a model would assess different conceptual models for both recharge/infiltration and geologic framework of the Culebra, other Rustler units, and overlying formations.
- A lithofacies modeling approach was proposed (Ravennes et al., 1991). Instead of describing spatial variability by just parameter variability, lithofacies models represent geometric descriptions of geologic strata by sequential stratigraphy in a stochastic framework. These models can be conditioned by geologic information.
- Upscaling block properties and modifying the governing equations appropriately is an approach that was also proposed.

These proposed methods will be assessed by the GXG after the results of the variability studies in the Culebra are available.

6.3 Selection of Transmissivity Fields—Walt Beyeler

At least three types of information are available for estimating values of Culebra transmissivity (T): slug tests, drill stem tests, and short-term pumping tests are interpreted to give estimates of T in the neighborhood of the tested well; long-term pumping tests with pressure observations made at several wells can yield a T value integrated over a large region surrounding the pumped well; and the distribution of pressures over the aquifer is related to the distribution of transmissivities by the flow equation.

The estimation procedure used in the present PA is intended to identify transmissivity fields which are consistent with both point observations of T and the equilibrium pressure distribution. An approach being developed for the 1992 PA (method 4, described above) will allow transmissivities to be constrained by both short- and long-term transient pressure data, in addition to the transmissivity observations and equilibrium pressures used in the present method. As an interim means of incorporating information about transmissivity from long-term transient observations, pilot points derived during calibration of the Culebra flow model (LaVenue et al., 1990) were introduced as additional observations of T.

The present method consists of four steps: generation of candidate transmissivities constrained by point data; determination of the sensitivity of pressure at all observation wells to changes in boundary pressure; assembly of an optimal boundary pressure function which minimizes the deviation of model pressures from estimated equilibrium pressures; and evaluation of acceptability of the resulting model. Detailed information on these four steps follows.

The CAMCON program GARFIELD (draft of SAND90-1983, Rechard et al., in preparation) was used to simulate transmissivity fields over the discretized model domain. GARFIELD uses a set of point observations, and a generalized covariance describing the spatial variability of the observations, to simulate any number of alternative fields conditioned by the point observations. The point observations of transmissivity, and the associated generalized covariance function, were identical to those used in the final calibrated flow model of LaVenue et al. (1990). Conditioning on both measured and pilot point values was done by a Cholesky decomposition of the full covariance matrix of the kriging estimation error. An IRF = 0 random function was considered with the linear variogram determined by LaVenue et al. (1990). Point simulations on a 32 x 25 km^2 grid (52 by 44 elements) were produced. The resulting realizations honor the point estimates of transmissivity (within bounds established by the variance of the point estimate), and the spatial variability of transmissivity reflected in the generalized covariance.

Since this conditioning on head measurements is only indirect, a systematic measurement of the coherence of the calculated heads with the measured heads was performed, but given the time constraint, only steady-state heads could be considered. Uncertainty in the value of the prescribed heads on the boundary was also taken into account. These prescribed heads on the boundary are

estimated by kriging the local head measurements at well locations. Therefore, they are given a variance of their estimation error. Programs GENOBS and SWIFT were then used to calculate sensitivity of steady-state model pressure with respect to pressure changes on segments of the model boundary. In order to reduce the number of independent pressures, the pressure distribution along a boundary segment was assumed to be piecewise linear.

Program FITBND then used the above sensitivity coefficients to derive fixed-pressure boundary conditions which optimized model agreement with estimates of pre-construction Culebra pressure at the 36 control points used in the LaVenue et al. (1990) study. The resulting pressure fields are optimal in the sense of minimizing the following objective function:

$$X^2 = \frac{1}{N_{obs} + N_{bound}} \left\{ \sum_{i=1}^{N_{obs}} \left(\frac{P_{obs} - P_{\mathrm{mod}}}{\sigma_{obs}} \right)^2 + \sum_{i=1}^{N_{bound}} \left(\frac{P_{bound} - P_{\mathrm{mod}}}{\sigma_{bound}} \right)^2 \right\} \qquad (6\text{-}1)$$

where N is the number of elements of a particular type, P is pressure, σ is the estimated standard deviation of the error of the observation, *obs* denotes an observation well location, *bound* denotes a model boundary element, and *mod* denotes a model-calculated pressure.

To decide on the acceptability of a conditionally simulated field, the boundary conditions of the calculated head fields were first optimized within their uncertainty range. Then, two acceptance criteria were used:

- The average standard deviation of the model error over all wells where steady-state head data are available should not exceed $\sqrt{2} \bullet s$ where s is the standard deviation of the measured head error.
- The corresponding flow field should be globally coherent with known flow in the area including general direction, recharge and discharge zones

6.3.1 RATIONALE FOR FIRST CRITERION

The value of model error (X^2) at the minimum was used as an indication of the plausibility of the underlying T field. X^2 is the average normalized squared deviation of the model pressure from the observed pressure or prior estimate of boundary pressure. If the variance of the observation and boundary errors have been correctly estimated, and the observation errors are normally distributed, the expected value of X^2 for the correct model would be 1. If the observation error distribution is less compact than the normal distribution, X^2 for the correct model would be larger than 1. To allow for this possibility, a threshold value of 2 was selected for X^2 (as discussed below, the particular threshold value selected has little effect on release). If the model error for a given transmissivity field was greater than this threshold, the transmissivity was considered irreconcilable

with pre-construction equilibrium pressures. Transmissivity fields (along with optimal boundary conditions) which produce an error less than the threshold were considered to be plausible. All plausible transmissivity fields were considered to be equally likely.

6.3.2 RATIONALE FOR SECOND CRITERION

Because pressure data near the model boundaries are sparse, the optimizing procedure has considerable latitude in assigning some boundary values. In a few cases, the location of minimum pressure in otherwise plausible fields was believed to be unrealistically located along the southeastern boundary. For this reason, a further screening of flow fields satisfying the maximum error criterion was made on the subjective basis of requiring discharge to occur along the southwestern boundary.

6.3.3 TRAVEL TIMES FOR RETAINED FIELDS

The procedure described above was applied to produce 60 plausible transmissivity fields and associated equilibrium boundary pressures. About 350 simulations conditioned on point transmissivities were generated. The first criterion selected 88 acceptable T fields. The second criterion, although subjective, reduced that number to 76.

The resulting flow fields control advection of radionuclides released into the Culebra Dolomite from an intrusion borehole. For this reason, the travel time of a neutrally buoyant particle from the hypothesized location of an intrusion borehole to the accessible environment boundary is an appropriate index of the influence of the flow field on discharge. The first 60 of the 76 T fields were retained and then ordered by travel time to the accessible environment. This travel time was calculated for each plausible flow field using the program TRACKER. Figure 6-2 is a cumulative distribution of travel times of the 60 flow fields. Figure 6-3 shows a scatter plot of model error X^2 versus travel time. There is no apparent relationship between the model error and travel time, so that the distribution of travel times is independent of the threshold model error used to define plausible flow fields. Figure 6-4 (part a through part o) shows the transmissivity distribution in each of the retained fields.

Flow fields were selected for the 1991 PA calculations using a single uniformly distributed random variable as an index of the flow field to be used in conjunction with all other parameters defining a sample vector. Travel time from the center of the waste panel region was used to impose a natural ordering on the flow fields to facilitate future sensitivity analyses (for example, the tenth smallest value of the sampled index was associated with the flow field having the tenth smallest travel time). Because the flow fields are considered to be equally likely, the rank of the sampled index value was used an an index of the flow field. The particular shape and range of the distribution is therefore irrelevant.

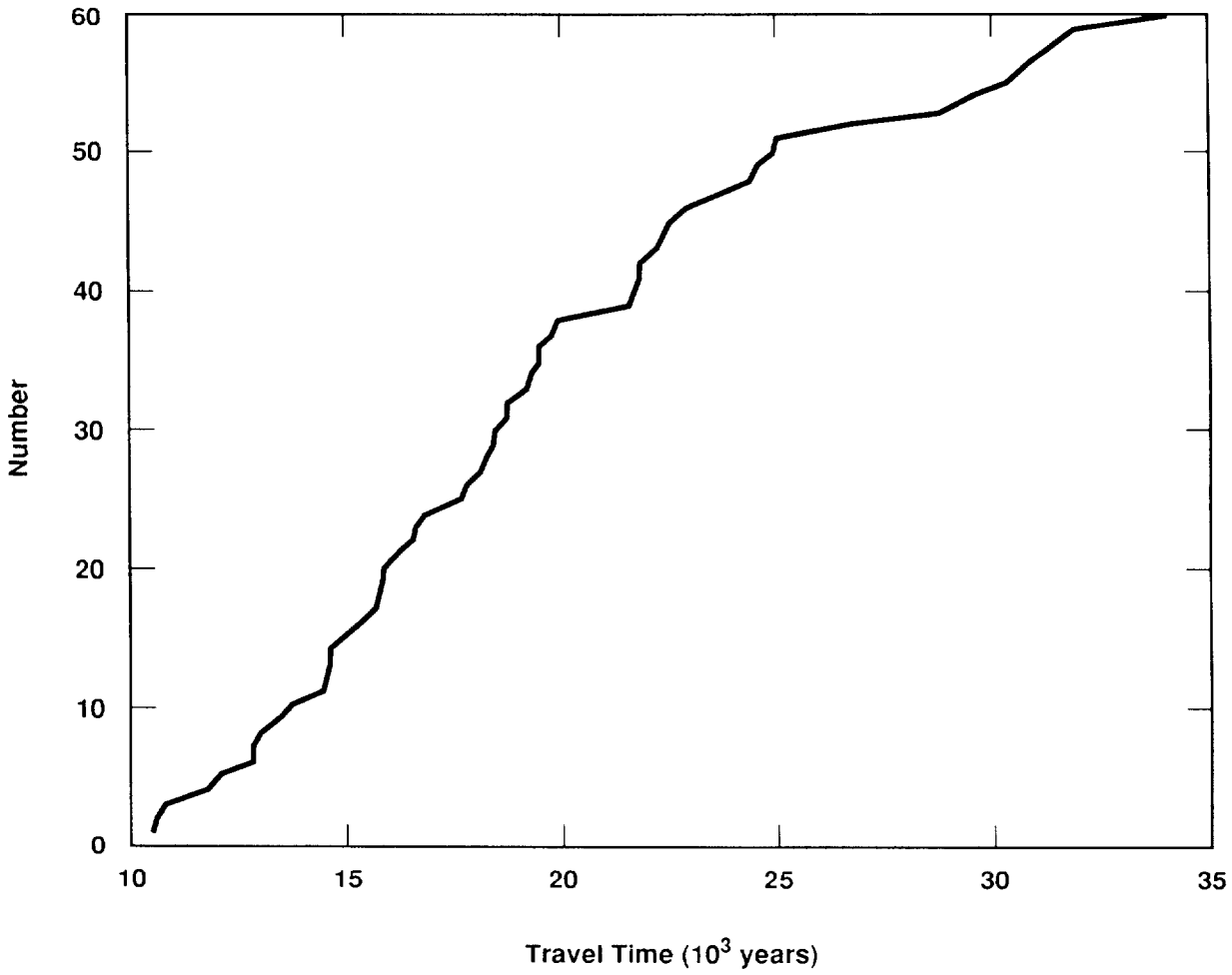

Figure 6-2. Cumulative Distribution of Travel Times of the 60 Flow Fields

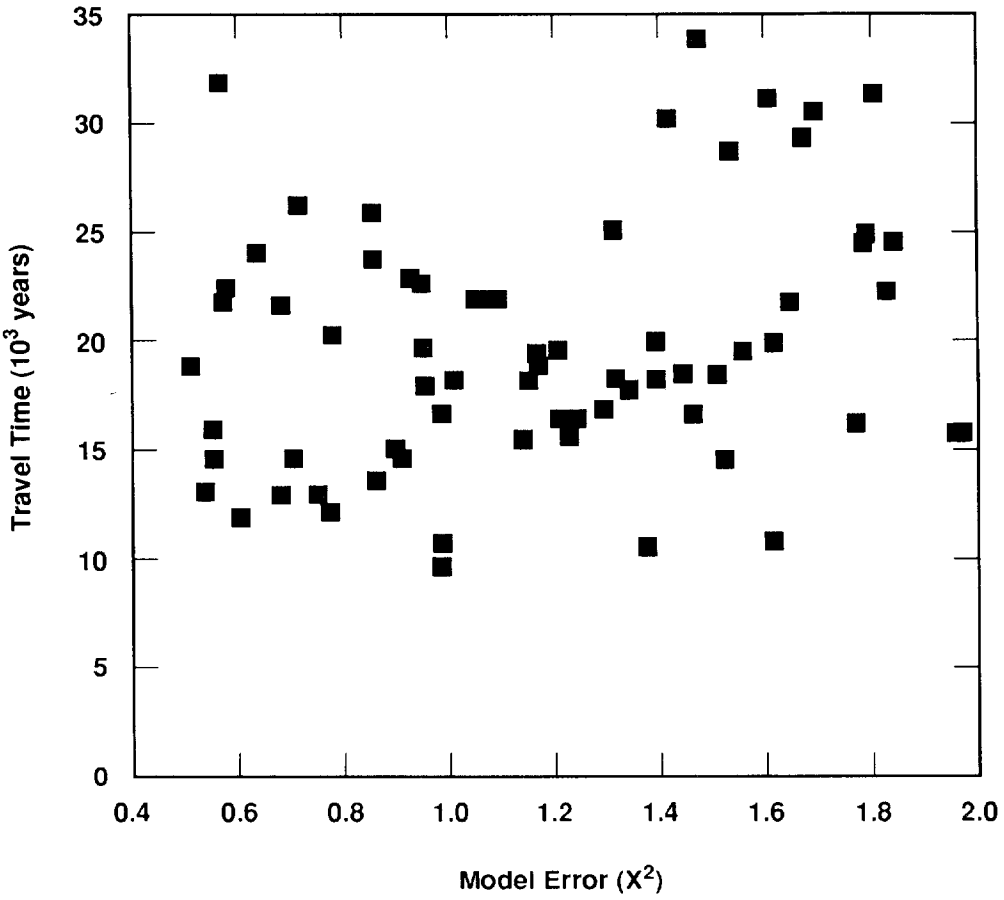

Figure 6-3. Scatter Plot of Model Error X^2 versus Travel Time

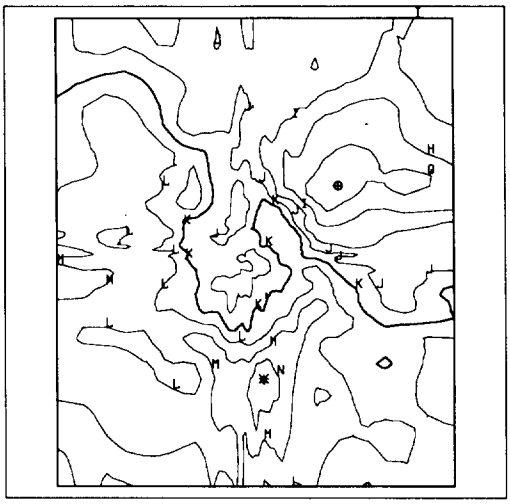

Field 1
⊕ = -9.781
★ = -0.875

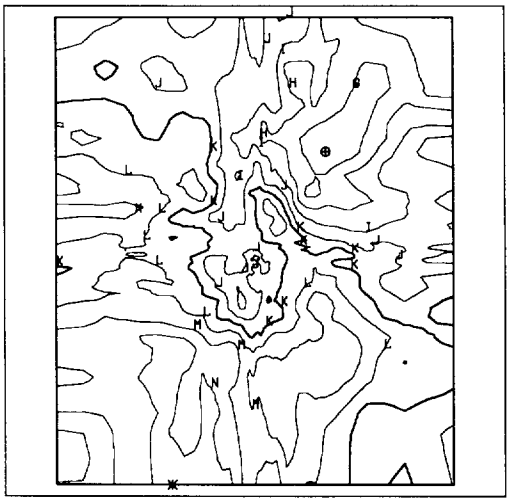

Field 2
⊕ = -9.627
★ = -1.231

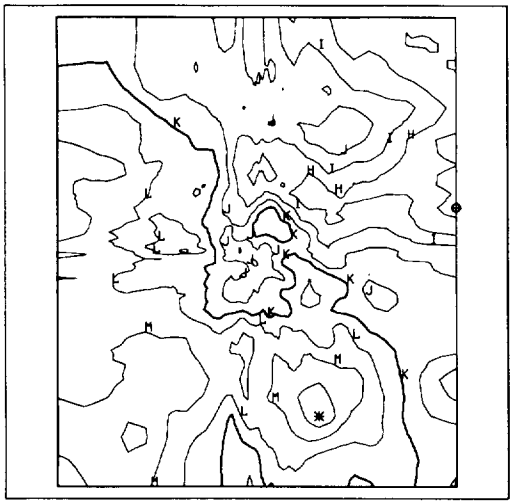

Field 3
⊕ = -9.502
★ = -1.141

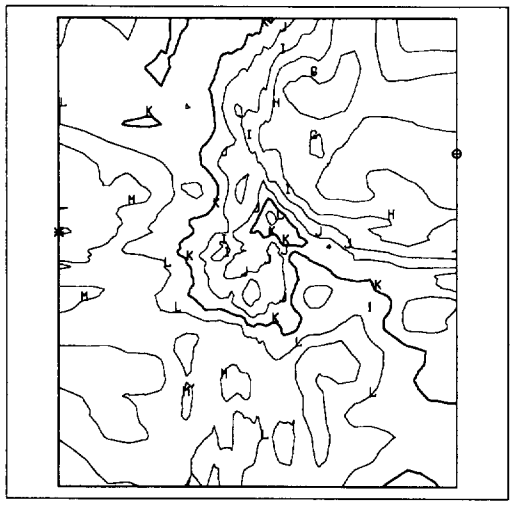

Field 4
⊕ = -9.972
★ = -1.860

Legend

LOGT (log_{10} m^2/s)

A = -15.00	**D = -12.00**	**G = -9.00**	**J = -6.00**
B = -14.00	**E = -11.00**	**H = -8.00**	⋮
C = -13.00	**F = -10.00**	**I = -7.00**	**Q = 1.00**

TRI-6342-1367-0

Figure 6-4a. Transmissivity Field Distribution (Fields 1-4)

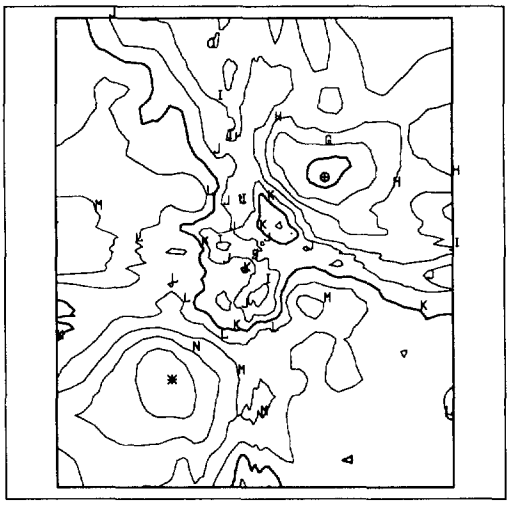

Field 5
⊕ = -10.74
★ = -0.16

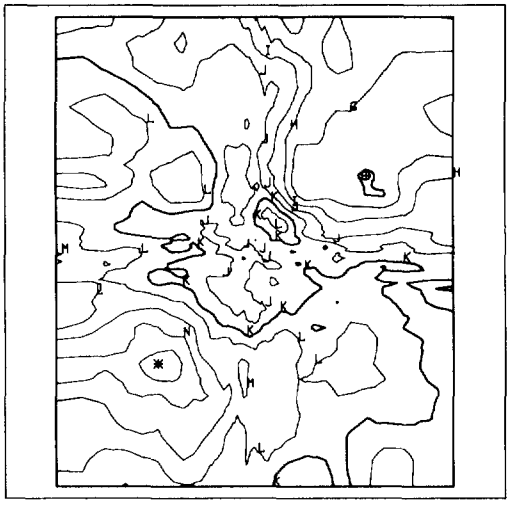

Field 6
⊕ = -10.22
★ = -0.24

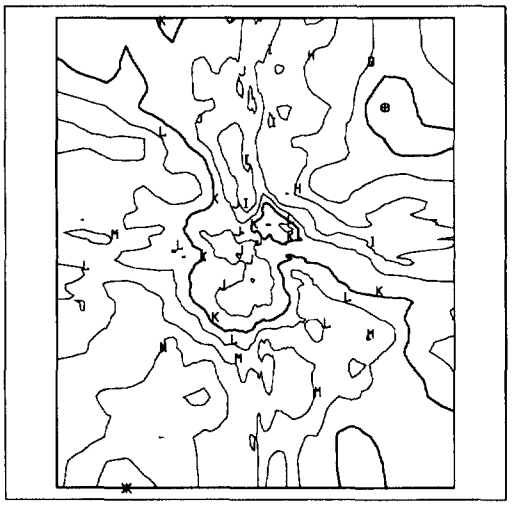

Field 7
⊕ = -10.78
★ = -0.23

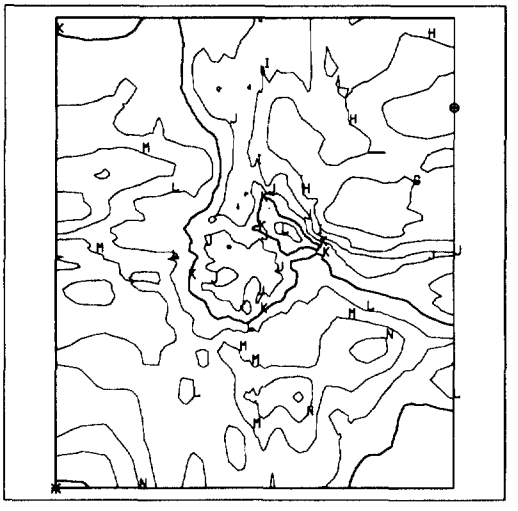

Field 8
⊕ = -10.01
★ = 0.28

Legend

LOGT (log_{10} m^2/s)

A = -15.00	D = -12.00	G = -9.00	J = -6.00
B = -14.00	E = -11.00	H = -8.00	●●●
C = -13.00	F = -10.00	I = -7.00	Q = 1.00

TRI-6342-1368-0

Figure 6-4b. Transmissivity Field Distribution (Fields 5-8)

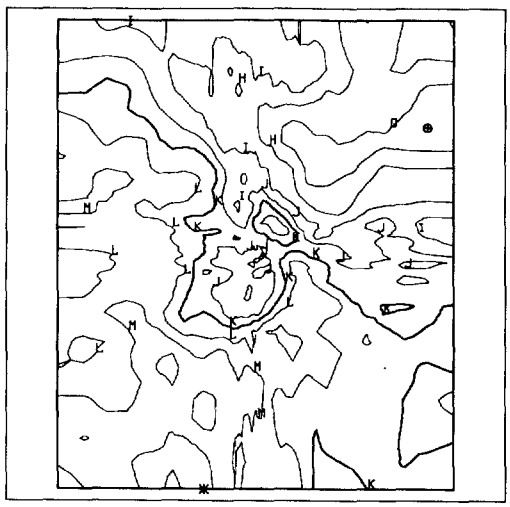

Field 9
⊕ = -9.722
★ = -1.186

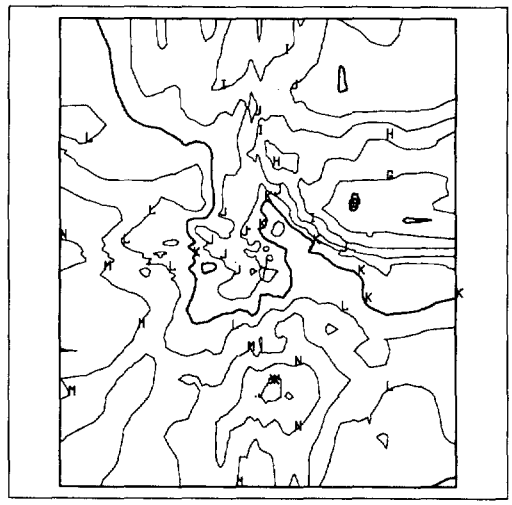

Field 10
⊕ = -10.13
★ = -0.72

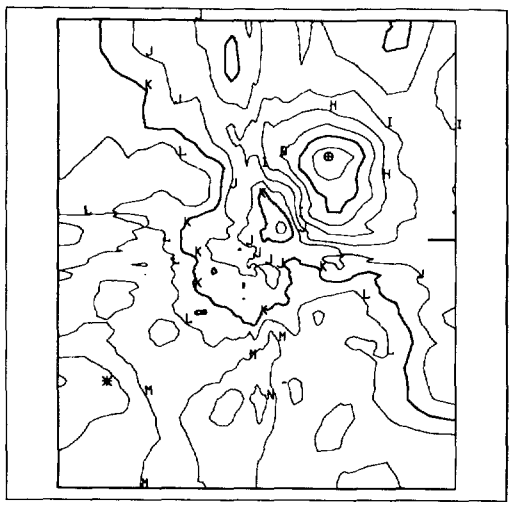

Field 11
⊕ = -11.72
★ = -1.57

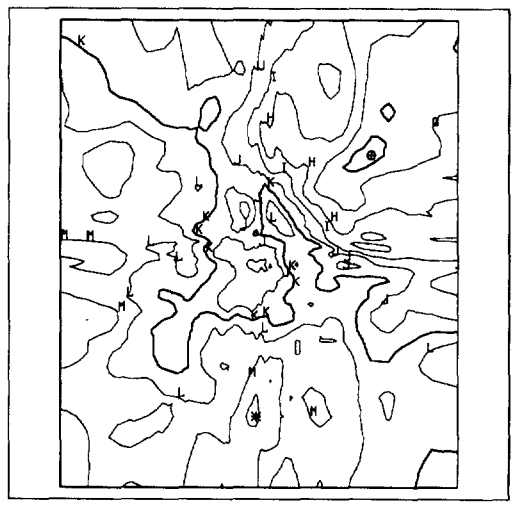

Field 12
⊕ = -10.39
★ = -1.61

Legend

LOGT ($\log_{10}$ m^2/s)

A = -15.00	D = -12.00	G = -9.00	J = -6.00
B = -14.00	E = -11.00	H = -8.00	●●●
C = -13.00	F = -10.00	I = -7.00	Q = 1.00

TRI-6342-1369-0

Figure 6-4c. Transmissivity Field Distribution (Fields 9-12)

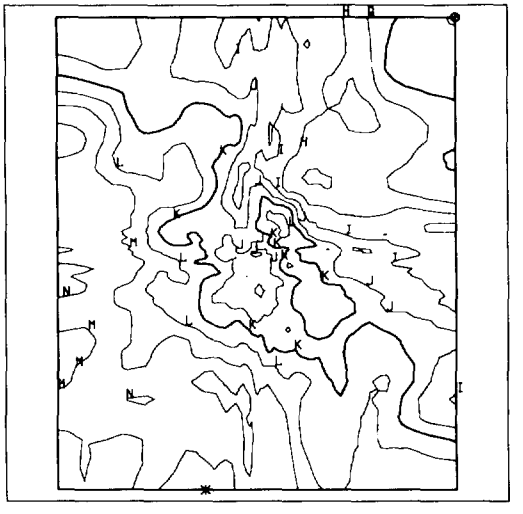

Field 13
⊕ = -11.13
★ = -1.21

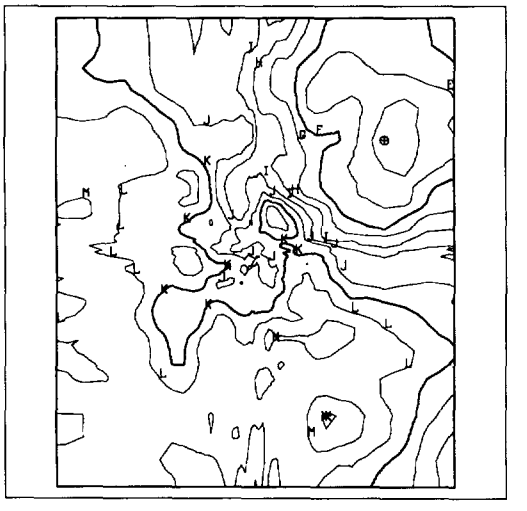

Field 14
⊕ = -12.57
★ = -1.79

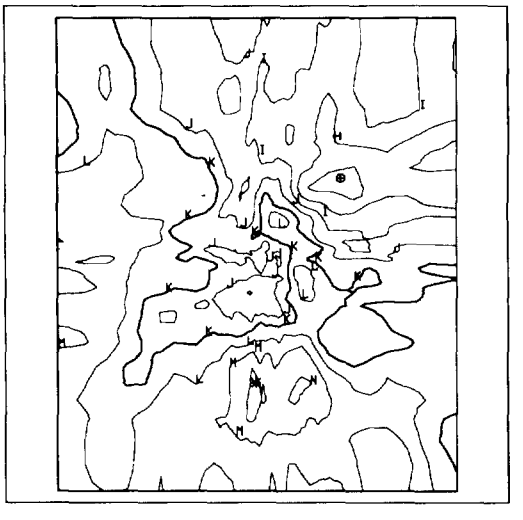

Field 15
⊕ = -9.351
★ = -1.664

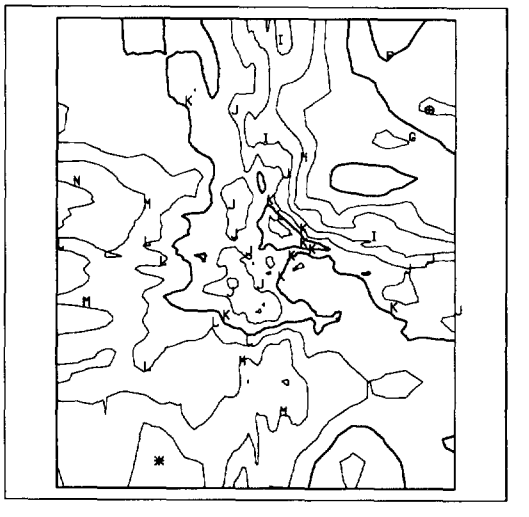

Field 16
⊕ = -11.15
★ = -1.10

Legend

LOGT ($\log_{10}$ m^2/s)

A = -15.00	**D = -12.00**	**G = -9.00**	**J = -6.00**
B = -14.00	**E = -11.00**	**H = -8.00**	**⋮**
C = -13.00	**F = -10.00**	**I = -7.00**	**Q = 1.00**

TRI-6342-1370-0

Figure 6-4d. Transmissivity Field Distribution (Fields 13-16)

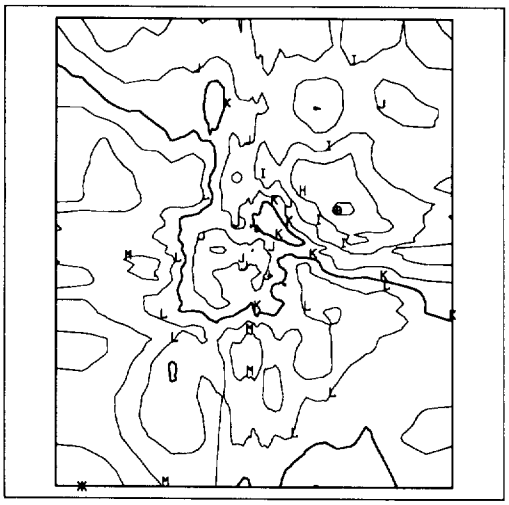

Field 17
⊕ = -9.306
★ = -1.206

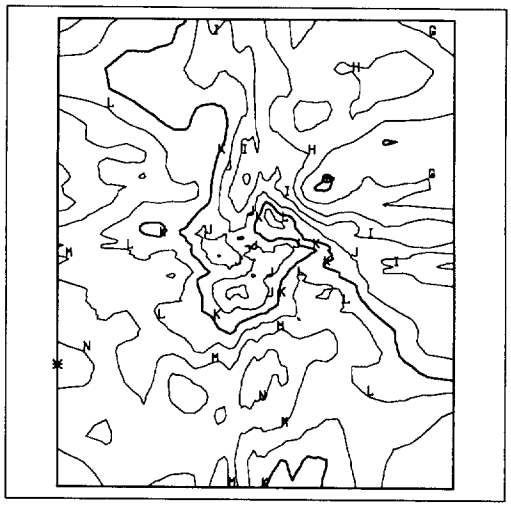

Field 18
⊕ = -10.16
★ = -1.41

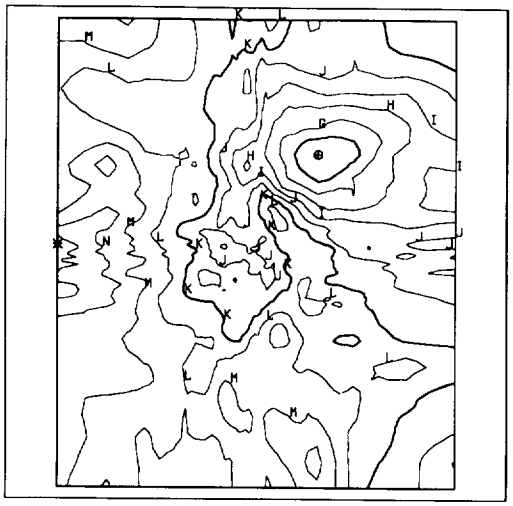

Field 19
⊕ = -10.99
★ = -0.43

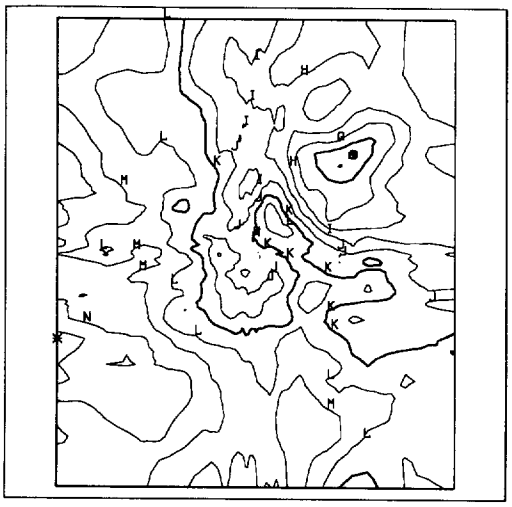

Field 20
⊕ = -11.15
★ = -0.46

Legend

LOGT ($\log_{10}$ m^2/s)

A = -15.00	D = -12.00	G = -9.00	J = -6.00
B = -14.00	E = -11.00	H = -8.00	⋮
C = -13.00	F = -10.00	I = -7.00	Q = 1.00

TRI-6342-1371-0

Figure 6-4e. Transmissivity Field Distribution (Fields 17-20)

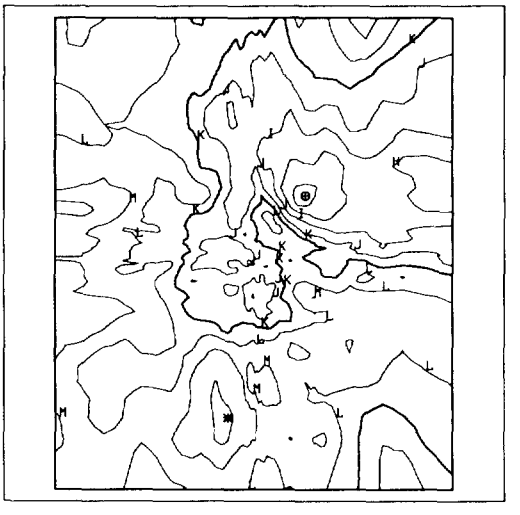

Field 21
⊕ = -9.431
★ = -1.579

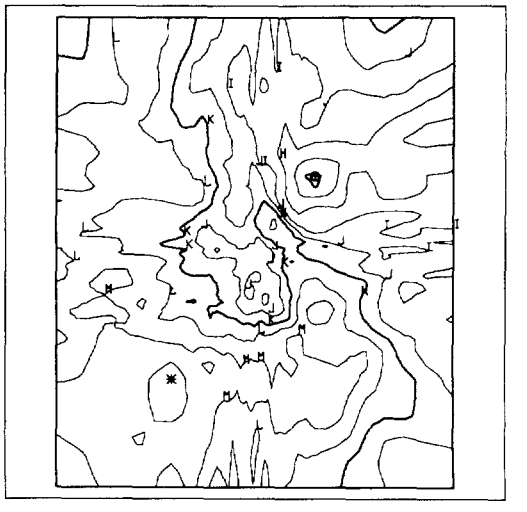

Field 22
⊕ = -10.17
★ = -1.36

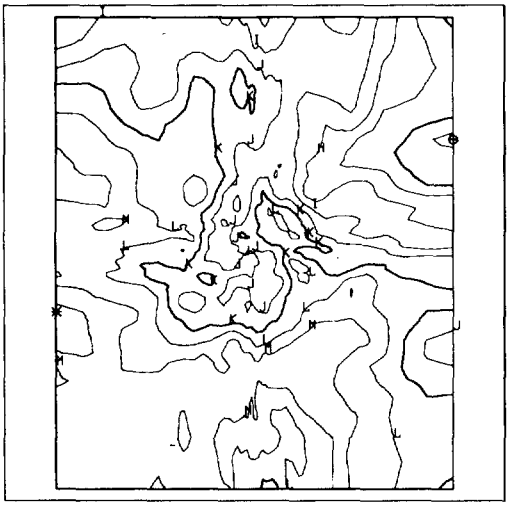

Field 23
⊕ = -11.41
★ = -1.71

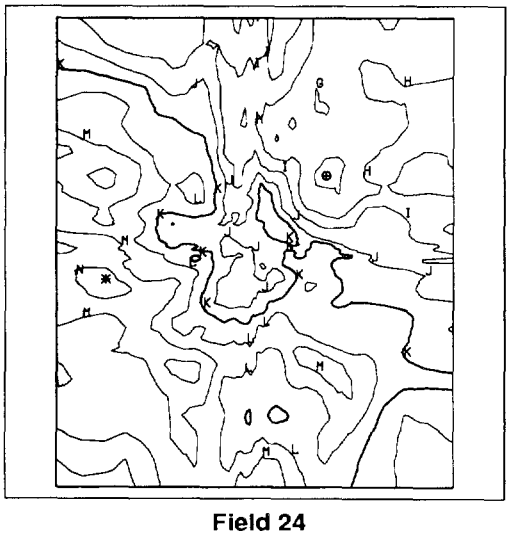

Field 24
⊕ = -9.337
★ = -1.438

Legend

LOGT (log_{10} m^2/s)

A = -15.00	**D = -12.00**	**G = -9.00**	**J = -6.00**
B = -14.00	**E = -11.00**	**H = -8.00**	**⋮**
C = -13.00	**F = -10.00**	**I = -7.00**	**Q = 1.00**

TRI-6342-1372-0

Figure 6-4f. Transmissivity Field Distribution (Fields 21-24)

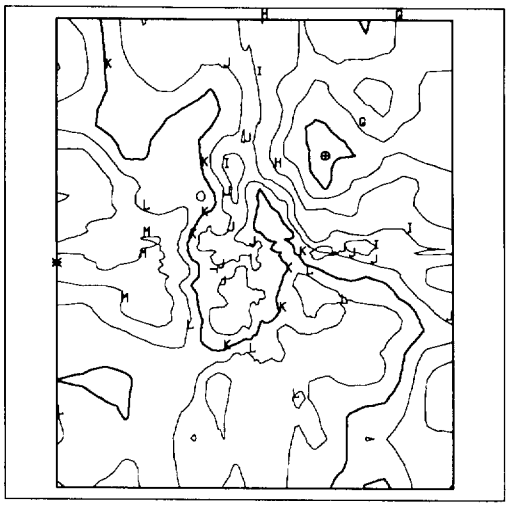

Field 25
⊕ = -10.48
★ = -1.93

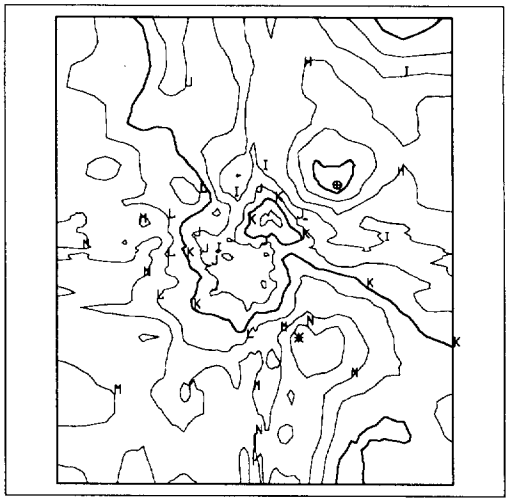

Field 26
⊕ = -10.62
★ = -1.10

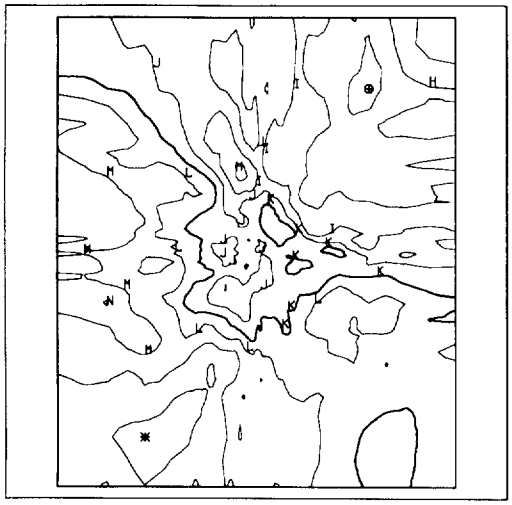

Field 27
⊕ = -9.388
★ = -1.168

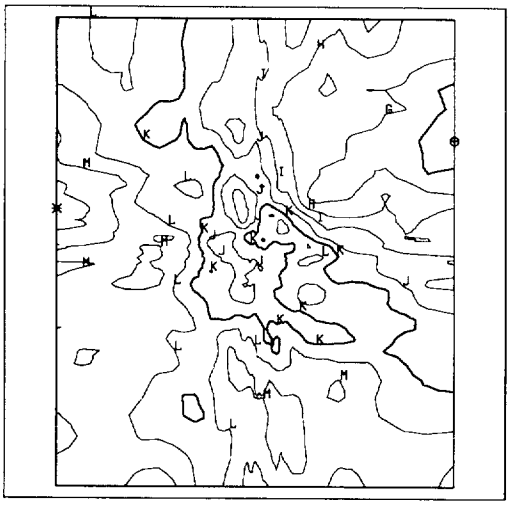

Field 28
⊕ = -11.03
★ = -1.19

Legend

LOGT (log_{10} m^2/s)

A = -15.00	D = -12.00	G = -9.00	J = -6.00
B = -14.00	E = -11.00	H = -8.00	⋮
C = -13.00	F = -10.00	I = -7.00	Q = 1.00

TRI-6342-1373-0

Figure 6-4g. Transmissivity Field Distribution (Fields 25-28)

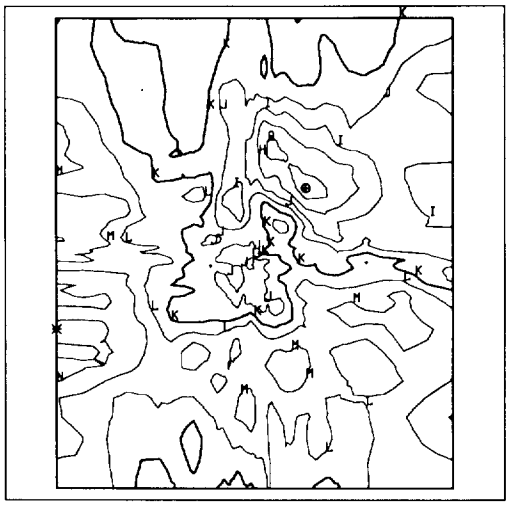

Field 29
⊕ = -9.654
★ = -1.620

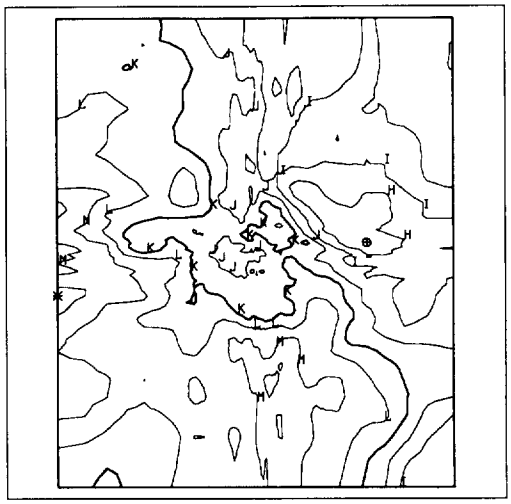

Field 30
⊕ = -8.811
★ = -1.466

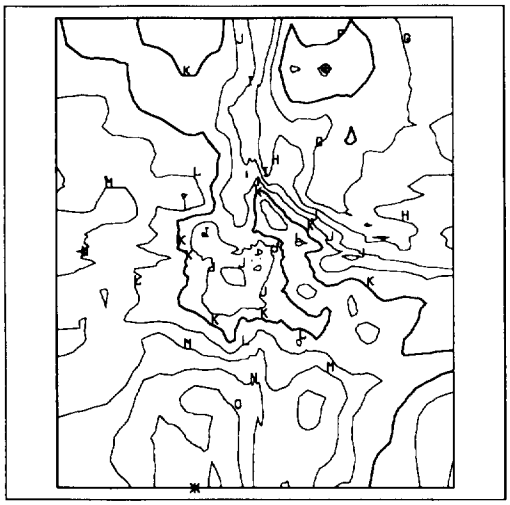

Field 31
⊕ = -11.19
★ = -0.06

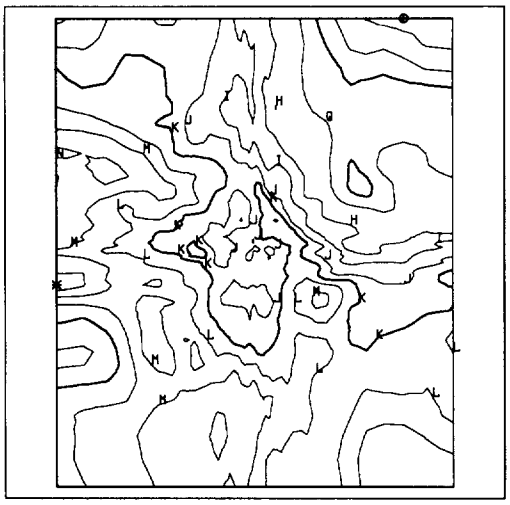

Field 32
⊕ = -12.42
★ = -1.53

Legend

LOGT ($\log_{10}$ m^2/s)

A = -15.00	**D = -12.00**	**G = -9.00**	**J = -6.00**
B = -14.00	**E = -11.00**	**H = -8.00**	**⋮**
C = -13.00	**F = -10.00**	**I = -7.00**	**Q = 1.00**

TRI-6342-1374-0

Figure 6-4h. Transmissivity Field Distribution (Fields 29-32)

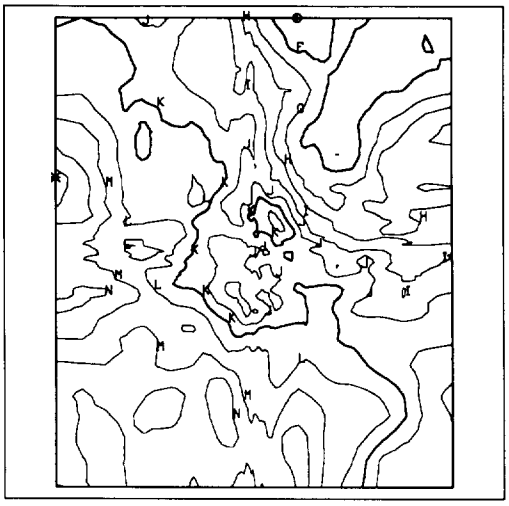

Field 33
⊕ = -11.03
★ = -0.52

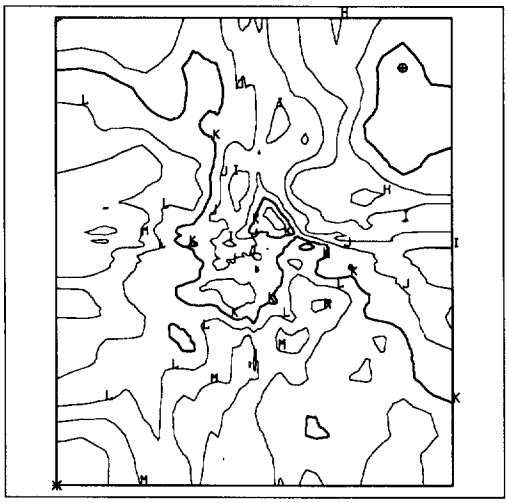

Field 34
⊕ = -10.67
★ = -1.27

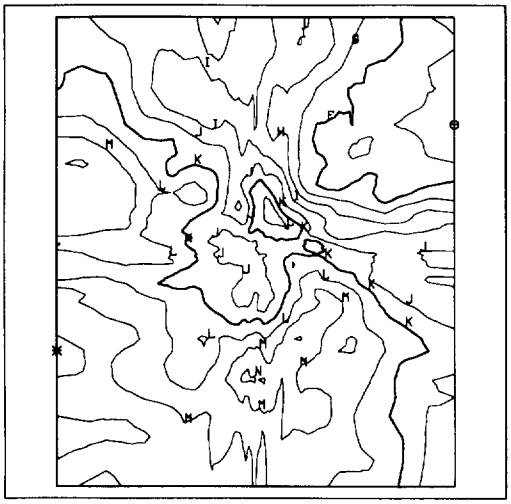

Field 35
⊕ = -11.46
★ = -1.56

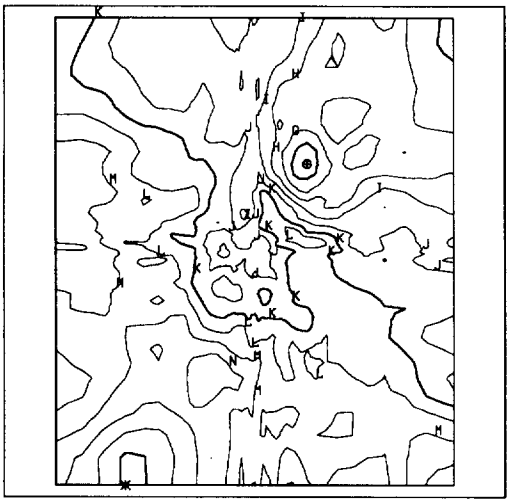

Field 36
⊕ = -10.71
★ = 0.25

Legend

LOGT (log_{10} m^2/s)

A = -15.00	D = -12.00	G = -9.00	J = -6.00
B = -14.00	E = -11.00	H = -8.00	⋮
C = -13.00	F = -10.00	I = -7.00	Q = 1.00

TRI-6342-1375-0

Figure 6-4i. Transmissivity Field Distribution (Fields 33-36)

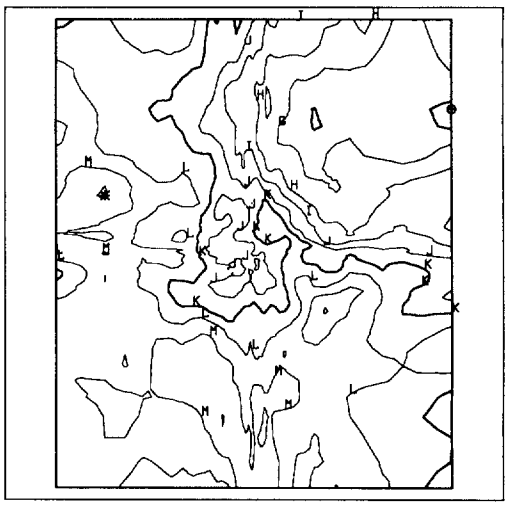

Field 37
⊕ = -10.33
★ = -1.88

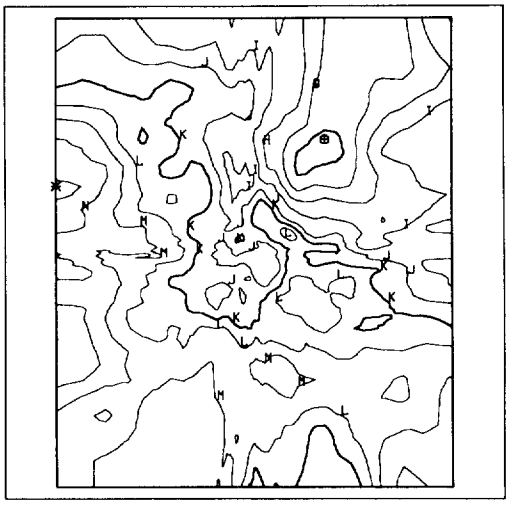

Field 38
⊕ = -10.41
★ = -0.48

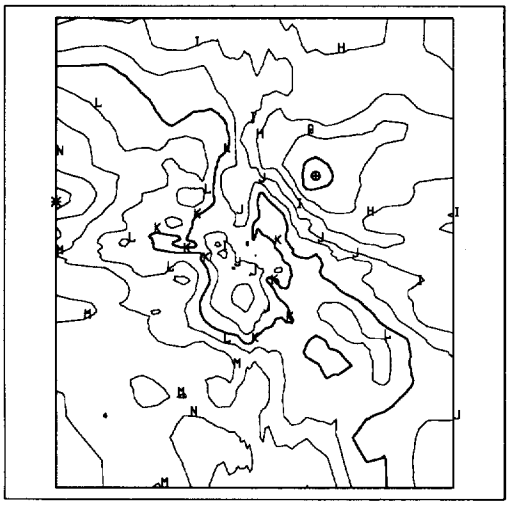

Field 39
⊕ = -10.49
★ = -0.58

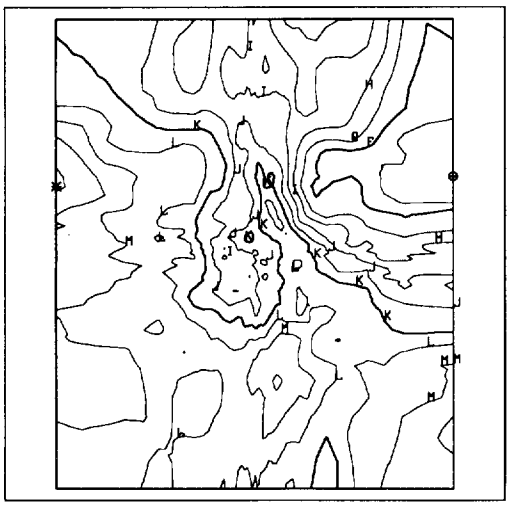

Field 40
⊕ = -11.69
★ = -0.79

Legend

LOGT ($\log_{10}$ m^2/s)

A = -15.00	**D = -12.00**	**G = -9.00**	**J = -6.00**
B = -14.00	**E = -11.00**	**H = -8.00**	**⋮**
C = -13.00	**F = -10.00**	**I = -7.00**	**Q = 1.00**

TRI-6342-1376-0

Figure 6-4j. Transmissivity Field Distribution (Fields 37-40)

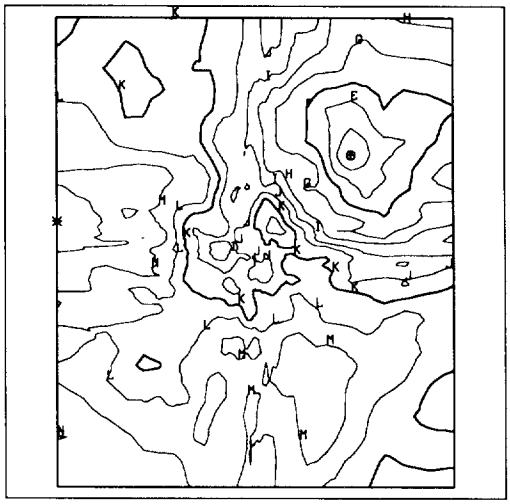

Field 41
⊕ = -13.08
★ = -0.94

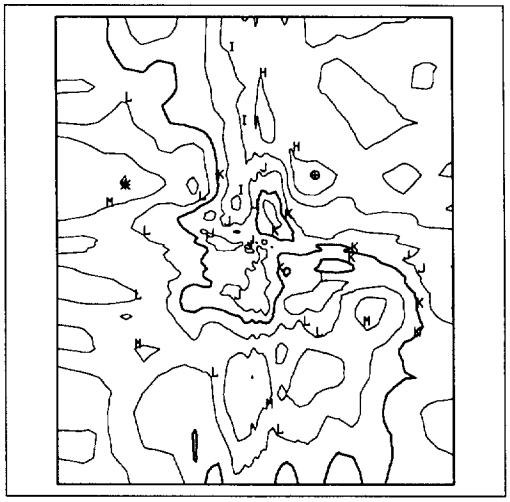

Field 42
⊕ = -8.797
★ = -1.963

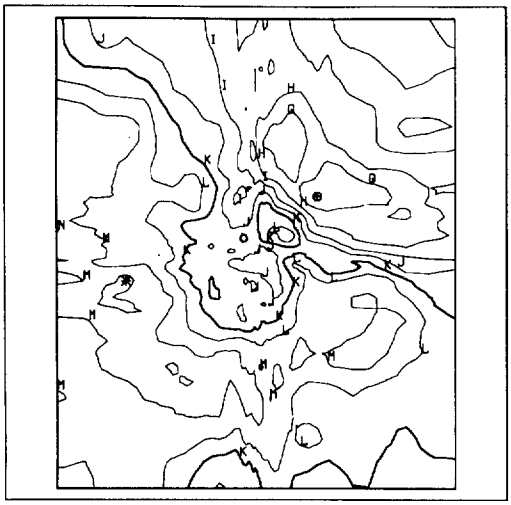

Field 43
⊕ = -10.04
★ = -1.80

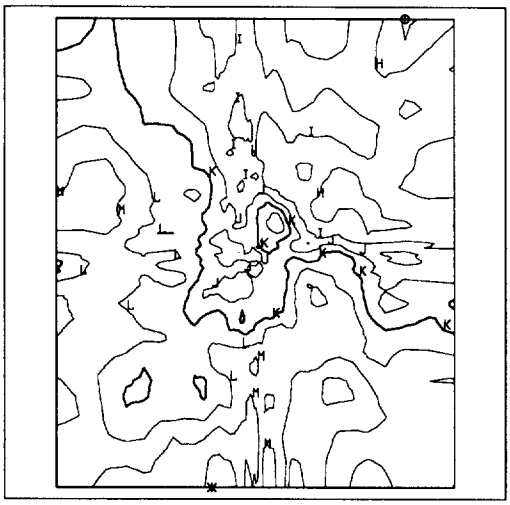

Field 44
⊕ = -9.172
★ = -1.630

Legend

LOGT ($\log_{10}$ m^2/s)

A = -15.00	D = -12.00	G = -9.00	J = -6.00
B = -14.00	E = -11.00	H = -8.00	⋮
C = -13.00	F = -10.00	I = -7.00	Q = 1.00

TRI-6342-1377-0

Figure 6-4k. Transmissivity Field Distribution (Fields 41-44)

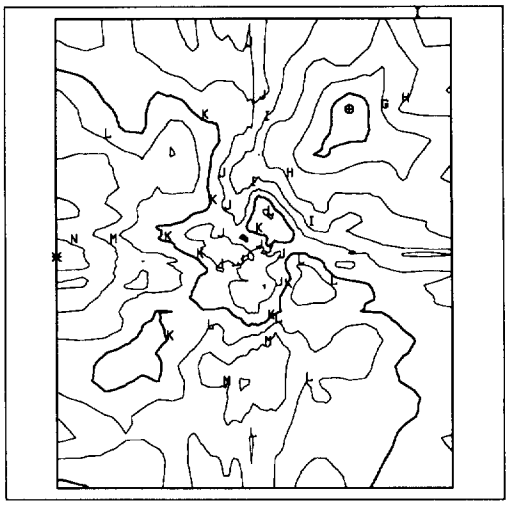

Field 45
⊕ = -10.68
★ = -1.46

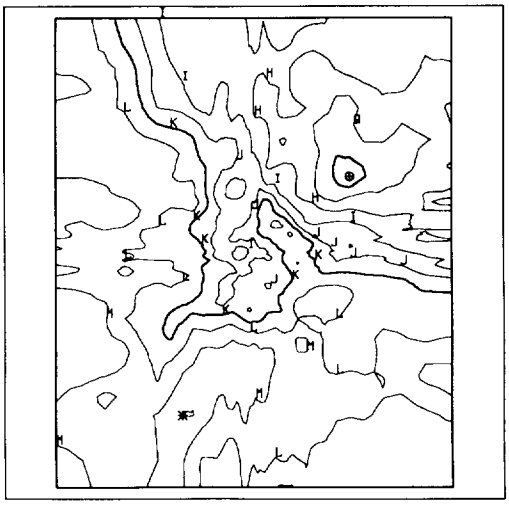

Field 46
⊕ = -10.62
★ = -1.96

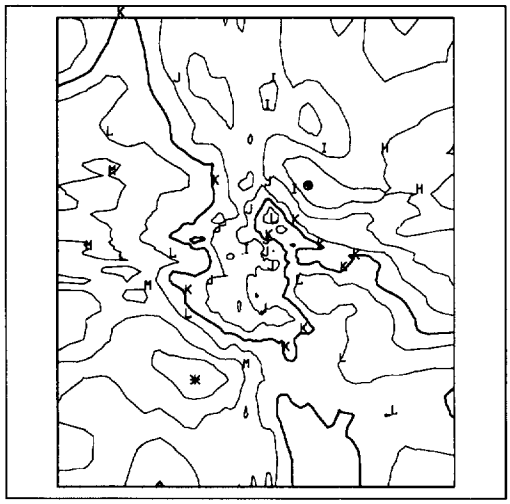

Field 47
⊕ = -9.118
★ = -1.194

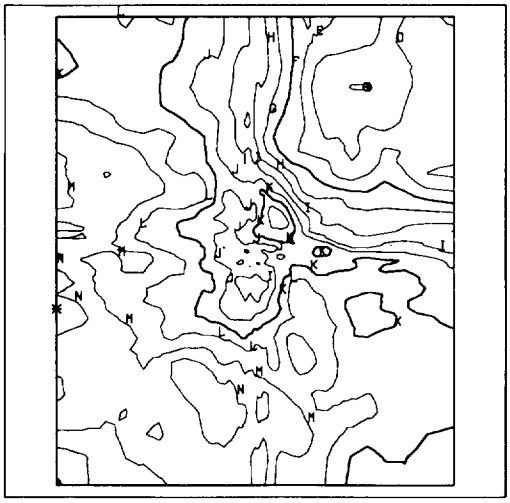

Field 48
⊕ = -13.06
★ = -1.13

Legend

LOGT (log_{10} m^2/s)

A = -15.00	**D = -12.00**	**G = -9.00**	**J = -6.00**
B = -14.00	**E = -11.00**	**H = -8.00**	⋮
C = -13.00	**F = -10.00**	**I = -7.00**	**Q = 1.00**

TRI-6342-1378-0

Figure 6-4l. Transmissivity Field Distribution (Fields 45-48)

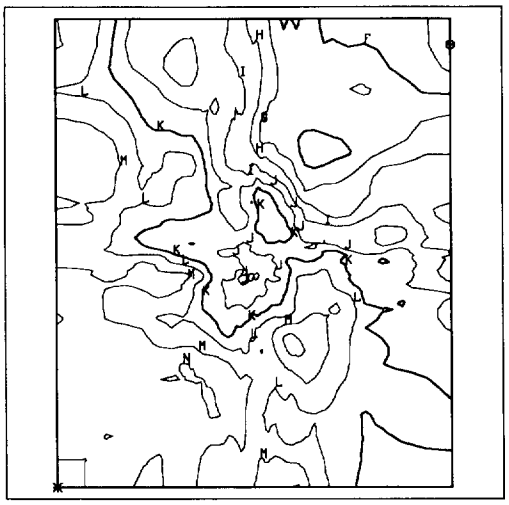

Field 49
⊕ = -11.45
★ = -1.24

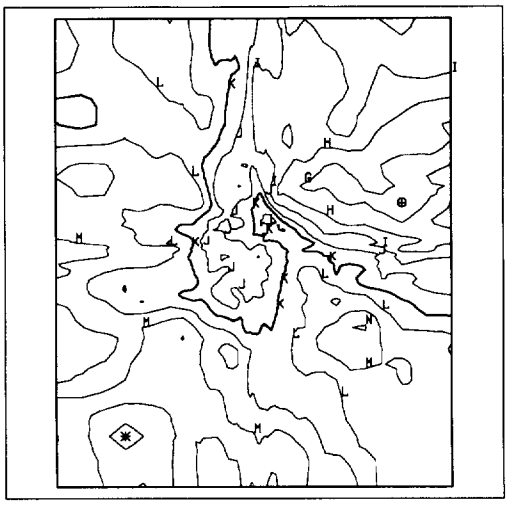

Field 50
⊕ = -9.929
★ = -0.655

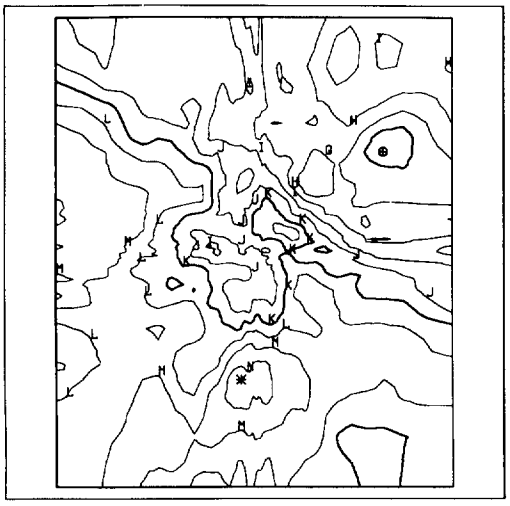

Field 51
⊕ = -10.80
★ = -1.22

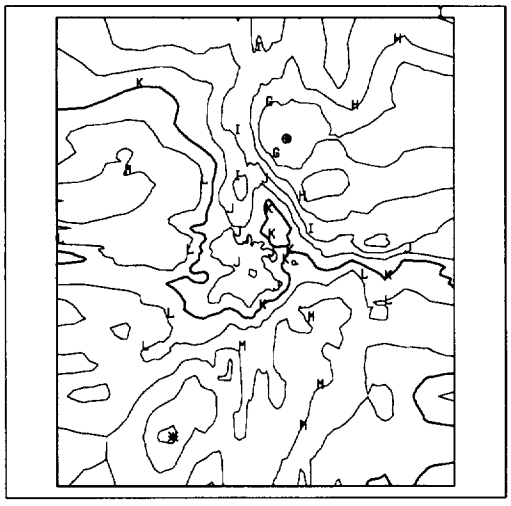

Field 52
⊕ = -10.02
★ = -0.72

Legend

LOGT ($\log_{10}$ m^2/s)

A = -15.00	D = -12.00	G = -9.00	J = -6.00
B = -14.00	E = -11.00	H = -8.00	⋮
C = -13.00	F = -10.00	I = -7.00	Q = 1.00

TRI-6342-1379-0

Figure 6-4m. Transmissivity Field Distribution (Fields 49-52)

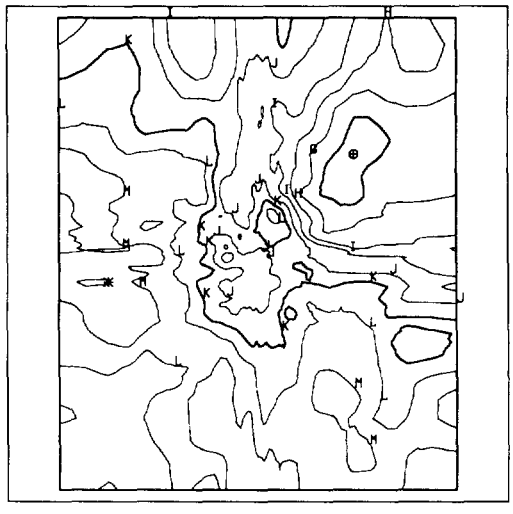

Field 53
⊕ = -10.66
★ = -1.88

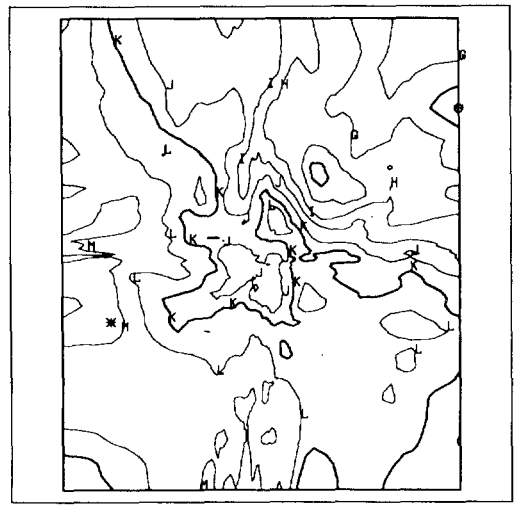

Field 54
⊕ = -10.78
★ = -2.33

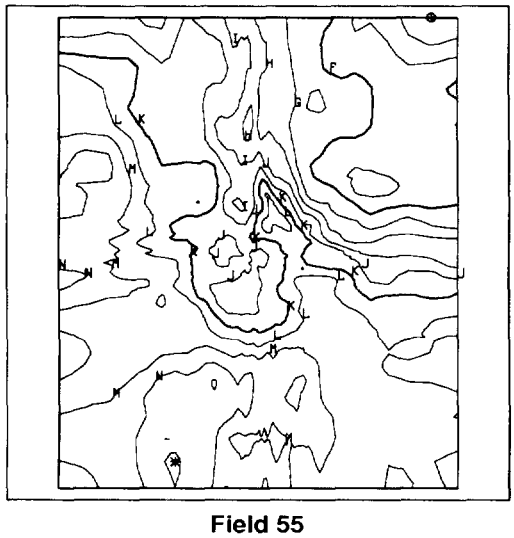

Field 55
⊕ = -12.67
★ = -0.81

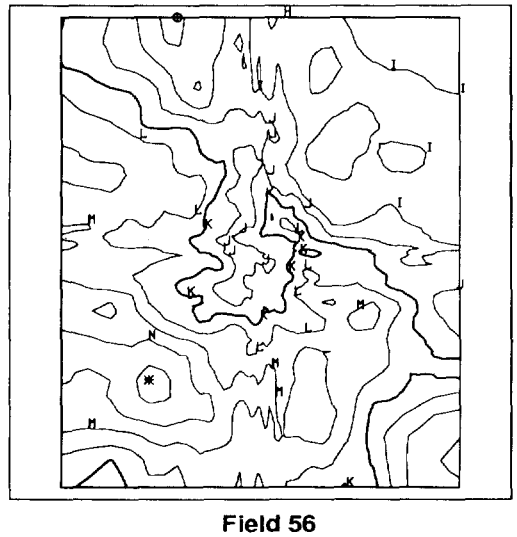

Field 56
⊕ = -8.359
★ = -0.562

Legend

LOGT ($\log_{10}$ m^2/s)

A = -15.00	**D = -12.00**	**G = -9.00**	**J = -6.00**
B = -14.00	**E = -11.00**	**H = -8.00**	⋮
C = -13.00	**F = -10.00**	**I = -7.00**	**Q = 1.00**

TRI-6342-1380-0

Figure 6-4n. Transmissivity Field Distribution (Fields 53-56)

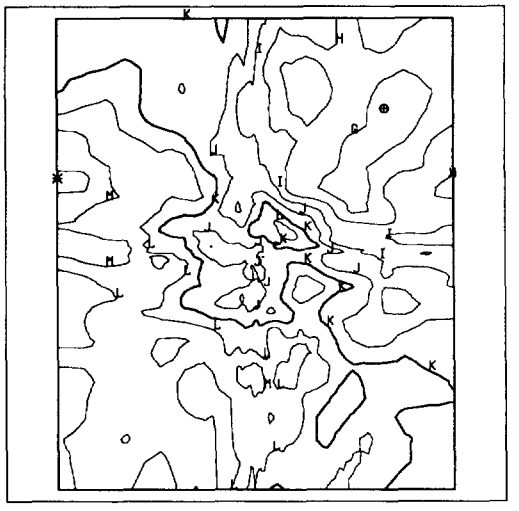

Field 57
⊕ = -9.951
★ = -1.383

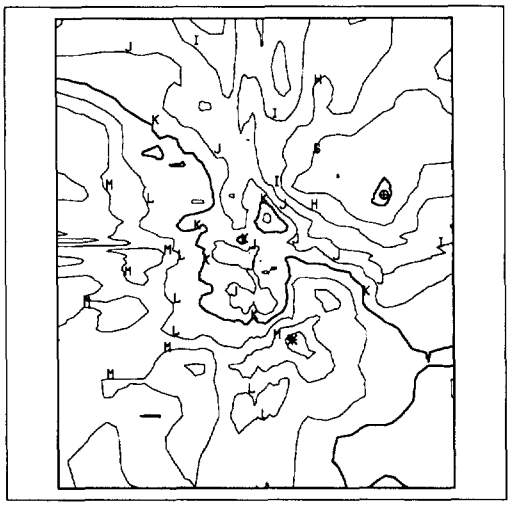

Field 58
⊕ = -10.36
★ = -1.30

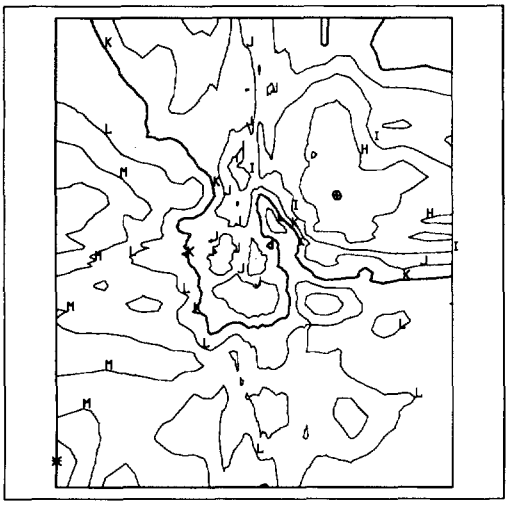

Field 59
⊕ = -8.787
★ = -1.298

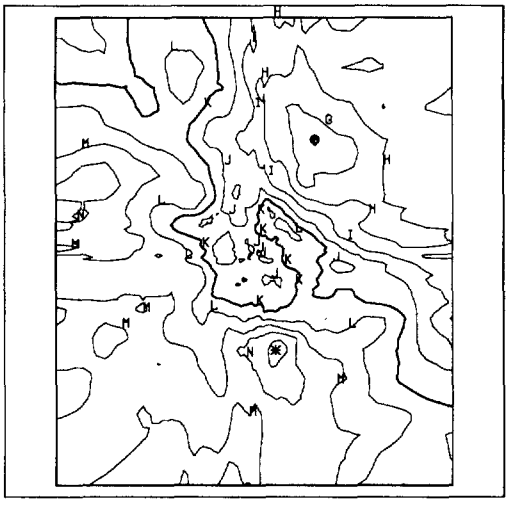

Field 60
⊕ = -10.09
★ = -0.47

Legend

LOGT ($\log_{10}$ m^2/s)

A = -15.00	**D = -12.00**	**G = -9.00**	**J = -6.00**
B = -14.00	**E = -11.00**	**H = -8.00**	⋮
C = -13.00	**F = -10.00**	**I = -7.00**	**Q = 1.00**

TRI-6342-1381-0

Figure 6-4o. Transmissivity Field Distribution (Fields 57-60)

6.4 Fluid Flow Modeling with SECO2D—Bruce L. Baker and Patrick J. Roache

The SECO_2DH code was used to model the effect of climate on groundwater flow in the Culebra Dolomite Member. Capabilities of SECO_2DH are fully documented in the SECO 2.1 User's Manual (draft of SAND90-7096, Roache et al., in preparation). A brief overview the SECO_2DH code is first described and then the specific options utilized to model the Culebra aquifer are detailed.

6.4.1 MODEL DESCRIPTION

SECO_2DH, a single-phase, two-dimensional flow code, was developed specifically for the WIPP project. For the 1991 PA calculations, SECO_2DH was used to estimate the regional steady-state flow fields for present and climatically perturbed boundaries.

6.4.1.1 Governing Equation

The partial differential equation solved for potentiometric head, h, is the following:

$$S_s \frac{\partial h}{\partial t} = \nabla \bullet (K \nabla h) - W \tag{6-2}$$

where K is the (tensor) hydraulic conductivity, S_s is the specific storage of the porous material, t is time, and W is a volumetric flux (out of the porous material) percent volume representing wells. The principal axes of K must be aligned along the coordinate directions x and y. S_s, K, and W may be functions of (x, y, t).

6.4.1.2 Discretization and Solvers

The above equation (or the steady-state version with $\partial h/\partial t = 0$) is discretized using standard second-order differences in space and first-order backward (fully implicit) differences in time (McDonald and Harbaugh, 1988; Roache, 1976). The fully implicit time differencing produces unconditional stability for this linear equation but requires solution of an elliptic (Helmholtz) equation at each time step. In MODFLOW and other common groundwater hydrology codes, this linear, elliptic equation is solved by either the 2-line successive over-relaxation (SOR) iterative method or by a direct solver. The direct solver is not considered to be practical for realistic grids (sufficiently fine resolution), being excessively sensitive to computer round-off error (especially on VAX class computers) and very slow. In SECO_2DH, the solver options are point SOR, (single)

line SOR (e.g., see Roache, 1976), and the semi-coarsening multigrid solver MGSS2, which was developed at Ecodynamics (Schaffer, 1991).

The semi-coarsening multigrid solver (MGSS2) is the default option. For very coarse resolution (e.g., a 6x6 grid that might be used for development of code enhancements), the point SOR solver is fastest. However, MGSS2 results in significantly increased efficiency for problems with fine resolution and strongly varying conductance (due to either hydraulic conductivity variations or highly stretched grids). Further, the MGSS2 solver does not require that the user estimate an optimum relaxation factor, as SOR solvers do.

6.4.1.3 Block-Centered Discretization

SECO_2DH has been written with an option flag called MAC to select either the most common block-centered discretization (MAC=1), with the cell edge coincident with the aquifer edge, or node-centered discretization (MAC=0), with the cell center (or node) on the aquifer edge. Unless required by a specific study, the default cell configuration is MAC=1. This configuration clearly more accurately locates the aquifer edge for both Dirichlet (fixed head) and Neumann (fixed gradient) boundary conditions. For QA purposes, MAC=0 is unsupported in SECO_2DH.

6.4.1.4 Problem Decoupling

To make the problem definition convenient and to facilitate the running of grid convergence tests and local-area simulations within the larger regional-area simulation, the problem definition is decoupled from the computational grid. The aquifer properties are defined on a discrete data base that can be independent of the computational grids. A sequence of grid solutions does not require the user to define aquifer properties point by point in each computational grid; likewise, the regional computational grid is decoupled from the local computational grid, both in space and time. A number of parameters, including the boundaries of the computational regions, the spatial increments (cell sizes), the simulation times, and the time steps, are all decoupled in both space and time. The only requirement is that the local grid problem domain of definition must lie within the regional grid problem domain of definition. Likewise, definition of boundary conditions (types and values) and wells (locations and pumping schedules) are decoupled from the computational grid and are defined in the continuum.

6.4.1.5 Initial Conditions

Initial conditions on hydraulic head may be specified by one of three methods: (1) by using the values set in the aquifer-defining grid; (2) by specifying other values by way of linear variations in

the x and y directions (the initial condition subroutine, SET IC, may be readily modified for other distributions); or (3) by solving the steady-state problem with the specified boundary conditions and all wells turned off.

6.4.1.6 Boundary Conditions

Unlike most groundwater hydrology codes, SECO_2DH allows a fairly general specification of boundary conditions. The SECO_2DH boundary conditions can be of the following types: Dirichlet (specified head), non-homogeneous Neumann (specified, possibly non-zero gradient), or Robin (mixed) conditions. A further option is an adaptive boundary condition, which sets specified flux at inflow boundaries and specified head at outflow boundaries. These types of boundaries may be set independently along each of the four rectangular boundaries of the grid or along an arbitrary number of user-specified sections on each boundary. (Following the basic philosophy of the SECO codes, the specification of these boundary sections is done in the continuum rather than being tied into the discretization.) In particular, sections of specified-gradient boundaries can be used to simulate recharge boundaries; these values can be modified by climatic variation.

Constant-head regions may also be set on interior regions, as can time-independent wells and lake/river levels, which differ from simple constant-head regions in that they affect the cell block heads via a riverbed conductance term. The specification of these interior boundaries is not automated at present: the user must specify each interior boundary on a cell-by-cell basis in the aquifer-defining grid, as is the case with other aquifer properties. However, once established, these values can be used without further user specification in any regional or local grid. In this sense, the interior boundaries are still defined independently of the discretization of the computational grids.

6.4.1.7 Additional Capabilities

Although the SECO codes solve the same equation for hydraulic head as the United States Geological Survey (USGS) code MODFLOW (McDonald and Harbaugh, 1988), the SECO codes have the following additional capabilities:

- Regional and local grid solutions
- General boundary conditions
- Interactive problem definition and output
- Options for initial condition specification
- Options for either cell-centered or node-centered grids

- Automated specification of grid spacing, including uniform spacing or power-law stretching for increased resolution near physical features
- Automated specification of time steps, including uniform spacing or power-law stretching for increased time resolution near events
- Parameterized climatic variations
- Particle-tracking capability

The regional and local grid capabilities include the following:

- Independent specification of aquifer properties in an aquifer-defining grid (independent of the computational grids)
- User-friendly specification of regional and local grid translation and rotation without the need for redefining aquifer properties
- A single specification of well properties and locations applicable to both the regional and local grids
- Independent specification of time stepping
- Time events such as well schedules, climatic variability, and time-dependent boundaries are defined independent of the modeled time.
- Automated, conservative interpolation of time-dependent or steady boundary conditions from the regional grid solution to the local grid boundaries
- Automated particle tracking from the local into the regional grid with the entire particle history expressed conveniently in the regional grid

Particle tracking is accomplished by the SECO Tracker codes (which are separate from the SECO_2DH flow codes) for the local and regional grid flow solutions with either time-dependent or steady-state solutions. For time-dependent solutions, the particle-tracking time intervals are equal to the flow-solution time intervals as output to a file. There is no requirement for separate time intervals because the nature of Darcy flow assures that the characteristic time for the particle motion will always be significantly less than the characteristic time for the flow solution. For steady-state flows, the particle-tracking time intervals are defined separately.

The particle-tracking algorithm is based on a linear interpolation of the Darcy velocities in space (consistent with the second-order spatial accuracy of the flow solution) and an adaptive fifth-order (Runge-Kutta-Fehlberg) integration in time. Note that the tracker integrator is a much higher order in time than the flow solution. This is not inconsistent or unbalanced because the flow solution involves an Eulerian description, whereas the particle solution is inherently Lagrangian. For example, even a steady-state flow solution with zero time truncation error and a velocity field linearly varying in space produces a particle path that involves exponential time functions, which justifies the higher order accuracy in time.

Three options govern the code performance if the tracked particle exits the computational grid within the simulation time: the code can simply stop computing as soon as the particle exits; it can continue the calculation over the entire tracking time step by extrapolation of the velocity field; or the code can repeat the previous step with a new time step adjusted so as to approximately place the particle at the grid boundary. Provision is made should the particle exit the grid within the first time step.

The particle history (position vs. time) is written to a file. The output file from the local grid particle tracker may be read by the regional grid tracker to set the initial position of the particle in the regional grid. In this option, the entire history in the local grid coordinates is read and translated to the regional grid coordinates, and the tracking is continued. The output file from the regional grid tracker then contains the entire particle history (local and regional grid) expressed in the regional grid coordinates.

The accuracy of the flow codes in SECO_2DH and the particle tracking codes SECO_TRACKER have been verified on model problems. The flow codes experimentally exhibit the expected $O(\Delta x^2, \Delta t)$ accuracy, and the particle tracking codes exhibit the expected $O(\Delta x^2, \Delta t^5)$ accuracy. See the internal code documentation or Roache et al. (1990).

6.4.2 OPTIONS USED FOR 1991 CALCULATIONS

The specific options utilized in the current calculations are mentioned here. Semi-coarsening multigrid solvers are used to increase solution efficiency. A point SOR solver is then used to check the convergence of the finite difference formulation of the fluid flow. Independent regional and local grid definition and orientation keep boundary effects from unduly influencing the fluid flow field input to the STAFF2D transport equations. Initial conditions on hydraulic head are set by solving the steady-state problem with the specified boundary conditions and all wells turned off. The user-modifiable nature of SECO_2DH is utilized to include a customized climatic variation for boundary recharge. The boundary conditions used include fixed head, fixed flux, and time-varying head. The SECO_2DH particle tracking capability is utilized to estimate path lines and fluid travel times for diagnostic analysis.

6.4.2.1 Spatial Grid

Regional gridding for SECO_2DH used for 1991 calculations is the same as used for the transmissivity sampling and is shown in Figure 6-5. The regional domain is shown in Figure 6-1. As this figure shows, the regional domain of the previous year's calculations has been shortened from 40 to 30 kilometers in length. Greater accuracy in modeling of the transmissivity

fields results because of the lack of control well data in this southern 10 km portion. The resulting 25 km by 30 km grid is still of sufficient size to keep effects of the regional boundary from adversely influencing the solution of the local domain simulation. The region retains its orientation along the natural boundary of Nash Draw but now has a power-law-stretched rectangular gridding. Initial testing has shown difficulties in utilizing the finite difference results of a SECO2 local fluid flow solution to solve the finite element transport equations of STAFF2D. For consistency, the local fluid flow and mass transport are both solved using STAFF2D using the regional SECO2D solutions as input boundary conditions. Saline concentration density and mass transport features are being added to SECO2D to solve these difficulties for next year's calculations.

6.4.2.2 Changing Climate Models

The climate model was planned to utilize the user-modifiable climate factor routines to input a modified sinusoidal variability of flux, including an LHS-sampled, uniformly distributed factor. This climatic variability was entered as a boundary recharge along 15 kilometers of the north and west regional boundaries. Difficulties arose from trying to apply a single average flux value along the entire recharge boundary. The variability of sampled transmissivities changed this property by six orders of magnitude along this boundary, requiring a similar range of head values. This required us to look at other ways to incorporate climatic change in the model. For preliminary analysis a steady-state simulation with heads along the same recharge boundary set to the land surface elevation was used to represent the effects on climatic change.

6.4.2.3 Climate Factors and Climatic Variability Calculations

For the 1991 preliminary comparison, climate variability was modeled by varying head along the recharge boundary. The amplitude of the climate function was bounded between present values and the land surface elevation, multiplied by a uniformly sampled value, ClimtIdx, ranging from zero to one. The user-modifiable climate function routine was utilized to model an equation with three peaks in ten thousand years (see Volume 3). This does not match the data base definition of five peaks in ten thousand years because it was written before the data base was defined. However, the integrated effect will be the same and the historical data show three minor climate peaks in the last ten thousand years. This model with its peaks occurring at exactly four thousand year intervals is not intended to predict the exact climatic change but only to model its effect.

6.4.2.4 Material Properties, Boundary Conditions, and Initial Conditions

The western regional boundary that corresponds to the center of Nash Draw is modeled as a no-flow symmetry boundary, except for the small portion (7.3 km) of the northern end that takes climatic boundary recharge. The head boundaries of the north, south, and east sides are fixed as part of the transmissivity sampling process. Each sample has a set of fixed head boundaries associated with it as part of the constraints on the transmissivity field. Initial conditions for interior head values are taken from a preliminary steady-state solution step computed by SECO_2DH.

6.4.3 RESULTS AND DISCUSSION

The sampled transmissivities resulted in a greater spatial variation of aquifer properties than were present in previous calculations. The variability in flow fields, travel times, and path lines were more realistic than the 1990 zoned calculations. There were no unphysical or unrealistic flow problems revealed by solving for these synthetically generated fields. The effect of the climatic variability calculations were shown to be less than 5000 years reduction in travel times, averaging about 3000 years. Characteristics of all modeled flows are illustrated by displaying results of the vector containing the largest sampled climate factor. Since this is an LHS uniformly sampled variable, the effect is to randomly select a synthetic transmissivity field.

The results of these calculations are shown in Figures 6-6 through 6-11:

- Figure 6-6 shows the 10,000-year history of the climate function, sampled at 1000-year time steps.
- The head contours in Figure 6-7 describe all time steps with a climate head boundary factor (HEAD_VAR) of 1. (See Figure 6-6 for the plot of HEAD_VAR.)
- Figure 6-8 shows the resulting flux vector representation of the velocity flow field. Small values of flux are thresholded to blanks. This illustrates the channelized nature of the flow in response to the transmissivity field which is described in Figure 6-9.
- Figure 6-10 has the elevated heads at the northwest corner set to the land surface elevation times ClimtIdx (=.985), which is the LHS sampled climate factor. These elevated heads are applied at 2000, 6000, and 10,000 years.
- The resulting increased flux is shown in Figure 6-11. Note the no-flow symmetry boundary on the west face representing the center of Nash Draw. The highly channelized flow was present in single or multiple flow paths for all the characterized fields.

This model of climatic variability will be refined for next year's calculations.

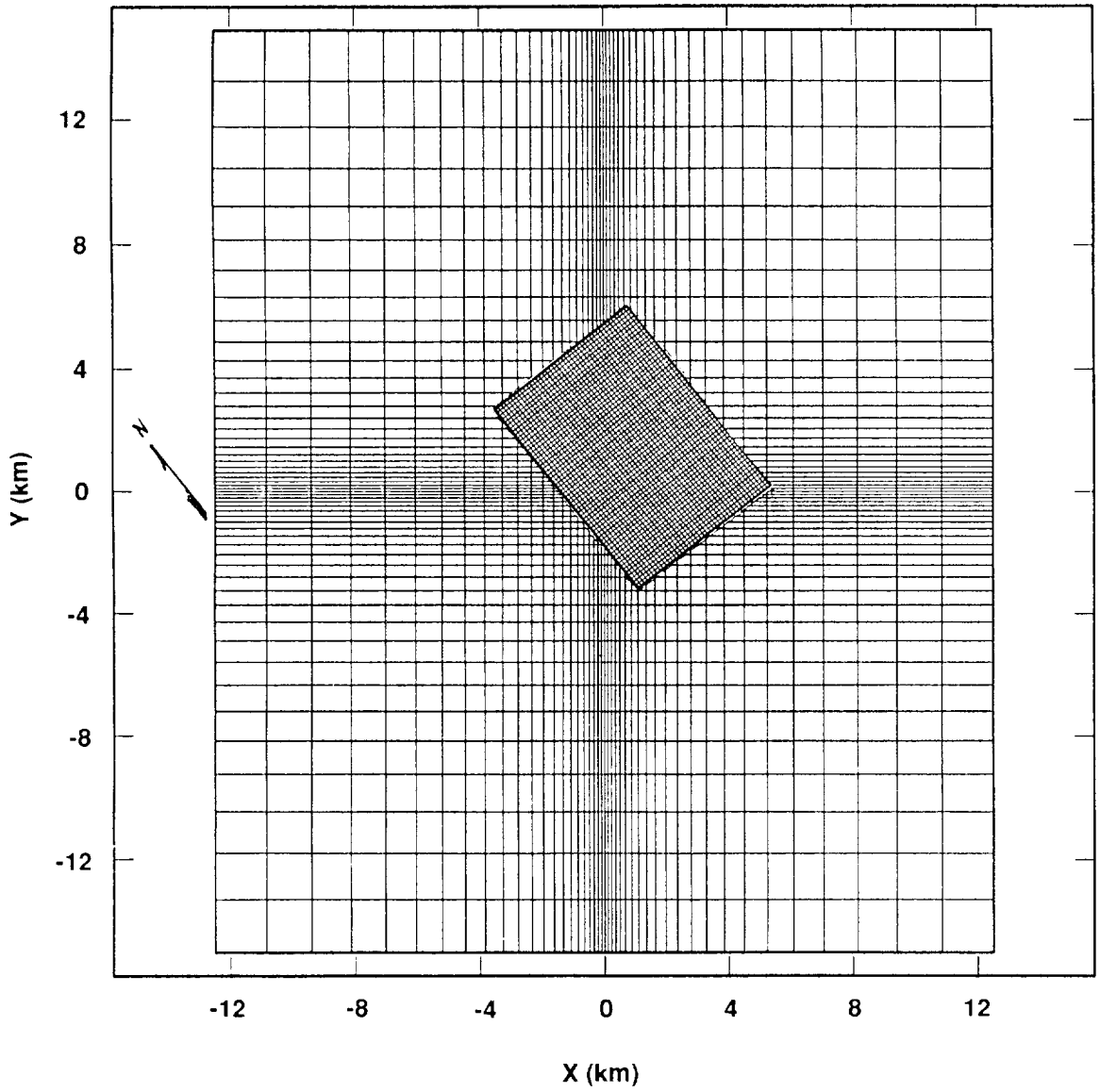

TRI-6342-1360-0

Figure 6-5. Regional and Local Grids Used for Disturbed Fluid Flow and Transport Calculations

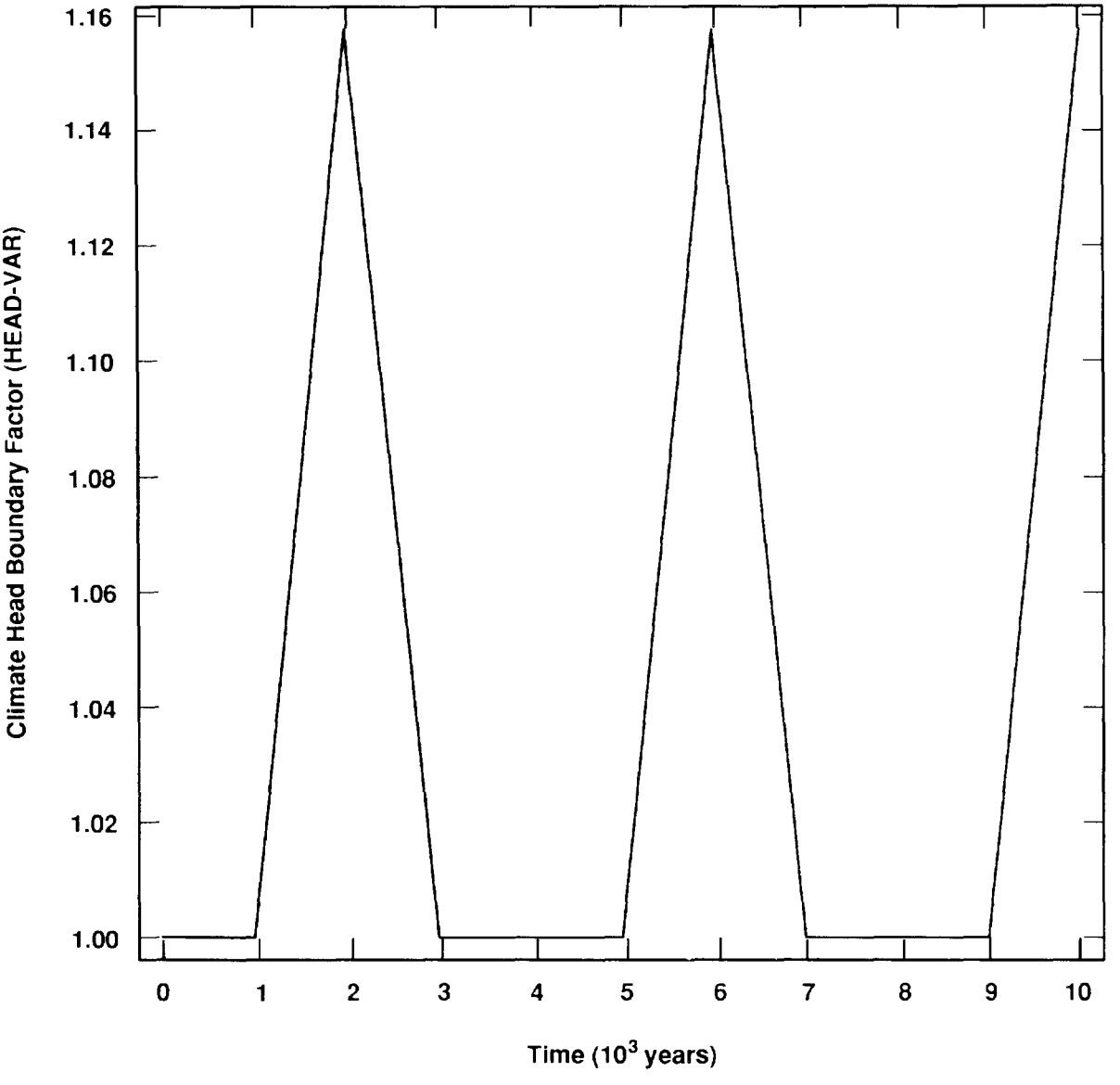

Figure 6-6. 10,000-Year History of Climate Function, Sampled at 1000-Year Time Steps

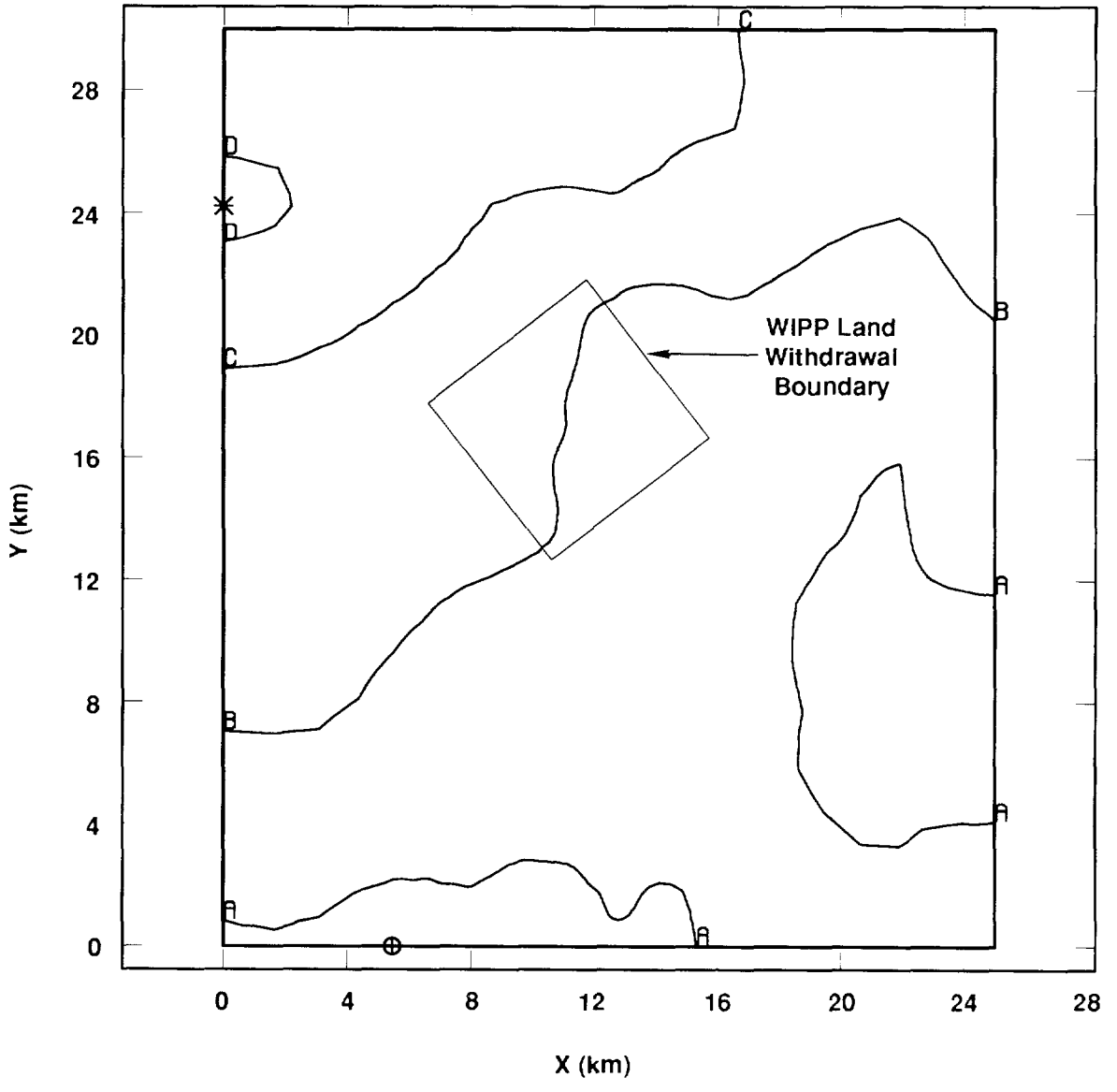

HEADEL (m x 10^{3})

A = 0.91	G = 0.97	M = 1.03
B = 0.92	H = 0.98	N = 1.04
C = 0.93	I = 0.99	0 = 1.05
D = 0.94	J = 1.00	P = 1.06
E = 0.95	K = 1.01	Q = 1.07
F = 0.96	L = 1.02	⊕ = 906.7
		* = 942.2

TRI-6342-1362-0

Figure 6-7. Head Contours at 1000 Years, Climate Minimum

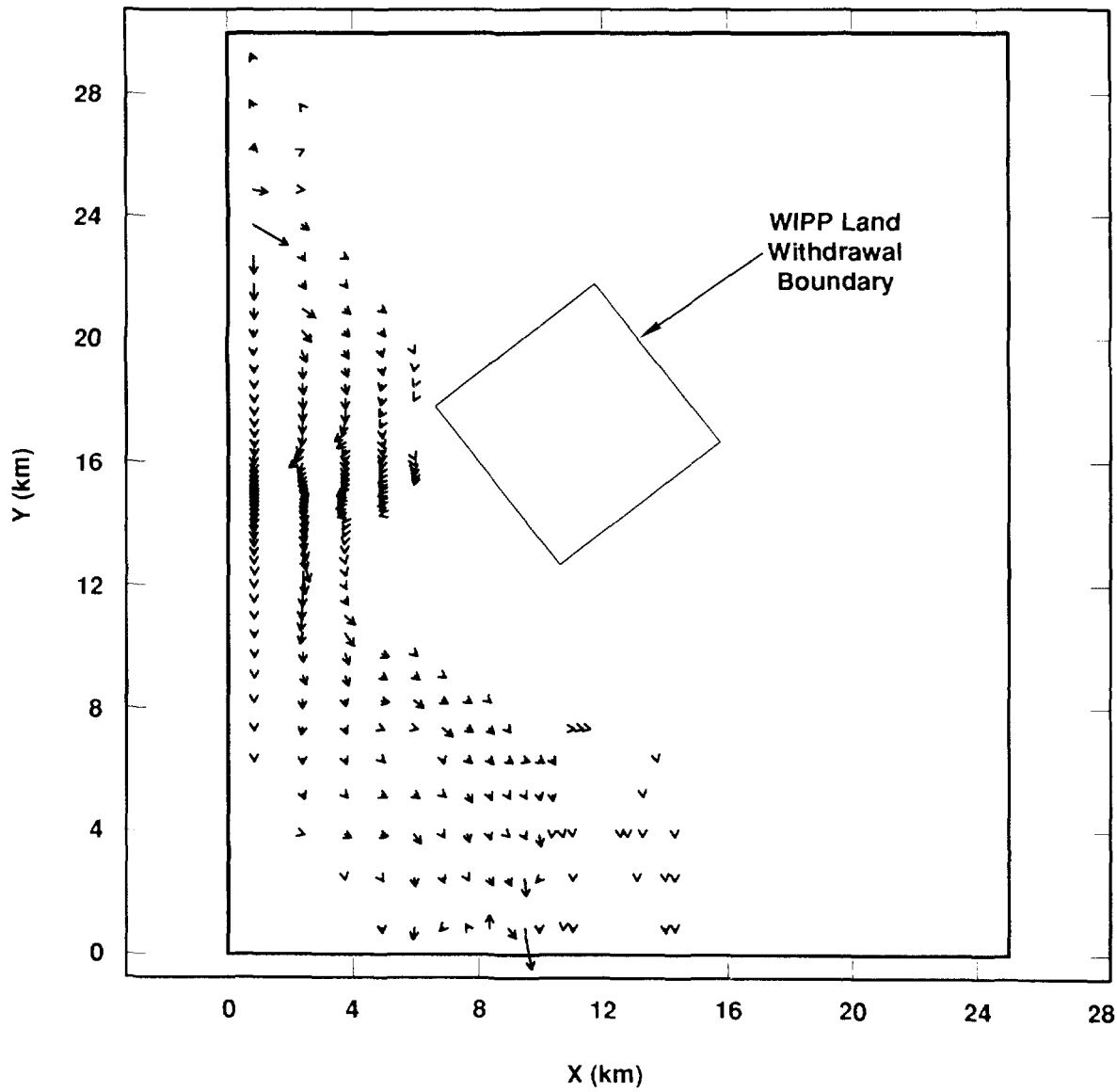

TRI-6342-1363-0

Figure 6-8. Flux Vector Representation of the Velocity Flow Field at 1000 Years, Climate Minimum

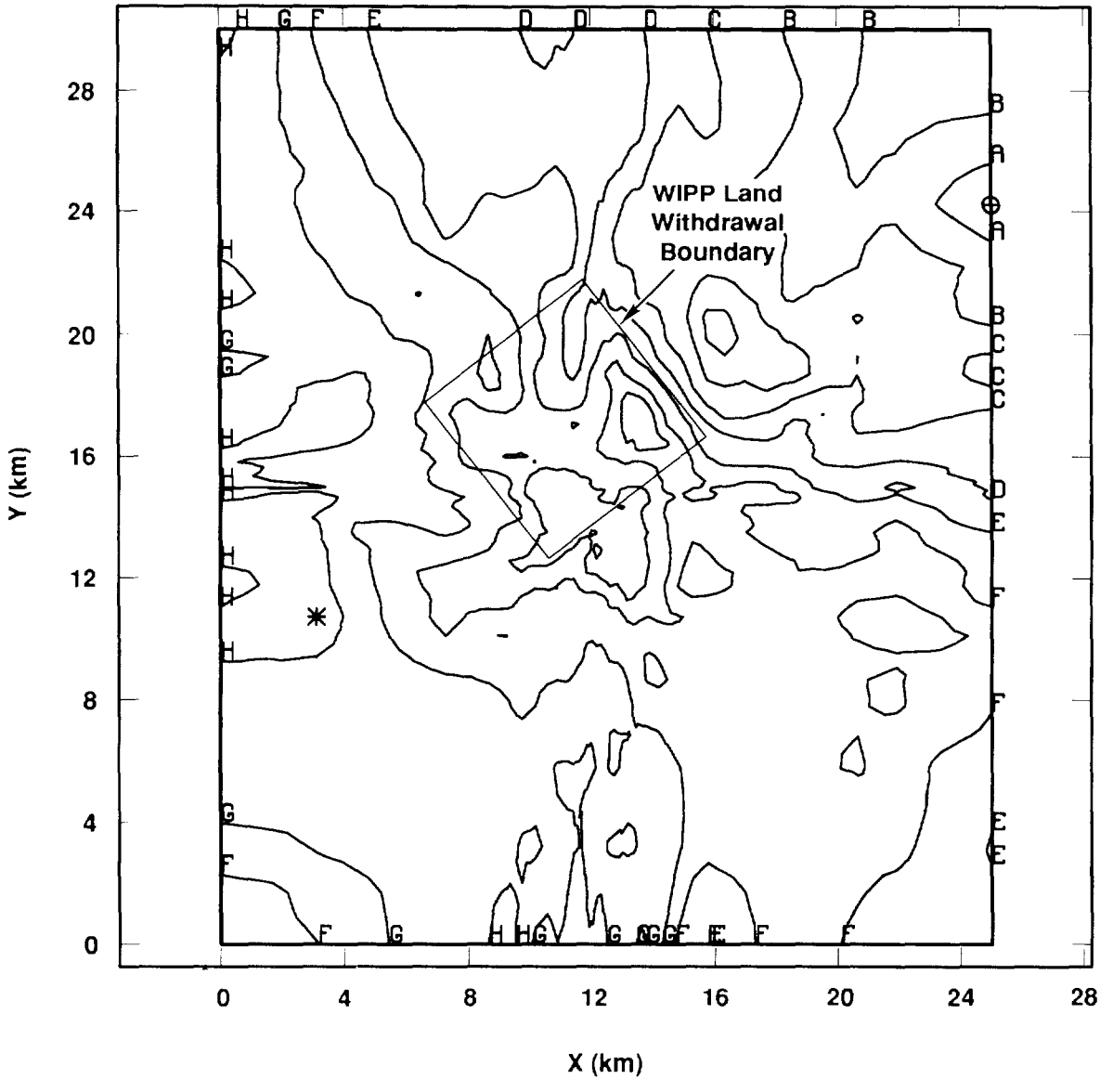

LOGT (log_{10} m^2/s)

A = -10.00 E = -6.00
B = -9.00 F = -5.00
C = -8.00 ⊕ = -10.75
D = -7.00 ✶ = -2.33

TRI-6342-1364-0

Figure 6-9. Log_{10} of Transmissivity Field for Vector 54

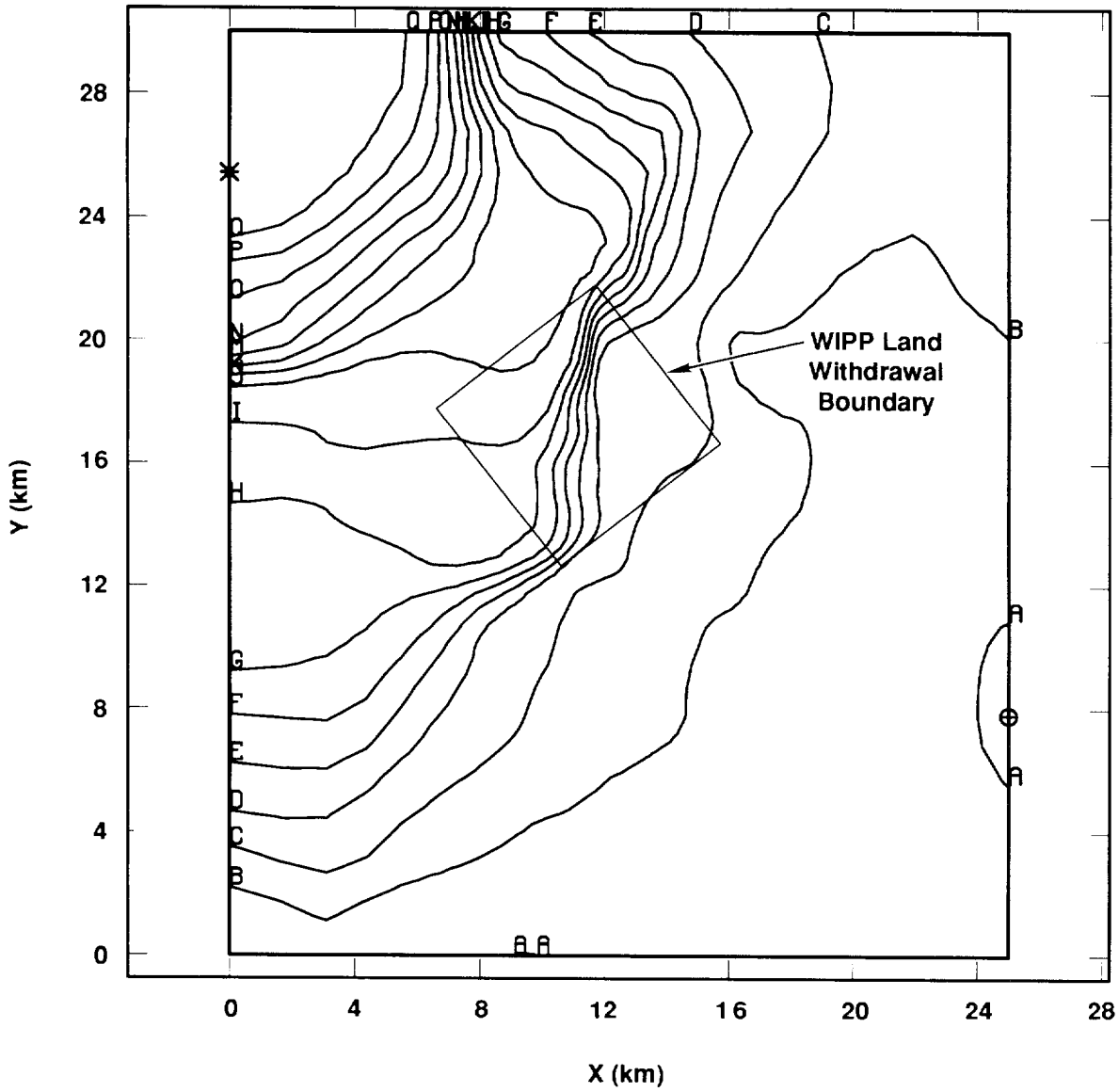

HEADEL (m x 10^3)

A = 0.910	H = 0.980	O = 1.05
B = 0.920	I = 0.990	P = 1.06
C = 0.930	J = 1.00	Q = 1.07
D = 0.940	K = 1.01	⊕ = 0.909
E = 0.950	L = 1.02	* = 1.084
F = 0.960	M = 1.03	
G = 0.970	N = 1.04	

TRI-6342-1365-0

Figure 6-10. Elevated Heads at the Northwest Corner Set to the Land Surface Elevation at 10,000 Years, Climate Maximum

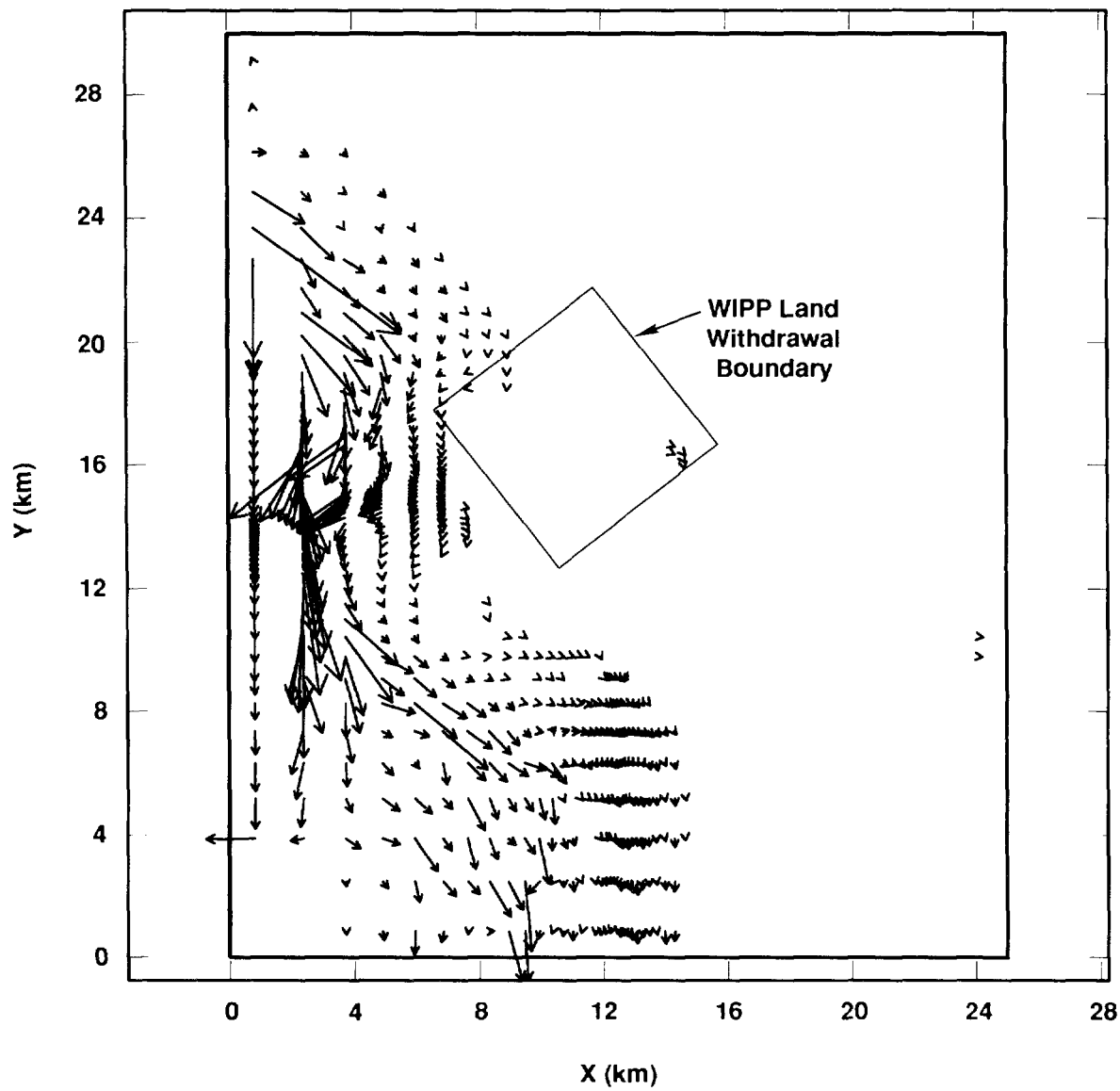

TRI-6342-1366

Figure 6-11. Resulting Increased Flux, Climate Maximum

6.5 Transport Modeling (STAFF2D)—David K. Rudeen

6.5.1 Local Flow Modeling With STAFF2D

The local flow fields calculations were generated with the STAFF2D finite element program. STAFF2D calculates either Darcy flow or radionuclide transport in two-dimensions. The flow and transport could be uncoupled because the rate of fluid injection into the Culebra from an intrusion borehole was assumed to have no impact on the prevailing flow-field and the injected nuclide concentration was assumed to be so small as to have no effect on Culebra fluid density. The local flow simulations were each run in two steps. The first step was a steady state calculation of initial conditions for a second transient calculation. The resulting transient flow fields were used for transport discussed below.

6.5.1.1 Fluid Flow Model Description

The model description that follows is based closely on the presentation in Huyakorn et al. (1991). The governing equation for fluid flow in STAFF2D is

$$\frac{\partial}{\partial x_i}\left(T_{ij}\frac{\partial h}{\partial x_j}\right) = S\frac{\partial h}{\partial t} - \Lambda - q,\ i = 1,2 \tag{6-3}$$

where,

h = hydraulic head (length)

T_{ij} = transmissivity tensor (length^2/time)

S = storage coefficient (dimensionless)

Λ = volumetric rate of fluid transfer per unit area from porous matrix blocks to the fracture when using dual-porosity flow (length^3/(time•length^2))

q = volumetric rate of fluid flow per unit area for sources or sinks (length^3/(time•length^2))

In accordance with standard definitions for transmissivity and storage coefficient, T_{ij} and S can be expressed as

$$T_{ij} = \phi_f H K_{ij} \tag{6-4}$$

and

$$S = \phi_f H S_s \text{ for confined aquifers} \tag{6-5}$$

where,

H = formation thickness (length)

K_{ij} = hydraulic conductivity tensor (length/time)

ϕ_f = porosity (fracture or secondary porosity for dual porosity) (dimensionless)

S_s = specific storage coefficient (1/length).

The term Λ represents the interaction between the porous rock matrix and fractures and is analogous to the Γ_ℓ in the transport equation. For the flow calculated here, Λ is assumed to be zero. The fluid exchange between the matrix and fractures in the Culebra dolomite is assumed to negligible. The q term is also zero. The fluid injected into the Culebra at the intrusion borehole that carries dissolved nuclides is assumed to have negligible effect on the existing flow field.

6.5.1.2 Space and Time Discretization

The spatial grid used for the fluid flow modeling in the Culebra was a subregion of the regional flow field (Section 6.4). The extent of the local grid region was chosen to minimize the size of the simulation and still cover the expected transport region to a boundary 5 km south of the center of the repository. TRACKER flow paths for a neutrally buoyant particle released at the intrusion borehole for all regional flow fields were examined to determine the extent of the east and west particle path positions. All zones in the grid were 125 m square. The region covered extended form 1500 m east to 3750 m west of the borehole and 1750 m north to 5375 m south. The grid and its relation to the regional and local flow fields is shown in Figure 6-5. UTM coordinates for the grid origin (south west corner) are 612094 m east and 3576025 m north. Equal times of 1000 years to the maximum time of 10,000 yr were used in all transient simulations.

6.5.1.3 Boundary and Initial Conditions

The zones (elements) in the local grid did not coincided with the zones in the regional grid so interpolation of the heads on to the boundaries of the grid was required. The head boundary conditions for the steady state calculation of initial conditions were interpolated from time zero SECO_2DH regional calculations using the RELATE computer program. The resulting steady-state hydraulic heads were used as initial conditions for the second step, which was a transient flow calculation with time dependent boundary heads interpolated from subsequent SECO_2DH time step results.

6.5.1.4 Results and Discussion

The resulting flow fields were used for radionuclide transport as discussed below. Figure 6-12 shows the spatial range of particle paths for a neutrally buoyant particle released at time 0 at the intrusion borehole. The 5 chosen paths are representative of the spread in the 60 sampled flow

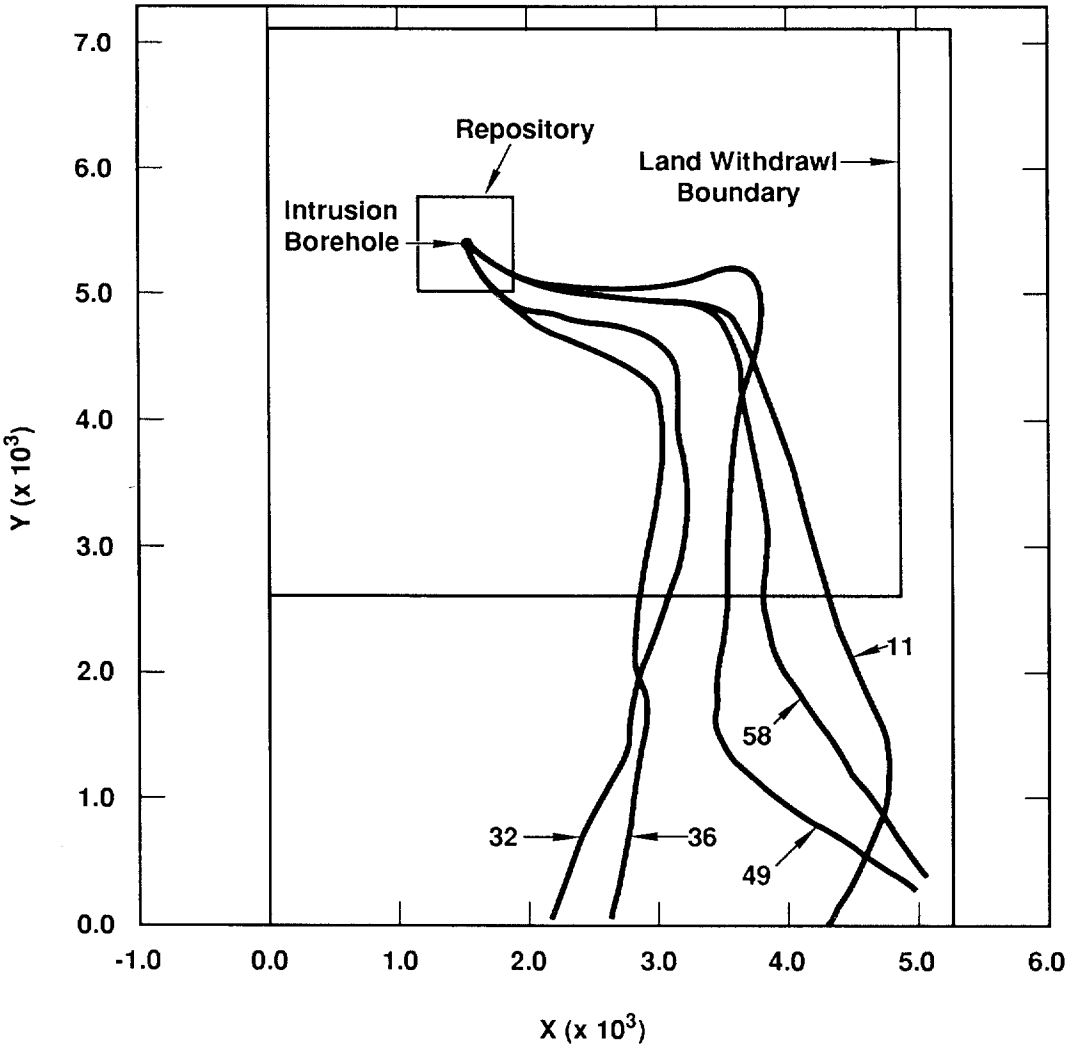

TRI-6342-1388-0

Figure 6-12. Representative Particle Paths for Local Fluid Flow Calculations

fields. Travel time variations were discussed in the section on transmissivity field generation (Section 6.3.3).

6.5.2 LOCAL TRANSPORT MODELING WITH STAFF2D

The local transport modeling was performed with the STAFF2D finite element program. STAFF2D calculates either Darcy fluid flow or radionuclide transport. The flow fields used in the transport calculations were also calculated with STAFF2D as discussed above. Transport was calculated using the dual-porosity conceptual model. The flow and transport are assumed to take place in the fractures with a solute exchange between the fractures and matrix controlled by a one-dimensional diffusion equation. Single porosity fracture transport was calculated using a fracture field derived from the specific discharge by scaling by fracture porosity. Dual porosity transport used the fracture flow field but included diffusion into the matrix. Transport was also calculated using single-porosity fracture transport with no diffusion into the matrix.

6.5.2.1 Transport Model Description

STAFF2D (Solute Transport and Fracture Flow in 2 Dimensions) is a two-dimensional, finite-element code designed to simulate groundwater flow and solute transport in fractured or granular aquifers (Huyakorn et al., 1991). The original version was developed through a joint effort by HydroGeoLogic, Inc., and the International Ground Water Modeling Center of the Holcomb Research Institute. Improved versions of the code have since been commercially available through HydroGeoLogic, the latest being Version 3.2. CAMCON originally adapted Version 2.0 of the code and has since included upgrades from Version 3.2. Additional changes to the code have been made to accommodate CAMCON input/output requirements and tailor code inputs to the WIPP database (Rechard et al., 1989). The model description that follows is based closely on the presentation in Huyakorn et al. (1991).

6.5.2.2 Governing Physical Equations

STAFF2D can perform both fluid flow and transport problems. The governing equations for transport in STAFF2D are

$$\frac{\partial}{\partial x_i}\left(D_{ij}\frac{\partial c_\ell}{\partial x_j}\right) - V_i\frac{\partial c_\ell}{\partial x_i} = \phi R_\ell\frac{\partial c_\ell}{\partial t} + \phi R_\ell\lambda_\ell c_\ell - \sum_{m=1}^{M}\xi_{\ell m}\phi R_m\lambda_m c_m - q\left(c_\ell^* - c_\ell\right) - \Gamma_\ell$$

$$\ell = 1, 2, \ldots, M \quad \textit{species} \tag{6-6}$$

where,

c_ℓ = concentration (mass/volume) of species ℓ,

D_{ij} = hydrodynamic dispersion tensor (length^2/time),

V_i = Darcy velocity (length/time) of the flow field,

ϕ = porosity (dimensionless),

λ_ℓ = first order decay constant (time^{-1}) of species ℓ,

R_ℓ = retardation coefficient (dimensionless) of species ℓ,

$\xi_{\ell m}$ = fraction of parent species m (dimensionless) that transforms into daughter species ℓ,

q = rate of fluid injection per unit volume of formation (length^3/(time•length^3)),

c_ℓ^* = concentration of species ℓ in the injected fluid, and

Γ_ℓ = rate of material transfer of component ℓ from the rock matrix to the fracture (see dual porosity model below).

In the transport mode, the Darcy velocity is considered as input to the code and is obtained from STAFF2D or other flow codes. The dispersion tensor is defined as (Scheideger, 1960),

$$D_{11} = \frac{\alpha_L V_1^2 + \alpha_T V_2^2}{|V|} + \phi D_1^*, \text{ [length}^2\text{/time]}$$

$$D_{12} = (\alpha_L - \alpha_T)\frac{V_1 V_2}{|V|}, \text{ [length}^2\text{/time]}$$

$$D_{22} = \frac{\alpha_L V_2^2 + \alpha_T V_1^2}{|V|} + \phi D_2^*, \text{ [length}^2\text{/time]} \qquad (6\text{-}7)$$

where α_L and α_T [length] are the longitudinal and transverse dispersivities, and D_1^* and D_2^* [length^2/time] are the effective coefficients of molecular diffusion, including tortuosity effects ($D_\ell^o \bullet \tau$) where D_ℓ^o is the free water molecular diffusion of species ℓ and τ [dimensionless] is the tortuosity.

The decay constant is

$$\lambda = \frac{\ln(2)}{T_{1/2}}, \text{ [time}^{-1}\text{]} \qquad (6\text{-}8)$$

where $T_{1/2}$ is the half-life of species ℓ.

Retardation is given by

$$R_\ell = 1 + \frac{\rho_s(1-\phi)}{\phi} K_{d,\ell}, \text{ [dimensionless]} \tag{6-9}$$

where K_d is the distribution coefficient, and ρ_s is the solid density.

In (6-6), Γ represents a source term modeling the matrix-fracture interaction. The dual porosity model involves the solution of both the two-dimensional, advective-dispersion equation for transport in the fracture (6-6) and a one-dimensional diffusion equation derived by assuming Fick's Law for solute exchange between the fracture and the matrix,

$$\frac{\partial}{\partial \chi'}\left(D' \frac{\partial c'_\ell}{\partial \chi'} \right) = \phi' R'_\ell \frac{\partial c'_\ell}{\partial t} + \phi' R'_\ell \lambda_\ell c'_\ell - \sum_{m=1}^{M} \xi_{lm} \phi' R'_m \lambda_m c'_m \tag{6-10}$$

where the prime indicates matrix properties and with the boundary condition requirement that the concentrations match at the interface. Refinements are made depending on the assumed geometry. For slab geometry:

$$\Gamma_\ell = \frac{2}{-b} D' \frac{\partial C'_\ell}{\partial \chi'}\bigg|_{\chi'=\alpha} \tag{6-11}$$

where,

b = fracture aperture (length)

α = fracture matrix interface.

The initial and boundary conditions for (6-10) are given by

$$C'_\ell(\chi', t=0) = C'^{o}_\ell \tag{6-12}$$

$$D' \frac{\partial C'}{\partial \chi}(0, y) = 0 \tag{6-13}$$

$$C'_\ell(b', t) = C_\ell - \zeta D' \frac{\partial C'}{\partial \chi'} \tag{6-14}$$

where ζ is a parameter characterizing the resistance of a thin skin adjacent to the fracture surface. The parameter is defined as $\zeta = b_s / D_s$, where b_s (length) and D_s (length^2/time) are the skin thickness and the effective skin diffusion coefficient, respectively.

The purpose of the dual-porosity term is to simulate solute storage within the matrix through diffusion processes. If the concentration in the fractures decreases with time, solute is returned to the fractures through diffusion out of the matrix. Note that there is no transport through the matrix; there is only an exchange between the fracture and matrix at discrete points. Details are given in Huyakorn et al. (1991, 1983a, and 1983b).

6.5.2.3 Physical Assumptions and Limitations

Assumptions are as follows:

- The code is limited to two dimensions.
- Transport is governed by Fick's Law.
- The dispersivity is assumed to correspond to an isotropic porous medium so that it can be represented by two constants in the principal direction of flow.
- In the fracture-flow-only model, the fractures are modeled as an equivalent porous medium.
- In the dual-porosity model, there is no flow or transport through the matrix, only an exchange between the matrix and fracture.
- Adsorption and decay of radionuclides obey a linear equilibrium isotherm.
- Solute concentration effects on fluid density are ignored.
- There is local chemical equilibrium between the liquid and the solid.

CAMCON Enhancement: Spatially Varying Material Properties. The HydroGeoLogic version of STAFF2D is limited to having distinct material regions over which physical properties do not vary. In the transport case, these include porosity and tortuosity. In addition, the free-water molecular diffusion parameter is independent of species in Version 3.2. The CAMCON database contains spatially varying data for tortuosity and porosity and species-dependent molecular diffusion parameters. The CAMCON version of STAFF2D was modified to permit input of these data.

6.5.2.4 Numerical Approach

As used in CAMCON, the fractured porous medium is represented by a "double-continuum" idealization, with a two-dimensional continuum representing the domain of fractures and a one-dimensional continuum representing the porous matrix (Figure 6-13). Transport is thus described by equations (6-6) and (6-10). These equations are solved using a finite-element technique, combining upstream weighting for the fracture domain and a Galerkin approximation for the porous medium. At each time level, tri-diagonal sets of algebraic equations for the matrix blocks are generated and solved using the standard Thomas algorithm to obtain the relation between the solute mass flux from the matrix and the nodal concentrations in the fractures. These flux terms

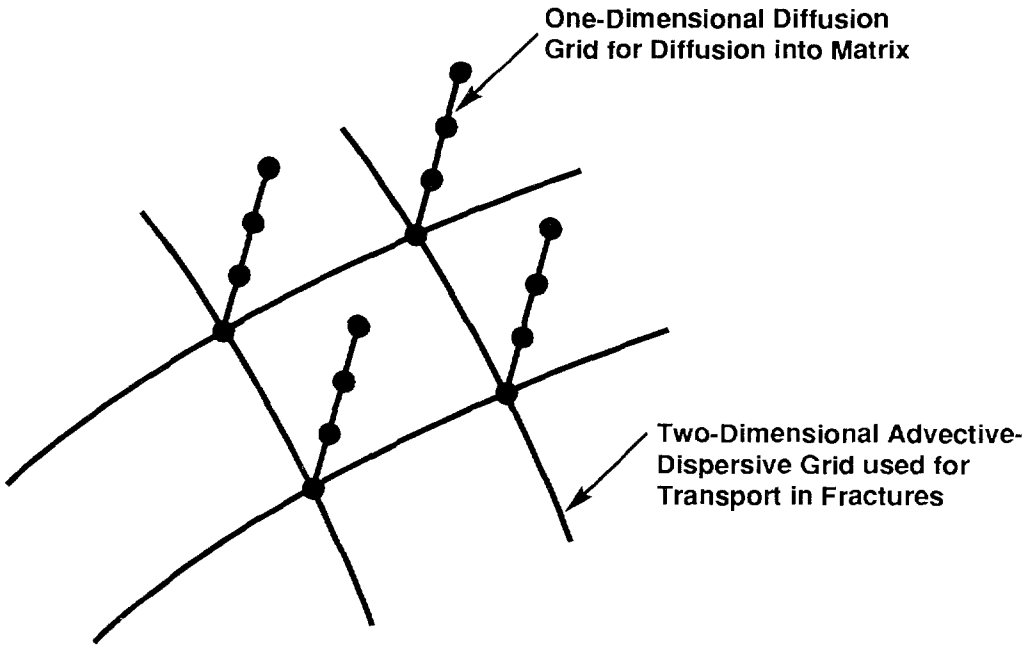

Note: No Transport Through Matrix

TRI-6342-1375-0

Figure 6-13. Schematic of Dual Porosity Double Continuum Idealization Used in STAFF2D

are treated implicitly when the equations for the two-dimensional fracture domain are generated and solved. The nodal concentrations in the matrix blocks can then be updated by performing the back-substitution step of the Thomas algorithm. The finite-element approximation technique applied to the convective-dispersive equation is an upstream-weighted residual technique (Huyakorn and Pinder, 1983) designed to overcome oscillations of the numerical solutions when the convective terms are dominant.

6.5.2.5 Benchmark Tests

Several benchmark calculations have been performed to compare STAFF2D with analytical solutions. Generally, good agreement with the analytic solutions is claimed. For the case of multiple decaying and interacting species transport, analytic solutions are currently confined to one-dimensional model problems. The following list of documented benchmark problems is discussed in Huyakorn et al. (1991):

- Longitudinal transport in fractures and transverse matrix diffusion
- Longitudinal transport in fractures and spherical matrix diffusion
- One-dimensional transport of a three-member radioactive decay chain
- Radial transport in fractures and transverse matrix diffusion
- Two-well transport in a porous medium system

6.5.2.6 Space and Time Discretization

The spatial grid used for the transport modeling in the Culebra was identical to the local flow field discussed above and is shown overlayed on the regional grid in Figure 6-5.

A time step of 1000 years was used in all simulations. The simulations were run from the time of intrusion (1000, 3000, 5000, 7000, 9000 yr) to 10,000 yr.

6.5.2.7 Boundary Conditions

The four boundaries surrounding the grid permitted flow. The discharge was determined by the velocities at the boundary. Flow out of the grid results in loss of fluid and solute. Flow into the grid had a solute concentration of zero.

A single intrusion borehole was modeled as a time dependent flux boundary (or source term) at a single node at the center of the repository with UTM coordinates of 613594 m east and 3581400 m north. The flux boundary requires the input of both the fluid flux rate and the solute flux rate. The STAFF code integrates the flux rates to obtain a total mass injected over the time step and determines an average rate to preserve total mass. The fluid flux into the Culebra from the borehole was assumed to have negligible effect on the Culebra flow field and was therefore set to 0. Solute mass flux history was supplied by the PANEL calculations. The simulations therefore

modeled the direct dumping of nuclides into Culebra flow. Transport effects between the repository and the Culebra has been ignored.

6.5.2.8 Material Properties

Up to three sets of properties are required for STAFF2D simulations of transport depending on wether the single or dual porosity conceptual models are used. For the the single porosity simulations only the fracture properties and solute (nuclide) properties are used. For the dual porosity simulations fracture, matrix and nuclide properties are required. Property values can found in Vol III. Fracture transport properties include porosity*, tortuosity, longitudinal dispersivity*, transverse dispersivity, retardations*, and effective diffusion coefficient. Matrix properties include porosity*, tortuosity, retardations*, fracture spacing*, and skin resistance effective diffusion coefficients. (Starred properties were sampled.) Nuclide properties include half life, specific activity, and chain description.

6.5.2.9 Nuclide Chains

A total of seven species broken down into 4 chains were transported. The chains are as follows:

- PU240
- AM241 -> NP237 -> U233
- U234 -> TH230
- PU239

6.5.2.10 Results

The primary results from the transport simulations is the integrated discharge across boundaries 3 and 5 km south of the repository. The 3 km boundary is actually located at the southern land withdrawal boundary. Each species flux is calculated from the y-component (south) of Darcy velocity, zone flux area (DX * thickness) and the species concentrations. The mass flux rate for each of the species is converted to activity rates across each boundary and stored for subsequent use in generating the CCDF curves. Results are tabulated for all scenarios and all vectors in Appendix B.

A typical solute plume is shown in Figure 6-14 at times of 2000 and 10,000 years. The results are for vector 9 (dual-porosity scenario E1E2 with an intrusion time of 1000 years). The effects of artificial numerical dispersion can be seen at the northeast and southwest corners of the repository. The oscillations are minimal and decrease with time. The results are typical of numerical algorithms that generate numerical oscillation transverse to the primary flow. The oscillations can be reduced by using more upwinding but only at the expense of increased dispersion throughout the entire problem. The current solution error is assumed to be more

localized near the source where concentration gradients are largest. This particular vector had the largest normalized EPA release (0.065) to the accessible environment, which was calculated as discharge across the 5-km boundary south of the repository. Normalized EPA release varied from 0 to 0.065. For the E1E2 dual-porosity scenario with a time of intrusion of 1000 years, only 10 vectors had EPA normalized releases greater than 10^{-7}. For the E2 scenario there were only five. The number of vectors with releases greater than 10^{-7} decreased with later times of intrusion. Fracture-only-transport releases were generally 150 times larger.

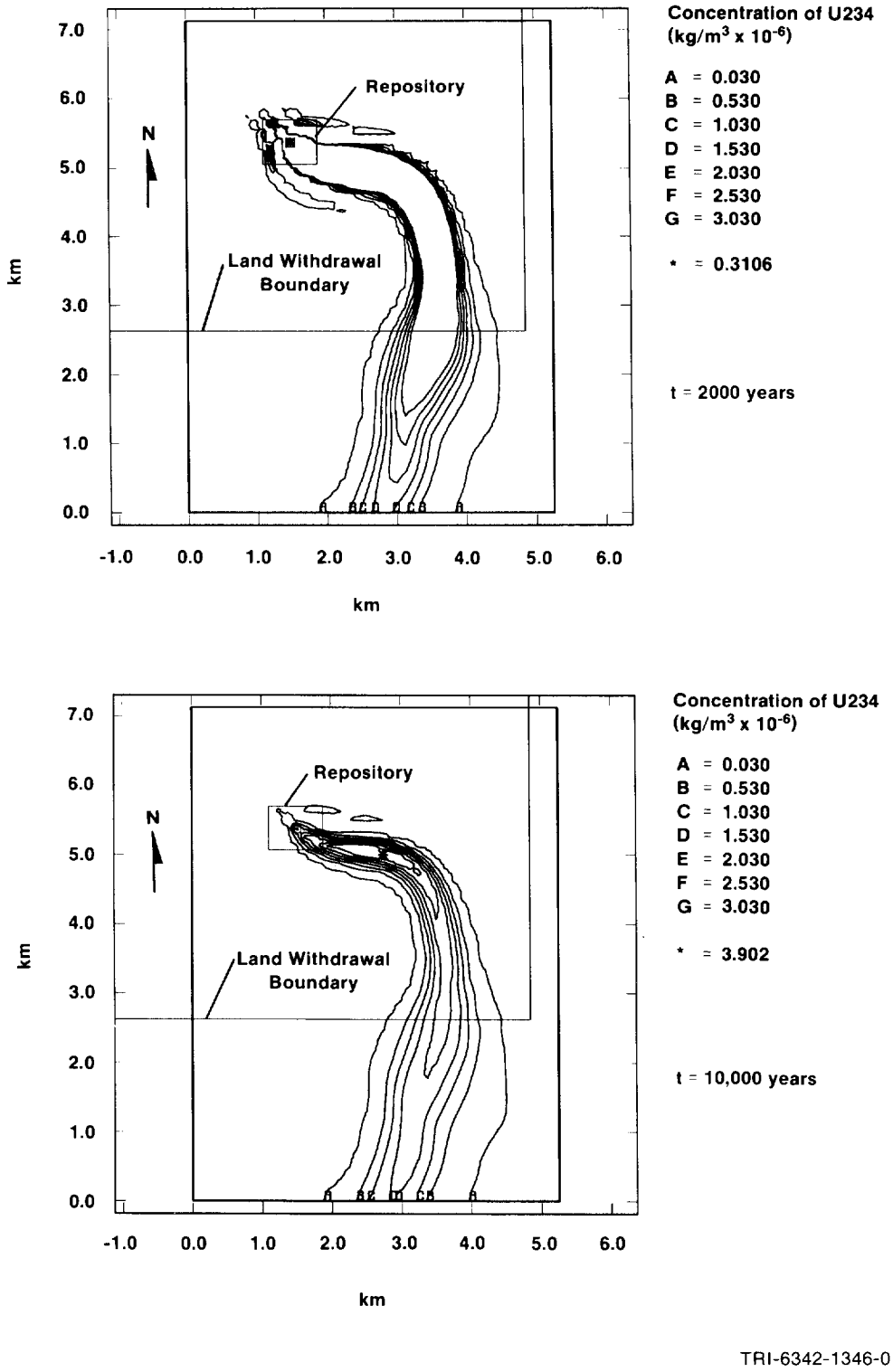

Figure 6-14. Sample Concentration Contours for Culebra Transport (Vector 9, E1E2, Dual Porosity, t_{int} = 1000 years)

7. CUTTINGS REMOVAL DURING DISTURBANCES—Jerry W. Berglund

One of the more important considerations in assessing the long term behavior of the WIPP repository involves the transport of radionuclides from the WIPP repository as the result of penetrating a panel by an exploratory borehole. If a borehole intrudes the repository, waste will be brought directly to the surface as particulates suspended in the circulating drilling fluid. This section addresses the assumptions, theory, and computational procedures governing direct waste removal due to drilling and summarizes some of the results obtained for the 1991 comparison to 40 CFR 191.

7.1 General Considerations

In the human intrusion type scenario, a hydrocarbon exploration well is drilled through a WIPP repository panel and into the underlying pressurized brine Castile formation. If rotary drilling is assumed, a volume of repository wastes is removed from the breached panel and is transported to the surface as cuttings and cavings suspended in the drilling fluid. The minimum volume of repository material removed is equal to the cross-sectional area of the drill bit multiplied by the repository thickness (cuttings). This minimum volume must be increased by material eroded from the borehole wall (cavings) by the scouring action of the swirling drilling fluid. Both cuttings and cavings will be released to the accessible environment in a settling pit at the surface.

In traditional rotary drilling, a cutting bit attached to a series of hollow drill collars and pipes is rotated at a fixed angular velocity and is directed to cut downward through the underlying strata. To remove the drill cuttings a fluid is pumped down the drill pipe through and around the drill bit and up to the surface within the annulus formed by the drill pipe and the borehole wall (Figure 7-1). In addition to the removal of cuttings, the drilling fluid (mud) serves to cool and clean the bit, reduce drilling friction, maintain borehole stability, prevent the inflow of unwanted fluids from permeable formations, and form a thin, low permeability filter cake on penetrated formations.

The volume of repository wastes removed by the cutting action of the bit is simple to calculate and is equal to the cross-sectional area of the drill bit multiplied by the thickness of the compacted repository panel. Calculating the volume of eroded waste, however, requires a more complex model. In the oil and gas drilling industry, it has been suggested (Broc, 1982) that drill hole wall erosion may be influenced by a number of factors:

- the shear stresses of the drilling fluid against the hole wall during circulation
- suction effect during pipe movement
- eccentricity of pipe with respect to the hole
- impact of the solid particles in the mud on the walls
- physical and chemical interaction between the mud and the exposed formation

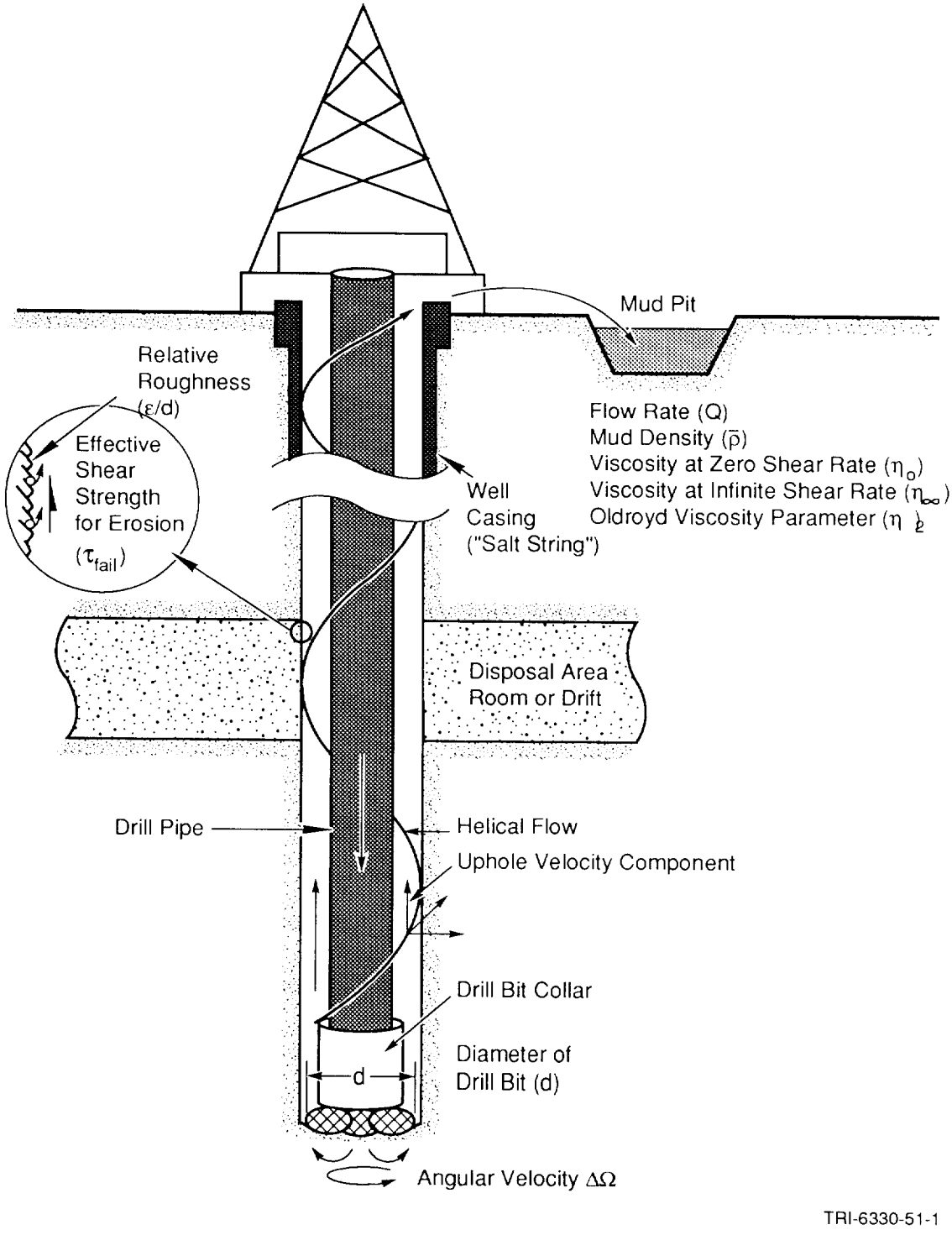

Figure 7-1. Rotary Drilling

- time of contact between the mud and the formation.

A number of investigators maintain that the flow pattern has a major effect on the stability of the walls. Walker and Holman (1971) defined an index of erosion that is a function of the shear stress acting on the walls and the type of flow opposite the drill collars. They postulated that erosion occurs primarily opposite the drill collars where the mud flow rates are greatest and is considerably more prevalent when the flow is turbulent rather than laminar. Darley (1969), in a number of laboratory experiments also showed that for aqueous drill fluids, erosion was sensitive to flow rates. For certain types of shales Darley showed that the material in the exposed borehole wall can undergo a swelling due to the decrease in the lateral effective stress and by undergoing surface hydration and osmotic action. In such cases the circulation of clear liquids caused severe erosion of the walls. Erosion was much less when colloidal suspensions were circulated partly because the formation of a filter cake inhibited the formation of a soft swollen zone. Brittle shales also exhibited a weakening when penetrated by a drill hole due in part to the infiltration of drilling fluid into old fracture or cleavage planes.

The mechanical and chemical properties of the compacted wastes in a WIPP panel sometime in the distant future will undoubtedly be quite different than any material encountered in today's oil and gas drilling industry. However, the behaviors that influence erosion are likely to be similar.

Although there are a number of factors that may influence borehole erosion, industry opinion appears to single out the effects of fluid shear stress acting on the borehole wall and the character of the fluid flow regime (laminar or turbulent). To consider these effects it is necessary to know the threshold fluid shear stress acting on the borehole wall that will initiate erosion. This "effective" borehole shear strength for erosion must be determined by experiment and may be different for laminar and turbulent flow. In the following analysis it is assumed that borehole erosion is caused primarily by the magnitude of the fluid shear stress acting on the borehole wall. Caving or spalling effects that may be caused by an encounter with gas-pressurized wastes are ignored. These effects will be addressed in a later study.

7.2 Analysis

In the annulus formed by the collars or drill pipe and the borehole wall, the flow of the drilling fluid has both a vertical and rotational component. Within this helical flow pattern shear stresses are generated by the relative motion of adjacent fluid regions and also by the motion of the fluid directly adjacent to the borehole wall and the borehole wall itself. In this analysis it is assumed that if the shear stress at the wall exceeds the effective shear strength for erosion of the wall material (filter cake or compacted repository wastes) erosion of the wall material will occur, increasing the diameter of the bored hole. The eroded material will be passed to the surface in the flowing drilling fluid.

Flow in the annulus between the drill pipe and borehole wall is usually laminar (Darley and Gray, 1988). Adjacent to the collar, however, the flow may be either laminar or turbulent as a consequence of the larger collar diameter and resulting higher mud velocities (Pace, 1990). For laminar flow, the analysis lends itself to classical solution methods. Turbulent flow requires a more approximate approach where the flow is assumed to be axial with no rotational component. Finally, the amount of radioactive material that is extracted from the repository depends on the extent of radioactive decay. A discussion on these three topics follows.

7.2.1 LAMINAR FLOW

Below Reynolds numbers of about 2100 for newtonian fluids and 2400 for some non-newtonian fluids (Walker, 1976), experiments have shown that the flow of a fluid in a circular pipe or annulus is well behaved and can be described using a well defined relationship between the velocity field and the fluid shear stress. This type of flow is called laminar.

Some of the early work on laminar, helical flow of a non-newtonian fluid in an annulus was performed by Coleman and Noll (1959) and Fredrickson (1960). The laminar helical flow solution procedure outlined below is, for the most part, an adaptation of methods described in a paper by Savins and Wallick (1966).

One of the principal difficulties in solving for the shear stresses within a helically flowing drilling fluid is the shear rate dependence of the fluid viscosity. This non-newtonian fluid behavior necessitates choosing a functional form for the variation of viscosity with shear rate for the fluid. There are several functional forms for the viscosity of drilling fluids that can be assumed. For example, in the oil and gas industry, the Bingham and power law models are often used to approximate the shear rate dependence of the fluid viscosity. A less common function is a form chosen by Oldroyd (1958) and used in the analyses by Savins and Wallick (1966). Oldroyd assumed that the viscosity varies according to the functional relation.

$$\eta = \eta_o \left[\frac{1+\sigma_2 \Gamma^2}{1+\sigma_1 \Gamma^2} \right] \tag{7-1}$$

where σ_1 and σ_2 are constants, η_o is the limiting viscosity at zero rate of shear, η_∞—defined as $\eta_o(\sigma_2/\sigma_1)$—is the limiting viscosity at infinite rate of shear, and Γ is the shear rate.

Viscous shear stress is described by

$$\tau = \eta\Gamma. \tag{7-2}$$

The above expression, developed using the Oldroyd viscosity equation (7-1), can be illustrated graphically as shown in Figure 7-2 This is a rate softening (pseudoplastic) model that has an initial slope of η_o and a limiting slope of η_∞ for large shear rates.

The Oldroyd model cannot account for drilling fluids that exhibit a yield stress. However, above a shear rate of zero, parameters can be chosen so that the model approximates the pseudoplastic rate response of many drilling fluids (see Figure 7-2).

Savins and Wallick (1966), expanding on the work of Coleman and Noll (1959) and Fredrickson (1960), showed that the solution for laminar helical flow of a non-newtonian fluid in an annulus could be written in terms of three nonlinear integral equations

$$F_1 = \int_{\alpha}^{1} \left(\frac{\rho^2 - \lambda^2}{\rho} \right) \frac{d\rho}{\eta} = 0$$

$$F_2 = C \int_{\alpha}^{1} \frac{d\rho}{\rho^3 \eta} - \Delta\Omega = 0$$

$$F_3 = \frac{4Q}{\pi R^3} + 4\left(\frac{RJ}{2}\right) \int_{\alpha}^{1} \left(\frac{\alpha^2 - \rho^2}{\eta} \right) \left(\frac{\rho^2 - \lambda^2}{\rho} \right) d\rho = 0 \qquad (7\text{-}3)$$

where α is the ratio of the collar radius over the cutting radius (R_i/R) (Figure 7-3), $\Delta\Omega$ is the drill string angular velocity, Q is the drilling fluid flow rate, r is the radial coordinate, and ρ is the non-dimensional radial coordinate representing the ratio r/R. The unknown parameters λ^2, $RJ/2$, and C are related to the fluid shear stresses through the relations

$$\tau_{r\theta} = \frac{C}{\rho^2}$$

$$\tau_{rz} = \frac{RJ}{2} \left(\frac{\rho^2 - \lambda^2}{\rho} \right)$$

$$\tau^2 = \tau_{r\theta}^2 + \tau_{rz}^2 \qquad (7\text{-}4)$$

where r, θ, and z represent radial, tangential, and vertical coordinates associated with the cylindrical geometry (Figure 7-3).

The three nonlinear integral equations represented by (7-3) in general must be solved numerically. By expanding each of the integral equations into a Taylor series and retaining only the linear terms, a recursive solution procedure can be used (Newton-Raphson) to find the solution for the unknowns $\delta\lambda^2$, $\delta(RJ/2)$, and δC. The three linear equations are

$$\frac{\partial F_1}{\partial \lambda^2} \delta\lambda^2 + \frac{\partial F_1}{\partial C} \delta C + \frac{\partial F_1}{\partial \left(\frac{RJ}{2}\right)} \delta\left(\frac{RJ}{2}\right) = -F_1$$

$$\frac{\partial F_2}{\partial \lambda^2} \delta\lambda^2 + \frac{\partial F_2}{\partial C} \delta C + \frac{\partial F_2}{\partial \left(\frac{RJ}{2}\right)} \delta\left(\frac{RJ}{2}\right) = -F_2$$

$$\frac{\partial F_3}{\partial \lambda^2}\delta\lambda^2 + \frac{\partial F_3}{\partial C}\delta C + \frac{\partial F_3}{\partial\left(\frac{RJ}{2}\right)}\delta\left(\frac{RJ}{2}\right) = -F_3 \tag{7-5}$$

The solution procedure consists of assuming initial values for λ^2, $RJ/2$, and C and solving the three linear equations in (7-5) for the corrections $\delta\lambda^2$, $\delta(RJ/2)$, and δC. The unknowns λ^2, $RJ/2$, and C are then replaced by $\lambda^2+\delta\lambda^2$, $(RJ/2)+\delta(RJ/2)$, and $C+\delta C$. This recursive solution procedure is repeated until $|\delta\lambda^2|$, $|\delta(RJ/2)|$, and $|\delta C|$ are all less than some specified limit. The coefficients of the unknowns $\delta\lambda^2$, $\delta(RJ/2)$, and δC in (7-5) are determined by differentiating the equations in (7-3):

$$\frac{\partial F_1}{\partial \lambda^2} = -\int_\alpha^1 \frac{1}{\eta\rho}\left[1+\frac{\left(\rho^2-\lambda^2\right)}{\eta}\frac{\partial\eta}{\partial\lambda^2}\right]d\rho$$

$$\frac{\partial F_1}{\partial C} = -\int_\alpha^1 \frac{1}{\eta\rho}\frac{\left(\rho^2-\lambda^2\right)}{\eta}\frac{\partial\eta}{\partial C}d\rho$$

$$\frac{\partial F_1}{\partial\left(\frac{RJ}{2}\right)} = -\int_\alpha^1 \frac{1}{\eta\rho}\frac{\left(\rho^2-\lambda^2\right)}{\eta}\frac{\partial\eta}{\partial\left(\frac{RJ}{2}\right)}d\rho$$

$$\frac{\partial F_2}{\partial \lambda^2} = -C\int_\alpha^1 \frac{1}{\eta^2\rho^3}\frac{\partial\eta}{\partial\lambda^2}d\rho$$

$$\frac{\partial F_2}{\partial C} = \int_\alpha^1 \frac{1}{\eta\rho^3}\left[1-\frac{C}{\eta}\frac{\partial\eta}{\partial C}\right]d\rho$$

$$\frac{\partial F_2}{\partial\left(\frac{RJ}{2}\right)} = -C\int_\alpha^1 \frac{1}{\eta^2\rho^3}\frac{\partial\eta}{\partial\left(\frac{RJ}{2}\right)}d\rho$$

$$\frac{\partial F_3}{\partial \lambda^2} = -4\left(\frac{RJ}{2}\right)\int_\alpha^1 \frac{\alpha^2-\rho^2}{\eta\rho}\left[1+\frac{\left(\rho^2-\lambda^2\right)}{\eta}\frac{\partial\eta}{\partial\lambda^2}\right]d\rho$$

$$\frac{\partial F_3}{\partial C} = -4\left(\frac{RJ}{2}\right)\int_\alpha^1 \frac{\left(\alpha^2-\rho^2\right)}{\eta\rho}\frac{\left(\rho^2-\lambda^2\right)}{\eta}\frac{\partial\eta}{\partial C}d\rho$$

$$\frac{\partial F_3}{\partial\left(\frac{RJ}{2}\right)} = 4\int_\alpha^1 \frac{\left(\alpha^2-\rho^2\right)}{\eta\rho}\left(\rho^2-\lambda^2\right)d\rho - 4\left(\frac{RJ}{2}\right)\int_\alpha^1 \frac{\left(\alpha^2-\rho^2\right)}{\eta\rho}\frac{\left(\rho^2-\lambda^2\right)}{\eta}\frac{\partial\eta}{\partial\left(\frac{RJ}{2}\right)}d\rho \tag{7-6}$$

The viscosity is related to the the shear rate function $Y(\Gamma)$ by the equation

$$\eta^2 Y = 2\left[\left(\frac{RJ}{2}\right)^2\left(\frac{\rho^2-\lambda^2}{\rho}\right)^2 + \frac{C^2}{\rho^4}\right] \tag{7-7}$$

where $Y = 2\Gamma^2$. (7-8)

For the Oldroyd viscosity function (7-1) the unknown derivatives of the viscosity in (7-6) can be determined by using the chain rule of differentiation and (7-7):

$$\frac{\partial\eta}{\partial\lambda^2} = \frac{\partial(\eta^2 Y)}{\partial\lambda^2}\frac{\partial\eta}{\partial(\eta^2 Y)} = -4\left(\frac{RJ}{2}\right)^2\left(\frac{\rho^2-\lambda^2}{\rho^2}\right)\frac{\partial\eta}{\partial(\eta^2 Y)}$$

$$\frac{\partial\eta}{\partial C} = \frac{\partial(\eta^2 Y)}{\partial C}\frac{\partial\eta}{\partial(\eta^2 Y)} = \frac{4C}{\rho^4}\frac{\partial\eta}{\partial(\eta^2 Y)}$$

$$\frac{\partial\eta}{\partial\left(\frac{RJ}{2}\right)} = \frac{\partial(\eta^2 Y)}{\partial\left(\frac{RJ}{2}\right)}\frac{\partial\eta}{\partial(\eta^2 Y)} = 4\left(\frac{RJ}{2}\right)\left(\frac{\rho^2-\lambda^2}{\rho}\right)^2\frac{\partial\eta}{\partial(\eta^2 Y)} \tag{7-9}$$

The derivative $\partial\eta/\partial(\eta^2 Y)$ can be determined by combining (7-1) and (7-8) and differentiating to obtain

$$\frac{\partial\eta}{\partial(\eta^2 Y)} = \frac{\left(\frac{\sigma_2}{2}\eta_o - \frac{\sigma_1}{2}\eta\right)^2}{\left(\frac{\sigma_2}{2}\eta_o - \frac{\sigma_1}{2}\eta\right)\left[\eta^2 + 2(\eta-\eta_o)\eta\right] + (\eta-\eta_o)\eta^2\frac{\sigma_1}{2}} \tag{7-10}$$

Based upon the preceding equations, a Fortran computer code was written to perform the necessary computations for a solution to the problem of laminar helical flow in an annulus.

For the specific case of borehole erosion, once a solution to the three integral equations in (7-3) is found, the shear stress in the fluid at the wall can be calculated by setting $\rho = 1$ in the equations in (7-4). By changing the outer radius of the hole, the fluid shear stress can be forced to equal the repository effective shear strength for erosion. The required outer hole radius is determined by iteration as shown in Figure 7-4. The derivatives required for the iteration $(d\tau/dR)$ are found numerically.

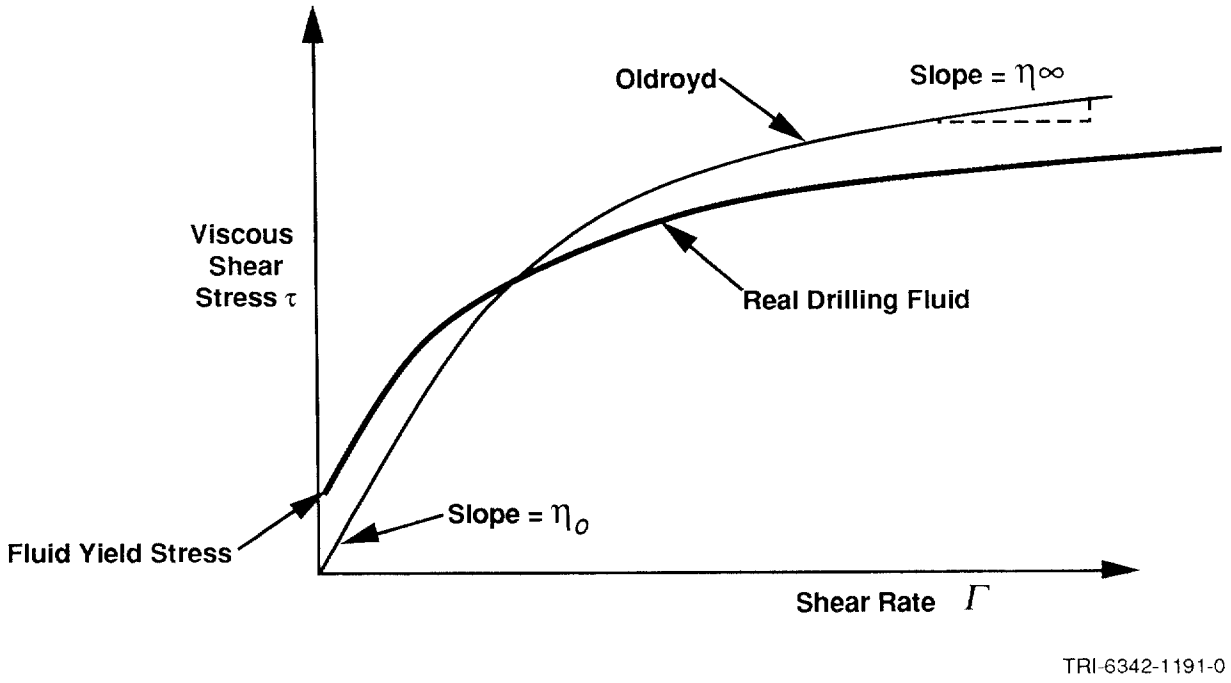

Figure 7-2. Viscous Shear Stress for Oldroyd and Real Drilling Fluid

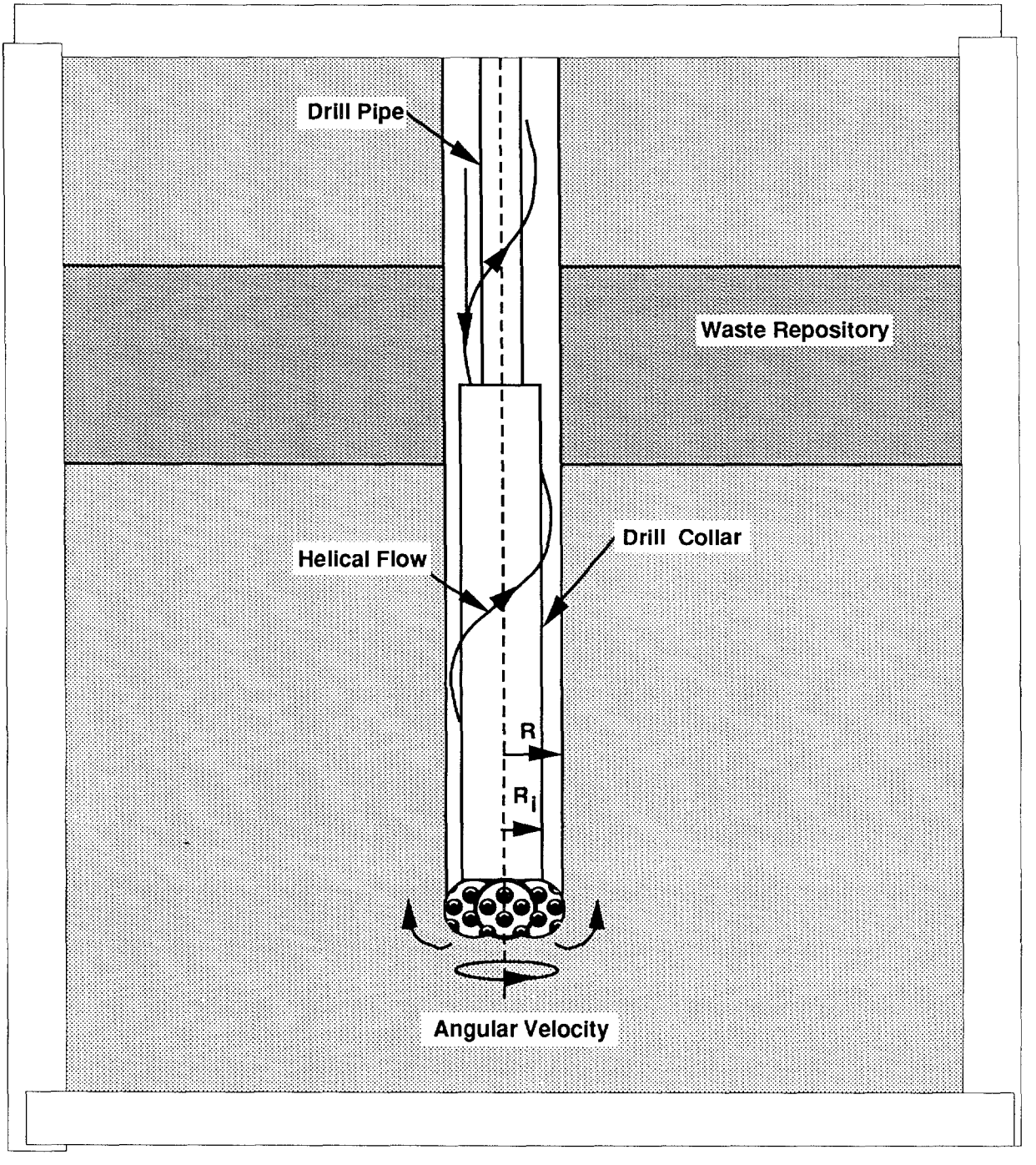

TRI-6342-1190-0

Figure 7-3. Detail of Rotary Drill String Adjacent to Drill Bit

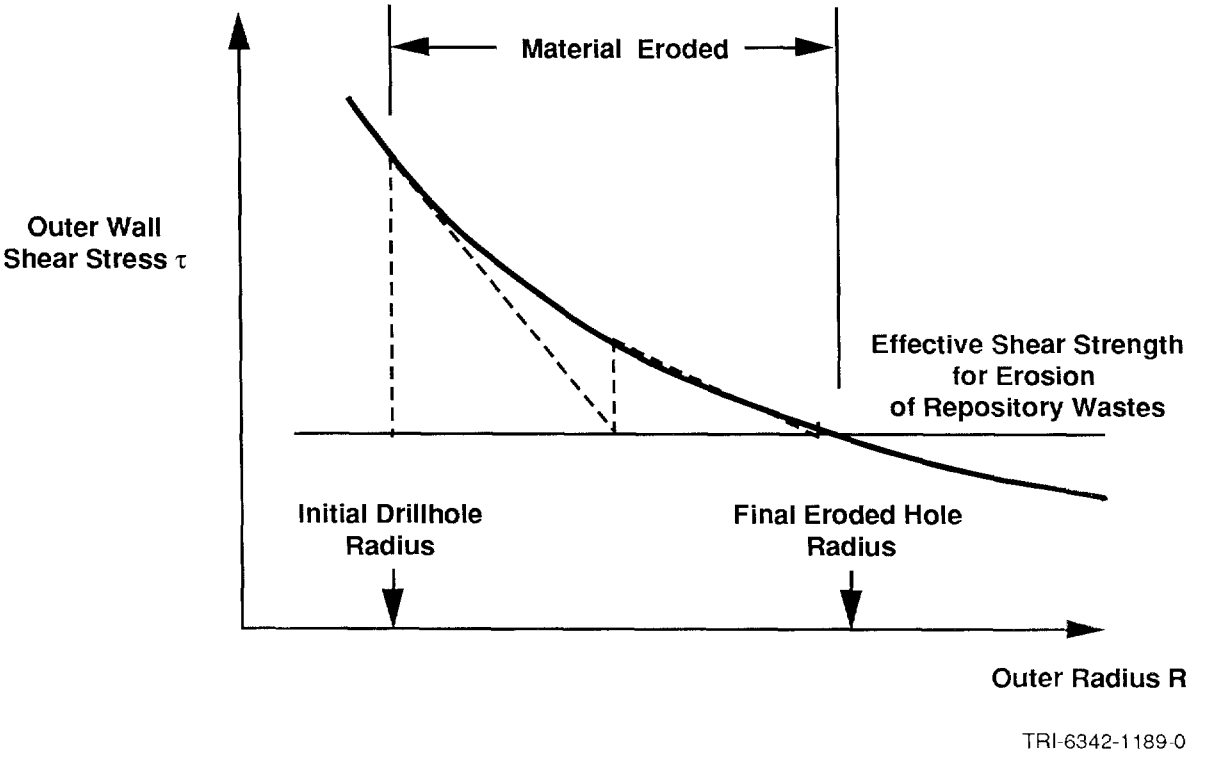

Figure 7-4. Iteration Procedure for Finding the Final Hole Radius

7.2.2 TURBULENT FLOW

For fluids with Reynolds numbers greater than about 2100, flow in a circular pipe or annulus starts to become more or less random in character, which makes orderly mathematical analysis of the flow difficult if not impossible. With increasing Reynolds numbers this random behavior increases until at a Reynolds number of about 3000 the flow becomes fully turbulent. In fully turbulent flow, momentum effects dominate and the fluid viscosity is no longer important in characterizing pressure losses.

The Reynolds number is defined as

$$R_e = \frac{\overline{\rho}\overline{V}D_e}{\overline{\eta}} \tag{7-11}$$

where D_e is the equivalent hydraulic diameter, $\overline{\rho}$ is the drill fluid density, $\overline{V}$ is the average fluid velocity, and $\overline{\eta}$ is the average fluid viscosity.

For newtonian fluids the value to use for the viscosity is clear since the viscosity is constant for all rates of shear. Non-newtonian fluids, which exhibit a changing viscosity with shear rate, present a special problem in calculating R_e.

For fluids that exhibit a limiting viscosity at high rates of shear (such as the Bingham model and in our case the Oldroyd model) it has been suggested (Broc, 1982) that the limiting viscosity ($\overline{\eta} = \eta_\infty$) be used in calculating the Reynolds number.

The Reynolds number for an Oldroyd fluid in an annulus can then be written as (Broc, 1982)

$$R_e = \frac{0.8165D\overline{V}\overline{\rho}}{\overline{\eta}} \tag{7-12}$$

where the hydraulic diameter is expressed as $D = 2(R - R_i)$ (see Figure 7-3).

The most important influence viscosity has on the calculation of pressure losses in fully turbulent flow of non-newtonian fluids appears to be in the calculation of the Reynolds number. A far more important parameter is the surface roughness past which the fluid must flow. The Reynolds number, however, does have a role in determining the onset of turbulence. For newtonian fluids this number is about 2100. For non-newtonian, rate thinning fluids the critical value of R_e tends to be greater than 2100 but less than 2400 (Walker, 1976). For our purposes a value of 2100 will be used to represent R_{e_C} (critical Reynolds number) for the Oldroyd fluid model. Since turbulent flow is more effective in generating fluid shear stresses at the borehole wall, this assumption is conservative.

There is a transition region beyond R_{e_C} before the development of fully turbulent flow. In this regime the flow has the character of both laminar and turbulent flow. However, since pressure

losses increase rapidly in turbulent flow and affect borehole shear stresses more severely it will be assumed that beyond R_{ec} the flow is fully turbulent.

To characterize the turbulent flow regime, the great bulk of analysis has concentrated on empirical procedures.

For axial flow in an annulus, the pressure loss under turbulent conditions can be written as (Whittaker, 1985)

$$\Delta P = \frac{2fL\bar{\rho}\bar{V}^2}{D} \tag{7-13}$$

where f is the Fanning friction factor and L is the borehole length.

If the shear stress due to the flowing fluid is uniformly distributed on the inner and outer surfaces of the annulus, it can be easily shown using equation (7-13) that the shear stress acting on the borehole wall is related to the average velocity through the relation

$$\tau = \frac{f\bar{\rho}\bar{V}^2}{2} \tag{7-14}$$

The Fanning friction factor is empirically related to the Reynolds number and relative roughness for pipe flow by the equation (Whittaker, 1985)

$$\frac{1}{\sqrt{f}} = -4\log_{10}\left[\frac{\varepsilon}{3.72D} + \frac{1.255}{R_e\sqrt{f}}\right] \tag{7-15}$$

where ε/D is the relative roughness. For pipes, D in this equation represents the inside diameter and ε is the absolute roughness or the average depth of pipe wall irregularities. In the absence of a similar equation for flow in an annulus, it will be assumed that this equation also applies here, where D is the hydraulic diameter as defined earlier and ε is the absolute roughness of the waste-borehole interface.

Based upon a calculated Reynolds number, a Fanning friction factor can be determined by numerically solving (7-15). The value of the shear stress acting on the borehole wall can then be determined from (7-14). Using an iterative procedure similar to that for the laminar flow problem (Figure 7-4), the fluid shear stress can be forced to equal the repository effective shear strength for erosion to obtain the final eroded borehole radius.

7.2.3 RADIOACTIVE DECAY

The quantity of radioactive material deposited in the settling pit as the result of drilling must be modified by the growth and decay of component radionuclides in the cuttings and cavings at the time of intrusion. The Bateman equations (Wehr et al., 1984) are used to calculate this decay.

For example, consider a chain of five radionuclides A, B, C, D, and E directly brought to the surface as the result of drilling. If N_a , N_b , N_c , N_d , and N_e represent the number of atoms of each of the radionuclides, then the differential equations that govern the decay and growth are (Wehr et al., 1984)

$$\frac{dN_a}{dt} = -\lambda_a N_a \qquad \frac{dN_b}{dt} = \lambda_a N_a - \lambda_b N_b$$

$$\frac{dN_c}{dt} = \lambda_b N_b - \lambda_c N_c \qquad \frac{dN_d}{dt} = \lambda_c N_c - \lambda_d N_d$$

$$\frac{dN_e}{dt} = \lambda_d N_d - \lambda_e N_e \tag{7-16}$$

If the initial number of atoms of radionuclide A is N_{a0} , the initial number of daughter atoms are N_{b0} , N_{c0} , N_{d0} , and N_{e0}, and the disintegration constants are λ_a, λ_b, λ_c, λ_d, and λ_e, then the half-lives of the radionuclides are related to the disintegration constants through the relation half-life = $\ln 2/\lambda$. Solving the differential equations in (7-16) sequentially yields.

$$N_a = N_{a0} \exp(-\lambda_a t)$$

$$N_b = \frac{\lambda_a N_{a0}}{\lambda_b - \lambda_a}\exp(-\lambda_a t) + C_1 \exp(-\lambda_b t)$$

$$N_c = \frac{\lambda_b \lambda_a N_{a0}}{\lambda_b - \lambda_a}\frac{\exp(-\lambda_a t)}{\lambda_c - \lambda_a} + C_1 \frac{\lambda_b}{\lambda_c - \lambda_b}\exp(-\lambda_b t) + C_2 \exp(-\lambda_c t)$$

$$N_d = \frac{\lambda_c \lambda_b \lambda_a N_{a0}}{(\lambda_b - \lambda_a)(\lambda_c - \lambda_a)}\frac{\exp(-\lambda_a t)}{(\lambda_d - \lambda_a)} + C_1 \frac{\lambda_c \lambda_b}{(\lambda_c - \lambda_b)}\frac{\exp(-\lambda_b t)}{(\lambda_d - \lambda_b)} + C_2 \frac{\lambda_c}{(\lambda_d - \lambda_c)}\exp(-\lambda_c t)$$

$$+C_3 \exp(-\lambda_d t)$$

and

$$N_e = \frac{\lambda_d \lambda_c \lambda_b \lambda_a N_{a0}}{(\lambda_b - \lambda_a)(\lambda_c - \lambda_a)}\frac{\exp(-\lambda_a t)}{(\lambda_d - \lambda_a)(\lambda_e - \lambda_a)} + C_1 \frac{\lambda_d \lambda_c \lambda_b}{(\lambda_c - \lambda_b)}\frac{\exp(-\lambda_b t)}{(\lambda_d - \lambda_b)(\lambda_e - \lambda_b)}$$

$$+C_2 \frac{\lambda_d \lambda_c \exp(-\lambda_c t)}{(\lambda_d - \lambda_c)(\lambda_e - \lambda_c)} + C_3 \frac{\lambda_d}{(\lambda_e - \lambda_d)}\exp(-\lambda_d t) + C_4 \exp(-\lambda_e t) \tag{7-17}$$

The constants of integration are

$$C_1 = -\frac{\lambda_a N_{a0}}{\lambda_b - \lambda_a} + N_{b0}$$

$$C_2 = -\frac{\lambda_b \lambda_a N_{a0}}{(\lambda_b - \lambda_a)(\lambda_c - \lambda_a)} - C_1 \frac{\lambda_b}{\lambda_c - \lambda_b} + N_{c0}$$

$$C_3 = -\frac{\lambda_c \lambda_b \lambda_a N_{a0}}{(\lambda_b - \lambda_a)(\lambda_c - \lambda_a)(\lambda_d - \lambda_a)} - C_1 \frac{\lambda_c \lambda_b}{(\lambda_c - \lambda_b)(\lambda_d - \lambda_b)} - C_2 \frac{\lambda_c}{(\lambda_d - \lambda_c)} + N_{d0}$$

$$C_4 = -\frac{\lambda_d \lambda_c \lambda_b \lambda_a N_{a0}}{(\lambda_b - \lambda_a)(\lambda_c - \lambda_a)(\lambda_d - \lambda_a)(\lambda_e - \lambda_a)} - C_1 \frac{\lambda_d \lambda_c \lambda_b}{(\lambda_c - \lambda_b)(\lambda_d - \lambda_b)(\lambda_e - \lambda_b)}$$

$$-C_2 \frac{\lambda_d \lambda_c}{(\lambda_d - \lambda_c)(\lambda_e - \lambda_c)} - C_3 \frac{\lambda_d}{(\lambda_e - \lambda_d)} + N_{e0} \qquad (7\text{-}18)$$

Since the above equations are based upon the number of atoms of each radionuclide, initial quantities in terms of activities would have to be changed to use these equations. The relative number of radionuclide atoms of each constituent can be obtained from the activities by multiplying each daughter activity by the ratio of daughter half-life to the half-life of the oldest parent. After the above equations are solved in terms of the relative number of atoms, the activities can be retrieved by inverting the above procedure, i.e., by multiplying the relative number of atoms by the ratio of the half-life of the oldest parent to the half-life of the daughter product.

7.3 Code Description

The CUTTINGS code, developed specifically for the WIPP, calculates the quantity of radioactive material (in curies) brought to the surface as cuttings generated by an exploratory drilling operation that penetrates the repository during the human intrusion type scenario. The code determines the amount of cuttings removed by drilling and mud erosion, and accounts for radioactive decay that has occurred up to the intrusion time.

It is assumed that the drilling operation uses techniques similar to the rotary drilling methods in use today and that the waste can be characterized as having an effective shear strength for erosion. When the effective shear strength for erosion of the compacted waste is exceeded by the drilling fluid shear stress acting on the borehole wall, it is assumed that erosion of the wall (waste) occurs and continues until a state of equilibrium exists between the effective shear strength for erosion and the applied fluid shear stress. Primary erosion occurs adjacent to the largest diameter of the drill string, namely the drill collar, which is assumed to be aligned concentrically with the hole. It is also assumed that erosion occurs during drilling operations when the drill bit lies on the

hole bottom and drilling mud is flowing up the annulus. Drilling time is not a variable in the analysis. It is assumed that if conditions are conducive to causing erosion, sufficient time is available to complete the erosion process.

The total volume of material removed by drilling is the sum of the eroded material and the material directly cut by the drill bit. Multiple borehole intrusions are permissible. The code is based on an exact analytical solution for laminar helical flow of a non-newtonian fluid in an annulus and on empirical equations for turbulent flow. Input for the code includes rotational speed of the drill string; drilling mud flow rate; cutting bit diameter; shear rate dependent viscosity parameters for the drilling mud; borehole roughness; compacted repository thickness and porosity; effective failure shear strength of the compacted repository material, radionuclide inventory, and the number of intrusions. If the Reynolds number is greater than 2100, the calculation is based on turbulent, axial, annular flow. If the Reynolds number is less than 2100, the calculation assumes that the flow is laminar and is governed by equations for the helical flow of a non-newtonian fluid. An Oldroyd type fluid is assumed.

The volume of material removed as the result of each intrusion is used with the intrusion times and the repository radionuclide inventory to calculate the total amount (in curies) of decayed radionuclides brought to the surface. The radioactive decay process is solved using the Bateman equations.

7.4 Drilling Parameters

The direct removal of wastes to the accessible environment is based on the assumption that rotary drilling will be used. The parameters associated with drilling are dependent upon the well type, predicted depth, and materials through which the drill will penetrate.

The ranges and distributions for the input variables used in generating the CCDF were chosen from data gathered from a number of sources:

- For drilling operations through salt in the Delaware basin (WIPP site), the drilling mud most likely to be used is a brine (Pace, 1990), with the density cut somewhat with an emulsified oil. The density and viscosity related variables were chosen for the calculations based on the assumption of the use of such a brine-based drilling mud.
- For drilling through salt, the drilling speeds can vary from 40 to 220 rpm (Austin, 1983; Pace, 1990), with the most probable speed about 70 rpm (Pace, 1990).
- Mud flow rates are usually selected to be from 30 to 50 gallons/minute per inch of drill diameter (Austin, 1983) and usually result in flow velocities in the annulus between the drill collars and the hole wall at or near the critical flow state (laminar-turbulent transition) (Pace, 1990).

- The drill diameter is related to the total planned depth of the hole to be drilled. For gas wells in the 4000- to 10000-foot range, it is likely that the drill used that passes through the repository would have a diameter of 10.5 to 17.5 inches. The collar diameter is assumed to be 2 inches less than the drill diameter.
- The amount of material eroded from the borehole wall is dependent upon the magnitude of the fluid-generated shear stress acting on the wall and the effective shear strength for erosion of the repository material. In the absence of experimental data, the effective shear strength for erosion of the repository material is assumed to be similar to that of a montmorillonite clay, with an effective shear strength for erosion of 1 Pa (Sargunam et al., 1973).
- For turbulent flow, the shear stress acting on the borehole wall at the repository is dependent upon the absolute surface roughness. The value chosen for the calculations exceeds that of very rough concrete or riveted steel piping (Streeter, 1958).
- For most input parameters the median values were chosen. However, to maximize cuttings removal, a lower bound for the effective shear strength for erosion was chosen. The drill bit diameter was sampled over its range. The specific input values chosen for the cuttings calculations appear in Volume 3.

7.5 Results and Discussion

Except for the five different times of intrusion and the sampling of the drill bit diameter, the input data used in the CUTTINGS code to characterize the drilling mud, drill string, and waste properties was fixed for all cases (see Volume 3). As an example of the type of results obtained from the 600 CUTTINGS calculations required to calculate a CCDF, one specific calculation set for the five intrusion times is shown in Tables 7-1 and 7-2 for a drill bit diameter of 0.4445 m (17.5 inches). The calculations indicated that borehole erosion increased the diameter of the borehole from an initial value of 0.4445 m to a final diameter of 0.994 m. During the erosion process the flow between the drill collar and borehole wall remained turbulent. The initial value of the Reynolds number was 7165, which decreased to 4319 when erosion ceased. Radionuclide release to the surface (in curies) from contact-handled (CH) and remote-handled (RH) waste for the five intrusion times are shown in Tables 7-1 and 7-2, respectively. The releases are ordered according to magnitude at the 1000-year intrusion.

Table 7-1. Radionuclide Release (CI) From Contact-Handled (CH) Waste Based on Eroded Volume and Intrusion Time

	1000 yrs	3000 yrs	5000 yrs	1000 yrs	9000 yrs
PU239	0.5817×10^{1}	0.5492×10^{1}	0.5184×10^{1}	0.4894×10^{1}	0.4620×10^{1}
AM241	0.2571×10^{1}	0.1040×10^{0}	0.4209×10^{-2}	0.1703×10^{-3}	0.6888×10^{-3}
PU240	0.6818×10^{0}	0.5515×10^{0}	0.4461×10^{0}	0.3608×10^{0}	0.2919×10^{0}
PU238	0.2433×10^{-1}	0.3344×10^{-8}	0.4596×10^{-15}	0.6317×10^{-22}	0.8682×10^{-29}
U234	0.2348×10^{-1}	0.2336×10^{-1}	0.2323×10^{-1}	0.2310×10^{-1}	0.2297×10^{-1}
NP237	0.2070×10^{-2}	0.2567×10^{-2}	0.2585×10^{-2}	0.2584×10^{-2}	0.2583×10^{-2}
U233	0.7375×10^{-3}	0.7523×10^{-3}	0.7682×10^{-3}	0.7840×10^{-3}	0.7997×10^{-3}
TH230	0.1842×10^{-3}	0.5989×10^{-3}	0.1004×10^{-2}	0.1399×10^{-2}	0.1785×10^{-2}
TH229	0.6628×10^{-4}	0.1831×10^{-3}	0.2824×10^{-3}	0.3674×10^{-3}	0.4405×10^{-3}
RA226	0.3141×10^{-4}	0.2577×10^{-3}	0.5900×10^{-3}	0.9612×10^{-3}	0.1343×10^{-2}
PB210	0.2934×10^{-4}	0.2530×10^{-3}	0.5842×10^{-3}	0.9551×10^{-3}	0.1337×10^{-2}
U236	0.2129×10^{-4}	0.5766×10^{-4}	0.8707×10^{-4}	0.1109×10^{-3}	0.1301×10^{-3}
PU242	0.1528×10^{-4}	0.1523×10^{-4}	0.1517×10^{-4}	0.1512×10^{-4}	0.1506×10^{-4}
U235	0.6824×10^{-5}	0.1796×10^{-4}	0.2847×10^{-4}	0.3839×10^{-4}	0.4776×10^{-4}
CM248	0.1014×10^{-5}	0.1010×10^{-5}	0.1006×10^{-5}	0.1002×10^{-5}	0.9974×10^{-6}
U238	0.2373×10^{-11}	0.7106×10^{-11}	0.1182×10^{-10}	0.1652×10^{-10}	0.2120×10^{-10}
TH232	0.5344×10^{-12}	0.4493×10^{-11}	0.1168×10^{-10}	0.2149×10^{-10}	0.3341×10^{-10}
CM244	0.3002×10^{-17}	0.0000	0.0000	0.0000	0.0000
PU241	0.4060×10^{-19}	0.0000	0.0000	0.0000	0.0000
CF252	0.0000	0.0000	0.0000	0.0000	0.0000

Table 7-2. Radionuclide Release (Ci) From Remote-Handled (RH) Waste Based on Eroded Volume and Intrusion Time

	1000 yrs	3000 yrs	5000 yrs	1000 yrs	9000 yrs
PU239	0.7065×10^{-1}	0.6669×10^{-1}	0.6296×10^{-1}	0.5943×10^{-1}	0.5611×10^{-1}
AM241	0.2145×10^{-1}	0.8678×10^{-3}	0.3511×10^{-4}	0.1420×10^{-5}	0.5746×10^{-7}
PU240	0.1547×10^{-1}	0.1251×10^{-1}	0.1012×10^{-1}	0.8189×10^{-2}	0.6624×10^{-2}
U233	0.1111×10^{-1}	0.1101×10^{-1}	0.1092×10^{-1}	0.1082×10^{-1}	0.1073×10^{-1}
TH229	0.1003×10^{-2}	0.2734×10^{-2}	0.4150×10^{-2}	0.5306×10^{-2}	0.6247×10^{-2}
NP237	0.8828×10^{-4}	0.9237×10^{-4}	0.9248×10^{-4}	0.9243×10^{-4}	0.9237×10^{-4}
PU238	0.2730×10^{-4}	0.3753×10^{-11}	0.5158×10^{-18}	0.7089×10^{-25}	0.9743×10^{-32}
U234	0.2635×10^{-4}	0.2622×10^{-4}	0.2607×10^{-4}	0.2592×10^{-4}	0.2577×10^{-4}
U238	0.4824×10^{-5}	0.4824×10^{-5}	0.4824×10^{-5}	0.4824×10^{-5}	0.4824×10^{-5}
U235	0.8403×10^{-6}	0.9756×10^{-6}	0.1103×10^{-5}	0.1224×10^{-5}	0.1337×10^{-5}
U236	0.4826×10^{-6}	0.1308×10^{-5}	0.1975×10^{-5}	0.2515×10^{-5}	0.2952×10^{-5}
PU242	0.2251×10^{-6}	0.2243×10^{-6}	0.2235×10^{-6}	0.2226×10^{-6}	0.2218×10^{-6}
TH230	0.2067×10^{-6}	0.6721×10^{-6}	0.1127×10^{-5}	0.1570×10^{-5}	0.2003×10^{-5}
CM248	0.5384×10^{-7}	0.5362×10^{-7}	0.5340×10^{-7}	0.5319×10^{-7}	0.5297×10^{-7}
RA226	0.3525×10^{-7}	0.2892×10^{-6}	0.6621×10^{-6}	0.1079×10^{-5}	0.1507×10^{-5}
PB210	0.3293×10^{-7}	0.2839×10^{-6}	0.6556×10^{-6}	0.1072×10^{-5}	0.1501×10^{-5}
CS137	0.3348×10^{-8}	0.2858×10^{-28}	0.0000	0.0000	0.0000
SR90	0.1327×10^{-8}	0.2803×10^{-29}	0.0000	0.0000	0.0000
TH232	0.1210×10^{-13}	0.1019×10^{-12}	0.2650×10^{-12}	0.4875×10^{-12}	0.7580×10^{-12}
CM244	0.6113×10^{-17}	0.0000	0.0000	0.0000	0.0000
PU241	0.9313×10^{-21}	0.0000	0.0000	0.0000	0.0000
PM147	0.0000	0.0000	0.0000	0.0000	0.0000
CF252	0.0000	0.0000	0.0000	0.0000	0.0000

REFERENCES

Austin, E. H. 1983. *Drilling Engineering Handbook.* Boston: International Human Resources Development Corporation.

Bear, J. 1972. Dynamics of Fluids in Porous Media. Elsevier, New York.

Beauheim, Richard L. 1987. *Interpretations of Single-Well Hydraulic Tests Conducted At and Near The Waste Isolation Pilot Plant (WIPP) Site, 1983-1987.* SAND87-0039. Albuquerque, NM: Sandia National Laboratories.

Bertram-Howery, S. G., and R. L. Hunter, eds. 1989. *Preliminary Plan for Disposal-System Characterization and Long-Term Performance Evaluation of the Waste Isolation Pilot Plant.* SAND89-0178. Albuquerque, NM: Sandia Naitonal Laboratories.

Bertram-Howery, S. G., M. G. Marietta, R. P. Rechard, P. N. Swift, D. R. Anderson, B. L. Baker, J. E. Bean, Jr., W. Beyeler, K. F. Brinster, R. V. Guzowski, J. C. Helton, R. D. McCurley, D. K. Rudeen, J. D. Schreiber, and P. Vaughn. 1990. *Preliminary Comparison with 40 CFR Part 191, Subpart B for the Waste Isolation Pilot Plant, December 1990.* SAND90-2347. Albuquerque, NM: Sandia National Laboratories.

Bras, R. L., and P. K. Kitanidis. 1991. *User's Manual for the INVS Computer Code.* SAND number not available. Albuquerque, NM: Sandia National Laboratories.

Brinster, Kenneth F. 1991. *Preliminary Geohydrologic Conceptual Model of the Los Medanos Region Near the Waste Isolation Pilot Plant for the Purpose of Performance Assessment.* SAND89-7147. Albuquerque, NM: Sandia National Laboratories.

Broc, R., ed. 1982. *Drilling Mud and Cement Slurry Rheology Manual.* Houston, Texas: Gulf Publishing Company.

Brush, L. H., and A. L. Lappin. 1990. *Appendix A, Memo 4: Additional Estimates of Gas Production Rates and Radionuclide Solubilities for Use in Models of WIPP Disposal Rooms* in Data Used in Preliminary Performance Assessment of the Waste Isolation Pilot Plant (1990). R. P. Rechard, H. Iuzzolino, and J. S. Sandha. SAND89-2408. Albuquerque, NM: Sandia National Laboratories.

Carnahan, B., H. A. Luther, J. O. Wilkes. 1969. "Applied Numerical Methods." John Wiley & Sons, Inc. New York, 1969.

Carrera, J., and S. P. Neuman. 1986a. "Estimation of Aquifer Parameters Under Transient and Steady State Conditions: 1. Maximum Likelihood Method Incorporating Prior Information." *Water Resources Research 22*: 199-210.

Carrera, J., and S. P. Neuman. 1986b. "Estimation of Aquifer Parameters Under Transient and Steady State Conditions: 2. Uniqueness, Stability, and Solution Algorithms." *Water Resources Research 22*: 211-227.

Carrera, J., and S. P. Neuman. 1986c. "Estimation of Aquifer Parameters Under Transient and Steady State Conditions: 3. Application to Synthetic and Field Data." *Water Resources Research 22*: 228-242.

Coats, K. H. 1980. "In-Situ Combustion Model." *Soc. Pet. Eng. J.* (Dec. 1980) 533-554.

Coleman, B. D., and W. Noll. 1959. "Helical Flow of General Fluids." *Journal of Applied Physics* vol. 30, no. 10: 1508.

Conte, S. D., and C. de Boor. 1972. *Elementary Numerical Analysis and Algorithm Approach.* McGraw Hill Book Company, New York, 1972.

Cox, D. R., and P. A. W. Lewis. 1966. *The Statistical Analysis of Series of Events.* London: Chapman and Hall.

Cox, D. R., and V. Isham. 1980. *Point Processes.* London: Chapman and Hall.

Cranwell, R. M., R. V. Guzowski, J. E. Campbell, and N. R. Ortiz. 1990. *Risk Methodology for Geologic Disposal of Radioactive Waste: Scenario Selection Procedure.* SAND80-1429, NUREG/CR-1667. Albuquerque, NM: Sandia National Laboratories.

Crichlow, H. B. 1977. *Modern Reservoir Engineering–A Simulation Approach.* Englewood Cliffs, NJ: Prentice Hall.

Crookston, H. B., W. E. Culham, and W. H. Chen. 1979. "Numerical Simulation Model for Thermal Recovery Processes". *Soc. Pet. Eng. J.* (Feb 1979) 37-58.

Darley, H. C. H. 1969. *"A Laboratory Investigation of Borehole Stability."* Journal of Petroleum Technology. Trans. AIME. Vol. 246 (July): 883-892.

Darley, H. C. H., and G. R. Gray. 1988. *Composition and Properties of Drilling and Completion Fluids.* Houston, TX: Gulf Publishing Company. 243.

Davies, Peter B. 1989. *Variable-Density Ground-Water Flow and Paleohydrology in the Waste Isolation Pilot Plant (WIPP) Region, Southeastern New Mexico.* U.S. Geological Survey Open-File Report 88-490. Albuquerque, NM: U.S. Geological Survey.

Davis, W. P., and J. A. Chatfield. 1970. "Concerning Product Integrals and Exponentials." *Proceeding of the American Mathematical Society 25*: 743-747.

Delhomme, J. P.. 1979. "Spatial Variability and Uncertainty in Groundwater Flow Parameters: a Geostatistical Approach." *Water Resources Research,* Vol. 15, No. 2: 269-289.

de Marsily, G. 1986. *Quantitative Hydrogeology.* Orlando, FL: Academic Press, Inc.

Dollard, J. D., and C. N. Friedman. 1979. *Product Integration with Applications to Differential Equations* (with an appendix by P. R. Masani). Reading, MA: Addison-Wesley.

Dongarra, J. J., J. R. Bonch, C. B. Moler, G. W. Stewart. 1979. *LINPACK User's Guide.* Philadelphia, PA. SIAM.

Earth Technology Corp. 1987. *Final Report for Time Domain Electromagnetic (TDEM) Survey of the WIPP.* SAND87-7144. Albuquerque, NM: Sandia National Laboratories.

Fanchi, J. R., K. J. Harpole, and S. W. Bujnowski. 1982. *BOAST III: A Three-Dimensional Three-Phase Black Well Applied Simulation Tool.* DOE/BC-10033-3. U.S. Department of Energy.

Fanchi, J. R., J. E. Kennedy, and D. L. Dauben. 1987. *BOAST II: A Three-Dimensional Three-Phase Black Oil Applied Simulation Tool.* DOE/BC-88/2/SP, DE 88001205. U.S. Department of Energy.

Fredrickson, A. G. 1960. "Helical Flow of an Annular Mass of Visco-Elastic Fluid." *Chemical Engineering Science 11*: 252-259.

Gellert, W., H. Guestner, M. Hellwich, and H. Kaestner, eds. 1977. *The VNR Concise Encyclopedia of Mathematics*. 1st American ed. New York: Van Nostrand Reinhold.

Gill, R. D., and S. Johansen. 1990. "A Survey of Product-Integration with a View Toward Application in Survival Analysis." *The Annals of Statistics 18*: 1501-1555.

Grindrod, P., and Capon, P. 1991. *Flow Through Fractured Rock: What Does the WIPP Site Culebra Data Reveal*. Draft report, version 2. NSARP 55(91)R9(IMI898-26). United Kingdom: INTERA SCIENCES.

Gutjahr, A. L. 1989. *Fast Fourier Transforms for Random Field Generation*. Socorro, NM: New Mexico Tech. Report. 106.

Guzowski, R. V. 1990. *Preliminary Identification of Scenarios that May Affect the Escape and Transport of Radionuclides from the Waste Isolation Pilot Plant, Southeastern New Mexico*. SAND89-7149. Albuquerque, NM: Sandia National Laboratories.

Guzowski, R. V. 1991. *Evaluation of Applicability of Probability Techniques to Determining the Probability of Occurrence of Potentially Disruptive Intrusive Events at the Waste Isolation Pilot Plant*. SAND90-7100. Albuquerque, NM: Sandia National Laboratories. In preparation.

Haight, F. A. 1967. *Handbook of the Poisson Distribution*. New York: Wiley.

Helton, J. C. 1973a. "Existence of Sum and Product Integrals." *Transactions of the American Mathematical Society 182*: 165-174.

Helton, J. C. 1973b. "Some Interdependencies of Sum and Product Integrals." *Proceedings of the American Mathematical Society 37*: 201-206.

Helton, J. C. 1977. "Existence of Integrals and the Solution of Integral Equations." *Transactions of the American Mathematical Society 229*: 307-327.

Helton, J. C., J. W. Garner, R. D. McCurley, and D. K. Rudeen. 1991. *Sensitivity Analysis Techniques and Results for Performance Assessment at the Waste Isolation Pilot Plant*. SAND90-7103. Albuquerque, NM: Sandia National Laboratories.

Hildebrand , F. B. 1974 *Introduction to Numerical Analysis*. McGraw-Hill, Inc. 1974.

Hoeksema, R. J., and P. K. Kitanidis. 1984. "An Application of the Geostatistical Approach to the Inverse Problem in Two-Dimensional Groundwater Modeling." *Water Resources Research 20*: 1003-1020.

Hoeksema, R. J., and P. K. Kitanidis. 1985a. "Analysis of the Spatial Structure of Properties of Selected Aquifers." *Water Resources Research 21*: 563-572.

Hoeksema, R. J., and P. K. Kitanidis. 1985b. "Comparison of Gaussian Conditional Mean and Kriging Estimation in the Geostatistical Solution of the Inverse Problem." *Water Resources Research 21*: 825-836.

Hora, S. C., D. von Winterfeldt, and K. Trauth. 1991. *Expert Judgment on Inadvertent Human Intrusion into the Waste Isolation Pilot Plant*. SAND90-3063. Albuquerque, NM: Sandia National Laboratories.

Hunter, R. L. 1989. *Events and Processes for Constructing Scenarios for the Release of Transuranic Waste from the Waste Isolation Pilot Plant, Southeastern New Mexico*. SAND89-2546. Albuquerque, NM: Sandia National Laboratories.

Hunter, R. L., and C. J. Mann, eds. 1989. *Techniques for Determining Probabilities of Events and Processes Affecting the Performance of Geologic Repositories: Literature Review*. Vol. 1. SAND86-0196, NUREG/CR-3964. Albuquerque, NM: Sandia National Laboratories.

Huyakorn, P. S., and G. F. Pinder. 1983. *Computational Methods in Subsurface Flow*. New York: Academic Press.

Huyakorn, P. S., B. H. Lester, and J. W. Mercer. 1983a. "An Efficient Finite Element Technique for Modeling Transport in Fractured Porous Media, 1, Single Species Transport." *Water Resources Research vol. 19, no. 3*: 841-854.

Huyakorn, P. S., B. H. Lester, and J. W. Mercer. 1983b. "An Efficient Finite Element Technique for Modeling Transport in Fractured Porous Media, 2, Nuclide Decay Chain Transport." *Water Resources Research vol. 19, no. 5*: 1286-1296.

Huyakorn, P. S., H. O. White, Jr., and S. Panday. 1989. *STAFF2D Solute Transport and Fracture Flow in Two Dimensions*. Herndon, VA: HydroGeologic, Inc.

Huyakorn, P. S., H. O. White, Jr., and S. Panday. 1991. *STAFF2D. Solute Transport and Fracture Flow in 2-Dimensions*. Herndon, VA: HydroGeoLogic, Inc.

IAEA (International Atomic Energy Agency). 1989. *Evaluating the Reliability of Predictions Made Using Environmental Transfer Models*. Vienna, Austria: Safety Series Report No. 100.

Kaplan, S., and B. J. Garrick. 1981. "On the Quantitative Definition of Risk." *Risk Analysis 1*: 11-27.

Kitanidis, P. K. and E. G. Vomvoris. 1983. "A Geostatistical Approach to the Inverse Problem in Groundwater Modeling (Steady State) and One-Dimensional Simulations." *Water Resources Research 19*: 677-690.

Lappin, A. R., R. L. Hunter, D. P. Garber, P. B. Davies, R. L. Beauheim, D. J. Borns, L. H. Brush, B. M. Butcher, T. Cauffman, M. S. Y. Chu, L. S. Gomez, R. V. Guzowski, H. J. Iuzzolino, V. Kelley, S. J. Lambert, M. G. Marietta, J. W. Mercer, E. J. Nowak, J. Pickens, R. P. Rechard, M. Reeves, K. L. Robinson, and M. D. Siegel. 1989. *Systems Analysis, Long-Term Radionuclide Transport, and Dose Assessments, Waste Isolation Pilot Plant (WIPP), Southeastern New Mexico; March 1989*. SAND89-0462. Albuquerque, NM: Sandia National Laboratories.

LaVenue, A. M., T. L. Cauffman, and J. F. Pickens. 1990. *Ground-Water Flow Modeling of the Culebra Dolomite - Volume I: Model Calibration*. SAND89-7068/1. Albuquerque, NM: Sandia National Laboratories.

McDonald, M. G., and A. W. Harbaugh. 1988. *A Modular Three-Dimensional Finite-Difference Ground-Water Flow Model*. Techniques of Water-Resources Investigations of the United States Geological Survey, Book 6, Modeling Techniques. Washington, D.C.: Scientific Software Group.

McKay, M. D., W. J. Conover, and R. J. Beckman. 1979. "A Comparison of Three Methods for Selecting Values of Input Variables in the Analysis of Output from a Computer Code." *Technometrics 21*: 239-245.

Mann, C. J., and R. L. Hunter. 1988. "Probabilities of Geologic Events and Processes in Natural Hazards." *Zeitschrift fuer Geomorphologie N.F. 67*: 39-52.

Marietta, M. G., S. G. Bertram-Howery, D. R. Anderson, K. Brinster, R. Guzowski, H. Iuzzolino, and R. P. Rechard. 1989. *Performance Assessment Methodology Demonstration: Methodology Development for Purposes of Evaluating Compliance with EPA 40 CFR Part 191, Subpart B, for the Waste Isolation Pilot Plant.* SAND89-2027. Albuquerque, NM: Sandia National Laboratories.

Masani, P. R. 1947. "Multiplicative Riemann Integration in Normed Rings." *Transactions of the American Mathematical Society 16*: 147-192.

Mercer, J. W. and B. R. Orr. 1979. *Interim Data Report on the Geohydrology of the Proposed Waste Isolation Pilot Plant Site Southeast New Mexico.* U.S. Geological Survey Water Resources Investigation, 79-98. Albuquerque, NM: U.S. Geological Survey.

Oldroyd, J. G. 1958. *Proceedings of the Royal Society* (London) A245: 278.

Pace, R. O. 1990. Manager, Technology Exchange Technical Services, Baroid Drilling Fluids, Inc., 3000 N. Sam Houston Pkwy. E , Houston, Texas. (Expert Opinion), Letter of 18 September 1990.

Peaceman, D. W. 1977. *Fundamentals of Numerical Reservoir Simulation: Developments in Petroleum Science, 6, Elsevier Scientific Publishing Company.* New York, 1977.

Powers, D. W., S. J. Lambert, S. E. Shaffer, L. R. Hill, and W. D. Weart, eds. 1978. *Geological Characterization Report, Waste Isolation Pilot Plant (WIPP) Site, Southeastern New Mexico.* SAND78-1596, Volume 1 and 2. Albuquerque, NM: Sandia National Laboratories.

Price, H. S., and K. H. Coats. 1974. "Direct Methods in Reservoir Simulation". *Soc. Pet. Eng. J.* (June 1974) 195-308.

Ravenne, C., A. Galli, H. Beucher, R. Eschard, D. Guerillot, and Heresim Group. 1991. *Outcrop Studies and Geostatistical Modelling of a Middle Jurassic Brent Analogue.* Paper distributed at the meeting of the WIPP performance-assessment geostatistics consultant group, April 22-23, 1991, Albuquerque, New Mexico.

Rechard, R. P., H. J. Iuzzolino, J. S. Rath, R. D. McCurley, and D. K. Rudeen. 1989. *User's Manual for CAMCON: Compliance Assessment Methodology Controller.* SAND88-1496. Albuquerque, NM: Sandia National Laboratories.

Rechard, R. P., H. J. Iuzzolino, and J. S. Sandha. 1990a. *Data Used in Preliminary Performance Assessment of the Waste Isolation Pilot Plant (1990).* SAND89-2408. Albuquerque, NM: Sandia National Laboratories.

Rechard, R. P., W. Beyeler, R. D., McCurley, D. K. Rudeen, J. E. Bean, and J. D. Schreiber. 1990b. *Parameter Sensitivity Studies of Selected Components of the WIPP Repository System.* SAND89-2030. Albuquerque, NM: Sandia National Laboratories.

Rechard, R. P., P. J. Roache, R. L. Blaine, A. P. Gilkey, and D. K. Rudeen. 1991. *Quality Assurance Procedures for Computer Software Supporting Performance Assessments of the Waste Isolation Pilot Plant.* SAND90-1240. Albuquerque, NM: Sandia National Laboratories.

Reeves, M., G. A. Freeze, V. A. Kelley, J. F. Pickens, and D. T. Upton. 1991. *Regional Double-Porosity Solute Transport in the Culebra Dolomite Under Brine-Rerservoir-Breach Release Conditions: An Analysis of Parameter Sensitivity and Importance.* SAND89-7069. Albuquerque, NM: Sandia National Laboratories.

Roache, P. J. 1976. *Computational Fluid Dynamics.* Rev. ed. Albuquerque, NM: Hermosa Publishers.

Roache, P. J., P. M. Knupp, S. Steinberg, and R. L. Blaine. 1990. *Experience with Benchmark Test Cases for Groundwater Flow in ASME FED. Benchmark Test Cases for Computational Fluid Dynamics.* Eds. I. Celik and C. J. Freitas. Vol. 93, no. H00598, (June): 49-56.

Ross, B. 1989. "Scenarios for Repository Safety Analysis." *Engineering Geology 26*: 285-299.

Rubin, B., and P. K. W. Vinsome. 1980. "The Simulation of the In Situ Combustion Process in One Dimension Using a Highly Implicit Finite-Difference Scheme". *J. Col. Pet. Tech* (Oct/Dec. 1980) 68-76.

Rubin, Y. 1990. "Stochastic Modeling of Macrodispersion in Heterogeneous Porous Media." *Water Resources Research 26*: 133-141.

Rubin, Y. 1991. "Prediction of Tracer Plume Migration in Disordered Porous Media by the Method of Conditional Probabilities." *Water Resources Research.* In press.

Rubin, Y., and G. Dagan. 1987a. "Stochastic Identification of Transmissivity and Effective Recharge in Steady Groundwater Flow: 1. Theory." *Water Resources Research 23*: 1185-1192.

Rubin, Y., and G. Dagan. 1987b. "Stochastic Identification of Transmissivity and Effective Recharge in Steady Groundwater Flow: 2. Case Study." *Water Resources Research 23*: 1193-1200.

Rubin, Y., and G. Dagan. 1988. "Stochastic Analysis of Boundary Effects on Head Spatial Variability in Heterogeneous Aquifers: 1. Constant Head Boundary." *Water Resources Research 24*: 1689-1697.

Ruge, J. W., and K. Stuben. 1987. *Algebraic Multigrid* in Multigrid Methods. Ed. S. McCormick. Philadelphia: SIAM.

Sargunam, A., P. Riley, K. Arulanandan, and R. B. Krone. 1973. "Physico-Chemical Factors in Erosion of Cohesive Soils." *Proceedings of the American Society of Civil Engineers, Journal of the Hydraulics Division vol. 99, no. HY3 99*, (March): 555-558.

Savins, J. G. and G. C. Wallick. 1966. "Viscosity Profiles, Discharge Rates, Pressures, and Torques for a Rheologically Complex Fluid in Helical Flow." *A.I.Ch.E. Journal vol. 12*, no. 2.

Schaffer, S. 1991. *An Efficient 'Black Box' Semi-coarsening Multigrid Algorithm for Two and Three Dimensional Symmetric Elliptic PDE's with Highly Varying Coefficients.* Proceedings of the Fifth Copper Mountain Conference on Multigrid Methods, March 31-April 5, 1991. Also, submitted to SIAM Journal of Numerical Analysis.

Scheideger, A. E. 1960. *The Physics of Flow Through Porous Media.* Toronto, Canada: University of Toronto Press.

Smith, G. D. 1965. *Numerical Solution of Partial Differential Equations.* Oxford University Press, New York, 1965.

Streeter, V. L. 1958. *Fluid Mechanics.* New York: McGraw-Hill.

U.S. EPA (Environmental Protection Agency). 1985. *Environmental Standards for the Management and Disposal of Spent Nuclear Fuel, High-Level and Transuranic Radioactive Waste*; Final Rule, 40 CFR Part 191, Federal Register 50: 38066-38089.

U.S. DOE (Department of Energy). 1991. *Strategy for the Waste Isolation Pilot Plant Test Phase*. Department of Energy Office of Waste Operations, DOE/EM/48063-2.

Vaughn, P. 1986. *A Numerical Model for Thermal Recovery Processes in Tar Sand: Description and Application*. April 1986, DOE Report #DOE/FE/60177-2219.

Voss, C. I. 1984. *SUTRA (Saturated-Unstaturated TRAnsport): A Finite-Element Simulation Model for Saturated-Unsaturated, Fluid-Density-Dependent Ground-Water Flow with Energy Transport or Chemically Reactive Single-Species Solute Transport*. Reston, VA: U.S. Geological Survey National Center.

Walker, R. E. 1976. "Hydraulic Limits Are Set by Flow Restrictions." *Oil and Gas Journal*. (October 4): 86-90.

Walker, R. E. and W. E. Holman. 1971. "Computer Program Predicting Drilling-Fluid Performance." Oil and Gas Journal (March 29): 80-90.

Wehr, R. M., J. A. Richards, Jr., and T. W. Adair III. 1984. *Physics of the Atom*. Reading, Massachusetts: Addison-Wesley.

Whittaker, A., ed. 1985. *Theory and Application of Drilling Fluid Hydraulics*. Boston: International Human Resources Development Corporation.

Yeh, W. W-G. 1986. "Review of Parameter Identification Procedures in Groundwater Hydrology: The Inverse Problem." *Water Resources Research* February 1986, Vol. 22, No. 2., 95-108

A. MULTIPHASE FLOW THROUGH POROUS MEDIA—Palmer Vaughn

Consequence modeling of WIPP for compliance assessment under both undisturbed and disturbed conditions involves quantification of the flow fields in and around the repository. Many of the models used by performance assessment (PA) rely on simulating the nature of the flow fields and are based on mathematical formulations that describe flow through porous media. Two models, BOAST (for undisturbed conditions) and BRAGFLO (for undisturbed and disturbed conditions) describe the simultaneous flow of brine and gas through porous media. Table A-1 provides list of terms commonly used when discussing multiphase flow through porous media. These PA models are based on the following general conceptualization of porous media flow.

A description of multi-phase porous media flow is necessary to understand the assumptions involved in modeling multi-phase flow through porous media. Details of equations of motion for multi-phase flow describing assumptions, derivations, and implementation are wide-spread throughout the petroleum and hydrology literature (Bear et al., 1968; Bear, 1975; Bear, 1979; Dake, 1978; Crichlow, 1977; Collins, 1961; Aziz, Settari, 1979; Peaceman, 1977; Crookston, Culhan, and Chen, 1979; Coats, 1980; Vaughn, 1986; Rubin, Vinsome, 1980; Scheidegger, 1960). The interested reader is referred to this literature for this background information. The nomenclature, assumptions, and conceptualization used here are typical with those found in much of the multiphase reservoir modeling literature referenced above.

BRAGFLO and BOAST are based on a description of porous media presented by Bear (1975) and Bear, Zaslavsky, and Irmay (1968). Bear (1975) points out that "no precise definition of porous media exists; however, the following characteristics, even though they are subjective, convey something about the nature of porous media:"

1. A portion of the space is occupied by heterogeneous or multiphase matter, with at least one of the phases being fluid.
2. The space within the porous media domain that is not part of the solid matrix is referred to as void space or pore space. The openings comprising the void space are relatively narrow. Some of the pores comprising the void space are interconnected (effective pore space) while unconnected pores are considered part of the solid matrix.
3. The solid phase is distributed throughout the porous media and solid must be present inside each representative elementary volume.
4. The specific surface (surface area of the pores per unit bulk volume) is relatively high.
5. "Any two points within the effective pore space may be connected by a curve that lies completely within it."

6. With respect to fluid flow, the porous media restricts the transport of the fluid to well defined channels and the velocity of a fluid particle at a point in the void space is parallel to the walls.

The term "distributed" in characteristic 3 above is somewhat general. PA adopts the Bear and Bachmat (1966 and 1967) visualization that "the void space of a porous media is composed of a spatial network of interconnected random passages of varying length, cross-section, orientation, and functions" (Bear, 1975, p. 93). Flow in the void space is laminar and each channel defines a stream tube in which the pattern of streamlines is fixed although the direction of flow along them may be reversed. The junctions where channels intersect occupy negligible pore space volume.

The fluids (either individually or combined) all occupy the pore space and are viscous and Newtonian and may be compressible. The active forces on the fluids are those due to pressure, gravity, capillarity, and shear resulting from the fluid's velocity. The fluid loses energy only during passage through the narrow channels and not through a junction. The network of channels connected to each other by junctions produces average gradients of pressure, density, and viscosity in any elementary volume that includes a sufficiently large number of channels and junctions. These average gradients are practically independent of the geometric shape of a single channel within the elementary volume (Bear 1975, p. 93).

BRAGFLO and BOAST simulate the flow of brine and gas through porous media. Two types of multi-phase flow are possible, miscible and immiscible. The PA conceptual models consider immiscible displacement only. In this case both fluids flow simultaneously through the porous network. The gas and brine phases are separated by an interface whose curvature and surface tension give rise to a capillary pressure difference across the interface (Brook, Corey, 1964; Corey, 1986; Peaceman, 1977; Dake, 1978; Crichlow, 1977; Collins, 1961). The interface is assumed to be abrupt and any transitions from one phase to another occur over a distance of negligible length compared to the channel diameter (Bear, 1975).

When brine and gas occupy void space, the concept of saturation is introduced. Saturation is defined as the volume fraction of void space occupied by a particular fluid. Interfacial tension exists where the two immiscible fluids contact each other. The shape of the resulting meniscus defines the wettability of the system (Brook, Corey, 1964; Bear, 1975). For example, the convex side of the meniscus faces toward the wetting phase while the concave side faces toward the non-wetting phase. The wetting phase for all the strata surrounding the WIPP is assumed to be brine. Interfacial tension and wettability may depend on the direction the interface is moving. This phenomenon is called hysteresis. Hysteresis is a secondary effect and is not currently modeled (Brook, Corey, 1964).

Three saturation regions are differentiated in the two-phase (brine and gas) system. Assuming a brine-wet reservoir, at low brine saturations water forms in isolated rings or exists as a thin film

of molecular thickness. As brine saturation increases, a condition is reached where the brine forms a continuous phase that is capable of transmitting pressure. Above this critical saturation or "irreducible saturation," brine flow is possible. Potential flow of brine below the irreducible brine saturation will not occur. At high brine saturation brine isolates the gas and the gas no longer forms a continuous phase. This occurs at the irreducible gas saturation.

In formulating the equations of motion for the simultaneous flow of two immiscible fluids through porous media, it is assumed that "each fluid establishes its own tortuous path, forming very stable channels, and that a unique set of channels corresponds to each degree of saturation" (Bear, 1975). Bear's continuum approach is used when two immiscible fluids simultaneously flow through porous media. Under these conditions "each of the fluids is regarded as a continuum completely filling the flow domain (at a fluid content that is a function of space coordinates and of time). The various continua occupy the entire flow domain simultaneously" (Bear, 1975 p. 457). The equations of motion for multi-phase flow used here are based on heuristic extensions of Darcy's law (Hubbert, 1956; Bear, 1975; Bear, 1979; Dake, 1978; Crichlow, 1977; Collins, 1961; Dullien, 1979; Hiatt, 1968); deMarsily, 1986; DeWest, 1965; Aziz, Settari, 1979).

The following is a statement of Darcy's law in differential form:

$$q_v = -\frac{k}{\mu}\left[\nabla P - \rho g\right] \tag{A-1}$$

where q_v is the volumetric flow rate per unit cross sectional area, k is the absolute or intrinsic permeability of the porous media, μ is the fluid viscosity, ρ is the fluid density, g is the gravitational constant, and P is the fluid pressure.

Darcy's original observations were made on the one-dimensional vertical flow of water through a fully saturated porous media (Hubbert, 1956). Darcy postulated the law, which states that the flow of water under these conditions is proportional to the change in potential. Many generalizations of Darcy's law can be found in the literature (Bear, 1975; Bear, 1979; Bear, 1968; Bear, 1966; Bear, 1967; Dake, 1978; Crichlow, 1977; Collins, 1961; Dullien, 1979; Hiatt, 1968; deMarsily, 1986; DeWest, 1965; Aziz, Settari, 1979). These generalizations extend Darcy's observation to other fluids, to the simultaneous flow of immiscible fluids, to multiple dimensions, and to compressible fluids. These generalizations are used in obtaining the equations of motion governing the two-phase flow assumed here and are discussed below.

The first extension is a generalization from an isotropic to an anisotropic medium. This extension is developed heuristically as well as theoretically in Bear (1975). Implicit in this generalization is the extension to two and three dimensions.

The second extension is that of accounting for fluid compressibility effects. Hubbert (1940) shows that extensions of Darcy's law to compressible fluids such as gas are valid provided the density of the fluid is only a function of pressure and the flow is irrotational "Darcy's law in its differential form is the same for a gas as for a liquid, provided that the flow behavior of a gas in small pore spaces, other than expansion, is similar to that of a liquid" (Hubbert, 1956). The two flows (of liquid and gas) for a given potential are not similar. Klinkenberg (1941) has shown that in general the permeability to gas (k_g) based on the assumed validity of Darcy's law for gases is not the same as the permeability to liquid (k_L) and is a function of pressure. This is a result of boundary slip associated with gas and the lower frictional resistances to flow of gas compared to a liquid of the same viscosity and velocity. However, at pressures in excess of 30 atm, k_g and k_L differ by only 1%. This Klinkenberg effect is assumed to be negligible in the WIPP environment and the equations of motion that are developed in Sections 4.2.1.2 and 5.2.2 are assumed to hold for compressible gas as well as the slightly compressible brine.

The third extension of Darcy's law accounts for the presence and flow of multiple immiscible phases. Once steady-state flow is achieved, Darcy's law may be extended to describe the separate flow of each phase (Bear, 1975). This extension introduces the concept of effective permeabilities, relative permeabilities, and capillary pressure.

For each phase, the absolute permeability of (A-1) is replaced by the effective phase permeability and the pressure of (A-1) is replaced by the phase pressure. These effective permeabilities are empirically determined by pressure drop and flow measurements. Numerous experiments verify the validity of this extension and suggest that the effective permeability depends on characteristics of the rock, the wettability characteristics, surface tension, the shape of the interface separating the phases, and on phase saturation. The effective permeabilities do not appear to depend on fluid viscosity or their specific discharges (Bear, 1975; Scheideggar, 1960). Instead of using effective permeabilities it is more convenient to refer to relative permeabilities, which are defined for each phase as the ratio of the effective phase permeability to the absolute or intrinsic permeability of the medium (measured when the medium is saturated with a single fluid).

As stated above, the relative permeabilities are empirical fits of pressure drop and flow data to extensions of Darcy's law. Measurements taken at different degrees of saturation result in differing relative permeabilities. The dependence on saturation results in the sum of the effective permeabilities being less than the absolute permeability at all values of saturation as long as more than one phase is present (Bear, 1975; Dake, 1978; Corey, 1986; Scheideggar, 1960). The typical dependence of relative permeability on saturation is shown in Figure A-1. For each phase its relative permeability increases with that phase's saturation. Below each phase's residual or irreducible saturation (S_{wo} for wetting and S_{nwo} for non-wetting) the relative permeability is zero,

indicating flows due to potential gradients in that phase will not occur. The effective permeability and its saturation dependence is an empirical way of accounting for the interference that one fluid makes on the other as they simultaneously flow through the porous media. Some researchers suggest that there may be a transfer of viscous forces across this interface and that a finite velocity exist at the interface (Russell and Charles, 1959; Yuster, 1953). This would result in effective permeabilities being dependent on the difference in the viscosities or viscosity ratio of the phases. Rose (1960) shows theoretically that this effect is secondary and most experimental data fail to substantiate this dependence (Bear, 1975 p. 462). Therefore the relative permeabilities used here are assumed independent of the viscosity ratio of the brine and gas phases. The relative permeabilities are assumed to depend on saturation according to relationships presented by Brooks and Corey (1964). Volume 3 of this report presents the Brooks and Corey parameters that define the relative permeabilities assumed for WIPP Brine and Gas.

Table A-1. Definitions for Terms Used to Describe Flow Through Porous Media.

permeability	Defined by Darcy's law as a conductivity of 1.0 darcy ($9.87 \times 10^{-13} m^2$) if a pressure difference of 1 atm produces a flow rate of 1 cm^3/sec of a fluid with 1 cp viscosity through a cube having sides 1 cm in length (Dullen, 1979). It is determined under single phase saturated flow conditions and is independent of the fluid used. Also the absolute permeability or specific permeability of porous media. [L^2], [m^2]
effective permeability	Defined for each phase and determined experimentally and defined by extensions of Darcy's law to immiscible multiple phase flow. It is dependent on both fluid and rock properties as well as fluid saturation. Assumed to vary with saturation according to Brooks and Corey relationship Brook and Corey (1964). [L^2], [m^2]
relative permeability	Defined for each phase as the ratio of effective permeability of a phase to the absolute permeability of the rock. [dimensionless]
saturation	Defined for each phase as the ratio of the volume of a phase to the pore volume. The volume of a fluid in a reservoir is then the product of that fluid's saturation, rock porosity, and reservoir volume. [dimensionless]
porosity	Volume fraction of the reservoir that is void (non-rock). The quantity 1.0-porosity is the reservoir's rock volume. [dimensionless]
Irreducible Saturation	Also the residual saturation and is defined for each phase as the saturation corresponding to the formation of a continuous flow path of that phase. Below irreducible saturation that phase will not flow under a potential gradient. [dimensionless]

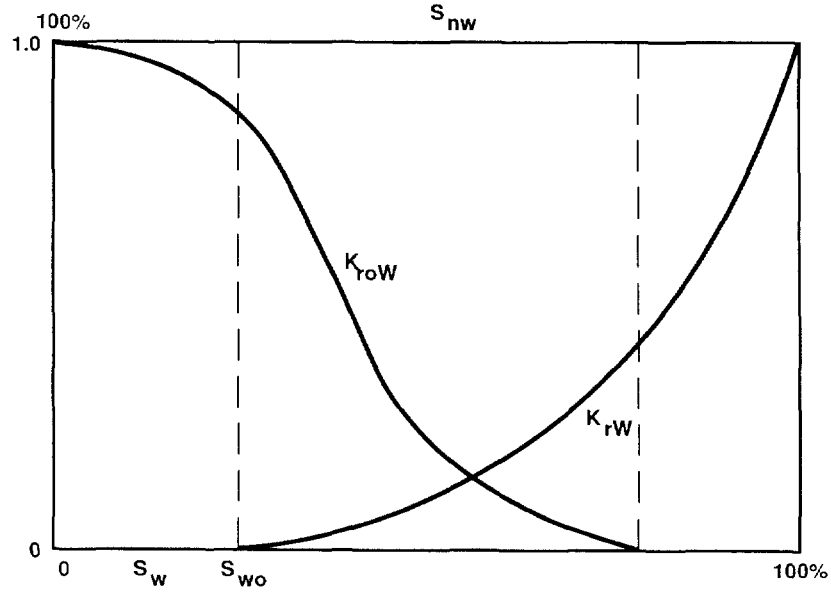

Figure A-1. Typical Relative Permeability Dependence on Saturation

References

Aziz, K., and A. Settari. 1979. *Petroleum Reservoir Simulation.* Applied Science, London.

Bear, J. 1975. *Dynamics of Fluids in Porous Media.* Elsevier Publishing Company, 1975, NY.

Bear, J. 1979. *Hydraulics of Groundwater.* McGraw-Hill, Inc., 1979, NY.

Bear, J., and Y. Bachmat. 1966. *Hydrodynamic Dispersion in Non-uniform Flow Through Porous Media, Taking into Account Density and Viscosity Differences (in Hebrew with English Summary),* Hydraulic Lab., Technion, Haifa, Israel, IASH, P.N. 4/66, 1966.

Bear, J., and Y. Bachmat. 1967. "A Generalized Theory on Hydrodynamic Dispersion in Porous Media," *I.A.S.H. Symp. Artificial Recharge and Management of Aquifers,* Haifa, Israel, IASH, P.N. 72, 7-16 (1967).

Bear, J., D. Zaslowsky, and S. Irmay. 1968. *Physical Principles of Water Percolation and Seepage,* UNESCO, Paris, 1968.

Brook, R. H., and A. T. Corey. 1964. *Hydraulic Properties of Porous Media.* Civil Engineering Department, Colorado State University, Fort Collins. Hydrology Paper No. 3.

Coats, K. H. 1980. "In-Situ Combustion Model." *Soc. Pet. Eng. J.,* Dec. 1980, 533-554.

Collins, R. E. 1961. *Flow of Fluids Through Porous Materials.* Reinhold Publishing Corporation, NY.

Corey, A. T. 1986. *Mechanics of Immiscible Fluids in Porous Media.* Water Resources Publication, Littleton, CO.

Crichlow, H. B. 1977. *Modern Reservoir Engineering - A Simulation Approach.* Prentice - Hall, Inc. 1977 Englewood Cliffs, NJ.

Crookston, H. B., W. E. Culham, and W. H. Chen. 1979. "Numerical Simulation Model for Thermal Recovery Processes." *Soc. Pet. Eng. J.,* Feb, 1979, 37-58.

Dake, L. P. 1978. *Fundamentals of Reservoir Engineering.* Elsevier Scientific Publishing Co., 1978, NY.

deMarsily, G. 1986. *Quantitative Hydrogeology.* Academic Press, Inc., Orlando, Florida, 440 pp.

DeWest, R. J. M. 1965. *Geohydrology.* John Wiley and Sons, New York, NY, 366 pp.

Dullien, F. A. L. 1979. *Porous Media Fluid Transport and Pore Structure.* Academic Press, 1979, NY.

Hiatt, W. N. 1968. *Mathematical Basis of Two-Phase, Incompressible, Vertical Flow Through Porous Media and Its Implications in the Study of Gravity-Drainage-Type Petroleum Reservoirs.*

Hubbert, M. K. 1956. "The Theory of Ground Water Motion." *J. Geol.* 48: 785-944 (1940).

Hubbert, M. K. 1956. "Darcy Law and the Field Equations of the Flow of Underground Fluids." *Trans. Amer. Inst. Min. Metal. Eng.* 207: 222-239 (1956).

Klinkenberg, L. J. 1941. "The Permeability of Porous Media to Liquids and Gases." *Amer. Petrol. Inst. Drilling Prod. Pract.* 200-213 (1941).

Peaceman, D. W. 1977. *Fundamentals of Numerical Reservoir Simulation.* Elsevier Scientific Publishing Company, New York.

Rose, W. 1953. "Fluid Flow in Petroleum Reservoirs III. Effect of Fluid-Fluid Interfacial Boundary Condition," *Ill. Geol. Survey Circ.* 291 (1960).

Rubin, B., and P. K. W. Vinsome. 1980. "The Simulation of the In-Situ Combustion Process in One Dimension Using a Highly Implicit Finite Difference Scheme." *J. Col. Pet. Tech.* (Oct/Dec 1980), 68-76.

Russell, T. W. F. and E. Charles. 1959. "Effect of the Less Viscous Liquid in the Laminar Flow of Two Immiscible Liquids." *Canad. J. Chem. Eng.* 37: 18-24 (1959).

Scheideggar, A. E. 1960. *The Physics of Flow Through Porous Media,* 2nd ed. University of Toronto Press, Toronto, 1960.

Vaughn, P. 1986. *A Numerical Model for Thermal Recovery Processes in Tar Sand: Description and Application.* April 1986, DOE Report #DOE/FE/60177-2219.

Yuster, S. T. 1953 "Theoretical Considerations of Multiphase Flow in Idealized Capillary Systems," *Proc. 3rd World Petrol., The Hague* 2: 437-445 (1953).

B. LHS SAMPLES AND CALCULATED NORMALIZED RELEASES

This appendix contains the 60 sample elements for each of the 45 parameters varied and sampled by LHS and summaries of radionuclide release to the 5-km, accessible environment boundary south of the WIPP for the E1 and E1E2 scenarios with intrusions at 1000, 3000, 5000, 7000, and 9000 yr. The simulations are run assuming a dual porosity model for transport in the Culebra Dolomite Member of the Rustler Formation.

This appendix also contains the summaries of release to the accessible environment from initially drilling into the repository and bringing up cuttings from one average activity of CH waste and one average activity of RH waste. (The CH waste activity is subsequently multiplied by a factor to account for the four CH activity levels. This modified activity along with the probability of actually hitting these various CH activity levels are used when constructing the CCDF.

Cuttings were calculated for the five different intrusion times but there is no difference between the E1, E2 or E1E2 scenarios. The different scenarios are accounted for by the CCDFPERM program. The output tables were created by the CCDFCALC computer code after reading the output databases created by STAFF2D and CUTTINGS and are the input to the CCDFPERM program which calculates the final CCDF.

Table B-1 lists the 45 parameters sampled and the distribution type used.

Table B-1. Numerical ID and Distributions of 45 Sampled Parameters in December 1991 WIPP PA Calculations

Parameter	Range		Distribution Type
Unmodified Waste Form			
1. Initial waste saturation	0	2.76×10^{-1}	Uniform
Gas Generation			
Corrosion			
2. Stoichiometry	0	1	Uniform
3. Relative humid rate	0	5×10^{-1}	Cumulative
4. Inundated rate, mol/m^2/s*	0	1.2×10^{-8}	Cumulative
Microbiological			
5. Relative humid rate	0	2×10^{-1}	Uniform
6. Inundated rate, mol/m^2/s**	0	1.6×10^{-8}	Cumulative
9. Stoichiometry	0	1.67	Uniform
Volume Fractions of IDB Categories			
7. Metal/Glass	2.76×10^{-1}	4.76×10^{-1}	Normal
8. Combustibles	2.84×10^{-1}	4.84×10^{-1}	Normal

* mole/m^2 surface area steel/s

** mole/kg cellulosics/s

Table B-1. Numerical ID and Distributions of 45 Sampled Parameters in December 1991 WIPP PA Calculations (Continued)

Parameter	Range		Distribution Type
18. Relative areas in Eh-pH Space (index)	0	1.0	Uniform
Dissolved Concentrations (Solubility)*			
19. Am3+, Molar	$5x10^{-14}$	1.4	Cumulative
20. Np4+, Molar	$3x10^{-16}$	$2x10^{-5}$	Cumulative
21. Np5+, Molar	$3x10^{-11}$	$1.2x10^{-2}$	Cumulative
22. Pu4+, Molar	2.0×10^{-16}	4×10^{-6}	Cumulative
23. Pu5+, Molar	$2.5x10^{-17}$	$5.5x10^{-4}$	Cumulative
24. Th4+, Molar	$5.5x10^{-16}$	$2.2x10^{-6}$	Cumulative
25. U4+, Molar	$1x10^{-15}$	$5x10^{-2}$	Cumulative
26. U6+, Molar	$1x10^{-7}$	1	Cumulative
Halite within Salado Formation			
10. Permeability (k), m^2	8.6×10^{-22}	5.4×10^{-20}	Data
Anhydrite Layers within Salado Formation			
11. Pore pressure (p), Pa	9.3×10^{6}	1.39×10^{7}	Data
12. Undisturbed, Permeability (k), m^{2**}	6.8×10^{-20}	9.5×10^{-19}	Data
13. Undisturbed Porosity (ϕ)	1×10^{-3}	3×10^{-2}	Cumulative
45. Threshold displacement index (p_t)	0	1	Normal
Castile Formation Brine Reservoir			
14. Initial pressure (p), Pa	1.1×10^{7}	2.1×10^{7}	Cumulative
15. Storativity, bulk (S_b), m^3	2×10^{-2}	2	Lognormal
16. Permeability (k), m^2	1×10^{-14}	1×10^{-11}	Lognormal
17. Diameter, m	2.67×10^{-1}	4.44×10^{-1}	Uniform
Culebra Dolomite Member			
27. Transmissivity field	0	60	Uniform
28. Climate index	0	1.0	Uniform
29. Dispersivity, longitudinal (α_L), m	5×10^{1}	3×10^{2}	Cumulative
30. Fracture porosity (ϕ_f)	1×10^{-4}	1×10^{-2}	Lognormal
Fracture Partition Coefficients, m^3/kg			
31. Americium	0.0	1×10^{3}	Cumulative

* For the following elements – Np, Pu, and Th – only one species was used in each sample. The species were rank correlated at r = 0.99.

** Permeability of the halite and anhydrite were rank correlated with an r = 0.80.

Table B-1. Numerical ID and Distributions of 45 Sampled Parameters in December 1991 WIPP PA Calculations (Concluded)

Parameter	Range		Distribution Type
32. Neptunium	0.0	1×10^{3}	Cumulative
33. Plutonium	0.0	1×10^{3}	Cumulative
34. Thorium	0.0	1×10^{1}	Cumulative
35. Uranium	0.0	1	Cumulative
36. Fracture spacing (2B), m	6×10^{-2}	8	Cumulative
37. Matrix porosity (ϕ_m)	9.6×10^{-2}	2.08×10^{-1}	Spatial
Matrix Partition Coefficients (m^3/kg)			
40. Am	0.0	1×10^{2}	Cumulative
41. Np	0.0	1×10^{2}	Cumulative
42. Pu	0.0	1×10^{2}	Cumulative
43. Th	0.0	1	Cumulative
44. U	0.0	1	Cumulative
Probability Model for Scenarios			
38. Rate constant in Poisson drilling model, $\Lambda(t)$, s-1	0 <	1.04×10^{-11}	Uniform
39. Area of pressurized brine reservoir	2.5×10^{-1}	5.52×10^{-1}	Cumulative

Table B-2 lists the Latin Hypercube sampled (LHS) values for each of the 45 parameters.

Table B-2. Sixty Values Sampled By LHS For 45 Parameters which Were Varied in December 1991 WIPP PA Calculations

Material Parameter RUN NO.	WastRef Brine Sat X(1)	WastRef CorRatFr X(2)	WastRef G RatCor H X(3)	WastRef GRatCorI X(4)	WastRef GRatMicH X(5)	WastRef GRatMicI X(6)
1	0.854	0.315	3.454E-02	6.775E-09	0.122	4.706E-09
2	0.810	0.459	0.436	7.461E-09	0.165	9.441E-10
3	0.611	0.850	0.372	1.128E-10	0.152	2.845E-09
4	0.139	0.254	0.194	4.313E-09	7.819E-02	3.106E-09
5	0.123	0.383	0.359	8.924E-09	0.198	1.265E-08
6	0.945	0.942	8.686E-02	2.106E-09	0.116	3.953E-10
7	0.725	0.653	5.686E-02	9.723E-09	0.138	1.608E-09
8	0.151	0.402	6.637E-02	1.164E-08	0.118	1.147E-09
9	0.469	0.818	7.563E-02	3.244E-09	0.146	1.392E-08
10	0.109	0.536	4.467E-02	1.073E-08	0.168	2.787E-10
11	0.236	0.361	1.606E-02	5.732E-09	8.184E-02	1.166E-08
12	4.723E-02	0.614	9.739E-02	7.308E-10	0.104	1.355E-08
13	0.738	0.478	2.705E-03	1.286E-08	6.507E-02	2.939E-09
14	0.259	0.892	1.952E-02	7.067E-09	8.896E-02	1.091E-08
15	0.923	4.737E-02	9.478E-02	6.221E-10	3.021E-02	1.019E-08

Table B-2. Sixty Values Samples By LHS For 45 Parameters Which Were Varied In December 1991 WIPP PA Calculations (Continued)

Material Parameter RUN NO.	WastRef Brine Sat X(1)	WastRef CorRatFr X(2)	WastRef GRadCorH X(3)	WastRef GRatCorI X(4)	WastRef GRatMicH X(5)	WastRef GRatMicI X(6)
16	0.288	0.212	0.327	1.172E-08	5.353E-02	2.291E-09
17	0.532	0.233	0.475	2.921E-09	4.978E-02	8.301E-10
18	0.331	0.671	8.471E-02	1.264E-08	0.173	5.550E-09
19	0.390	5.652E-02	0.464	9.104E-09	6.868E-02	1.206E-08
20	0.229	0.190	0.495	6.679E-09	1.346E-02	3.723E-09
21	0.960	0.447	0.413	4.429E-09	0.177	1.736E-09
22	0.355	0.523	0.157	7.330E-09	7.233E-02	2.464E-09
23	8.905E-02	0.152	0.232	3.525E-09	5.874E-02	5.234E-09
24	0.537	0.574	0.421	1.194E-08	0.162	2.172E-09
25	0.650	0.905	0.300	1.084E-08	3.453E-02	9.966E-10
26	0.847	1.134E-02	9.080E-03	1.140E-08	9.785E-02	6.680E-09
27	1.635E-02	0.563	8.296E-02	1.600E-09	0.189	3.508E-09
28	0.446	0.732	6.049E-02	9.515E-09	4.091E-03	1.586E-08
29	0.278	0.285	0.271	3.914E-09	5.248E-02	2.067E-09
30	0.817	0.789	0.325	4.136E-09	7.454E-02	2.424E-09
31	0.967	0.685	9.240E-02	1.232E-08	0.148	1.474E-08
32	0.404	0.427	5.519E-03	8.680E-09	9.438E-02	2.646E-09
33	0.787	0.986	0.192	2.488E-09	4.027E-02	1.367E-09
34	5.649E-02	0.933	0.142	5.351E-09	3.841E-02	5.767E-09
35	2.096E-02	0.328	3.873E-02	1.140E-09	2.195E-02	5.228E-10
36	0.773	8.698E-02	6.932E-02	9.337E-09	0.100	6.373E-10
37	0.760	0.170	0.385	6.332E-09	0.193	1.515E-08
38	0.496	0.588	2.427E-02	7.912E-09	9.186E-02	1.554E-10
39	0.454	0.500	0.398	4.872E-09	1.698E-02	6.403E-09
40	0.341	0.134	0.114	2.099E-09	0.142	1.184E-09
41	0.554	0.781	0.249	8.331E-09	6.304E-02	1.435E-09
42	0.697	0.649	1.021E-02	1.834E-09	2.670E-02	1.430E-08
43	0.372	0.125	7.764E-02	5.941E-09	0.130	1.599E-09
44	0.575	0.766	0.127	3.583E-09	0.185	1.906E-09
45	0.679	0.342	0.108	5.081E-09	2.491E-02	1.313E-08
46	0.883	0.383	4.118E-02	2.651E-09	0.110	7.384E-10
47	0.642	0.868	2.058E-02	1.438E-09	0.156	2.737E-09
48	0.707	0.742	0.288	7.857E-09	7.898E-03	1.076E-08
49	0.624	0.486	2.742E-02	5.668E-09	0.195	9.775E-09
50	0.432	0.862	7.281E-02	9.637E-10	0.173	8.372E-09
51	0.906	0.983	0.450	8.089E-09	0.111	7.530E-09
52	0.209	0.816	0.353	1.112E-08	1.258E-02	1.254E-08
53	0.182	0.627	0.217	1.237E-08	0.128	4.370E-09
54	0.190	0.961	4.961E-02	6.227E-09	0.159	7.458E-09
55	0.890	0.104	3.077E-02	2.446E-10	4.374E-02	9.474E-09
56	0.989	0.271	0.274	1.036E-08	8.555E-02	8.150E-09
57	7.286E-02	0.243	0.172	1.020E-08	0.136	8.908E-09
58	0.507	0.701	5.553E-02	9.999E-09	3.208E-03	1.051E-10
59	0.303	3.048E-02	5.130E-02	3.006E-09	0.124	1.937E-09
60	0.586	7.983E-02	0.242	4.754E-09	0.182	3.053E-09

Table B-2. Sixty Values Sampled By LHS For 45 Parameters which Were Varied in December 1991 WIPP PA Calculations (Continued)

RUN NO.	Wast Ref VolMetal X(7)	Wast Ref Vol Wood X(8)	Wast Ref SH2Mic X(9)	Salado Prm_X_U X(10)	MB139 Pressure X(11)	MB139 Prm_X_U X(12)
1	0.358	0.316	0.595	1.027E-19	1.473E+07	1.077E-18
2	0.350	0.301	1.48	3.989E-20	1.267E+07	1.530E-18
3	0.385	0.284	1.11	2.341E-21	8.502E+06	5.455E-20
4	0.334	0.339	1.17	5.593E-21	1.280E+07	1.309E-19
5	0.385	0.376	0.200	3.348E-22	1.277E+07	3.839E-20
6	0.412	0.396	0.785	1.207E-19	8.415E+06	8.435E-19
7	0.339	0.401	0.773	2.347E-20	1.208E+07	1.035E-18
8	0.380	0.340	0.888	1.544E-21	1.308E+07	6.800E-20
9	0.321	0.351	0.856	6.585E-21	1.425E+07	1.170E-18
10	0.345	0.358	0.335	5.878E-21	1.280E+07	6.800E-20
11	0.314	0.388	0.927	1.115E-19	9.027E+06	1.257E-18
12	0.371	0.374	1.47	7.331E-21	1.262E+07	7.853E-20
13	0.361	0.370	1.03	5.402E-21	1.280E+07	6.800E-20
14	0.318	0.395	1.66	1.337E-21	1.396E+07	7.291E-20
15	0.336	0.382	1.33	6.438E-21	9.176E+06	7.900E-20
16	0.352	0.413	7.328E-02	7.433E-20	1.280E+07	1.319E-18
17	0.432	0.378	1.58	1.120E-21	1.445E+07	2.595E-20
18	0.368	0.305	0.331	5.046E-21	1.280E+07	4.760E-19
19	0.392	0.384	0.650	1.416E-20	1.235E+07	6.631E-19
20	0.344	0.404	0.464	5.972E-21	8.738E+06	8.099E-20
21	0.399	0.409	1.23	1.429E-21	1.264E+07	7.665E-20
22	0.404	0.329	0.153	3.508E-20	1.406E+07	1.395E-18
23	0.326	0.414	1.00	5.577E-20	1.417E+07	7.307E-20
24	0.382	0.434	1.50	1.334E-19	1.280E+07	1.659E-18
25	0.424	0.446	1.27	9.770E-20	1.272E+07	1.798E-18
26	0.398	0.360	0.479	7.504E-22	8.542E+06	6.949E-20
27	0.427	0.409	0.817	3.469E-21	1.154E+07	8.143E-20
28	0.378	0.439	1.07	6.086E-22	8.816E+06	4.557E-20
29	0.293	0.387	1.13	4.162E-22	1.186E+07	7.475E-20
30	0.330	0.424	3.803E-02	2.715E-21	1.286E+07	6.800E-20
31	0.390	0.353	1.21	8.079E-21	1.082E+07	8.161E-20
32	0.395	0.399	0.299	1.571E-20	1.012E+07	7.446E-19
33	0.369	0.365	0.133	4.489E-22	1.358E+07	6.623E-20
34	0.365	0.379	2.110E-02	8.179E-21	9.254E+06	7.930E-20
35	0.356	0.334	0.432	4.234E-21	1.336E+07	7.568E-20
36	0.413	0.453	1.28	3.414E-21	1.428E+07	7.031E-20
37	0.388	0.322	0.956	6.083E-21	1.280E+07	7.837E-20
38	0.440	0.406	1.35	7.230E-22	8.220E+06	3.247E-20
39	0.476	0.350	0.383	7.050E-21	9.657E+06	1.946E-19
40	0.423	0.362	1.63	4.941E-21	1.274E+07	7.742E-20
41	0.283	0.443	1.60	4.762E-20	9.389E+06	2.843E-19
42	0.465	0.356	1.43	2.632E-20	1.457E+07	8.934E-19
43	0.365	0.455	0.726	5.509E-21	1.388E+07	5.972E-20
44	0.379	0.428	9.182E-02	5.749E-21	1.269E+07	6.800E-20
45	0.363	0.422	1.15	6.070E-21	1.467E+07	8.059E-20
46	0.407	0.369	0.516	8.084E-20	1.297E+07	1.574E-18
47	0.298	0.346	1.37	1.881E-21	1.257E+07	6.800E-20
48	0.453	0.371	0.614	3.919E-21	1.280E+07	3.026E-20
49	0.374	0.466	0.671	1.258E-21	1.326E+07	6.834E-20
50	0.402	0.484	0.407	9.420E-22	1.280E+07	8.007E-20
51	0.347	0.384	0.572	1.702E-21	1.442E+07	6.800E-20
52	0.393	0.416	0.705	7.265E-21	1.280E+07	5.837E-19
53	0.442	0.398	1.42	2.025E-22	1.376E+07	1.397E-20
54	0.417	0.392	0.995	6.918E-20	1.259E+07	6.800E-20
55	0.373	0.430	0.269	1.929E-21	1.098E+07	6.800E-20

Table B-2. Sixty Values Samples By LHS For 45 Parameters Which Were Varied In December 1991 WIPP PA Calculations (Continued)

RUN NO.	Wast Ref VolMetal X(7)	Wast Ref Vol Wood X(8)	Wast Ref SH2Mil X(9)	Salado Prm_X_U X(10)	MB139 Pressure X(11)	MB139 Prm_X_U X(12)
56	0.341	0.345	0.538	5.744E-22	8.910E+06	1.867E-20
57	0.420	0.366	1.55	4.587E-20	1.029E+07	7.999E-20
58	0.354	0.331	0.891	8.206E-22	1.318E+07	6.800E-20
59	0.407	0.391	0.171	7.766E-21	1.280E+07	4.111E-19
60	0.311	0.419	0.225	5.680E-21	1.348E+07	7.135E-20

RUN NO.	MB139 Pore_U X(13)	Castile_R Pressure X(14)	Castile_R StorBulk X(15)	Borehole Prm_X X(16)	Borehole DiamMod X(17)	Wast Ref RelAEhpH X(18)
1	2.337E-02	1.232E+07	0.118	2.050E-14	0.410	0.276
2	2.329E-02	1.202E+07	0.156	1.047E-12	0.294	0.160
3	2.840E-02	1.426E+07	1.08	1.019E-13	0.377	0.841
4	2.413E-02	1.940E+07	0.465	3.905E-14	0.424	0.666
5	6.626E-03	1.174E+07	5.452E-02	2.271E-13	0.273	0.977
6	3.835E-03	1.486E+07	0.212	4.515E-12	0.361	0.588
7	1.423E-02	1.408E+07	0.143	6.181E-13	0.339	0.389
8	4.976E-03	1.890E+07	0.808	7.856E-13	0.329	0.473
9	2.194E-02	1.147E+07	8.365E-02	1.000E-11	0.333	0.576
10	2.797E-02	1.544E+07	0.191	2.681E-12	0.277	0.870
11	2.062E-03	1.172E+07	0.566	4.298E-14	0.345	0.715
12	1.298E-02	1.654E+07	9.906E-02	1.116E-13	0.307	0.209
13	1.080E-02	1.242E+07	0.138	1.200E-12	0.420	0.381
14	1.831E-02	1.575E+07	0.373	2.276E-12	0.422	0.623
15	7.069E-03	1.503E+07	0.269	1.578E-12	0.328	0.903
16	9.040E-03	1.321E+07	0.541	3.537E-12	0.434	0.789
17	8.390E-03	1.607E+07	0.113	1.462E-12	0.387	0.820
18	1.706E-02	1.157E+07	0.655	5.053E-13	0.405	0.945
19	1.487E-02	1.548E+07	0.411	2.393E-13	0.442	0.284
20	6.341E-03	1.117E+07	0.501	2.491E-13	0.318	9.611E-02
21	2.927E-02	1.271E+07	0.157	4.819E-14	0.390	2.648E-02
22	4.805E-03	1.833E+07	9.589E-02	1.309E-13	0.286	0.329
23	1.893E-02	1.222E+07	0.177	3.888E-13	0.311	0.998
24	8.745E-03	1.362E+07	3.996E-02	1.714E-12	0.427	0.695
25	1.142E-02	1.167E+07	1.81	1.462E-13	0.283	0.648
26	2.559E-02	1.243E+07	0.174	2.628E-13	0.349	0.429
27	5.575E-03	1.154E+07	0.257	2.004E-13	0.398	0.510
28	8.070E-03	1.993E+07	0.122	5.495E-12	0.363	0.526
29	1.360E-02	1.124E+07	0.126	5.953E-13	0.337	0.342
30	2.517E-02	1.762E+07	0.228	4.873E-13	0.380	0.739
31	1.423E-03	1.790E+07	0.295	1.366E-13	0.311	0.403
32	9.893E-03	1.191E+07	3.792E-02	7.621E-14	0.365	0.923
33	7.770E-03	1.851E+07	9.060E-02	7.112E-14	0.369	0.866
34	2.105E-02	1.811E+07	0.326	4.470E-13	0.299	5.813E-02
35	1.131E-03	1.129E+07	0.284	1.162E-13	0.439	0.230
36	1.941E-02	1.141E+07	0.637	2.267E-14	0.270	0.893
37	2.930E-03	1.258E+07	0.370	8.042E-13	0.375	4.848E-02
38	2.650E-02	1.188E+07	0.224	9.055E-14	0.391	0.246
39	1.631E-02	2.033E+07	6.140E-02	1.806E-13	0.415	0.759
40	2.335E-03	1.911E+07	0.134	3.546E-13	0.326	0.810
41	9.117E-03	1.266E+07	2.229E-02	3.225E-14	0.352	0.546
42	1.266E-02	1.227E+07	1.40	9.110E-13	0.305	0.683

Table B-2. Sixty Values Sampled By LHS For 45 Parameters Which Were Varied In December 1991 WIPP PA Calculations (Continued)

RUN NO.	MB139 Pore_U X(13)	Castile_R Pressure X(14)	Castile_R StorBulk X(15)	Borehole Prm_X X(16)	Borehole DiamMod X(17)	Wast Ref RelAEhpH X(18)
43	2.551E-03	1.463E+07	0.973	9.961E-13	0.372	0.134
44	4.061E-03	1.685E+07	0.197	5.514E-13	0.384	0.185
45	1.038E-02	1.686E+07	6.910E-02	1.622E-13	0.268	7.773E-02
46	3.131E-03	1.261E+07	4.850E-02	6.654E-13	0.431	0.610
47	5.274E-03	1.216E+07	7.638E-02	2.959E-13	0.355	0.307
48	2.973E-02	1.122E+07	7.937E-02	2.038E-12	0.320	0.365
49	1.539E-02	2.046E+07	0.315	9.869E-14	0.396	0.255
50	4.433E-03	1.249E+07	0.761	1.770E-13	0.288	0.726
51	5.830E-03	1.101E+07	0.411	4.306E-13	0.417	0.438
52	6.889E-03	1.721E+07	0.105	1.088E-14	0.401	0.780
53	3.539E-03	1.136E+07	6.601E-02	2.975E-13	0.407	0.178
54	2.214E-02	1.185E+07	0.206	6.375E-14	0.315	0.127
55	2.691E-02	1.109E+07	0.169	7.211E-13	0.436	0.461
56	1.662E-03	1.208E+07	0.343	5.933E-14	0.291	0.960
57	1.752E-02	1.338E+07	0.255	3.631E-13	0.342	0.559
58	7.443E-03	1.972E+07	0.438	3.211E-13	0.300	1.443E-02
59	9.428E-03	1.205E+07	2.587E-02	1.289E-12	0.281	0.108
60	2.006E-02	2.088E+07	0.245	2.084E-13	0.356	0.489

RUN NO.	Am^{+3} Solm X(19)	Np^{+4} Sol M X(20)	Np^{+5} Sol M X(21)	Pu^{+4} Sol M X(22)	Pu^{+5} Sol M X(23)	Th^{+4} Sol M X(24)
1	1.080E-10	1.850E-09	1.680E-07	1.909E-09	8.394E-10	9.272E-11
2	0.203	2.844E-09	2.737E-07	4.096E-12	2.675E-13	8.644E-09
3	6.019E-07	3.912E-11	1.812E-08	3.772E-07	5.302E-05	1.736E-06
4	5.557E-04	2.247E-07	3.421E-06	1.518E-12	1.207E-13	6.645E-11
5	3.634E-10	3.763E-09	3.346E-07	1.071E-08	1.656E-08	7.327E-09
6	9.860E-10	5.273E-07	9.456E-06	4.490E-08	1.361E-07	5.318E-09
7	5.988E-11	3.122E-07	5.483E-06	1.185E-06	1.819E-04	1.681E-11
8	2.781E-10	2.321E-09	2.480E-07	3.083E-06	4.131E-04	4.808E-13
9	1.671E-11	5.633E-09	5.552E-07	4.300E-08	1.491E-07	2.787E-13
10	8.132E-07	1.117E-06	4.670E-04	1.524E-08	4.692E-08	2.532E-11
11	2.993E-11	1.024E-05	5.006E-03	1.176E-07	9.552E-06	9.457E-08
12	9.701E-07	1.441E-05	8.102E-03	3.231E-08	1.084E-07	8.285E-16
13	2.183E-10	1.151E-11	3.920E-09	3.652E-10	3.954E-10	4.555E-09
14	8.734E-10	4.735E-11	2.490E-08	2.283E-10	1.333E-10	7.170E-11
15	4.189E-07	2.963E-11	1.570E-08	3.920E-06	5.035E-04	4.317E-11
16	3.680E-07	5.202E-06	3.436E-03	3.186E-07	3.679E-05	6.307E-09
17	3.626E-12	1.274E-06	6.182E-04	1.686E-08	6.375E-08	2.722E-09
18	7.520E-10	1.384E-05	8.770E-03	1.239E-11	3.273E-11	6.262E-07
19	1.798E-10	3.306E-06	2.750E-03	1.449E-10	2.012E-10	3.824E-13
20	3.046E-04	1.716E-07	2.557E-06	8.286E-08	3.996E-06	9.174E-10
21	8.743E-11	7.438E-08	1.383E-06	5.463E-10	5.535E-10	5.955E-11
22	7.906E-10	1.626E-09	1.827E-07	4.900E-08	1.664E-07	2.065E-06
23	1.956E-07	3.346E-08	7.398E-07	1.628E-15	1.981E-16	2.966E-15
24	4.831E-08	3.268E-16	4.467E-11	2.953E-08	8.233E-08	1.470E-07
25	3.420E-11	2.614E-10	4.306E-08	2.426E-12	1.677E-13	8.038E-11
26	0.264	5.686E-07	8.172E-06	7.384E-16	7.319E-17	1.183E-07
27	6.281E-04	1.146E-07	2.131E-06	4.139E-10	4.138E-10	1.345E-06
28	1.896E-10	5.198E-07	8.881E-06	1.036E-13	1.769E-14	3.244E-07
29	9.571E-07	5.595E-09	5.869E-07	1.747E-06	2.312E-04	8.050E-13
30	1.09	4.793E-07	8.085E-06	3.012E-10	3.010E-10	5.456E-08

Table B-2. Sixty Values Samples By LHS For 45 Parameters Which Were Varied In December 1991 WIPP PA Calculations (Continued)

RUN NO.	Am^{+3} SolM X(19)	Np^{+4} Sol M X(20)	Np^{+5} Sol M X(21)	Pu^{+4} Sol M X(22)	Pu^{+5} Sol M X(23)	Th^{+4} Sol M X(24)
31	1.174E-03	3.317E-07	6.160E-06	3.382E-07	4.807E-05	1.400E-15
32	1.811E-05	4.613E-09	4.694E-07	2.079E-08	6.791E-08	3.560E-15
33	8.906E-04	4.398E-09	4.301E-07	4.995E-12	3.209E-13	5.334E-15
34	4.235E-11	1.209E-15	1.473E-10	4.091E-16	5.546E-17	3.534E-11
35	9.258E-10	1.835E-11	7.314E-09	7.517E-09	3.293E-08	3.322E-09
36	7.585E-11	1.508E-07	3.933E-06	4.428E-10	4.665E-10	9.268E-13
37	1.517E-10	2.665E-09	3.169E-07	9.479E-13	4.702E-14	4.353E-15
38	7.496E-07	1.881E-06	1.083E-03	5.445E-08	1.890E-07	9.794E-14
39	4.825E-10	5.145E-09	5.039E-07	5.188E-10	5.098E-10	5.993E-13
40	5.348E-10	1.723E-06	9.840E-04	8.352E-16	1.028E-16	1.782E-07
41	9.668E-04	5.750E-11	2.749E-08	2.695E-12	1.861E-13	7.915E-09
42	1.25	2.348E-15	2.503E-10	5.757E-10	5.648E-10	6.032E-09
43	0.729	2.517E-07	4.545E-06	3.763E-12	2.398E-13	4.818E-10
44	4.592E-10	4.237E-07	7.075E-06	1.277E-15	1.722E-16	2.925E-11
45	3.467E-04	1.931E-05	1.113E-02	1.895E-10	1.724E-10	9.875E-07
46	0.645	6.832E-07	1.195E-04	9.900E-11	8.268E-11	1.599E-13
47	1.384E-11	1.394E-06	7.828E-04	3.232E-10	3.259E-10	6.413E-08
48	6.415E-10	1.538E-06	8.646E-04	9.944E-07	6.953E-05	3.658E-09
49	5.225E-07	9.042E-07	1.942E-04	2.764E-06	3.780E-04	1.073E-08
50	1.268E-10	4.502E-11	2.249E-08	2.637E-08	9.569E-08	4.453E-12
51	1.105E-06	1.030E-06	3.380E-04	2.551E-10	2.792E-10	1.213E-11
52	6.115E-10	3.229E-09	3.990E-07	2.451E-07	2.753E-05	1.594E-07
53	1.160E-06	5.299E-12	2.819E-09	1.850E-07	2.362E-05	4.930E-11
54	1.332E-03	3.842E-07	6.378E-06	3.963E-08	1.299E-07	1.994E-07
55	1.494E-10	2.916E-15	2.994E-10	7.244E-11	5.394E-11	9.515E-11
56	1.168E-07	2.439E-11	1.034E-08	1.827E-15	2.238E-16	8.833E-09
57	6.740E-07	1.756E-15	1.884E-10	5.735E-12	3.906E-13	7.314E-13
58	3.571E-10	7.851E-10	8.756E-08	5.673E-08	1.806E-07	7.562E-11
59	7.249E-10	8.958E-10	1.155E-07	1.599E-07	1.526E-05	9.512E-09
60	3.166E-07	9.088E-16	1.095E-10	2.707E-07	3.460E-05	1.940E-09

RUN NO.	U^{+4} SolM X(25)	U^{+6} SolM X(26)	Culebra FieldIdx X(27)	Culebra ClimtIdx X(28)	Culebra Disp_Ing X(29)	Culebra FPore X(30)
1	5.674E-03	3.843E-02	0.612	4.754E-02	59.3	3.373E-04
2	1.097E-02	6.729E-02	0.842	0.153	72.2	6.051E-03
3	9.926E-07	2.984E-05	0.506	0.846	165.	7.606E-04
4	6.936E-04	6.966E-03	0.597	0.464	282.	2.647E-03
5	8.458E-05	1.690E-03	0.701	0.470	206.	1.304E-03
6	2.561E-03	2.338E-02	0.896	0.222	77.8	1.554E-03
7	4.323E-09	5.469E-07	3.516E-03	0.969	272.	4.447E-03
8	4.543E-03	4.310E-02	0.243	3.045E-02	208.	1.676E-04
9	4.988E-02	0.914	4.062E-02	0.833	61.4	1.048E-03
10	1.221E-02	8.384E-02	0.285	0.125	131.	3.211E-04
11	3.876E-02	0.790	0.820	0.813	238.	1.487E-03
12	6.470E-07	2.179E-05	0.216	5.657E-02	52.8	7.358E-03
13	2.796E-04	3.463E-03	0.186	0.381	50.0	5.535E-04
14	6.245E-04	6.241E-03	0.973	0.789	241.	1.208E-03
15	2.420E-02	0.361	0.344	0.605	232.	4.104E-04
16	8.701E-07	1.851E-05	0.562	0.204	82.8	1.343E-03
17	8.932E-09	9.753E-07	0.173	0.728	118.	9.504E-04
18	1.215E-09	2.477E-07	0.687	0.587	74.5	1.760E-03

Table B-2. Sixty Values Sampled By LHS For 45 Parameters which Were Varied in December 1991 WIPP PA Calculations (Continued)

RUN NO.	U^{+4} SolM X(25)	U^{+6} SolM X(26)	Culebra Field Idx X(27)	Culebra ClimtIdx X(28)	Culebra Disp_Ing X(29)	Culebra FPore X(30)
19	1.425E-02	0.173	0.964	0.940	89.4	1.868E-03
20	2.912E-07	8.830E-06	0.374	0.660	54.7	2.624E-04
21	4.443E-05	9.478E-04	0.464	0.716	159.	9.785E-04
22	8.125E-03	5.940E-02	0.311	0.536	213.	1.000E-02
23	4.534E-07	1.426E-05	0.815	0.739	153.	3.304E-03
24	3.771E-07	1.278E-05	0.399	0.233	276.	1.041E-03
25	3.158E-05	5.836E-04	0.662	0.417	90.1	5.374E-04
26	8.859E-05	1.820E-03	0.490	0.755	188.	7.807E-04
27	9.102E-04	9.377E-03	0.223	0.438	81.4	1.057E-04
28	1.477E-03	1.812E-02	8.122E-02	0.674	63.5	2.506E-03
29	4.153E-04	5.334E-03	0.914	0.626	126.	4.657E-04
30	5.708E-05	1.120E-03	2.404E-02	0.334	86.4	1.099E-03
31	6.229E-09	6.672E-07	0.351	0.502	184.	6.819E-04
32	7.956E-09	8.273E-07	0.778	0.868	220.	4.368E-04
33	1.298E-07	6.962E-06	0.628	0.523	57.3	4.906E-04
34	4.829E-05	9.888E-04	0.861	0.485	292.	2.950E-04
35	7.281E-05	1.466E-03	0.166	0.366	265.	2.212E-03
36	7.892E-04	8.364E-03	0.413	0.896	84.6	8.208E-04
37	4.445E-06	1.240E-04	0.325	0.297	97.3	6.090E-04
38	9.433E-04	9.696E-03	9.229E-02	9.709E-03	258.	4.138E-03
39	3.127E-02	0.402	0.281	0.768	113.	2.490E-04
40	7.894E-05	1.529E-03	0.647	0.695	75.4	3.947E-04
41	7.015E-04	7.338E-03	0.528	0.389	61.9	8.872E-04
42	7.791E-07	2.551E-05	0.785	0.327	95.0	2.086E-03
43	2.738E-05	4.406E-04	0.436	0.416	67.9	6.894E-04
44	8.777E-04	8.649E-03	0.872	0.191	99.3	2.870E-03
45	2.079E-05	4.199E-04	0.149	0.146	296.	2.151E-04
46	1.333E-02	9.681E-02	0.728	0.932	167.	8.718E-04
47	3.163E-09	2.668E-07	0.767	0.306	138.	1.604E-04
48	3.208E-04	4.162E-03	0.984	7.205E-02	198.	6.467E-04
49	9.799E-05	1.958E-03	0.945	0.559	68.9	7.244E-04
50	3.567E-04	4.030E-03	0.549	0.167	87.1	1.968E-03
51	3.656E-02	0.600	0.127	0.912	248.	5.944E-04
52	6.680E-05	1.319E-03	0.431	0.106	70.4	1.647E-03
53	4.857E-04	4.822E-03	0.919	0.647	141.	3.767E-03
54	1.385E-04	2.415E-03	0.104	0.985	92.0	1.458E-03
55	1.176E-07	1.638E-06	0.261	9.896E-02	178.	2.335E-03
56	8.334E-03	7.984E-02	0.469	0.278	105.	3.189E-03
57	5.626E-04	6.579E-03	6.127E-02	0.264	79.2	3.790E-04
58	3.794E-05	7.308E-04	0.742	0.959	66.3	1.234E-03
59	1.077E-05	2.459E-04	0.583	0.854	56.2	1.807E-03
60	1.715E-04	2.653E-03	0.675	0.578	93.7	1.138E-03

RUN NO.	Culebra FKd_Am_C X(31)	Culebra FKd_Np_C X(32)	Culebra FKd_Pu_C X(33)	Culebra FKd_Th_C X(34)	Culebra FKd_U_C X(35)	Culebra FrctrSp X(36)
1	39.8	419.	494.	6.560E-02	5.791E-04	7.31
2	247.	690.	690.	2.64	0.992	0.329
3	77.9	9.821E-03	180.	1.240E-02	3.464E-03	0.546
4	1.28	202.	1.97	7.925E-04	1.156E-02	7.12
5	1.141E-02	5.075E-03	728.	0.893	3.841E-03	1.40
6	577.	1.365E-02	69.0	1.704E-02	9.744E-03	5.59
7	647.	201.	825.	1.52	7.360E-03	0.298
8	1.10	991.	0.178	4.030E-02	6.461E-03	0.273

Table B-2. Sixty Values Samples By LHS For 45 Parameters Which Were Varied In December 1991 WIPP PA Calculations (Continued)

RUN NO.	Culebra FKd_Am_C X(31)	Culebra FKd_Np_C X(32)	Culebra FKd_Pu_C X(33)	Culebra FKd_Th_C X(34)	Culebra FKd_U_C X(35)	Culebra FrctrSp X(36)
9	2.49	7.655E-04	541.	4.526E-02	1.095E-02	4.56
10	733.	333.	145.	7.714E-02	1.183E-02	0.356
11	1.06	27.4	910.	8.19	0.392	0.776
12	412.	2.326E-03	306.	3.005E-02	1.300E-02	0.192
13	525.	1.676E-03	4.27	2.122E-02	4.144E-03	0.283
14	7.79	595.	565.	8.80	1.487E-02	3.75
15	477.	6.809E-03	394.	5.028E-02	9.550E-03	0.165
16	0.482	286.	5.18	2.501E-02	0.885	0.115
17	2.06	129.	351.	3.26	0.573	4.86
18	824.	8.876E-02	576.	0.217	9.142E-04	0.248
19	561.	343.	1.43	9.376E-02	2.982E-03	0.215
20	697.	643.	230.	4.925E-02	5.271E-03	6.80
21	0.836	5.578E-03	2.94	2.18	8.966E-03	0.201
22	0.878	558.	1.20	0.426	6.140E-03	0.238
23	1.43	134.	0.480	0.837	2.968E-04	5.37
24	379.	90.0	812.	2.723E-02	1.405E-03	0.393
25	0.626	1.637E-03	0.591	6.779E-02	0.133	6.25
26	193.	4.429E-03	0.370	0.151	0.801	6.18
27	0.295	0.263	7.37	4.03	5.564E-03	8.236E-02
28	2.24	833.	319.	1.623E-02	1.159E-03	0.352
29	346.	64.4	459.	9.065E-02	2.117E-03	2.95
30	16.5	8.359E-03	161.	9.02	1.035E-02	7.82
31	0.424	8.528E-04	3.600E-03	6.79	2.373E-03	4.10
32	856.	507.	262.	8.353E-02	0.643	0.287
33	0.967	625.	943.	9.904E-02	0.307	8.809E-02
34	302.	2.558E-03	890.	3.856E-02	6.744E-03	0.375
35	772.	1.584E-04	7.73	0.956	1.277E-02	3.20
36	5.33	395.	776.	9.255E-03	1.349E-02	0.138
37	121.	733.	974.	6.023E-02	1.426E-02	2.53
38	1.53	1.311E-02	852.	0.530	1.985E-04	1.97
39	6.53	7.243E-03	99.3	0.729	0.204	2.25
40	990.	4.154E-03	431.	0.332	7.072E-04	0.336
41	1.25	1.096E-02	1.79	0.273	5.420E-03	0.141
42	9.23	7.525E-03	657.	0.377	4.273E-03	0.121
43	0.181	1.468E-02	966.	0.520	5.984E-03	5.92
44	507.	3.378E-03	0.733	4.61	7.163E-03	6.751E-02
45	617.	0.923	203.	5.644E-02	8.681E-03	0.254
46	1.39	937.	499.	7.216E-02	1.644E-03	6.62
47	3.02	792.	2.644E-02	5.968E-02	1.055E-02	1.84
48	3.89	0.445	374.	5.80	1.963E-03	1.09
49	715.	6.182E-03	618.	8.906E-02	0.448	4.22
50	924.	860.	4.605E-02	7.509E-02	4.654E-03	7.68
51	956.	0.781	2.55	0.781	2.606E-03	0.103
52	888.	496.	743.	5.77	5.088E-02	1.50
53	218.	1.019E-02	5.78	5.650E-03	0.694	5.10
54	3.36	900.	11.5	3.466E-02	8.154E-03	2.76
55	3.76	736.	2.38	0.637	1.232E-02	0.155
56	332.	451.	632.	8.234E-02	7.691E-03	0.378
57	807.	883.	3.29	9.49	1.406E-02	0.311
58	152.	264.	72.6	7.29	3.160E-03	0.227
59	173.	1.171E-02	9.15	3.82	4.964E-03	3.61
60	436.	0.514	35.8	0.655	1.736E-03	0.176

Table B-2. Sixty Values Samples By LHS For 45 Parameters Which Were Varied In December 1991 WIPP PA Calculations (Continued)

RUN NO.	Culebra Porosity X(37)	Culebra Kd_Am_C X(38)	Culebra Kd_Np_C X(39)	Culebra Kd_Pu_C X(40)	Culebra Kd_Th_C X(41)	Culebra Kd_U_C X(42)
1	0.133	3.609E-02	3.549E-02	0.116	6.603E-02	3.237E-02
2	0.185	0.333	91.2	0.938	7.053E-03	6.583E-04
3	9.854E-02	8.183E-02	4.062E-03	40.0	1.304E-03	6.137E-04
4	0.207	0.998	4.849E-04	92.7	8.686E-03	0.194
5	0.178	0.169	0.121	7.642E-03	8.653E-03	9.397E-04
6	0.163	0.136	9.27	0.694	0.438	2.061E-04
7	0.121	1.356E-02	5.16	2.551E-02	5.029E-03	1.087E-02
8	0.115	0.150	87.3	32.1	0.863	5.635E-04
9	0.122	0.130	5.562E-02	0.381	5.662E-03	1.233E-04
10	0.120	0.347	5.154E-05	4.398E-04	4.605E-03	9.050E-02
11	0.118	53.7	4.957E-02	47.3	1.333E-02	0.462
12	0.138	57.2	1.798E-04	6.307E-02	0.594	0.261
13	0.172	26.7	1.92	0.133	5.899E-03	6.630E-02
14	0.163	9.28	7.942E-04	4.185E-02	0.580	9.994E-02
15	0.127	3.01	5.651E-04	1.633E-03	2.108E-02	3.970E-02
16	0.147	2.285E-02	6.25	7.772E-02	9.823E-03	0.868
17	0.203	77.1	1.082E-03	1.887E-02	0.668	2.298E-04
18	0.179	87.3	1.476E-03	0.186	2.294E-02	1.460E-03
19	9.539E-02	4.874E-02	1.312E-03	3.274E-03	8.440E-02	5.483E-05
20	0.154	39.7	1.195E-03	8.434E-02	6.482E-03	1.077E-03
21	0.101	0.892	69.4	5.077E-03	0.803	0.672
22	0.121	4.91	2.688E-04	0.488	4.851E-03	4.451E-02
23	0.140	2.802E-02	51.1	0.210	7.909E-03	8.371E-04
24	0.106	0.182	1.426E-04	8.96	4.954E-02	9.392E-02
25	0.180	0.105	1.085E-04	0.456	6.317E-02	2.458E-02
26	8.716E-02	0.200	0.107	1.418E-02	4.187E-02	1.278E-03
27	0.138	6.201E-02	3.811E-04	4.911E-02	0.706	4.344E-04
28	0.139	0.142	8.994E-02	61.5	9.644E-03	2.714E-03
29	0.175	9.405E-02	0.184	0.963	3.327E-03	7.931E-02
30	7.623E-02	0.159	7.131E-04	70.4	5.371E-02	5.547E-02
31	0.179	8.15	6.753E-02	0.332	4.306E-03	0.171
32	0.131	6.41	1.410E-02	82.2	0.981	2.157E-05
33	0.120	5.884E-02	0.136	0.531	7.392E-02	0.704
34	0.164	0.393	20.1	6.405E-03	3.292E-02	0.125
35	0.158	9.895E-02	0.195	0.269	0.181	3.412E-02
36	0.123	12.4	1.115E-03	79.1	1.484E-03	5.997E-02
37	0.116	6.892E-02	2.141E-04	16.4	7.680E-02	1.560E-02
38	0.199	0.148	2.704E-02	0.630	3.740E-02	8.225E-04
39	0.211	0.752	28.6	0.767	2.164E-03	4.912E-02
40	0.111	7.509E-02	11.3	0.797	9.168E-03	0.963
41	0.120	0.115	7.210E-02	7.407E-02	9.183E-02	1.056E-03
42	0.126	0.129	3.80	9.461E-02	8.103E-03	4.007E-04
43	0.130	72.3	59.2	0.217	2.844E-03	3.562E-04
44	0.121	0.300	6.381E-04	46.6	7.663E-05	1.614E-04
45	0.166	8.802E-02	0.102	0.166	6.933E-03	4.879E-04
46	0.145	6.56	6.736E-04	1.181E-03	1.844E-03	7.486E-02
47	0.143	0.536	8.125E-02	0.846	4.462E-04	1.173E-03
48	0.119	0.247	9.876E-04	2.15	9.892E-02	0.183
49	0.222	3.250E-03	4.349E-04	0.301	6.014E-03	1.340E-03
50	0.119	0.645	0.709	8.558E-03	0.284	0.163
51	0.204	1.59	8.578E-02	54.6	0.276	0.135
52	0.124	30.7	7.87	2.796E-03	2.634E-03	2.579E-04
53	0.100	0.122	4.651E-02	0.239	3.503E-03	8.507E-02
54	0.178	0.191	0.147	4.400E-03	0.157	0.111
55	0.179	0.271	8.473E-04	3.573E-02	3.700E-03	0.152
56	0.214	3.176E-02	3.086E-04	9.532E-03	0.922	2.324E-02
57	0.179	4.474E-02	2.752E-02	26.0	8.412E-04	7.041E-02

Table B-2. Sixty Values Samples By LHS For 45 Parameters Which Were Varied In December 1991 WIPP PA Calculations (Continued)

RUN NO.	Culebra Porosity X(37)	Culebra Kd_Am_C X(38)	Culebra Kd_Np_C X(39)	Culebra Kd_Pu_C X(40)	Culebra Kd_Th_C X(41)	Culebra Kd_U_C X(42)
58	0.122	9.340E-02	4.317E-06	5.528E-02	7.517E-03	7.079E-04
59	0.180	0.113	1.355E-03	99.9	0.350	0.474
60	0.179	97.2	0.172	0.651	0.471	8.230E-03

RUN NO.	Global Lambda X(43)	Castile_R AreaFrc X(44)	MB139 ThrsPIdx X(45)
1	9.787E-12	0.443	0.215
2	8.358E-12	0.489	0.286
3	6.893E-12	0.416	0.517
4	4.289E-12	0.354	0.747
5	5.988E-12	0.407	0.709
6	5.181E-12	0.257	0.898
7	5.544E-12	0.362	0.163
8	2.465E-12	0.348	0.111
9	9.137E-12	0.368	0.823
10	1.795E-12	0.462	0.611
11	8.574E-13	0.418	0.374
12	9.401E-12	0.361	0.236
13	9.402E-13	0.342	0.589
14	7.739E-12	0.352	0.594
15	6.288E-12	0.483	0.434
16	7.511E-12	0.439	0.813
17	1.287E-12	0.345	0.258
18	2.946E-12	0.429	0.190
19	1.659E-12	0.372	0.488
20	2.857E-12	0.432	0.783
21	5.290E-12	0.470	0.961
22	8.232E-12	0.306	0.642
23	4.004E-12	0.382	0.580
24	7.884E-12	0.423	0.385
25	6.472E-12	0.456	0.308
26	7.221E-12	0.340	0.331
27	7.001E-12	0.336	0.405
28	8.930E-12	0.491	0.506
29	5.471E-12	0.318	8.115E-02
30	1.118E-12	0.385	0.477
31	7.402E-12	0.366	0.525
32	1.017E-11	0.425	0.688
33	3.789E-12	0.410	0.527
34	1.917E-12	0.325	0.418
35	8.128E-12	0.514	0.632
36	4.408E-12	0.392	0.650
37	5.373E-13	0.377	0.537
38	1.481E-12	0.412	0.761
39	3.220E-12	0.464	-1.192E-07
40	9.590E-12	0.331	0.566
41	3.511E-13	0.402	0.297
42	8.838E-14	0.445	0.561
43	1.030E-11	0.358	0.358
44	5.872E-12	0.476	0.271
45	3.828E-12	0.420	0.616
46	2.675E-12	0.450	0.549
47	2.141E-12	0.453	0.703
48	9.991E-12	0.458	0.439

Table B-2. Sixty Values Samples By LHS For 45 Parameters Which Were Varied In December 1991 WIPP PA Calculations (Concluded)

RUN NO.	Global Lambda X(43)	Castile_R Area Frc X(44)	MB139 ThrsPIdx X(45)
49	3.318E-12	0.386	0.413
50	3.483E-12	0.468	0.396
51	4.560E-12	0.333	0.449
52	4.821E-12	0.324	0.728
53	2.393E-12	0.394	0.499
54	8.728E-12	0.435	0.354
55	8.595E-12	0.311	0.339
56	6.666E-12	0.397	0.465
57	6.100E-12	0.374	0.877
58	9.295E-12	0.399	0.678
59	2.908E-13	0.390	0.464
60	4.940E-12	0.441	0.659

Table B-3 lists the ranks of samples.

Table B-3. Ranks of Sixty Values Sampled

Material Parameter RUN NO.	WastRef Brine Sat X(1)	WastRef CorRatFr X(2)	WastRef GRatCorH X(3)	WastRef GRatCorI X(4)	WastRef GRatMicH X(5)	WastRef G Rat Mic I X(6)	Wast Ref VolMetal X(7)	Wast Ref VolWood X(8)
1	52.	19.	11.	33.	37.	34.	21.	4.
2	49.	28.	56.	36.	50.	9.	17.	2.
3	37.	51.	51.	1.	46.	27.	36.	1.
4	9.	16.	38.	21.	24.	30.	10.	9.
5	8.	23.	50.	42.	60.	53.	35.	26.
6	57.	57.	27.	11.	35.	4.	48.	37.
7	44.	40.	18.	46.	42.	16.	12.	40.
8	10.	25.	20.	54.	36.	11.	33.	10.
9	29.	50.	23.	16.	44.	56.	7.	14.
10	7.	33.	14.	50.	51.	3.	15.	17.
11	15.	22.	5.	28.	25.	50.	5.	33.
12	3.	37.	30.	4.	32.	55.	28.	25.
13	45.	29.	1.	60.	20.	28.	22.	23.
14	16.	54.	6.	34.	27.	49.	6.	36.
15	56.	3.	29.	3.	10.	47.	11.	29.
16	18.	13.	48.	55.	17.	22.	18.	45.
17	32.	14.	59.	14.	15.	8.	55.	27.
18	20.	41.	26.	59.	52.	36.	26.	3.
19	24.	4.	58.	43.	21.	51.	39.	30.
20	14.	12.	60.	32.	5.	32.	14.	41.
21	58.	27.	54.	22.	54.	17.	43.	44.
22	22.	32.	35.	35.	22.	24.	45.	6.
23	6.	10.	40.	17.	18.	35.	8.	46.
24	33.	35.	55.	56.	49.	21.	34.	53.
25	40.	55.	46.	51.	11.	10.	53.	56.
26	51.	1.	3.	53.	30.	39.	42.	18.
27	1.	34.	25.	8.	57.	31.	54.	43.
28	27.	44.	19.	45.	2.	60.	31.	54.
29	17.	18.	43.	19.	16.	20.	2.	32.
30	50.	48.	47.	20.	23.	23.	9.	50.
31	59.	42.	28.	57.	45.	58.	38.	15.
32	25.	26.	2.	41.	29.	25.	41.	39.

Table B-3. Ranks of Sixty Values Sampled (Continued)

Material Parameter RUN NO.	WastRef Brine Sat X(1)	WastRef CorRatFr X(2)	WastRef GRatCorH X(3)	WastRef GRatCorI X(4)	WastRef GRatMicH X(5)	WastRef GRatMicI X(6)	Wast Ref VolMetal X(7)	Wast Ref VolWood X(8)
33	48.	60.	37.	12.	13.	13.	27.	20.
34	4.	56.	34.	26.	12.	37.	25.	28.
35	2.	20.	12.	6.	7.	5.	20.	8.
36	47.	6.	21.	44.	31.	6.	49.	57.
37	46.	11.	52.	31.	58.	59.	37.	5.
38	30.	36.	8.	38.	28.	2.	56.	42.
39	28.	31.	53.	24.	6.	38.	60.	13.
40	21.	9.	32.	10.	43.	12.	52.	19.
41	34.	47.	42.	40.	19.	14.	1.	55.
42	42.	39.	4.	9.	9.	57.	59.	16.
43	23.	8.	24.	29.	40.	15.	24.	58.
44	35.	46.	33.	18.	56.	18.	32.	51.
45	41.	21.	31.	25.	8.	54.	23.	49.
46	53.	24.	13.	13.	33.	7.	46.	22.
47	39.	53.	7.	7.	47.	26.	3.	12.
48	43.	45.	45.	37.	3.	48.	58.	24.
49	38.	30.	9.	27.	59.	46.	30.	59.
50	26.	52.	22.	5.	53.	43.	44.	60.
51	55.	59.	57.	39.	34.	41.	16.	31.
52	13.	49.	49.	52.	4.	52.	40.	47.
53	11.	38.	39.	58.	39.	33.	57.	38.
54	12.	58.	15.	30.	48.	40.	50.	35.
55	54.	7.	10.	2.	14.	45.	29.	52.
56	60.	17.	44.	49.	26.	42.	13.	11.
57	5.	15.	36.	48.	41.	44.	51.	21.
58	31.	43.	17.	47.	1.	1.	19.	7.
59	19.	2.	16.	15.	38.	19.	47.	34.
60	36.	5.	41.	23.	55.	29.	4.	48.

RUN NO.	Wast Ref SH2Mil X(9)	Salado Prm_X_U X(10)	MB139 Pressure X(11)	MB139 Prm_X_U X(12)	MB139 Pore_U X(13)	Castile_R Pressure X(14)	Castile_R StorBulk X(15)	Borehole Prm_X X(16)
1	22.	57.	60.	52.	51.	24.	18.	2.
2	54.	49.	25.	57.	50.	18.	24.	48.
3	40.	19.	3.	8.	58.	36.	58.	14.
4	43.	29.	36.	41.	52.	55.	49.	5.
5	8.	2.	29.	6.	19.	14.	6.	25.
6	29.	59.	2.	49.	10.	38.	32.	58.
7	28.	46.	19.	51.	37.	35.	23.	41.
8	32.	15.	43.	16.	14.	53.	56.	44.
9	31.	37.	54.	53.	48.	9.	12.	60.
10	13.	32.	36.	16.	57.	40.	29.	56.
11	34.	58.	8.	54.	4.	13.	52.	6.
12	53.	40.	23.	32.	35.	44.	15.	15.
13	38.	27.	36.	16.	32.	25.	22.	49.
14	60.	13.	51.	25.	43.	42.	45.	55.
15	48.	36.	9.	33.	21.	39.	38.	52.
16	3.	54.	36.	55.	27.	32.	51.	57.
17	57.	11.	57.	3.	25.	43.	17.	51.
18	12.	26.	36.	45.	41.	11.	54.	38.
19	24.	44.	20.	47.	38.	41.	47.	26.
20	17.	33.	5.	38.	18.	3.	50.	27.
21	45.	14.	24.	29.	59.	31.	25.	7.
22	6.	48.	52.	56.	13.	51.	14.	17.

Table B-3. Ranks of Sixty Values Sampled (Continued)

RUN NO.	Wast Ref SH2Mil X(9)	Salado Prm_X_U X(10)	MB139 Pressure X(11)	MB139 Prm_X_U X(12)	MB139 Pore_U X(13)	Castile_R Pressure X(14)	Castile_R StorBulk X(15)	Borehole Prm_X X(16)
23	37.	52.	53.	26.	44.	22.	28.	34.
24	55.	60.	36.	59.	26.	34.	4.	53.
25	46.	56.	27.	60.	33.	12.	60.	19.
26	18.	8.	4.	22.	54.	26.	27.	28.
27	30.	22.	17.	39.	16.	10.	37.	23.
28	39.	6.	6.	7.	24.	57.	19.	59.
29	41.	3.	18.	27.	36.	5.	20.	40.
30	2.	20.	41.	16.	53.	48.	34.	37.
31	44.	42.	15.	40.	2.	49.	40.	18.
32	11.	45.	13.	48.	30.	17.	3.	11.
33	5.	4.	48.	10.	23.	52.	13.	10.
34	1.	43.	10.	34.	47.	50.	42.	36.
35	16.	24.	46.	28.	1.	6.	39.	16.
36	47.	21.	55.	23.	45.	8.	53.	3.
37	35.	35.	36.	31.	7.	28.	44.	45.
38	49.	7.	1.	5.	55.	16.	33.	12.
39	14.	38.	12.	42.	40.	58.	7.	22.
40	59.	25.	28.	30.	5.	54.	21.	32.
41	58.	51.	11.	43.	28.	30.	1.	4.
42	52.	47.	58.	50.	34.	23.	59.	46.
43	27.	28.	50.	9.	6.	37.	57.	47.
44	4.	31.	26.	16.	11.	45.	30.	39.
45	42.	34.	59.	37.	31.	46.	9.	20.
46	19.	55.	42.	58.	8.	29.	5.	42.
47	50.	17.	21.	16.	15.	21.	10.	29.
48	23.	23.	36.	4.	60.	4.	11.	54.
49	25.	12.	45.	21.	39.	59.	41.	13.
50	15.	10.	36.	36.	12.	27.	55.	21.
51	21.	16.	56.	16.	17.	1.	46.	35.
52	26.	39.	30.	46.	20.	47.	16.	1.
53	51.	1.	49.	1.	9.	7.	8.	30.
54	36.	53.	22.	16.	49.	15.	31.	9.
55	10.	18.	16.	16.	56.	2.	26.	43.
56	20.	5.	7.	2.	3.	20.	43.	8.
57	56.	50.	14.	35.	42.	33.	36.	33.
58	33.	9.	44.	16.	22.	56.	48.	31.
59	7.	41.	36.	44.	29.	19.	2.	50.
60	9.	30.	47.	24.	46.	60.	35.	24.

RUN NO.	Borehole DiamMod X(17)	Wast Ref RelAEhpH X(18)	Amt^{+3} Sol M X(19)	Np^{+4} Sol M X(20)	Np^{+5} Sol M X(21)	Pu^{+4} Sol M X(22)	Pu^{+5} Sol M X(23)	Th^{+4} Sol M X(24)
1	49.	17.	10.	20.	19.	31.	31.	29.
2	10.	10.	55.	23.	22.	13.	13.	43.
3	38.	51.	38.	12.	12.	54.	54.	59.
4	54.	40.	49.	36.	35.	9.	9.	25.
5	3.	59.	19.	25.	24.	33.	32.	41.
6	32.	36.	30.	44.	45.	42.	41.	38.
7	25.	24.	7.	38.	38.	56.	56.	18.
8	22.	29.	17.	21.	21.	59.	59.	11.
9	23.	35.	3.	30.	29.	41.	42.	9.
10	4.	53.	41.	49.	49.	34.	34.	19.
11	27.	43.	4.	57.	57.	47.	47.	49.
12	14.	13.	43.	59.	58.	39.	39.	1.

Table B-3. Ranks of Sixty Values Sampled (Continued)

RUN NO.	Borehole DiamMod X(17)	Wast Ref RelAEhpH X(18)	Amt^{+3} Sol M X(19)	Np^{+4} Sol M X(20)	Np^{+5} Sol M X(21)	Pu^{+4} Sol M X(22)	Pu^{+5} Sol M X(23)	Th^{+4} Sol M X(24)
13	52.	23.	16.	8.	8.	25.	25.	37.
14	53.	38.	28.	14.	14.	21.	19.	26.
15	21.	55.	36.	11.	11.	60.	60.	22.
16	57.	48.	35.	56.	56.	52.	52.	40.
17	41.	50.	1.	50.	50.	35.	35.	34.
18	47.	57.	26.	58.	59.	16.	16.	56.
19	60.	18.	14.	55.	55.	19.	21.	10.
20	18.	6.	47.	35.	34.	46.	46.	32.
21	42.	2.	9.	32.	32.	29.	29.	24.
22	7.	20.	27.	19.	20.	43.	43.	60.
23	16.	60.	33.	31.	31.	5.	5.	3.
24	55.	42.	31.	1.	1.	38.	37.	51.
25	6.	39.	5.	16.	16.	10.	10.	28.
26	28.	26.	56.	45.	43.	2.	2.	50.
27	45.	31.	50.	33.	33.	26.	26.	58.
28	33.	32.	15.	43.	44.	7.	7.	55.
29	24.	21.	42.	29.	30.	57.	57.	14.
30	39.	45.	59.	42.	42.	23.	23.	47.
31	15.	25.	53.	39.	39.	53.	53.	2.
32	34.	56.	46.	27.	27.	36.	36.	4.
33	35.	52.	51.	26.	26.	14.	14.	6.
34	11.	4.	6.	3.	3.	1.	1.	21.
35	59.	14.	29.	9.	9.	32.	33.	35.
36	2.	54.	8.	34.	36.	27.	27.	15.
37	37.	3.	13.	22.	23.	8.	8.	5.
38	43.	15.	40.	54.	54.	44.	45.	7.
39	50.	46.	21.	28.	28.	28.	28.	12.
40	20.	49.	22.	53.	53.	3.	3.	53.
41	29.	33.	52.	15.	15.	11.	11.	42.
42	13.	41.	60.	5.	5.	30.	30.	39.
43	36.	9.	58.	37.	37.	12.	12.	31.
44	40.	12.	20.	41.	41.	4.	4.	20.
45	1.	5.	48.	60.	60.	20.	20.	57.
46	56.	37.	57.	46.	46.	18.	18.	8.
47	30.	19.	2.	51.	51.	24.	24.	48.
48	19.	22.	24.	52.	52.	55.	55.	36.
49	44.	16.	37.	47.	47.	58.	58.	46.
50	8.	44.	11.	13.	13.	37.	38.	16.
51	51.	27.	44.	48.	48.	22.	22.	17.
52	46.	47.	23.	24.	25.	50.	50.	52.
53	48.	11.	45.	7.	7.	49.	49.	23.
54	17.	8.	54.	40.	40.	40.	40.	54.
55	58.	28.	12.	6.	6.	17.	17.	30.
56	9.	58.	32.	10.	10.	6.	6.	44.
57	26.	34.	39.	4.	4.	15.	15.	13.
58	12.	1.	18.	17.	17.	45.	44.	27.
59	5.	7.	25.	18.	18.	48.	48.	45.
60	31.	30.	34.	2.	2.	51.	51.	33.

Table B-3. Ranks of Sixty Values Sampled (Continued)

RUN NO.	U^{+4} Sol M X(25)	U^{+6} Sol M X(26)	Culebra Field Idx X(27)	Culebra Climt Idx X(28)	Culebra Disp_Ing X(29)	Culebra FPore X(30)	Culebra FKd_Am_C X(31)	Culebra FKd_Np_C X(32)
1	49.	48.	37.	3.	6.	9.	29.	43.
2	52.	51.	51.	10.	14.	58.	36.	51.
3	15.	15.	31.	51.	40.	24.	30.	18.
4	40.	40.	36.	28.	58.	51.	13.	37.
5	28.	28.	43.	29.	46.	37.	1.	11.
6	47.	47.	54.	14.	17.	41.	47.	23.
7	3.	3.	1.	59.	56.	57.	49.	36.
8	48.	49.	15.	2.	47.	3.	11.	60.
9	60.	60.	3.	50.	7.	32.	19.	2.
10	53.	53.	18.	8.	35.	8.	52.	40.
11	59.	59.	50.	49.	51.	40.	10.	31.
12	12.	13.	13.	4.	2.	59.	41.	6.
13	33.	33.	12.	23.	1.	17.	45.	5.
14	39.	38.	59.	48.	52.	35.	26.	48.
15	56.	56.	21.	37.	50.	12.	43.	14.
16	14.	12.	34.	13.	20.	38.	5.	39.
17	6.	6.	11.	44.	33.	29.	17.	34.
18	1.	1.	42.	36.	15.	43.	55.	25.
19	55.	55.	58.	57.	24.	45.	46.	41.
20	9.	9.	23.	40.	3.	6.	50.	50.
21	22.	22.	28.	43.	39.	30.	7.	12.
22	50.	50.	19.	33.	48.	60.	8.	47.
23	11.	11.	49.	45.	38.	54.	15.	35.
24	10.	10.	24.	15.	57.	31.	40.	33.
25	20.	20.	40.	26.	25.	16.	6.	4.
26	29.	29.	30.	46.	44.	25.	34.	10.
27	44.	44.	14.	27.	19.	1.	3.	26.
28	46.	46.	5.	41.	9.	50.	18.	55.
29	36.	37.	55.	38.	34.	14.	39.	32.
30	24.	24.	2.	21.	22.	33.	28.	17.
31	4.	4.	22.	31.	43.	21.	4.	3.
32	5.	5.	47.	53.	49.	13.	56.	46.
33	8.	8.	38.	32.	5.	15.	9.	49.
34	23.	23.	52.	30.	59.	7.	37.	7.
35	26.	26.	10.	22.	55.	48.	53.	1.
36	42.	42.	25.	54.	21.	26.	24.	42.
37	16.	16.	20.	18.	29.	19.	31.	52.
38	45.	45.	6.	1.	54.	56.	16.	22.
39	57.	57.	17.	47.	32.	5.	25.	15.
40	27.	27.	39.	42.	16.	11.	60.	9.
41	41.	41.	32.	24.	8.	28.	12.	20.
42	13.	14.	48.	20.	28.	47.	27.	16.
43	19.	19.	27.	25.	11.	22.	2.	24.
44	43.	43.	53.	12.	30.	52.	44.	8.
45	18.	18.	9.	9.	60.	4.	48.	30.
46	54.	54.	44.	56.	41.	27.	14.	59.
47	2.	2.	46.	19.	36.	2.	20.	54.
48	34.	35.	60.	5.	45.	20.	23.	27.
49	30.	30.	57.	34.	12.	23.	51.	13.
50	35.	34.	33.	11.	23.	46.	58.	56.
51	58.	58.	8.	55.	53.	18.	59.	29.
52	25.	25.	26.	7.	13.	42.	57.	45.
53	37.	36.	56.	39.	37.	55.	35.	19.
54	31.	31.	7.	60.	26.	39.	21.	58.
55	7.	7.	16.	6.	42.	49.	22.	53.
56	51.	52.	29.	17.	31.	53.	38.	44.

Table B-3. Ranks of Sixty Values Sampled (Continued)

RUN NO.	U^{+4} Sol M X(25)	U^{+6} Sol M X(26)	Culebra Field Idx X(27)	Culebra Climt Idx X(28)	Culebra Disp_lng X(29)	Culebra FPore X(30)	Culebra FKd_Am_C X(31)	Culebra FKd_Np_C X(32)
57	38.	39.	4.	16.	18.	10.	54.	57.
58	21.	21.	45.	58.	10.	36.	32.	38.
59	17.	17.	35.	52.	4.	44.	33.	21.
60	32.	32.	41.	35.	27.	34.	42.	28.

RANKS OF LATIN HYPERCUBE SAMPLE INPUT VECTORS

RUN NO.	Culebra FKd_Pu_C X(33)	Culebra FKd_Th_C X(34)	Culebra FKd_U_C X(35)	Culebra FrctrSp X(36)	Culebra Porosity X(37)	Culebra Kd_Am_C X(38)	Culebra Kd_Np_C X(39)	Culebra Kd_Pu_C X(40)
1	41.	20.	3.	58.	28.	6.	29.	24.
2	49.	48.	60.	24.	53.	36.	60.	44.
3	30.	4.	16.	31.	4.	13.	25.	51.
4	12.	1.	40.	57.	57.	43.	11.	59.
5	50.	44.	17.	34.	45.	29.	40.	9.
6	25.	6.	36.	51.	39.	24.	52.	40.
7	54.	46.	30.	22.	18.	2.	49.	14.
8	4.	13.	27.	19.	9.	27.	59.	50.
9	43.	14.	39.	47.	20.	23.	32.	34.
10	28.	24.	41.	27.	15.	37.	2.	1.
11	57.	57.	53.	32.	11.	55.	31.	53.
12	34.	10.	44.	12.	29.	56.	5.	19.
13	17.	7.	18.	20.	42.	52.	47.	25.
14	44.	58.	48.	44.	38.	50.	16.	16.
15	38.	16.	35.	10.	25.	45.	12.	3.
16	18.	8.	59.	5.	35.	3.	50.	21.
17	36.	49.	55.	48.	55.	58.	19.	13.
18	45.	32.	5.	17.	48.	59.	24.	27.
19	10.	29.	14.	14.	3.	8.	22.	5.
20	32.	15.	22.	56.	36.	54.	21.	22.
21	15.	47.	34.	13.	6.	42.	58.	7.
22	9.	36.	26.	16.	17.	46.	7.	36.
23	6.	43.	2.	50.	32.	4.	56.	28.
24	53.	9.	7.	30.	7.	30.	4.	47.
25	7.	21.	50.	54.	52.	18.	3.	35.
26	5.	31.	58.	53.	2.	32.	39.	12.
27	20.	51.	24.	2.	30.	10.	9.	17.
28	35.	5.	6.	26.	31.	25.	37.	55.
29	40.	28.	11.	41.	43.	16.	44.	45.
30	29.	59.	37.	60.	1.	28.	15.	56.
31	1.	55.	12.	45.	48.	49.	33.	33.
32	33.	26.	56.	21.	27.	47.	26.	58.
33	58.	30.	52.	3.	14.	9.	41.	37.
34	56.	12.	28.	28.	40.	38.	54.	8.
35	21.	45.	43.	42.	37.	17.	45.	31.
36	52.	3.	45.	7.	22.	51.	20.	57.
37	60.	19.	47.	39.	10.	11.	6.	48.
38	55.	38.	1.	37.	54.	26.	27.	38.
39	27.	41.	51.	38.	58.	41.	55.	41.
40	39.	34.	4.	25.	8.	12.	53.	42.
41	11.	33.	23.	8.	16.	20.	34.	20.
42	48.	35.	19.	6.	24.	22.	48.	23.
43	59.	37.	25.	52.	26.	57.	57.	29.
44	8.	52.	29.	1.	19.	35.	13.	52.
45	31.	17.	33.	18.	41.	14.	38.	26.
46	42.	22.	8.	55.	34.	48.	14.	2.

Table B-3. Ranks of Sixty Values Sampled (Continued)

RUN NO.	Culebra FKd_Pu_C X(33)	Culebra FKd_Th_C X(34)	Culebra FKd_U_C X(35)	Culebra FrctrSp X(36)	Culebra Porosity X(37)	Culebra Kd_Am_C X(38)	Culebra Kd_Np_C X(39)	Culebra Kd_Pu_C X(40)
47	2.	18.	38.	36.	33.	39.	35.	43.
48	37.	54.	10.	33.	12.	33.	18.	46.
49	46.	27.	54.	46.	60.	1.	10.	32.
50	3.	23.	20.	59.	13.	40.	46.	10.
51	14.	42.	13.	4.	56.	44.	36.	54.
52	51.	53.	49.	35.	23.	53.	51.	4.
53	19.	2.	57.	49.	5.	21.	30.	30.
54	23.	11.	32.	40.	44.	31.	42.	6.
55	13.	39.	42.	9.	46.	34.	17.	15.
56	47.	25.	31.	29.	59.	5.	8.	11.
57	16.	60.	46.	23.	49.	7.	28.	49.
58	26.	56.	15.	15.	21.	15.	1.	18.
59	22.	50.	21.	43.	51.	19.	23.	60.
60	24.	40.	9.	11.	50.	60.	43.	39.

RUN NO.	Culebra Kd_Th_C X(41)	Culebra Kd_U_C X(42)	Global Lambda X(43)	Castile_R AreaFrc X(44)	MB139 ThrsPIdx X(45)
1	40.	31.	57.	46.	6.
2	22.	14.	49.	58.	10.
3	4.	13.	40.	36.	32.
4	27.	53.	25.	15.	53.
5	26.	18.	35.	33.	51.
6	51.	5.	30.	1.	59.
7	16.	27.	33.	18.	4.
8	58.	12.	15.	13.	3.
9	17.	3.	53.	20.	57.
10	14.	43.	11.	52.	42.
11	31.	55.	5.	37.	17.
12	54.	54.	55.	17.	7.
13	18.	38.	6.	11.	40.
14	53.	45.	45.	14.	41.
15	32.	33.	37.	57.	23.
16	30.	59.	44.	44.	56.
17	55.	6.	8.	12.	8.
18	33.	24.	18.	41.	5.
19	43.	2.	10.	21.	29.
20	20.	20.	17.	42.	55.
21	57.	57.	31.	55.	60.
22	15.	34.	48.	2.	45.
23	24.	17.	24.	24.	39.
24	37.	44.	46.	39.	18.
25	39.	30.	38.	50.	12.
26	36.	22.	42.	10.	13.
27	56.	10.	41.	9.	20.
28	29.	25.	52.	59.	31.
29	10.	41.	32.	4.	2.
30	38.	36.	7.	25.	28.
31	13.	51.	43.	19.	33.
32	60.	1.	59.	40.	49.
33	41.	58.	22.	34.	34.
34	34.	47.	12.	6.	22.
35	47.	32.	47.	60.	44.
36	5.	37.	26.	28.	46.

Table B-3. Ranks of Sixty Values Sampled (Concluded)

RUN NO.	Culebra Kd_Th_C X(41)	Culebra Kd_U_C X(42)	Global Lambda X(43)	Castile_R Area Frc X(44)	MB139 ThrsPIdx X(45)
37	42.	28.	4.	23.	35.
38	35.	16.	9.	35.	54.
39	7.	35.	19.	53.	1.
40	28.	60.	56.	7.	38.
41	44.	19.	3.	32.	11.
42	25.	9.	1.	47.	37.
43	9.	8.	60.	16.	16.
44	1.	4.	34.	56.	9.
45	21.	11.	23.	38.	43.
46	6.	40.	16.	48.	36.
47	2.	21.	13.	49.	50.
48	45.	52.	58.	51.	24.
49	19.	23.	20.	26.	21.
50	49.	50.	21.	54.	19.
51	48.	48.	27.	8.	25.
52	8.	7.	28.	5.	52.
53	11.	42.	14.	29.	30.
54	46.	46.	51.	43.	15.
55	12.	49.	50.	3.	14.
56	59.	29.	39.	30.	27.
57	3.	39.	36.	22.	58.
58	23.	15.	54.	31.	48.
59	50.	56.	2.	27.	26.

Table B-4 lists the total and percentage release for the 3 radionuclides contributing the most for each vector showing integrated discharge to the accessible environment for the E2 scenario assuming the dual porosity conceptual model for contaminant transport in the Culebra Dolomite Member. Values are normalized by the EPA factor for each radionuclide. Vectors are ordered from most to least release. Vectors which have no release are omitted.

Table B-4. Vectors with Integrated Discharge through the Culebra Dolomite Member to the Accessible Environment for E2 Scenario and Assuming a Dual Porosity Conceptual Model.

Comp. Scen ID	Vector	Total Integrated Discharge	Top 3 Radionuclides Contribution to Integrated Discharge								
(Time of Intrusion, 1000 years)											
00	9	7.4111E-03	U234	7.0062E-03	95%	U233	3.6317E-04	5%	TH230	4.1754E-0	51%
	46	9.9224E-06	TH230	9.9224E-06	100%	NP237	1.5441E-29	0%			
	23	1.0705E-06	U234	9.4263E-07	88%	U233	1.1494E-07	11%	TH230	1.2899E-0	81%
	6	4.8043E-07	U234	3.8823E-07	81%	U233	9.2155E-08	19%	TH230	4.6176E-1	10%
	25	3.8288E-07	NP237	3.8286E-07	100%	U233	2.3849E-11	0%			
	19	1.0095E-08	U234	9.7562E-09	97%	U233	3.3807E-10	3%	TH230	1.2177E-1	20%
	32	2.2144E-09	U234	2.1328E-09	96%	U233	8.1490E-11	4%	TH230	7.6370E-1	40%
	59	2.1210E-14	NP237	2.1210E-14	100%	U233	3.2312E-19	0%			
	44	2.6502E-17	U234	2.5213E-17	95%	U233	8.7023E-19	3%	TH230	4.1842E-1	92%
	42	9.1316E-22	U234	8.7683E-22	96%	U233	3.0992E-23	3%	TH230	5.3350E-2	41%
	7	1.7848E-24	TH230	1.7848E-24	100%	U233	8.1346E-30	0%			
(Time of Intrusion, 3000 years)											
01	9	3.5231E-03	U234	3.3285E-03	94%	U233	1.7981E-04	5%	TH230	1.4770E-0	50%
	46	2.5066E-06	TH230	2.5066E-06	100%	NP237	1.7962E-29	0%			
	23	2.7330E-07	U234	2.4171E-07	88%	U233	2.8615E-08	10%	TH230	2.9758E-0	91%
	25	1.0827E-07	NP237	1.0827E-07	100%	U233	4.6077E-12	0%			
	6	6.3414E-08	U234	5.0573E-08	80%	U233	1.2837E-08	20%	TH230	4.7593E-1	20%
	19	8.0444E-10	U234	7.7627E-10	96%	U233	2.8085E-11	3%	TH230	8.1208E-1	40%
	32	4.6991E-10	U234	4.5277E-10	96%	U233	1.7118E-11	4%	TH230	.6213E-1	40%
	59	5.4216E-15	NP237	5.4215E-15	100%	U233	7.4345E-20	0%			
	42	1.5283E-22	U234	1.4662E-22	96%	U233	5.3403E-24	3%	TH230	8.7202E-2	51%
	7	2.5804E-25	TH230	2.5804E-25	100%	U233	8.4656E-31	0%			
(Time of Intrusion, 5000 years)											
02	9	1.7559E-03	U234	1.6583E-03	94%	U233	9.2364E-05	5%	TH230	5.2346E-06	0%
	46	3.6100E-07	TH230	3.6100E-07	100%	NP2371	.2852E-29	0%			
	23	3.7514E-08	U234	3.3300E-08	89%	U2333.	9436E-09	11%	TH230	2.6985E-10	1%
	25	3.3973E-08	NP237	3.3972E-08	100%	U2331.	0815E-12	0%			
	6	4.9214E-09	U234	3.8830E-09	79%	U2331.	0382E-09	21%	TH230	2.4932E-13	0%
	19	3.5557E-11	U234	3.4292E-11	96%	U2331.	2618E-12	4%	TH230	3.5873E-15	0%
	59	3.3202E-16	NP237	3.3201E-16	100%	U2334	.5529E-21	0%			
	42	2.3845E-24	U234	2.2851E-24	96%	U2338	.7434E-26	4%	TH230	1.2055E-26	1%
	7	3.0110E-26	TH230	3.0110E-26	100%						
(Time of Intrusion, 7000 years)											
03	9	9.1063E-05	U234	8.6037E-05	94%	U233	4.7559E-06	5%	TH230	2.7082E-07	0%
	46	7.7239E-08	TH230	7.7239E-08	100%	NP23	74.2876E-30	0%			
	23	4.6506E-09	U234	4.1516E-09	89%	U233	4.6541E-10	10%	TH230	3.3642E-11	1%
	25	1.7391E-09	NP237	1.7391E-09	100%	U233	5.5235E-14	0%			
	6	7.6023E-10	U234	6.0262E-10	79%	U233	1.5757E-10	21%	TH230	3.7913E-14	0%
	42	2.4243E-25	U234	2.3209E-25	96%	U233	9.1288E-27	4%	TH230	1.2172E-27	1%
	7	2.0199E-27	TH230	2.0199E-27	100%						
(Time of Intrusion, 9000 years)											
04	No Release										

Table B-5 lists the total and percentage release for the 3 radionuclides contributing the most for each vector showing integrated discharge to the accessible environment for the E1E2 scenario assuming the dual porosity conceptual model for contaminant transport in the Culebra Dolomite Member. Values are normalized by the EPA factor for each radionuclide. Vectors are ordered from most to least release. Vectors which have no release are omitted.

Table B-5. Vectors with Integrated Discharge through the Culebra Dolomite Member to the Accessible Environment for E1E2 Scenario and Assuming a Dual Porosity Conceptual Model. (Time of Intrusion, 1000 yr)

Comp. Scen ID	Vector	Total Integrated Discharge	Top 3 Radionuclides Contribution to Integrated Discharge (Time of Intrusion, 1000 years)								
05	9	6.5082E-02	U234	6.1583E-02	95%	U233	2.7365E-03	4%	TH230	7.6209E-04	1%
	43	1.2666E-03	U234	1.1239E-03	89%	U233	9.9814E-05	8%	TH230	4.2823E-05	3%
	30	1.7067E-04	NP237	1.7065E-04	100%	U233	2.1216E-08	0%			
	46	1.4798E-05	TH230	1.4798E-05	100%	NP23	71.5120E-29	0%			
	17	9.6709E-06	U234	8.6384E-06	89%	U233	1.0299E-06	11%	TH230	2.5980E-09	0%
	6	5.4014E-06	U234	4.4395E-06	82%	U233	9.6131E-07	18%	TH230	6.2036E-10	0%
	23	1.6703E-06	U234	1.4698E-06	88%	U233	1.7879E-07	11%	TH230	2.1675E-08	1%
	19	1.5696E-06	U234	1.5197E-06	97%	U233	4.9715E-08	3%	TH230	2.2826E-10	0%
	25	3.5095E-07	NP237	3.5093E-07	100%	U233	2.1724E-11	0%			
	32	1.3396E-07	U234	1.2926E-07	96%	U233	4.6924E-09	4%	TH230	6.3923E-12	0%
	26	4.9229E-08	U234	4.5890E-08	93%	U233	3.0312E-09	6%	TH230	3.0864E-10	1%
	20	4.5796E-08	U234	4.0527E-08	88%	U233	3.9738E-09	9%	TH230	1.2953E-09	3%
	49	3.6983E-08	NP237	3.6838E-08	100%	U233	1.1942E-10	0%	U234	2.3882E-11	0%
	39	1.0609E-08	TH230	1.0609E-08	100%						
	47	4.1081E-10	TH230	4.1081E-10	100%	U233	4.9310E-18	0%	U234	1.1139E-18	0%
	44	4.7679E-11	U234	4.5269E-11	95%	U233	1.3956E-12	3%	TH230	1.0151E-12	2%
	59	6.6671E-12	NP237	6.6669E-12	100%	U233	1.6261E-16	0%			
	3	2.1841E-13	U234	1.3545E-13	62%	TH230	5.1161E-14	23%	U233	3.1807E-14	15%
	12	1.4713E-13	NP237	1.4713E-13	100%	U233	7.5906E-19	0%			
	53	6.6924E-14	TH230	6.6924E-14	100%						
	15	5.2519E-14	NP237	5.2514E-14	100%	U233	5.2241E-18	0%	PU239	1.8186E-29	0%
	45	2.0295E-14	U234	1.9207E-14	95%	U233	9.0038E-16	4%	TH230	1.8702E-16	1%
	58	1.1489E-14	U234	1.0746E-14	94%	U233	6.2401E-16	5%	TH230	1.1905E-16	1%
	29	8.6867E-17	TH230	8.6867E-17	100%						
	5	4.2155E-17	U233	2.8583E-17	68%	U234	1.3338E-17	32%	TH230	2.3335E-19	1%
	38	2.5094E-18	U233	1.8804E-18	75%	U234	6.2730E-19	25%	TH230	1.7421E-21	0%
	4	7.9147E-19	TH230	7.9147E-19	100%	NP237	9.5638E-31	0%			
	27	3.6659E-19	U234	2.5720E-19	70%	NP237	9.6979E-20	26%	U233	1.2401E-20	3%
	42	1.4259E-20	U234	1.3698E-20	96%	U233	4.7139E-22	3%	TH230	9.0300E-23	1%
	8	2.1725E-22	U234	2.0266E-22	93%	U233	1.4567E-23	7%	TH230	1.6082E-26	0%
	7	3.2895E-23	TH230	3.2895E-23	100%	U233	1.6574E-28	0%	U234	1.6483E-29	0%
	31	2.4636E-23	TH230	2.4636E-23	100%						
	48	1.3068E-23	NP237	1.3067E-23	100%	U233	6.2704E-28	0%			
	28	5.4726E-26	U233	3.8690E-26	71%	U234	1.4905E-26	27%	TH230	1.1309E-27	2%
	50	1.5237E-26	PU239	1.5147E-26	99%	PU240	8.9241E-29	1%			
	37	4.6066E-30	U234	4.6066E-30	100%						

Table B-5. (Continued)

Comp. Scen ID	Vector	Total Integrated Discharge	Top 3 Radionuclides Contribution to Integrated Discharge								
			(Time of Intrusion, 3000 years)								
06	9	2.6392E-02	U234	2.4918E-02	94%	U233	1.2978E-03	5%	TH230	1.7603E-04	1%
	43	5.1662E-04	U234	4.5947E-04	89%	U233	4.4436E-05	9%	TH230	1.2714E-05	2%
	30	5.1104E-05	NP237	5.1099E-05	100%	U233	5.1087E-09	0%			
	46	5.0816E-06	TH230	5.0816E-06	100%	NP237	2.3186E-29	0%			
	17	2.4671E-06	U234	2.1575E-06	87%	U233	3.0909E-07	13%	TH230	5.2258E-10	0%
	6	9.7589E-07	U234	7.7604E-07	80%	U233	1.9976E-07	20%	TH230	8.1581E-11	0%
	23	6.2387E-07	U234	5.5077E-07	88%	U233	6.5860E-08	11%	TH230	7.2476E-09	1%
	19	3.0330E-07	U234	2.9333E-07	97%	U233	9.9359E-09	3%	TH230	3.9213E-11	0%
	25	1.3413E-07	NP237	1.3413E-07	100%	U233	6.7511E-12	0%			
	32	2.4762E-08	U234	2.3841E-08	96%	U233	9.2059E-10	4%	TH230	8.5369E-13	0%
	49	2.1552E-08	NP237	2.1472E-08	100%	U233	6.6478E-11	0%	U234	1.3549E-11	0%
	26	1.3023E-08	U234	1.2163E-08	93%	U233	7.8152E-10	6%	TH230	7.8647E-11	1%
	20	8.7469E-09	U234	7.7873E-09	89%	U233	7.5096E-10	9%	TH230	2.0867E-10	2%
	39	3.8495E-09	TH230	3.8495E-09	100%						
	47	1.9020E-10	TH230	1.9020E-10	100%	U233	1.6989E-18	0%	U234	3.9167E-19	0%
	44	3.9860E-12	U234	3.7902E-12	95%	U233	1.2082E-13	3%	TH230	7.4998E-14	2%
	59	2.5793E-12	NP237	2.5793E-12	100%	U233	5.2276E-17	0%			
	3	6.6863E-14	U234	3.9930E-14	60%	TH230	1.6579E-14	25%	U233	1.0354E-14	15%
	53	1.5144E-14	TH230	1.5144E-14	100%						
	12	9.2273E-15	NP237	9.2273E-15	100%	U233	4.5082E-20	0%			
	58	2.3430E-15	U234	2.1859E-15	93%	U233	1.3523E-16	6%	TH230	2.1813E-17	1%
	45	2.0100E-15	U234	1.8998E-15	95%	U233	9.2425E-17	5%	TH230	1.7740E-17	1%
	15	7.2103E-16	NP237	7.2097E-16	100%	U233	6.1399E-20	0%	PU239	1.7431E-29	0%
	29	2.1674E-17	TH230	2.1674E-17	100%						
	5	4.7979E-18	U233	3.4424E-18	72%	U234	1.3376E-18	28%	TH230	1.7910E-20	0%
	27	1.0718E-19	U234	7.5530E-20	70%	NP237	2.7985E-20	26%	U233	3.6592E-21	3%
	38	9.2118E-20	U233	7.1491E-20	78%	U234	2.0578E-20	22%	TH230	4.9476E-23	0%
	4	7.0047E-20	TH230	7.0047E-20	100%	NP237	4.7296E-31	0%			
	42	6.8662E-22	U234	6.5899E-22	96%	U233	2.3691E-23	3%	TH230	3.9367E-24	1%
	8	1.0383E-23	U234	9.6239E-24	93%	U233	7.5799E-25	7%	TH230	6.3983E-28	0%
	7	5.5810E-24	TH230	5.5809E-24	100%	U233	2.7528E-29	0%	PU239	1.7850E-29	0%
	31	3.1870E-24	TH230	3.1870E-24	100%						
	48	1.2971E-24	NP237	1.2970E-24	100%	U233	5.0439E-29	0%			
	28	2.9754E-27	U233	2.2082E-27	74%	U234	7.4297E-28	25%	TH230	2.4159E-29	1%
	50	1.4106E-27	PU239	1.4106E-27	100%						
	14	3.7900E-32	NP237	3.7900E-32	100%						

Table B-5. (Continued)

Comp. Scen ID	Vector	Total Integrated Discharge	Top 3 Radionuclides Contribution to Integrated Discharge								
			(Time of Intrusion, 5000 years)								
07	9	3.6213E-02	U234	3.4237E-02	95%	U233	1.7311E-03	5%	TH230	2.4524E-04	1%
	43	1.8519E-04	U234	1.6547E-04	89%	U233	1.5778E-05	9%	TH230	3.9396E-06	2%
	30	1.2139E-05	NP237	1.2138E-05	100%	U233	1.0635E-09	0%			
	46	1.3415E-06	TH230	1.3415E-06	100%	NP237	2.2848E-29	0%			
	17	8.1064E-07	U234	7.0772E-07	87%	U233	1.0275E-07	13%	TH230	1.6014E-10	0%
	6	7.6053E-07	U234	6.1091E-07	80%	U233	1.4956E-07	20%	TH230	6.2342E-11	0%
	23	7.2613E-08	U234	6.4280E-08	89%	U233	7.8127E-09	11%	TH230	5.2095E-10	1%
	25	3.8589E-08	NP237	3.8587E-08	100%	U233	1.2360E-12	0%			
	19	3.0801E-08	U234	2.9760E-08	97%	U233	1.0364E-09	3%	TH230	3.6252E-12	0%
	32	7.4968E-09	U234	7.2230E-09	96%	U233	2.7353E-10	4%	TH230	2.5864E-13	0%
	49	4.2624E-09	NP237	4.2523E-09	100%	U233	8.7013E-12	0%	U234	1.4183E-12	0%
	20	1.9746E-09	U234	1.7719E-09	90%	U233	1.6741E-10	8%	TH230	3.5369E-11	2%
	26	1.1727E-09	U234	1.0977E-09	94%	U233	6.9746E-11	6%	TH230	5.2587E-12	0%
	39	8.2784E-10	TH230	8.2784E-10	100%						
	47	2.4072E-11	TH230	2.4072E-11	100%	U233	1.5621E-19	0%	U234	2.6333E-20	0%
	59	8.4104E-13	NP237	8.4103E-13	100%	U233	1.5783E-17	0%			
	44	4.6382E-13	U234	4.4103E-13	95%	U233	1.4391E-14	3%	TH230	8.3947E-15	2%
	3	5.9903E-15	U234	3.2579E-15	54%	TH230	1.7440E-15	29%	U233	9.8838E-16	16%
	53	1.1622E-15	TH230	1.1622E-15	100%						
	12	1.9101E-16	NP237	1.9101E-16	100%	U233	8.5407E-22	0%			
	58	1.8512E-16	U234	1.7228E-16	93%	U233	1.1252E-17	6%	TH230	1.5877E-18	1%
	45	1.0401E-16	U234	9.7996E-17	94%	U233	5.2142E-18	5%	TH230	8.0178E-19	1%
	15	9.3804E-17	NP237	9.3796E-17	100%	U233	7.7804E-21	0%	PU239	1.1183E-29	0%
	5	2.2931E-18	U233	1.6703E-18	73%	U234	6.1464E-19	27%	TH230	8.1531E-21	0%
	29	1.5233E-18	TH230	1.5233E-18	100%						
	4	9.9425E-21	TH230	9.9425E-21	100%	NP237	1.0015E-31	0%			
	27	3.7151E-21	U234	2.5701E-21	69%	NP237	1.0187E-21	27%	U233	1.2617E-22	3%
	38	2.2066E-21	U233	1.7398E-21	79%	U234	4.6573E-22	21%	TH230	1.0354E-24	0%
	42	7.4086E-23	U234	7.1043E-23	96%	U233	2.6250E-24	4%	TH230	4.1849E-25	1%
	7	1.0809E-24	TH230	1.0809E-24	100%	PU239	1.6208E-29	0%	U233	7.3469E-30	0%
	8	3.9691E-25	U234	3.6534E-25	92%	U233	3.1568E-26	8%			
	31	1.6184E-25	TH230	1.6184E-25	100%						
	48	1.3572E-25	NP237	1.3572E-25	100%	U233	3.5373E-30	0%			
	28	2.8333E-27	U233	2.1761E-27	77%	U234	6.3627E-28	22%	TH230	2.0733E-29	1%
	50	2.4960E-29	PU239	2.4960E-29	100%						

Table B-5. (Continued)

Comp. Scen ID	Vector	Total Integrated Discharge	Top 3 Radionuclides Contribution to Integrated Discharge								
			(Time of Intrusion, 7000 years)								
08	9	6.5008E-03	U234	6.1261E-03	94%	U233	3.5508E-04	5%	TH230	1.9603E-05	0%
	43	3.9312E-05	U234	3.5309E-05	90%	U233	3.5109E-06	9%	TH230	4.9273E-07	1%
	30	1.3132E-06	NP237	1.3131E-06	100%	U233	8.1087E-11	0%			
	46	3.1618E-07	TH230	3.1618E-07	100%	NP237	1.4399E-29	0%			
	17	1.3816E-07	U234	1.1817E-07	86%	U233	1.9966E-08	14%	TH230	1.9207E-11	0%
	6	6.0202E-08	U234	4.7013E-08	78%	U233	1.3186E-08	22%	TH230	2.9586E-12	0%
	23	2.5024E-08	U234	2.2265E-08	89%	U233	2.5786E-09	10%	TH230	1.8042E-10	1%
	25	1.4402E-08	NP237	1.4401E-08	100%	U233	4.5752E-13	0%			
	19	3.9838E-09	U234	3.8442E-09	96%	U233	1.3919E-10	3%	TH230	4.0215E-13	0%
	49	2.0283E-09	NP237	2.0234E-09	100%	U233	4.1459E-12	0%	U234	7.1708E-13	0%
	26	3.4243E-10	U234	3.2110E-10	94%	U233	1.9792E-11	6%	TH230	1.5382E-12	0%
	39	2.7854E-10	TH230	2.7854E-10	100%						
	20	2.7115E-10	U234	2.4478E-10	90%	U233	2.1486E-11	8%	TH230	4.8862E-12	2%
	47	9.8228E-12	TH230	9.8228E-12	100%	U233	4.8780E-20	0%	U234	9.4011E-21	0%
	59	1.5256E-13	NP237	1.5255E-13	100%	U233	2.0920E-18	0%			
	44	1.0365E-14	U234	9.8679E-15	95%	U233	3.3335E-16	3%	TH230	1.6389E-16	2%
	3	1.9539E-15	U234	9.7441E-16	50%	TH230	6.5519E-16	34%	U233	3.2431E-16	17%
	53	2.2807E-16	TH230	2.2807E-16	100%						
	58	3.7253E-17	U234	3.4576E-17	93%	U233	2.3892E-18	6%	TH230	2.8786E-19	1%
	45	7.2069E-18	U234	6.7808E-18	94%	U233	3.7069E-19	5%	TH230	5.5477E-20	1%
	15	5.3191E-18	NP237	5.3187E-18	100%	U233	3.6843E-22	0%			
	12	3.7488E-18	NP237	3.7488E-18	100%	U233	1.6490E-23	0%			
	29	4.0059E-19	TH230	4.0059E-19	100%						
	27	9.8198E-22	U234	6.8113E-22	69%	NP237	2.6707E-22	27%	U233	3.3734E-23	3%
	5	2.4982E-22	U233	1.8242E-22	73%	U234	6.6519E-23	27%	TH230	8.8236E-25	0%
	42	2.3004E-24	U234	2.2035E-24	96%	U233	8.5296E-26	4%	TH230	1.1625E-26	1%
	7	1.4039E-25	TH230	1.4038E-25	100%	PU239	8.8810E-30	0%			
	31	1.6678E-26	TH230	1.6678E-26	100%						
	48	4.6182E-27	NP237	4.6182E-27	100%						
	8	4.0428E-27	U234	3.6903E-27	91%	U233	3.5247E-28	9%			
	28	7.6283E-29	U233	6.0913E-29	80%	U234	1.5370E-29	20%			
	10	1.3532E-29	NP237	1.3532E-29	100%						
	14	1.9103E-31	NP237	1.9103E-31	100%						

Table B-5. (Concluded)

Comp. Scen ID	Vector	Total Integrated Discharge	Top 3 Radionuclides Contribution to Integrated Discharge								
			(Time of Intrusion, 9000 years)								
09	9	9.3121E-03	U234	8.7988E-03	94%	U233	4.8564E-04	5%	TH230	2.7696E-05	0%
	43	9.4847E-06	U234	8.5607E-06	90%	U233	8.0461E-07	8%	TH230	1.1932E-07	1%
	30	1.6783E-07	NP237	1.6782E-07	100%	U233	1.0297E-11	0%			
	46	5.0795E-08	TH230	5.0795E-08	100%	NP237	3.3970E-30	0%			
	6	4.3087E-08	U234	3.4178E-08	79%	U233	8.9065E-09	21%	TH230	2.1503E-12	0%
	17	3.6881E-08	U234	3.1801E-08	86%	U233	5.0747E-09	14%	TH230	5.1686E-12	0%
	19	1.9423E-10	U234	1.8731E-10	96%	U233	6.8974E-12	4%	TH230	1.9595E-14	0%
	39	1.5154E-11	TH230	1.5154E-11	100%						
	47	2.3617E-13	TH230	2.3617E-13	100%	U233	9.4620E-22	0%	U234	2.1175E-22	0%
	59	3.6621E-14	NP237	3.6621E-14	100%	U233	5.0218E-19	0%			
	44	8.3026E-16	U234	7.8985E-16	95%	U233	2.7302E-17	3%	TH230	1.3108E-17	2%
	58	1.9070E-18	U234	1.7663E-18	93%	U233	1.2592E-19	7%	TH230	1.4705E-20	1%
	15	9.8113E-19	NP237	9.8106E-19	100%	U233	6.7959E-23	0%			
	42	2.1272E-25	U234	2.0359E-25	96%	U233	8.0601E-27	4%	TH230	1.0677E-27	1%
	7	2.1828E-26	TH230	2.1824E-26	100%	PU239	3.3538E-30	0%			
	48	3.0377E-28	NP237	3.0377E-28	100%						
	28	7.9241E-29	U233	6.4883E-29	82%	U234	1.4229E-29	18%	NP237	1.2864E-31	0%
	8	4.5490E-29	U234	4.1792E-29	92%	U233	3.6982E-30	8%			
	10	7.6689E-30	NP237	7.6689E-30	100%						

CCDFCALC C-4.06VV (09/23/91) 10/07/91 14:09:58

Table B-6 lists total EPP summed normalized release and the percentages contribution for the 3 radionuclides contributing the most release for each vector when drilling into a CH waste drum with an average activity level. Vectors are ordered from most to least release. All vectors have some release when intruding into the repository from drilling.

Table B-6. Integrated Discharge to the Accessible Environment by Bringing Average CH-Activity Cuttings to the Surface when Initially Drilling through the Repository.

Comp. Scen ID	Vector	Total Integrated Discharge	Top 3 Radionuclides Contribution to Integrated Discharge (Time of Intrusion, 1000 years)								
00	19	7.6179E-03	PU239	4.8576E-03	64%	AM241	2.1471E-03	28%	PU240	5.6927E-04	7%
	35	7.5567E-03	PU239	4.8185E-03	64%	AM241	2.1299E-03	28%	PU240	5.6470E-04	7%
	55	7.4956E-03	PU239	4.7796E-03	64%	AM241	2.1127E-03	28%	PU240	5.6013E-04	7%
	16	7.4550E-03	PU239	4.7537E-03	64%	AM241	2.1012E-03	28%	PU240	5.5710E-04	7%
	46	7.3941E-03	PU239	4.7149E-03	64%	AM241	2.0841E-03	28%	PU240	5.5255E-04	7%
	24	7.3132E-03	PU239	4.6633E-03	64%	AM241	2.0612E-03	28%	PU240	5.4650E-04	7%
	4	7.2527E-03	PU239	4.6247E-03	64%	AM241	2.0442E-03	28%	PU240	5.4198E-04	7%
	14	7.2124E-03	PU239	4.5990E-03	64%	AM241	2.0328E-03	28%	PU240	5.3897E-04	7%
	13	7.1722E-03	PU239	4.5734E-03	64%	AM241	2.0215E-03	28%	PU240	5.3596E-04	7%
	51	7.1120E-03	PU239	4.5350E-03	64%	AM241	2.0045E-03	28%	PU240	5.3147E-04	7%
	39	7.0719E-03	PU239	4.5094E-03	64%	AM241	1.9932E-03	28%	PU240	5.2847E-04	7%
	1	6.9720E-03	PU239	4.4457E-03	64%	AM241	1.9651E-03	28%	PU240	5.2101E-04	7%
	53	6.9123E-03	PU239	4.4076E-03	64%	AM241	1.9482E-03	28%	PU240	5.1654E-04	7%
	18	6.8725E-03	PU239	4.3823E-03	64%	AM241	1.9370E-03	28%	PU240	5.1357E-04	7%
	52	6.7932E-03	PU239	4.3317E-03	64%	AM241	1.9147E-03	28%	PU240	5.0764E-04	7%
	27	6.7338E-03	PU239	4.2939E-03	64%	AM241	1.8980E-03	28%	PU240	5.0321E-04	7%
	49	6.6944E-03	PU239	4.2687E-03	64%	AM241	1.8868E-03	28%	PU240	5.0026E-04	7%
	38	6.5959E-03	PU239	4.2059E-03	64%	AM241	1.8591E-03	28%	PU240	4.9290E-04	7%
	21	6.5763E-03	PU239	4.1934E-03	64%	AM241	1.8535E-03	28%	PU240	4.9143E-04	7%
	17	6.5174E-03	PU239	4.1559E-03	64%	AM241	1.8370E-03	28%	PU240	4.8704E-04	7%
	44	6.4587E-03	PU239	4.1184E-03	64%	AM241	1.8204E-03	28%	PU240	4.8265E-04	7%
	30	6.3807E-03	PU239	4.0687E-03	64%	AM241	1.7984E-03	28%	PU240	4.7682E-04	7%
	3	6.3223E-03	PU239	4.0314E-03	64%	AM241	1.7820E-03	28%	PU240	4.7246E-04	7%
	37	6.2835E-03	PU239	4.0067E-03	64%	AM241	1.7710E-03	28%	PU240	4.6955E-04	7%
	43	6.2253E-03	PU239	3.9696E-03	64%	AM241	1.7546E-03	28%	PU240	4.6521E-04	7%
	33	6.1673E-03	PU239	3.9326E-03	64%	AM241	1.7383E-03	28%	PU240	4.6087E-04	7%
	32	6.0902E-03	PU239	3.8834E-03	64%	AM241	1.7165E-03	28%	PU240	4.5511E-04	7%
	28	6.0517E-03	PU239	3.8589E-03	64%	AM241	1.7057E-03	28%	PU240	4.5223E-04	7%
	6	6.0132E-03	PU239	3.8344E-03	64%	AM241	1.6949E-03	28%	PU240	4.4936E-04	7%
	60	5.9175E-03	PU239	3.7733E-03	64%	AM241	1.6679E-03	28%	PU240	4.4220E-04	7%
	47	5.8984E-03	PU239	3.7611E-03	64%	AM241	1.6625E-03	28%	PU240	4.4077E-04	7%
	41	5.8411E-03	PU239	3.7246E-03	64%	AM241	1.6463E-03	28%	PU240	4.3650E-04	7%
	26	5.7840E-03	PU239	3.6882E-03	64%	AM241	1.6302E-03	28%	PU240	4.3223E-04	7%
	11	5.7081E-03	PU239	3.6398E-03	64%	AM241	1.6088E-03	28%	PU240	4.2655E-04	7%
	57	5.6513E-03	PU239	3.6036E-03	64%	AM241	1.5928E-03	28%	PU240	4.2231E-04	7%
	7	5.5946E-03	PU239	3.5674E-03	64%	AM241	1.5769E-03	28%	PU240	4.1808E-04	7%
	29	5.5569E-03	PU239	3.5434E-03	64%	AM241	1.5662E-03	28%	PU240	4.1526E-04	7%
	9	5.4817E-03	PU239	3.4954E-03	64%	AM241	1.5450E-03	28%	PU240	4.0964E-04	7%
	8	5.4068E-03	PU239	3.4476E-03	64%	AM241	1.5239E-03	28%	PU240	4.0404E-04	7%
	15	5.3881E-03	PU239	3.4357E-03	64%	AM241	1.5186E-03	28%	PU240	4.0264E-04	7%
	40	5.3507E-03	PU239	3.4119E-03	64%	AM241	1.5081E-03	28%	PU240	3.9985E-04	7%
	48	5.2390E-03	PU239	3.3406E-03	64%	AM241	1.4766E-03	28%	PU240	3.9150E-04	7%
	20	5.2019E-03	PU239	3.3170E-03	64%	AM241	1.4662E-03	28%	PU240	3.8873E-04	7%
	54	5.1463E-03	PU239	3.2815E-03	64%	AM241	1.4505E-03	28%	PU240	3.8457E-04	7%
	31	5.0724E-03	PU239	3.2344E-03	64%	AM241	1.4297E-03	28%	PU240	3.7905E-04	7%
	23	5.0724E-03	PU239	3.2344E-03	64%	AM241	1.4297E-03	28%	PU240	3.7905E-04	7%
	12	4.9988E-03	PU239	3.1875E-03	64%	AM241	1.4089E-03	28%	PU240	3.7355E-04	7%
	42	4.9621E-03	PU239	3.1641E-03	64%	AM241	1.3986E-03	28%	PU240	3.7081E-04	7%
	58	4.8705E-03	PU239	3.1057E-03	64%	AM241	1.3728E-03	28%	PU240	3.6396E-04	7%
	34	4.8522E-03	PU239	3.0940E-03	64%	AM241	1.3676E-03	28%	PU240	3.6260E-04	7%
	2	4.7611E-03	PU239	3.0359E-03	64%	AM241	1.3419E-03	28%	PU240	3.5579E-04	7%
	56	4.7066E-03	PU239	3.0012E-03	64%	AM241	1.3266E-03	28%	PU240	3.5172E-04	7%

Table B-6. (Continued)

Comp. Scen ID	Vector	Total Integrated Discharge	Top 3 Radionuclides Contribution to Integrated Discharge								
			(Time of Intrusion, 1000 years)								
	50	4.6523E-03	PU239	2.9665E-03	64%	AM241	1.3113E-03	28%	PU240	3.4766E-04	7%
	22	4.6161E-03	PU239	2.9435E-03	64%	AM241	1.3011E-03	28%	PU240	3.4496E-04	7%
	25	4.5620E-03	PU239	2.9090E-03	64%	AM241	1.2858E-03	28%	PU240	3.4091E-04	7%
	59	4.5260E-03	PU239	2.8860E-03	64%	AM241	1.2757E-03	28%	PU240	3.3822E-04	7%
	10	4.4542E-03	PU239	2.8402E-03	64%	AM241	1.2554E-03	28%	PU240	3.3285E-04	7%
	5	4.3826E-03	PU239	2.7946E-03	64%	AM241	1.2352E-03	28%	PU240	3.2750E-04	7%
	36	4.3290E-03	PU239	2.7604E-03	64%	AM241	1.2201E-03	28%	PU240	3.2350E-04	7%
	45	4.2934E-03	PU239	2.7377E-03	64%	AM241	1.2101E-03	28%	PU240	3.2084E-04	7%

Comp. Scen ID	Vector	Total Integrated Discharge	Top 3 Radionuclides Contribution to Integrated Discharge								
			(Time of Intrusion, 3000 years)								
01	19	5.1607E-03	PU239	4.5856E-03	89%	PU240	4.6049E-04	9%	AM241	8.6864E-05	2%
	35	5.1193E-03	PU239	4.5488E-03	89%	PU240	4.5679E-04	9%	AM241	8.6166E-05	2%
	55	5.0779E-03	PU239	4.5120E-03	89%	PU240	4.5310E-04	9%	AM241	8.5470E-05	2%
	16	5.0504E-03	PU239	4.4876E-03	89%	PU240	4.5064E-04	9%	AM241	8.5006E-05	2%
	46	5.0091E-03	PU239	4.4509E-03	89%	PU240	4.4696E-04	9%	AM241	8.4313E-05	2%
	24	4.9543E-03	PU239	4.4022E-03	89%	PU240	4.4207E-04	9%	AM241	8.3390E-05	2%
	4	4.9133E-03	PU239	4.3658E-03	89%	PU240	4.3841E-04	9%	AM241	8.2700E-05	2%
	14	4.8860E-03	PU239	4.3416E-03	89%	PU240	4.3598E-04	9%	AM241	8.2241E-05	2%
	13	4.8588E-03	PU239	4.3173E-03	89%	PU240	4.3355E-04	9%	AM241	8.1782E-05	2%
	51	4.8180E-03	PU239	4.2811E-03	89%	PU240	4.2991E-04	9%	AM241	8.1096E-05	2%
	39	4.7909E-03	PU239	4.2570E-03	89%	PU240	4.2749E-04	9%	AM241	8.0639E-05	2%
	1	4.7232E-03	PU239	4.1969E-03	89%	PU240	4.2145E-04	9%	AM241	7.9500E-05	2%
	53	4.6827E-03	PU239	4.1609E-03	89%	PU240	4.1784E-04	9%	AM241	7.8818E-05	2%
	18	4.6558E-03	PU239	4.1370E-03	89%	PU240	4.1543E-04	9%	AM241	7.8365E-05	2%
	52	4.6020E-03	PU239	4.0892E-03	89%	PU240	4.1064E-04	9%	AM241	7.7461E-05	2%
	27	4.5618E-03	PU239	4.0535E-03	89%	PU240	4.0705E-04	9%	AM241	7.6784E-05	2%
	49	4.5351E-03	PU239	4.0297E-03	89%	PU240	4.0466E-04	9%	AM241	7.6334E-05	2%
	38	4.4684E-03	PU239	3.9705E-03	89%	PU240	3.9871E-04	9%	AM241	7.5211E-05	2%
	21	4.4551E-03	PU239	3.9586E-03	89%	PU240	3.9753E-04	9%	AM241	7.4987E-05	2%
	17	4.4152E-03	PU239	3.9232E-03	89%	PU240	3.9397E-04	9%	AM241	7.4316E-05	2%
	44	4.3755E-03	PU239	3.8879E-03	89%	PU240	3.9042E-04	9%	AM241	7.3647E-05	2%
	30	4.3226E-03	PU239	3.8409E-03	89%	PU240	3.8570E-04	9%	AM241	7.2757E-05	2%
	3	4.2831E-03	PU239	3.8058E-03	89%	PU240	3.8217E-04	9%	AM241	7.2091E-05	2%
	37	4.2567E-03	PU239	3.7824E-03	89%	PU240	3.7983E-04	9%	AM241	7.1648E-05	2%
	43	4.2173E-03	PU239	3.7474E-03	89%	PU240	3.7631E-04	9%	AM241	7.0985E-05	2%
	33	4.1780E-03	PU239	3.7124E-03	89%	PU240	3.7280E-04	9%	AM241	7.0324E-05	2%
	32	4.1258E-03	PU239	3.6660E-03	89%	PU240	3.6814E-04	9%	AM241	6.9444E-05	2%
	28	4.0997E-03	PU239	3.6428E-03	89%	PU240	3.6581E-04	9%	AM241	6.9005E-05	2%
	6	4.0737E-03	PU239	3.6197E-03	89%	PU240	3.6349E-04	9%	AM241	6.8567E-05	2%
	60	4.0088E-03	PU239	3.5621E-03	89%	PU240	3.5770E-04	9%	AM241	6.7475E-05	2%
	47	3.9958E-03	PU239	3.5506E-03	89%	PU240	3.5655E-04	9%	AM241	6.7257E-05	2%
	41	3.9571E-03	PU239	3.5161E-03	89%	PU240	3.5309E-04	9%	AM241	6.6604E-05	2%
	26	3.9184E-03	PU239	3.4817E-03	89%	PU240	3.4963E-04	9%	AM241	6.5953E-05	2%
	11	3.8669E-03	PU239	3.4360E-03	89%	PU240	3.4504E-04	9%	AM241	6.5087E-05	2%
	57	3.8285E-03	PU239	3.4018E-03	89%	PU240	3.4161E-04	9%	AM241	6.4440E-05	2%
	7	3.7901E-03	PU239	3.3677E-03	89%	PU240	3.3819E-04	9%	AM241	6.3794E-05	2%
	29	3.7645E-03	PU239	3.3450E-03	89%	PU240	3.3591E-04	9%	AM241	6.3364E-05	2%
	9	3.7136E-03	PU239	3.2998E-03	89%	PU240	3.3136E-04	9%	AM241	6.2506E-05	2%
	8	3.6628E-03	PU239	3.2546E-03	89%	PU240	3.2683E-04	9%	AM241	6.1652E-05	2%
	15	3.6501E-03	PU239	3.2434E-03	89%	PU240	3.2570E-04	9%	AM241	6.1438E-05	2%
	40	3.6248E-03	PU239	3.2209E-03	89%	PU240	3.2344E-04	9%	AM241	6.1012E-05	2%
	48	3.5491E-03	PU239	3.1536E-03	89%	PU240	3.1669E-04	9%	AM241	5.9738E-05	2%
	20	3.5240E-03	PU239	3.1313E-03	89%	PU240	3.1444E-04	9%	AM241	5.9315E-05	2%
	54	3.4864E-03	PU239	3.0979E-03	89%	PU240	3.1108E-04	9%	AM241	5.8682E-05	2%
	31	3.4363E-03	PU239	3.0534E-03	89%	PU240	3.0662E-04	9%	AM241	5.7839E-05	2%
	23	3.4363E-03	PU239	3.0534E-03	89%	PU240	3.0662E-04	9%	AM241	5.7839E-05	2%

Table B-6. (Continued)

Comp. Scen ID	Vector	Total Integrated Discharge	Top 3 Radionuclides Contribution to Integrated Discharge								
			(Time of Intrusion, 3000 years)								
	12	3.3864E-03	PU239	3.0091E-03	89%	PU240	3.0217E-04	9%	AM241	5.6999E-05	2%
	42	3.3615E-03	PU239	2.9869E-03	89%	PU240	2.9995E-04	9%	AM241	5.6581E-05	2%
	58	3.2995E-03	PU239	2.9318E-03	89%	PU240	2.9441E-04	9%	AM241	5.5537E-05	2%
	34	3.2871E-03	PU239	2.9208E-03	89%	PU240	2.9331E-04	9%	AM241	5.5328E-05	2%
	2	3.2254E-03	PU239	2.8660E-03	89%	PU240	2.8780E-04	9%	AM241	5.4290E-05	2%
	56	3.1885E-03	PU239	2.8332E-03	89%	PU240	2.8451E-04	9%	AM241	5.3668E-05	2%
	50	3.1517E-03	PU239	2.8005E-03	89%	PU240	2.8122E-04	9%	AM241	5.3049E-05	2%
	22	3.1272E-03	PU239	2.7787E-03	89%	PU240	2.7904E-04	9%	AM241	5.2636E-05	2%
	25	3.0905E-03	PU239	2.7461E-03	89%	PU240	2.7577E-04	9%	AM241	5.2019E-05	2%
	59	3.0661E-03	PU239	2.7245E-03	89%	PU240	2.7359E-04	9%	AM241	5.1609E-05	2%
	10	3.0175E-03	PU239	2.6812E-03	89%	PU240	2.6925E-04	9%	AM241	5.0789E-05	2%
	5	2.9690E-03	PU239	2.6381E-03	89%	PU240	2.6492E-04	9%	AM241	4.9973E-05	2%
	36	2.9327E-03	PU239	2.6059E-03	89%	PU240	2.6168E-04	9%	AM241	4.9363E-05	2%
	45	2.9086E-03	PU239	2.5844E-03	89%	PU240	2.5953E-04	9%	AM241	4.8956E-05	2%

Comp. Scen ID	Vector	Total Integrated Discharge	Top 3 Radionuclides Contribution to Integrated Discharge								
			(Time of Intrusion, 5000 years)								
02	19	4.7364E-03	PU239	4.3289E-03	91%	PU240	3.7249E-04	8%	U234	1.9395E-05	0%
	35	4.6984E-03	PU239	4.2942E-03	91%	PU240	3.6950E-04	8%	U234	1.9239E-05	0%
	55	4.6604E-03	PU239	4.2595E-03	91%	PU240	3.6651E-04	8%	U234	1.9084E-05	0%
	16	4.6351E-03	PU239	4.2364E-03	91%	PU240	3.6453E-04	8%	U234	1.8980E-05	0%
	46	4.5973E-03	PU239	4.2018E-03	91%	PU240	3.6155E-04	8%	U234	1.8825E-05	0%
	24	4.5470E-03	PU239	4.1558E-03	91%	PU240	3.5759E-04	8%	U234	1.8619E-05	0%
	4	4.5093E-03	PU239	4.1214E-03	91%	PU240	3.5464E-04	8%	U234	1.8465E-05	0%
	14	4.4843E-03	PU239	4.0985E-03	91%	PU240	3.5267E-04	8%	U234	1.8363E-05	0%
	13	4.4593E-03	PU239	4.0757E-03	91%	PU240	3.5070E-04	8%	U234	1.8260E-05	0%
	51	4.4219E-03	PU239	4.0415E-03	91%	PU240	3.4776E-04	8%	U234	1.8107E-05	0%
	39	4.3970E-03	PU239	4.0187E-03	91%	PU240	3.4580E-04	8%	U234	1.8005E-05	0%
	1	4.3349E-03	PU239	3.9619E-03	91%	PU240	3.4091E-04	8%	U234	1.7751E-05	0%
	53	4.2977E-03	PU239	3.9280E-03	91%	PU240	3.3799E-04	8%	U234	1.7598E-05	0%
	18	4.2730E-03	PU239	3.9054E-03	91%	PU240	3.3605E-04	8%	U234	1.7497E-05	0%
	52	4.2237E-03	PU239	3.8603E-03	91%	PU240	3.3217E-04	8%	U234	1.7295E-05	0%
	27	4.1868E-03	PU239	3.8266E-03	91%	PU240	3.2927E-04	8%	U234	1.7144E-05	0%
	49	4.1622E-03	PU239	3.8041E-03	91%	PU240	3.2734E-04	8%	U234	1.7044E-05	0%
	38	4.1010E-03	PU239	3.7482E-03	91%	PU240	3.2252E-04	8%	U234	1.6793E-05	0%
	21	4.0888E-03	PU239	3.7370E-03	91%	PU240	3.2156E-04	8%	U234	1.6743E-05	0%
	17	4.0522E-03	PU239	3.7036E-03	91%	PU240	3.1868E-04	8%	U234	1.6593E-05	0%
	44	4.0157E-03	PU239	3.6703E-03	91%	PU240	3.1581E-04	8%	U234	1.6444E-05	0%
	30	3.9672E-03	PU239	3.6259E-03	91%	PU240	3.1200E-04	8%	U234	1.6245E-05	0%
	3	3.9309E-03	PU239	3.5927E-03	91%	PU240	3.0914E-04	8%	U234	1.6096E-05	0%
	37	3.9067E-03	PU239	3.5706E-03	91%	PU240	3.0724E-04	8%	U234	1.5997E-05	0%
	43	3.8706E-03	PU239	3.5376E-03	91%	PU240	3.0440E-04	8%	U234	1.5849E-05	0%
	33	3.8345E-03	PU239	3.5046E-03	91%	PU240	3.0156E-04	8%	U234	1.5702E-05	0%
	32	3.7865E-03	PU239	3.4608E-03	91%	PU240	2.9779E-04	8%	U234	1.5505E-05	0%
	28	3.7626E-03	PU239	3.4389E-03	91%	PU240	2.9591E-04	8%	U234	1.5407E-05	0%
	6	3.7387E-03	PU239	3.4171E-03	91%	PU240	2.9403E-04	8%	U234	1.5310E-05	0%
	60	3.6792E-03	PU239	3.3627E-03	91%	PU240	2.8935E-04	8%	U234	1.5066E-05	0%
	47	3.6673E-03	PU239	3.3518E-03	91%	PU240	2.8841E-04	8%	U234	1.5017E-05	0%
	41	3.6317E-03	PU239	3.3193E-03	91%	PU240	2.8561E-04	8%	U234	1.4871E-05	0%
	26	3.5962E-03	PU239	3.2868E-03	91%	PU240	2.8282E-04	8%	U234	1.4726E-05	0%
	11	3.5490E-03	PU239	3.2437E-03	91%	PU240	2.7911E-04	8%	U234	1.4533E-05	0%
	57	3.5137E-03	PU239	3.2114E-03	91%	PU240	2.7633E-04	8%	U234	1.4388E-05	0%
	7	3.4785E-03	PU239	3.1792E-03	91%	PU240	2.7356E-04	8%	U234	1.4244E-05	0%
	29	3.4550E-03	PU239	3.1578E-03	91%	PU240	2.7172E-04	8%	U234	1.4148E-05	0%
	9	3.4083E-03	PU239	3.1151E-03	91%	PU240	2.6804E-04	8%	U234	1.3956E-05	0%
	8	3.3617E-03	PU239	3.0725E-03	91%	PU240	2.6438E-04	8%	U234	1.3765E-05	0%
	15	3.3500E-03	PU239	3.0618E-03	91%	PU240	2.6346E-04	8%	U234	1.3718E-05	0%
	40	3.3268E-03	PU239	3.0406E-03	91%	PU240	2.6163E-04	8%	U234	1.3623E-05	0%
	48	3.2573E-03	PU239	2.9771E-03	91%	PU240	2.5617E-04	8%	U234	1.3338E-05	0%
	20	3.2343E-03	PU239	2.9560E-03	91%	PU240	2.5436E-04	8%	U234	1.3244E-05	0%

Table B-6. (Continued)

Comp. Scen ID	Vector	Total Integrated Discharge	Top 3 Radionuclides Contribution to Integrated Discharge							
			(Time of Intrusion, 5000 years)							
	54	3.1997E-03	PU239	2.9244E-03	91%	PU240	2.5164E-04	8%	U234	1.3102E-05	0%
	31	3.1538E-03	PU239	2.8825E-03	91%	PU240	2.4803E-04	8%	U234	1.2914E-05	0%
	23	3.1538E-03	PU239	2.8825E-03	91%	PU240	2.4803E-04	8%	U234	1.2914E-05	0%
	12	3.1080E-03	PU239	2.8406E-03	91%	PU240	2.4443E-04	8%	U234	1.2727E-05	0%
	42	3.0852E-03	PU239	2.8197E-03	91%	PU240	2.4263E-04	8%	U234	1.2633E-05	0%
	58	3.0282E-03	PU239	2.7677E-03	91%	PU240	2.3815E-04	8%	U234	1.2400E-05	0%
	34	3.0169E-03	PU239	2.7573E-03	91%	PU240	2.3726E-04	8%	U234	1.2354E-05	0%
	2	2.9602E-03	PU239	2.7056E-03	91%	PU240	2.3281E-04	8%	U234	1.2122E-05	0%
	56	2.9263E-03	PU239	2.6746E-03	91%	PU240	2.3014E-04	8%	U234	1.1983E-05	0%
	50	2.8926E-03	PU239	2.6437E-03	91%	PU240	2.2748E-04	8%	U234	1.1845E-05	0%
	22	2.8701E-03	PU239	2.6232E-03	91%	PU240	2.2572E-04	8%	U234	1.1753E-05	0%
	25	2.8364E-03	PU239	2.5924E-03	91%	PU240	2.2307E-04	8%	U234	1.1615E-05	0%
	59	2.8140E-03	PU239	2.5719E-03	91%	PU240	2.2131E-04	8%	U234	1.1523E-05	0%
	10	2.7694E-03	PU239	2.5311E-03	91%	PU240	2.1780E-04	8%	U234	1.1340E-05	0%
	5	2.7249E-03	PU239	2.4904E-03	91%	PU240	2.1430E-04	8%	U234	1.1158E-05	0%
	36	2.6916E-03	PU239	2.4600E-03	91%	PU240	2.1168E-04	8%	U234	1.1022E-05	0%
	45	2.6694E-03	PU239	2.4398E-03	91%	PU240	2.0994E-04	8%	U234	1.0931E-05	0%

Comp. Scen ID	Vector	Total Integrated Discharge	Top 3 Radionuclides Contribution to Integrated Discharge							
			(Time of Intrusion, 7000 years)							
03	19	4.4232E-03	PU239	4.0866E-03	92%	PU240	3.0131E-04	7%	U234	1.9285E-05	0%
	35	4.3876E-03	PU239	4.0538E-03	92%	PU240	2.9889E-04	7%	U234	1.9130E-05	0%
	55	4.3522E-03	PU239	4.0210E-03	92%	PU240	2.9648E-04	7%	U234	1.8976E-05	0%
	16	4.3286E-03	PU239	3.9992E-03	92%	PU240	2.9487E-04	7%	U234	1.8873E-05	0%
	46	4.2933E-03	PU239	3.9666E-03	92%	PU240	2.9246E-04	7%	U234	1.8719E-05	0%
	24	4.2463E-03	PU239	3.9232E-03	92%	PU240	2.8926E-04	7%	U234	1.8514E-05	0%
	4	4.2111E-03	PU239	3.8907E-03	92%	PU240	2.8687E-04	7%	U234	1.8361E-05	0%
	14	4.1877E-03	PU239	3.8691E-03	92%	PU240	2.8527E-04	7%	U234	1.8259E-05	0%
	13	4.1644E-03	PU239	3.8475E-03	92%	PU240	2.8368E-04	7%	U234	1.8157E-05	0%
	51	4.1294E-03	PU239	3.8152E-03	92%	PU240	2.8130E-04	7%	U234	1.8004E-05	0%
	39	4.1062E-03	PU239	3.7937E-03	92%	PU240	2.7972E-04	7%	U234	1.7903E-05	0%
	1	4.0482E-03	PU239	3.7401E-03	92%	PU240	2.7577E-04	7%	U234	1.7650E-05	0%
	53	4.0135E-03	PU239	3.7081E-03	92%	PU240	2.7340E-04	7%	U234	1.7499E-05	0%
	18	3.9904E-03	PU239	3.6868E-03	92%	PU240	2.7183E-04	7%	U234	1.7398E-05	0%
	52	3.9443E-03	PU239	3.6442E-03	92%	PU240	2.6869E-04	7%	U234	1.7197E-05	0%
	27	3.9099E-03	PU239	3.6124E-03	92%	PU240	2.6635E-04	7%	U234	1.7047E-05	0%
	49	3.8870E-03	PU239	3.5912E-03	92%	PU240	2.6478E-04	7%	U234	1.6947E-05	0%
	38	3.8298E-03	PU239	3.5384E-03	92%	PU240	2.6089E-04	7%	U234	1.6698E-05	0%
	21	3.8184E-03	PU239	3.5278E-03	92%	PU240	2.6011E-04	7%	U234	1.6648E-05	0%
	17	3.7842E-03	PU239	3.4963E-03	92%	PU240	2.5779E-04	7%	U234	1.6499E-05	0%
	44	3.7501E-03	PU239	3.4648E-03	92%	PU240	2.5546E-04	7%	U234	1.6351E-05	0%
	30	3.7048E-03	PU239	3.4229E-03	92%	PU240	2.5238E-04	7%	U234	1.6153E-05	0%
	3	3.6709E-03	PU239	3.3916E-03	92%	PU240	2.5007E-04	7%	U234	1.6005E-05	0%
	37	3.6484E-03	PU239	3.3708E-03	92%	PU240	2.4853E-04	7%	U234	1.5907E-05	0%
	43	3.6146E-03	PU239	3.3396E-03	92%	PU240	2.4623E-04	7%	U234	1.5760E-05	0%
	33	3.5809E-03	PU239	3.3084E-03	92%	PU240	2.4394E-04	7%	U234	1.5613E-05	0%
	32	3.5361E-03	PU239	3.2671E-03	92%	PU240	2.4089E-04	7%	U234	1.5418E-05	0%
	28	3.5138E-03	PU239	3.2464E-03	92%	PU240	2.3936E-04	7%	U234	1.5320E-05	0%
	6	3.4915E-03	PU239	3.2258E-03	92%	PU240	2.3784E-04	7%	U234	1.5223E-05	0%
	60	3.4359E-03	PU239	3.1744E-03	92%	PU240	2.3406E-04	7%	U234	1.4980E-05	0%
	47	3.4248E-03	PU239	3.1642E-03	92%	PU240	2.3330E-04	7%	U234	1.4932E-05	0%
	41	3.3915E-03	PU239	3.1335E-03	92%	PU240	2.3104E-04	7%	U234	1.4787E-05	0%
	26	3.3584E-03	PU239	3.1028E-03	92%	PU240	2.2878E-04	7%	U234	1.4643E-05	0%
	11	3.3143E-03	PU239	3.0621E-03	92%	PU240	2.2577E-04	7%	U234	1.4450E-05	0%
	57	3.2813E-03	PU239	3.0316E-03	92%	PU240	2.2353E-04	7%	U234	1.4307E-05	0%
	7	3.2484E-03	PU239	3.0012E-03	92%	PU240	2.2129E-04	7%	U234	1.4163E-05	0%
	29	3.2265E-03	PU239	2.9810E-03	92%	PU240	2.1980E-04	7%	U234	1.4068E-05	0%
	9	3.1829E-03	PU239	2.9407E-03	92%	PU240	2.1682E-04	7%	U234	1.3877E-05	0%
	8	3.1393E-03	PU239	2.9005E-03	92%	PU240	2.1386E-04	7%	U234	1.3688E-05	0%
	15	3.1285E-03	PU239	2.8904E-03	92%	PU240	2.1312E-04	7%	U234	1.3640E-05	0%

Table B-6. (Continued)

Comp. Scen ID	Vector	Total Integrated Discharge	Top 3 Radionuclides Contribution to Integrated Discharge							
			(Time of Intrusion, 7000 years)							
	40	3.1068E-03	PU239	2.8704E-03	92%	PU240	2.1164E-04	7%	U234	1.3546E-05	0%
	48	3.0419E-03	PU239	2.8105E-03	92%	PU240	2.0722E-04	7%	U234	1.3263E-05	0%
	20	3.0204E-03	PU239	2.7905E-03	92%	PU240	2.0575E-04	7%	U234	1.3169E-05	0%
	54	2.9881E-03	PU239	2.7607E-03	92%	PU240	2.0355E-04	7%	U234	1.3028E-05	0%
	31	2.9452E-03	PU239	2.7211E-03	92%	PU240	2.0063E-04	7%	U234	1.2841E-05	0%
	23	2.9452E-03	PU239	2.7211E-03	92%	PU240	2.0063E-04	7%	U234	1.2841E-05	0%
	12	2.9024E-03	PU239	2.6816E-03	92%	PU240	1.9772E-04	7%	U234	1.2655E-05	0%
	42	2.8811E-03	PU239	2.6619E-03	92%	PU240	1.9627E-04	7%	U234	1.2562E-05	0%
	58	2.8280E-03	PU239	2.6128E-03	92%	PU240	1.9264E-04	7%	U234	1.2330E-05	0%
	34	2.8174E-03	PU239	2.6030E-03	92%	PU240	1.9192E-04	7%	U234	1.2284E-05	0%
	2	2.7645E-03	PU239	2.5541E-03	92%	PU240	1.8832E-04	7%	U234	1.2053E-05	0%
	56	2.7328E-03	PU239	2.5249E-03	92%	PU240	1.8616E-04	7%	U234	1.1915E-05	0%
	50	2.7013E-03	PU239	2.4957E-03	92%	PU240	1.8401E-04	7%	U234	1.1778E-05	0%
	22	2.6803E-03	PU239	2.4763E-03	92%	PU240	1.8258E-04	7%	U234	1.1686E-05	0%
	25	2.6488E-03	PU239	2.4473E-03	92%	PU240	1.8044E-04	7%	U234	1.1549E-05	0%
	59	2.6279E-03	PU239	2.4280E-03	92%	PU240	1.7902E-04	7%	U234	1.1458E-05	0%
	10	2.5862E-03	PU239	2.3894E-03	92%	PU240	1.7618E-04	7%	U234	1.1276E-05	0%
	5	2.5447E-03	PU239	2.3510E-03	92%	PU240	1.7335E-04	7%	U234	1.1095E-05	0%
	36	2.5136E-03	PU239	2.3223E-03	92%	PU240	1.7123E-04	7%	U234	1.0959E-05	0%
	45	2.4929E-03	PU239	2.3032E-03	92%	PU240	1.6982E-04	7%	U234	1.0869E-05	0%

Table B-6. (Concluded)

Comp. Scen ID	Vector	Total Integrated Discharge	Top 3 Radionuclides Contribution to Integrated Discharge (Time of Intrusion, 9000 years)								
04	19	4.1403E-03	PU239	3.8579E-03	93%	PU240	2.4373E-04	6%	U234	1.9176E-05	0%
	35	4.1070E-03	PU239	3.8269E-03	93%	PU240	2.4178E-04	6%	U234	1.9022E-05	0%
	55	4.0738E-03	PU239	3.7959E-03	93%	PU240	2.3982E-04	6%	U234	1.8868E-05	0%
	16	4.0517E-03	PU239	3.7753E-03	93%	PU240	2.3852E-04	6%	U234	1.8766E-05	0%
	46	4.0186E-03	PU239	3.7445E-03	93%	PU240	2.3657E-04	6%	U234	1.8613E-05	0%
	24	3.9747E-03	PU239	3.7036E-03	93%	PU240	2.3399E-04	6%	U234	1.8409E-05	0%
	4	3.9418E-03	PU239	3.6729E-03	93%	PU240	2.3205E-04	6%	U234	1.8257E-05	0%
	14	3.9199E-03	PU239	3.6525E-03	93%	PU240	2.3076E-04	6%	U234	1.8155E-05	0%
	13	3.8980E-03	PU239	3.6321E-03	93%	PU240	2.2947E-04	6%	U234	1.8054E-05	0%
	51	3.8653E-03	PU239	3.6017E-03	93%	PU240	2.2755E-04	6%	U234	1.7903E-05	0%
	39	3.8435E-03	PU239	3.5814E-03	93%	PU240	2.2627E-04	6%	U234	1.7802E-05	0%
	1	3.7892E-03	PU239	3.5308E-03	93%	PU240	2.2307E-04	6%	U234	1.7550E-05	0%
	53	3.7568E-03	PU239	3.5005E-03	93%	PU240	2.2116E-04	6%	U234	1.7400E-05	0%
	18	3.7352E-03	PU239	3.4804E-03	93%	PU240	2.1989E-04	6%	U234	1.7300E-05	0%
	52	3.6920E-03	PU239	3.4402E-03	93%	PU240	2.1735E-04	6%	U234	1.7100E-05	0%
	27	3.6598E-03	PU239	3.4102E-03	93%	PU240	2.1545E-04	6%	U234	1.6951E-05	0%
	49	3.6383E-03	PU239	3.3902E-03	93%	PU240	2.1419E-04	6%	U234	1.6851E-05	0%
	38	3.5848E-03	PU239	3.3403E-03	93%	PU240	2.1104E-04	6%	U234	1.6604E-05	0%
	21	3.5742E-03	PU239	3.3304E-03	93%	PU240	2.1041E-04	6%	U234	1.6554E-05	0%
	17	3.5422E-03	PU239	3.3006E-03	93%	PU240	2.0853E-04	6%	U234	1.6406E-05	0%
	44	3.5103E-03	PU239	3.2708E-03	93%	PU240	2.0665E-04	6%	U234	1.6258E-05	0%
	30	3.4679E-03	PU239	3.2313E-03	93%	PU240	2.0415E-04	6%	U234	1.6062E-05	0%
	3	3.4361E-03	PU239	3.2017E-03	93%	PU240	2.0228E-04	6%	U234	1.5915E-05	0%
	37	3.4150E-03	PU239	3.1821E-03	93%	PU240	2.0104E-04	6%	U234	1.5817E-05	0%
	43	3.3834E-03	PU239	3.1526E-03	93%	PU240	1.9918E-04	6%	U234	1.5671E-05	0%
	33	3.3519E-03	PU239	3.1232E-03	93%	PU240	1.9732E-04	6%	U234	1.5525E-05	0%
	32	3.3100E-03	PU239	3.0842E-03	93%	PU240	1.9485E-04	6%	U234	1.5330E-05	0%
	28	3.2890E-03	PU239	3.0647E-03	93%	PU240	1.9362E-04	6%	U234	1.5234E-05	0%
	6	3.2682E-03	PU239	3.0452E-03	93%	PU240	1.9239E-04	6%	U234	1.5137E-05	0%
	60	3.2161E-03	PU239	2.9967E-03	93%	PU240	1.8933E-04	6%	U234	1.4896E-05	0%
	47	3.2057E-03	PU239	2.9870E-03	93%	PU240	1.8872E-04	6%	U234	1.4848E-05	0%
	41	3.1746E-03	PU239	2.9581E-03	93%	PU240	1.8689E-04	6%	U234	1.4704E-05	0%
	26	3.1436E-03	PU239	2.9291E-03	93%	PU240	1.8506E-04	6%	U234	1.4560E-05	0%
	11	3.1023E-03	PU239	2.8907E-03	93%	PU240	1.8263E-04	6%	U234	1.4369E-05	0%
	57	3.0714E-03	PU239	2.8619E-03	93%	PU240	1.8081E-04	6%	U234	1.4226E-05	0%
	7	3.0406E-03	PU239	2.8332E-03	93%	PU240	1.7900E-04	6%	U234	1.4083E-05	0%
	29	3.0202E-03	PU239	2.8141E-03	93%	PU240	1.7779E-04	6%	U234	1.3988E-05	0%
	9	2.9793E-03	PU239	2.7761E-03	93%	PU240	1.7539E-04	6%	U234	1.3799E-05	0%
	8	2.9385E-03	PU239	2.7381E-03	93%	PU240	1.7299E-04	6%	U234	1.3610E-05	0%
	15	2.9284E-03	PU239	2.7286E-03	93%	PU240	1.7239E-04	6%	U234	1.3563E-05	0%
	40	2.9081E-03	PU239	2.7097E-03	93%	PU240	1.7120E-04	6%	U234	1.3469E-05	0%
	48	2.8473E-03	PU239	2.6531E-03	93%	PU240	1.6762E-04	6%	U234	1.3188E-05	0%
	20	2.8272E-03	PU239	2.6343E-03	93%	PU240	1.6643E-04	6%	U234	1.3094E-05	0%
	54	2.7970E-03	PU239	2.6062E-03	93%	PU240	1.6466E-04	6%	U234	1.2955E-05	0%
	31	2.7568E-03	PU239	2.5688E-03	93%	PU240	1.6229E-04	6%	U234	1.2769E-05	0%
	23	2.7568E-03	PU239	2.5688E-03	93%	PU240	1.6229E-04	6%	U234	1.2769E-05	0%
	12	2.7168E-03	PU239	2.5315E-03	93%	PU240	1.5994E-04	6%	U234	1.2583E-05	0%
	42	2.6968E-03	PU239	2.5129E-03	93%	PU240	1.5876E-04	6%	U234	1.2491E-05	0%
	58	2.6471E-03	PU239	2.4665E-03	93%	PU240	1.5583E-04	6%	U234	1.2260E-05	0%
	34	2.6371E-03	PU239	2.4573E-03	93%	PU240	1.5525E-04	6%	U234	1.2214E-05	0%
	2	2.5876E-03	PU239	2.4111E-03	93%	PU240	1.5233E-04	6%	U234	1.1985E-05	0%
	56	2.5580E-03	PU239	2.3835E-03	93%	PU240	1.5059E-04	6%	U234	1.1848E-05	0%
	50	2.5285E-03	PU239	2.3560E-03	93%	PU240	1.4885E-04	6%	U234	1.1711E-05	0%
	22	2.5088E-03	PU239	2.3377E-03	93%	PU240	1.4769E-04	6%	U234	1.1620E-05	0%
	25	2.4794E-03	PU239	2.3103E-03	93%	PU240	1.4596E-04	6%	U234	1.1484E-05	0%
	59	2.4598E-03	PU239	2.2921E-03	93%	PU240	1.4481E-04	6%	U234	1.1393E-05	0%
	10	2.4208E-03	PU239	2.2557E-03	93%	PU240	1.4251E-04	6%	U234	1.1212E-05	0%
	5	2.3819E-03	PU239	2.2194E-03	93%	PU240	1.4022E-04	6%	U234	1.1032E-05	0%
	36	2.3528E-03	PU239	2.1923E-03	93%	PU240	1.3851E-04	6%	U234	1.0897E-05	0%
	45	2.3334E-03	PU239	2.1743E-03	93%	PU240	1.3737E-04	6%	U234	1.0808E-05	0%

Table B-7 lists total EPA summed normalized release and the percentage contribution for the top 3 radionuclides for each vector when drilling into an RH waste cask with an average activity level. Vectors are ordered from most to least release. All vectors have some small release when intruding into the repository from drilling.

Table B-7. Integrated Discharge to the Accessible Environment by Bringing Average RH-Activity Cuttings to the Surface when Initially Drilling through the Repository.

Comp. Scen ID	Vector	Total Integrated Discharge	Top 3 Radionuclides Contribution to Integrated Discharge (Time of Intrusion, 1000 years)								
00	19	1.0006E-04	PU239	5.8991E-05	59%	AM241	1.7911E-05	18%	PU240	1.2919E-05	13%
	35	9.9256E-05	PU239	5.8517E-05	59%	AM241	1.7767E-05	18%	PU240	1.2815E-05	13%
	55	9.8453E-05	PU239	5.8044E-05	59%	AM241	1.7624E-05	18%	PU240	1.2711E-05	13%
	16	9.7919E-05	PU239	5.7730E-05	59%	AM241	1.7528E-05	18%	PU240	1.2642E-05	13%
	46	9.7120E-05	PU239	5.7259E-05	59%	AM241	1.7385E-05	18%	PU240	1.2539E-05	13%
	24	9.6057E-05	PU239	5.6632E-05	59%	AM241	1.7195E-05	18%	PU240	1.2402E-05	13%
	4	9.5262E-05	PU239	5.6163E-05	59%	AM241	1.7053E-05	18%	PU240	1.2299E-05	13%
	14	9.4733E-05	PU239	5.5851E-05	59%	AM241	1.6958E-05	18%	PU240	1.2231E-05	13%
	13	9.4205E-05	PU239	5.5540E-05	59%	AM241	1.6863E-05	18%	PU240	1.2163E-05	13%
	51	9.3414E-05	PU239	5.5074E-05	59%	AM241	1.6722E-05	18%	PU240	1.2061E-05	13%
	39	9.2888E-05	PU239	5.4764E-05	59%	AM241	1.6628E-05	18%	PU240	1.1993E-05	13%
	1	9.1576E-05	PU239	5.3990E-05	59%	AM241	1.6393E-05	18%	PU240	1.1823E-05	13%
	53	9.0791E-05	PU239	5.3527E-05	59%	AM241	1.6252E-05	18%	PU240	1.1722E-05	13%
	18	9.0269E-05	PU239	5.3219E-05	59%	AM241	1.6159E-05	18%	PU240	1.1655E-05	13%
	52	8.9227E-05	PU239	5.2605E-05	59%	AM241	1.5972E-05	18%	PU240	1.1520E-05	13%
	27	8.8448E-05	PU239	5.2146E-05	59%	AM241	1.5833E-05	18%	PU240	1.1419E-05	13%
	49	8.7929E-05	PU239	5.1840E-05	59%	AM241	1.5740E-05	18%	PU240	1.1352E-05	13%
	38	8.6636E-05	PU239	5.1078E-05	59%	AM241	1.5508E-05	18%	PU240	1.1185E-05	13%
	21	8.6378E-05	PU239	5.0925E-05	59%	AM241	1.5462E-05	18%	PU240	1.1152E-05	13%
	17	8.5605E-05	PU239	5.0470E-05	59%	AM241	1.5324E-05	18%	PU240	1.1052E-05	13%
	44	8.4834E-05	PU239	5.0015E-05	59%	AM241	1.5186E-05	18%	PU240	1.0953E-05	13%
	30	8.3809E-05	PU239	4.9411E-05	59%	AM241	1.5002E-05	18%	PU240	1.0820E-05	13%
	3	8.3042E-05	PU239	4.8959E-05	59%	AM241	1.4865E-05	18%	PU240	1.0721E-05	13%
	37	8.2532E-05	PU239	4.8658E-05	59%	AM241	1.4774E-05	18%	PU240	1.0656E-05	13%
	43	8.1768E-05	PU239	4.8208E-05	59%	AM241	1.4637E-05	18%	PU240	1.0557E-05	13%
	33	8.1006E-05	PU239	4.7758E-05	59%	AM241	1.4501E-05	18%	PU240	1.0459E-05	13%
	32	7.9993E-05	PU239	4.7161E-05	59%	AM241	1.4319E-05	18%	PU240	1.0328E-05	13%
	28	7.9488E-05	PU239	4.6863E-05	59%	AM241	1.4229E-05	18%	PU240	1.0263E-05	13%
	6	7.8983E-05	PU239	4.6565E-05	59%	AM241	1.4138E-05	18%	PU240	1.0197E-05	13%
	60	7.7725E-05	PU239	4.5824E-05	59%	AM241	1.3913E-05	18%	PU240	1.0035E-05	13%
	47	7.7474E-05	PU239	4.5676E-05	59%	AM241	1.3868E-05	18%	PU240	1.0003E-05	13%
	41	7.6722E-05	PU239	4.5232E-05	59%	AM241	1.3734E-05	18%	PU240	9.9054E-06	13%
	26	7.5972E-05	PU239	4.4790E-05	59%	AM241	1.3599E-05	18%	PU240	9.8086E-06	13%
	11	7.4974E-05	PU239	4.4202E-05	59%	AM241	1.3421E-05	18%	PU240	9.6798E-06	13%
	57	7.4229E-05	PU239	4.3762E-05	59%	AM241	1.3287E-05	18%	PU240	9.5835E-06	13%
	7	7.3484E-05	PU239	4.3324E-05	59%	AM241	1.3154E-05	18%	PU240	9.4874E-06	13%
	29	7.2989E-05	PU239	4.3032E-05	59%	AM241	1.3066E-05	18%	PU240	9.4235E-06	13%
	9	7.2001E-05	PU239	4.2449E-05	59%	AM241	1.2889E-05	18%	PU240	9.2960E-06	13%
	8	7.1017E-05	PU239	4.1869E-05	59%	AM241	1.2712E-05	18%	PU240	9.1689E-06	13%
	15	7.0771E-05	PU239	4.1724E-05	59%	AM241	1.2668E-05	18%	PU240	9.1371E-06	13%
	40	7.0280E-05	PU239	4.1435E-05	59%	AM241	1.2581E-05	18%	PU240	9.0738E-06	13%
	48	6.8813E-05	PU239	4.0570E-05	59%	AM241	1.2318E-05	18%	PU240	8.8843E-06	13%
	20	6.8325E-05	PU239	4.0282E-05	59%	AM241	1.2231E-05	18%	PU240	8.8214E-06	13%
	54	6.7596E-05	PU239	3.9852E-05	59%	AM241	1.2100E-05	18%	PU240	8.7272E-06	13%
	31	6.6625E-05	PU239	3.9280E-05	59%	AM241	1.1926E-05	18%	PU240	8.6019E-06	13%
	23	6.6625E-05	PU239	3.9280E-05	59%	AM241	1.1926E-05	18%	PU240	8.6019E-06	13%
	12	6.5658E-05	PU239	3.8710E-05	59%	AM241	1.1753E-05	18%	PU240	8.4770E-06	13%
	42	6.5176E-05	PU239	3.8425E-05	59%	AM241	1.1667E-05	18%	PU240	8.4147E-06	13%
	58	6.3973E-05	PU239	3.7716E-05	59%	AM241	1.1452E-05	18%	PU240	8.2594E-06	13%
	34	6.3733E-05	PU239	3.7575E-05	59%	AM241	1.1409E-05	18%	PU240	8.2285E-06	13%
	2	6.2536E-05	PU239	3.6869E-05	59%	AM241	1.1194E-05	18%	PU240	8.0740E-06	13%
	56	6.1821E-05	PU239	3.6447E-05	59%	AM241	1.1066E-05	18%	PU240	7.9816E-06	13%
	50	6.1107E-05	PU239	3.6026E-05	59%	AM241	1.0939E-05	18%	PU240	7.8894E-06	13%
	22	6.0632E-05	PU239	3.5746E-05	59%	AM241	1.0853E-05	18%	PU240	7.8281E-06	13%

Table B-7. (Continued)

Comp. Scen ID	Vector	Total Integrated Discharge	Top 3 Radionuclides Contribution to Integrated Discharge								
			(Time of Intrusion, 1000 years)								
00	25	5.9921E-05	PU239	3.5327E-05	59%	AM241	1.0726E-05	18%	PU240	7.7363E-06	13%
	59	5.9448E-05	PU239	3.5048E-05	59%	AM241	1.0642E-05	18%	PU240	7.6752E-06	13%
	10	5.8505E-05	PU239	3.4492E-05	59%	AM241	1.0473E-05	18%	PU240	7.5534E-06	13%
	5	5.7564E-05	PU239	3.3938E-05	59%	AM241	1.0304E-05	18%	PU240	7.4320E-06	13%
	36	5.6861E-05	PU239	3.3523E-05	59%	AM241	1.0178E-05	18%	PU240	7.3412E-06	13%
	45	5.6393E-05	PU239	3.3247E-05	59%	AM241	1.0095E-05	18%	PU240	7.2808E-06	13%

Table B-7. (Continued)

Comp. Scen ID	Vector	Total Integrated Discharge	Top 3 Radionuclides Contribution to Integrated Discharge								
			(Time of Intrusion, 3000 years)								
01	19	7.8452E-05	PU239	5.5689E-05	71%	PU240	1.0450E-05	13%	U233	9.1950E-06	12%
	35	7.7822E-05	PU239	5.5242E-05	71%	PU240	1.0366E-05	13%	U233	9.1211E-06	12%
	55	7.7193E-05	PU239	5.4795E-05	71%	PU240	1.0282E-05	13%	U233	9.0474E-06	12%
	16	7.6774E-05	PU239	5.4498E-05	71%	PU240	1.0226E-05	13%	U233	8.9983E-06	12%
	46	7.6148E-05	PU239	5.4053E-05	71%	PU240	1.0143E-05	13%	U233	8.9249E-06	12%
	24	7.5314E-05	PU239	5.3462E-05	71%	PU240	1.0032E-05	13%	U233	8.8272E-06	12%
	4	7.4691E-05	PU239	5.3019E-05	71%	PU240	9.9489E-06	13%	U233	8.7541E-06	12%
	14	7.4276E-05	PU239	5.2725E-05	71%	PU240	9.8937E-06	13%	U233	8.7055E-06	12%
	13	7.3862E-05	PU239	5.2431E-05	71%	PU240	9.8385E-06	13%	U233	8.6570E-06	12%
	51	7.3242E-05	PU239	5.1991E-05	71%	PU240	9.7559E-06	13%	U233	8.5843E-06	12%
	39	7.2830E-05	PU239	5.1698E-05	71%	PU240	9.7009E-06	13%	U233	8.5360E-06	12%
	1	7.1801E-05	PU239	5.0968E-05	71%	PU240	9.5639E-06	13%	U233	8.4154E-06	12%
	53	7.1186E-05	PU239	5.0531E-05	71%	PU240	9.4820E-06	13%	U233	8.3433E-06	12%
	18	7.0776E-05	PU239	5.0240E-05	71%	PU240	9.4274E-06	13%	U233	8.2953E-06	12%
	52	6.9959E-05	PU239	4.9660E-05	71%	PU240	9.3186E-06	13%	U233	8.1995E-06	12%
	27	6.9348E-05	PU239	4.9227E-05	71%	PU240	9.2372E-06	13%	U233	8.1279E-06	12%
	49	6.8941E-05	PU239	4.8938E-05	71%	PU240	9.1830E-06	13%	U233	8.0803E-06	12%
	38	6.7928E-05	PU239	4.8218E-05	71%	PU240	9.0480E-06	13%	U233	7.9614E-06	12%
	21	6.7725E-05	PU239	4.8075E-05	71%	PU240	9.0211E-06	13%	U233	7.9377E-06	12%
	17	6.7119E-05	PU239	4.7645E-05	71%	PU240	8.9404E-06	13%	U233	7.8667E-06	12%
	44	6.6515E-05	PU239	4.7215E-05	71%	PU240	8.8598E-06	13%	U233	7.7959E-06	12%
	30	6.5711E-05	PU239	4.6645E-05	71%	PU240	8.7528E-06	13%	U233	7.7016E-06	12%
	3	6.5110E-05	PU239	4.6218E-05	71%	PU240	8.6727E-06	13%	U233	7.6312E-06	12%
	37	6.4710E-05	PU239	4.5934E-05	71%	PU240	8.6194E-06	13%	U233	7.5843E-06	12%
	43	6.4111E-05	PU239	4.5509E-05	71%	PU240	8.5396E-06	13%	U233	7.5141E-06	12%
	33	6.3514E-05	PU239	4.5085E-05	71%	PU240	8.4600E-06	13%	U233	7.4441E-06	12%
	32	6.2719E-05	PU239	4.4521E-05	71%	PU240	8.3542E-06	13%	U233	7.3510E-06	12%
	28	6.2323E-05	PU239	4.4240E-05	71%	PU240	8.3014E-06	13%	U233	7.3045E-06	12%
	6	6.1927E-05	PU239	4.3959E-05	71%	PU240	8.2487E-06	13%	U233	7.2581E-06	12%
	60	6.0941E-05	PU239	4.3259E-05	71%	PU240	8.1173E-06	13%	U233	7.1425E-06	12%
	47	6.0744E-05	PU239	4.3119E-05	71%	PU240	8.0911E-06	13%	U233	7.1194E-06	12%
	41	6.0154E-05	PU239	4.2700E-05	71%	PU240	8.0126E-06	13%	U233	7.0504E-06	12%
	26	5.9566E-05	PU239	4.2283E-05	71%	PU240	7.9342E-06	13%	U233	6.9814E-06	12%
	11	5.8784E-05	PU239	4.1728E-05	71%	PU240	7.8301E-06	13%	U233	6.8898E-06	12%
	57	5.8199E-05	PU239	4.1313E-05	71%	PU240	7.7522E-06	13%	U233	6.8212E-06	12%
	7	5.7616E-05	PU239	4.0899E-05	71%	PU240	7.6745E-06	13%	U233	6.7528E-06	12%
	29	5.7228E-05	PU239	4.0623E-05	71%	PU240	7.6228E-06	13%	U233	6.7073E-06	12%
	9	5.6453E-05	PU239	4.0073E-05	71%	PU240	7.5196E-06	13%	U233	6.6166E-06	12%
	8	5.5681E-05	PU239	3.9525E-05	71%	PU240	7.4168E-06	13%	U233	6.5261E-06	12%
	15	5.5489E-05	PU239	3.9388E-05	71%	PU240	7.3911E-06	13%	U233	6.5035E-06	12%
	40	5.5104E-05	PU239	3.9115E-05	71%	PU240	7.3399E-06	13%	U233	6.4584E-06	12%
	48	5.3953E-05	PU239	3.8299E-05	71%	PU240	7.1866E-06	13%	U233	6.3236E-06	12%
	20	5.3571E-05	PU239	3.8027E-05	71%	PU240	7.1357E-06	13%	U233	6.2788E-06	12%
	54	5.2999E-05	PU239	3.7621E-05	71%	PU240	7.0595E-06	13%	U233	6.2117E-06	12%
	31	5.2238E-05	PU239	3.7081E-05	71%	PU240	6.9581E-06	13%	U233	6.1225E-06	12%
	23	5.2238E-05	PU239	3.7081E-05	71%	PU240	6.9581E-06	13%	U233	6.1225E-06	12%
	12	5.1480E-05	PU239	3.6543E-05	71%	PU240	6.8571E-06	13%	U233	6.0336E-06	12%
	42	5.1101E-05	PU239	3.6274E-05	71%	PU240	6.8067E-06	13%	U233	5.9893E-06	12%
	58	5.0158E-05	PU239	3.5605E-05	71%	PU240	6.6811E-06	13%	U233	5.8788E-06	12%
	34	4.9970E-05	PU239	3.5471E-05	71%	PU240	6.6561E-06	13%	U233	5.8567E-06	12%
	2	4.9032E-05	PU239	3.4805E-05	71%	PU240	6.5311E-06	13%	U233	5.7468E-06	12%
	56	4.8471E-05	PU239	3.4407E-05	71%	PU240	6.4564E-06	13%	U233	5.6810E-06	12%
	50	4.7911E-05	PU239	3.4010E-05	71%	PU240	6.3818E-06	13%	U233	5.6154E-06	12%
	22	4.7539E-05	PU239	3.3745E-05	71%	PU240	6.3322E-06	13%	U233	5.5718E-06	12%
	25	4.6982E-05	PU239	3.3350E-05	71%	PU240	6.2580E-06	13%	U233	5.5064E-06	12%
	59	4.6611E-05	PU239	3.3087E-05	71%	PU240	6.2086E-06	13%	U233	5.4630E-06	12%
	10	4.5871E-05	PU239	3.2561E-05	71%	PU240	6.1100E-06	13%	U233	5.3763E-06	12%
	5	4.5134E-05	PU239	3.2038E-05	71%	PU240	6.0118E-06	13%	U233	5.2899E-06	12%
	36	4.4582E-05	PU239	3.1647E-05	71%	PU240	5.9384E-06	13%	U233	5.2252E-06	12%
	45	4.4215E-05	PU239	3.1386E-05	71%	PU240	5.8895E-06	13%	U233	5.1822E-06	12%

Table B-7. (Continued)

Comp. Scen ID	Vector	Total Integrated Discharge	Top 3 Radionuclides Contribution to Integrated Discharge								
			(Time of Intrusion, 5000 years)								
02	19	7.3751E-05	PU239	5.2572E-05	71%	U233	9.1156E-06	12%	PU240	8.4530E-06	11%
	35	7.3158E-05	PU239	5.2149E-05	71%	U233	9.0423E-06	12%	PU240	8.3851E-06	11%
	55	7.2567E-05	PU239	5.1728E-05	71%	U233	8.9692E-06	12%	PU240	8.3173E-06	11%
	16	7.2173E-05	PU239	5.1447E-05	71%	U233	8.9206E-06	12%	PU240	8.2722E-06	11%
	46	7.1584E-05	PU239	5.1028E-05	71%	U233	8.8478E-06	12%	PU240	8.2047E-06	11%
	24	7.0801E-05	PU239	5.0469E-05	71%	U233	8.7510E-06	12%	PU240	8.1149E-06	11%
	4	7.0215E-05	PU239	5.0051E-05	71%	U233	8.6785E-06	12%	PU240	8.0478E-06	11%
	14	6.9825E-05	PU239	4.9773E-05	71%	U233	8.6303E-06	12%	PU240	8.0031E-06	11%
	13	6.9436E-05	PU239	4.9496E-05	71%	U233	8.5822E-06	12%	PU240	7.9584E-06	11%
	51	6.8853E-05	PU239	4.9080E-05	71%	U233	8.5102E-06	12%	PU240	7.8916E-06	11%
	39	6.8465E-05	PU239	4.8804E-05	71%	U233	8.4622E-06	12%	PU240	7.8472E-06	11%
	1	6.7498E-05	PU239	4.8115E-05	71%	U233	8.3427E-06	12%	PU240	7.7363E-06	11%
	53	6.6919E-05	PU239	4.7702E-05	71%	U233	8.2712E-06	12%	PU240	7.6700E-06	11%
	18	6.6535E-05	PU239	4.7428E-05	71%	U233	8.2237E-06	12%	PU240	7.6259E-06	11%
	52	6.5767E-05	PU239	4.6880E-05	71%	U233	8.1287E-06	12%	PU240	7.5379E-06	11%
	27	6.5192E-05	PU239	4.6471E-05	71%	U233	8.0577E-06	12%	PU240	7.4721E-06	11%
	49	6.4810E-05	PU239	4.6198E-05	71%	U233	8.0105E-06	12%	PU240	7.4282E-06	11%
	38	6.3857E-05	PU239	4.5519E-05	71%	U233	7.8927E-06	12%	PU240	7.3190E-06	11%
	21	6.3667E-05	PU239	4.5384E-05	71%	U233	7.8692E-06	12%	PU240	7.2972E-06	11%
	17	6.3097E-05	PU239	4.4978E-05	71%	U233	7.7988E-06	12%	PU240	7.2319E-06	11%
	44	6.2529E-05	PU239	4.4572E-05	71%	U233	7.7285E-06	12%	PU240	7.1668E-06	11%
	30	6.1773E-05	PU239	4.4034E-05	71%	U233	7.6351E-06	12%	PU240	7.0802E-06	11%
	3	6.1208E-05	PU239	4.3631E-05	71%	U233	7.5653E-06	12%	PU240	7.0154E-06	11%
	37	6.0832E-05	PU239	4.3363E-05	71%	U233	7.5188E-06	12%	PU240	6.9723E-06	11%
	43	6.0269E-05	PU239	4.2961E-05	71%	U233	7.4492E-06	12%	PU240	6.9078E-06	11%
	33	5.9707E-05	PU239	4.2561E-05	71%	U233	7.3798E-06	12%	PU240	6.8434E-06	11%
	32	5.8960E-05	PU239	4.2029E-05	71%	U233	7.2875E-06	12%	PU240	6.7578E-06	11%
	28	5.8588E-05	PU239	4.1763E-05	71%	U233	7.2414E-06	12%	PU240	6.7151E-06	11%
	6	5.8216E-05	PU239	4.1498E-05	71%	U233	7.1955E-06	12%	PU240	6.6725E-06	11%
	60	5.7288E-05	PU239	4.0837E-05	71%	U233	7.0808E-06	12%	PU240	6.5662E-06	11%
	47	5.7103E-05	PU239	4.0705E-05	71%	U233	7.0580E-06	12%	PU240	6.5450E-06	11%
	41	5.6549E-05	PU239	4.0310E-05	71%	U233	6.9895E-06	12%	PU240	6.4815E-06	11%
	26	5.5996E-05	PU239	3.9916E-05	71%	U233	6.9211E-06	12%	PU240	6.4181E-06	11%
	11	5.5261E-05	PU239	3.9392E-05	71%	U233	6.8303E-06	12%	PU240	6.3338E-06	11%
	57	5.4711E-05	PU239	3.9000E-05	71%	U233	6.7623E-06	12%	PU240	6.2708E-06	11%
	7	5.4163E-05	PU239	3.8609E-05	71%	U233	6.6945E-06	12%	PU240	6.2079E-06	11%
	29	5.3798E-05	PU239	3.8349E-05	71%	U233	6.6494E-06	12%	PU240	6.1661E-06	11%
	9	5.3070E-05	PU239	3.7830E-05	71%	U233	6.5594E-06	12%	PU240	6.0827E-06	11%
	8	5.2344E-05	PU239	3.7313E-05	71%	U233	6.4697E-06	12%	PU240	5.9995E-06	11%
	15	5.2163E-05	PU239	3.7184E-05	71%	U233	6.4474E-06	12%	PU240	5.9787E-06	11%
	40	5.1802E-05	PU239	3.6926E-05	71%	U233	6.4026E-06	12%	PU240	5.9373E-06	11%
	48	5.0720E-05	PU239	3.6155E-05	71%	U233	6.2690E-06	12%	PU240	5.8133E-06	11%
	20	5.0361E-05	PU239	3.5899E-05	71%	U233	6.2245E-06	12%	PU240	5.7721E-06	11%
	54	4.9823E-05	PU239	3.5515E-05	71%	U233	6.1581E-06	12%	PU240	5.7105E-06	11%
	31	4.9107E-05	PU239	3.5005E-05	71%	U233	6.0697E-06	12%	PU240	5.6285E-06	11%
	23	4.9107E-05	PU239	3.5005E-05	71%	U233	6.0697E-06	12%	PU240	5.6285E-06	11%
	12	4.8394E-05	PU239	3.4497E-05	71%	U233	5.9815E-06	12%	PU240	5.5468E-06	11%
	42	4.8039E-05	PU239	3.4244E-05	71%	U233	5.9376E-06	12%	PU240	5.5060E-06	11%
	58	4.7152E-05	PU239	3.3612E-05	71%	U233	5.8280E-06	12%	PU240	5.4044E-06	11%
	34	4.6976E-05	PU239	3.3486E-05	71%	U233	5.8062E-06	12%	PU240	5.3842E-06	11%
	2	4.6094E-05	PU239	3.2857E-05	71%	U233	5.6972E-06	12%	PU240	5.2831E-06	11%
	56	4.5566E-05	PU239	3.2481E-05	71%	U233	5.6320E-06	12%	PU240	5.2226E-06	11%
	50	4.5040E-05	PU239	3.2106E-05	71%	U233	5.5669E-06	12%	PU240	5.1623E-06	11%
	22	4.4690E-05	PU239	3.1856E-05	71%	U233	5.5237E-06	12%	PU240	5.1222E-06	11%
	25	4.4166E-05	PU239	3.1483E-05	71%	U233	5.4589E-06	12%	PU240	5.0621E-06	11%
	59	4.3817E-05	PU239	3.1234E-05	71%	U233	5.4158E-06	12%	PU240	5.0222E-06	11%
	10	4.3122E-05	PU239	3.0739E-05	71%	U233	5.3299E-06	12%	PU240	4.9425E-06	11%
	5	4.2429E-05	PU239	3.0245E-05	71%	U233	5.2442E-06	12%	PU240	4.8630E-06	11%
	36	4.1910E-05	PU239	2.9875E-05	71%	U233	5.1801E-06	12%	PU240	4.8036E-06	11%
	45	4.1566E-05	PU239	2.9629E-05	71%	U233	5.1375E-06	12%	PU240	4.7641E-06	11%

Table B-7. (Continued)

Comp. Scen ID	Vector	Total Integrated Discharge	Top 3 Radionuclides Contribution to Integrated Discharge (Time of Intrusion, 7000 years)								
03	19	7.0056E-05	PU239	4.9629E-05	71%	U233	9.0369E-06	13%	PU240	6.8377E-06	10%
	35	6.9493E-05	PU239	4.9230E-05	71%	U233	8.9642E-06	13%	PU240	6.7828E-06	10%
	55	6.8931E-05	PU239	4.8832E-05	71%	U233	8.8918E-06	13%	PU240	6.7279E-06	10%
	16	6.8557E-05	PU239	4.8567E-05	71%	U233	8.8436E-06	13%	PU240	6.6915E-06	10%
	46	6.7998E-05	PU239	4.8171E-05	71%	U233	8.7714E-06	13%	PU240	6.6369E-06	10%
	24	6.7254E-05	PU239	4.7644E-05	71%	U233	8.6754E-06	13%	PU240	6.5642E-06	10%
	4	6.6697E-05	PU239	4.7250E-05	71%	U233	8.6036E-06	13%	PU240	6.5099E-06	10%
	14	6.6327E-05	PU239	4.6987E-05	71%	U233	8.5558E-06	13%	PU240	6.4737E-06	10%
	13	6.5957E-05	PU239	4.6725E-05	71%	U233	8.5081E-06	13%	PU240	6.4377E-06	10%
	51	6.5403E-05	PU239	4.6333E-05	71%	U233	8.4367E-06	13%	PU240	6.3836E-06	10%
	39	6.5035E-05	PU239	4.6072E-05	71%	U233	8.3892E-06	13%	PU240	6.3477E-06	10%
	1	6.4116E-05	PU239	4.5421E-05	71%	U233	8.2707E-06	13%	PU240	6.2580E-06	10%
	53	6.3567E-05	PU239	4.5032E-05	71%	U233	8.1998E-06	13%	PU240	6.2044E-06	10%
	18	6.3201E-05	PU239	4.4773E-05	71%	U233	8.1526E-06	13%	PU240	6.1687E-06	10%
	52	6.2472E-05	PU239	4.4256E-05	71%	U233	8.0585E-06	13%	PU240	6.0975E-06	10%
	27	6.1926E-05	PU239	4.3870E-05	71%	U233	7.9881E-06	13%	PU240	6.0442E-06	10%
	49	6.1563E-05	PU239	4.3612E-05	71%	U233	7.9413E-06	13%	PU240	6.0088E-06	10%
	38	6.0657E-05	PU239	4.2971E-05	71%	U233	7.8245E-06	13%	PU240	5.9204E-06	10%
	21	6.0477E-05	PU239	4.2843E-05	71%	U233	7.8012E-06	13%	PU240	5.9028E-06	10%
	17	5.9936E-05	PU239	4.2460E-05	71%	U233	7.7314E-06	13%	PU240	5.8500E-06	10%
	44	5.9396E-05	PU239	4.2077E-05	71%	U233	7.6618E-06	13%	PU240	5.7973E-06	10%
	30	5.8678E-05	PU239	4.1569E-05	71%	U233	7.5692E-06	13%	PU240	5.7272E-06	10%
	3	5.8141E-05	PU239	4.1188E-05	71%	U233	7.5000E-06	13%	PU240	5.6748E-06	10%
	37	5.7784E-05	PU239	4.0935E-05	71%	U233	7.4539E-06	13%	PU240	5.6400E-06	10%
	43	5.7249E-05	PU239	4.0557E-05	71%	U233	7.3849E-06	13%	PU240	5.5878E-06	10%
	33	5.6716E-05	PU239	4.0179E-05	71%	U233	7.3161E-06	13%	PU240	5.5357E-06	10%
	32	5.6006E-05	PU239	3.9676E-05	71%	U233	7.2246E-06	13%	PU240	5.4664E-06	10%
	28	5.5652E-05	PU239	3.9425E-05	71%	U233	7.1789E-06	13%	PU240	5.4319E-06	10%
	6	5.5299E-05	PU239	3.9175E-05	71%	U233	7.1333E-06	13%	PU240	5.3974E-06	10%
	60	5.4418E-05	PU239	3.8551E-05	71%	U233	7.0197E-06	13%	PU240	5.3114E-06	10%
	47	5.4242E-05	PU239	3.8427E-05	71%	U233	6.9970E-06	13%	PU240	5.2943E-06	10%
	41	5.3716E-05	PU239	3.8054E-05	71%	U233	6.9291E-06	13%	PU240	5.2429E-06	10%
	26	5.3191E-05	PU239	3.7682E-05	71%	U233	6.8614E-06	13%	PU240	5.1916E-06	10%
	11	5.2493E-05	PU239	3.7187E-05	71%	U233	6.7713E-06	13%	PU240	5.1235E-06	10%
	57	5.1970E-05	PU239	3.6817E-05	71%	U233	6.7039E-06	13%	PU240	5.0725E-06	10%
	7	5.1449E-05	PU239	3.6448E-05	71%	U233	6.6367E-06	13%	PU240	5.0217E-06	10%
	29	5.1103E-05	PU239	3.6202E-05	71%	U233	6.5920E-06	13%	PU240	4.9878E-06	10%
	9	5.0411E-05	PU239	3.5712E-05	71%	U233	6.5028E-06	13%	PU240	4.9203E-06	10%
	8	4.9722E-05	PU239	3.5224E-05	71%	U233	6.4139E-06	13%	PU240	4.8530E-06	10%
	15	4.9550E-05	PU239	3.5102E-05	71%	U233	6.3917E-06	13%	PU240	4.8363E-06	10%
	40	4.9206E-05	PU239	3.4859E-05	71%	U233	6.3474E-06	13%	PU240	4.8027E-06	10%
	48	4.8179E-05	PU239	3.4131E-05	71%	U233	6.2148E-06	13%	PU240	4.7024E-06	10%
	20	4.7837E-05	PU239	3.3889E-05	71%	U233	6.1708E-06	13%	PU240	4.6691E-06	10%
	54	4.7326E-05	PU239	3.3527E-05	71%	U233	6.1049E-06	13%	PU240	4.6192E-06	10%
	31	4.6647E-05	PU239	3.3046E-05	71%	U233	6.0172E-06	13%	PU240	4.5529E-06	10%
	23	4.6647E-05	PU239	3.3046E-05	71%	U233	6.0172E-06	13%	PU240	4.5529E-06	10%
	12	4.5970E-05	PU239	3.2566E-05	71%	U233	5.9299E-06	13%	PU240	4.4868E-06	10%
	42	4.5632E-05	PU239	3.2327E-05	71%	U233	5.8863E-06	13%	PU240	4.4539E-06	10%
	58	4.4790E-05	PU239	3.1730E-05	71%	U233	5.7777E-06	13%	PU240	4.3717E-06	10%
	34	4.4622E-05	PU239	3.1611E-05	71%	U233	5.7560E-06	13%	PU240	4.3553E-06	10%
	2	4.3784E-05	PU239	3.1018E-05	71%	U233	5.6480E-06	13%	PU240	4.2735E-06	10%
	56	4.3283E-05	PU239	3.0663E-05	71%	U233	5.5833E-06	13%	PU240	4.2246E-06	10%
	50	4.2783E-05	PU239	3.0309E-05	71%	U233	5.5189E-06	13%	PU240	4.1758E-06	10%
	22	4.2451E-05	PU239	3.0073E-05	71%	U233	5.4760E-06	13%	PU240	4.1434E-06	10%
	25	4.1953E-05	PU239	2.9720E-05	71%	U233	5.4118E-06	13%	PU240	4.0948E-06	10%
	59	4.1622E-05	PU239	2.9486E-05	71%	U233	5.3690E-06	13%	PU240	4.0625E-06	10%
	10	4.0961E-05	PU239	2.9018E-05	71%	U233	5.2838E-06	13%	PU240	3.9980E-06	10%
	5	4.0303E-05	PU239	2.8551E-05	71%	U233	5.1989E-06	13%	PU240	3.9337E-06	10%
	36	3.9811E-05	PU239	2.8203E-05	71%	U233	5.1354E-06	13%	PU240	3.8857E-06	10%
	45	3.9483E-05	PU239	2.7971E-05	71%	U233	5.0931E-06	13%	PU240	3.8537E-06	10%

Table B-7. (Concluded)

Comp. Scen ID	Vector	Total Integrated Discharge	Top 3 Radionuclides Contribution to Integrated Discharge (Time of Intrusion, 9000 years)								
04	19	6.6682E-05	PU239	4.6851E-05	70%	U233	8.9588E-06	13%	PU240	5.5311E-06	8%
	35	6.6146E-05	PU239	4.6474E-05	70%	U233	8.8868E-06	13%	PU240	5.4866E-06	8%
	55	6.5611E-05	PU239	4.6099E-05	70%	U233	8.8150E-06	13%	PU240	5.4423E-06	8%
	16	6.5256E-05	PU239	4.5849E-05	70%	U233	8.7672E-06	13%	PU240	5.4128E-06	8%
	46	6.4723E-05	PU239	4.5475E-05	70%	U233	8.6957E-06	13%	PU240	5.3686E-06	8%
	24	6.4015E-05	PU239	4.4977E-05	70%	U233	8.6005E-06	13%	PU240	5.3099E-06	8%
	4	6.3485E-05	PU239	4.4605E-05	70%	U233	8.5293E-06	13%	PU240	5.2659E-06	8%
	14	6.3132E-05	PU239	4.4357E-05	70%	U233	8.4820E-06	13%	PU240	5.2367E-06	8%
	13	6.2780E-05	PU239	4.4110E-05	70%	U233	8.4347E-06	13%	PU240	5.2075E-06	8%
	51	6.2253E-05	PU239	4.3739E-05	70%	U233	8.3639E-06	13%	PU240	5.1638E-06	8%
	39	6.1903E-05	PU239	4.3493E-05	70%	U233	8.3168E-06	13%	PU240	5.1347E-06	8%
	1	6.1028E-05	PU239	4.2879E-05	70%	U233	8.1993E-06	13%	PU240	5.0621E-06	8%
	53	6.0505E-05	PU239	4.2511E-05	70%	U233	8.1290E-06	13%	PU240	5.0188E-06	8%
	18	6.0157E-05	PU239	4.2267E-05	70%	U233	8.0823E-06	13%	PU240	4.9899E-06	8%
	52	5.9463E-05	PU239	4.1779E-05	70%	U233	7.9890E-06	13%	PU240	4.9323E-06	8%
	27	5.8944E-05	PU239	4.1414E-05	70%	U233	7.9192E-06	13%	PU240	4.8892E-06	8%
	49	5.8598E-05	PU239	4.1171E-05	70%	U233	7.8727E-06	13%	PU240	4.8605E-06	8%
	38	5.7736E-05	PU239	4.0566E-05	70%	U233	7.7570E-06	13%	PU240	4.7891E-06	8%
	21	5.7564E-05	PU239	4.0445E-05	70%	U233	7.7339E-06	13%	PU240	4.7748E-06	8%
	17	5.7049E-05	PU239	4.0083E-05	70%	U233	7.6647E-06	13%	PU240	4.7321E-06	8%
	44	5.6535E-05	PU239	3.9722E-05	70%	U233	7.5957E-06	13%	PU240	4.6895E-06	8%
	30	5.5852E-05	PU239	3.9242E-05	70%	U233	7.5039E-06	13%	PU240	4.6328E-06	8%
	3	5.5341E-05	PU239	3.8883E-05	70%	U233	7.4352E-06	13%	PU240	4.5904E-06	8%
	37	5.5001E-05	PU239	3.8644E-05	70%	U233	7.3895E-06	13%	PU240	4.5622E-06	8%
	43	5.4492E-05	PU239	3.8286E-05	70%	U233	7.3211E-06	13%	PU240	4.5200E-06	8%
	33	5.3984E-05	PU239	3.7929E-05	70%	U233	7.2529E-06	13%	PU240	4.4779E-06	8%
	32	5.3309E-05	PU239	3.7455E-05	70%	U233	7.1622E-06	13%	PU240	4.4218E-06	8%
	28	5.2972E-05	PU239	3.7218E-05	70%	U233	7.1169E-06	13%	PU240	4.3939E-06	8%
	6	5.2636E-05	PU239	3.6982E-05	70%	U233	7.0717E-06	13%	PU240	4.3660E-06	8%
	60	5.1797E-05	PU239	3.6393E-05	70%	U233	6.9591E-06	13%	PU240	4.2965E-06	8%
	47	5.1630E-05	PU239	3.6275E-05	70%	U233	6.9366E-06	13%	PU240	4.2826E-06	8%
	41	5.1129E-05	PU239	3.5923E-05	70%	U233	6.8693E-06	13%	PU240	4.2410E-06	8%
	26	5.0629E-05	PU239	3.5572E-05	70%	U233	6.8021E-06	13%	PU240	4.1996E-06	8%
	11	4.9965E-05	PU239	3.5105E-05	70%	U233	6.7128E-06	13%	PU240	4.1444E-06	8%
	57	4.9467E-05	PU239	3.4756E-05	70%	U233	6.6461E-06	13%	PU240	4.1032E-06	8%
	7	4.8972E-05	PU239	3.4408E-05	70%	U233	6.5794E-06	13%	PU240	4.0621E-06	8%
	29	4.8642E-05	PU239	3.4176E-05	70%	U233	6.5351E-06	13%	PU240	4.0347E-06	8%
	9	4.7983E-05	PU239	3.3713E-05	70%	U233	6.4467E-06	13%	PU240	3.9801E-06	8%
	8	4.7327E-05	PU239	3.3252E-05	70%	U233	6.3585E-06	13%	PU240	3.9257E-06	8%
	15	4.7163E-05	PU239	3.3137E-05	70%	U233	6.3365E-06	13%	PU240	3.9121E-06	8%
	40	4.6836E-05	PU239	3.2907E-05	70%	U233	6.2926E-06	13%	PU240	3.8850E-06	8%
	48	4.5858E-05	PU239	3.2220E-05	70%	U233	6.1612E-06	13%	PU240	3.8038E-06	8%
	20	4.5534E-05	PU239	3.1992E-05	70%	U233	6.1175E-06	13%	PU240	3.7769E-06	8%
	54	4.5047E-05	PU239	3.1650E-05	70%	U233	6.0522E-06	13%	PU240	3.7365E-06	8%
	31	4.4400E-05	PU239	3.1196E-05	70%	U233	5.9653E-06	13%	PU240	3.6829E-06	8%
	23	4.4400E-05	PU239	3.1196E-05	70%	U233	5.9653E-06	13%	PU240	3.6829E-06	8%
	12	4.3756E-05	PU239	3.0743E-05	70%	U233	5.8787E-06	13%	PU240	3.6294E-06	8%
	42	4.3434E-05	PU239	3.0517E-05	70%	U233	5.8355E-06	13%	PU240	3.6028E-06	8%
	58	4.2633E-05	PU239	2.9954E-05	70%	U233	5.7278E-06	13%	PU240	3.5363E-06	8%
	34	4.2473E-05	PU239	2.9842E-05	70%	U233	5.7063E-06	13%	PU240	3.5230E-06	8%
	2	4.1676E-05	PU239	2.9281E-05	70%	U233	5.5992E-06	13%	PU240	3.4569E-06	8%
	56	4.1199E-05	PU239	2.8946E-05	70%	U233	5.5351E-06	13%	PU240	3.4173E-06	8%
	50	4.0723E-05	PU239	2.8612E-05	70%	U233	5.4712E-06	13%	PU240	3.3779E-06	8%
	22	4.0406E-05	PU239	2.8390E-05	70%	U233	5.4287E-06	13%	PU240	3.3516E-06	8%
	25	3.9933E-05	PU239	2.8057E-05	70%	U233	5.3650E-06	13%	PU240	3.3123E-06	8%
	59	3.9618E-05	PU239	2.7835E-05	70%	U233	5.3227E-06	13%	PU240	3.2862E-06	8%
	10	3.8989E-05	PU239	2.7394E-05	70%	U233	5.2382E-06	13%	PU240	3.2340E-06	8%
	5	3.8362E-05	PU239	2.6953E-05	70%	U233	5.1540E-06	13%	PU240	3.1820E-06	8%
	36	3.7893E-05	PU239	2.6624E-05	70%	U233	5.0910E-06	13%	PU240	3.1432E-06	8%
	45	3.7582E-05	PU239	2.6405E-05	70%	U233	5.0492E-06	13%	PU240	3.1173E-06	8%

Distribution

FEDERAL AGENCIES

U. S. Department of Energy (4)
Office of Environmental Restoration
and Waste Management
Attn: L. P. Duffy, EM-1
J. E. Lytle, EM-30
S. Schneider, EM-342
C. Frank, EM-50
Washington, DC 20585

U.S. Department of Energy (5)
WIPP Task Force
Attn: M. Frei, EM-34 (2)
G. H. Daly
S. Fucigna
J. Rhoderick
12800 Middlebrook Rd.
Suite 400
Germantown, MD 20874

U.S. Department of Energy (4)
Office of Environment, Safety and
Health
Attn: R. P. Berube, EH-20
C. Borgstrum, EH-25
R. Pelletier, EH-231
K. Taimi, EH-232
Washington, DC 20585

U. S. Department of Energy (4)
WIPP Project Integration Office
Attn: W. J. Arthur III
L. W. Gage
P. J. Higgins
D. A. Olona
P.O. Box 5400
Albuquerque, NM 87115-5400

U. S. Department of Energy (12)
WIPP Project Site Office (Carlsbad)
Attn: A. Hunt (4)
M. McFadden
V. Daub (4)
J. Lippis
K. Hunter
R. Becker
P.O. Box 3090
Carlsbad, NM 88221-3090

U. S. Department of Energy, (5)
Office of Civilian Radioactive Waste
Management
Attn: Deputy Director, RW-2
Associate Director, RW-10
Office of Program
Administration and
Resources Management
Associate Director, RW-20
Office of Facilities
Siting and
Development
Associate Director, RW-30
Office of Systems
Integration and
Regulations
Associate Director, RW-40
Office of External
Relations and Policy
Office of Geologic Repositories
Forrestal Building
Washington, DC 20585

U. S. Department of Energy
Attn: National Atomic Museum Library
Albuquerque Operations Office
P.O. Box 5400
Albuquerque, NM 87185

U. S. Department of Energy
Research & Waste Management Division
Attn: Director
P.O. Box E
Oak Ridge, TN 37831

U. S. Department of Energy (2)
Idaho Operations Office
Fuel Processing and Waste
Management Division
785 DOE Place
Idaho Falls, ID 83402

U.S. Department of Energy
Savannah River Operations Office
Defense Waste Processing
Facility Project Office
Attn: W. D. Pearson
P.O. Box A
Aiken, SC 29802

U.S. Department of Energy (2)
Richland Operations Office
Nuclear Fuel Cycle & Production Division
Attn: R. E. Gerton
825 Jadwin Ave.
P.O. Box 500
Richland, WA 99352

U.S. Department of Energy (3)
Nevada Operations Office
Attn: J. R. Boland
D. Livingston
P. K. Fitzsimmons
2753 S. Highland Drive
Las Vegas, NV 87183-8518

U.S. Department of Energy (2)
Technical Information Center
P.O. Box 62
Oak Ridge, TN 37831

U.S. Department of Energy (2)
Chicago Operations Office
Attn: J. C. Haugen
9800 South Cass Avenue
Argonne, IL 60439

U.S. Department of Energy
Los Alamos Area Office
528 35th Street
Los Alamos, NM 87544

U.S. Department of Energy (3)
Rocky Flats Area Office
Attn: W. C. Rask
G. Huffman
T. Lukow
P.O. Box 928
Golden, CO 80402-0928

U.S. Department of Energy
Dayton Area Office
Attn: R. Grandfield
P.O. Box 66
Miamisburg, OH 45343-0066

U.S. Department of Energy
Attn: E. Young
Room E-178
GAO/RCED/GTN
Washington, DC 20545

U.S. Bureau of Land Management
101 E. Mermod
Carlsbad, NM 88220

U.S. Bureau of Land Management
New Mexico State Office
P.O. Box 1449
Santa Fe, NM 87507

U.S. Environmental Protection Agency (2)
Office of Radiation Protection Programs (ANR-460)
Attn: Richard Guimond (2)
Washington, D.C. 20460

U.S. Nuclear Regulatory Commission
Division of Waste Management
Attn: H. Marson
Mail Stop 4-H-3
Washington, DC 20555

U.S. Nuclear Regulatory Commission (4)
Advisory Committee on Nuclear Waste
Attn: Dade Moeller
Martin J. Steindler
Paul W. Pomeroy
William J. Hinze
7920 Norfolk Avenue
Bethesda, MD 20814

Defense Nuclear Facilities Safety Board
Attn: Dermot Winters
625 Indiana Avenue NW
Suite 700
Washington, DC 20004

Nuclear Waste Technical Review Board (2)
Attn: Dr. Don A. Deere
Dr. Sidney J. S. Parry
Suite 910
1100 Wilson Blvd.
Arlington, VA 22209-2297

Katherine Yuracko
Energy and Science Division
Office of Management and Budget
725 17th Street NW
Washington, DC 20503

U.S. Geological Survey (2)
Water Resources Division
Attn: Cathy Peters
Suite 200
4501 Indian School, NE
Albuquerque, NM 87110

INSTITUTIONAL DISTRIBUTION

NEW MEXICO CONGRESSIONAL DELEGATION:

Jeff Bingaman
U.S. Senate
524 SHOB
Washington, DC 20510

Pete V. Domenici
U.S. Senate
427 SDOB
Washington, DC 20510

Bill Richardson
House of Representatives
332 CHOB
Washington, DC 20510

Steven H. Schiff
House of Representatives
1520 LHOB
Washington, DC 20510

Joe Skeen
House of Representatives
1007 LHOB
Washington, DC 20510

STATE AGENCIES

Environmental Evaluation Group (5)
Attn: Robert Neill
Suite F-2
7007 Wyoming Blvd., N.E.
Albuquerque, NM 87109

New Mexico Bureau of Mines
and Mineral Resources
Socorro, NM 87801

New Mexico Department of Energy & Minerals
Attn: Librarian
2040 S. Pacheco
Santa Fe, NM 87505

New Mexico Radioactive Task Force (2)
(Governor's WIPP Task Force)
Attn: Anita Lockwood, Chairman
Chris Wentz, Coordinator/Policy Analyst
2040 Pacheco
Santa Fe, NM 87505

Bob Forrest
Mayor, City of Carlsbad
P.O. Box 1569
Carlsbad, NM 88221

Chuck Bernard
Executive Director
Carlsbad Department of Development
P.O. Box 1090
Carlsbad, NM 88221

Robert M. Hawk (2)
Chairman, Hazardous and Radioactive Materials Committee
Room 334
State Capitol
Sante Fe, NM 87503

New Mexico Environment Department
Secretary of the Environment
Attn: J. Espinosa (3)
P.O. Box 968
1190 St. Francis Drive
Santa Fe, NM 87503-0968

New Mexico Environment Department
Attn: Pat McCausland
WIPP Project Site Office
P.O. Box 3090
Carlsbad, NM 88221-3090

ADVISORY COMMITTEE ON NUCLEAR FACILITY SAFETY

John F. Ahearne
Executive Director, Sigma Xi
99 Alexander Drive
Research Triangle Park, NC 27709

James E. Martin
109 Observatory Road
Ann Arbor, MI 48109

Dr. Gerald Tape
Assoc. Universities
1717 Massachusetts Ave. NW
Suite 603
Washington, DC 20036

WIPP PANEL OF NATIONAL RESEARCH COUNCIL'S BOARD ON RADIOACTIVE WASTE MANAGEMENT

Charles Fairhurst, Chairman
Department of Civil and
Mineral Engineering
University of Minnesota
500 Pillsbury Dr. SE
Minneapolis, MN 55455-0220

John O. Blomeke
3833 Sandy Shore Drive
Lenoir City, TN 37771-9803

John D. Bredehoeft
Western Region Hydrologist
Water Resources Division
U.S. Geological Survey (M/S 439)
345 Middlefield Road
Menlo Park, CA 94025

Fred M. Ernsberger
1325 NW 10th Avenue
Gainsville, FL 32601

Rodney C. Ewing
Department of Geology
University of New Mexico
200 Yale, NE
Albuquerque, NM 87131

B. John Garrick
Pickard, Lowe & Garrick, Inc.
2260 University Drive
Newport Beach, CA 92660

Leonard F. Konikow
U.S. Geological Survey
431 National Center
Reston, VA 22092

Jeremiah O'Driscoll
505 Valley Hill Drive
Atlanta, GA 30350

Christopher Whipple
Clement International Corp.
160 Spear St.
Suite 1380
San Francisco, CA 94105-1535

National Research Council (3)
Board on Radioactive
Waste Management
RM HA456
Attn: Peter B. Myers, Staff Director (2)
Dr. Geraldine J. Grube
2101 Constitution Avenue
Washington, DC 20418

PERFORMANCE ASSESSMENT PEER REVIEW PANEL

G. Ross Heath
College of Ocean and
Fishery Sciences HN-15
583 Henderson Hall
University of Washington
Seattle, WA 98195

Thomas H. Pigford
Department of Nuclear Engineering
4159 Etcheverry Hall
University of California
Berkeley, CA 94720

Thomas A. Cotton
JK Research Associates, Inc.
4429 Butterworth Place, NW
Washington, DC 20016

Robert J. Budnitz
President, Future Resources
Associates, Inc.
2000 Center Street
Suite 418
Berkeley, CA 94704

C. John Mann
Department of Geology
245 Natural History Bldg.
1301 West Green Street
University of Illinois
Urbana, IL 61801

Frank W. Schwartz
Department of Geology and Mineralogy
The Ohio State University
Scott Hall
1090 Carmack Rd.
Columbus, OH 43210

FUTURE SOCIETIES EXPERT PANEL

Theodore S. Glickman
Resources for the Future
1616 P St., NW
Washington, DC 20036

Norman Rosenberg
Resources for the Future
1616 P St., NW
Washington, DC 20036

Max Singer
The Potomac Organization, Inc.
5400 Greystone St.
Chevy Chase, MD 20815

Maris Vinovskis
Institute for Social Research
Room 4086
University of Michigan
426 Thompson St
Ann Arbor, MI 48109-1045

Gregory Benford
University of California, Irvine
Department of Physics
Irvine, CA 92717

Craig Kirkwood
College of Business Administration
Arizona State University
Tempe, AZ 85287

Harry Otway
Health, Safety, and Envir. Div.
Mail Stop K-491
Los Alamos National Laboratory
Los Alamos, NM 87545

Martin J. Pasqualetti
Department of Geography
Arizona State University
Tempe, AZ 85287-3806

Michael Baram
Bracken and Baram
33 Mount Vernon St.
Boston, MA 02108

Wendell Bell
Department of Sociology
Yale University
1965 Yale Station
New Haven, CT 06520

Bernard L. Cohen
Department of Physics
University of Pittsburgh
Pittsburgh, PA 15260

Ted Gordon
The Futures Group
80 Glastonbury Blvd.
Glastonbury, CT 06033

Duane Chapman
5025 S. Building, Room S5119
The World Bank
1818 H Street NW
Washington, DC 20433

Victor Ferkiss
23 Sage Brush Circle
Corrales, NM 87048

Dan Reicher
Senior Attorney
Natural Resources Defense Council
1350 New York Ave. NW, #300
Washington, DC 20005

Theodore Taylor
P.O. Box 39
3383 Weatherby Rd.
West Clarksville, NY 14786

MARKERS EXPERT PANEL

Dr. Dieter Ast
Department of Materials Science
Bard Hall
Cornell University
Ithaca, NY 14853-1501

Dr. Victor Baker
Department of Geosciences
Building #77, Gould-Simpson Building
University of Arizona
Tucson, AZ 85721

Mr. Michael Brill
President
BOSTI
1479 Hertel Ave.
Buffalo, NY 14216

Dr. Frank Drake
Board of Studies in Astronomy and
Astrophysics
Lick Observatory
University of California, Santa Cruz
Santa Cruz, CA 95064

Dr. Ben Finney
University of Hawaii at Manoa
Department of Anthropology
Porteus Hall 346, 2424 Maile Way
Honolulu, HI 96822

Dr. David Givens
American Anthropological Association
1703 New Hampshire Ave., NW
Washington, D.C. 20009

Dr. Ward Goodenough
Department of Anthropology
University of Pennsylvania
325 University Museum
33rd and Spruce Streets
Philadelphia, PA 19104-6398

Dr. Maureen Kaplan
Eastern Research Group, Inc.
6 Whittemore Street
Arlington, MA 02174

Mr. Jon Lomberg
P.O. Box 207
Honaunau, HI 96726

Dr. Louis Narens
Department of Cognitive Sciences
School of Social Sciences
University of Califorrnia, Irvine
Irvine, CA 92717

Dr. Frederick Newmeyer
Department of Linguistics
GN-40
University of Washington
Seattle, WA 98195

Dr. Woodruff Sullivan
Department of Astonomy
FM-20
University of Washington
Seattle, WA 98195

Dr. Wendell Williams
Materials Science and Engineering
White Building
Case Western Reserve University
Cleveland, OH 44106

NATIONAL LABORATORIES

Argonne National Labs (2)
Attn: A. Smith
D. Tomasko
9700 South Cass, Bldg. 201
Argonne, IL 60439

Battelle Pacific Northwest Laboratories (3)
Attn: R. E. Westerman
S. Bates
H. C. Burkholder
Battelle Boulevard
Richland, WA 99352

Lawrence Livermore National Laboratory
Attn: G. Mackanic
P.O. Box 808, MS L-192
Livermore, CA 94550

Los Alamos National Laboratories
Attn: B. Erdal, CNC-11
P.O. Box 1663
Los Alamos, NM 87544

Los Alamos National Laboratories
Attn: A. Meijer
Mail Stop J514
Los Alamos, NM 87545

Los Alamos National Laboratories (3)
HSE-8
Attn: M. Enoris
L. Soholt
J. Wenzel
P.O. Box 1663
Los Alamos, NM 87544

Los Alamos National Laboratories (2)
HSE-7
Attn: A. Drypolcher
S. Kosciewiscz
P.O. Box 1663
Los Alamos, NM 87544

Oak Ridge National Labs
Martin Marietta Systems, Inc.
Attn: J. Setaro
P.O. Box 2008, Bldg. 3047
Oak Ridge, TN 37831-6019

Savannah River Laboratory (3)
Attn: N. Bibler
M. J. Plodinec
G. G. Wicks
Aiken, SC 29801

Savannah River Plant (2)
Attn: Richard G. Baxter
Building 704-S
K. W. Wierzbicki
Building 703-H
Aiken, SC 29808-0001

CORPORATIONS/MEMBERS OF THE PUBLIC

Benchmark Environmental Corp. (3)
Attn: John Hart
C. Frederickson
K. Lickliter
4501 Indian School Rd., NE
Suite 105
Albuquerque, NM 87110

Deuel and Associates, Inc.
Attn: R. W. Prindle
7208 Jefferson, NE
Albuquerque, NM 87109

Disposal Safety, Inc.
Attn: Benjamin Ross
Suite 314
1660 L Street NW
Washington, DC 20006

Ecodynamics Research Associates (2)
Attn: Pat Roache
Rebecca Blaine
P.O. Box 8172
Albuquerque, NM 87198

E G & G Idaho (3)
1955 Fremont Street
Attn: C. Atwood
C. Hertzler
T. I. Clements
Idaho Falls, ID 83415

Geomatrix
Attn: Kevin Coppersmith
100 Pine Street #1000
San Francisco, CA 94111

Golden Associates, Inc. (3)
Attn: Mark Cunnane
Richard Kossik
Ian Miller
4104 148th Avenue NE
Redmond, WA 98052

In-Situ, Inc. (2)
Attn: S. C. Way
C. McKee
209 Grand Avenue
Laramie, WY 82070

INTERA, Inc.
Attn: A. M. LaVenue
8100 Mountain Road NE
Suite 213
Albuquerque, NM 87110

INTERA, Inc.
Attn: J. F. Pickens
Suite #300
6850 Austin Center Blvd.
Austin, TX 78731

INTERA, Inc.
Attn: Wayne Stensrud
P.O. Box 2123
Carlsbad, NM 88221

INTERA, Inc.
Attn: William Nelson
101 Convention Center Drive
Suite 540
Las Vegas, NV 89109

IT Corporation (2)
Attn: P. Drez
J. Myers
Regional Office - Suite 700
5301 Central Avenue, NE
Albuquerque, NM 87108

IT Corporation
R. J. Eastmond
825 Jadwin Ave.
Richland, WA 99352

MACTEC (2)
Attn: J. A. Thies
D. K. Duncan
8418 Zuni Road SE
Suite 200
Albuquerque, NM 87108

Pacific Northwest Laboratory
Attn: Bill Kennedy
Battelle Blvd.
P.O. Box 999
Richland, WA 99352

RE/SPEC, Inc. (2)
Attn: W. Coons
Suite 300
4775 Indian School NE
Albuquerque, NM 87110

RE/SPEC, Inc.
Attn: J. L. Ratigan
P.O. Box 725
Rapid City, SD 57709

Reynolds Elect/Engr. Co., Inc.
Building 790, Warehouse Row
Attn: E. W. Kendall
P.O. Box 98521
Las Vegas, NV 89193-8521

Roy F. Weston, Inc.
CRWM Tech. Supp. Team
Attn: Clifford J. Noronha
955 L'Enfant Plaza, S.W.
North Building, Eighth Floor
Washington, DC 20024

Science Applications International Corporation
Attn: Howard R. Pratt,
Senior Vice President
10260 Campus Point Drive
San Diego, CA 92121

Science Applications International Corporation (2)
Attn: George Dymmel
Chris G. Pflum
101 Convention Center Dr.
Las Vegas, NV 89109

Science Applications International Corporation (2)
Attn: John Young
Dave Lester
18706 North Creek Parkway
Suite 110
Bothell, WA 98011

Southwest Research Institute
Center for Nuclear Waste Regulatory Analysis (2)
Attn: P. K. Nair
6220 Culebra Road
San Antonio, Texas 78228-0510

Systems, Science, and Software (2)
Attn: E. Peterson
P. Lagus
Box 1620
La Jolla, CA 92038

TASC
Attn: Steven G. Oston
55 Walkers Brook Drive
Reading, MA 01867

Tech. Reps., Inc. (5)
Attn: Janet Chapman
Terry Cameron
Debbie Marchand
John Stikar
Denise Bissell
5000 Marble NE
Suite 222
Albuquerque, NM 87110

Tolan, Beeson, & Associates
Attn: Terry L. Tolan
2320 W. 15th Avenue
Kennewick, WA 99337

TRW Environmental Safety Systems (TESS)
Attn: Ivan Saks
10306 Eaton Place
Suite 300
Fairfax, VA 22030

Westinghouse Electric Corporation (4)
Attn: Library
L. Trego
C. Cox
L. Fitch
R. F. Kehrman
P.O. Box 2078
Carlsbad, NM 88221

Westinghouse Hanford Company
Attn: Don Wood
P.O. Box 1970
Richland, WA 99352

Western Water Consultants
Attn: D. Fritz
1949 Sugarland Drive #134
Sheridan, WY 82801-5720

Western Water Consultants
Attn: P. A. Rechard
P.O. Box 4128
Laramie, WY 82071

Neville Cook
Rock Mechanics Engineering
Mine Engineering Dept.
University of California
Berkeley, CA 94720

Dennis W. Powers
Star Route Box 87
Anthony, TX 79821

Shirley Thieda
P.O. Box 2109, RR1
Bernalillo, NM 87004

Jack Urich
c/o CARD
144 Harvard SE
Albuquerque, NM 87106

UNIVERSITIES

University of California
Mechanical, Aerospace, and
Nuclear Engineering Department (2)
Attn: W. Kastenberg
D. Browne
5532 Boelter Hall
Los Angeles, CA 90024

University of Hawaii at Hilo
Attn: S. Hora
Business Administration
Hilo, HI 96720-4091

University of New Mexico
Geology Department
Attn: Library
Albuquerque, NM 87131

University of New Mexico
Research Administration
Attn: H. Schreyer
102 Scholes Hall
Albuquerque, NM 87131

University of Wyoming
Department of Civil Engineering
Attn: V. R. Hasfurther
Laramie, WY 82071

University of Wyoming
Department of Geology
Attn: J. I. Drever
Laramie, WY 82071

University of Wyoming
Department of Mathematics
Attn: R. E. Ewing
Laramie, WY 82071

LIBRARIES

Thomas Brannigan Library
Attn: Don Dresp, Head Librarian
106 W. Hadley St.
Las Cruces, NM 88001

Hobbs Public Library
Attn: Marcia Lewis, Librarian
509 N. Ship Street
Hobbs, NM 88248

New Mexico State Library
Attn: Norma McCallan
325 Don Gaspar
Santa Fe, NM 87503

New Mexico Tech
Martin Speere Memorial Library
Campus Street
Socorro, NM 87810

New Mexico Junior College
Pannell Library
Attn: Ruth Hill
Lovington Highway
Hobbs, NM 88240

Carlsbad Municipal Library
WIPP Public Reading Room
Attn: Lee Hubbard, Head Librarian
101 S. Halagueno St.
Carlsbad, NM 88220

University of New Mexico
General Library
Government Publications Department
Albuquerque, NM 87131

NEA/PSAC USER'S GROUP

Timo K. Vieno
Technical Research Centre of Finland (VTT)
Nuclear Engineering Laboratory
P.O. Box 169
SF-00181 Helsinki
FINLAND

Alexander Nies (PSAC Chairman)
Gesellschaft für Strahlen- und
Institut für Tieflagerung
Abteilung für Endlagersicherheit
Theodor-Heuss-Strasse 4
D-3300 Braunscheweig
GERMANY

Eduard Hofer
Gesellschaft für Reaktorsicherheit (GRS)
MBH
Forschungsgelände
D-8046 Garching
GERMANY

Takashi Sasahara
Environmental Assessment Laboratory
Department of Environmental Safety Research
Nuclear Safety Research Center,
Tokai Research Establishment, JAERI
Tokai-mura, Naka-gun
Ibaraki-ken
JAPAN

Alejandro Alonso
Cátedra de Tecnología Nuclear
E.T.S. de Ingenieros Industriales
José Gutiérrez Abascal, 2
E-28006 Madrid
SPAIN

Pedro Prado
CIEMAT
Instituto de Tecnología Nuclear
Avenida Complutense, 22
E-28040 Madrid
SPAIN

Miguel Angel Cuñado
ENRESA
Emilio Vargas, 7
E-28043 Madrid
SPAIN

Francisco Javier Elorza
ENRESA
Emilio Vargas, 7
E-28043 Madrid
SPAIN

Nils A. Kjellbert
Swedish Nuclear Fuel and Waste Management Company (SKB)
Box 5864
S-102 48 Stockholm
SWEDEN

Björn Cronhjort
Swedish National Board for Spent Nuclear Fuel (SKN)
Sehlsedtsgatan 9
S-115 28 Stockholm
SWEDEN

Richard A. Klos
Paul-Scherrer Institute (PSI)
CH-5232 Villingen PSI
SWITZERLAND

NAGRA (2)
Attn: Charles McCombie
Fritz Van Dorp
Parkstrasse 23
CH-5401 Baden
SWITZERLAND

Brian G. J. Thompson
Department of the Environment
Her Majesty's Inspectorate of Pollution
Room A5.33, Romney House
43 Marsham Street
London SW1P 2PY
UNITED KINGDOM

INTERA/ECL (2)
Attn: Trevor J. Sumerling
Daniel A. Galson
Chiltern House
45 Station Road
Henley-on-Thames
Oxfordshire RG9 1AT
UNITED KINGDOM

U.S. Nuclear Regulatory Commission (2)
Attn: Richard Codell
Norm Eisenberg
Mail Stop 4-H-3
Washington, D.C. 20555

Paul W. Eslinger
Battelle Pacific Northwest Laboratories (PNL)
P.O. Box 999, MS K2-32
Richland, WA 99352

Andrea Saltelli
Commission of the European Communities
Joint Resarch Centre od Ispra
I-21020 Ispra (Varese)
ITALY

Budhi Sagar
Center for Nuclear Waste Regulatory Analysis (CNWRA)
Southwest Research Institute
P.O. Drawer 28510
6220 Culebra Road
San Antonio, TX 78284

Shaheed Hossain
Division of Nuclear Fuel Cycle and Waste Management
International Atomic Energy Agency
Wagramerstrasse 5
P.O. Box 100
A-1400 Vienna
AUSTRIA

Claudio Pescatore
Division of Radiation Protection and Waste Management
38, Boulevard Suchet
F-75016 Paris
FRANCE

FOREIGN ADDRESSES

Studiecentrum Voor Kernenergie
Centre D'Energie Nucleaire
Attn: A. Bonne
SCK/CEN
Boeretang 200
B-2400 Mol
BELGIUM

Atomic Energy of Canada, Ltd. (3)
Whiteshell Research Estab.
Attn: Michael E. Stevens
Bruce W. Goodwin
Donna Wushke
Pinewa, Manitoba
ROE 1L0
CANADA

Ghislain de Marsily
Lab. Géologie Appliqué
Tour 26, 5 étage
4 Place Jussieu
F-75252 Paris Cedex 05
FRANCE

Jean-Pierre Olivier
OECD Nuclear Energy Agency (2)
38, Boulevard Suchet
F-75016 Paris
FRANCE

D. Alexandre, Deputy Director
ANDRA
31 Rue de la Federation
75015 Paris
FRANCE

Claude Sombret
Centre D'Etudes Nucleaires
De La Vallee Rhone
CEN/VALRHO
S.D.H.A. BP 171
30205 Bagnols-Sur-Ceze
FRANCE

Bundesministerium fur Forschung und Technologie
Postfach 200 706
5300 Bonn 2
GERMANY

Bundesanstalt fur Geowissenschaften und Rohstoffe
Attn: Michael Langer
Postfach 510 153
3000 Hannover 51
GERMANY

Gesellschaft fur Reaktorsicherheit (GRS) mb (2)
Attn: Bruno Baltes
Wolfgang Muller
Schwertnergasse 1
D-5000 Cologne
GERMANY

Hahn-Mietner-Institut fur Kernforschung
Attn: Werner Lutze
Glienicker Strasse 100
100 Berlin 39
GERMANY

Institut fur Tieflagerung (2)
Attn: K. Kuhn
Theodor-Heuss-Strasse 4
D-3300 Braunschweig
GERMANY

Physikalisch-Technische Bundesanstalt
Attn: Peter Brenneke
Postfach 33 45
D-3300 Braunschweig
GERMANY

Shingo Tashiro
Japan Atomic Energy Research Institute
Tokai-Mura, Ibaraki-Ken
319-11
JAPAN

Netherlands Energy Research Foundation
ECN
Attn: L. H. Vons
3 Westerduinweg
P.O. Box 1
1755 ZG Petten
THE NETHERLANDS

Johan Andersson
Statens Kärnkraftinspektion
SKI
Box 27106
S-102 52 Stockholm
SWEDEN

Fred Karlsson
Svensk Karnbransleforsorjning AB
SKB
Box 5864
S-102 48 Stockholm
SWEDEN

Nationale Genossenschaft fur die Lagerung
Radioaktiver Abfalle (NAGRA) (2)
Attn: Stratis Vomvoris
Piet Zuidema
Hardstrasse 73
CH-5430 Wettingen
SWITZERLAND

D. R. Knowles
British Nuclear Fuels, plc
Risley, Warrington, Cheshire WA3 6AS
1002607 UNITED KINGDOM

AEA Technology
Attn: J.H. Rees
D5W/29 Culham Laboratory
Abington
Oxfordshire OX14 3DB
UNITED KINGDOM

AEA Technology
Attn: W. R. Rodwell
O44/A31 Winfrith Technical Centre
Dorchester
Dorset DT2 8DH
UNITED KINGDOM

AEA Technology
Attn: J. E. Tinson
B4244 Harwell Laboratory
Didcot
Oxfordshire OX11 ORA
UNITED KINGDOM

INTERNAL

1	A. Narath
20	O. E. Jones
1510	J. C. Cummings
1511	D. K. Gartling
3151	S. M. Wayland
3200	N. R. Ortiz
6000	D. L. Hartley
6233	J. C. Eichelberger
6300	T. O. Hunter
6301	E. Bonano
6310	T. E. Blejwas, Acting
6313	L. E. Shephard
6312	F. W. Bingham
6313	L. S. Costin
6315	Supervisor
6316	R. P. Sandoval
6320	R. E. Luna, Acting
6340	W. D. Weart
6340	S. Y. Pickering
6341	J. M. Covan
6341	D. P. Garber
6341	R. C. Lincoln
6341	J. Orona*
6341	Sandia WIPP Central Files (250)
6342	D. R. Anderson
6342	B. M. Butcher
6342	D. P. Gallegos
6342	L. S. Gomez
6342	M. Gruebel
6342	R. Guzowski
6342	R. D. Klett
6342	M. G. Marietta
6342	D. Morrison
6342	A. C. Peterson
6342	R. P. Rechard
6342	P. Swift
6342	M. Tierney
6342	K. M. Trauth
6342	B. L. Baker*
6342	J. Bean*
6342	J. Berglund*
6342	W. Beyeler*
6342	T. Blaine*
6342	K. Brinster*
6342	K. Byle*
6342	L. Clements*
6342	J. Garner*
6342	A. Gilkey*
6342	H. Iuzzolino*
6342	J. Logothetis*
6342	R. McCurley*
6342	J. Rath*
6342	D. Rudeen*
6342	J. Sandha*
6342	J. Schreiber*
6342	P. Vaughn*
6343	T. M. Schultheis
6344	R. L. Beauheim
6344	P. B. Davies
6344	S. J. Finley
6344	E. Gorham
6344	C. F. Novak
6344	S. W. Webb
6345	R. Beraun
6345	L. Brush
6345	A. R. Lappin
6345	M. A. Molecke
6346	D. E. Munson
6346	E. J. Nowak
6346	J. R. Tillerson
6347	A. L. Stevens
6400	D. J. McCloskey
6413	J. C. Helton
6415	R. M. Cranwell
6415	C. Leigh
6415	R. L. Iman
6622	M.S.Y. Chu
9300	J. E. Powell
9310	J. D. Plimpton
9325	J. T. McIlmoyle
9325	R. L. Rutter
9330	J. D. Kennedy
8523-2	Central Technical Files
3141	S. A. Landenberger (5)
3145	Document Processing (8) for DOE/OSTI
3151	G. C. Claycomb (3)

*6342/Geo-Centers

☆ U.S. GOVERNMENT PRINTING OFFICE: 1991—673-122/60036